Fake lepton determination, Supersymmetry searches in di-lepton final states, and sharing ATLAS research with young students

Maiken Pedersen
Department of Physics
University of Oslo
Norway

Dissertation presented for the degree of
Philosophiae Doctor (PhD) in Physics

March 2014

Series of dissertations submitted to the
Faculty of Mathematics and Natural Sciences, University of Oslo
No. 1518

ISSN 1501-7710

Cover: Inger Sandved Anfinsen.
Printed in Norway: AIT Oslo AS.

Produced in co-operation with Akademika Publishing.
The thesis is produced by Akademika Publishing merely in connection with the thesis defence. Kindly direct all inquiries regarding the thesis to the copyright holder or the unit which grants the doctorate.

Fake lepton determination,
Supersymmetry searches in di-lepton final states,
and sharing ATLAS research with young students

Maiken Pedersen

Abstract

The world around us seems concrete and apparent. However, it is in fact governed by what goes on at the sub-atomic level, hidden from immediate experience. We describe this microscopic world by a theory we call the Standard Model (SM). Since its formation in the 1970s, collecting the physics of electromagnetism, the weak and the strong forces, into one coherent theory, it has proven extremely successful. Experimental evidence however, tells us that the Universe consists of 26.8% of dark matter, a type of matter that the SM does not describe. If we had a theory that predicted a symmetry in Nature where each type of particle came in two versions, only separated by their spin, we would have a promising pool of candidate dark-matter particles. Supersymmetry (SUSY) is exactly this type of theory. It even addresses other fundamental short-comings of the SM. Why we have not earlier discovered such particles can be explained by the nature of symmetries, they are often *broken*, in this case leading to very massive copies of the SM particles. Which means we need large energies in order to discover them.

This thesis performs a search for SUSY in ATLAS, using 4.7 fb^{-1} of data collected in 2011, at center of mass energy of $\sqrt{s} = 7$ TeV, focusing on the direct production of charginos, neutralinos, and sleptons. On route to this search, I have worked on the careful estimation of part of the background of a SUSY signal, namely the fake lepton background, using the Matrix Method. Since we can only hope to find SUSY if we understand the SM and the experimental environment well, the prediction of the expected overall background, including the fake leptons, is essential. Two approaches are successfully followed for the fake lepton estimation, a semi data-driven one, as implemented in a publication in Physics Lett. B, and a new fully data-driven approach, with slight improvements, yielding compatible results with the first in the important SUSY signal region.

No SUSY signal was found, and we therefore use the lack of observation to set upper limits on the cross sections and masses of new physics phenomena such as SUSY. The current $\sqrt{s} = 7$ TeV mass limits extend earlier SUSY limits.

An important part of my work has been dedicated to education and outreach. How can we let high school students follow along with the discoveries made at the LHC? I describe an educational tool we developed in the framework of the IPPOG International Masterclasses, namely the Z-path. Already, high school students around the world have themselves measured the properties of the Z boson, and discovered the Higgs boson. In the future we hope to discover SUSY, and also bring this discovery out to the public.

Acknowledgements

Thank you, Farid Ould-Saada for being such a dedicated, enthusiastically driving, and goal-oriented supervisor. As my main supervisor you have provided the principal academic support to this work. Since encountering your energetic personality for the first time as a Master Student, not yet sure of what to choose among theory, astrophysics, and particle physics, I was convinced that if you could be my supervisor, it would all turn out well. And it did.

I want to thank my colleagues from the High Energy Particle Physics group at the University of Oslo. Three people deserve special mention. It has been invaluable to work with Eirik Gramstad, which has been my main analysis partner during the course of this PhD degree. We have had many essential discussions both around theory, but not least around analysis approach and development. Børge Kile Gjelsten has been a great support, both in analysis, theory, and with technical aspects. Finally, my second supervisor Alex Lincoln Read has contributed with very useful feedback and discussions. All in all, I feel lucky to have been part of the great HEPP group at UiO, for the way it has contributed to my academic and personal development.

Doing a PhD in experimental particle physics has given me invaluable experience on many levels. I have had the possibility to develop my presentation skills through numerous meetings, presenting analysis results both in informal, and more formal settings. I have also been fortunate to have been encouraged by Farid, to work with more educational aspects of particle physics, by taking active part in the IPPOG Masterclasses program. I am very happy to have had this experience. Finally, the opportunity to travel to meetings and conferences, and in particular the stays at CERN, have been a great inspiration.

It is with great pride and thankfulness that I sign these acknowledgements

Oslo, March 2014
Maiken Pedersen

Contents

Introduction **1**

1 Theory and modelling nature **4**
1.1 General Introduction . . . 4
1.2 The Standard Model and its particle content . . . 6
1.2.1 Symmetries . . . 8
1.2.2 The quantum world and particle-waves . . . 9
1.2.3 The Lagrangian formalism . . . 11
1.2.4 The Gauge Principle applied to Electromagnetism . . . 13
1.2.5 Strong force, weak force, and the Standard Model . . . 15
1.2.6 Spontaneous symmetry breaking . . . 17
1.2.7 Forces, running couplings . . . 21
1.2.8 The success of the SM, and the need for a model beyond it . . . 23
1.3 Supersymmetry . . . 24
1.3.1 Observational arguments to physics beyond the Standard Model . . . 24
1.3.2 Theoretical arguments for physics beyond the Standard Model . . . 25
1.3.3 The hierarchy problem . . . 26
1.3.4 What is Supersymmetry . . . 30
1.3.5 The supersymmetric particle content . . . 31
1.3.6 Soft symmetry breaking and the MSSM . . . 36
1.3.7 Sparticle decays and mass spectra . . . 37
1.3.8 Viable SUSY models . . . 38
1.3.8.1 mSUGRA . . . 38
1.3.8.2 GMSB . . . 40
1.3.8.3 Simplified models . . . 41
1.3.8.4 Phenomenological MSSM . . . 42

2 Describing the pp collision **43**
2.1 The overall picture . . . 43
2.2 The hard interaction . . . 45
2.3 Structure and parton distribution functions . . . 48
2.4 Bringing it all together, including fragmentation and hadronization . . . 51

3 LHC, ATLAS, and how to find what we are looking for **55**
3.1 The Large Hadron Collider . . . 55
3.2 The ATLAS detector . . . 57
3.2.1 Some kinematic variables . . . 58
3.2.2 Magnet system . . . 60
3.2.3 The inner detector - the tracker . . . 61

3.2.4 The Calorimetry . . . 63
3.2.5 Muon system . . . 64
3.2.6 Trigger and Data Acquisition . . . 65
3.3 From simulation or detector signals to analysis files . . . 66
3.4 Analysis variables . . . 69
3.5 Object definitions . . . 72
3.5.1 Electrons (and photons) . . . 72
3.5.2 Muons . . . 75
3.5.3 Jets . . . 77
3.5.4 Invisible particles and the $E_{\mathrm{T}}^{\mathrm{miss}}$ variable . . . 80
3.6 Commissioning and monitoring of ATLAS . . . 82
3.6.1 Noise monitoring of SCT modules . . . 82
3.6.2 Commissioning ATLAS with cosmic muons . . . 86

4 SUSY signal and SM background processes 92
4.1 Cross sections at the LHC . . . 92
4.2 Signal processes . . . 95
4.2.1 Production mechanisms of gaugino and sleptons, and decays leading to leptons . . . 96
4.2.2 Direct gaugino production with the pMSSM grid . . . 98
4.2.3 Direct gaugino production with simplified model grids . . . 101
4.2.4 Direct slepton production . . . 102
4.2.5 Di-leptonic final states in direct gaugino and slepton production . . . 103
4.2.6 Signal footprints . . . 106
4.3 Standard Model background processes, and the means to suppress them . . . 107
4.3.1 $t\bar{t} \to (bl^{+}\nu) + (\bar{b}l^{-}\bar{\nu})$ . . . 108
4.3.2 Z/γ^{*}+jets . . . 110
4.3.3 WZ, WW, ZZ . . . 111
4.3.4 Background processes involving fake leptons . . . 112

5 Signal regions, the data, and the event selection procedure 118
5.1 Signal regions . . . 118
5.1.1 SR-OSjveto . . . 119
5.1.2 SR-SSjveto . . . 121
5.1.3 SR-2jets . . . 122
5.1.4 SR-m_{T2} . . . 124
5.2 General event selection . . . 126
5.3 Data sets and triggers . . . 128
5.3.1 Monte Carlo SM background samples . . . 132
5.3.2 Monte Carlo signal grid files . . . 135

6 Fake lepton background estimation with the Matrix Method 136
6.1 Fake leptons in MC, and the need for a data-driven estimation method . . . 137
6.2 The Matrix Method (MM) . . . 140
6.3 Real efficiency . . . 145

6.4 Fake rates . . . 146
6.4.1 Fake leptons from hadrons . . . 147
6.4.1.1 Single lepton CR-A . . . 148
6.4.1.2 Di-lepton same-sign CR-B . . . 152
6.4.1.3 Heavy flavour CR-C . . . 154
6.4.1.4 Comparison of QCD control regions . . . 158
6.4.1.5 Data and MC comparison for QCD fakes . . . 161
6.4.2 Fake rate from conversion electrons . . . 167

7 Implementation of the fake lepton estimation with the Matrix Method 171
7.1 Semi-data driven procedure . . . 171
7.1.1 Calculating fake rate weights . . . 172
7.1.2 Systematic uncertainty on the QCD MC fake rate . . . 175
7.1.2.1 $E_{\mathrm{T}}^{\mathrm{miss,rel}}$ MC QCD fake rate dependency . . . 175
7.1.2.2 Heavy flavour QCD MC ($b\bar{b}$) versus $t\bar{t}$ MC fake rates . . . 176
7.1.2.3 Light versus heavy flavour fakes in the MC QCD fake rate . . . 178
7.1.2.4 SS and OS MC QCD fake rate comparison . . . 180
7.1.2.5 QCD control region systematics . . . 182
7.1.2.6 Summary of the MC QCD fake rate uncertainty . . . 183
7.1.3 Conversion systematics . . . 184
7.1.4 Real efficiency systematics . . . 184
7.1.5 Uncertainty due to η dependency . . . 185
7.1.6 Final fake rates and real efficiencies, including systematic uncertainties 186
7.1.7 Obtaining the fake lepton estimates with the Matrix Method . . . 187
7.1.8 Validation of semi data-driven fake lepton estimation . . . 189
7.2 Fully data-driven fake lepton background estimation . . . 192
7.2.1 Data-driven fake rates and real efficiencies . . . 192
7.2.2 Data-driven $E_{\mathrm{T}}^{\mathrm{miss,rel}}$ dependency . . . 193
7.2.3 Systematic uncertainties and final fake rates . . . 196
7.2.4 Validation of the fully data-driven fake lepton estimation . . . 199
7.3 Comparison of data and MC agreement using the two fake lepton estimation methods . . . 202

8 Search for direct gauginos and sleptons in di-lepton final states 205
8.1 SUSY search based on the semi data-driven fake lepton estimation . . . 205
8.2 SUSY search based on the fully data-driven fake lepton estimation . . . 210
8.3 Statistical method for interpretation of results . . . 214
8.4 Systematic uncertainties . . . 215
8.5 Interpretation of SUSY search results . . . 219

9 Communicating the excitement of discovery 223
9.1 The LHC Z-Path emerges . . . 223
9.2 Tools used in the Z-path . . . 225
9.3 The Z-path web-material . . . 226
9.4 Analysis results in OPloT . . . 232

9.5 Discussion of results . . . 234
9.6 Experiences and improvements, and outlook . . . 235

Conclusions and outlook **237**

Appendices **240**

A Semi Conducter Tracker noise-occupancy monitoring **241**
A.1 ATLAS DAQ Monitoring . . . 241
A.2 The ratio-noise method . . . 243
A.3 Study of the ratio-noise results . . . 245
A.3.1 Explanation of online and offline discrepancy . . . 249
A.3.2 Improvement of online and offline results . . . 250
A.4 Conclusion . . . 251

B Details on object definitions, event selection and data and MC samples **252**
B.1 Electron object definitions . . . 252
B.2 Muon and electron reconstruction efficiency . . . 253
B.3 Monte Carlo background samples . . . 253
B.4 Simulated luminosity and luminosity scale factors . . . 258

C Supporting material for the Matrix Method fake estimation **260**
C.1 Purity, statistics and fake rates in all control regions . . . 260
C.2 Data and MC comparison before and after statistical subtraction of MC leptons 266
C.3 Relative importance of processes versus $E_{\mathrm{T}}^{\mathrm{miss,rel}}$ in MC . . . 269
C.4 Relative amount of real MC leptons to total data leptons . . . 270
C.5 Effect on fake rate versus p_{T} when varying MC cross section . . . 272
C.6 Subtracting conversion electrons in QCD control regions . . . 274
C.7 $E_{\mathrm{T}}^{\mathrm{miss,rel}}$ dependency QCD control regions . . . 275
C.8 MC subtraction uncertainty on data fake rate versus $E_{\mathrm{T}}^{\mathrm{miss,rel}}$ . . . 278
C.9 Data based QCD fake rate versus p_{T} for different $E_{\mathrm{T}}^{\mathrm{miss,rel}}$ ranges . . . 280
C.10 QCD and conversion weights in signal regions . . . 280

D Charge flip, data and MC **283**

List of Figures **285**

List of Tables **293**

Bibliography **297**

Introduction

Far underground just outside of Geneva in Switzerland, stretching into the French countryside, lies the world's biggest machine, whose purpose is to study the very smallest: the elementary particles. If you are new to physics this might sound like a contradiction, but in fact it is not. The smaller objects you want to study, the more energy you will need to do exactly that. And the more energy you need, the larger machine you have to build. The newest and biggest of the kind is The Large Hadron Collider (LHC) [1]. From this machine, and another equally important apparatus, namely the ATLAS detector, comes the results of this thesis.

CERN, the "Européen pour la Recherche Nucléaire", is the host of LHC and its experiments. More than 10000 physicists are connected to CERN, out of which around 3000 are part of the ATLAS International Collaboration [2]. While the subject of this thesis is on particle physics, and on physics beyond the current understanding of nature, CERN is the home for a wide range of experiments, ranging from high energy heavy ion physics (ALICE [3], nuclear physics (Isolde [4]), Big-Bang matter-antimatter asymmetry (LHCb [5]), anti-matter physics (Anti Proton Decelerator [6]), neutrino physics ([7]) to cloud formation physics (Cloud experiment [8]). CERN is therefore a melting pot of people from all around the world and from many disciplines. In other words: a great place to belong to!

The LHC adventure has already been ongoing for years. Its first mention was in the 1980's, as the planned successor of LEP (The Large Electron Positron Collider), the reigning particle accelerator at the time. In year 2000 the construction started, and finally in 2008 the switch was turned on for the very first time, and the first high energy proton beams found themselves circulating in the LHC rings. It is clear that LHC is a big investment, both in money and manpower, and has, and will still require years and years of both preparation and study of results. So why such an investment? Simply because humans will never stop trying to understand how the Universe we live in is assembled. I dare say it is an inherit human behaviour to seek understanding, and what could be more fundamental than the attempt to start from the smallest, indivisible entities, those of the elementary particles, and from that construct the whole Universe.

However, the particle physics adventure is more than just stimuli for our curiosity. Without it, we would not live in the advanced world we do today, with lasers, thin, ultralight laptop computers, proton beam cancer radiation facilities, to mention just a few aspects of modern life. To understand nature, one needs basics science such as particle physics, and even though its application sometimes is not apparent before years later, one can never know what the revelations of nature might bring us of useful insight.

A tiny contribution to the immense task of understanding nature, is the study of Supersymmetry. And yet another tiny fraction of this study is the determination of a particular background

which is dubbed “fake” . These are the main topics of my thesis. Its content is arranged in the following way:

First, in Chapter 1, I introduce you to the basics of Quantum Field Theory, leading to the theory we know as the Standard Model (SM), which encompasses our current understanding of physics at the elementary particle level. This involves explaining the importance of symmetries in nature, which lead to conservation laws, and the principle of gauge invariance which leads to interaction between matter particles and forces. I use the theory of Quantum Electro Dynamics (QED) to outline the way gauge invariance leads to the interaction between the electron and the photon. Through this example, the theory is extended to include the weak and strong interactions. The final component requires electroweak spontaneous symmetry breaking in order to generate elementary particle masses, leading to the prediction of the Higgs particle. I then go through the basics of Supersymmetry (SUSY), which is an extension of the Standard Model. Finding supersymmetric particles in the data from ATLAS would prove that Supersymmetry is actually a symmetry of nature, and not a hypothetical symmetry which is the current status. SUSY predicts that each SM particle has a supersymmetric twin sister, which is identical except for spin (and mass). SUSY is a very interesting theory as it predicts a candidate for dark matter observed in the Universe. This thesis performs a search for supersymmetric particles, targeting particularly the so-called charginos, neutralinos and sleptons, the hypothetical partners of the electroweak SM bosons and of the leptons, respectively.

Then, in Chapter 2, I explain what goes on in a proton-proton collision at the LHC, and how it all can be modelled such that we can make predictions to test in experiment. In Chapter 3 I turn toward the actual experimental part, explaining the basics of LHC and of the ATLAS detector, where the search is performed. In particular I share with you my personal involvement in preparing ATLAS with cosmic rays, and in monitoring the SemiConductor Tracker.

In Chapter 4 I look closer at the signatures of the Supersymmetry signal, and what SM background can mimic the signal. This analysis focuses on gauginos and sleptons that produce two leptons, and missing transverse energy from the lightest neutralinos, the dark matter candidate. This forms the basis for the determination of the signal regions, four in total, which are discussed more closely in Chapter 5. In this chapter, the data samples are also presented, and the selection criteria used to find interesting collision events.

Then, in Chapter 6 we embark on the main subject of this thesis, namely the background estimation of so-called fake leptons. Fake leptons mimic the signal leptons which stem from decay of heavy particles such as the SUSY gauginos and sleptons, or from SM background processes through gauge bosons, the top quark or tau lepton decays. Fake leptons stem from heavy or light flavour hadron decay, or conversions. They are not well modelled in simulation data, and therefore require special care. The general procedure, introducing the Matrix Method, and the detailed study of control regions is performed in this chapter. The Matrix Method transforms measured quantities, namely the number of di-lepton events categorized into combinations of “loose” and “tight” leptons, into a fake lepton prediction, once fake rates and real efficiencies are measured.

Chapter 7 presents the implementation of the procedure, using two main approaches, that of the semi data-driven one, partly relying on Monte Carlo simulations, and the fully data-driven one, where Monte Carlo is used only for the validation of the method.

The results of the fake lepton estimation and the search for supersymmetric particles are

presented in Chapter 8.

In Chapter 9 I finish off with outreach to the public. How would I share a hypothetical discovery of supersymmetric particles with high-school students? Here I detail the way we shared ATLAS data - and the Higgs discovery - with them. The educational material I have developed has been successfully deployed in the International particle physics Masterclasses. Finally conclusions are drawn and an outlook presented.

Chapter 1

Theory and modelling nature

"I like relativity and quantum theories
because I don't understand them"

David Herbert Lawrence [9]

1.1 General Introduction

Quantum physics is the language of a hidden and mystical world, out of reach of a direct conceptual understanding. For many, including myself, this is exactly what makes quantum physics such a tempting field. The struggle to understand, and find ways to link Nature at the subatomic level to Nature at the observable level offers rewarding challenges. I by no means pretend to have found the key to unlock the mysteries of quantum physics; even after a century of development in the field, experts disagree on the theory's interpretation and conceptual framework. I here rather try to draw the big, but rough picture of the particle physics world.

As a student getting to grips with quantum physics, one of the challenges is to see the full picture of how the theory developed, and especially why one necessarily needed Quantum Field Theory (QFT) to reach the goal. The educational path usually starts at the non-relativistic Schrödinger equation (SE). The Schrödinger equation is the matter analogue of the description of waves, and is useful since it builds on the conceptually familiar mathematics of waves and oscillators. Next step is usually the matrix-algebra formulation of the non-relativistic quantum mechanics, before dealing with the relativistic extensions of the SE, the Dirac[1] and Klein-Gordon[2] equations. Finally one tackles the relativistically manifest QFT leading to what culminated in the "Standard Model" (SM). This long and historically motivated route is preferred since QFT involves some rather advanced mathematics, and the concepts to do with the quantum world are new and challenging. However, it can be hard to see how the different approaches relate to each other, and what limitations drove the development of new theories.

[1] Paul Dirac 1920-1984

[2] Oskar Klein 1894-1977, Walter Gordon 1893-1939

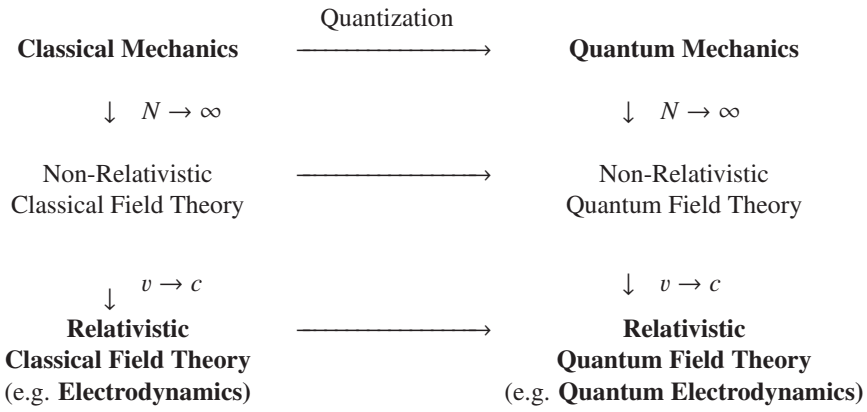

Figure 1.1: The connections between the various formulations of quantum physics, a simplified version, inspired from [10]. $N \to \infty$ means the number of particles goes to infinity, and $v \to c$ means when the velocity approaches the speed of light c.

Figure 1.1 attempts to visualize the connection between the different approaches used to describe the sub-atomic world. It suggests possible paths starting from Classical Mechanics used to describe macroscopic non-relativistic systems, and ending with the final quantum field theory of the SM. The steps in the figure do not necessarily reflect how history lead us to the "final" theory, but are the configuration of possibilities when considering the three main steps necessary to arrive to it. These are the extension from handling single to an infinite number of particles ($N \to \infty$) (when moving from a particle to a field, we effectively move from one degree of freedom to infinite degrees of freedom, i.e. $N \to \infty$), the quantization of waves (or fields) to describe particles, and the incorporation of Special Relativity Theory as the velocity approaches the speed of light, i.e. $v \to c$. These are the main ingredients of QFT.

But why the need of a quantum field theory? Experimental observations showed that particles can behave like waves, and electromagnetic radiation (waves) can behave like particles. This so-called "particle-wave duality", inspired the attempt to describe both particles and fields with the same underlying formalism. In addition it can be mentioned that the relativistic version of the SE, namely the Klein Gordon (deals with spin-less particles) and Dirac (deals with spin 1/2 particles) equations, which potentially could form a sufficient theory, unfortunately could not account for a variable number of particles. Therefore hard scattering processes where a set of incoming particles, e.g. an electron and its antiparticle the positron meet, and annihilate into a photon, could not be described. The only way to deal with varying particle numbers is with treating particles as fields within the framework of quantum field theory. But what is really a field? Temperature is a good example, each space-time point has a certain magnitude of temperature, and the collection of temperatures makes up the temperature field. The fields we deal with in QFT are scalar fields (the Higgs field), spinor fields (matter fields), and vector fields (force fields). While a scalar field just consists of pure values for each space-time point, a spinor field is a collection of magnitudes (numbers) *and* spins, and a vector field is a collection of magnitudes and directions. More on the various fields and spin later. What is important to

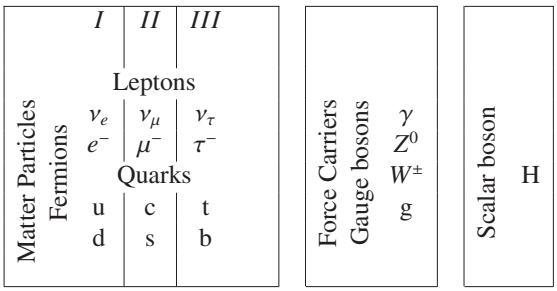

Figure 1.2: The particle content of the SM. In addition to these: each fermion has an anti-particle, a duplicate but with opposite charge, and other quantum numbers. The γ, Z^0, g and H are their own anti-particles. W^+ and W^- are anti-particles.

understand is that a field is not an abstract nonphysical object, but transfers energy and acts in dynamical ways much like particles. In fact, in a quantized field, the energy comes in quantized energy packets which in all respect act like elementary particles. So, one can regard fields as the more fundamental objects: *"Quantum fields, and not particles, are the primary reality"* [11]

1.2 The Standard Model and its particle content

The first successful QFT is Quantum Electro Dynamics (QED, 1950s, Nobel prize in 1965 to Feynman, Schwinger, Tomonaga [12]) which describes how matter and light interact through the electromagnetic force. I first start by outlining the steps leading to QED. Similar basic principles are used to derive the three forces of Nature relevant to the microscopic world, namely the electromagnetic, the weak and the strong forces of Nature. In the 1970's the QED and the weak force - unified in the Electroweak (EW) force - and Quantum ChromoDynamics (QCD) - the strong force, culminated in one joint theory given the name the "Standard Model" (Nobel Prize in Physics 1979 for Glashow, Salam, Weinberg [13]).

There is no doubt that the SM is a theory developed in close synergy between theoretical principles and experimental results. An apparent abundance of "elementary" hadrons (particles interacting strongly) discovered in the early 1900s, first from cosmic ray experiments, later in particle colliders, screamed for more fundamental explanations. One needed a way to build matter out of orderly building blocks following predictable rules. The resulting theory explained the patterns seen in Nature: the many "elementary" particles discovered were in fact built up of smaller constituents, namely quarks. This together with several other assumptions lead to the "periodic table" of the SM, namely the elementary particle content depicted in Figure 1.2.

The SM arranges particles into two main groups, matter particles which are fermions (half-numbered spin) and force-carrier particles which are bosons (integer spin). Matter particles are further divided into leptons and quarks, where leptons interact electroweakly, and quarks in addition interact strongly. Furthermore, leptons and quarks come in 3 "generations" or "families" (*I*,*II*,*III*), where the lightest set of particles are defined as the first generation, and the heaviest

group as the third generation. In the first generation we find the most familiar particles. These are for leptons, the electron (e^-), and for quarks, the up (u) and down (d) quarks. All three particles are constituents of atoms. In fact, electrons, up and down quarks, in addition to gluons to hold the quarks together, are all we need to build the ordinary matter we find in Nature. The last particle that belongs to the first generation is the electron-neutrino ν_e, which is important in transformation of matter, such as in nuclear radioactive decay and fusion reactions in the sun.

Whereas charged leptons have integer electric charge, -1 or +1 for particle and anti-particle respectively, quarks exhibit fractional charge, +2/3 for up-type quarks, and -1/3 for down-type quarks. Furthermore, each quark comes in three copies or "colours", and it is this property that is transmitted by gluons when quarks interact and lead to the name of the strong force: Quantum Chromo Dynamics (QCD). Neutrinos are neutral (0 electric charge). When it comes to the bosons, all are neutral except the W^+, W^- bosons which evidently have charge +1 and -1 respectively.

Like for matter fields, the quantization of the force fields (the electromagnetic, weak and strong) result in a set of particles called “gauge bosons” which are responsible for transmitting force, or said in another way: involved when particles interact. The photon (γ) mediates the electromagnetic force, the electrically neutral Z^0, and charged $W^\pm$ bosons mediate the weak force, and the gluons (g) the strong force. As the names hint of, the forces’ strengths differ (at low energies). The weak force is (not surprisingly) the weakest, only a billionth of the electromagnetic force, while the strong force is 100 times stronger than the electromagnetic force. Gravity, some 10^{40} times weaker than the strong force is negligible at the microscopic scale at hand.

The Higgs boson (H) (spin 0, and therefore scalar) is the quantum of the Higgs field, which is responsible for allowing elementary particles to acquire mass. While the photon of the infinite-range Electromagnetism is massless, the gauge bosons of the short-range Weak force are massive. Mass explains the different ranges of these forces. Ultimately it is the Spontaneous symmetry breaking mechanism, connected to the Higgs field, that explains why a macroscopic force (Electromagnetic) and a microscopic force (Weak), although unified at high energies, behave very differently at low energies, where we observe them. In addition to the particles shown in Figure 1.2 there exists a set of duplicates or *antiparticles*. These are blueprints of the particles except with reversed electric charge, and other quantum properties we shall meet in this chapter. Electrically neutral particles like the photon, the Z boson, the gluons and the Higgs boson are their own antiparticles.

All particles (and antiparticles) of Figure 1.2 have been discovered. One of the last, but crucial discoveries was of the top quark in 1995 by the CDF and D0 collaborations [14, 15] at Fermilab in the US. It was found 18 years after its prediction with the bottom quark discovery [16], also at Fermilab. According to the Standard Model, fermions, which quarks are, come in pairs, and therefore the discovery of the bottom quark’s partner, the top quark, was a(nother) triumph of the theory. After year 2000 when the ν_τ was directly proven [17], only a single particle was missing to complete the SM. This was the Higgs boson, one of the main missions of the searches at the LHC.

On 4 July 2012, the two general purpose experiments at LHC, CMS ([18, 19]) and ATLAS

([2, 20]) finally announced the observation of a new particle consistent with the SM Higgs boson. This was a historical moment, after decades of searching for the boson which is a very important ingredient in the SM, and its final missing piece.

The LHC has only taken 2% of the data it is expected to during its lifetime. With the high energies planned already from April 2015, prospects for precision measurements, and possibly new discoveries are excellent.

Let us now have a look at how QFT leads to the SM. When doing so we need to understand several important concepts. In the following section, I touch on a few of these.

1.2.1 Symmetries

Symmetries are of great importance in the description and understanding of Nature. Historically, people like Kepler, Galileo, Newton and Maxwell, to mention a few, saw its relevance. But it was not until the early 1900's that Einstein elevated symmetry to a fundamental principle, claiming that the symmetries dictated the underlying laws and not the opposite. He went ahead an derived Maxwell's equations from symmetry principles, by realizing the symmetry between space and time, thus requiring invariance of the speed of light. In 1915 another significant contribution was made to acknowledge the importance of symmetries. Emily Noether formulated a theorem which stated that any *continuous* symmetry implies some conserved quantity, and vice versa. One of the simplest examples of this is spatial symmetry which leads to conservation of momentum. It is maybe easier to see the connection if one instead of saying "symmetries", says "invariance", which is equivalent. An experiment done here or there, today, or tomorrow must lead to the same outcome, given the conditions are identical. This might seem obvious, but is in fact much deeper than what it seems, since invariance in space (here or there) and invariance in time (today or tomorrow) imply conservation of important physical quantities such as momentum and energy. Luckily Nature behaves in such a way, otherwise it would be impossible to attain scientifically predictable results.

In particle physics and quantum field theory, symmetries are not as straight forward and obvious as in the spatial case. We talk about symmetries in some abstract space, for instance phase-invariance in quantum physics. However, the principle is the same, and it is of fundamental importance to the considered theory. In fact, today we believe that symmetry is the underlying principle of all laws of Nature, and that the laws arise in order to preserve symmetry. "Symmetries are laws, which the laws of Nature have to observe" [21].

Symmetries can be divided into two main groups, namely discrete and continuous, and the continuous again come in two versions: local and global. I discuss for the most part continuous symmetries, but discrete symmetries are equally important. In Nature the simultaneous transformation of charge conjugation (matter antimatter), parity transformation (mirroring of space), and time reversal is postulated in QFT to be absolutely conserved. This is the so-called CPT theorem, an exact symmetry of Nature that has so far never been defied. However, let us turn our attention back to the continuous symmetries. While the *global* symmetries are connected to conservation laws, the *local* symmetries are of equal or maybe even larger importance. They

lead to the automatic introduction of interaction terms in the equations describing free particles.

1.2.2 The quantum world and particle-waves

In the macroscopic world we are used to handle quantities such as position and momentum directly as physical variables. In the microscopic world of quantum physics we take one step back and define a particle's *wavefunction* and apply position or momentum *operators* on that wavefunction in order to generate the observable quantities. This can be seen as a more fundamental approach, and is the only way to handle the subtleties of the quantum world, as it naturally incorporates the Heisenberg uncertainty principle dominant at this scale. Heisenberg's uncertainty principle states that you can not at the same time exactly determine momentum and position (or energy and time) of a system. This is formulated by relating the uncertainty σ of the position x and momentum p by $\sigma_x \sigma_p \leq \hbar/2$, where $\hbar$ is the reduced Planck's constant $\hbar = h/2\pi$. In the following I show how a particle's wave equation and corresponding wavefunction can be found, and at the same time define the operator substitution known as the first quantization. In short the first quantization lets us go from describing waves to particles, by moving from wave parameters such as frequency and wavelength, to particle parameters such as momentum and energy.

We start by the familiar (one-dimensional) wave-equation

$$\frac{1}{c^2}\frac{\partial^2}{\partial^2 t}\phi - \frac{\partial^2}{\partial^2 x}\phi = 0\,,$$

which has a plane-wave solution expressed through the wavenumber k and the angular momentum ω

$$\phi = \phi_0 e^{i(kx-\omega t)}\,.$$

Moving from classical waves to particles is done by altering $(kx - \omega t)$ above by means of de Broglie's wave-particle duality relation, connecting particles of momentum p and energy E, to waves with wavelength λ and angular velocity ω

$$\lambda = h/p \quad \text{or equally} \quad k = \frac{2\pi}{\lambda} = p/\hbar\,.$$

We must also transform ω in a similar manner. Using the fact that $E = h\nu$ and $\omega = 2\pi\nu$, we find $\omega = E/\hbar$, which then leads to the particle wavefunction

$$\phi = \phi_0 e^{(i/\hbar)(px-Et)}\,, \tag{1.1}$$

and a particle wave equation which reads

$$\left[\frac{1}{c^2}\frac{\partial^2}{\partial^2 t} - \frac{\partial^2}{\partial^2 x}\right]\phi_0 e^{(i/\hbar)(px-Et)} = 0\,.$$

We can therefore infer that the wave equation for particle with mass m simply would be

$$\left[\frac{1}{c^2}\frac{\partial^2}{\partial^2 t} - \frac{\partial^2}{\partial^2 x} + \frac{m^2c^2}{\hbar^2}\right]\phi = 0\,.$$

Let us now extend this to all three space-dimensions, and at the same time write the formula in a relativistic covariant form, which ensures that we obey special relativity. We do this by connecting space and time into the contravariant space-time coordinate $x^\mu = (ct, x, y, z)$ (and the covariant space-time coordinate is then $x_\mu = (ct, -x, -y, -z)$).

$$\begin{aligned}\left[\frac{1}{c^2}\frac{\partial^2}{\partial^2 t} - \frac{\partial^2}{\partial^2 x} - \frac{\partial^2}{\partial^2 y} - \frac{\partial^2}{\partial^2 z} + \frac{m^2c^2}{\hbar^2}\right]\phi &= 0\\ \left[\frac{1}{c^2}\frac{\partial^2}{\partial^2 t} - \boldsymbol{\nabla}^2 + \frac{m^2c^2}{\hbar^2}\right]\phi &= 0\\ \left[\partial_\mu\partial^\mu + \frac{m^2c^2}{\hbar^2}\right]\phi &= 0\,,\end{aligned}$$

where $\boldsymbol{\nabla}$ the so-called Del-operator, which is just a short-hand notation for the three-dimensional partial derivative, and $\partial_\mu\partial^\mu$ is the short-hand for denoting the space-time derivative, as the expression above shows. More specifically $\partial_\mu = \frac{\partial}{\partial x^\mu}$, and $\partial^\mu = \frac{\partial}{\partial x_\mu}$, which is needed since when working in Lorentz manifest notation, then the inner-product between two vectors is defined as $x^2 = x_\mu x^\mu = t^2 - x^2 - y^2 - z^2$.

We have now in fact arrived to the relativistic Klein Gordon (KG) equation for a spin-less particle, described by the field ϕ , and with mass m

$$\left(\partial_\mu\partial^\mu + m^2\right)\phi = 0\,, \tag{1.2}$$

where we have switched to natural units $c = \hbar = 1$. Performing the derivation on the left hand side of Equation 1.2, or said in another way, letting the *operator* ∂_μ work on ϕ, with a plane-wave solution as in (1.1), yields

$$\left(E^2 - p^2 - m^2\right)\phi = 0\,, \tag{1.3}$$

which we recognize as the energy-momentum relation. We could have arrived to the same result, i.e. the KG equation, if we just directly had substituted

$$p_\mu \to i\partial_\mu = \left(E \to i\frac{\partial}{\partial t}, \boldsymbol{p} \to -i\boldsymbol{\nabla}\right),$$

in the energy-momentum relation (1.3). This is the correspondence principle, and the procedure is commonly known as the first quantization. It is the usual prescription to quantize classical systems, motivated by the necessary steps needed to move from classical to quantized systems via de Broglie's relation.

The KG equation which we have worked with so far, is quadratic in time and space. And it

only describes scalar (spin 0) particles. A very nice property of an equation if it is *linear* in time however, is that it predicts time-evolution, and likewise it predicts evolution in space if linear in space. The Dirac equation operates with terms linear in ∂_μ, i.e. linear in both space and time

$$\left(i\gamma^\mu\partial_\mu - m\right)\psi = 0 \tag{1.4}$$

This requires that γ^μ, the so-called γ matrices, are 4×4 spin matrices, and the solutions are four component spinors ψ.

The Dirac equation resulted in a profound prediction, namely that of the existence of antiparticles. The four components of the field ψ thus corresponds to the spin-orientations up ($\psi_1 = \psi_\uparrow$) or down ($\psi_2 = \psi_\downarrow$) for matter particles, and up ($\psi_3 = \psi^\dagger_\uparrow$) or down ($\psi_4 = \psi^\dagger_\downarrow$) for anti-matter particles (the dagger † represents the antiparticle). The first antiparticle, the positive electron (called positron) was discovered shortly after its prediction, in 1932.

We have already introduced the KG and Dirac fields. A very elegant way to deal with fields is through the Lagrangian formalism. The next section gives a brief overview of this. We see how starting with a Lagrangian describing a system, we derive the equations of motion just by requiring some symmetry arguments. In the following sections I to a large extent use the notation and procedures as in Ref. [22].

1.2.3 The Lagrangian formalism

In field theory (both classical and quantized), the *Lagrangian* holds all necessary dynamical information about the system. It is constructed in such a way that it, via the "principle of least action", leads to the equations of motion. The principle reflects Nature's tendency to always choose the most efficient path from a to b, and is a fundamental property of Nature.

Classically, the Lagrangian L is the system's kinetic energy T minus the potential energy V

$$L = T - V\,,$$

while the *action* S is the integral over the time coordinate $S = \int L dt$, and represents the system's path in space-time. It is practical to operate with *generalized* coordinates q and their time-derivative $\dot{q}$, i.e. $L = L(q, \dot{q})$. The principle of least action requires that we minimize the action S, i.e $\delta S = 0$. This results in the Euler-Lagrange (EL) equation

$$\frac{\partial L}{\partial q_i} - \frac{d}{dt}\frac{\partial L}{\partial \dot{q}_i} = 0\,, \tag{1.5}$$

leading to the equations of motion. I show this using a very simple example. Let us look at a system with a (non-relativistic) particle with kinetic energy $T = 1/2mv^2 = (1/2)m\dot{x}^2$, in a potential $V(x)$. We then have $q_i = x$, and $\dot{q}_i = \dot{x}$. Applying the EL equation on $L = (1/2)m\dot{x}^2 - V(x)$ yields

$$\frac{\partial L}{\partial x} = -\frac{\partial V}{\partial x}$$

$$\frac{d}{dt}\left(\frac{\partial L}{\partial \dot{x}}\right) = \frac{d}{dt}(m\dot{x}) = m\ddot{x}\,,$$

which we recognize as Newtons second law of motion $F = -dV/dx = m\ddot{x}$, where the derivative of the potential describes the (conservative) force. In a similar way we can use the Lagrangian formalism for other types of interactions. Thus the principle of least action is a compact and powerful method incorporating all necessary dynamical information about the system.

In quantum field theory we operate with the Lagrangian *density* $\mathcal{L}$. The Lagrangian is then an integral over the three space-coordinates, which is a functional of the fields (ξ) and their derivatives, which are themselves functions of the space-time coordinates of the Lagrangian density

$$L = \int d^3x\, \mathcal{L}(\xi, \partial_\mu(\xi))$$

The Lagrangian density $\mathcal{L}$ satisfies the EL equations

$$\partial_\mu\left(\frac{\partial \mathcal{L}}{\partial(\partial_\mu \xi_i)}\right) - \frac{\partial \mathcal{L}}{\partial \xi_i} = 0\,, \tag{1.6}$$

where we see that the coordinate q_i is now replaced by the field ξ_i, and the time derivatives of the coordinate $\dot{q}$ are replaced by the derivatives of the fields with respect to the four space-time coordinates, i.e. $\partial_\mu \xi_i = \partial \xi_i / \partial x^\mu$.

How do we build Lagrangians[3] for scalars and spinors? The only rule we need to go by, is that for the fields to be of general use, they must obey special relativity, which implies that the Lagrangian must stay invariant under Lorentz transformation when defining kinetic, potential and mass terms. The following minimal free Lagrangians satisfy this condition

$$\mathcal{L}_{\text{scalar(KG)}} = \frac{1}{2}(\partial_\mu \phi)(\partial^\mu \phi) - \frac{1}{2}m^2\phi^2 \tag{1.7}$$

$$\mathcal{L}_{\text{spinor(Dirac)}} = \bar{\psi} i\gamma^\mu \partial_\mu \psi - m\bar{\psi}\psi\,. \tag{1.8}$$

In the Dirac Lagrangian we encounter $\bar{\psi}$ which is the "adjoint spinor" which briefly explained tells us how to complex conjugate ψ in a coherent manner. It is defined $\bar{\psi} = \psi^\dagger \gamma^0$, where the $\dagger$ tells us to transpose the vector (column vector $\rightarrow$ row vector, or vice-versa), and complex conjugate each element of the vector, i.e. $A^\dagger = (a + ib)^* = a - ib$. Furthermore γ^0 (gamma matrix) is needed in order to follow the algebraic rules of spinors. Complex conjugation in fact also applies when multiplying complex scalars, namely $\phi^*\phi$. Here however, I have chosen a real scalar field. We now use the same procedure as outlined above, by applying the EL principle to the Lagrangian of the fields (KG, or Dirac) as in Equation 1.6, and from this derive the KG and Dirac equations of motion. The reader can now easily check that applying the EL equation (1.6) to the KG Lagrangian (1.7), yields the KG equation (1.2). And likewise applying the EL equation to Dirac Lagrangian (1.8) yields the Dirac equation (1.4).

Now that we have established a few basic Lagrangians, let us consider what happens when we rotate the system.

[3]From now on we work with Lagrangian densities $\mathcal{L}$, but refer to them as Lagrangians for simplicity.

1.2.4 The Gauge Principle applied to Electromagnetism

If we apply a global phase transition to some system, the system stays unchanged, i.e. all observables are the same. This means that phase is irrelevant. For a wave ψ this means that when its phase changes by some constant phase χ, nothing changes. This is because the multiplicative factor that enters ($e^{iq\chi}$) in fact cancels out. To outline the idea of gauge invariance in the microscopic word, I shall use the Lagrangian of the free Dirac electron

$$\mathcal{L}_0 \;=\; i\,\overline{\psi}(x)\gamma^{\mu}\partial_{\mu}\psi(x) \;-\; m\,\overline{\psi}(x)\psi(x)\,. \tag{1.9}$$

It is well known that the dynamical properties of a wave function (or here field) stay unchanged if a *global* phase-transformation takes place:

$$\psi(x) \quad \rightarrow \quad \psi'(x) \;\equiv\; e^{iq\chi}\,\psi(x)\,, \tag{1.10}$$

where the $e^{iq\chi}$ is just an ordinary phase-term, with constant phase χ, and q a real constant. This does not change the physical system, as it is straightforward to see that since $\partial_{\mu}\psi'(x) = e^{iq\chi}\partial\psi(x)$ the Lagrangian transforms as

$$\begin{aligned}
\mathcal{L}_0 \rightarrow \mathcal{L}_0^{'} &= i\bar{\psi}^{'}\gamma^{\mu}\partial_{\mu}\psi^{'} - m\bar{\psi}^{'}\psi^{'} \\
&= ie^{-iq\chi}\psi\gamma^{\mu}\partial_{\mu}e^{iq\chi}\psi - me^{-iq\chi}\bar{\psi}e^{iq\chi}\psi \\
&= i\,\overline{\psi}\gamma^{\mu}\partial_{\mu}\psi \;-\; m\,\overline{\psi}\psi \\
&= \mathcal{L}_0\,,
\end{aligned}$$

since the global phase terms $e^{-iq\chi}\bar{\psi}\cdot e^{iq\chi}$ just cancel out, we have arrived back to (1.9), thus demonstrating invariance.

We saw that global phase transition is irrelevant. What about *local* phase transitions, i.e. $\chi = \chi(x)$, where χ is a phase-factor dependent on space-point x? When applying such a local phase transformation, and requiring *local gauge invariance* of the Lagrangian we will see that something very interesting occurs in order to communicate the phase transformation from one part of the system to another. The derivation $\partial_{\mu}\psi^{'}(x)$ when introducing a local phase transition yields

$$\partial_{\mu}\psi^{'}(x) \quad = \quad e^{iq\chi(x)}\,\Big(\partial_{\mu} + iq\,\partial_{\mu}\chi(x)\Big)\,\psi(x)\;, \tag{1.11}$$

where contrary to the previous global phase transformation, we now have an extra term from the derivative ($\partial_{\mu}\chi(x)$) which breaks invariance; unless we introduce a new field which transforms such that it exactly cancels the additional term. The new field must take the form of a vector (spin 1) field A_{μ} and transforms as

$$A_{\mu}(x) \quad \rightarrow \quad A'_{\mu}(x) \;\equiv\; A_{\mu}(x) - \partial_{\mu}\chi(x)\,, \tag{1.12}$$

When ψ and A^{μ} undergo the *combined* transformations $\psi \rightarrow \psi^{'}$ and $A^{\mu} \rightarrow A^{'\mu}$, the Lagrangian stays invariant under local phase transformation. The new field is called a *gauge field*. In

practice the above transformation is taken care of by introducing the *covariant* derivative D_μ

$$\partial_\mu \psi(x) \rightarrow D_\mu \psi(x) \equiv \left[\partial_\mu + iqA_\mu(x)\right] \psi(x)\,, \tag{1.13}$$

which transforms exactly as the field itself. The Lagrangian thus becomes

$$\mathcal{L} \equiv i\overline{\psi}\gamma^\mu D_\mu \psi - m\overline{\psi}\psi = \mathcal{L}_0 - q\overline{\psi}\gamma^\mu A_\mu \psi\,, \tag{1.14}$$

where $\mathcal{L}_0$ is the free electron Lagrangian we started with. The whole Lagrangian now stays invariant under local phase-transformation, since the extra term from the derivative of the exponential term is exactly cancelled out by the added field. What is very interesting now is that the right-hand term in Equation 1.14 in fact is an interaction term between the Dirac electron and the 4-vector field A^μ, which is nothing but the electromagnetic four-potential, the photon field, defining the electromagnetic tensor

$$F_{\mu\nu} \equiv \partial_\mu A_\nu - \partial_\nu A_\mu\,. \tag{1.15}$$

This means that the resulting Lagrangian went from describing a free charged particle, to the particle in an electromagnetic field, and the gauge principle completely determines the way the electron couples to the photon, and with what strength, namely q, identified as the charge of the particle! We can write q in a more obvious form: $q = eQ$, where e is the unit electric charge, and Q is a real number. Then in the case of an electron in an electromagnetic field: $Q = -1$ and therefore $q = -e$.

For A_μ to be a real propagating field, one must just add the gauge-invariant kinetic term

$$\mathcal{L}_{\text{Kin}} \equiv -\frac{1}{4} F_{\mu\nu} F^{\mu\nu}\,, \tag{1.16}$$

finally giving the following full QED Lagrangian

$$\begin{aligned} \mathcal{L}_{QED} &= \overline{\psi}(i\gamma^\mu D_\mu - m_e)\psi - \frac{1}{4} F_{\mu\nu} F^{\mu\nu} \\ &= \overline{\psi}(i\gamma^\mu \partial_\mu - m_e)\psi + e\bar{\psi}\gamma^\mu \psi A_\mu - \frac{1}{4} F_{\mu\nu} F^{\mu\nu}\,, \end{aligned} \tag{1.17}$$

where we now have identified q as the electric charge $-e$.

QED is one of the most successful theories known to man. To mention just one of the most significant achievements: The theoretical prediction of the anomalous magnetic momentum, which arises strictly due to virtual electrons and photons, and thus only relies on QED, agrees with measurement to more than 10 significant digits! No other prediction of any quantity throughout history agrees to this level.

So, with the powerful tool of gauge invariance in hand, and successfully having derived QED, we can move along and have a look at the two other forces in the microscopic Nature, namely the weak and the strong forces.

1.2.5 Strong force, weak force, and the Standard Model

The set of phase transformations described in the example above, form a symmetry group of type U(1), or Unitary group U(n) (group of n×n unitary matrices) of dimension n=1, and as we saw describes Quantum Electro Dynamics (QED). The symmetry groups that encompass the phase transformations for the weak and strong interactions are the $SU(2)_L$ and $SU(3)_C$ Special (S) Unitary symmetry groups, with dimension n=2, and n=3, respectively. The "special" refers to the fact that it is a sub-group of the unitary group, namely with matrix determinant of 1. Although the resulting gauge fields and the mathematical calculations are more complicated than in the U(1) case, the recipe for constructing a local gauge invariant theory is the same for all. I here briefly outline the procedures, starting with SU(3), and in the course of it, point out some important differences with QED.

In QED we encountered the electric charges Q, which is conserved as a consequence of gauge invariance. In Quantum Chromo Dynamics (QCD), governing the interaction between quarks, coming in three *colours*: red, blue, and green. Hence we must use the $SU(3)_C$ symmetry group (where C is for color), in order to describe the phase transformations in "colour-space". The Dirac field $\psi = (q_r, q_g, q_b)$ where q_α represents the three colour-states α, transforms under $SU(3)_C$ as

$$\psi(x) \rightarrow \psi'(x) = e^{ig_S \alpha(x)\cdot\hat{\boldsymbol{T}}}\psi(x)\,.$$

Here we identify g_S as the strong coupling constant, and $\hat{\boldsymbol{T}} = \{T^a\}$, where $T^a = 1/2\lambda^a$ and $a = (1, 2, ..., 8)$. λ^a are the 3×3 (Gell-Mann) matrices, the eight $(n^2 - 1)$ generators of the $SU(3)_C$ symmetry group. When we demand local gauge invariance the Dirac field equation becomes

$$i\gamma^\mu \left[\partial_\mu + ig_S(\partial_\mu \boldsymbol{\alpha}) \cdot \hat{\boldsymbol{T}}\right]\psi - m\psi = 0\,,$$

which has the same form as the resulting Dirac field from the corresponding U(1) transformation (1.11). This means that we must construct a covariant derivative that transforms exactly like the above, such that the extra term $(\partial_\mu \boldsymbol{\alpha}) \cdot \hat{\boldsymbol{T}}$ cancels, namely

$$D_\mu \psi = \left[\partial_\mu + ig_S G^a_\mu T^a\right]\,.$$

So far everything looks similar to QED. However, the now 8 new gauge fields G^k_μ introduced to restore gauge invariance, must transform as

$$G^k_\mu \rightarrow G^{k'}_\mu = G^k_\mu - \partial_\mu \alpha_k - g_S f_{ijk}\alpha_i G^j_\mu\,,$$

and we notice that there is an additional term $g_S f_{ijk}\alpha_i G^j_\mu$, where f_{ijk} are so-called structure constants which determine the commutation relations of the SU(3) group. This in contrast to the QED theory, where no such term arises. The underlying reason for this is that while QED is an Abelian theory where the generators of the U(1) group commute[4], SU(3) is non-Abelian, i.e. the generators do not commute.

[4](as ordinary numbers do $a \cdot b = b \cdot a$

When we write down the kinetic Lagrangian of the fields

$$\mathcal{L} = -\frac{1}{4}\boldsymbol{G}^{\mu\nu} \cdot \boldsymbol{G}_{\mu\nu}\,,$$

with

$$G_{\mu\nu} = \partial_\mu G^i_\nu - \partial_\nu G^i_\mu + g_S f_{ijk} G^j_\mu G^k_\nu\,,$$

we observe that there is an extra term compared to the corresponding expression for the photon field (Equation 1.15), namely $g_S f_{ijk} G^j_\mu G^k_\nu$. This is a significant term, as it describes the gluon *self-interaction* and gives rise to triple and quartic (tree-level) gluon vertices. Whereas photons do not interact because they do not carry electric charge, gluons do interact, as they carry colour-charge. This is in fact the underlying reason for the "asymptotic freedom" of quarks, which I come back to in Section 1.2.7.

What about the weak force? Well, things become slightly more complicated, and we must introduce a new concept, namely that of "handedness". Experiment shows that fermions come in two types, left-handed and right-handed, where only the left-handed particles (or right-handed anti-particles) couple to the $W^\pm$ of the weak force. To account for this we introduce the concept of *weak isospin* I_W. Left-handed particles are organized in weak isospin doublets with $I_W = 1/2$, and right-handed particles in weak isospin singlets with $I_W = 0$. This organizational principle is in fact already implied in the SM particle content structure in Table 1.2, where leptons and quarks are set up as they would be in weak isospin doublets. Taking first generation of leptons and quarks as an example, this is

$$\ell_L = \begin{pmatrix} \nu_e \\ e^- \end{pmatrix} \qquad q_L = \begin{pmatrix} u \\ d \end{pmatrix} \qquad e_R,\ u_R,\ d_R\,,$$

(assuming massless neutrino, hence no ν_R). All lepton and quark generations follow this structure, grouped as given in Table 1.2. The gauge fields of $\mathrm{SU}(2)_L$ govern the weak force, and there are $n^2-1 = 3$ gauge fields W^k_μ, $k = 1, 2, 3$, which correspond to three gauge bosons W^1, W^2, and W^3. However, the gauge bosons mentioned here are not the physical $W^\pm$, and Z bosons listed in Table 1.2. To find those we need yet another ingredient: we must marry $\mathrm{SU}(2)_L$ with $\mathrm{U}(1)_Y$. We already know $\mathrm{SU}(2)_L$, however $\mathrm{U}(1)_Y$ is new, and is called the U(1) *hypercharge* group. It is similar to the $\mathrm{U}(1)_{EM}$ of QED, and the Lagrangian transforms as with $\mathrm{U}(1)_{EM}$, however, the resulting gauge field is B_μ, with the charge $Yg'/2$ now (where g' is the coupling constant of the $\mathrm{U}(1)_Y$ interaction), in place of $q = eQ$ in QED. It turns out that the third component of weak isospin and hypercharge relate to electric charge Q in the following way: $Q = Y/2 + I^3_W$. In an electroweak unified model, W^1_μ and W^2_μ mix to form the physical W-bosons $W^\pm_\mu$, and B_μ and W^3 mix to form the physical photon field A_μ, and the Z-boson Z^0:

$$\begin{aligned} W^\pm_\mu &= \frac{1}{\sqrt{2}}\left(W^1_\mu \mp i W^2_\mu\right) \\ A_\mu &= +B_\mu \cos\theta_W + W^3_\mu \sin\theta_W \\ Z_\mu &= -B_\mu \sin\theta_W + W^3_\mu \cos\theta_W\,, \end{aligned}$$

where θ_W is the *weak mixing angle*. So, we have found the correct symmetry group combination, and successfully generated the physical photon and Z^0 boson, in addition to the $W^\pm$ bosons.

We have now applied the gauge principle and successfully generated the three forces, electromagnetism, the strong force, and the weak force. However, all gauge bosons are massless. The formalism in fact requires this, otherwise we would break gauge invariance. In fact, the fermions are also massless. The experimentally determined short range reach of the weak force on the other hand, can only be explained by massive force carriers $W^\pm$ and Z^0. In order to maintain a mathematically valid theory, and allow necessary mass terms, the symmetry can be "spontaneously" broken. This ensures the stability of the theory, but has some important consequences: the vacuum can not be empty!

1.2.6 Spontaneous symmetry breaking

A desirable feature of a quantum field theory is that it is "renormalizable" which has to do with its ability to avoid breaking down at very low (infrared) or very high (ultraviolet) scales. Writing up a theory describing massive particles challenges this goal, since explicit mass-terms in the Lagrangian break gauge invariance and thus renormalizability is not guarantied. However, it turns out that by introducing a "new" scalar field with a particular type of potential, the symmetry is "spontaneously broken". This in fact maintains the original symmetry of the theory, and at the same time gives mass to the gauge bosons of the weak force and in addition allows mass terms for fermions!

The term "spontaneous symmetry breaking" requires some explanation. It refers to the "procedure" of choosing a specific gauge for a non-vanishing and degenerate vacuum state of some system. The simplest example is of a pencil standing upright on its tip in a perfectly symmetric state[5]. It is not energetically favourable to maintain the upright position, and sooner or later it will fall down into its energy ground state. But which direction the pencil falls is arbitrary, and does not affect the system's ground state, which is the same independent on direction. Once a certain direction is "chosen" though, the symmetry is spontaneously broken.

In the case of quantum field theories the vacuum expectation value, denoted v, is that of some field, and the only way of introducing a non-vanishing vacuum expectation value without breaking invariance under Lorentz transformation and translations, is to choose a *scalar* field. But what kind of symmetry should the scalar field obey? First of all, the most important goal of the symmetry breaking is to allow massive weak gauge bosons. They belong to the $\mathrm{SU}(2)_L$ groups, (whose generators were the W^1, W^2 and W^3 weak fields). But, the W-boson is electrically charged, suggesting that the U(1) symmetry group should be included, as we saw in the previous section. The $\mathrm{SU}(2)_L\times \mathrm{U}(1)_Y$ electroweak unifying group marries $\mathrm{SU}(2)_L$ and $\mathrm{U}(1)_Y$ at high energies, and is what has been proved to work (Glashow, Salam and Weinberg [23–25]). A complex scalar field ϕ that obeys the $\mathrm{SU}(2)_L\times\mathrm{U}(1)_Y$ arranged in form of an isospin doublet is

$$\phi = \begin{pmatrix} \phi^+ \\ \phi^0 \end{pmatrix}, \tag{1.18}$$

[5]Assuming a perfect pencil tip, a perfectly smooth surface, and no external forces affecting the pencil.

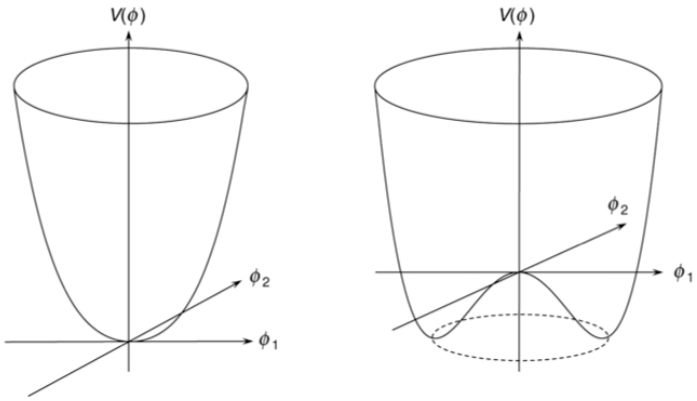

Figure 1.3: Parabolic (left) and mexican hat (right) scalar potential. Extracted from Ref. [22]

where ϕ^+ is charged, and ϕ^0 is neutral. How does ϕ transform under the local gauge transformation of $SU(2)_L \times U(1)_Y$?

It is the choice of the form of the potential V that leads to spontaneous symmetry breaking, hence generating mass to the weak gauge bosons. Figure 1.3 illustrates two possible choices, one described by a parabolic function (left), and the second by a "Mexican hat" potential (right). As we see, the parabolic curve offers only a single solution to the ground state energy, namely $V = 0$. This can therefore not be the potential we are seeking, since we want a degenerate ground state. However, the mexican hat potential is promising. Its ground state corresponds to a whole set of solutions in ϕ forming a ring around the z-axis, in other words a degenerate ground state.

To outline how fields acquire mass through spontaneous symmetry breaking, through the BEH (Brout-Englert-Higgs) mechanism [26–31], I use the U(1) symmetry group. I therefore start with a complex scalar field $\phi = (1/\sqrt{2})(\phi_1 + i\phi_2)$ as above, in an electromagnetic field B_μ, and with the scalar potential $V = \mu^2\phi^*\phi + \lambda(\phi^*\phi)^2$, where μ and λ are some constants. In order for the potential to actually be bounded (have a finite minimum) we must require $\lambda > 0$. The Lagrangian of such a system is

$$\mathcal{L} = (\partial_\mu\phi)^*(\partial^\mu\phi) - V(\phi)$$

where we recognize the dynamic term from the free scalar Lagrangian of Equation 1.7. By following the usual gauge invariance principle applied to the Lagrangian above, we get

$$\mathcal{L} = -\frac{1}{4}F_{\mu\nu}F^{\mu\nu} + (D_\mu\phi)^*(D^\mu\phi) - \mu^2(\phi^*\phi) - \lambda(\phi^*\phi)^2\,, \tag{1.19}$$

where the covariant derivative $D_\mu = \partial_\mu + igB_\mu$ has been introduced in order to preserve gauge invariance, i.e. to cancel out the extra terms which occur as usual when performing a *local* gauge transformation, $\phi \to e^{i\alpha}\phi$.

With $\mu^2 < 0$ (corresponding to a non-trivial ground state of the mexican hat potential)

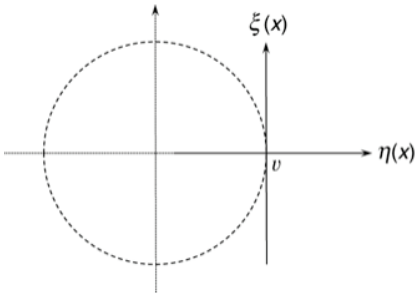

Figure 1.4: The η, ξ plane of the Higgs potential. Extracted from Ref. [22]

the ground state is degenerate, thus the symmetry is spontaneously broken. The dashed circle in Figure 1.3 (right) illustrates the $\mu^2 < 0$ minima, which corresponds to an infinite set of ground states. We further express ϕ in terms v, η, and ξ, which are just the "coordinates" in the complex-scalar phase space of the mexican hat potential, see Figure 1.4. We then get $\phi(x) = (1/\sqrt{2})(v + \eta(x) + i\xi(x))$. Here ξ is along the tangent of the degenerate ground state v (circle when projected from above), and η is the radial component. When moving in the ξ direction, at constant η, we move effortlessly along the valley (ground state) of the potential , and varying η while keeping ξ constant we move away from the ground state, to more energetic states, moving up in the potential. Therefore ξ is interpreted as a massless Goldstone field [32], while η is a massive field. When inserting this back into the Lagrangian in (1.19) we get

$$\mathcal{L} = \underbrace{\frac{1}{2}(\partial_\mu \eta)(\partial^\mu \eta) - \lambda v^2 \eta^2}_{\text{massive } \eta} + \underbrace{\frac{1}{2}(\partial_\mu \xi)(\partial^\mu \xi)}_{\text{massless } \xi} - \underbrace{\frac{1}{4}F_{\mu\nu}F^{\mu\nu} + \frac{1}{2}g^2 v^2 B_\mu B^\mu}_{\text{massive gauge field}} - V_{int} + gvB\mu(\partial^\mu \xi) \quad (1.20)$$

We now have five main components, which are the kinematic and mass components of the (massive) η, the kinematic term of the (massless) ξ field, the kinematic and mass term of the gauge field, which now has acquired mass through v^2 (which is exactly the goal), the interaction term V_{int}, and finally a term which seems to couple the gauge field B_μ with the massless ξ field. However, it turns out that the field ξ is not physical: no massless Goldstone boson ξ is observed in Nature. What we therefore do is to choose a gauge that rotates us into a physical system, which we are completely free to do. By choosing the *Unitary* gauge, ϕ transforms as

$$\phi(x) \rightarrow \phi(x)' = \frac{1}{\sqrt{2}} e^{-i\xi(x)/v} \left[v + \eta(x)\right] e^{i\xi(x)/v} = \frac{1}{\sqrt{2}}(v + \eta(x)),$$

and where ϕ now is entirely real. We can write ϕ out in a more obvious way

$$\phi(x) = \frac{1}{\sqrt{2}}(v + \eta(x)) \equiv \frac{1}{\sqrt{2}}(v + h(x)),$$

where $\eta(x)$ has been written as the physical Higgs field $h(x)$ [30], and v is the vacuum expectation value. If we now write out the resulting Lagrangian, and use $\mu^2 = -\lambda v^2$, we finally arrive

to

$$\mathcal{L} = \underbrace{\frac{1}{2}(\partial_\mu h)(\partial^\mu h) - \lambda v^2 h^2}_{\text{massive } h \text{ scalar}} - \underbrace{\frac{1}{4}F_{\mu\nu}F^{\mu\nu} + \frac{1}{2}g^2 v^2 B_\mu B^\mu}_{\text{massive gauge boson}} + \underbrace{g^2 v B_\mu B^\mu h + \frac{1}{2}g^2 B_\mu B^\mu h^2}_{h,B \text{ interactions}} - \underbrace{\lambda v h^3 - \frac{1}{4}\lambda h^4}_{h \text{ self-interactions}} . \tag{1.21}$$

The nonphysical Goldstone field is now gauged away, and the field's degree of freedom is absorbed into the B field. The effect is that B becomes massive. Furthermore we see that the resulting Lagrangian contains a massive scalar Higgs (boson), interaction between the gauge bosons and the Higgs, and finally Higgs self-interactions.

Now, this example used the U(1) symmetry group. As outlined in the start of this section we are interested in breaking the $\mathrm{SU}(2)_L \times \mathrm{U}(1)_Y$ symmetry spontaneously. This requires, in a minimal Higgs model, two complex scalar fields as follows

$$\phi = \begin{pmatrix} \phi^+ \\ \phi^0 \end{pmatrix} = \frac{1}{\sqrt{2}}\begin{pmatrix} \phi_1 + i\phi_2 \\ \phi_3 + i\phi_4 \end{pmatrix} .$$

We now end up with one massive scalar and *three* massless Goldstone bosons. This turns out to be exactly what we need. When we again choose the unitary gauge, the spectacular effect is that the three non-physical fields are absorbed into the three gauge bosons thus giving them mass, while the photon stays massless. Exactly what Nature requires!

A consequence of spontaneous symmetry breaking is that the actual masses of the weak gauge bosons are predicted by the theory. With some work, one can infer from a similar Lagrangian as (1.21), but with more mass terms and interactions between the gauge bosons and the Higgs, that the masses of A_μ and Z_μ, corresponding to the photon and the Z-boson are

$$m_A = 0 \quad \text{and} \quad m_Z = \frac{1}{2}v\sqrt{g_W^2 + g'^2} ,$$

respectively, where g_W is the weak gauge interaction coupling constant, and g' the coupling constant of the hypercharge field. Furthermore $g'/g_W = tan\theta_W$, with θ_W the well known weak mixing angle. The W boson mass is also given:

$$m_W = m_Z \cos\theta_W .$$

We can also express the W boson mass as $m_W = g_W v/2$, which means that we can infer the vacuum expectation value of the Higgs $v = 246$ GeV. Now, with the mass of the Higgs boson

$$m_H^2 = 2\lambda v^2 ,$$

now measured to ~126 GeV, we can in fact deduce the value of λ, namely $\lambda \sim 0.13$.

Fermion masses introduces interaction terms between the scalar field and the fermion field,

so-called Yukawa-couplings g_e. Using the $SU(2)_L$ electron doublet as an example, and already having assumed the unitary gauge

$$\mathcal{L}_e = \frac{g_e}{\sqrt{2}} v(\bar{e}_L e_R + \bar{e}_R e_L) - \frac{g_e}{\sqrt{2}} h(\bar{e}_L e_R + \bar{e}_R e_L)\,.$$

If this is to represent the observed electron mass m_e we must require

$$g_e = \sqrt{2}\frac{m_e}{v}\,.$$

which yields

$$\mathcal{L}_e = -m_e \bar{e}e - \frac{m_e}{v}\bar{e}eh\,,$$

where the first term is just the electron mass term, and the second is the coupling with the Higgs boson. We can naturally exchange the electron in this example with a muon or tau lepton. And in a similar fashion, the Higgs doublet gives masses to the up-type quarks. The neutrinos and down-type quarks acquire mass through the conjugate of the Higgs doublet ($\phi_c = (-\phi^0, \phi^-)$). So with the Higgs mechanism, and through Yukawa couplings, the Higgs field induces masses not only to the gauge bosons, but also to fermions!

How do we interpret the Higgs field? It is as a field that permeates all space, and at all points the vacuum expectation value is the same. The Universe is embedded in the Higgs field, and particles that feel the weak force acquire mass through this field. Before the spontaneous symmetry breaking kicked in (at high energies), the world was described by the perfectly symmetric SM, with the electromagnetic and weak forces unified into a single electroweak force (making up the symmetry group $U(1)_Y \times SU(2)_L$). The underlying symmetry is not lost with spontaneous symmetry breaking, but it is hidden by an apparent asymmetric state with massive particles. One can of course dream of further unification, and extended symmetries, incorporating $SU(3)_C$, but that lies beyond the SM itself.

I have now discussed the main ingredients of a Quantum Field Theory, and how a basic principle like symmetry generates the forces of Nature, and how the breaking of (the $SU(2)_L \times U(1)_Y$ symmetry induces masses to the elementary particles. Together all the pieces form the SM. The final subject I would like to discuss in this introduction to the SM, is the interaction strength between particles, which in fact leads us nicely to the next section, which is on Supersymmetry.

1.2.7 Forces, running couplings

The strength of the force between particles is decided by its coupling strength, manifest in coupling constants. It turns out that they are in fact not constants, but a function of energy. At energies of the order of the Z boson mass , the coupling strengths of the electromagnetic (α_1), weak (α_2) and strong force (α_3) are [22]

$$\alpha_1 \sim \frac{1}{128}\,, \quad \alpha_2 \sim \frac{1}{30}\,, \quad \alpha_3 \sim \frac{1}{9}\,.$$

How the couplings evolve with energy is summarized with the following general formula

(and it is practical to work with the inverse of α_i) [34]

$$\frac{1}{\alpha_i}(q^2) = \frac{1}{\alpha_i}(\mu^2) + \frac{B}{12\pi}\ln\frac{q^2}{\mu^2},$$

where the B is related to the so-called β function, and encodes the different contributing particles that cause so-called "loop-effects" which is the underlying reason for running couplings. They are for the electromagnetic (em), strong (S) and weak (W) force

$$B_{em} = -1, \quad B_S = 33 - 2n_f, \quad B_W = 22 - 2n_f - 1/2\,.$$

Here n_f is the number of fermion generations that actually contribute at the given energy, the number 33 in B_S is connected to the gluon contributions, the number 22 in B_W to the W and Z boson contribution, and the factor 1/2 in B_W from the Higgs boson entering the EW loops. What is important to realize here is that both the strong force and the weak force experience so-called "anti-screening" effect from the self-interacting bosons (gluons or W and Z bosons respectively), whereas the electromagnetic force has no such contribution. The effect (somewhat larger for the strong force), means that the coupling strengths of elementary strongly and weakly interacting particles decrease with energy, contrary to the electromagnetic which increases, see Figure 1.5 (left) which illustrates how the inverse of three couplings α_1, α_2, and α_3 evolve as a function of the energy scale. The weakly interacting particles increase more slowly due to the smaller anti-screening effect. At high energies therefore, the coloured quarks and gluons in fact experience a very weak strong force between them, leaving them practically free inside e.g. a nucleon. However, at low energies, they are strongly bound together, explaining why free quarks have never been seen in experiments, only so-called colour-less objects such as mesons ($q\bar{q}$) and baryons (qqq or $\bar{q}\bar{q}\bar{q}$). The theoretical discovery of the negative β function, so-called asymptotic freedom, in 1973 by H. D. Politzer, F. Wilczek and D. J. Gross ([35, 36]), was awarded the Nobel Prize in Physics in 2004.

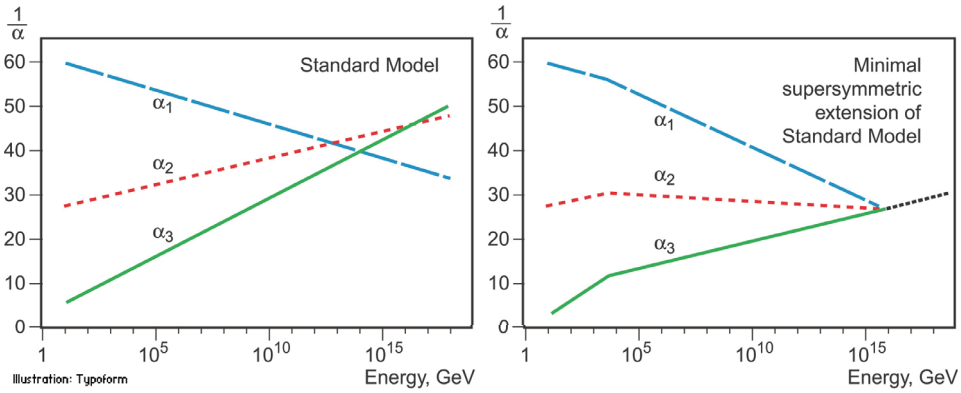

Figure 1.5: The evolution of the electromagnetic, weak and strong coupling constants α_1, α_2, and α_3 as a function of the energy scale. The left figure shows the evolution assuming the SM, and the right in a Supersymmetric extension of the SM. Figure extracted from [33].

The left plot of Figure 1.5 gives tantalizing hints of a possible Grand Unification Theory (GUT) of all three forces at some high energy scale of order 10^{16} GeV. While the electromagnetic and weak forces are unified at the scale of the weak gauge bosons, the strong force is not. GUT theories, based on a higher group embedding the $SU(3)_C \times SU(2)_L \times U(1)_Y$ of the SM and incorporating a new symmetry between leptons and quarks, propose to unify all three interactions. New gauge bosons X and Y are predicted to allow transitions between leptons and quarks. Dramatic predictions of such GUT theories are proton decay. However, if some additional new physics entered at around 1 TeV, the slope of the running couplings would alter as in the right plot of Figure 1.5. This is because additional particles would contribute to the loop corrections encoded in the β function. As we see, the effect is that all forces meet at one point. This is in fact one of the arguments why Supersymmetry, a symmetry between fermions and bosons, adding a whole range of new particles, is a favoured extension of the SM. In the next section I present Supersymmetry, but first let us take a final assessment of the SM, in order to understand its importance.

1.2.8 The success of the SM, and the need for a model beyond it

The SM has been a great success, correctly predicting the behaviour of elementary particles at energy ranges from a fraction of an eV to more than 100 GeV. The theory has been tested to predictions of the order of at least per-mille, and up until now, no experimental evidence has defied the SM. However, the SM itself is known to be incomplete, it can be seen as an *effective* theory, which works excellent at the mentioned energy-ranges, but which is not suited at much higher energies. The next sections deal with this, and suggest how Supersymmetry could help out.

"Just because it is infinite does not mean it does not exist".

author not known

1.3 Supersymmetry

In the Standard Model we encountered the unification of the electromagnetic and the weak theory into the electroweak forces. Supersymmetry[6] is yet another unification, namely between fermions and bosons. Why would one want to unify fermions and bosons? The answer is, that even as successful as the SM has been, there are strong arguments that suggest that this is not the end of the story. We can think of the SM as an *effective theory*, that can precisely explain physics within a certain energy range, but which is not sufficient at ranges far beyond.

What are the arguments to expect beyond the SM theories? It makes sense to divide the arguments into two categories, namely observational and theoretical.

1.3.1 Observational arguments to physics beyond the Standard Model

Elementary particle physics has a strong connection to cosmology and astrophysics. It turns out that in order to explain some important observations of the Universe, the SM will not do. We would need a theory beyond the SM.

The first important observation I wish to mention is that of the neutrino mass. The original formulation of the SM assumed massless neutrinos, or equivalently only left-handed neutrinos. The fermion mass terms enter via Yukawa couplings which couple right and left-handed fermions with the scalar, so with only left-handed particles, they stay massless. There has of yet been no direct observation of right-handed neutrinos. However, observations of solar ([38]) and atmospheric ([39]) neutrinos give evidence of massive neutrinos through the inference of *neutrino oscillations* from one neutrino flavour to another. Oscillations are not possible for massless particles, since they depend on mass-squared differences (in addition to mixing angles between the three neutrino mass eigenstates). Thus neutrino masses must be non-zero. They are however extremely small, the upper limit of the electron neutrino is 2 eV [40]. As the right-handed neutrinos do not interact via the W boson, they are said to be "sterile", which explains why they are so difficult to observe. Whether the neutrino is of Dirac (particles and antiparticles are distinct) or Majorana (particle is its own antiparticle) is not yet settled. Any observation of neutrino-less double beta decay would hint to Majorana, in which case the lepton number would be violated by 2 units.

Why the neutrinos are so light compared to the other fermions (where the electron is the lightest of 0.511 MeV), can be due to a so-called "seesaw" mechanism, which is part of a Grand Unified Theory (unifying $SU(3)_C \times SU(2)_L \times U(1)_Y$. The name comes from the prediction that there exists very heavy neutrinos (additional right-handed neutrino fields), that effectively mix in an asymmetric way like on a seesaw, explaining the very light neutrino masses.

[6] For an introduction to SUSY see for instance [37], which has been used in this account of SUSY.

Another observational argument, is the inference of *dark matter* which can be seen indirectly due to its gravitational effects, but that has not yet been directly detected. Dark matter is thought to be composed of some different type of matter than that of the SM. It is dark, which means that it does not radiate, and must be very weakly interacting (since it is extremely difficult to detect). The neutrinos could seem to be the perfect candidate, but even though they contribute to some of the dark matter, their masses are too small to play any significant role. The very first hints of such matter was found in the early 1930s when the astrophysicist Fritz Zwicky tried to explain the rotational speed of spiral galaxies (like our own), and found that the matter accounted for was not sufficient to actually hold the galaxy together ([41]). There had to be a large amount of some type of non-radiating, or dark matter in order to gain enough gravitational attraction to balance the speed of the outer spiral legs. What this dark matter is, has not yet been determined, but a popular hypothesis is that it is made up of so-called *WIMP*s, Weakly Interacting Massive Particles. As we shall see, Supersymmetry has such candidate particles.

In addition to dark matter, the Universe seems to be filled mostly with *dark energy*. The most recent results from the Planck satellite ([42]), which has measured the relic density[7] limit of $\omega_\chi h^2 = 0.1199 \pm 0.027$, suggest that as much as 68.3% of the Universe's energy is so-called dark energy. This is the energy responsible for the newly discovered *accelerated* expansion of the Universe observed through large red-shifts which were first measured in supernovae. The Planck satellite measurements furthermore indicate that dark matter accounts for about 26.8% of the total energy of the Universe. This means that the SM only concerns as little as 4.9% (!). However, it might be a consolation that we at least explain this 4.9% very well, and are aware that 95.1% is missing.

There is a final popular example of observational arguments pointing to physics beyond the SM, and that is that gravity exists. It is not a problem in itself, but through the view of quantum field theory it is, since one so far has not succeeded to incorporate gravity into it. Gravity itself can very well be formulated as a gauge theory, but the attempt of quantization has failed miserably. If the goal of elementary particle physics is to explain Nature at its most fundamental, then it is clear that all forces must be included in a consistent way. We have not yet reached that goal.

1.3.2 Theoretical arguments for physics beyond the Standard Model

When it comes to the theoretical arguments, they tend to address issues concerning "naturalness" ([43, 44]) and aesthetics of the current SM, and many of these relate to issues with mass.

Although we have found a prescription to incorporate fermion masses, there is no theoretical explanation why the fermion masses are so different among themselves, unless we go beyond the SM, as for instance with the seesaw mechanism briefly introduced above. The lightest quark, the up quark, is around 2.3 MeV while the heaviest is the top quark of 173.3 GeV [45]. All these different fermion mass terms are free parameters, hence not predicted by the theory. A certain pattern is visible, thus the division into so-called *generations* where each generation

[7] Density of particles left over from the Big Bang

is heavier than the next, as we saw in the SM chapter, but other than that there is no hint of why the masses are as they are. However, as explained in Section 1.2.6, the gauge boson masses are predicted by the theory.

Another argument, also to do with the way masses are introduced in the SM, is that the scalar potential responsible for the Higgs mechanism is chosen completely arbitrarily. It works, but it is not understood why the potential has that particular shape.

With the Higgs mechanism explaining mass terms in the SM, the mass of scalar Higgs boson itself offers some challenge. In general when explaining particle masses, one must take into account radiative corrections. These are visualized by loop diagrams up to arbitrarily high order. The virtual particles in a loop contribute to the experimentally measured mass of the particle, and the heavier the particle in the loop, the more it contributes. Since fermions couple to the Higgs boson via their mass term, especially the top quark, but also the weak gauge bosons are important. The Higgs boson mass is measured to be around 125 GeV, and a top quark mass of ~173 GeV turns out to give problematic loop corrections. This is because unlike the self-energy of for instance electrons that are cancelled out by the existence of positrons (ending up with only logarithmic divergent terms), the fermion loops to the Higgs mass do not naturally cancel out in this way. One is therefore left with quadratic divergences which are clearly a problem. It turns out that if one in addition to the fermions have some new scalars with the same mass, a bit like the symmetry between particle, anti-particle, the contributions to loop corrections cancel, only leaving logarithmic divergences. This is in fact one of the strongest motivations for Supersymmetry, which offers exactly such a symmetry between fermions bosons. Since this issue, known as the "hierarchy problem" is perceived to be of such importance, I discuss it further in the next section.

A final motivation for Supersymmetry is worth mentioning, and it has to do with unification of forces. It is natural to think that like the electromagnetic and weak force unify, the strong force may ultimately be unified with the two others, in order that all forces can be explained on the same footing. Such a unification is part of the "Grand Unified Theory", which, a hypothetical theory governing at high energy scales. In the SM we saw (Figure 1.5) that the three gauge couplings do not ever meet at a single point. Including Supersymmetry however, with new heavy particles entering around 1 TeV, the slope of the gauge couplings as they run from low to high energies changes in such a way that unification of all three forces in one point seems possible. Thus all SM forces can be explained as stemming from one and the same origin, and Nature would prove its simplicity.

Now that we have firmly motivated the need of physics beyond the SM, let's have a closer look a the so-called Hierarchy problem.

1.3.3 The hierarchy problem

Higher order corrections to a process, so-called loop corrections, are known to diverge. For a theory which is "renormalizable" one relies on a technique in which radiative corrections are calculated up to a certain cutoff energy-scale Λ. The divergent terms are taken care of by re-

arranging them in such a way that they cancel each other out. After appropriate cancellations the theory is well-behaved. This is the normal technique used for the gauge theories of the SM and results in finite calculations to all orders. Although there was quite some resistance to this procedure when it originally was proposed, hence the epigraph introducing Section 1.3, it is now accepted as a valid procedure reflecting the nature of modern physics.

Since renormalization is a highly technical and intricate procedure, it is not straight forward to give a qualitative description of it, therefore the overview given here is highly general.

The theoretical objects that we operate with in physics, and hence QFT, are those of mathematical perfection, for instance the Dirac electron, which is regarded as a point object. But what is a point in the real world? It has no spatial extension, and thus must be thought of as a purely mathematical object. However, the various quantities we measure in the laboratory experiments are "real", like for instance the electric charge. These values will however, vary according to our instrument's resolution. We can say that they depend on the scale (energy or distance) achieved in the experiment. The observed charge of an electron measured from "a-far" would give you a certain value, which can be regarded as the "global" charge of the electron, often called the "dressed" charge. If you zoom in, however, you will realize that the electron cannot be seen as a single entity. Adding to its properties is a swarm of electron-positron pairs popping in and out of vacuum, in addition to the electrons awareness of its own electromagnetic field. Zooming further in the pattern repeats itself again and again, and just simply adding up all the "zoom-levels" will lead to divergences. The fact is that you already have a measured quantity and since this measured quantity is supposed to be a sort of representative for the other terms you are adding up, they must naturally be speaking the same language. And by that I mean that they must both represent the same zoom-level, or cutoff scale.

An example helps illustrate the procedure of renormalization. I use the electron and the measurement of its mass starting from classical electrodynamics, mainly following the procedure of [46].

Since the electron's Coulomb electric field cannot be removed, it must be seen as an inseparable part of the electron mass. This energy can be expressed as

$$\Delta E_{\text{Coulomb}} = \frac{1}{4\pi\epsilon_0}\frac{e^2}{r_e} + \text{h.o.c}$$

where ϵ_0 is the permittivity constant, e the electric charge, r_e the "size" of the electron which has been introduced in order to cutoff the divergent Coulomb self-energy, and "h.o.c." are the higher order corrections. Figure 1.6 (a) depicts the Feynman diagram of this term. We can construct the experimentally observed electron mass m_e as a sum of the "bare" electron mass[8], and the additional Coulomb term

$$(m_e c^2)_{\text{obs}} = (m_e c^2)_{\text{bare}} + \Delta E_{\text{Coulomb}}$$

[8]The bare mass would be the mathematical mass of a Dirac electron

(a) Coulomb self-energy

(b) Electron which annihilates with a positron and is recreated

Figure 1.6: The Coulomb self-energy term of the electron to the left, and the electron's annihilation with a positron (where the positron comes from a photon from the vacuum which has split into an electron positron pair), and its subsequent recreation to the right. The two terms cancel each other.

However, we know from experiment that the electron is very small, with an upper limit of $r_e \leq 10^{-17}$ cm, which would lead to a Coulomb term > 10 GeV (!). This means that in order for the experimentally observed electron mass of 0.511 MeV to be respected, the "bare" mass must be equally large and negative

$$0.511 \text{ MeV} = (-9999.489 + 10000.000) \text{ MeV}$$

Even when ignoring the conceptual problem of negative mass, it seems extremely improbable that Nature has provided such a degree of fine-tuning. To avoid this problem, the only sensible conclusion is that the classical theory is only valid down to a certain minimum distance (sufficiently) larger than r_e, such that the correction from the Coulomb term keeps within an acceptable size.

However, it is of course desirable to be able to make calculations beyond the classical limit. The problem was overcome with the prediction (Dirac [47]) and later observation of the positron. Once positrons were proven to exist, one in addition to the Coulomb term needed to account for the electron self-energy term(s) which play a role at distances of the order r_e. It turned out that the contribution from such a term was exactly the same as the Coulomb term, but of opposite sign

$$\Delta E_{\text{self-energy}} = -\frac{1}{4\pi\epsilon_0}\frac{e^2}{r_e} \; + \; \text{h.o.c}$$

hence cancelling the large extra contributions, and ultimately only depending logarithmically on r_e, which is completely acceptable:

$$(m_e c^2)_{obs} = (m_c c^2)_{bare}\left[1 + \frac{3\alpha}{4\pi}\log\frac{\hbar}{m_e c r_e}\right]$$

Thus, with the newly discovered symmetry between matter and antimatter at very small distances (allowing a doubling of the number of particles), one could proceed with the calculations and ultimately let r_e become as small as the Plank scale (corresponding to 10^{-35} m).

This shows that when operating with *effective* theories such as classical electromagnetism, one needs to limit the calculations to the scale in which the theory is valid. Going beyond this scale leads to divergent terms. However, at the scale r_e a new symmetry had to be taken into

account, namely the one between the electron and positron, which solved the divergence problem. It is the *chiral* symmetry that protects the electron from acquiring a mass from self-energy corrections. In a similar fashion gauge symmetry protects the photon from acquiring mass from radiative corrections.

The hierarchy problem and scalar particles

For all fermions the dependency on the cutoff scale turns out to be logarithmic, as the electron example above. However, there is still a problem with scalar particles, like the Higgs boson, which is the only scalar particle of the SM. For such particles the dependency is quadratic, since there turns out to be no cancellations taming the divergences, which again leads to unacceptable need of fine-tuning. In the introduction to this section I mentioned that the top quark in the Higgs loop illustrates the problems with scalar bosons and large loop corrections. Now, if we could find a symmetry, much like that of the electron-positron symmetry, that could cancel the top quark contribution, we "would be done". Such a symmetry has in fact been "found" (mathematically), namely Supersymmetry, where fermions have scalar superpartners. Figure 1.7 shows the Higgs boson line with loop contributions from a top quark to the left, and from a scalar superpartner of the top quark, the $\tilde{t}$ to the right. Similar diagrams involve Higgs, W and Z bosons and their superpartners.

Following the exact same reasoning as with the electron, we write down the Higgs mass-term resulting from the top-loop (t), which is

$$\Delta\mu_t^2 = -6\frac{h_t^2}{4\pi^2}\frac{1}{r_H^2} \quad + \text{ h.o.c.},$$

where h_t is the Yukawa coupling of the top to the Higgs field and is roughly 1, and r_H is the "size" of the Higgs boson. Again, we would like to apply the SM below this size, which is of the order 10^{-17} cm, and would therefore need a similar term to remove the divergence when $r_H \to 0$. Now when applying supersymmetry, such that the top quark has a scalar superpartner, the stop ($\tilde{t}$), with a Higgs loop correction:

$$\Delta\mu_{\tilde{t}}^2 = +6\frac{h_t^2}{4\pi^2}\frac{1}{r_H^2} \quad + \text{ h.o.c.},$$

we see that this will work very well. In fact, the resulting loop correction from both terms turn out to be

$$\Delta\mu_t^2 + \Delta\mu_{\tilde{t}}^2 = -6\frac{h_t^2}{4\pi^2}\frac{1}{r_H^2}\left(m_{\tilde{t}}^2 - m_t^2\right)\log\frac{1}{r_H^2 m_{\tilde{t}}^2}.$$

So, in a similar way as chiral symmetry protected the electron mass from its self-energy terms, SUSY protects theories with scalar particles from suffering from unacceptably large loop corrections ([48–53]). If the top and stop masses are identical the two terms cancel exactly. However, if SUSY is *broken*, there would still be a logarithmic dependency. This assumes that m_t and $m_{\tilde{t}}$ are not too different. So m_H is in fact still sensitive to the largest (superpartner) masses in the loop. In order for $\Delta\mu^2$ to be of the same order as the measured tree-level value μ^2, we must require that $m_{\tilde{t}}^2$ is not too far above the electroweak scale. This applies also for

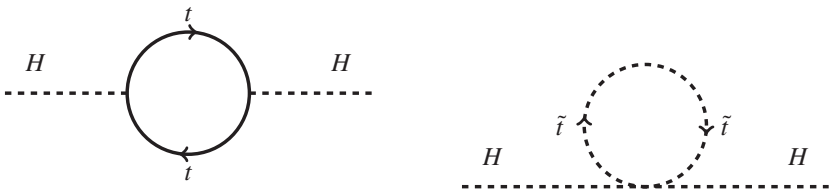

(a) Fermion loop contribution from t (b) Scalar loop contribution from $\tilde{t}$

Figure 1.7: One-loop quantum corrections to the Higgs (scalar) squared mass parameter.

the other loop-contributions, and in turn restricts the SUSY masses to not be much larger than $\mathcal{O}(1\ \text{TeV})$.

This, and the previous sections have shown that there are plenty of reasons why one should strive for a more fundamental theory. Since Supersymmetry can explain at least some of the open questions of the Standard Model, it could be a step in the right direction.

1.3.4 What is Supersymmetry

Although Supersymmetry (SUSY) was first seen as nothing much but a beautiful mathematical model, its application to the SM and thereby its solutions to important SM shortcomings have firmly linked it with possible phenomena in Nature, and resulted in a large popularity. Today many thousand physicists, both experimental and theoretical, work with SUSY.

SUSY proposes a symmetry between fermions and bosons. It predicts that swapping one for the other does not change the fundamental laws of Nature. Symbolically we can write the symmetry as a fermion $|\text{Fermion}\rangle$ or boson $|\text{Boson}\rangle$ state under influence of an operator Q, such that the fermion is transformed into a boson, or vice versa

$$Q\,|\text{Fermion}\rangle = |\text{Boson}\rangle\,, \quad Q\,|\text{Boson}\rangle = |\text{Fermion}\rangle$$

One of the important physical consequences of Supersymmetry is an approximate doubling of Nature's particle content, since for every SM fermion (degree of freedom), there should be a bosonic superpartner, and for every SM boson (degree of freedom) there should be a fermionic superpartner. The new particles are, in an unbroken symmetry, exact blueprints of their SM partners, except for spin which transforms in the following way: a fermion (spin 1/2) transforms to a scalar superpartner (spin 0), a vector boson (spin 1) transforms to a fermion superpartner (spin 1/2), likewise the Higgs scalar (spin 0) transforms to a fermion superpartner (spin 1/2). All these new particles are naturally experimentally interesting since they should be detectable in particle colliders. But there has been no sign of them yet, which can mean that either Supersymmetry is just a mathematical exercise after all, or the symmetry is broken, inducing additional masses to the supersymmetric particles has made them energetically inaccessible so far. Naturally, the latter is the working hypothesis.

Although I do not go into the technical details of the Supersymmetry formalism, it is worth mentioning at least a few main points. In particular there are a multitude of ways to form a supersymmetric theory. I only discuss certain aspects of the *superfield* formalism which allows for a procedure to write down theories which are guaranteed to be supersymmetric, and can handle non-Abelian gauge symmetries. This formalism leads to the simplest supersymmetric extension of the SM, the so-called Minimal Supersymmetric Standard Model (MSSM) [48, 54–57], which is state of the art today. First though, let us have a look at the particle content of the MSSM.

1.3.5 The supersymmetric particle content

The naming convention in supersymmetry is the following: The supersymmetric partners of the fermions are called the same as their SM particles, except with an *s* stuck in the front, so that for instance the *selectron* is the superpartner of an electron. For the supersymmetric partners of the gauge bosons, an *ino* is appended to the name, like the *photino* which is the superpartner of the photon. All the gauge-boson partners are commonly addressed as *gauginos*, and the fermion partners as *sfermions*, while a short-hand for all supersymmetric particles in general is *sparticles*. A tilde (˜) is used to denote supersymmetric particles.

	Particles			Spin		Sparticles			
quarks	$u_{L,R}$	$c_{L,R}$	$t_{L,R}$	1/2	0	$\tilde{t}_{1,2}$	$\tilde{c}_{L,R}$	$\tilde{u}_{L,R}$	squarks
	$d_{L,R}$	$s_{L,R}$	$b_{L,R}$	1/2	0	$\tilde{b}_{1,2}$	$\tilde{s}_{L,R}$	$\tilde{d}_{L,R}$	
leptons	ν_e	ν_μ	ν_τ	1/2	0	$\tilde{\nu}_\tau$	$\tilde{\nu}_\mu$	$\tilde{\nu}_e$	sleptons
	$e_{L,R}$	$\mu_{L,R}$	$\tau_{L,R}$	1/2	0	$\tilde{\tau}_{1,2}$	$\tilde{\mu}_{L,R}$	$\tilde{e}_{L,R}$	
gauge bosons	g			1	1/2	$\tilde{g}$			gauginos
	$W^\pm$, Z^0			1	1/2	Neutralinos $\tilde{\chi}^0_{1-4}$ Charginos $\tilde{\chi}^\pm_{1-2}$			
	γ			1					
	$H^\pm, H^0, A^0, h^0$			0					

Table 1.1: The full particle content of the MSSM after electroweak symmetry breaking (mass eigenstates). The third generation left- and right-handed quarks and lepton partners mix, such that the mass eigenstates are denoted $1, 2$ rather than L, R. The superpartners of the gauge bosons, and the higgs boson mix to form the neutralinos and charginos, see details in text.

The minimal MSSM particle content (with spontaneous electroweak breaking assumed) is shown in Table 1.1. Each right or left-handed SM fermion has its scalar superpartner, denoted with a superscript L or R. So even though scalars naturally do not convey handedness, there still exists two distinct particles, one partner for each SM helicity state, obeying the same gauge interaction rules.

One thing to notice is the extended Higgs sector. We have five Higgs-es, charged Higgs: $H^{\pm}$, heavy CP-even: H^0, heavy CP-odd: A^0, and a light Higgs: h. These five Higgses come from the fact that we in SUSY need two Higgs doublets, one doublet to give mass to the up-type fermions, and one for the down-type. In the SM, one Higgs doublet accounts for both, as the original Higgs field itself gives mass to down-type fermions, and its right-handed charge conjugate to up-type fermions. However in SUSY, this is not possible, as the superpotential does not allow the charge conjugates of a field, otherwise it does not stay invariant under gauge and SUSY transformations [58]. The minimal solution includes two doublets [37]

$$H_u = \begin{pmatrix} H_u^+ \\ \\ H_u^0 \end{pmatrix}, \quad H_d = \begin{pmatrix} H_d^0 \\ \\ H_d^- \end{pmatrix}. \tag{1.22}$$

We thus have two vacuum expectation values, namely $v_u =< H_u^0 >$ and $v_d =< H_d^0 >$. From these we define the ratio:

$$\tan\beta \equiv \frac{v_u}{v_d}, \tag{1.23}$$

which we encounter later.

After electroweak symmetry breaking, 3 out of the original 8 degrees of freedom of the Higgs field, are absorbed into the W_μ as before, and we are left with 5 physical Higgs bosons as given in Table 1.1. Each Higgs has a superpartner, the Higgsino. With EW symmetry breaking, the gauge bosons with the same quantum numbers mix, so that the gauge and mass eigenstates differ (as in the SM). The gauge eigenstates (which is before EW symmetry breaking) are listed in Tables 1.2 and 1.3 for the chiral and gauge fields respectively (we get back to these in more detail later). The superpartners of the SM B, W, and H fields, the Bino $\widetilde{B}^0$, Wino $\widetilde{W}$, and Higgsino $\widetilde{H}_{u,d}$ fields respectively, mix to form the charginos and neutralinos we already encountered in Table 1.1. Specifically: $\widetilde{B}^0, \widetilde{W}^0, \widetilde{H}_u^0$, and $\widetilde{H}_d^0$ mix to form the four neutralinos χ_{1-4}^0, and $\widetilde{W}^{\pm}, \widetilde{H}_u^+$, and $\widetilde{H}_d^-$ mix to form the two charginos $\chi_{1-2}^{\pm}$. The CP-odd higgs A^0 does not mix, as all the other states are CP-even, thus it does not share the same quantum numbers.

In addition to the gauginos, the right and left-handed third generation sleptons and squarks also mix to form mass eigenstates different than their weak eigenstates. This is indicated with the subscript $_{1,2}$ in the Table 1.1. Mixing in the first two generations is considered negligible, due to their relatively small coupling to the Higgs compared to the third generation particles.

The table does not include the hypothetical graviton (spin 2), and its superpartner gravitino (spin 3/2). But in supergravity models, which are theories that combine general relativity and supersymmetry, the graviton and gravitino are included, and are indeed important, as the gravitino can take the role of the lightest SUSY particle (LSP), and hence a dark matter candidate.

Names		spin 0	spin 1/2	$SU(3)_c$	$SU(2)_L$	$U(1)_y$
squarks, quarks	Q	$(\tilde{u}_L, \tilde{d}_L)$	(u_L, d_L)	**3**	**2**	1/3
(× 3 families)	$\bar{u}$	$\bar{\tilde{u}}_L(\tilde{u}_R)$	$\bar{u}_L \sim (u_R)^c$	$\bar{\mathbf{3}}$	**1**	-4/3
	$\bar{d}$	$\bar{\tilde{d}}_L(\tilde{d}_R)$	$\bar{d}_L \sim (d_R)^c$	$\bar{\mathbf{3}}$	**1**	2/3
sleptons, leptons	L	$(\tilde{\nu}_{eL}, \tilde{e}_L)$	(ν_{eL}, e_L)	**1**	**2**	-1
(× 3 families)	$\bar{e}$	$\bar{\tilde{e}}_L(\tilde{e}_R)$	$\bar{e}_L \sim (e_R)^c$	**1**	**1**	2
higgs, higgsinos	H_u	(H_u^+, H_u^0)	$(\tilde{H}_u^+, \tilde{H}_u^0)$	**1**	**2**	1
	H_d	(H_d^0, H_d^-)	$(\tilde{H}_d^0, \tilde{H}_d^-)$	**1**	**2**	-1

Table 1.2: Chiral supermultiplet fields in the MSSM. The right-handed terms are written in two ways, either in terms of the left-handed fields, or as charge-conjugates of the right-handed fields. Extracted from Ref. [37]

Names	spin 1/2	spin 1	$SU(3)_c$	$SU(2)_L$	$U(1)_y$
gluinos, gluons	$\tilde{g}$	g	**8**	**1**	0
winos, W bosons	$\widetilde{W}^{\pm}, \widetilde{W}^0$	$W^{\pm}, W^0$	**1**	**3**	0
bino, B boson	$\tilde{B}$	B	**1**	**1**	0

Table 1.3: Gauge supermultiplet fields in the MSSM. Extracted from Ref. [37]

Let us now turn to the basics of the superfield formalism to get a rough overview of SUSY's mathematical framework. In a supersymmetric world, our concepts of space-time have to be extended, since SUSY can be thought of as living in *superspace*. This is an extension of the ordinary (commuting) space-time coordinates $x^\mu = (t, x, y, z)$, with four new anti-commuting coordinates θ_α. The new coordinates θ_α are so-called Grassman numbers[9]. They are spinors, and built by four independent quantities θ_a, which can be split into two-component θ, $,\bar{\theta}$ or θ_L, θ_R and needed for a consistent treatment of scalar and fermion fields in the theory.

To go with superspace, *superfields* are introduced to account for the new fermion-boson symmetry. Superfields depend on the superspace coordinates $\hat{x} = (x^\mu, \theta_\alpha)$. The chiral supermultiplet fields are listed in Table 1.2, while the gauge supermultiplet fields are shown in Table 1.3. As we see they are constructed of the ordinary SM fields (spin 1/2 fermions and spin 1 vector bosons) and the new SUSY fields (spin 0 sfermions and spin 1/2 gauginos), sharing the same quantum numbers, as they should. Using the leptons as an example, and now with e denoting any family, the left-handed superfields L contain the left-handed lepton fields (e_L) and slepton

[9]Grassmann numbers differ from ordinary numbers in that they anticommute with each other (but commute with ordinary numbers). A discussion on whether the new coordinates have any physical significance, goes beyond the scope of this overview.

$(\widetilde{e}_L)$ fields which are $SU(2)_L$ doublets **2** containing the neutral and charged leptons. The right-handed lepton supermultiplets $\widetilde{e}$ contain right-handed lepton fields (e_R) and sleptons fields $(\widetilde{e}_R)$ and are $SU(2)_L$ singlets **1**. An explicit example of how the superfield $(\mathcal{S})$ is constructed is shown in Equation 1.24 for a fermion doublet [59]. Here we define the variable $\hat{x_\mu} = x_\mu + \frac{1}{2}\bar{\theta}\gamma_5\gamma_\mu\theta$ for convenience, where γ are the gamma-matrices we have encountered earlier, and x_μ is the usual space-time variable. As we see it is made up of a scalar field $\mathcal{S}$ (which is the supersymmetric sfermion), and a Dirac field ψ_L (the SM fermion). In addition we need a so-called *auxiliary field* $\mathcal{F}$. Auxiliary fields are needed in order to balance degrees of freedom, but they are not dynamical and therefore do not change the physics of the theory. They are merely there for "book-keeping" reasons. The Grassmann numbers θ and the conjugates are multiplied appropriately with the fermion, and auxiliary fields, in order for all terms to be scalars of the Lagrangian. Similar expressions are built for the right-handed $SU(2)_L$ singlets, see Equation 1.25.

$$\hat{\mathcal{S}}_L(x,\theta) = \mathcal{S}(\hat{x}) + i\sqrt{2}\bar{\theta}\psi_L(\hat{x}) + i\bar{\theta}\theta_L\mathcal{F}(\hat{x}) \quad (1.24)$$

$$\hat{\mathcal{S}}_R(x,\theta) = \mathcal{S}(\hat{x}^\dagger) - i\sqrt{2}\bar{\theta}\psi_R(\hat{x}^\dagger) - i\bar{\theta}\theta_R\mathcal{F}(\hat{x}^\dagger)\,. \quad (1.25)$$

The rest of the fermion fields are extended in the same way. The gauge fields are also formulated in a similar manner, with the new supersymmetric gauginos and the auxiliary field, included in a gauge potential superfield together with the well-known gauge fields. As with the gauge fields in the Standard Model, the super gauge fields are a consequence of spontaneous (super) electroweak symmetry breaking. One can then build a Lagrangian as usual consisting of the relevant terms, but now instead of the ordinary SM fields, we use the new superfields, which include all features of the SM, but augments the terms with the supersymmetric part.

An important point to realize before we go on, is that when building a general SUSY Lagrangian there appears terms which break baryon and lepton number conservation, contrary to the SM where lepton and baryon number conservation is a consequence of a renormalizable theory. Such terms are of the form [37]:

$$W_{\Delta L=1} = \frac{1}{2}\lambda^{ijk}L_iL_j\bar{e}_k + \frac{1}{2}\lambda^{'ijk}L_iQ_j\bar{d}_k + \mu^{'i}L_iH_u$$

$$W_{\Delta B=1} = \frac{1}{2}\lambda^{''ijk}\bar{u}_i\bar{d}_j\bar{d}_k\,.$$

The second top term for instance, breaks lepton number conservation by allowing left-handed lepton super-fields (L_i) interact with left-handed quark super-fields (Q_j) and right-handed quark superfield $(\bar{d}_k)$ with coupling strength $\lambda^{'ijk}$. The bottom term allows breaking of baryon number conservation by letting three right-handed squark super-fields ($\bar{u}_i$, $\bar{d}_j$, and $\bar{d}_k$) interact (with coupling strength $\lambda^{''ijk}$). All particles(antiparticles) have baryon number +1/3(-1/3) and lepton number +1(-1). Thus the reader can easily check that the top term breaks lepton number by 1 unit, and the bottom term breaks baryon number by 1 unit. An example of a diagram explicitly illustrating these terms is the proton decay via a right-handed squark in Figure 1.8. Here an initial proton decays to a positron and pion, via a right-handed squark. Although it is not a problem in itself that the theory allows proton decay, GUT theories which propose to unify

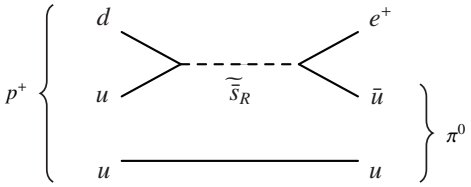

Figure 1.8: Example of proton decay through a squark. ([37])

all three forces in one have these types of processes also, by exchange of new heavy bosons, allowing transitions between quarks and leptons, and vice-versa. However, the problem in this SUSY process is the extremely *rapid* proton decay such a process would induce. Typically protons would decay in a split second, if the couplings $\lambda^{'ijk}$ and $\lambda^{''ijk}$ were of the order of unity, and the squark mass of the order of TeV. The current limit of the proton lifetime is $> 10^{33}$ years ([40]), which is 21 orders of magnitude larger than the lifetime of the Universe[10]. So, these terms are clearly a problem.

One way to remedy this is to either set all such terms to 0 by hand, by assuming some unknown mechanism is at play which suppresses them. However, another more elegant way is to introduce a new symmetry. This is matter-parity $P_M = (-1)^{3(B-L)}$, or R-parity [48, 54–57] which is often used instead

$$P_R = (-1)^{3(B-L)+2s},$$

where s is spin, and as before, B and L are the baryon and lepton numbers. In this scheme, all supersymmetric particles carry $P_R = -1$, while all SM particles carry $P_R = +1$. Thus interaction terms inducing the proton decay above would be forbidden, since each vertex breaks R-parity.

R-parity conservation leads to very interesting phenomenology. For instance: all SUSY particles must be produced in pairs, and a sparticle must decay to an odd number of supersymmetric particles. But more importantly: there must be a lightest supersymmetric particle (LSP) that is absolutely stable. If this particle in addition is electrically neutral and weakly interacting, it is a prime candidate for dark matter. Such a particle is a so-called WIMP (Weakly Interacting Massive Particle). In mSUGRA (minimal Gravity Mediated Symmetry breaking model [60–65]) the LSP can for instance be the lightest neutralino $\tilde{\chi}_1^0$, which fulfils the WIMP requirements (since it is heavy, neutral and weakly interacting). It is also possible to construct a viable supersymmetric model with a dark matter candidate even if R-parity is violated. In such models the *gravitino*, the hypothetical superpartner of the hypothetical graviton, is the lightest supersymmetric particle and can act as a the LSP, and is also a prime dark matter candidate. As already mentioned, the dark matter candidate is one of the most compelling reasons for supersymmetry's popularity.

[10]The most recent measurements of the age of the universe from the Big Bang occurred from Planck ([42]), is $13.798 \pm 0.037\ 10^9$ years.

1.3.6 Soft symmetry breaking and the MSSM

A SUSY Lagrangian with the minimal amount of new particles is the Minimal Supersymmetric SM (MSSM [48, 54–57]). It is a result of a direct supersymmetrization of the SM, and with two Higgs doublets. As pointed out, no supersymmetric particles have yet been found, which implies that Supersymmetry is broken, if it exists. Naturally one would like the symmetry to be broken spontaneously, particularly because this ensures that no new quadratic loop terms appear. However, this has proven difficult, and there is so far no consensus between theorists as how the actual symmetry breaking should be performed, and no help from experimental data to guide by. The general approach is therefore to add the necessary mass terms to the Lagrangian by hand, and allow all that do not spoil the protection against large loop-corrections. The protection was achieved with the fermion-boson symmetry, and after all one of the main incentives for SUSY, thus important to preserve. The resulting soft susy-breaking Lagrangian $\mathcal{L}_{\text{soft}}$ assuming R-parity is given by [37]:

$$\begin{aligned}
\mathcal{L}_{\text{soft}}^{\text{MSSM}} \;=\; & -\frac{1}{2}\left(M_3\widetilde{g}\widetilde{g} + M_2\widetilde{W}\widetilde{W} + M_1\widetilde{B}\widetilde{B} + \text{c.c.}\right) \\
& -\left(\widetilde{\overline{u}}\,\mathbf{a_u}\,\widetilde{Q}H_u - \widetilde{\overline{d}}\,\mathbf{a_d}\,\widetilde{Q}H_d - \widetilde{\overline{e}}\,\mathbf{a_e}\,\widetilde{L}H_d + \text{c.c.}\right) \\
& -\widetilde{Q}^{\dagger}\,\mathbf{m_Q^2}\,\widetilde{Q} - \widetilde{L}^{\dagger}\,\mathbf{m_L^2}\,\widetilde{L} - \widetilde{\overline{u}}\,\mathbf{m_{\overline{u}}^2}\,\widetilde{\overline{u}}^{\dagger} - \widetilde{\overline{d}}\,\mathbf{m_{\overline{d}}^2}\,\widetilde{\overline{d}}^{\dagger} - \widetilde{\overline{e}}\,\mathbf{m_{\overline{e}}^2}\,\widetilde{\overline{e}}^{\dagger} \\
& - m_{H_u}^2 H_u^* H_u - m_{H_d}^2 H_d^* H_d - (bH_uH_d + \text{c.c.})\,.
\end{aligned} \tag{1.26}$$

In the first line we have the gaugino mass-terms: M_3, M_2, and M_1, which are the gluino, wino, and bino terms respectively. In the second line we have the trilinear couplings: $\mathbf{a_u}$, $\mathbf{a_d}$, and $\mathbf{a_e}$. These are 3×3 matrices in family space, and are in one-to-one correspondence with the Yukawa couplings. In the third line, the squark and slepton mass terms are given (tildes omitted to avoid clutter): $\mathbf{m_Q^2}$, $\mathbf{m_L^2}$, $\mathbf{m_u^2}$, $\boldsymbol{m_d^2}$, and $\mathbf{m_e^2}$, for left-handed squarks (up and down-types), for left-handed sfermions (up and down-types), for right-handed up-squarks, right-handed down-squarks, and finally for right-handed sleptons. These terms are also 3×3 matrices in family space. Finally in the last line, the SUSY-breaking contribution to the Higgs potential is given, namely $m_{H_u}^2$, $m_{H_d}^2$, and b. These last terms go into the visible Higgs parameters m_A, μ, $\tan\beta$ and v after electroweak symmetry breaking.

Unfortunately the breaking terms introduce a whole set of new free parameters. Due to our ignorance of the SUSY breaking mechanism, the MSSM contributes with an additional 105 ([66]) free parameters. Such an amount of free parameters makes phenomenological studies and searches very difficult. However, several well motivated assumptions and constraints can be enforced in order to simplify the picture. For instance: off-diagonal terms in the $\mathbf{m_e^2}$ matrix result in the family number violation decay $\mu \to e\gamma$ via loops, for instance through the term $(\mathbf{m_e^2})_{21}\tilde{\mu}_R^*\tilde{e}_R$. The strong upper experimental limit for such a process is $\text{Br}(\mu \to e\gamma) < 1.2\times10^{-11}$ [67]. To this decay, the off-diagonal terms in $(a_e)_{12}$ and $(a_e)_{21}$ would also contribute. And similarly, the off-diagonal terms $(a_e)_{13}$, $(a_e)_{31}$ and $(a_e)_{23}$, $(a_e)_{32}$ contribute to $\tau \to e\gamma$ and $\tau \to \mu\gamma$ respectively, which also are constrained through experiment. Also in the squark sector off-diagonal terms are constrained, as they otherwise would result in too large CP-violation in Kaon decays. So, to avoid these dangerous flavour and CP violating terms we can impose the

following constraint: all off-diagonal terms of $\mathbf{m}$ are 0:

$$\mathbf{m}_{\mathbf{Q}}^{\mathbf{2}} = m_Q^2\mathbf{1}, \quad \mathbf{m}_{\tilde{\mathbf{u}}}^{\mathbf{2}} = m_{\tilde{u}}^2\mathbf{1}, \quad \mathbf{m}_{\tilde{\mathbf{d}}}^{\mathbf{2}} = m_{\tilde{d}}^2\mathbf{1}, \quad \mathbf{m}_{\mathbf{L}}^{\mathbf{2}} = m_L^2\mathbf{1}, \quad \mathbf{m}_{\tilde{\mathbf{e}}}^{\mathbf{2}} = m_e^2\mathbf{1}\,.$$

If we also require that the $\mathbf{a}$ terms are proportional to the Yukawa couplings

$$\mathbf{a_u} = A_{u0}\mathbf{y_u}, \quad \mathbf{a_d} = A_{d0}\mathbf{y_d}, \quad \mathbf{a_e} = A_{e0}\mathbf{y_e}\,,$$

then we in fact avoid most of the flavour violating neutral currents and CP-violating phases (except those that are already contained in the SM through the quark sector CKM mixing matrix [68, 69]).

There are other constraints not mentioned here, but as a total result, the additional 105 parameters which were a consequence of the soft SUSY breaking terms, can be reduced to around 20. To reduce the parameter space further one must assume a particular supersymmetry breaking mechanism. Although this leads to theories which are much easier to interpret phenomenologically, and have enabled the exclusion of a large part of the SUSY parameter-space, they are generally considered too restrictive, as they result in models with unnecessary limited phenomenology (e.g. mSUGRA). In the end, only observation of sparticles will help us determine what mechanism Nature has chosen (assuming supersymmetry exists). However, a large amount of studies have been performed assuming specific breaking mechanisms, and they are therefore worth mentioning. Two of the most popular ones are the gravity-mediated supersymmetry breaking (minimal supergravity: mSUGRA or also called Constrained MSSM: CMSSM), and Gauge Mediated Supersymmetry breaking (GMSB, [70–75]). I will get back to these models, but first I want to briefly present the sparticle decays and example of some mass-spectra.

1.3.7 Sparticle decays and mass spectra

I have already implied, but not specifically stated that all sparticles obey the same gauge interactions as their SM partners. Therefore the way the superpartner gauge eigenstates Zino, Wino, Bino, and Higgsino, mix to form mass eigenstates charginos and neutralinos dictates the probable decay mechanisms. For instance does a purely Wino-like neutralino not decay into right-handed sfermions, since only left-handed couple to the W boson. A Zino-like neutralino will however have an equal probability to decay to left- and right handed sfermions, and so on.

Possible two-body decays assuming R-parity conservation are shown below. Depending on the mass hierarchy, the decays are kinematically allowed or not, however, assuming all are allowed, the following two-body decays are possible (now using N to denote neutralinos, and C to denote charginos) [37]:

$$\begin{aligned}
\widetilde{N}_i &\rightarrow Z\widetilde{N}_j, \;\; W\widetilde{C}_j, \;\; h^0\widetilde{N}_j, \;\; \ell\widetilde{\ell}, \;\; \nu\widetilde{\nu}, \;\; [A^0\widetilde{N}_j, \;\; H^0\widetilde{N}_j, \;\; H^{\pm}\widetilde{C}_j^{\mp}, \;\; q\widetilde{q}] \\
\widetilde{C}_i &\rightarrow W\widetilde{N}_j, \;\; Z\widetilde{C}_1, \;\; h^0\widetilde{C}_1, \;\; \ell\widetilde{\nu}, \;\; \nu\widetilde{\ell}, \;\; [A^0\widetilde{C}_1, \;\; H^0\widetilde{C}_1, \;\; H^{\pm}\widetilde{N}_j, \;\; q\widetilde{q}'] \\
\widetilde{\ell} &\rightarrow \ell\widetilde{N}_i, \;\; \nu\widetilde{C}_i,
\end{aligned}$$

$$\begin{aligned} \widetilde{\nu} &\rightarrow \nu\widetilde{N}_i, \quad \ell\widetilde{C}_i \\ \tilde{q} &\rightarrow q\tilde{g}, \quad q\widetilde{C}_i, \quad q\widetilde{N}_i \\ \tilde{g} &\rightarrow q\tilde{q} \end{aligned} \tag{1.27}$$

For the neutralinos and charginos the less kinematically probable decays are listed in brackets of Equation 1.27. The mass spectrum, and thus the kinematically allowed decays, is highly sensitive to the particular mixing of the mass parameters, and in general to the relation between the underlying mass parameters. For instance can the gluino be heavier than all squarks and sleptons in one scenario, while in another it can be light, see Figure 1.9 which illustrates the mass spectrum in two different mSUGRA SUSY models, after SUSY breaking. Here the actual mass ranges are omitted deliberately, since the figure is meant only to give a qualitative idea of the diversity of mass gaps between sparticles.

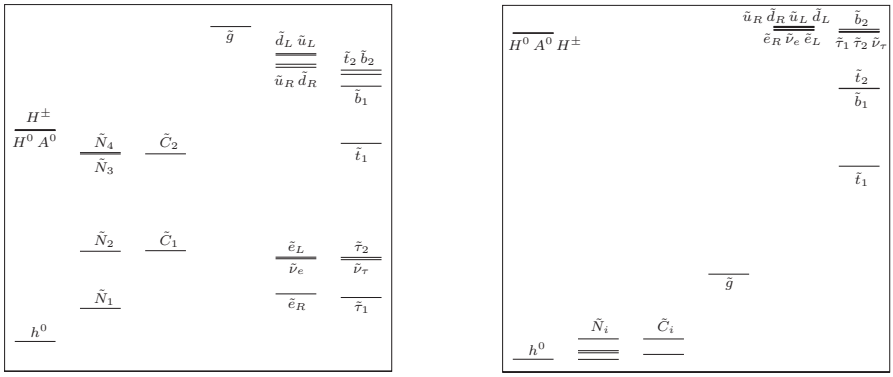

Figure 1.9: Examples of two mass spectres obtained assuming two different mSUGRA SUSY models. The left has $m_0^2 << m_{1/2}$ and the LSP is h^0, and in the right $m_0^2 \gg m_{1/2}$, with LSP N_1. From [37].

1.3.8 Viable SUSY models

I have briefly mentioned mSUGRA above. Let us have a closer look at what mSUGRA is, and also discuss several other SUSY models: GMSB (Gauge mediated symmetry breaking model), pMSSM (phenomenological MSSM) and simplified models.

1.3.8.1 mSUGRA

In Planck-scale-mediated symmetry breaking models, gravitational interactions induce the breaking, not surprisingly at the Planck-scale M_P. Since gravity couples to energy-momentum, there can be interaction between the MSSM fields and *hidden sector* fields (X) through gravity, even though there might not be any other types of interaction between the fields. The hidden sector is typically at some high scale where the supersymmetry breaking occurs, and it is communicated to the particles in the MSSM through *messenger interactions*. As the hidden sector field acquires a vacuum expectation value (vev) $\langle F_X \rangle$ (here assumed to be of the order of 10^{10} GeV [37]), the

soft SUSY terms of the MSSM fields arise. The typical mass-scale is

$$m_{\text{soft}} = \frac{\langle F_X \rangle}{M_P},$$

which means that with the well-founded restriction of m_{susy} of a few hundred GeV(at last below TeV), the scale of the broken symmetry must be $\sqrt{\langle F_X \rangle} \sim 10^{11}$ GeV.

In a Minimal Supergravity Model (mSUGRA), one constrains the theory assuming universality, i.e. that at the SUSY-breaking scale, all the different coupling strengths (g_i), the different gaugino masses (M_i), the different scalar masses (m_i) and the different Yukawa-like couplings (a_i), of the SUSY soft mass breaking terms from Equation 1.26, are identical, so

$$\begin{aligned}
&g_1 = g_2 = g_3 \equiv g_{GUT} \\
&M_3 = M_2 = M_1 \equiv m_{1/2} \\
&\mathbf{m_Q^2} = \mathbf{m_{\bar{u}}^2} = \mathbf{m_{\bar{d}}^2} = \mathbf{m_L^2} = \mathbf{m_{\bar{e}}^2} \equiv \mathrm{m}_0^2\mathbf{1}, \quad m_{H_u}^2 = m_{H_d}^2 \equiv m_0^2 \\
&\mathbf{a_u} = A_0\mathbf{y_u}, \quad \mathbf{a_d} = A_0\mathbf{y_d}, \quad \mathbf{a_e} = A_0\mathbf{y_e} \\
&b \equiv B_0\mu\,.
\end{aligned} \tag{1.28}$$

We have here assumed that all off-diagonal terms of $\mathbf{a}$ and $\mathbf{m^2}$ are zero (as discussed earlier). The masses are then run down to low energies using the Renormalization Group Equations - RGEs - which are a set of equations extracted following the scheme explained for the β functions in Section 1.2.7. This produces the observable mass-spectra as Figure 1.10 shows. The evolution of the first and second generation squark and slepton masses is governed by their gauge interactions (ignoring the small Yukawa couplings), which increase as we move towards lower energies. Differences between the squark and slepton mass spectrum are due to the gauge couplings, with the strong couplings resulting in a more dramatic evolution (and higher masses). Yukawa couplings reduce the masses as we go from high to low energies, thus the third generation species are expected to be lighter than the first and second which have smaller Yukawa couplings.

This leaves only 4 free parameters to decide through experiment, namely $m_{1/2}, m_0^2, A_0, \tan\beta$ and the sign of μ, where $m_{1/2}$ is the universal gaugino mass, m_0 the universal scalar mass, A_0 the universal trilinear coupling related to the Yukawa couplings, $\tan\beta$ the ratio of the two expectation values as given in Equation 1.23, and finally μ is the Higgs and Higgsino mass term, where the sign is not given by the theory.

It turns out that the scheme outlined about results in a predictable relationship between the gaugino masses at low energy, which is roughly $M_1 : M_2 : M_3 = g_1 : g_2 : g_3 \sim 1 : 2 : 7$. This, and μ, control the allowed mass-gap between the gluinos and charginos or neutralinos, which as the relation shows can not be much larger than 7 times M_1.

mSUGRA has been used extensively for many years to set limits on SUSY. Although restrictive, it has therefore been very useful, and still serves its purpose. This applies also to GMSB, which I describe next.

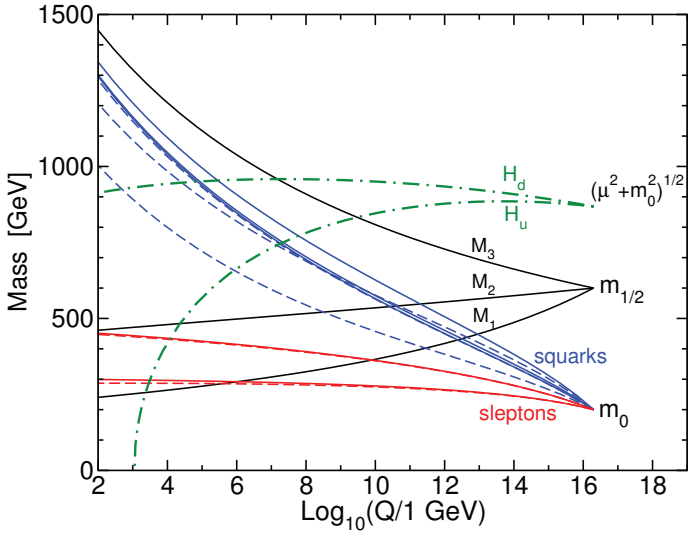

Figure 1.10: The running of the mSUGRA mass parameters from the unified high energy scale, to the low observable scale [37].

1.3.8.2 GMSB

Another way of mediating supersymmetry breaking is through the ordinary gauge interactions. This is the case, as the name implies, in the Gauge Mediated Supersymmetry Breaking model (GMSB). One here imagines non-MSSM messenger (s)quark and s(lepton) fields that couple directly to a chiral superfield S in the hidden sector. The field S itself, and its auxiliary field (F) both acquire a vev, which then result in (very) massive messenger fields. The messenger fields further interact with gauginos through loops at first order, and with scalar SUSY particles through second order loops, which induce sparticle soft SUSY breaking masses. Examples of such loop interactions can be found in Figure 1.11, where the left Feynman diagram shows a gaugino interacting with messenger fields through a first order loop, and scalar sparticles interacting with messenger in a second order loop, with either a gauge boson (two centre diagrams) or a gaugino (right diagram) in the first loop. The messenger fields are messenger scalars and fermions, as indicated by the dashed scalar loops, or solid fermion loops in the Feynman diagrams of Figure 1.11. In a minimal version of GMSB the resulting (new) free parameters are

$$M_s,\ M_m,\ \tan\beta,\ n,\ \mathrm{sign}(\mu)$$

where M_s is the supersymmetry breaking scale, M_m is the messenger scale, and $\tan\beta$ the usual ratio shown in (1.23), n the number of messenger fields. So again, a small set of free parameters allows for more or less straight forward interpretation.

One of the challenges in SUSY searches is the vast range of possible scenarios one must consider, due to our ignorance of the SUSY breaking mechanism. Thus the probability to miss a signal just because the experimental method is tuned to a given type of phenomenology, is

Figure 1.11: Example of messenger fields connecting to sparticles by loops, directly to gauginos (left), and indirectly to scalars via gauge (two centre graphs) and gaugino (right) loops.

very large. The traditional search-strategies such as those aimed at mSUGRA and (m)GMSB signature certainly suffer from this. Hence the motivation to broaden the view and rather take MSSM as the base, with no explicit breaking mechanism assumed. The *simplified models* ([76–80]) are a step in the direction of model-independent searches. So is the *phenomenological* MSSM (pMSSM [81–83]), and they are both eagerly used in today's SUSY searches in ATLAS and CMS.

1.3.8.3 Simplified models

A simplified model is an effective model which assumes the smallest particle spectrum necessary to produce the final state of interest. It is a very generic approach, and can even be used for general searches beyond the SM, if these models include SM partner particles.

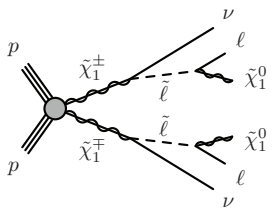

Figure 1.12: An example of a suitable diagram to be interpreted in a Simplified Model.

It is possibly the simplest way to set limits on processes where the underlying parameters or even models are not really known. Limits are set on the crossection times branching ratio, or directly on the SUSY particle masses, and answers the question: "If there exists a possibility to pair-produce sleptons or gauginos that directly decay to a lepton and the LSP, would we have seen it? If not, what are the corresponding limits on the slepton and gaugino masses?". It is much more generic than for instance mSUGRA or even pMSSM, as the scan is simply over the masses of the few contributing SUSY sparticles in the selected diagrams, and produces the expected event-yield for each point, with no further restrictions or assumptions. One example is the SUSY production diagram shown in Figure 1.12, where the final-state of interest is a pair of opposite sign leptons and missing energy (in form of the undetected LSPs and ν's). We will in fact encounter this process later, in Section 4.2.3. Limits can here be set directly on the masses of $\tilde{\chi}_1^{\pm}$ and $\tilde{\chi}_1^0$, as we see later.

Although the approach can seem sensible due to our ignorance of the SUSY breaking mechanism and corresponding parameters, there is a challenge with the interpretation, as a point in the simplified model parameter space does not necessarily correspond to an actual physical model point. However, simplified models have still been used in several analyses, since it is

considered a straightforward, generic, and minimal approach to get a first hint of physics beyond the SM, and specifically of SUSY.

In Section 4.2.3 I go further in detail of the simplified models, particularly concentrating on the ones used in the direct gaugino search discussed in this thesis.

1.3.8.4 Phenomenological MSSM

In phenomenological MSSM (pMSSM [81–83]) we as before apply the well-motivated theoretical constraints, as e.g. in mSUGRA, namely CP conservation (no new phases), minimal flavour violation (no off-diagonal mass terms), negligible 1st and 2nd generation trilinear couplings, and degenerate 1st and 2nd generation sfermion masses. With these restrictions the parameter space is reduced from 105 after SUSY breaking, to 19. All in all these constraints give a (large) set of viable models which are scanned in predefined soft SUSY breaking parameter ranges. However, in contrast to mSUGRA we do not chose a specific breaking mechanism, thus the phase-space is much larger. The 19 free parameters still left to determine include: 3 gaugino mass parameters M_1, M_2, and M_3, 3 Higgs parameters μ, m_A, $\tan\beta$, 6 squark mass parameters (two right-handed and four left-handed), 4 slepton masses (two right-handed and two left-handed), and 3 trilinear couplings of 3rd generation sfermions A_t, A_b, A_τ. For actual searches, there is need to simplify further, which are discussed in Section 4.2.2.

We have then arrived to a more or less model-independent SUSY phase-space, where there is a much bigger freedom of scenarios. In particular we are no longer bound by the $M_1 : M_2 : M_3 \sim 1 : 2 : 7$ relation which mSUGRA yields. Or in other words: pMSSM considers areas of parameter space which are not reached by constrained models such as mSUGRA. The mass-patterns can be almost arbitrary above the LSP mass scale, since no specific SUSY breaking mechanism is assumed. For instance, unlike the mSUGRA model, there can be rather light gluinos and squarks in pMSSM, and with a small mass energy splitting down to the LSPs, this could lead to soft jets. Possibly missed by earlier searches. There can also be scenarios where all coloured particles are extremely heavy, while charginos, neutralinos, and sleptons are light and accessible at LHC. The latter is exactly the scenario which this analysis is based on. Earlier, most SUSY analysis focused on chains of decaying squarks and gluinos, since it was assumed that these would be abundantly produced due to the strong interaction. However, with the research into pMSSM, one has realized that processes pair-producing gauginos or sleptons, like for instance already illustrated in Figure 1.12, might turn out to be the only visible scenarios, if squarks and gluinos are sufficiently heavy.

This finalizes the introduction to the SM and SUSY. In the next section I move towards the more experimental side of particle physics, and describe what goes on in a pp collision.

Chapter 2

Describing the pp collision

Particle physics describes elementary particles and their interactions. The Large Hadron Collider (LHC) however collides protons, and they are definitely not elementary particles. Three valence quarks build a nucleon, and gluons hold them together. Even more particles are involved: At high collision energies such as those at the LHC, the quarks are relativistic, and are therefore likely to emit gluons. The gluons themselves can split into gluon or quark anti-quark pairs, the latter called sea quarks.

Together, the gluons and the valence- and sea-quarks, which are jointly called *partons* (R. Feynman [84]), make up a very complex object. Which of the partons actually end up in the hard interaction process is therefore not obvious.

In order to make predictions about the physics at the LHC we must be able to accurately model the collision process. Luckily, it can be factorized into manageable parts. These are: the probability that parton i takes fraction x_i of the proton momentum, initial state radiation, the hard interaction, final state radiation, fragmentation, and hadronization[1], in addition to the beam remnant or *underlying event*. Finally, with millions of protons in each bunch crossing, several collisions occur at the same time. This is known as *pile-up*.

The following sections explain how we see a pp collision, and goes through each of the important concepts and steps needed to give a full account of the process.

2.1 The overall picture

A simplified illustration of a pp collision, is shown in Figure 2.1. Time can be pictured as going from left to right. The figure shows two incoming protons which meet in a head-on collision. The upper proton emits a gluon which splits into a $u\bar{u}$-quark pair. From the lower proton a quark interacts with the $\bar{u}$-quark that originated from the gluon splitting above (and also itself emits a gluon on its way). Then the $\bar{u}$-quark and u-quark annihilates into a Z/γ^*. The hard interaction process $u\bar{u} \to Z/\gamma^* \to q\bar{q}$ is outlined inside the blue inner solid box. As we can see from the figure, there is initial state radiation (ISR) from the partons, and from the "beam remnants"

[1] In literature the terms fragmentation and hadronization are used differently depending on author. Here hadronization strictly refers to the process where partons form hadrons, and fragmentation all what happens before in the strong force showering process.

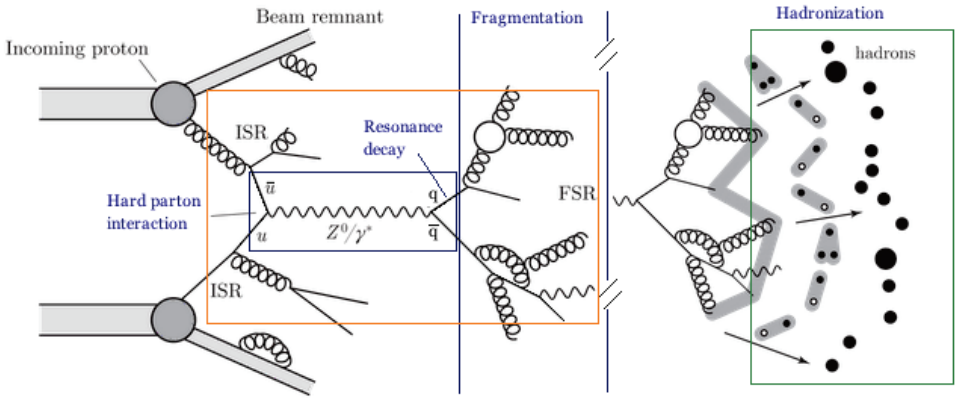

Figure 2.1: A proton proton collision with the hard interaction process $u\bar{u} \rightarrow Z/\gamma^* \rightarrow q\bar{q}$, with its subsequent decay, and with initial and final state radiation (ISR and FSR). The hard interaction process is outlined with blue box in the inner part of the figure. The orange outer box is drawn to indicate what part of the process is (in principle) analytically calculable. The hadronization part to the right of the illustration repeats the drawing of the resonance decay, but in addition illustrates hadronization, drawn inside the solid line box.

which refer to the rest of the proton which did not join in the hard interaction process. At the other end of the diagram, there is "final state radiation" (FSR) from the decay products. The initial and final state radiation can refer to both electromagnetic and strong radiation depending on the emitting particle. For instance: a lepton (which as we know does not carry colour charge) only emits photons, a gluon can emit more gluons or split into a $q\bar{q}$ pair, and quarks can emit both photons and gluons. The terms initial and final state radiation are most commonly used for electromagnetic and strong radiation, but can also be used for weak emission of Z^0 or $W^{\pm}$. What is important to note, independent on radiation type, is that the particles that join the hard interaction process are highly relativistic, and are therefore likely to radiate. This means that additional photons and gluons (and to much less extent W and Z) are part of any event, and both can lead to yet more particles, either quarks, gluons or leptons.

The fragmentation and hadronization process (re-drawn to the right of the figure) then follows after the initial hard scattering process. This is due to the phenomenon of confinement inherent to the strong colour force presented in Section 1.2.7. The fact that the colour force increases as the quarks separate, induces the fragmentation, and ultimately hadronization.

The final component in the pp collision depicted in Figure 2.1, is the underlying event which is defined as any hadronic activity not connected to the hard interaction process. This therefore includes anything that happens to the "spectator" partons left over in the proton. These can naturally also interact, although not with the large energy momentum transfer as the hard interaction process, and these partons also inevitably undergo hadronization. Thus the underlying event is an additional source of (soft) QCD jets.

To complicate the picture further there can be several pp collisions recorded during the same event, this is referred to as "pile-up", and is touched upon further in Section 3.1.

How then to deal with such complicated pp collision events? As mentioned, we can treat each component rather independently, or in other words: the process can be factorized into separate pieces. The hard interaction process is one piece, the structure of the proton another, the initial and final state radiation a third, and finally the hadronization process a fourth part.

I start by the most straight forward part, the hard interaction.

2.2 The hard interaction

The only thing we can know precisely when it comes to a pp collision and the hard interaction process that occurs, is what we observe as the end product. Let us say an electron-positron pair is produced and measured[2]. If we then want to calculate the probability of such an outcome, we must consider (the superposition of) all possible hard interaction processes that could lead to this final-state, which would include all allowed initial states, and all allowed interactions. This could seem like a very difficult task, needing endless calculations, but it turns out that we can use *perturbation* theory. Perturbation theory is a mathematical approach that allows a calculation to be carried out by series expansion around some small parameter ϵ, in this case the coupling constants α. A total cross section σ can then be computed by summing up all the individual terms as the following expression illustrates

$$\begin{aligned} \sigma &= \sum_{O=0}^{N} \sigma = \sigma_0 + \sigma_1 + \sigma_2 + \cdots + \sigma_N \\ &= A_0\alpha^0 + A_1\alpha^1 + A_2\alpha^2 + \cdots + A_N\alpha^N \end{aligned} \tag{2.1}$$

which is just the sum of leading order (LO), next to leading order terms (NLO), and so on, and A_i are constants. If $\alpha << 1$, then the total cross section can be approximated to n-th order (for example 2$^{\text{nd}}$) by $\sigma \simeq A_0 + A_1\alpha$, so only including the LO and NLO terms. That α must be small is important, otherwise the power series does not converge. For the high energy inelastic scattering processes considered here, even QCD is weak (small α_s, roughly 0.12 at M_Z), as explained in Chapter 1.2.7, which means that perturbation theory can safely be applied for all interaction types, electromagnetic, weak and strong.

I have mentioned the total cross section σ above. This is calculated from the differential cross section $d\sigma$ for a certain initial and final state, considered within a certain theory (for instance QED), by first integrating over the momenta of final-state particles, and then summing up all the individual contributions, or sub-processes to a certain level of precision n, as explained above. The differential cross section for a $2 \to X$ hard scattering process is expressed as ([85])

$$d\sigma = \frac{|\mathcal{M}|^2}{4\sqrt{(p_1 \cdot p_2)^2 - m_1^2 m_2^2}} \left(\prod_f \int \frac{d^3 p_f}{(2\pi)^3 2E_f} \right) (2\pi)^4 \delta^{(4)} \left(p_1 + p_2 - \sum p_f \right), \tag{2.2}$$

[2]Leptonic final-states are simpler to use as an example, since we can confine the discussion to electroweak production, leaving out QCD.

where p_1, m_1 and p_2, m_2 are the four-momenta and mass of the incoming particles, and p_f and E_f the momentum and energy of the outgoing particles. The four-dimensional Kroenecker delta $\delta^{(4)}$ ensures energy-momentum conservation. Any value different from 0 of its argument (here, the sum over momenta) yields 0. Finally $\mathcal{M}$ is the Feynman amplitude. It is calculated from Feynman diagrams and their corresponding Feynman rules [86]. An example of a Feynman diagram is the hard interaction diagram (solid inner box) already encountered in Figure 2.1. A Feynman diagram pictures the particle interaction as happening in space-time where space is along one axis, and time the other (here I operate with space along y- and time along the x-axis). The incoming, outgoing and intermediate particles are connected in space-time vertices, and each have their particular representation according to the Feynman rules. Fermions are straight lines (with an arrow indicating the path of travel), bosons are wiggly lines, gluons are spiral lines, and scalar particles are dashed lines.

Feynman diagrams are extremely useful, since each vertex, and each internal line (lines between vertices) and external line (lines from initial or to final particles), correspond to a mathematical expression. Figure 2.2 gives an example of of a QED Feynman diagram, showing the incoming and outgoing spinors as well as the vertex and propagator terms entering the amplitude calculation. This is a diagram much like the one in Figure 2.1, but where the incoming and outgoing lines just are general fermions, instead of specifically $u\bar{u}$ and $q\bar{q}$, and for simplicity the internal line is here represented by a photon.

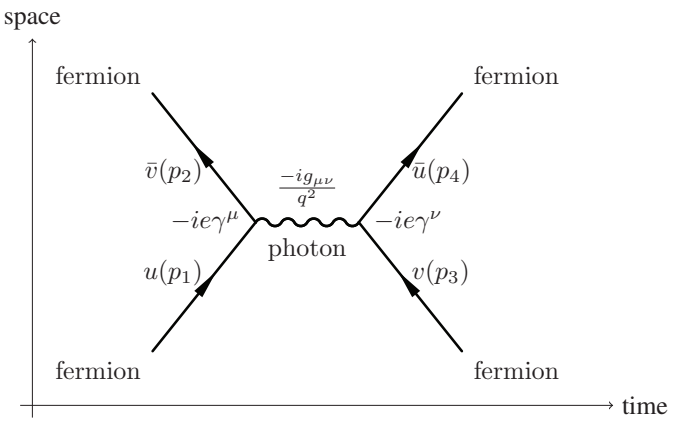

Figure 2.2: A Feynman diagram of a fermion-fermion annihilation process. The Feynman rules corresponding to each fermion line, vertex and internal boson line are shown. Time is on the x-axis and space on the y-axis. v, u, $\bar{v}$, and $\bar{u}$ are Dirac spinors, which hold all the kinematic information about the incoming and outgoing fermions.

The Feynman amplitude for the exact diagram in Figure 2.2 would be the following

$$\mathcal{M} = \bar{u}(p_4)(-ie\gamma^\nu)v(p_3)\left(\frac{-ig_{\mu\nu}}{q^2}\right)\bar{v}(p_2)(ie\gamma^\mu)u(p_1)\,, \tag{2.3}$$

where u and $\bar{v}$ are Dirac spinors representing the incoming fermion, and anti-fermion, and $\bar{v}$ and u the outgoing fermion and anti-fermion respectively. Furthermore γ are the 4×4 γ matrices

built up of Pauli spin matrices, q^2 the momentum transfer squared, and e the magnitude of the coupling constant g_e, which is related to the fine structure constant $\alpha = \frac{g_e^2}{4\pi}$, and $g_{\mu\nu}$ the usual space-time metric tensor, a 4×4 matrix with diagonal entries (1, -1, -1, -1) and otherwise 0's. From this expression, and Equation 2.2 the probability for this process to occur, assuming certain initial and final state particles can readily be calculated.

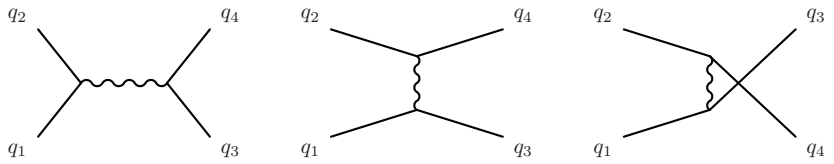

(a) s-channel (b) t-channel (c) u-channel

Figure 2.3: The three diagrams illustrating the s- t- and u-channels defining the Mandelstam variables in Equation 2.4, using incoming $q_{1,2}$ and outgoing $q_{3,4}$ quarks as an example. They can be particles or anti-particles depending on the exact process. The superscripts 1-4 are used to separate one particle from another and correspond to the numbering in Equation 2.4.

I have mentioned sub-processes, but not yet exactly defined what these are. Figure 2.3 shows how three different (LO) *channels*, or sub-processes, can lead to the same final state. This is the s-channel (a) (which we have already encountered above), the t-channel (b), and the u-channel (c). The last channel is only relevant in processes where the final-state particles are identical, i.e: $q_3 = q_4$. In such processes (b) and (c) cannot be distinguished, and must be summed over.

The energy-momentum conservation is described differently in each case, and the invariant *Mandelstam* variables s, t and u are useful here:

$$\begin{aligned} s &= (p_1 + p_2)^2 = (p_3 + p_4)^2 \\ t &= (p_1 - p_3)^2 = (p_2 - p_4)^2 \\ u &= (p_1 - p_4)^2 = (p_2 - p_3)^2 \,. \end{aligned} \tag{2.4}$$

Here $\sqrt{s}$ is the centre of mass energy, t the square of the four-momentum transfer, while u is the four-momentum transfer with the two outgoing particles exchanged.

To illustrate the simple expressions obtained when applying the Mandelstam variables, I use the strong process $qq' \rightarrow qq'$ via the t-channel process in Figure 2.3 (b) (assuming a gluon exchange). The squared Feynman amplitudes (matrix elements) for this process (when assuming a scattering angle of $\theta = \pi/2$) is ([85])

$$(M)^2(qq' \rightarrow qq') \quad \hat{=} \quad \frac{4g_s^4}{9}\frac{(s^2 + u^2)}{t}\,, \tag{2.5}$$

where the factor 4/9 is a "colour-factor", and g_s is the gauge coupling factor $g_s^2 = 4\pi\alpha_s$. The value of this expression turns out to be 2.22, and relates to the size of the cross section. The

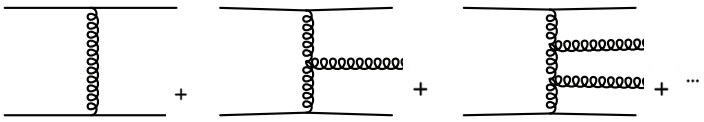

(a) LO (b) NLO (c) NNLO

Figure 2.4: Feynman diagrams illustrating the leading order (a) and real corrections to the leading order (b) and (c) as formulated in perturbation theory.

abundant process $gg \rightarrow gg$ gives for comparison 30.4.

An example of how the LO, NLO and NNLO could look like for a strong interaction process, is shown in Figure 2.4. Naturally, this is only a limited example, all possible combinations leading to topologically different diagrams must be considered. Adding up all sub-processes (for instance the tree-level s, t and u-channels), and all higher order processes (to the decided cut-off), finally gives the total scattering amplitude $\mathcal{M}_{fi}$.

I have now outlined how the hard interaction process can be calculated. But this assumes certain initial state particles. I started the introduction of this chapter by reminding that we are dealing with complex protons. Thus, we cannot know exactly *what* initial partons actually joined in the hard interaction, neither with exactly what energy. For this we need to involve *structure functions* or the related *parton distribution functions*, which is the topic of the next section.

2.3 Structure and parton distribution functions

To calculate cross sections involving protons, structure functions are involved, with the role of parametrizing the momentum-energy distribution of the partons in the proton. Structure functions are universal (valid for all protons), and we can therefore use the results from Deep Inelastic Scattering (DIS) where electrons are used to probe protons. The differential cross section for DIS with electrons as probes is ([85])

$$\frac{d^2\sigma}{dq^2 d\nu} = \frac{4\pi\alpha^2}{q^4}\frac{E_f}{E_i M_N}\left[\frac{M_N}{\nu}F_2(q^2,\nu)\cos^2\frac{\theta}{2} + 2F_1(q^2,\nu)\sin^2\frac{\theta}{2}\right]. \tag{2.6}$$

Here M_N is the mass of the nucleon, E_i and E_f the initial and final energy of the incoming and scattered electron, q^2 the four momentum transfer squared, ν the energy lost by the electron in the process, i.e. $\nu = E_i - E_f$, and θ the scattering angle. Finally, F_1 and F_2 are the structure functions, which I explain further in the following.

In Equation 2.6 the structure functions $F_{1,2}$ enter as functions of two variables, namely the momentum transfer squared q^2, and the energy loss of the probe ν. However, it is a pure number, and hence the dimension dependence must be cancelled out. J. Bjørken suggested in [87] that

the structure functions depend on the ratio

$$x = q^2/(2M_N\nu)\,, \tag{2.7}$$

where the Lorentz invariant variable x is interpreted as the fractional nucleon momentum carried by the parton. $F_1(q^2,\nu)$ and $F_2(q^2,\nu)$ in Equation 2.6 can therefore instead be expressed by $F_1(x)$ and $F_2(x)$ in agreement with the data not showing any explicit dependence on q^2 at high energies. An interesting feature with the Bjørken x is that at high q^2 the dependency on M_N is irrelevant. This is reasonable, because as the probe energy becomes large compared to the scale of QCD, i.e. $p_T >> \Lambda_{\mathrm{QCD}}$, where $\Lambda_{\mathrm{QCD}} \sim 200$ MeV, and hence the wavelength small $1/p_T << 1/\Lambda_{\mathrm{QCD}}$, the probe does not see the nucleon as a whole, but as consisting of single point-like objects, namely the quarks. In fact, the structure functions in the electron-nucleon DIS can be expressed as a sum over the individual parton momentum distributions, or parton density functions (PDF's) $f(x)$ and their charge Q_i as follows

$$\begin{aligned} F_1^{eN} &= \sum_{i\,\mathrm{partons}} f_i(x)\, Q_i^2 \\ F_2^{eN} &= x \sum_{i\,\mathrm{partons}} f_i(x)\, Q_i^2\,. \end{aligned}$$

It is then evident that the nucleon structure functions are directly related to the PDFs.

Parton distribution functions cannot, as explained earlier, be deduced from first principles, but must be extracted from experiment. One needs a series of experiments to determine the functions for varying $Q^2 = -q^2$. Recent results obtained from HERA [88] with $E_{e^-,e^+} = 27.5$ GeV, $E_p = 920$ GeV, for $Q^2 = 10\,\mathrm{GeV}^2$ and $Q^2 = 10000\,\mathrm{GeV}^2$, are shown in Figure 2.5. Here we see that at low fractional momentum x it is far more probable to find a gluon (xg) or a sea-quark (xS), than a valence quark ($\mathrm{xu_v}$ or $\mathrm{xd_v}$, subscript v for valence), but that the probability to find one of the valence quarks steeply increases with x. One can also see by comparing the two plots that when Q^2 is large (right) the probability that the gluons or sea quarks are found at a certain x increases more steeply with decreasing x compared to lower Q^2 (left).

In order to make predictions at other energies than those the PDF's are calculated at, one needs to extrapolate. This is accomplished by applying the so-called DGLAP (Dokshitzer-Gribov-Lipatov-Altarelli-Parisi) equations ([89–92]), or QCD evolution equations. I do not go into any further details about these.

To understand the shape of the PDF's, a simple example serves the purpose. If the proton strictly consisted of three valence quarks (three partons), and no interquark forces (assuming negligible strong force), the PDF of each of the partons would be a very simple Dirac delta function at 1/3 of the protons momentum. Naturally, since there are double as many up quarks as down quarks, the probability of finding an up quark with that fractional momentum is double that of finding a down quark. Which means that each of the three partons share the momentum equally among themselves. This is also what a probe would see if its energy was large enough to probe the nucleon, but too small to see beyond the valence quark structure (very low Q^2). We know however, that the gluons hold the quarks together inside the nucleon, so there must be

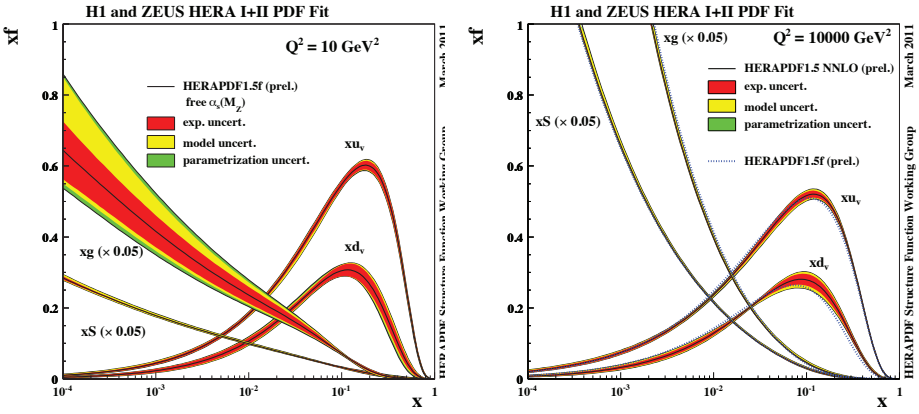

Figure 2.5: Proton parton distribution function as measured at HERA, plotted as a function of Bjørken x. The gluon (xg) and sea quark (xS) distributions are scaled down by a factor of 20. To the left with transferred momentum squared $Q^2 = 10$ GeV^2 and to the right with $Q^2 = 10000$ GeV^2, the latter relevant for energies at the LHC. Figures from [93].

interquark forces. Therefore, if one gives the probe more energy such that the resolution power grows, this allows the probe to see the gluons and sea quark-antiquark pairs that surround the valence quarks. This ultimately means that the proton momentum must be shared by more partons, hence the fractional momentum decreases resulting in a smeared distribution as in Figure 2.5.

An important note to mention here is that at large energies such as those at the LHC, the probability of a quark-antiquark interaction from the proton-proton pair is as probable as a quark-antiquark interaction from a proton-antiproton accelerator, as Fermilab, which means that the sea quarks are in fact very important.

An overview over how the LHC (at nominal $\sqrt{s} = 14$ TeV) reaches in Q^2 versus x, and the relation to the rapidity range y, is shown in Figure 2.6. One can read from the plot that an object of mass $M = 100$ GeV is produced over a rapidity range ($\Delta y \sim 5$), corresponding to a range of fractional momentum $\sim 10^{-1} < x < 1$. The LHC range is compared to HERA and fixed target experiments, and it is clear that the LHC probes a very large area, far exceeding both. The plot shows that very high mass-scales can be reached, up to $M = 10$ TeV at very high Q^2 and x.

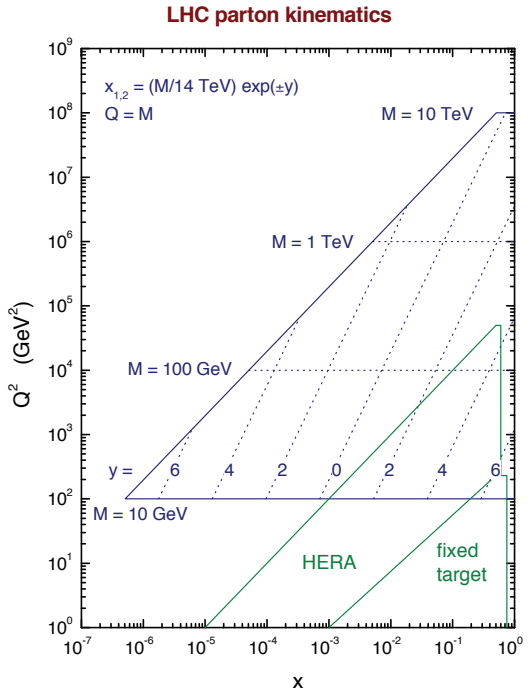

Figure 2.6: The reach of LHC (blue), HERA and fixed target experiments as a function of momentum transfer Q^2 and fractional momentum x. Figure from [94]

2.4 Bringing it all together, including fragmentation and hadronization

I have discussed how a total differential cross section can be calculated if one knows the initial and final state particles, and given the order of magnitude the calculation should be done at. I have also introduced the parton distribution functions that give the parton's probability to take on a certain proton momentum fraction. If we then take all possible initial parton combinations and convolute the analytic hard scattering expression with the parton distribution function for the interacting partons, we have solved the problem of dealing with a complex proton, where we cannot know for certain which initial parton contributed. Schematically speaking for a hard scattering process in a hadron-hadron collision we can express the total inclusive production cross section σ into some (heavy) particle X (for instance a Z boson) through annihilation of the participating partons as

$$\sigma_X = \sum_{a,b} \int_0^1 dx_1 dx_2 f_a(x_1, \mu_F^2) f_b(x_2, \mu_F^2) \times \hat{\sigma}_{ab\to X}(p_1, p_2, \alpha_s(\mu_R), Q^2; \mu_F^2, \mu_R^2) \tag{2.8}$$

where f_i are the structure functions, α_S is the strong coupling constant, μ_F and μ_R are the factorization scale and renormalization scale respectively, and $\hat{\sigma}_{ab\to X}$ is the calculable pertubative partonic cross section. For Z production it is mainly quark a from proton 1 and antiquark b from proton 2 (or vice-versa). The scales μ_F and μ_R should typically be chosen of the order of the soft and hard scale Q respectively. In an annihilation process like $q\bar{q} \to Z$, the hard scale would

typically correspond to the mass of Z, while the soft scale would relate to the long-distance soft QCD processes. As described in the sections above, we now have all the ingredients to predict the production cross section of X when colliding proton 1 with proton 2. Furthermore the particle X would decay into some final-state particles $f\bar{f}$ for instance, in which case the elementary process to calculate pertubatively is $\hat{\sigma}_{ab\to X\to f\bar{f}}$.

This brings us as far as to the final-state of the hard interaction process, and what happens further depends on this final-state. If the products are 1$^{\text{nd}}$ or 2$^{\text{nd}}$ generation leptons they will shoot out into the detector without changing identity. If the products on the other hand are quarks or gluons, or hadronically decaying τ particles (leptonic decays lead to electrons, muons and corresponding neutrinos), a more complicated chain of events takes place, due to the nature of the strong force. As already explained in Section 1.2.7, quarks are confined into colour-less objects inside hadrons, and therefore no single free parton can be observed, nor colourful combinations such as qq. The experimental effect of this is that quarks and gluons produced in pp collisions are surrounded by a shower of partons which quickly form hadrons, such as pions, kaons, protons, and neutrons, to mention some of the most common types. Going back to Figure 2.1 I am now referring to the "Fragmentation" and "Hadronization" sections of the figure. In the detector we therefore see, in addition to leptons and photons, collimated jets of hadrons, and not single final-state quarks or gluons.

To describe the complicated process involved in these steps, so-called parton showering models are needed since part of this process occurs at the non-pertubative scale and cannot be approximated with perturbation theory. The showering models typically work in a step-by-step procedure, producing gluon radiation from the highly accelerated and virtual quarks, until the quark itself has lost so much energy/virtuality from the radiation that fragmentation stops. Similarly gluons split into pairs of gluons and quark-antiquarks. Then hadronization takes over, at the $Q^2 \sim (1\text{ GeV})^2$ scale (where Q^2 is the momentum transfer squared). The showering process is angular/p_{T} ordered, which means that a quark emitting a gluon always emits the next more collinear compared to the previous. This is related to the fact that each step in the process is less energetic than the first. This forms collimated *parton jets* illustrated in Figure 2.7, by the circles around the quark and gluon jet direction.

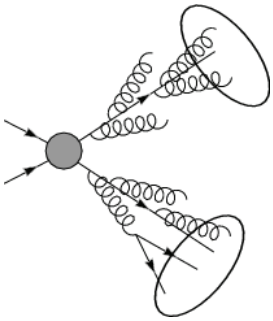

Figure 2.7: An illustration of gluon showering from two quarks, giving rise to parton jets.

Two main models dominate the parton showering picture. This is the (Lund) string model [95] and the cluster model [96]. I use an $e^+e^- \to q\bar{q}$ process to illustrate the two models. Figure 2.8 shows how the string (left) and cluster (right) models schematically visualize the fragmentation and hadronization process in an e^+e^- collision. The iterative process starts with a quark emitting a gluon, followed by gluon splitting to gluon or quark pairs.

In the string model in Figure 2.8 (a), the outgoing partons are connected with "strings", which represents the colour flux between the partons. The string's endpoints are always connected with a quark and an anti-quark, but the string itself goes via gluons when present, as the figure shows. The process starts off with the string connected between the initial $q\bar{q}$ pair, but as the quarks move apart the string tension will reach a predefined limit, and then the string breaks, resulting in the two asymmetric string pieces in Figure 2.8 (a). The two resulting strings will again stretch as the quarks keep moving away from each other, and breaks if the tension becomes too large, and so on until a certain cut-off energy scale, which is linked to the non-pertubative regime, is reached. Eventually the hadronization takes place coupling quarks and anti-quarks into mesons or baryons.

The cluster model illustrated in Figure 2.8 (b) on the other hand, forms parton showers by exploiting the fact that the showering happens at scales much smaller than the initial hard process scale Q^2, and here so-called *pre-confinement* properties [97] dominate. At these scales, partons form clusters of colourless states which form so-called *proto-hadrons*. This is an intermediate state which is only dependent on the evolution scale q, and the fundamental QCD scale λ_{QCD}, and not on the nature and scale Q^2 of the subprocess itself. Observable final-state hadrons are formed when the proto-hadrons decay (typically 2-body) into hadrons in form of collimated jet-like objects.

The only thing that now must be added in order for a full description of the pp collision, is

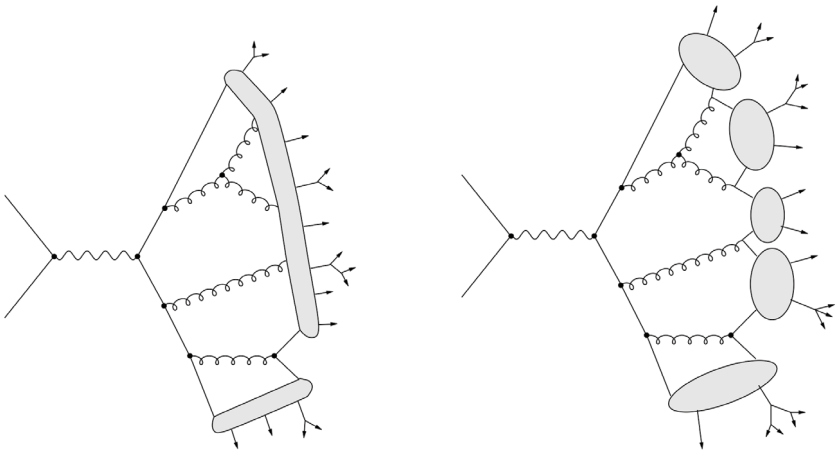

(a) String model (b) Cluster model

Figure 2.8: Schematic presentation of the string (left) and cluster (right) QCD models.

the additional initial state radiation (assuming the final-state radiation is added by the showering processes above), which can be thought of as part of the underlying event, and finally the pile-up. It can be the same programs that treat the showering process described above, that also have implementation of these components. And we finally have the full pp event modelled, by piecing the process up into manageable parts.

Finally a quick note about what kind of programs do all this. All steps described in this section use Monte Carlo[3] (MC) simulation programs [98]. It is a class of algorithms that rely on repeated random sampling in order to produce numerical results, and is not only used in particle physics, but for a vast spectrum of mathematical and physics applications.

I am sure I have convinced the reader that pp collisions are very complex. Luckily the detectors that register the collisions are highly sophisticated, and so is the software that interprets the data from the detectors. Therefore we successfully extract interesting physics even in such a challenging environment. The next chapter presents The Large Hadron Collider (LHC) and the ATLAS detector, and also explains how physics objects such as muons, electrons, photons, and jets are defined.

[3]Naturally, the name directly refers to the gamble scenes in the district Monte Carlo of Monaco, where the same random and statistical rules apply as those of these numerical methods.

Chapter 3

LHC, ATLAS, and how to find what we are looking for

> "It doesn't matter how beautiful your theory is, it doesn't matter how smart you are. If it doesn't agree with experiment, it's wrong."
>
> Richard P. Feynman

Up until now I have discussed particle physics and pp collisions mainly from a theoretical point of view. It is now time to turn the focus to the experimental side. First to the apparatus itself, the LHC accelerator and the ATLAS detector. Then to particles in the analysis' point of view, the so-called object definitions. This chapter also includes definitions of important kinematical variables used throughout. Finally it describes the qualification work-task I performed on monitoring of the Semi Conducter Tracker noise measurement, followed by the commissioning of the ATLAS detector with cosmic muons.

3.1 The Large Hadron Collider

The Large Hadron Collider (LHC), is the current work horse of the CERN complex. It is built underground as a two-ring circular machine, 27 km in circumference inside the already existing LEP[1] tunnel. Proton beams circulate inside each of the rings, in opposite directions, and are made to collide inside four main detectors, one of which is the ATLAS detector.

An advanced system of magnets is needed to control the beam. Superconducting magnets provide an 8T magnetic field in order to bend the beams around the ring. The magnets are cooled down to 1.9K, and this is achieved by using liquid helium as cooling agent. In addition to the bending dipole magnets, a sophisticated set of quadrupole magnets are used to focus the beam. And finally a separate system of magnets squeeze the beam just before the collision in the detectors. In this way a high intensity beam is achieved. Since the protons must move through

[1] LEP is an acronym for The Large Electron Positron Collider and was in operation during the years 1989-2000

the ring without colliding with air molecules, the beams are kept in ultra vacuum of 10^{-10} Torr, which is popularly said to be better than vacuum in outer space.

The beam must not only circulate in an orderly manner around the ring, it must naturally also be accelerated! This is the job of the superconducting radio frequency (RF) system, which supply a pulsating electric field which accelerates the (positively charged) protons. It is installed at dedicated sections around the ring, between the detectors and the bending and optics magnets.

A key accelerator parameter is the machine instantaneous luminosity $\mathcal{L}$, and it is determined solely by the beam parameters. It is a quantitative measure for the number of collisions per squared area per second, and is defined through the number of colliding particles in each direction (n_1, n_2), the collision frequency (f), and their cross section in the x-y direction $(\sigma_x \sigma_y)$ through

$$\mathcal{L} = \frac{n_1 n_2 f}{4\pi\sigma_x\sigma_y}$$

The time-integrated total luminosity L is then $L = \int \mathcal{L}\, dt$.

The LHC proton beams are divided into bunches. The design parameters quote $1.15 \cdot 10^{11}$ protons in each bunch and 2808 bunches per beam. With a design collision frequency of 40 MHz (collisions each 25 ns), the delivered luminosity is $\mathcal{L} = 10^{34} cm^{-2} s^{-1}$, to be reached in 2015. In the 2011 run, the peak luminosity achieved was $3.6 \times 10^{33} cm^{-2} s^{-1}$ at a center of mass energy (CM) $\sqrt{s} = 7$ TeV. Since then the LHC has increased the CM energy to $\sqrt{s} = 8$ TeV and reached a record luminosity of $7.7 \times 10^{33} cm^{-2} s^{-1}$, not far from the nominal value.

The luminosity is directly related to the experiment's discovery power, once a threshold energy for producing a new particle is reached. Interesting physics processes such as the production of a Higgs boson have tiny cross sections ($\mathcal{O}(10^{-35})$ cm^2 which correspond to 10^{-2} nb, compared to a dijet cross section of about 10^8 nb), and since the number of times a certain process happens is a product of luminosity and cross section

$$N = L \times \sigma$$

the larger luminosity, the more frequent the process occurs.

In the previous section pile-up was briefly touched upon. Pile-up is strongly correlated with the instantaneous luminosity and bunch-spacing, and one therefore expects this to be more and more important as the instantaneous luminosity increases in the future. In the last period of the 2011 data-taking, the average number of inelastic pp collisions per bunch crossing was around 10, and at the end of the 2012 run, it had more than doubled. Matching the particles in an event with the right interaction point thus becomes an increasing challenge. So although high luminosity is a main goal, the effect of pile-up is an important ingredient when considering increased luminosity.

The LHC accelerator is not a solitary player at CERN. It is in fact part of a large accelerator complex, illustrated in Figure 3.1. This means that before the beam reaches the LHC it has already been through several steps of bunching, focusing, and acceleration. First hydrogen atoms

are stripped from their electrons providing bare protons. Then the first stage of acceleration starts in a linear accelerator (LINAC), before the beam is passed on to the Booster. After circulating through the booster the beam reaches an energy of 1.4 GeV. Next stage is the PS (Proton Synchrotron) accelerator, where the beams reach 25 GeV, and the final step before the LHC is in the SPS (Super Proton Synchrotron), where the beam reaches 450 GeV and a speed close to the speed of light. For completeness, the figure also depicts the storage complex used for the ion beams (in green).

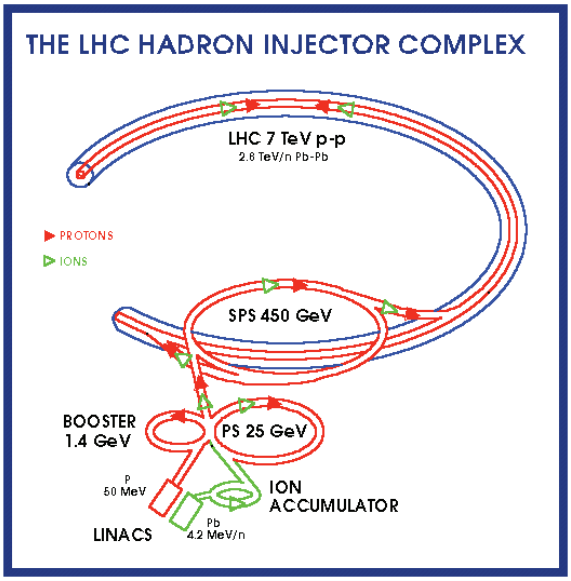

Figure 3.1: The LHC accelerator complex including the LINAC, Booster, PS, SPS and the LHC. The Ion Accumulator and accelerators are also sketched in green. [99]

After this brief overview of the LHC, let us turn to the experimental detection and measuring instrument itself, namely the ATLAS detector.

3.2 The ATLAS detector

The ATLAS detector [100] illustrated in Figure 3.2, is a "general purpose" detector, and as such is built with layers of several different detector technologies in order to measures all important particles and phenomena from the debris of the pp collision. It is built to accommodate new physics searches in addition to SM physics measurements, and in particular to find the Higgs boson. As the discovery of a boson was announced on 4th of July 2012, one of the main goals has already been achieved. Now the focus is on precision measurements of the Higgs boson properties, and on searches for physics beyond the SM, such as Supersymmetry.

In the following subsections I give a brief overview of the detector components. I start off however, by introducing the coordinate system used by the LHC and ATLAS, and by defining some important kinematical variables used throughout the thesis.

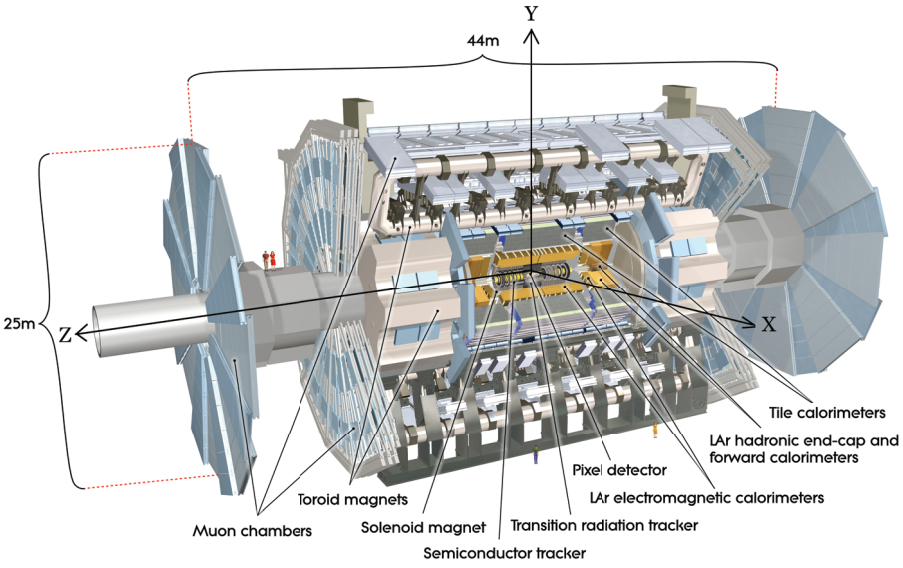

Figure 3.2: Schematic overview of the ATLAS detector, with all the sub-detectors indicated. A coordinate system is superposed on top of the detector. The x-axis direction is defined to point towards the centre of the LHC ring.

3.2.1 Some kinematic variables

The ATLAS coordinate system (Figure 3.2) is a right-handed system with z along the beam axis and the x-y plane transverse to the beam direction. The x-axis direction is defined to point towards the centre of the LHC ring. As usual for polar coordinates, we define the azimuthal angle ϕ around the z-axis in the x-y plane, and the polar angle θ is defined as the angle with respect to the z-axis.

Rapidity

With the coordinate system defined as above, a useful variable is *rapidity*, y defined as

$$y = \frac{1}{2} ln\left(\frac{E + p_z}{E - p_z}\right). \tag{3.1}$$

Rapidity gives us an intuitive understanding of the direction of the outgoing particle in the collision, since the momentum pointing in the z-direction, p_z, is part of the expression. Two examples illustrate the point: Let's say an outgoing particle is directed 90° with respect to the beam axis, hence $p_z << E$. This leaves the argument of the logarithmic expression tending towards 1, and hence the rapidity approaches 0, since $ln(1) = 0$. However, if the outgoing particle is directed almost parallel to the beam axis, we have $E \sim p_z$, and the argument in the logarithmic expression will tend toward 0, hence $y \to \infty$.

So the rapidity is related to the polar angle θ, but this is not only why it is such a useful variable. It turns out that rapidity transforms particularly easily under Lorentz transformation

along the z-axis, which is very useful as the centre of mass frame is most often boosted along the z-axis with respect to the lab-frame. The transformation can be written as

$$y^{'} = y - \tanh^{-1}\beta\,,$$

where β is the usual relativistic quantity v/c. This again means that if we take take the difference between two particles rapidities, this value is Lorenz invariant: $y_1^{'} - y_2^{'} = y_1 - y_2$.

In high energy physics where we are dealing with relativistic particles, it is more practical to work with the *pseudorapidity* η, since the rapidity requires the knowledge of both the energy and the total momentum. For $pc \gg mc^2$, which is often the case in pp collisions at the LHC, then

$$y \sim -ln\tan\left(\frac{\theta}{2}\right) \equiv \eta\,. \tag{3.2}$$

Another very important reason for using the (pseudo)rapidity instead of θ is related to particle densities. In high energy particle collisions particle density is highly dependent on θ, but nearly constant in most of phase space in unit rapidity. When measuring the particle density per rapidity, a so-called rapidity plateau is observed. In fact, particle detectors are built to exploit the given rapidity plateau, with best coverage in this region. At the LHC the rapidity plateau at $\sqrt{s} = 14$ TeV stretches from about $\Delta\eta = 5$, and depends on the energy/momentum of the particle. However as it only depends logarithmically on these kinematic quantities, the plateau is for most practical purposes independent of the dynamics of the particle, except in the case of very massive particles.

Based on pseudo-rapidity (which depend on the polar angle θ) and on the azimuthal angle ϕ, we define the distance or separation between two particles as:

$$\Delta R = \sqrt{(\Delta\phi)^2 + (\Delta\eta)^2}\,. \tag{3.3}$$

Transverse momentum and energy

When protons collide inside the ATLAS detector, a large fraction of particles continue in the direction of the beam-pipe, and hence do not hit the detector. This is because the detector necessarily sits outside the beam-pipe (starting at $\theta \sim 0.8\,\text{deg}$, or $\eta = 4.9$), and therefore particles travelling at very small angles close to the beam-pipe never enter the detector. This makes it impossible to make a complete account of the longitudinal energy-momentum account. The protons move along the beam pipe which means that most of the momentum points in this direction, and we can approximate the total momentum in the transverse plane to 0. Since the detector is (approximately) hermetic in the transverse plane, most of the outgoing energy and momentum is accounted for in this plane. This allows us to apply the rules of energy and momentum conservation, which is the reason why *transverse* energy E_T and momentum p_T have such a central role at hadron colliders.

Starting by the four-momentum $p_\mu = (E, -p_x, -p_y, -p_z)$, and the three-momentum $\boldsymbol{p} = (p_x, p_y, p_z)$, which are related by the Lorentz invariant quantity $E^2 - \boldsymbol{p}^2 = m^2$, the transverse

momentum p_T and transverse energy E_T are defined as follows

$$p_T = \sqrt{p_x^2 + p_y^2} \tag{3.4}$$

$$E_T = \sqrt{m^2 + p_T^2} \tag{3.5}$$

Other kinematic analysis variables, such as the invariant mass (m defined already in the energy-momentum relation above), the transverse mass (m_{T}), the contransverse (m_{CT}) mass, and the stransverse mass (m_{T2}) are detailed and presented in Section 3.4 just after the description of the ATLAS detector to follow. So, with the coordinate system set up, and the most important kinematic variables defined, we can go on to describe ATLAS's magnet system, and each of the sub-detectors.

3.2.2 Magnet system

Charged particles moving in a magnetic field follow a circular or helix trajectory[2], whose radius depends on the particle's momentum. The ATLAS superconducting magnet system provides bending power for precise momentum measurement of charged particles and charge determination, since positive and negative charges are bent in opposite directions.

The ATLAS magnet system consists of a solenoid magnet encapsulating the inner detector, one outer toroidal magnet placed around the barrel, and which is part of the muon system, and one toroidal magnet for each end-cap. Figure 3.3 shows a schematic overview of the magnets. In the center is shown the solenoid magnet, followed by the eight coils that make up the central toroid. At each end an end-cap toroid is also shown. The solenoid magnet provides a 2T central magnetic field parallel to the beam pipe. The ATLAS toroids provide approximately 0.5 Tesla field in the barrel, and 1 Tesla field in the end-caps.

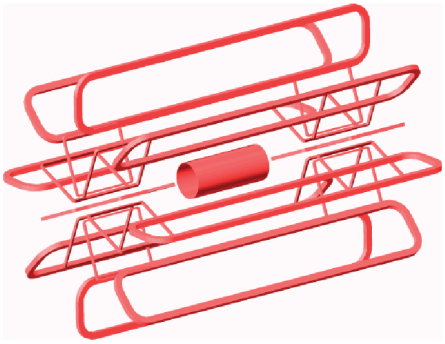

Figure 3.3: The ATLAS Magnet system, built up of three toroids and one solenoid. Each toroid consists of eight coils resulting in a magnetic field of concentric circles in respect to the beam axis.

[2]The circular motion is due to the transverse velocity component, and the helix motion a result of a longitudinal velocity component

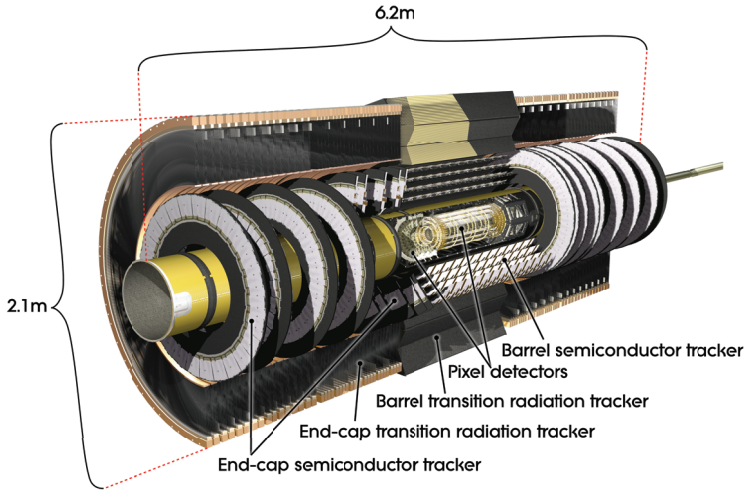

Figure 3.4: Overview of the ATLAS inner detector including the barrel and end-cap sections, of the pixel, silicon strip, and transition radiation tracker.

3.2.3 The inner detector - the tracker

The inner detector (see Figure 3.4) is contained within the solenoid and is a high resolution detector built up of 3 main parts: The Pixel detector, the Silicon Strip Semi Conductor Tracker (SCT), and the Transition Radiation Tracker (TRT). The inner detector provides excellent momentum resolution, primary and secondary vertex measurements, pattern recognition, and electron identification. The required momentum resolution for the tracking system is $\sigma_{P_T}/p_T = 0.05\%$ with an uncertainty on the momentum p_T of 1% [100]. It is built hermetically and serves over a range $|\eta|$=[0,2.5].

Pixel detector

The silicon pixel tracker is placed as close to the interaction point as possible, and is the most precise sub-detector in ATLAS. The granularity and precision is very high, and balance between performance and material density has been met by only allowing 3 layers around the barrel. They are placed concentrically at radii of 4, 11 and 14 cm. There are 5 layers at each end-cap placed perpendicular to the beam pipe. Intrinsic measurement accuracies in the barrel are 10 μm in (R-ϕ) and 115 μm in z ([100]).

Not only does the pixel detector measure charged particles, it also contains a buffer which stores data, to allow for the slight delay of the first level trigger (Level 1) decision as described in Section 3.2.6.

The main physics tasks are vertexing and b-tagging, where secondary vertex measurements are important. A new pixel layer (the insertible b-layer, IBL [101]) even closer to the beam (placed at radius 3cm, requiring a new smaller beam-pipe) is being installed and will be used from 2015 when collecting data at higher energy and luminosity.

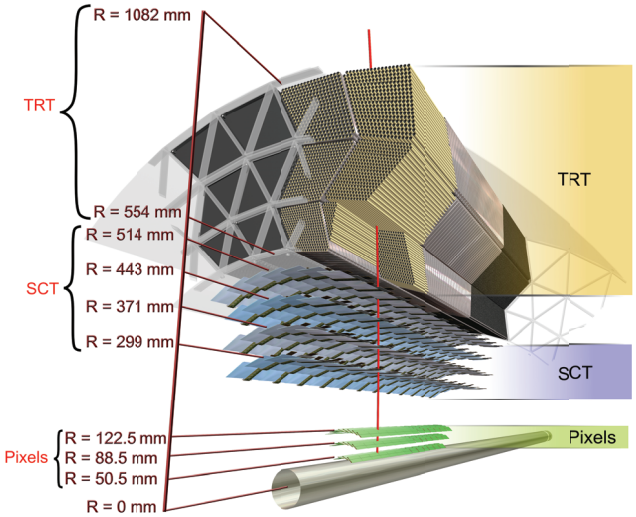

Figure 3.5: Layout of the ATLAS inner detector showing the positioning of the pixel detector, the silicon strip detector and the transition radiation tracker.

Semi Conductor Tracker

The Semi Conductor Tracker (SCT) [100], made up of silicon micro-strips, extends the Pixel detector. There are four barrel layers and nine end-cap disk layers. Each module has two detector pairs glued back to back at an angle of 40 milliradians. A pitch of 80 μm gives a spatial resolution of 17 μm in the Rϕ plane and 580 μm in the z direction. The readout electronics is mounted on-top of the detectors and as for the pixel detector contains a system for storing data until the Level 1 trigger decision has been made. The SCT is the most important tracker in the transverse plane since it measures a traversing particle over a much larger area than the Pixel Detector and sample more points (maximum 3 hits in the Pixel detector and 8 in the SCT) with roughly the same (transverse) accuracy as the Pixel Detector.

Transition Radiation Tracker

A straw detector filled with a gas-mixture of Xenon-CO_2 and O_2 makes up the last layers of the inner detector. Its precision is lower than the Pixel and SCT detectors, but it is capable of a larger number of measurements, as each charged track will at least cross 36 straws in the central barrel region, and 22 in the end-caps [100] compared to 3 and 8 for the Pixel and SCT.

A total of 500k straws make up the TRT barrel detector, while another 420k equip the end-caps. Intrinsic spatial resolution is 130 μm per straw.

The TRT functions as a combination of a straw tracker and a transition radiation detector. Each straw uses separate low- and high- thresholds in the read-out electronics to separate the

tracking pulses (low threshold) and the transition radiation pulses (high threshold). The transition radiation produced when a particle traverses the different materials depends on the mass of the particles and this is used for particle identification, as it identifies and differentiates electrons and hadrons.

3.2.4 The Calorimetry

The calorimetry is placed outside the solenoidal magnet and consists of the Electromagnetic (ECal) and the Hadronic (HCal) Calorimeters. The calorimeter's main task is to measure the energy of (certain) particles by absorbing them. Particle showers are caused when the traversing particles interact with the detector material. Purely electromagnetically interacting particles like the electron, positron and photon are absorbed in the ECal, while strongly interacting hadrons pass through the ECal (depositing some energy), and are absorbed in the HCal. Both calorimeters have a full η coverage up to $|\eta|$ <4.9, and consist of barrel and end-cap components.

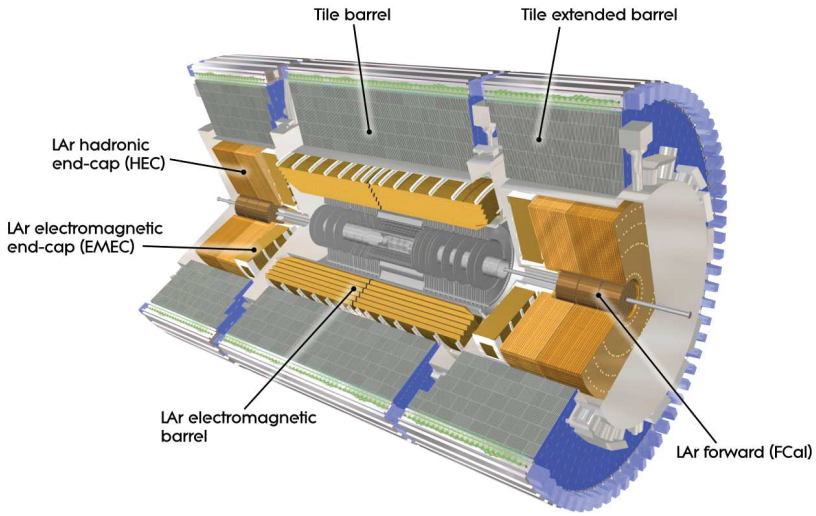

Figure 3.6: The ATLAS electromagnetic and hadronic calorimeters.

The Electromagnetic Calorimeter

An accordion shaped geometry with layers of lead as absorbing material in between liquid argon as active detector material, is used for the ECal. The accordion waves in the barrel are parallel to the beam-pipe and run in the ϕ direction. In the end-caps the waves are parallel to the radial direction and run in z. The ECal operates at high precision, both in energy resolution and location of the energy deposit. Since the particles already suffer from energy loss due to interaction with the material in the inner detector the electromagnetic calorimeters have an innermost pre-sampler layer which measure energy lost in front of the ECal. Coverage is divided into precision sections at 0< $|\eta|$ <2.5 and a higher η region 2.5< $|\eta|$ <3.2. The required ECal energy resolution is σ_E/E = 10% / $\sqrt{E}$, plus a constant term of 0.7%. ([100]).

The Hadronic Calorimeter

The hadronic calorimeter (HCal) is divided into 3 main parts: the tile calorimeter in the central barrel region, the liquid argon end-cap calorimeter (HEC) and the liquid argon forward calorimeter (FCal). The coverage range for the barrel part of HCal is $0< |\eta| <1.7$. The end-cap section covers the ranges $1.5< |\eta| <3.2$ and the forward hadronic calorimeter FCAL extends out to $|\eta| =4.9$. The central barrel tile calorimeter uses scintillators as the active detector material, and steel plates as absorbing material. As already mentioned both the HEC and FCal have liquid argon as the active detector material. For absorption the HEC uses copper, while the FCAL uses a copper/tungsten combination. The required energy resolution in the barrel and end-cap hadronic calorimetry is $\sigma_E/E = 50\% / \sqrt{E}$ plus a constant term of 3%. The forward hadronic calorimeter is required to have an energy resolution of $\sigma_E/E = 100\% / \sqrt{E}$ plus a constant term of 10%.

3.2.5 Muon system

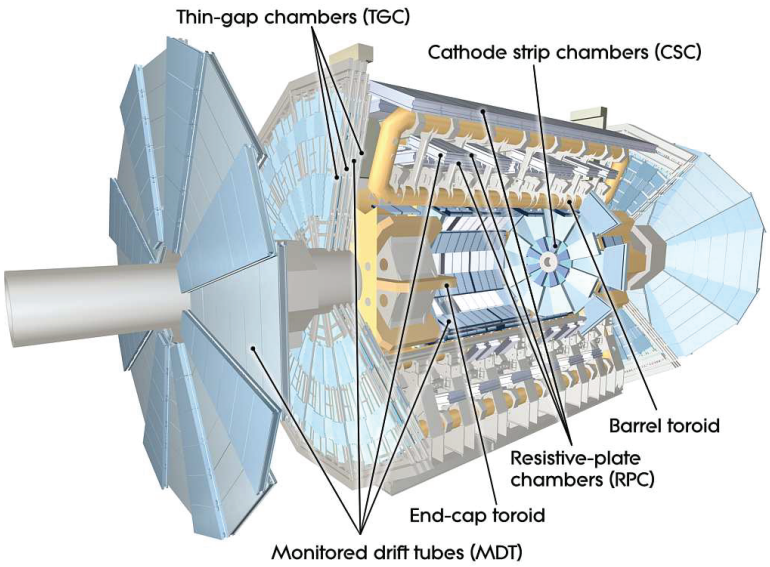

Figure 3.7: Overview of the ATLAS Muon system.

Finally there is the muon system illustrated in Figure 3.7, which extends out to the 22x46 meters that ATLAS measures. It is divided into a barrel part and an end-caps part. The muon chambers in the barrel are placed in between the toroid magnets and contain 3 layers at radii about 5, 7 and 10 meters. The end-caps are formed out of 4 circular disks at 7.4, 10, 13 and 21 m from the center of the detector and perpendicular to the beam axis. They are positioned both in front and behind the end-cap toroids. The muon system has coverage up to $|\eta| <2.7$, however at $\eta = 0$ a gap is made to allow for services to the solenoid magnet, the calorimeters, and the ID. The construction performance goal is to measure 1 TeV-tracks with a precision of 10%, i.e requiring a momentum resolution of $\sigma_{p_T}/p_T = 10\%$.

The muon system (Figure 3.7) uses 4 different detectors, for precision measurements: the Monitored Drift Tube Chamber (MDT) and the Cathode Strip Chambers (CSC), and for trigger: the Resistive Plate Chambers (RPC) and the Thin Gap Chambers (TGC). The MDTs have high measuring accuracy, about 80 μm per tube and are the most important for precise measurements of momentum. The CSCs are placed to cover the very forward region 2< $|\eta|$ <2.7. The CSCs have high rate capability and time resolution. For fast triggering on muon tracks the RPCs are used in the barrel and the TGCs for the end-caps. Within 15-20 ns a signal of a muon track is delivered, which makes the muon systems capable of performing bunch tagging, and triggering on high p_{T} muons.

3.2.6 Trigger and Data Acquisition

When LHC runs with nominal parameters, 40 million events are produced per second. No processing equipment is able to handle such large loads of data, and therefore it must be reduced drastically to around 100Hz for final storage. This is the trigger's job. ATLAS' trigger performs real-time (online) event selection in 3 stages, the Level 1 Trigger (L1), the Level 2 Trigger (L2) and the Event Filter (EF). L2 and EF make up the High Level Trigger (HLT).

The L1 trigger must deliver its decision in time for the next collision, which nominally is each 25 ns. The overall duration of the whole process from receiving data to sending the decision back must be less than 2.5 μs. The Level 1 trigger reduces the rate to about 100 kHz by triggering on high-p_T muons, electrons/photons, jets, hadronic decays of τ-leptons, and on large missing transverse energy ($E_{\mathrm{T}}^{\mathrm{miss}}$).

L2 uses information from the L1 trigger to select Regions of Interest (RoI). It then extracts full-granularity and full-precision data from the appropriate detector parts and uses dedicated algorithms for its decision. The L2 trigger sends 3.5 kHz of events along to the Event Filter, and on average each event is evaluated in 10 ms.

To reduce the rate to the requested 100 Hz which is the allowed permanent storage rate for ATLAS, the Event Filter uses offline algorithms on fully built events.

A schematic overview of the ATLAS Trigger and DataAquisition system is shown in Figure 3.8, and reads from top to bottom. Indicated in the figure are the different trigger levels to the left (L1, L2, EF), and the data flow and processing to the right, together with the rate achieved after each stage. The HLT is indicated with the curly bracket to the left.

The final piece in the data chain involves data storage, and computing power to perform the reconstruction of the raw data, MC simulation, and also for user analysis (such as the analysis performed in this thesis). CERN has developed the World-Wide-GRID for this, which is a network of computers spread around the world. The computers are typically hosted by computing centers and member institutes, such as for instance the University of Oslo. In this way the necessary storage capacity and processing needed to reprocess raw data, produce large amounts of MC data, and to perform analysis is covered.

This finalizes the description of the LHC complex, and the ATLAS detector. In the following section I discuss data formats, followed by object definitions in Section 3.5.

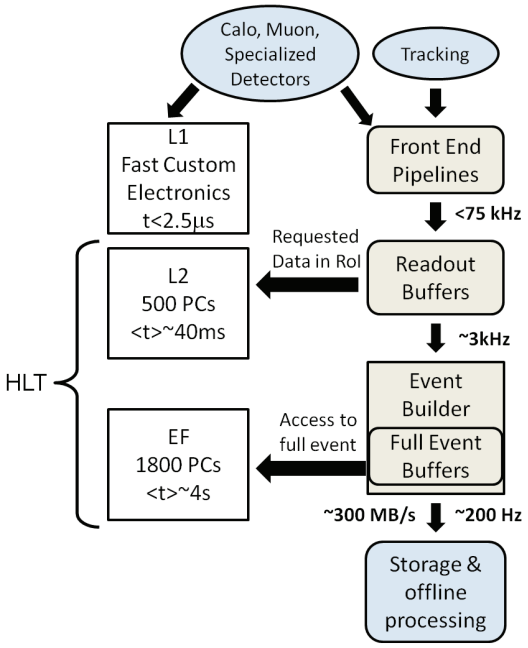

Figure 3.8: Schematic overview of the ATLAS Trigger system [102].

3.3 From simulation or detector signals to analysis files

The ATLAS community is large and complex, and relies on a common software framework, and practical data formats for analysis. Athena [103], which is written in C++, serves this function. It is the framework which allows the processing of all steps in the ATLAS data chain schematically depicted in Figure 3.9. In the following I explain briefly each of the steps in the figure, and also mention what software is used in each case.

When discussing collision data in ATLAS, the concept of an "event" is useful, and I have in fact used this term several times already. An event can be seen as a snapshot of a pp-collision, and each of these "snapshots" or events are (more or less) independent incidences, and are therefore processed independently. The typical information an analyst is interested in are the particles (objects) in the event, and all relevant information about these particles, like mass, charge, energy, momentum, and so on. Also interesting, are which triggers fired, how much energy-momentum is missing, and for instance information on whether objects have passed through problem-areas in the detector. For this the electric signals fired in the detector modules must be processed in order to lead to quantified information in terms of physics variables and particle identities.

Particles created at the interaction point in a pp-collision traverse and leave signals in the detector directly. For MC on the other hand, several steps must first be taken.

The first step is, as Figure 3.9 shows, the event generation, produced by a class of software

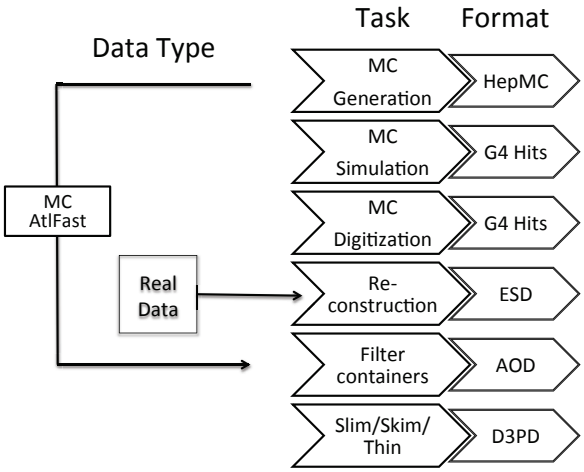

Figure 3.9: Schematic overview of the ATLAS data chain.

suitably named Event Generators. Their job is to produce a set of final state particles according to some distributions and rules based on some input theory (Standard Model or beyond). The data-format produced from this step is the so-called HepMC event record. In these files, all necessary kinematic information is linked to the particle, and also the particle's history and future in terms of its production mechanism and (possible) decay products. Vertices are also stored, including information about incoming and outgoing particles.

Computing power and numerical challenges unfortunately hinder the existence of an "optimal-ultimate-all-purpose" event generator. In addition we in fact do not necessarily know which generator is "best", since for instance the hadronization process is very complicated to understand. Among the various on the market, each with its customized speciality, a subset relevant for this analysis is quickly presentated below.

Pythia [104], Herwig [105] and Sherpa [106] are all general purpose generators that compute matrix elements to leading order (LO). These generators handle the interaction process, including initial and final state radiation, all the way to hadronization and decay into final state particles.

While Pythia, Herwig and Sherpa are all self-contained, MC@NLO [107], Alpgen [108], and PowHeg [109] need to be interfaced with tools that handle particle showering and hadronization, as they only supply the matrix element calculations. Therefore MC@NLO is interfaced with Herwig, while PowHeg uses either Pythia, Herwig or Jimmy [110][3], while Alpgen [108] uses Jimmy or Pythia. As the name implies, MC@NLO and also the newer PowHeg calculate the matrix elements to NLO in α_s, which leads to more precise predictions than LO generators.

For each event generated, the resulting particles journey through the detector, and their re-

[3]In fact Jimmy is just a library of routines linked with Herwig.

sponse to the detector material is mimicked. This is referred to as the simulation step of the MC production. To achieve this, the detector description is supplied to the software, which provides awareness about both material type and material density at each coordinate point. A toolkit named GEANT4 [111, 112] is used. This step of the MC production is extremely time-consuming (especially the particle's response to the Calorimeters), as each event takes approximately 10 minutes to fully simulate. As millions of events must be simulated it is clear that this step should not be repeated too often. Due to this time-consuming simulation process, a fast-track simulation has been developed, namely AtlFast. This instead parametrizes the particles expected behaviour in the detector, by using a smearing technique with resolutions measured from full simulation studies[4]. In Figure 3.9 the AtlFast step is shown as it skips all steps between *generation* and the creation of analysis files, thus increasing the processing speed by about 1 order of magnitude (Atlfast II). The simulation step returns a G4 Hits file, which is a type of raw data.

After simulation follows digitization. Here the detector's response to the particles, in form of times and voltages, are emulated as though real particles were passed through detector. After this step MC and data have caught up and can be treated in the same way as data, going through *reconstruction* and finally production of data files for analysis.

In the reconstruction step, all the information in the sub-detectors is run through various algorithms to match up hits to form tracks, and match tracks to energy deposits in the calorimeter. In this way the separate signals in each detector module are compiled to reconstruct particle trajectories, energies, momenta, and identification. The output of this step is the Event Summary Data format (ESD roughly 1MB/ev [113]), ready for analysis. The EDS files contain enough information for reconstruction to be rerun without going back to the G4Hits files (Raw data roughly 1.6MB/ev [113]). Rerunning reconstruction is necessary when important updates in for instance the detector calibration and/or alignement are available. Since this data format is so large, the ESDs are not distributed widely enough for users to access them frequently. Instead, another level of data files serves this purpose, namely the smaller Analysis Object data files (AODs roughly 0.1MB/ev [113]). These are files created from the ESDs and are of the same format, but contain less detailed information (they are a summary of the ESDs) and thus faster to work with. And maybe even more importantly, the smaller size allows for replication to several storage sites, which is important when many users from around the world need to access the files.

Although the AODs are smaller than ESDs, they are not practical for the "everyday" analysis. Therefore even smaller data formats exist, the so-called ntuples, which are made from the AODs, using various reduction procedures[5]. This removes whole sets of objects, for instance all the separate track information, or keeps only events with certain particles present, like for instance at least one electron with $p_{\mathrm{T}} > 5$ GeV. Both these examples are very useful in particular in an analysis such as this di-lepton search, as we are only interested in a particular final state. In this way the original data file can be significantly reduced by removing objects and information that are not needed in the analysis. The resulting files are built up with an event-by-event

[4]The actual gain is from the calorimeter simulation which is parametrized.

[5]Technically the reduction procedure is divided into three types: slimming, skimming and thinning.

structure, and are given the name DPDs, Derived Physics Data files. Several iterations of these exist, and the one used in this analysis are so-called D3PDs. These are files that are not read in the general Athena framework, but rather in ROOT [114]. ROOT which among other things, provides histogramming and statistical interpretation tools, operates with user-scripts written either in C++ or python, and is used for looping over events for analysis and plotting. With ROOT and D3PDs the demand for a fast turnaround of results is met. In fact, the results in this thesis are mainly produced with ROOT.

Now that I have presented the LHC, the whole ATLAS detector, and the full data processing chain from detector signals to analysis files, let us go back to the physics, and define some useful physics analysis variables such as the invariant mass, transverse mass, the stranverse mass, and the contransverse mass, which all are derived from the energy-momentum relation. Together with the physics objects defined in Section 3.5, we have all necessary tools to tackle the actual analysis.

3.4 Analysis variables

Invariant mass and transverse mass

The invariant mass m^2 is a conserved quantity as follows from $E^2 = p^2 + m^2$, where energy and momentum are conserved, hence also m. It is a very useful quantity since it can be used to calculate the mass of short-lived particles such as the π^0 or Z-boson which decay immediately, and thus cannot be measured directly. We can instead construct the combined invariant mass of the decay products, which is equal to the mass of the mother particle, as with the Z boson-decay into $\mu^+\mu^-$:

$$m(\mu^+\mu^-) = \sqrt{(E_{\mu^+} + E_{\mu^-})^2 - (\boldsymbol{p}_{\mu^+} + \boldsymbol{p}_{\mu^-})^2}\,.$$

The energy and the momentum of the two muons are readily available, and we therefore have a way to reconstruct the mass of the illusive Z-boson.

A more detailed description of the invariant-mass technique and its importance in measuring properties of know short-lived particles and discovering new particles, is presented in Chapter 9 where I describe the "Z-Path", an educational particle physics program aimed at high school students.

The transverse mass m_{T}, is a version of the invariant mass restricted to the transverse plane, and is defined, for a set of two particles with total energy $E_{T,tot} = E_{T,1} + E_{T,2}$, and total momentum $\mathbf{p_{tot}} = \mathbf{p_1} + \mathbf{p_2}$

$$m_{\mathrm{T}} = \sqrt{(E_{T,tot})^2 - (\mathbf{p_{tot}})^2} \tag{3.6}$$

This variable is useful when decay products are not fully reconstructed, such as with a W boson-decay to a visible charged lepton, and an invisible neutrino. The neutrino is as we know extremely weakly interacting and neutral, and hence unlikely to be detected in ATLAS. The resulting *missing energy-momentum* is therefore assigned to the neutrino. This is explained in more

detail in Section 3.5.4. We know from the discussion in Section 3.2.1 that we can only reliably determine the total energy-momentum in the transverse plane. This is therefore the reason why instead of constructing the invariant mass, must use the transverse mass. Using the example of a leptonic decay of a W-boson, and assuming the missing energy-momentum match the energy-momentum of the neutrino, the transverse mass constructed from the decay products, namely the charged and neutral leptons (ℓ and ν respectively) is

$$\begin{aligned} m_{\mathrm{T}} &= \sqrt{(E_{T,\nu} + E_{T,\ell})^2 - (\boldsymbol{p}_{T,\nu} + \boldsymbol{p}_{T,\ell})^2} \\ &= \sqrt{E_{T,\nu}^2 + E_{T,\ell}^2 + 2E_{T,\nu}E_{T,\ell} - \boldsymbol{p}_{T,\nu}^2 - \boldsymbol{p}_{T,\ell}^2 - 2\boldsymbol{p}_{T,\nu}\boldsymbol{p}_{T,\ell}}\,. \end{aligned}$$

Using the expression for transverse mass from Equation 3.5 ($E_T = \sqrt{m^2 + \boldsymbol{p}_T^2}$) and approximating the lepton masses to 0 we have $E_T = |\mathbf{p}_T|$

$$m_{\mathrm{T}} = \sqrt{2(E_{T,\nu}E_{T,\ell} - \boldsymbol{p}_{T,\nu}\boldsymbol{p}_{T,\ell})} = \sqrt{2E_{T,\nu}E_{T,\ell}(1 - \cos\phi)}\,, \tag{3.7}$$

where ϕ is a short-hand here for $\Delta\phi(\ell, \nu)$. The transverse mass m_{T} gives an upper value for the mother particle mass, i.e. for the W-boson here $m_{\mathrm{T}} \leq m(W)$.

Stransverse mass m_{T2}

Another variable we encounter is the stransverse mass m_{T2} [115]. It is analogous to transverse mass, but is constructed to account for more than one invisible particle. It is a function of the mass and momentum of the particles taking part in the interaction, and its kinematic endpoint is related to the mass of the primary (or mother) particle.

A simple SUSY production and decay chain with direct production of two sleptons, with consequent decay into a lepton and LSP, i.e. $\tilde{\ell}\tilde{\ell} \to \ell\tilde{\chi}_1^0\ell\tilde{\chi}_1^0$ is used to illustrate the application and definition of m_{T2}. Let us start by defining the transverse mass m_{T} for a single decay leg $\tilde{\ell} \to \ell\tilde{\chi}_1^0$

$$m_{\mathrm{T}}{}^2(\boldsymbol{p}_T^{\ell}, \boldsymbol{p}_T^{\tilde{\chi}_1^0}; m_{\tilde{\chi}_1^0}) \equiv m_{\ell}^2 + m_{\tilde{\chi}_1^0}^2 + 2(E_T^{\ell} \cdot E_T^{\tilde{\chi}_1^0} - \boldsymbol{p}_T^{\ell} \cdot \boldsymbol{p}_T^{\tilde{\chi}_1^0})\,, \tag{3.8}$$

where $\boldsymbol{p}_T$ is the transverse three-momentum and E_T the transverse energy of the lepton (ℓ) or LSP ($\tilde{\chi}_1^0$). This quantity is at most equal to the mass squared of the mother particle, i.e. $m_{\mathrm{T}}{}^2 \leq m_{\tilde{\ell}}^2$.

However, in this event there are two invisible particles, namely two $\tilde{\chi}_1^0$. We can therefore not know the individual momentum of each invisible particle, only the combined (missing) momentum $\not{p}_T = \not{\boldsymbol{p}}_T^{(1)} + \not{\boldsymbol{p}}_T^{(2)}$. The best we can do is therefore to evaluate the quantity

$$\min\left[\max\left\{m_{\mathrm{T}}{}^2(p_T^{\ell(1)}, \not{\boldsymbol{p}}_T^{(1)}; m_{\tilde{\chi}_1^0}), m_{\mathrm{T}}{}^2(p_T^{\ell(2)}, \not{\boldsymbol{p}}_T^{(2)}; m_{\tilde{\chi}_1^0})\right\}\right], \tag{3.9}$$

which means that the larger of the two transverse masses undergoes a minimization, by scanning the space of momentum combinations of the lepton and $\tilde{\chi}_1^0$. This results in the lower bound on

the square of the transverse mass m_T.

The equations above include the $\tilde{\chi}_1^0$ mass, which in fact is typically unknown. It is customary to substitute the unknown $m_{\tilde{\chi}_1^0}$ with a trial-mass m_χ, and with the latter substitution, we arrive to the actual definition of m_{T2}.

$$m_{\mathrm{T2}}{}^2(\chi) \equiv \min\left[\max\left\{m_{\mathrm{T2}}(p_T^{\ell(1)}, \not{p}_T^{(1)}; \chi), m_{\mathrm{T2}}(p_T^{\ell(2)}, \not{p}_T^{(2)}; \chi)\right\}\right] . \tag{3.10}$$

It can be shown that ([115]) when the trial mass equals the LSP mass, $m_{\mathrm{T2}}{}^{\max}$ in fact equals the mass of the mother particle, so

$$m_{\mathrm{T2}}^{\max}(m_\chi = m_{\tilde{\chi}_1^0}) = m_{\tilde{\ell}} \equiv \text{mother particle mass}\,.$$

The contransverse mass m_{CT}

M_{CT}, or contransverse mass [116, 117] is calculated from the kinematical properties of a pair of visible particles $v1$ and $v2$, and is typically useful in pair-production with semi-invisible decays:

$$\begin{aligned} M_{CT}^2(v1, v2) &\equiv [E_T(v1) + E_T(v2)]^2 - [\boldsymbol{p}_T(v1) - \boldsymbol{p}_T(v2)]^2 \\ &= m^2(v1) + m^2(v2) + 2[E_T(v1)E_T(v2) + \boldsymbol{p}_T(v1) \cdot \boldsymbol{p}_T(v2)]\,. \end{aligned} \tag{3.11}$$

The contransverse mass can as such be constructed from all visible pair-combinations of the two decay legs.

A suitable SM example is the semi-leptonic decay of $t\bar{t}$ pairs $t \to b\ell^+\nu_\ell$, $\bar{t} \to \bar{b}\ell^-\bar{\nu}_\ell$. Another example is the slepton pair-production considered for the variable m_{T2} above: $\tilde{\ell}^\pm\tilde{\ell}^\mp \to \ell^\pm\tilde{\chi}_1^0\ell^\mp\tilde{\chi}_1^0$.

In these cases the possible combinations of M_{CT} from a given pair-production and decay-chain is useful both as a tagger, and for extracting mass-measurements from the observables in the decay chain. The key feature is that M_{CT} is bounded from above and depends on the masses of the heavy initial particle and the invisible decay product, in addition to the mass of the visible decay products $(v1, 2)$ (when v_1 and v_2 above are the same) [118].

With a two-step decay chain, using $t\bar{t}$ as an example, we can form one invariant mass (3.12), and three M_{CT} combinations (3.13-3.15) according to Ref. [116] as follows:

$$m^{max}(b, \ell) = \frac{\sqrt{[m^2(t) - m^2(W)][m^2(W) - m^2(\nu)]}}{m(W)} \equiv k_1, \tag{3.12}$$

$$M_{CT}^{max}(b, b') = \frac{m^2(t) - m^2(W)}{m(t)} \equiv k_2, \tag{3.13}$$

$$M_{CT}^{max}(\ell, \ell') = \frac{m^2(W) - m^2(\nu)}{m(W)} \equiv k_3, \tag{3.14}$$

$$M_{CT}^{max}([b\ell], [b'\ell']) = \frac{m^2(t) - m^2(W)}{m(t)} + m(t)\left(\frac{m^2(W) - m^2(\nu)}{m^2(W)}\right) \equiv k_4 \tag{3.15}$$

which according to 3.15, form a distinct identification of the process in question. In this anal-

ysis, the set of upper bounds is specifically exploited in order to tag $t\bar{t}$ events for background suppression, and is called the "top-tagger". Another useful feature is that from the equations above, the mass of the parent particle can be calculated from

$$m(t) = \frac{k_1^4 k_2}{k_1^4 - k_2^2 k_3^2}. \tag{3.16}$$

We have all the variables we need now, so let us turn to the object definitions used in this analysis, and together with that, an explanation how ATLAS actually measures and defines particles.

3.5 Object definitions

From the detector point of view, particles are just a collection of electric signals. The object definitions are a set of rules of how to interpret these in the various sub detectors, in order to decide whether or not a (certain) particle was the source of the signals. In this section I go through the object definitions used by ATLAS, and in particular detail the ones relevant for the direct gaugino and slepton search.

3.5.1 Electrons (and photons)

Electrons are electrically charged particles, and therefore leave tracks in the Inner Detector (ID) before being slowed down and stopped by the Electromagnetic Calorimeter (ECal). In the stopping process, the electron emits bremsstrahlung photons, which convert into electron anti-electron pairs, that again emit photons and so on, creating an electromagnetic cascade or "shower". Each radiation step depletes the electron energy, until it finally is absorbed in ECal.

Electron identification software (the `egamma` Athena algorithm) uses both the tracks in the ID and the energy deposit in the ECal. First electromagnetic clusters are identified with a sliding window algorithm scanning over the η, ϕ plane. These are used as seeds for further identification. Clusters are then attempted to be geometrically matched with tracks using ΔR. If a match is found, this is an electron candidate, if not it is a photon candidate. Naturally each cluster can match more than one track. In this case the best match, corresponding to the smallest $\Delta R = \sqrt{(\Delta\phi)^2 + (\Delta\eta)^2}$ value is chosen, in addition to prioritizing tracks with most pixel hits.

Electron (and photon) identification follows a complex scheme summarized in Appendix Table B.1. Most of the cuts are η and p_{T} dependent, and here I therefore only give a qualitative review of the procedure. I also only concentrate on electrons in the barrel region with $|\eta| < 2.47$.

ATLAS operates with three e/γ quality levels, `loose`, `medium` and `tight`, each including the requirements of the previous, but either adding new requirements, or tightening the existing ones. The loose requirement is used for both e/γ, while the medium and tight only apply to electrons.

In the `loose` requirement only the shower energy and shape, in addition to its leakage into the first layer of the hadronic calorimeter are evaluated.

For `medium` electrons, there are in addition requirements on the number of hits in the pixel and SCT trackers (≥ 1 and ≥ 7 respectively), and extra requirements on the cluster and track matching ($\Delta\eta < 0.005$), as well as additional requirements on the cluster shape and energy distribution, plus a cut on the transverse impact parameter $d_0 < 5$ mm. The impact parameter measures the distance of closest approach of the electron track to the primary vertex, and is useful for suppressing electrons from γ conversions.

The `tight` electrons are constructed in order to be especially robust against fake electrons. The Transition Radiation Tracker (TRT) is utilized through its particle identification capabilities. A tight electron must have at least 15 hits in the TRT, and a certain amount of high to low threshold TRT hits (depending on p_{T} and η). TRT operates with two thresholds in order to effectively separate hadrons with a ratio of high to low TRT hits close to 0, from electrons with a non-zero ratio. Besides TRT-cuts, the ratio of cluster energy to track momentum (E/p) also separates hadrons from electrons. Hadrons deposit little energy in the ECal giving a small E/p ratio, while electrons deposit most of their energy in the ECal, and the ratio E/p is close to 1. Finally the cluster and track must be close together in $\Delta\phi$, and to suppress conversion electrons, a B-layer hit is required.

There is a potentially large contribution of electron candidates from misidentified $\pi^0 \to \gamma\gamma$ when the two photon ECal towers merge into one, and if a track (for instance from one of the many $\pi^{\pm}$s) by chance is aligned to the merged 2γ cluster. Even though the first layer of the ECal is designed with the main purpose to separate γ and π^0, a substantial amount of these fake electrons can still be reconstructed due to the huge amount of π^0s produced in connection with QCD jets. Naturally not only collimated $\gamma\gamma$ pairs can be wrongly coupled with a track, and thus fake an electron, this applies equally well to single photons. Therefore there are many possible sources of fake electrons. I discuss this further in Section 4.3.4.

To fight the fake electron background, an isolation requirement is added on top of the

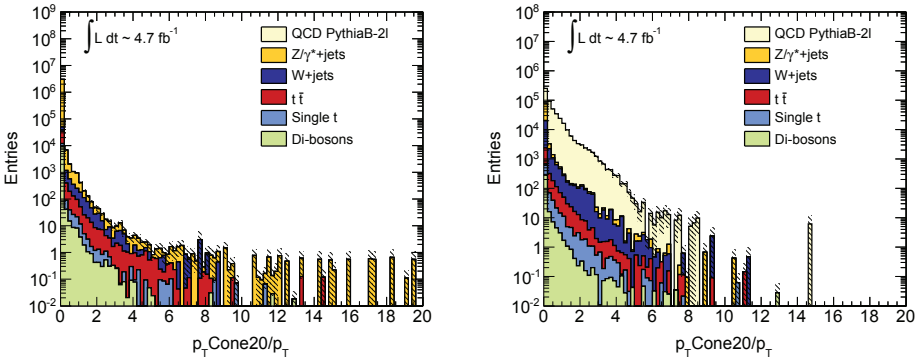

(a) Real e (b) Fake e

Figure 3.10: Isolation variable `pTcone20`$/p_{\mathrm{T}}$ for real (left) and fake (right) electrons for various SM MC processes.

egamma algorithm. Several isolation variables exist, but they all apply restrictions on the allowed energy, momentum or amount of tracks within a certain cone size ΔR around the electron. In this analysis an isolated electron satisfies pTcone20/p_{T}< 0.1. Or said in other words, the sum of p_{T} of tracks in a cone $\Delta R < 0.2$ from the electron (omitting the electron p_{T} itself) divided by the electron p_{T} should be less than 0.1. The isolation is shown in Figure 3.10 for real (left) and fake (right) simulated electrons from various Standard Model MC processes. One can clearly see the different shape of the fake and real leptons. With a cut at pTcone20/p_{T}< 0.1 63% of the fake electrons are rejected, while 99.6% of the real electrons are kept.

The electron identification scheme described above is general and was based on MC studies. After 2 years of data taking, a review of the electron (and photon) identification scheme was performed, and many improvements to the selection cuts were done. As a consequence the naming of the identification levels underwent a change, adding a ++ or PP, to indicate that they use the re-optimized identification menu.

The analysis of this thesis uses two types of electrons. These are baseline (mediumPP) and signal (tightPP) electrons defined in Table 3.1. In addition, signal electrons satisfy the isolation requirement. Both use the same $|\eta|$ and p_{T} acceptance of < 2.47 and < 10 GeV respectively. Since both a track and a cluster is associated to the electron, η and ϕ could be taken from either. Here, the track is used if it contains more than 3 silicon hits, otherwise the cluster is used. In the latter case the p_{T} of the electron (or E_T) is defined as $E^{\mathrm{clus}}/Cosh(\eta)$.

Electron definition		
	Baseline	Signal
Cut	Value/Description	Value/Description
Algorithm	egamma	egamma
p_T	> 10 GeV	> 10 GeV
η	< 2.47	< 2.47
quality	mediumPP	tightPP
isolation	-	pTcone20/p_T < 0.1

Table 3.1: The baseline and signal electron.

Besides applying the electron definitions, MC and data electrons are corrected for energy resolution and energy scale discrepancies. In data, electrons are scaled, using a scale factor sf with an uncertainty of σ_{sf} which is extracted from electromagnetic cluster energy measurements, after comparing resonance decays such as $Z \to e^{\pm}e^{\mp}$ and $J/\Psi \to e^{\pm}e^{\mp}$ in bins of η, ϕ in data. The scale factor is then applied to data as $E_{\mathrm{corr}} = E/(1 + \mathrm{sf})$, while it is usual to apply the correction uncertainty to MC in the following way $\sigma_{\mathrm{corr}}(E) = E \cdot (1 + \sigma_{\mathrm{sf}})$. MC is in addition smeared, to account for the uncertainty in the energy resolution. Finally each electron in a MC

event is given a weight (which is multiplied with the other MC-event weights) to adjust for different identification, reconstruction and track quality efficiency between data and MC.

A dedicated tool is used for the smearing and energy scale procedures, developed to work within SUSYTools, a software framework which is interfaced with Athena and ROOT in order to handle the implementation of common analysis software packages. The actual scale and smearing maps are the official Egamma Performance groups `EnergyRescaler` tool in the `egammaAnalysisUtils` Athena package. The current analysis uses the tool with tag `00-02-76`. The efficiency maps supplying the electron event weights mentioned above, are also included in this package.

3.5.2 Muons

Muons are the only charged particles that traverse the whole ATLAS detector, and leave hits in both Inner Detector (ID) and the Muon Spectrometer system (MS). Identification of muons mainly involves extrapolating tracks either from the MS to the ID, or the other way around, and matching these tracks, taking energy loss in (mainly) the calorimeter into account. The muon identification has historically used two different main types of identification algorithms, the Staco [119, 120] and the MuId [120] algorithms, often denoted as "chain 1" and "chain 2" respectively. They follow different pattern recognition algorithms, and as a result, the muon is defined (slightly) differently using the two chains.

While the Staco algorithm weights the separate tracks in the ID and in the MS based on their p_{T}, and statistically combines the tracks according to these weights, the MuId fits a combined track to the hits in the ID + MS tracks, and from this defines its muons. The Staco algorithm is the current default for analysis, including this SUSY search.

ATLAS operates with four types of muons, depending on the available information from the various detector systems. These are: Standalone (SA) muons where the muon is reconstructed from tracks in the MS only, Combined (CB) muons where both ID and MS tracks are reconstructed, and then combined, Segment-tagged (ST) muons where the ID track can be matched with at least one segment of the MS, and finally Calorimeter-tagged (CaloTag) muons where a track in the ID is matched with energy deposits in the calorimeter if this corresponds to what is expected from a minimum ionizing particle. In this analysis, the CB and ST muons are used.

The CaloTag muons provide the lowest, while the CB the highest purity, but they are all important in order to also reconstruct muons in difficult areas of the detector where the acceptance is lower, particularly in the "crack-region" at $\eta \sim 0$ (providing services for the ID, Calorimeters and magnets), and in the transition region $1.1 < \eta < 1.3$ between the barrel and the end-caps, where not all chambers have been installed (but will after the current LHC phase 0 shutdown).

For practical physics analysis, the ST and CB muons are put together in a collective "muon container", taking care of removing any overlaps between the two muon types. This analysis uses such muons.

Good quality muons are essential for any physics analysis, thus also for SUSY searches with leptons. The definitions we use for quality muons is presented in Table 3.2, including both baseline and signal muons. Staco muons must have $p_{\mathrm{T}} > 10$ GeV, and $|\eta| < 2.4$. Cosmic muons,

although useful for commissioning, are not welcome in the SUSY event selection. Therefore all cosmic muons are rejected, in fact the whole event is rejected. Cosmic muons are defined by their track's impact parameters with respect to the primary vertex of the event. Muons are defined as cosmic, if their transverse impact parameter $d_0 > 0.2$ mm or longitudinal impact parameter $z_0 > 1$ mm.

If the covariance matrix[6] of q/p is larger than 20% of the absolute value of q/p, the muon is bad, and the event is not used.

Muon definition		
	Baseline (Loose)	Signal (Tight)
Cut	Value/Description	Value/Description
Algorithm	Staco	Staco
p_T	> 10 GeV	> 10 GeV
η	< 2.4	< 2.4
cosmic μ rejection	$d_0 < 0.2$ mm, $z_0 < 1$ mm	$d_0 < 0.2$ mm, $z_0 < 1$ mm
bad μ rejection	$\mathrm{Cov}(q/p)/\lvert q/p\rvert < 0.2$	$\mathrm{Cov}(q/p)/\lvert q/p\rvert < 0.2$
isolation		`pTcone20` < 1.8 GeV

Table 3.2: The baseline (loose) and signal (tight) muon selection criteria. The Staco algorithm for muons includes both combined tracks (Inner Detector and Muon Spectrometer) in addition to Segment Tagged muons.

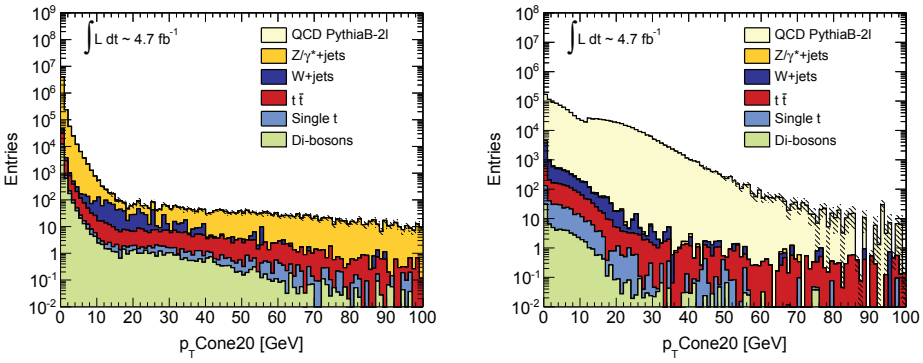

(a) Real μ (b) Fake μ

Figure 3.11: Isolation variable `pTcone20` for real (left) and fake (right) muons from various SM MC processes.

[6]which is calculated based on the χ^2 of the fit of the expected track parameter to the measured track parameter

All these are basic requirements valid for both (ST and CB) muon definitions. A tight muon is in addition asked to be isolated, with `pTcone20` < 1.8 GeV. Isolation is a handle to distinguish prompt (here called real) muons from heavy bosons or from top or tau decays, from secondary leptons (here called fakes), typically from jets. Figure 3.11 shows how the two types of leptons behave with respect to the isolation variable. A clear distinction is seen between the two, with the real muons peaking at low `pTcone20`, while the fake muons are much broader distributed at higher values. A cut at `pTcone20`< 1.8 GeV keeps as much as 95.78% of the real muons, while 79% of the fake muons are rejected.

Like for electrons, the muons must be adjusted for the observed differences in data and MC. Therefore MC muon p_{T} is smeared with the `MuonMomentumCorrections` Athena tool, and muon efficiency discrepancies are corrected with the `MuonEfficiencyCorrections` Athena tool.

3.5.3 Jets

A jet is a collimated spray of particles which, as it passes through the hadronic calorimeter (HCal), creates a broad shower from the strong interaction with the detector material. The hadrons can deposit some energy in the ECal, but the major energy release is in the HCal. The showers contain hadrons such as for instance pions, kaons, protons and neutrons, and are formed due to the nature of the strong force. When the initial partons produced in the hard interaction move away from each other in the centre of mass frame, new partons (quark, anti-quark pairs or gluons) are created in a shower-like process from the colour potential created between them. The partons in the shower form hadrons, which are the particles we finally observe in the detector. The most frequent particles are the pions (π^+, π^-, π^0), while heavier hadrons typically are produced on average by fractions of an order of magnitude smaller. The hadrons can be stable (or semi-stable) like for instance protons and neutrons, or decay via the weak (for instance $\pi^+ \to \mu^+\nu_\mu$ or $\Lambda^0 \to p\pi^-$), electromagnetic force ($\pi^0 \to \gamma\gamma$), or strong force ($\rho \to \pi\pi$).

It is important to be aware that jets do not only stem from the hard interaction process, but are a natural part of a pp collision, both from initial- and final-state radiation, but also from the so-called "underlying event", which refers to the rest of the proton which does not participate in the hard process, and finally from other soft pp collisions (pile-up) occurring at the same time. This was discussed in more detail in Section 2.1. Jets also originate from hadronic decay of for instance τ's, or other particle decays through quarks.

Identification of jets is based on techniques to find clusters of energy that can be uniquely identified with a single jet. The early jet algorithms created simple cones of a certain ΔR width, seeded by the object (a calorimeter cell) with the highest transverse energy above some lower threshold (typically above a few GeV). A proto-jet is built around the seed, gathering energy-clusters in a cone of a defined width around the seed cluster. This is done until all seeds have been assigned a proto-jet. From this an iterative process starts, where proto-jets are joined into larger jet structures, until a stable jet is found. This happens when the energy of the proto-jet typically changes with less than the order of 1%, and direction less than $\Delta R = 0.01$ (to give some ballpark sizes). These cone algorithms are intuitive algorithms, but unfortunately too

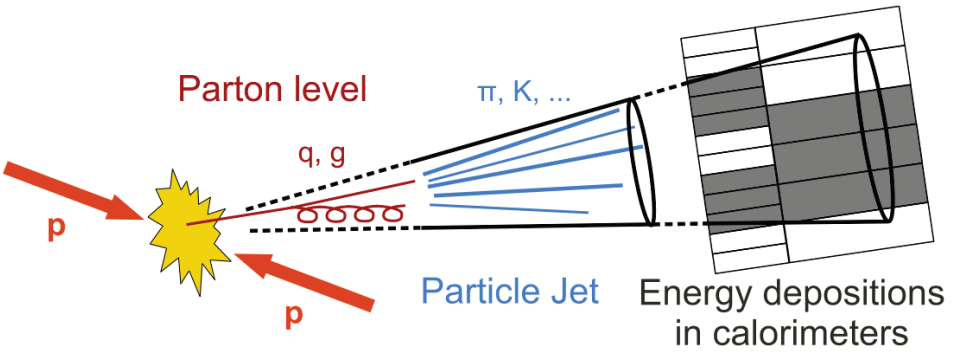

Figure 3.12: Illustration of the stages forming a QCD jet, from the parton level, via the particle jet when hadrons are formed, and finally to the energy clusters in the HCal.

simple, as they can not accommodate difficulties such as divergences due to "infrared" ($E \to 0$) and/or "collinear" (parallel to the jet direction) soft gluon emissions. More powerful cone-finding algorithms have emerged, with more refined "recombination" procedures, which have made them infrared and collinear safe, and therefore more suitable for the harsh environment of the LHC. "Recombination" procedures refer to the way particles and objects are merged together when they are believed to be part of single jet structure. ATLAS physics groups have converged to mostly using the anti-k_t algorithm [121] to reconstruct jets, which is a version of the more general k_t algorithm ([122]). Jets are identified based on distances measured between objects (stable particle tracks or calorimeter cells) defined as ([85])

$$\begin{aligned} d_{iB} &= (k_{t,i})^{2p} \\ d_{ij} &= \min\{k_{t,i}^{2p}, k_{t,j}^{2p}\}\,\Delta R_{ij}^2/R^2 \end{aligned} \tag{3.17}$$

Here i, j denotes two distinct objects, $k_{t,i}$ the transverse momentum of object i with respect to the beam axis (B), and ΔR is the usual distance in ϕ and η, i.e. $(\Delta R_{ij})^2 = (\eta_i - \eta_j)^2 + (\phi_i - \phi_j)^2$. The parameter R defines the cone width, usually spanning from 0.1 to 1.0 depending on the desired jet-width. The current value used by the SUSY group is $R = 0.4$. Three values of p are commonly used, 1, 0 and -1. While the original k_t algorithm has used p=1, the Cambridge Achen algorithm [123] uses $p = 0$, the anti-k_t combines inverse momentum, thus p=-1. ATLAS uses p=-1, as the algorithm is better protected against infrared and collinear divergences.

Once jets are reconstructed, this SUSY analysis applies a set of additional cuts, summarized in Table 3.3. A baseline jet must be found within $|\eta| < 4.9$, and with $p_{\mathrm{T}} > 20$ GeV, while a signal jet features tighter cuts: $|\eta| < 2.5$ and $p_{\mathrm{T}} > 30$ GeV[7], and a "Jet Vertex Fraction" (JVF) > 0.75. JVF measures the probability that a jet originates from a certain vertex, and the larger the value, the smaller the risk of picking up jets that stem from uncorrelated soft collisions, mostly from pile-up.

[7]These values were a result of optimization of the SUSY signal regions with jets, as is explained in Section 5.1

Jet definition		
	Baseline	Signal
Cut	Value/Description	Value/Description
Algorithm	anti-k_t ($\Delta R = 0.4$)	anti-k_t ($\Delta R = 0.4$)
p_T	> 20 GeV	> 30 GeV
$\|\eta\|$	< 4.9	< 2.5
JVF	–	JVF > 0.75
b-jet definition		
tag	`JetFitterCombNN` > -1.25	`JetFitterCombNN` > -1.25

Table 3.3: Baseline and signal jet definitions used in this direct gaugino and slepton SUSY search.

The above described jet algorithm and jet definition, are used for all sorts of jet, also jets stemming from b-quarks. However, b-jets are special. If a $b\bar{b}$ pair is produced in the hard interaction process, there is a large probability that B-hadrons form before further fragmentation. B-hadrons have a finite lifetime, which allows them to travel a small distance inside the beam-pipe before they decay. This produces a *secondary vertex*, which can be reconstructed by the pixel detector, especially designed for this.

B-tagging algorithms typically use (a combination of) secondary vertices, impact parameters, and topology to identify b-jets. The concept of impact parameter (in fact transverse impact parameter d_0) is illustrated in Figure 3.13. This SUSY analysis uses the `JetFitterCombNN` (where the `NN` refers to the use of neural networks) variable, which is a combination of the so-called IP3D variable and the JetFitter. IP3D primarily uses the track impact parameter to define the b-jet, while the the JetFitter mainly uses the b (and c-) hadron topologies. Topologies in this case refer to the assumption that the primary vertex, the b-hadron and subsequent c-hadron vertices all lie along a common line, namely the flight direction of the b-hadrons.

In this analysis, a b-jet is defined if its `JetFitterCombNN` value is > -1.25, as shown in Table 3.3. The identification efficiency is high, about 80% using this definition, when estimated using $t\bar{t}$ MC. The mis-identification rate is very low, with a probability of the order of 1% to wrongly identify a light jet as a b-jet.

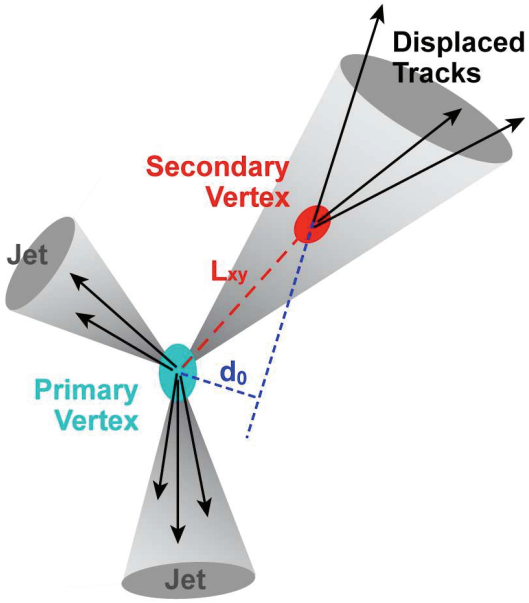

Figure 3.13: Cartoon showing the definition of the transverse impact parameter d_0, between a track from a secondary vertex and the primary vertex. L_{xy} is the distance between the secondary and primary vertex in the transverse plane. From Ref. [124].

3.5.4 Invisible particles and the $E_{\mathrm{T}}^{\mathrm{miss}}$ variable

Electrons, photons, muons and hadrons from jet production, are all observable in the detector. The neutrinos on the other hand are not, as they are neutral and only interact very weakly. Thus they pass through the whole detector without leaving a trace. Neutrinos are very important in particle physics, and they are crucial for a full understanding of the collision event.

Another interesting (so far hypothetical) invisible particle is naturally the lightest hypothetical neutralino $\tilde{\chi}_1^0$, which is the LSP and thus is stable in an R-parity conserving Minimal Supersymmetric Standard Model (MSSM). This means it behaves just like a neutrino from the detector point of view, but is much more massive, thus escaping with even more energy.

Assuming a perfect collision (head-on) in a perfect detector (100% efficient and hermetic), a neutrino can be inferred from *missing* energy, when comparing the initial and final states in the process. As a real high energy particle collision is far from "perfect", the situation is somewhat more complicated. Firstly we remember that it is the *transverse* energy that must be used, as discussed in Section 3.2.1. Secondly, missing energy can come from the detector itself, due to inefficient instrumentation, or wrongly measured energy of the accompanying objects in the event due to mis-calibration issues. The missing energy variables we use are therefore defined in order to reduce these effects. We define E^{miss} projections as follows

$$E_{x(y)}^{\mathrm{miss}} = E_{x(y)}^{\mathrm{miss,calo}} + E_{x(y)}^{\mathrm{miss},\mu} \tag{3.18}$$

deduced from the calorimeter (Ecal and HCal measurements), and the muon contributions (μ). If the event is perfectly balanced this sum is zero, hence the missing energy is a result of the energy imbalance ideally caused by a particle that escaped. In more detail, the calo and μ terms are defined as

$$E_x^{\text{miss,calo}} = -\sum_{i=1}^{N_{\text{cell}}} E_i \sin\theta_i \cos\phi_i \tag{3.19}$$

$$E_y^{\text{miss,calo}} = -\sum_{i=1}^{N_{\text{cell}}} E_i \sin\theta_i \sin\phi_i \tag{3.20}$$

$$E_{x(y)}^{\text{miss},\mu} = -\sum_{\text{selected } \mu' s} p_{x(y)}^{\mu} \tag{3.21}$$

i.e. the negative sum of each contribution's energy or momentum projection onto x(y).

From these variables the transverse missing energy $E_{\text{T}}^{\text{miss}}$ is thus defined by

$$E_{\text{T}}^{\text{miss}} = \sqrt{(E_x^{\text{miss}})^2 + (E_y^{\text{miss}})^2} \tag{3.22}$$

In this particular analysis, $E_T^{\text{miss,rel}}$ (and therefore also E_T^{miss}) is based on actual reconstructed objects, such as the jets, electrons, and muons, in addition to the topological calorimeter clusters outside any reconstructed jet or electron (CellOut). The latter term is to account for stray energy deposits. The objects and the Cell-Out terms included have certain quality cuts, and their calibration is taken into account in the $E_{\text{T}}^{\text{miss}}$ calculation. This reduces the contribution from calorimeter noise and fake muons.[8]

To reduce sensitivity to detector effects, the $E_{\text{T}}^{\text{miss,rel}}$ variable is instead used in this analysis. It is defined as

$$E_{\text{T}}^{\text{miss,rel}} = \begin{cases} E_{\text{T}}^{\text{miss}} & \text{if } \Delta\phi_{\ell,j} \geq \pi/2 \\ E_{\text{T}}^{\text{miss}} \times \sin\Delta\phi_{\ell,j} & \text{if } \Delta\phi_{\ell,j} < \pi/2 \end{cases} \tag{3.23}$$

where the "rel" refers to the relative distance in ϕ between the $E_{\text{T}}^{\text{miss}}$ and the nearest lepton or jet in the event. We see from the equation that when $E_{\text{T}}^{\text{miss}}$ is more aligned with a lepton or jet ($\Delta\phi_{\ell,j} < \pi/2$), only the $E_{\text{T}}^{\text{miss}}$ component perpendicular to this lepton or jet is used. An object is most probably badly reconstructed if most of its energy is aligned with the $E_{\text{T}}^{\text{miss}}$.

This concludes the definition of the objects important in characterizing SM processes and in the search for SUSY direct gaugino and slepton production. With these tools and methods we can now confidently identify the hard interaction process from the many overlapping processes occurring in the particle collision. We can identify and measure decay products like photons, leptons, and jets, and account for missing energy. And finally, the fine tracking resolution allows us to resolve secondary vertices (mostly) from b-hadrons, such that we can identify

[8] The calculation is done with the `METUtility` Athena package, and is based on the `Simplified20_RefFinal` E^{miss} variable.

$t\bar{t}$ production for instance, which is an important background for direct gaugino and slepton SUSY searches. This is to be explained in later chapters.

In the next section I present a summary of my qualification task performed on monitoring the noise in the SCT modules. This is followed by work performed during the commissioning period of the ATLAS detector with cosmic muons.

3.6 Commissioning and monitoring of ATLAS

3.6.1 Noise monitoring of SCT modules

An ATLAS member must perform a certain amount of service-work in order to qualify as ATLAS author. My qualification task was done within the SCT, a historically important detector for the Oslo group, as we were one of the institutes building the modules.

The task was to look closer at the noise-measurements performed within the monitoring framework of the SCT, especially investigating the performance of a newly implemented noise-algorithm dubbed the ratio-noise algorithm. Details on the study can be found in Appendix A, including an overview over the monitoring services. Here, however, I give a quick summary of the study and result.

The ratio-noise algorithm

The ratio-noise algorithm is a simple way to measure noise in the modules of the SCT. It relies on the ratio

$$R = \frac{\text{Hits on one side}}{\text{No hits on either side}} \tag{3.24}$$

which is just the ratio of occurrences of hits on a single side of the two-sided SCT module strips, divided by the occurrences of strips with no hits on either sides. This is measured in empty events, where no physics objects are expected to pass the detector, thus in a perfectly mathematically world, all strips should have no hits on either sides. The noise is built from the ratio R above in the following way

$$\text{NO} = \frac{1}{768}\frac{R}{2+R} \tag{3.25}$$

where 768 stems from the total number of strips in each SCT module. For a derivation of the expression, see Appendix Section A.2.

Online and offline measurements

The ratio-noise was implemented as part of the SCT Monitoring package with its own tool, the SCTRatioNoiseMonTool. This tool was used both for online real-time assessment of the module-noise, and offline analysis. My main task was to compare results obtained in the online versus offline implementation of the tool. I did most of this work using the event-wise ratio-

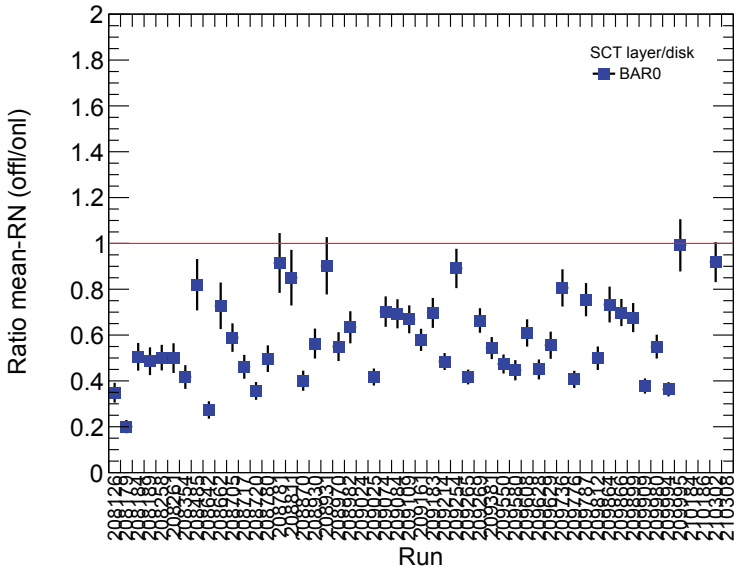

Figure 3.14: Ratio of ratio-noise measured offline versus online versus run-number.

noise.

Although the same tool is used both online and offline, the frequency in which the actual noise is calculated differs. In the online implementation the calculation is done every 1000 events, while in offline mode, the ratio-noise calculation is called at the very end of each run, and therefore hits are accumulated over a longer period of time. This automatically results in differences when comparing online and offline measurements, as the noise is in fact a ratio, and a sum of ratios is not the same as the ratio of the sum of the denominator and numerator. One must also have in mind that the noise level can evolve during the run, and that the offline measurement is an integral of the whole run. So whereas the online noise measurement gives a snapshot of the noise level at this instance, the offline gives an integrated measurement. However, the results are not expected to differ by large values, and certainly not by as much shown in Figure 3.14, where the online and offline results are divided and displayed as a function of run number.

These discrepancies resulted in more detailed investigation of the SCTRatioNoiseMonTool. The distribution in Figure 3.15 revealed interesting results. The plot shows how the ratio-noise evolves as a function of time for run 209980. Here we see that during STANDBY, when the modules are in a low voltage configuration (50 V, blue hatched area), the ratio noise is high, but after the detector is switched ON and modules are set in their nominal voltage configuration (150 V, green hatched area), the noise is gradually reduced. The noise is expected to be lower when the detector is ON compared to in STANDBY, however, the fall-off curve was unexpected, and an investigation was initiated to determine what the effect could stem from.

A special sequence of runs revealed the underlying reason for the noise development, see Figure 3.16. While the SCT modules were running with nominal voltage, the data-taking

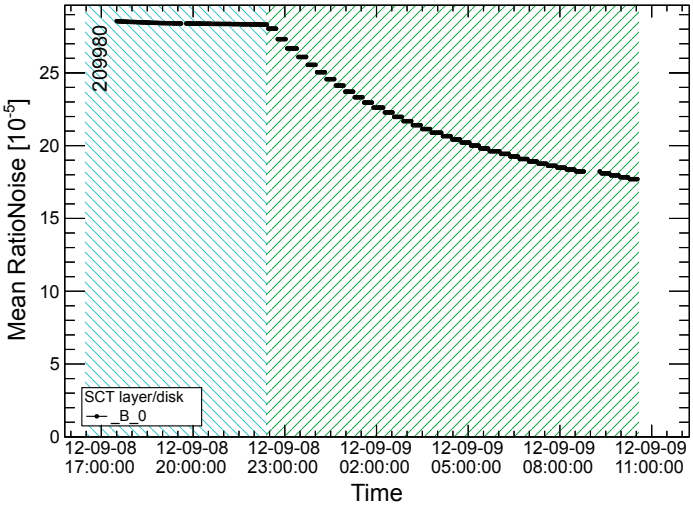

Figure 3.15: Mean ratio-noise in run 209980 measured by DQMF versus time. The blue area marks the STANDBY-period, the green when SCT in ON.

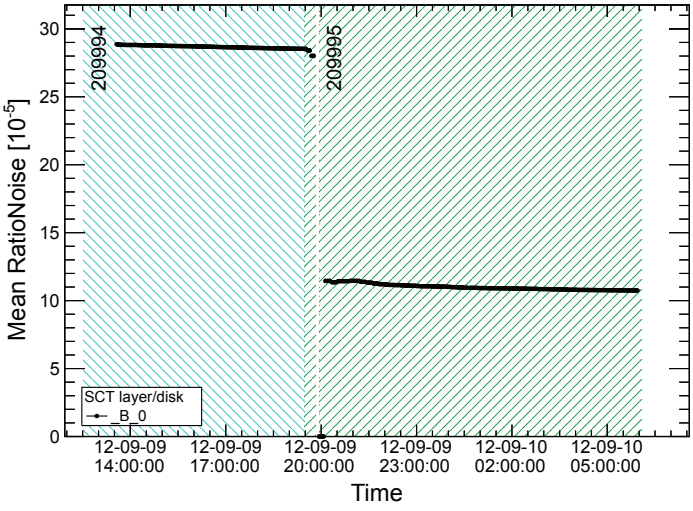

Figure 3.16: Mean ratio-noise for consecutive runs 20994 and 20995. The blue area marks the STANDBY-period, the green when SCT in ON.

stopped (run was killed), and then re-initiated (a new run started), without powering down the modules. The figure shows how the the SCT modules were set ON in run 209994, and shortly after the data-taking stopped. As the second run started, still with SCT ON, the noise-level had decreased substantially, without the characteristic fall-off curve seen earlier. This prompted a bug-finding search, resulting in the detection of a hits counting variable that was not refreshed

as it should. After the bug was fixed, the noise versus time showed the expected behaviour as Figure 3.17 presents. The noise now falls immediately after turn-on, and shows a more natural fluctuation compared to the very smooth distribution in earlier runs.

Figure 3.18 summarizes the improvement between the online and offline results. The left plot shows the relative difference (diff) between the online (ONL) and offline (OFFL) ratio-noise (RN) measurement defined as

$$\text{diff} = \frac{<\text{RN}^{\text{OFFL}}> - <\text{RN}^{\text{ONL}}>}{<\text{RN}^{\text{OFFL}}>}$$

A clear improvement can be seen by comparing the left and right plot which show the relative difference between the offline and online ratio-noise before the bug-fix and after. The distribution is now centred around 0, and has a much narrower width.

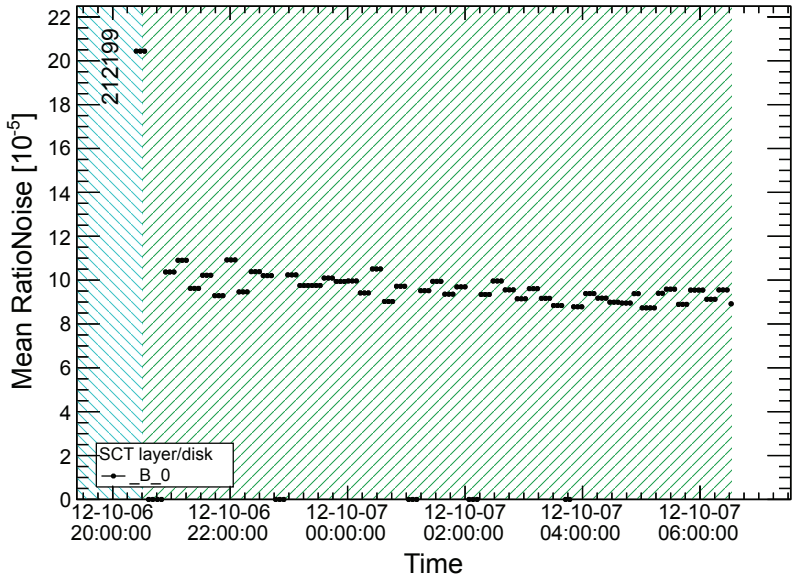

Figure 3.17: Mean ratio-noise versus time from DQMF for run 212199. The blue area indicates the period of the run before stable beam, and the green area the period with stable beam. The measurement ends when the run stops (white area).

This concludes the summary of my qualification work, performed during summer and fall of 2012. In the next section I present work done in connection to the pre-data-taking period with cosmic muons.

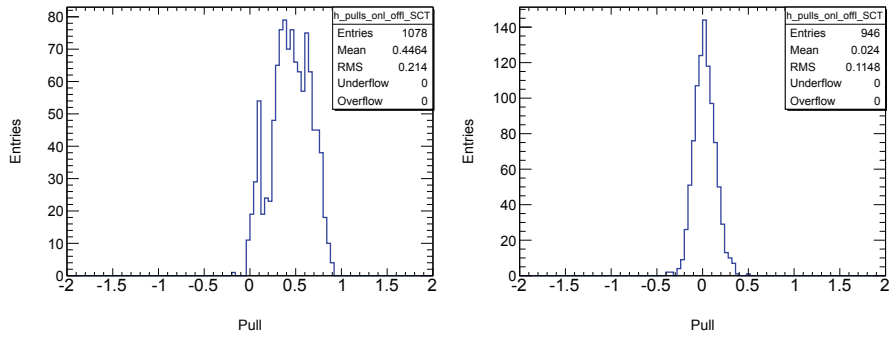

(a) Pre fix, onl-offl

(b) Post fix, onl-offl

Figure 3.18: Difference between ratio-noise online and offline measurements. The left plot shows the results before the bug-fix, and the right after.

3.6.2 Commissioning ATLAS with cosmic muons

Muons were used extensively to commission the detector before collision data came (at last) in 2009. Several hundred million cosmic ray events were collected between 2008 and 2009. I was involved in this work as part of the Muon Combined Performance Group (MCPG), investigating charge asymmetry, comparing the tracks in the Inner Detector (ID) and Muon Spectrometer (MS), their alignment, energy loss, and resolution, among other things. The analysis was done directly on ESD files, so the flexibility for detailed analysis was (practically) unlimited, with the possibility to go down to hit-level on each detector module. In the following I use public ATLAS plots where available, and my private distributions otherwise[9].

In the commissioning period extensive work was put into correcting for any possible misalignement, both within the MS itself, but even more importantly between the ID and the MS. Figure 3.19 shows the transverse and longitudinal impact parameter difference between the tracks measured in the MS and the ID, after alignement corrections were made. The results are shown using cosmic data collected in 2009. In Figure 3.20 the angular correlation in the ID and MS is visualized for ϕ_0 (left) and θ_0 (right). Both figures display excellent alignement between the two detectors. In Table 3.4 the fit results extracted from the above distributions are summarized. The alignement is impressive, with the transverse impact parameter differing only by -0.9±0.7 μm, and the longitudinal by 2.0±3.7 μm, while the azimuthal alignement is -0.053±0.005, and polar alignement 0.27±0.03.

In Figure 3.21 the relative transverse momentum resolution is plotted as a function of p_{T} for three types of tracks, namely the standalone ID and MS tracks, and for the combined muon (CB) tracks. As the figure shows the resolution of the combined track is driven by the ID at low momentum, and by the MS at high momentum. Up to ~100 GeV the resolution is well below 10%.

[9]It must be noted that although my distributions were presented in various meetings within the MCPG, they are not official ATLAS plots, and therefore do not carry the "ATLAS"-label, but are instead marked "Work in progress".

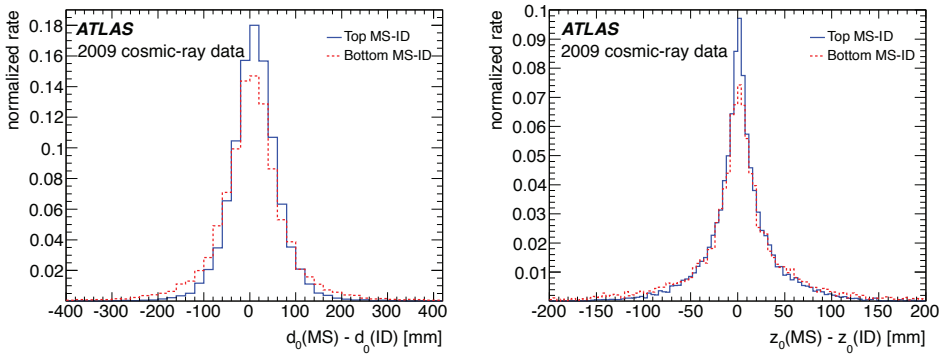

(a) (b)

Figure 3.19: The difference between MS and ID measured transverse (left) and longitudinal (right) impact parameters , both in mm. As the muon passes the detector from top to bottom, the measurement is performed separately for the top half and the bottom half of the detector, as indicated in the legend. From [125]

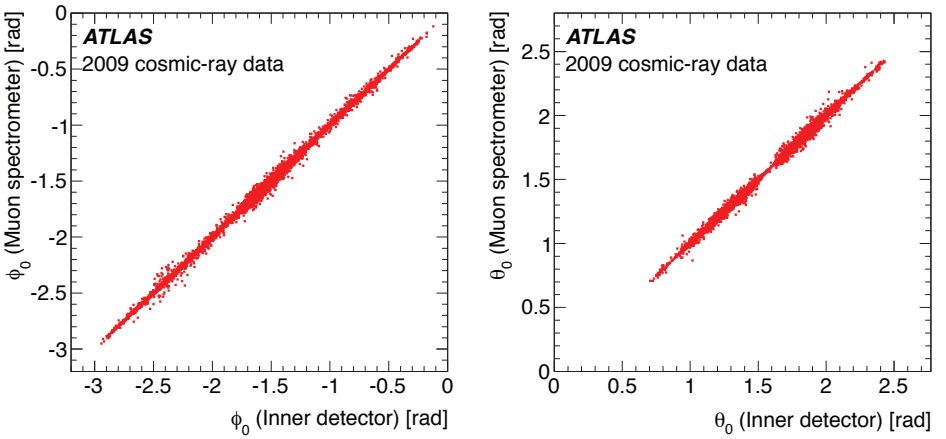

(a) (b)

Figure 3.20: The correlation between ϕ (left) and θ (right) in the bottom MS and ID detectors. From [125]

Besides the importance of good resolution both with respect to geometry and energy, the charge identification must also be determined reliably. Since this depends on the curvature of the track, the charge misidentification rate increases with p_{T}. During the course of working with the cosmic muon data within the ATLAS Muon Combined Performance Group, I attempted to determine the charge misidentification rate by comparing the charge measured separately in the ID and MS. The charge misidentification rate is then the number of instances the charges disagree (two tracks with opposite charges) relative to all track combinations measured (opposite

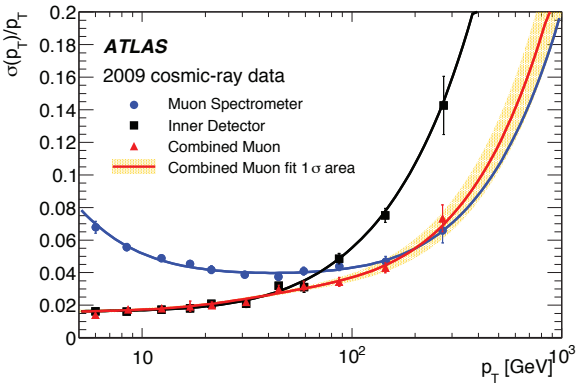

Figure 3.21: The relative p_{T} resolution as a function of p_{T} for standalone Inner Detector (ID) and Muon Spectrometer (MS) tracks, and for combined muon (CB) tracks. The yellow band shows the $\pm 1\sigma$ region of the fit to the curve of the CB tracks. From [125]

Parameter	Mean	Resolution
ϕ_0 (mrad)	-0.053±0.005	0.164±0.004
θ_0 (mrad)	0.27±0.03	0.80±0.02
d_0 (μm)	-0.9± 0.7	26.8 ± 0.8
z_0 (μm)	2.0 ± 3.7	116.6 ± 2.9

Table 3.4: Alignement between the Inner Detector (ID) and the Muon Spectrometer (MS) sub-detectors measured in the transverse and longitudinal impact parameters d_0 and z_0. [125].

(OS) and same sign (SS)), i.e. the ratio

$$R = \frac{N(OS)}{N(OS) + N(SS)}$$

This ratio is shown in Figure 3.22, and as expected increases with p_{T}. Up to ~100 GeV the charge-misidentification stays well below 1%, but rises to around 10% above 300 GeV.

Using this definition of charge mis-identification gives a larger rate than reported with truth studies, which typically lie at the order of a few percent at TeV energies ([126]). One of the explanations is that for large momentum the MS is expected to be able to determine the charge exactly, and not the ID. Therefore it is to some extent too conservative to compare the two, as the MS measurement should be given priority. Another important aspect is that the alignement was still in early stages of calibration and not yet completely optimized, affecting the measurements in the detector. However, the study still gives useful insight into the charge identification abilities in the two detector systems.

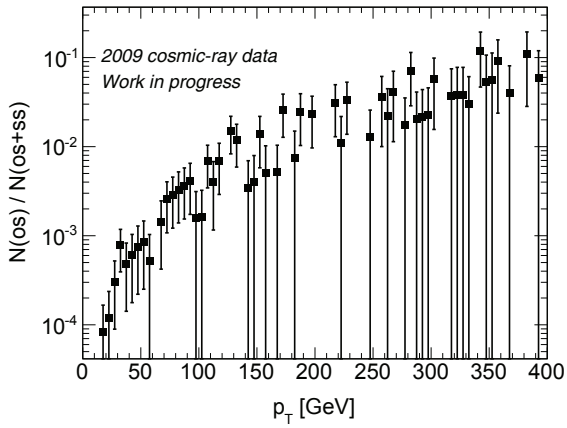

Figure 3.22: The frequency in which charges in the ID and MS disagree (OS).

An attempt was also made to measure the cosmic muon charge asymmetry. Cosmic muons are created as a result of (mostly) proton collision with molecules in the atmosphere, producing secondary pions and kaons, which consequently decay to muons (and neutrinos). Due to the primary cosmic-ray abundance of protons (over neutrons and anti-protons), the collisions favour positive meson production. Therefore the relative amount of μ^+ to μ^- should be > 1. An illustration of a cosmic ray shower resulting from the cosmic-ray impact on the air-molecules in the atmosphere is shown in Figure 3.23. The figure shows primary meson production, and the secondary muon, hadron and electron production. Here I am interested only in the muon component, which makes up more than half the cosmic radiation (at sea-level).

Figure 3.24 (a) shows the muon charge asymmetry I obtained in ATLAS, with a mean value of 1.27±0.01(stat.). Note that the errors are expected to be larger when taking into account systematic uncertainties. The ratio compares well with measurements done by other experiments, for instance BESS (Baloon-borne Experiment with Superconducting Spectrometer) [128], whose results are shown in Figure 3.24 (b). BESS is an experiment whose scientific mission is to detect antiparticles in the cosmic radiation. They measure a p_T dependent ratio, with a value around 1.3 above 10 GeV. So although ATLAS is underground and BESS in the air, the measurements are consistent.

With the large amount of cosmic muons studied, adjustments to the detector calibration were successfully performed. At the turn on of the beam in 2010 with $\sqrt{s} = 7$ TeV, ATLAS could therefore immediately produce invariant mass spectrum plots showing the well-known $\mu^+\mu^-$ mass-peaks in a spectrum ranging from below 1 GeV to the Z-boson ~91 GeV, using a simple level 1 trigger, and loose muon quality cuts. With the experience from the cosmic muon work, I too could produce such a plot at once, and the excitement of the result (now updated with 2011 data) shown in Figure 3.25 can not be exaggerated. The distribution shows 7 di-muon resonances, starting with ρ/ω just below 800 MeV, continuing with ϕ at ~1 GeV, with J/Ψ at ~3 GeV and just above Ψ', further along comes $\Upsilon(1S)$ at ~9.5 GeV, $\Upsilon(2S)$ just above, and

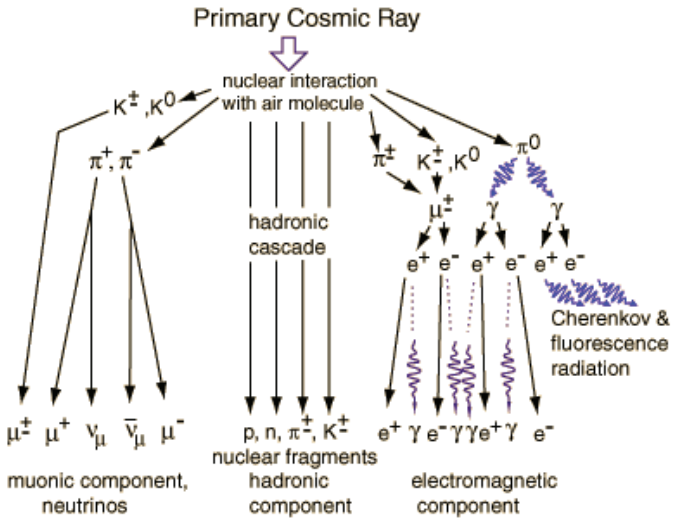

Figure 3.23: Illustration of cosmic ray showers from cosmic ray collisions with the earth's atmosphere. Figure from [127].

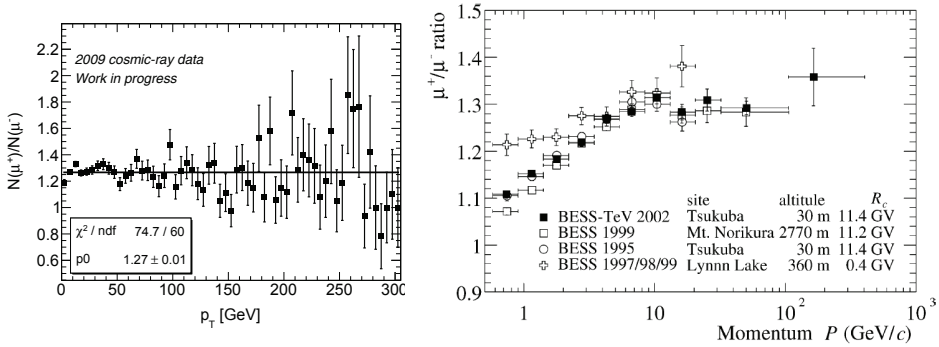

(a) ATLAS cosmic muon charge ratio

(b) BESS cosmic muon charge ratio [128]

Figure 3.24: Cosmic muon charge ratio as measured underground in ATLAS (a) and in the balloon experiment BESS (b).

finally the Z-boson at ~91 GeV.

Still today, this is the finest plot I made, and I find great inspiration to look back on it.

Taking part of the commissioning of the ATLAS detector was a very useful entry point into collider physics, which is the theme of the rest of this thesis. The next chapter presents the relevant SUSY signal and SM background processes and how we successfully can separate the two, in order to win over the large background cross section.

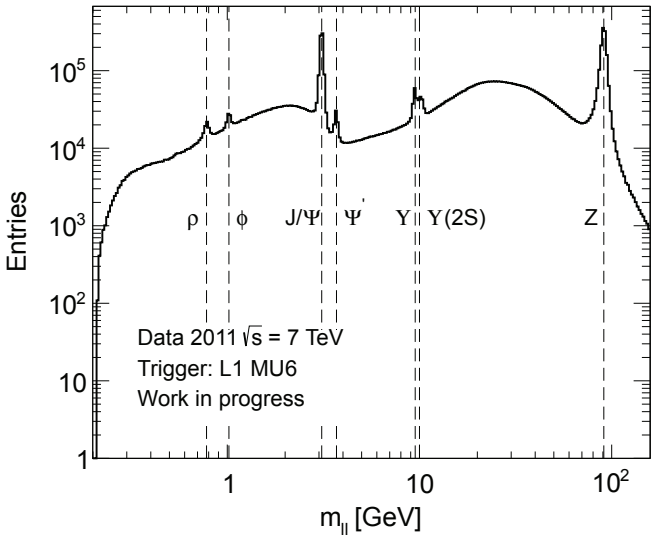

Figure 3.25: The invariant mass spectrum for opposite sign di-muons. The mass peaks are clearly visible with ρ/ω just below 800 MeV, the ϕ at ~1 GeV, the J/Ψ at ~3 GeV, and Ψ' just above, then the $\Upsilon(1S)$ and $\Upsilon(2S)$ at ~ 10 GeV, and finally the Z-boson at around 91 GeV.

Chapter 4

SUSY signal and SM background processes

4.1 Cross sections at the LHC

Out of the large number of pp collisions at the LHC, only a small fraction are of real interest. In this section I briefly present the total inelastic pp cross section measured by ATLAS with the 2010 $\sqrt{s} = 7$ TeV data, and compare to the expected cross sections of the Standard Model, as well as some SUSY scenarios.

Total pp (and $\bar{p}p$) collision cross sections cannot (yet) be calculated theoretically with pertubative QCD, and it is therefore of great interest to determine these experimentally. To do this, ATLAS uses Minimum Bias Trigger Scintillators (MBTS) installed in front of each of the end-cap calorimeters. As the name implies they serve both as a trigger and as a detector. When attempting to measure the total inelastic cross section it is important to get "everything", and not bias the measurement in one way or the other. Naturally it is impossible to not be biased at all, the best we can do is to be minimally biased, hereof the name. The MBTS therefore triggers if at least one charged track is registered (above the threshold 0.15 pC to suppress noise [129]) in either of the detectors. This is needed since the total inelastic cross section can be decomposed into four main components. These are the single diffractive processes (SD, $pp \rightarrow pX$), double diffractive processes (DD, $pp \rightarrow XY$), central diffractive (CD) ($pp \rightarrow pXp$), and non-diffractive processes (ND) ($pp \rightarrow XY$). The central-diffractive processes are less important, suppressed by a factor of 10 compared to SD at high energies [129]. The first three of these are in Figure 4.1, and the non-diffractive events are those that belong to the pertubative regime which were already discussed in Section 2.2 (hard interaction). In the single diffractive processes one proton (p) continues unperturbed, while the other fragments into a set of tracks X, with mass M_x. In the double diffractive processes, both protons fragment. This can result in tracks in just one of the MBTS or both, depending on whether the collision is SD or DD.

As the diffractive collisions are expected to make up around 25%-30% ([129]) of the total inelastic cross section, and are part of the underlying event, they are important to take into account for an inclusive measurement. The results from ATLAS [130] performed on 20 μb^{-1} of

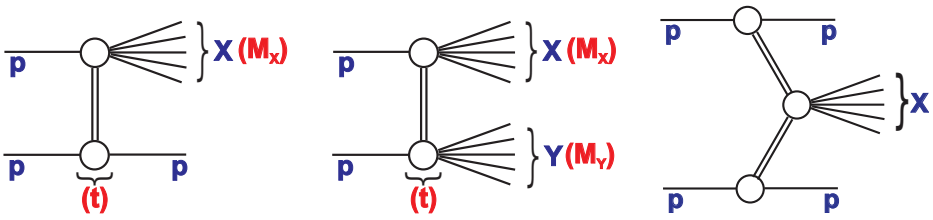

(a) SD (b) DD (c) CD

Figure 4.1: Illustration of the single diffractive (a), double-diffractive (b), and central-diffractive (c) processes [129].

data, and with events selected by requiring hits on scintillation counters in the forward region of the detector, a total inelastic cross section of 60.33±2.10 mb was measured within the detector acceptance. The result has also been extrapolated to full acceptance, and is then found to be 69.4±2.4±6.9, where the last error is related to the extrapolation procedure.

The majority of the events used in the total cross section measurement are in form of jets, and only a small fraction comes from electroweak SM processes, as Figure 4.2 shows. Here the cross sections are shown as a function of energy for all important SM production processes, including some Higgs boson production processes. The total cross section σ_{tot}, at $\sqrt{s} = 7$ TeV is close to 10^8 nb, which translates to 100 mb, not far from the measured total cross section from ATLAS (60.33 mb). The single W boson production which is the largest of the SM electroweak processes is very small compared to this, only at the order of 100 nb. And in comparison to this the Higgs boson production is vanishingly small with the largest cross section production mechanism through gluon-gluon fusion (σ_{ggH}), at around $2{\cdot}10^{-2}$ nb.

How does the electroweak SUSY production compare to the above? This is discussed in more depth in Section 4.2. However, it is interesting already now to look at the expected cross sections as function of the gaugino masses using mSUGRA (Figure 4.3). In this model the gauginos have low mass, and the highest cross sections range from 10^{-4}-10^{-2} nb (at $\sqrt{s} = 14$ TeV). So in this optimistic scenario the production cross section is comparable with the Higgs cross section. However, with higher masses the cross section quickly decreases by several orders of magnitude.

In order to be able to discover SUSY particles with such small production cross sections, it is essential to identify decay channels which have the potential for an experimentally significant signal to noise ratio. But even more important is to evaluate other less constrained models. Especially those that might yield larger cross sections for the electroweak signal, and no strong production. This is favourable since any new physics driven by the strong production will inevitably be swamped by more abundant QCD processes. This can for instance be obtained in models where the squark and gluino masses are beyond LHC reach, opening up the possibility for detection of direct electroweak SUSY production. Naturally this still assumes that the cross sections are large enough, and that we can control the background processes.

The next sections go through the decay channels that are considered in this analysis, and the signal footprints used in the search, in addition to the background processes that contribute.

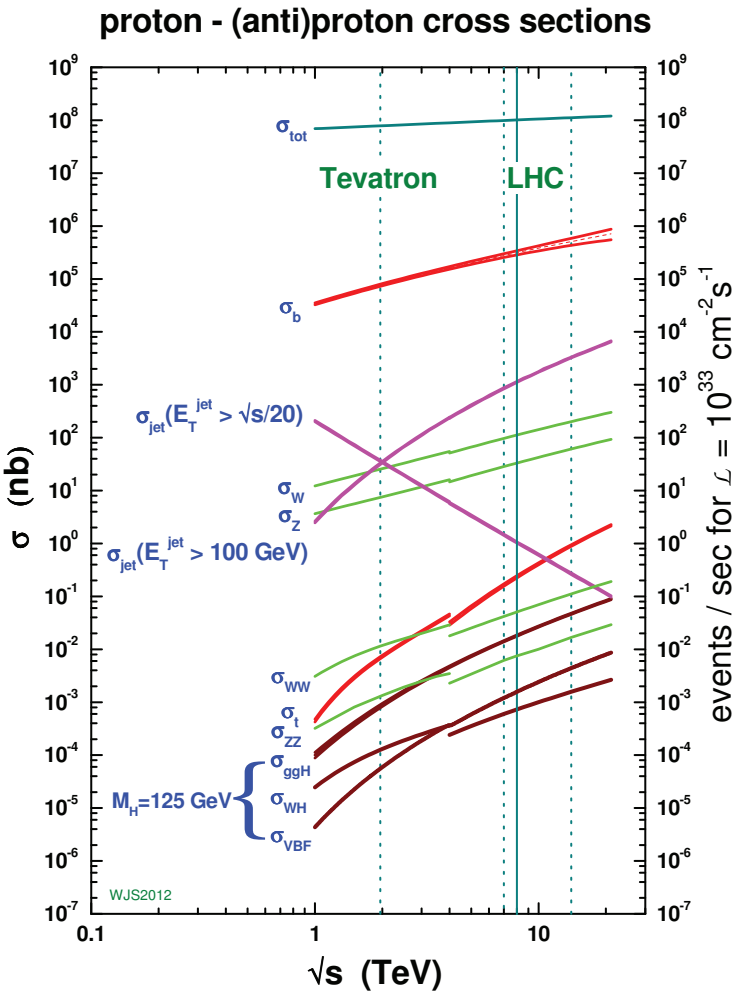

Figure 4.2: Predicted SM cross sections as a function of energy. The $\sqrt{s} = 7$ TeV line relevant for the LHC is marked by the second stapled line from the left. [131].

These sections are a description of the analysis as carried out in the supporting ATLAS internal note [133], which is the basis for the publication "Search for direct slepton and gaugino production in final states with two leptons and missing transverse momentum with the ATLAS detector in pp collisisons at $\sqrt{s} = 7$ TeV" [134].

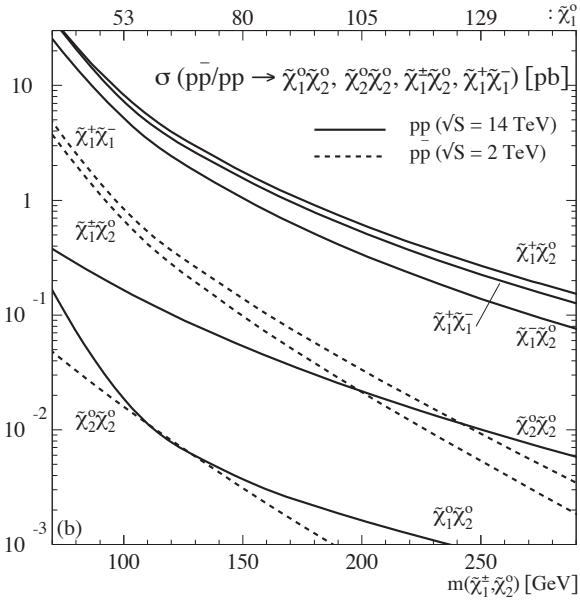

Figure 4.3: Expected cross sections for gaugino production at $\sqrt{s} = 2$ ($p\bar{p}$) or 14 GeV (pp) calculated assuming SUSY realized in mSUGRA [132].

4.2 Signal processes

With the LHC proton-proton beams, the dominant particle production is through colour exchange, and as SUSY obeys the gauge interactions of the SM, the squark and gluino production cross-sections are expected to be the largest. Still, this analysis focuses on direct gaugino and slepton production, which can be favoured if nature has constructed SUSY with very large squark and gluino masses, so large that the abundant strong production at the LHC is inaccessible. The current limits [135] on the gluino and squark masses are 1.35 TeV, and 0.78 TeV respectively[1] which are getting close to the kinematic limit, and hence makes direct gaugino and slepton production a probable scenario (assuming SUSY is true).

With squarks and gluinos out of the way, lepton final states from electroweak decays become important. Gauginos and W and Z-bosons have a relatively large branching ratio to leptons, which are known to give very clean detector signatures. When it comes to direct production of sleptons, the cross section at the LHC is very small. However, it is a very interesting channel, as direct decays into leptons plus an LSP feature short decay chains and simple signatures.

Many SUSY models such as mSUGRA, assuming a specific breaking mechanism, do not allow for arbitrarily large mass-differences between coloured and non-coloured sparticles, since the mass-hierarchy is set by the symmetry breaking[2]. However, in the phenomenological MSSM (pMSSM) the parameter-space is much larger and scenarios where direct production of non-

[1] Evaluated in simplified models: $\tilde{q}\tilde{q}$, $\tilde{q} \to q\tilde{\chi}_1^0$ and $\tilde{g}\tilde{g}$, $\tilde{g} \to q\bar{q}\tilde{\chi}_1^0$.

[2] See Chapter 1.3.8.1 for details.

coloured sparticles dominate are perfectly attainable. The underlying reason for this is that the pair-production of neutralinos and charginos and their subsequent decay is highly sensitive to their gaugino/higgsino content, which in the pMSSM is not fixed as in constrained models like mSUGRA.

In the next couple of sections I present the general production mechanisms and decay chains relevant for the direct gaugino and slepton searches. Details on the actual model assumptions follow from Section 4.2.2.

4.2.1 Production mechanisms of gaugino and sleptons, and decays leading to leptons

The most important direct gaugino and slepton production channels (which can result in at least one lepton) are shown in Figure 4.4.

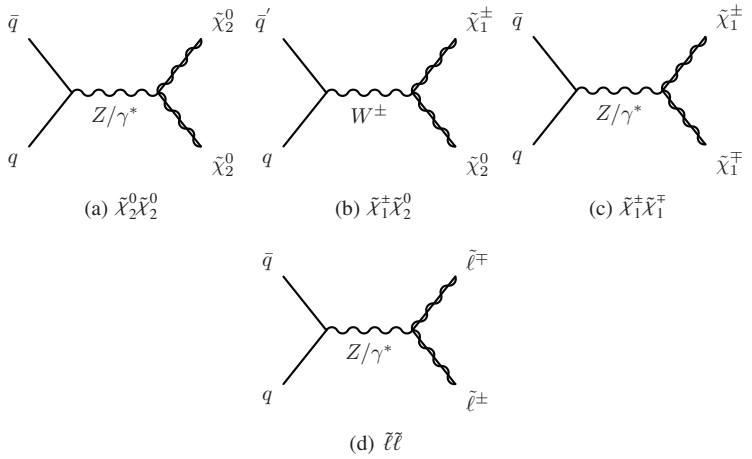

Figure 4.4: The dominant gaugino and slepton production channels which (can) result in final state leptons.

The lightest gauginos dominate over the heavier, and therefore only $\tilde{\chi}_1^\pm$ and $\tilde{\chi}_2^0$ are presented. However, in the pMSSM, the heavier gauginos contribute to some extent. Typically the decay-chains are more complicated than the ones resulting from decay of the lighter gaugino production processes depicted in Figure 4.4, involving cascade decays such as $\tilde{\chi}_3^0 \rightarrow Z\tilde{\chi}_2^0 \rightarrow Z\ell\tilde{\ell} \rightarrow Z\ell\ell\tilde{\chi}_1^0$, or $\tilde{\chi}_2^\pm \rightarrow W\tilde{\chi}_2^0, \rightarrow W\ell\tilde{\ell} \rightarrow W\ell\ell\tilde{\chi}_1^0$, and so on, following the rules of Equation 1.27 in Section 1.3.7. Furthermore, the direct production of the invisible channel $\tilde{\chi}_1^0\tilde{\chi}_1^0$ is omitted in the further presentation, since it is experimentally very challenging, and does not lead to leptons. Note that in general t-channel diagrams would also contribute. However, in this direct gaugino and slepton search, the squarks and gluinos are out of reach. That means that any t-channel diagram, which must involve squarks (due to the incoming quarks) by construction does not contribute in this scenario.

For the direct slepton search only a single diagram contributes, namely the s-channel diagram in Figure 4.4 (d).

In this direct gaugino and slepton search we target di-lepton final states. We also consider direct gaugino decay chains which give 3 leptons, but where one lepton is mis-reconstructed (and hence the final state is defined to belong to the di-lepton channel). This is because the best sensitivity is obtained if the direct gaugino search is divided into lepton final states (2,3,4), and then statistically combined. A separate analysis is therefore performed by the "Multilepton SUSY Working Group", aiming at three and four leptons. The three-lepton search is documented in Ref. [136], while the four-lepton search did not result in any publications at that stage. Then with the strategy of including the mis-reconstructed three lepton final states, we obtain close to 100% efficiency for the three lepton channel after statistical combination.

In the following discussion I outline what signal processes can contribute to this search, and roughly to what degree.

The most important tree-level production channels leading to gauginos and sleptons were shown in Figure 4.4. The possible leptonic decay chains are given in Table 4.1. By combining the production and decay chains we arrive to the list of sub-processes which are presented in the sections to follow.

Only the hard interaction processes are shown and discussed. However, it is important to remember that initial and final state radiation of gluons can in all diagrams to follow, lead to (more) jets in the final state. The same applies for initial state photon radiation, which can lead to electrons in case of subsequent conversion.

In the Feynman diagrams to follow, different quark flavours (up or down-type) are indicated with a super-script apostrophe as follows: q and $q^{'}$, respectively (or vice-versa). In cases where precise labelling of charge and flavour make the diagrams cluttered, these are omitted.

Notice also that some of the decay chains to follow involve decays via Z-bosons. This search is not sensitive to such processes however, as all OS signal regions which are defined in Section 5.1 include a Z-veto to suppress SM background[3]. Still, the processes that include a Z-boson are mentioned in the discussion to follow for the sake of completeness.

The possible decay chains of gauginos and sleptons leading to lepton final states given in Table 4.1 only include two-body decays, but the processes can naturally also go via three-body decays, with off-shell heavy intermediate sparticles. In the column "Decay chain", two-step decay chains are shown separated by a comma. Only the particle that decays further is then specified. Each line represents a possible decay path. In the last column, the resulting final state particles are shown. As the table shows, $\tilde{\chi}_1^{\pm}$ gives at most one charged lepton, while $\tilde{\chi}_2^0$ leads to two charged leptons. In some decay chains neutrinos are also produced. For the slepton decay (bottom row), the only allowed decay in this search is directly to the LSP and lepton ($\tilde{\chi}_1^0 l^{\pm}$), as it is assumed that all gauginos (except the LSP) are heavier than the sleptons in the direct slepton scenario, as is detailed in Section 4.2.4. All decay chains necessarily result in two $\tilde{\chi}_1^0$, as R-parity is assumed.

[3]It could however still pick up chains where the Z-boson decays to e^+e^-, and where one of the reconstructed electrons flips charge. Recent ATLAS SUSY analysis have dedicated search channels including Z in the cascade.

Sparticle	Decay chain	Final state
$\tilde{\chi}_1^{\pm}$	$\rightarrow \tilde{\chi}_1^0 W^{\pm}$, $W^{\pm} \rightarrow l^{\pm}\nu$	$\tilde{\chi}_1^0 l^{\pm}\nu$
	$\rightarrow \tilde{\ell}_{\mathrm{L}}^{\pm}\nu$, $\tilde{\ell}_{\mathrm{L}}^{\pm} \rightarrow \tilde{\chi}_1^0 l^{\pm}$	
	$\rightarrow \tilde{\nu}_{\mathrm{L}} l^{\pm}$, $\tilde{\nu}_{\mathrm{L}} \rightarrow \tilde{\chi}_1^0 \nu$	
$\tilde{\chi}_2^0$	$\rightarrow \tilde{\chi}_1^0 Z$, $Z \rightarrow l^{\pm} l^{\mp}$	$\tilde{\chi}_1^0 l^{\pm} l^{\mp}$
	$\rightarrow \tilde{\ell}_{\mathrm{L,R}}^{\pm} l^{\mp}$, $\tilde{\ell}_{\mathrm{L,R}}^{\pm} \rightarrow \tilde{\chi}_1^0 l^{\pm}$	
	$\rightarrow \tilde{\chi}_1^{\pm} l^{\mp}\nu$, $\tilde{\chi}_1^{\pm} \rightarrow \tilde{\chi}_1^0 l^{\pm}\nu$	$\tilde{\chi}_1^0 l^{\mp}\nu\, l^{\pm}\nu$
$\tilde{\ell}^{\pm}$	$\rightarrow \tilde{\chi}_1^0 l^{\pm}$	$\tilde{\chi}_1^0 l^{\pm}$

Table 4.1: Possible decays of $\tilde{\chi}_1^{\pm}, \tilde{\chi}_2^0$ and $\tilde{\ell}$, leading to lepton(s) and missing energy in form of $\tilde{\chi}_1^0$ and ν(s) in the final state.

In order to study the direct gaugino and slepton processes, Monte Carlo signal grids which scan over the (most important) free model-parameters are defined. Three different grids were used for this study, these are the Direct Gaugino pMSSM grids (DGgrid), as the name implies for the direct gaugino production, the simplified model grids, also constructed to study direct gaugino production, and finally the direct slepton pMSSM grid. In the following I first describe the two grids developed to simulate direct gauginos, namely the DGemt (emt stands for electron, muon and tau), and the simplified model grids, before presenting the direct slepton grids.

4.2.2 Direct gaugino production with the pMSSM grid

As explained in Section 1.3.8.4, 19 MSSM parameters are left free after phenomenological constraints are taken into account. These are three gaugino mass parameters M_1, M_2, and M_3, three Higgs(ino) parameters μ, m_A, $\tan\beta$, six squark mass parameters, four slepton masses, and three trilinear couplings of 3$^{\mathrm{rd}}$ generation sfermions A_t, A_b, A_τ. Even though 19 parameters already is a large reduction from the ~100 parameters of the MSSM, the parameter space must be reduced further, in order to make it practically possible to extract useful experimental constraints from the analysis. For this two pMSSM grids were set up by the ATLAS SUSY Working group to accommodate the di- (and tri-lepton) direct gaugino search(es) with e, μ, τ final states, the so-called Direct Gaugino electron muon tau (DGemt) grids: One with and one without intermediate sleptons, both simulated with a full detector description [4].

Since squarks and gluinos are out of reach, the six squark and the one gluino mass parameters (M_3) can be ignored, together with the two squark trilinear couplings, since they do not affect the chargino and neutralino sector. Furthermore, the stau trilinear coupling is set to zero,

[4] pMSSM scenarios are defined at the electroweak scale using ISASUSY/ISAJet 7.80 [137] as spectrum generator. Cross-sections are calculated by Prospino2.1 [138, 139], and event generation is done by HERWIG [105].

as it does not affect the model.

We are then left with M_1, M_2, μ, $\tan\beta$. For the grid including sleptons we need additional parameters that increase the complexity, since the slepton masses either must be fixed by hand, or varied in a mass-scan. To limit the complexity, only the right-handed sleptons are considered within LHC reach, and their mass is set midway between the two lightest neutralinos, i.e. $m(\tilde{\ell}_R) = 0.5 \cdot (m(\tilde{\chi}_2^0) - m(\tilde{\chi}_1^0))$. With these assumptions the two DGemt grids are defined with $\tan\beta = 6$, $m_A = 500$ GeV and with (μ,M_2) both $\in \{100, 110, 120, 140, 160, 180, 250\}$ GeV. This set is used for optimization studies. For the actual SUSY search, the grid was extended up to 500 GeV. Three values are chosen for M_1: 100, 140 and 250 GeV. This gives a total of 147 points in a two-dimensional μ,M_2 grid for the first set, and more than 300 points in the extended set. The number of points selected is a careful balance between resolution and computational limits.

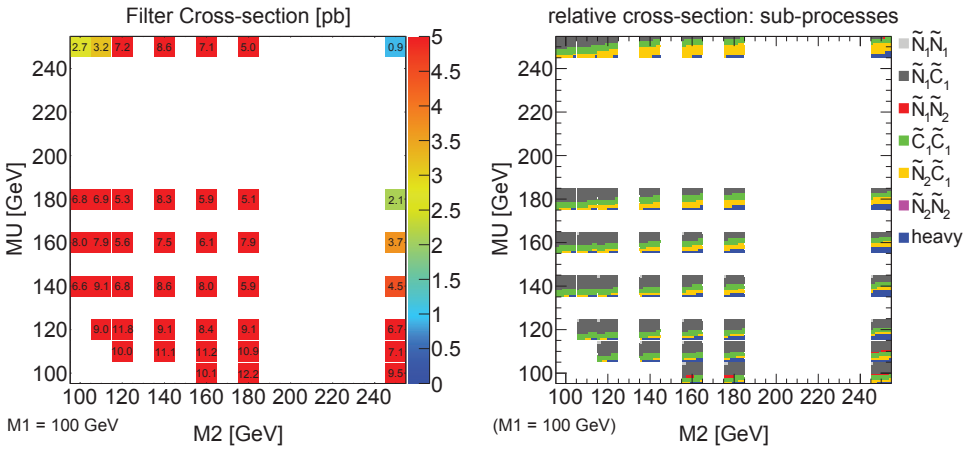

Figure 4.5: The total cross-section after two-lepton filter (left), and the breakdown into gaugino sub-processes in pMSSM (right, no filter). The collection named "heavy" contains all processes involving one or more $\tilde{\chi}_2^{\pm}$ or $\tilde{\chi}_{3,4}^0$. From Ref. [133].

As the direct gaugino search involves many possible production and decay channels, the DGemt grid in Ref. [133, 134] is used to explore which sub-processes are the dominant contributions, which in turn is used for optimizing the signal regions. The left plot in Figure 4.5, shows the total cross section as given by Prospino2.1 [138][5], in this case for M_1=100 GeV, after requiring 2 leptons. In this particular parameter space the total cross section is of the order 10 pb. With higher M_1 values, the cross sections decrease, with a minimum cross section of 0.2 pb.

In the right plot of Figure 4.5, the total cross section for each grid point is broken down into relative cross sections per sub-process. The relative amount is illustrated by how much each sub-process, represented by the colours given in the legend, populate the grid point. In this, and following related figures, MU is the Higgs mass-parameter μ, while $\tilde{N}_i$ and $\tilde{C}_i$, where $i \in (1, 2)$,

[5]Quoting from Prospino home-page: "A computer program which computes next-to-leading order cross-sections for the production of supersymmetric particles at hadron colliders". `http://www.thphys.uni-heidelberg.de/~plehn/index.php?show=prospino&visible=tools`

denote the lightest and second-lightest neutralino and chargino mass eigenstates ($\tilde{\chi}^0_{1,2}, \tilde{\chi}^\pm_{1,2}$). The grid in Figure 4.5 is dominated by $\tilde{\chi}^0_1\tilde{\chi}^\pm_1$, $\tilde{\chi}^\pm_1\tilde{\chi}^\mp_1$ and $\tilde{\chi}^0_2\tilde{\chi}^\pm_1$ production (dark grey, green, and yellow respectively), but there is also some contribution from the heavy gaugino sector (blue) which includes $\tilde{\chi}^0_{3,4}$ and $\tilde{\chi}^\pm_2$. The contribution from $\tilde{\chi}^0_1\tilde{\chi}^0_2$, $\tilde{\chi}^0_2\tilde{\chi}^0_2$, $\tilde{\chi}^0_1\tilde{\chi}^0_1$ is very small. With higher M_1 masses the main effect is that the $\tilde{\chi}^0_{3,4}$ and $\tilde{\chi}^\pm_2$ (heavy) contributions become even smaller [133].

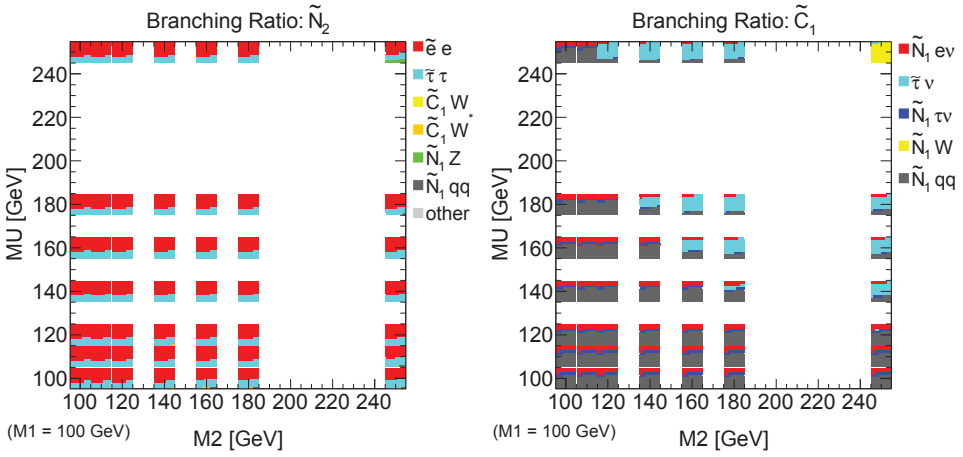

Figure 4.6: pMSSM Direct Neutralino-Chargino signal grids: Branching ratios of $\tilde{\chi}^0_2$ and $\tilde{\chi}^\pm_1$. MU is the μ parameter. Note: $e/\tilde{e}$ is here used for both electron/selectron and muon/smuon. From Ref. [133].

Figure 4.6 again from Ref. [133], depicts relative branching ratios in the M_2, μ plane for M_1=100 GeV, for $\tilde{\chi}^\pm_1$ and $\tilde{\chi}^0_1$, following the same scheme as in the left plot of Figure 4.5. Note that in the legend the symbols e and $\tilde{e}$ represent both (s)electrons and (s)muons. As the figure shows, especially the decay of $\tilde{\chi}^0_2$ (left, N2 in the figure) leads to a large amount of leptons (red fill), and that the total branching ratio is shared (more or less) equally between the three lepton flavours. The $\tilde{\chi}^\pm_1$ (C1 in the figure) decay topology (Figure 4.6 right) is more complex with a fairly large fraction of $\tilde{\tau}\nu$ (azure) and $\tilde{\chi}^0_1 qq$ (grey), but still with a significant $\tilde{\chi}^0_1 e\nu$ (red) contribution. In Ref. [133] it is shown that with increasing M_1, the $\tilde{\tau}\nu$ contribution is overtaken by $\tilde{\chi}^0_1 qq$, while the for us interesting leptonic final state (where leptonic again means e, μ) $\tilde{\chi}^0_1 e\nu$ remains (mainly) unchanged. The decay chains with Z and W bosons (green and yellow fills respectively in Figure 4.6) also naturally give a certain amount of leptonic final states, either directly from the bosons, or from the further decay of the $\tilde{\chi}^\pm_1$ and $\tilde{\chi}^0_2$.

Based on Figure 4.5, the gaugino production channels with significant cross-sections are $\tilde{\chi}^\pm_1\tilde{\chi}^\mp_1$ (C1C1, green) $\tilde{\chi}^0_2\tilde{\chi}^\pm_1$ (N2C1, yellow) and $\tilde{\chi}^0_1\tilde{\chi}^\pm_1$(N1C1, dark grey). Only the two first are relevant for this direct gaugino search, since we require two (reconstructed) leptons in the final state. This therefore rules out $\tilde{\chi}^\pm_1\tilde{\chi}^0_1$ which would at most yield a single lepton from the $\tilde{\chi}^\pm_1$ leg.

4.2.3 Direct gaugino production with simplified model grids

Simplified models were developed to study direct gauginos in a complementary way to the pMSSM DGgrids. Three grids are produced based on the two production channels with the largest cross section, out of four originally considered: $\tilde{\chi}_1^{\pm}\tilde{\chi}_2^0$ (mode A), $\tilde{\chi}_1^{\pm}\tilde{\chi}_1^0$ (mode B), $\tilde{\chi}_1^{\pm}\tilde{\chi}_1^{\mp}$ (mode C), and $\tilde{\chi}_2^0\tilde{\chi}_2^0$ (mode D). The diagrams corresponding to the four modes are shown in Figure 4.7, however Mode B is not relevant for this SUSY search, as it would at most result in only a single lepton, from the decay of $\tilde{\chi}_1^{\pm}$. Modes A and mode C were in Ref. [133] chosen for further studies, as their cross sections are three to four orders of magnitude larger than mode D, see Figure 4.8.

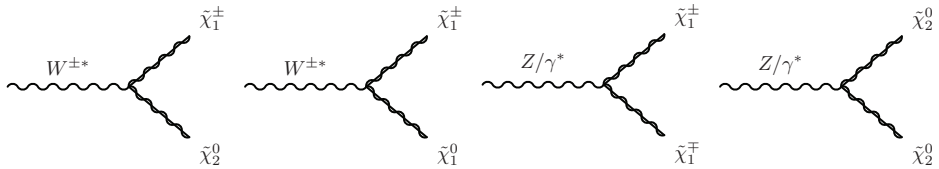

(a) Mode A (b) Mode B (c) Mode C (d) Mode D

Figure 4.7: Feynman diagrams for simplified model decay modes A, B, C, and D.

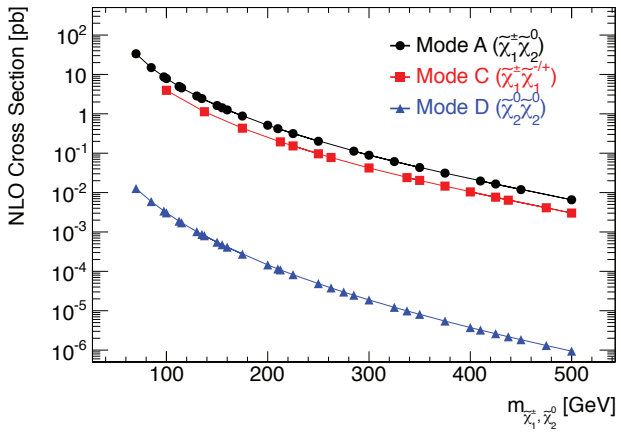

Figure 4.8: Cross sections for simplified models mode A, C and D versus the mass of $\tilde{\chi}_1^{\pm}$ and $\tilde{\chi}_2^0$ (degenerate). From Ref. [133].

Mode A consists of two grids, with or without intermediate sleptons, while mode C only operates *with* intermediate sleptons. The slepton mass is in both modes set half-way between the mass of $\tilde{\chi}_2^0$ and $\tilde{\chi}_1^0$, i.e $m(\tilde{\ell}_R) = 0.5 \cdot (m(\tilde{\chi}_2^0) - m(\tilde{\chi}_1^0))$, and the slepton and sneutrino branching ratios are set to be equally large. Both the $\tilde{\chi}_1^{\pm}$ and $\tilde{\chi}_2^0$ are purely wino-like, and their masses are identical in these grids. Mode A without intermediate sleptons therefore features branching

ratios $\tilde{\chi}_1^\pm \rightarrow W^\pm\tilde{\chi}_1^0$ and $\tilde{\chi}_2^0 \rightarrow Z\tilde{\chi}_1^0$ of 100%. All squark and gluino masses, as well as right-handed slepton masses and $\tilde{\chi}_2^\pm$, $\tilde{\chi}_3^0$, and $\tilde{\chi}_4^0$ are set to several hundred TeV, well beyond LHC reach.

With the identical masses of $\tilde{\chi}_1^\pm$ and $\tilde{\chi}_2^0$, and the slepton masses dictated by $\tilde{\chi}_2^0$ and $\tilde{\chi}_1^0$, limits can be quoted as function of $\tilde{\chi}_1^\pm$ and $\tilde{\chi}_1^0$ sparticle masses only. Each grid consists of 31 points distributed over the $\tilde{\chi}_1^\pm$ and $\tilde{\chi}_1^0$ mass plane, with a higher density at low masses.

4.2.4 Direct slepton production

A separate grid was produced for studying the direct sleptons. This is a very simple grid, which could equally well be described in a full pMSSM model as in simplified models. The grid itself is produced within pMSSM, but the limits are set directly on the slepton and $\tilde{\chi}_1^0$ masses. This is because we only consider the first and second generation sleptons, where the mass mixing is negligible, hence the weak and mass eigenstates are basically identical. In addition, M_1 is approximately equal $M(\tilde{\chi}_1^0)$. Furthermore, M_2 (gaugino mass parameter), M_3 (gluino mass parameter), L_3 (third generation slepton mass) and Q_3 (third generation squark mass) and M_A are all set to several TeV. The stau contribution is suppressed through L_3, since we only want to study the first two generations of sleptons. The chosen $\tan\beta$ value is 10, and slepton and $\tilde{\chi}_1^0$ masses are varied in a grid of $m(\tilde{\ell}) = 70 - 170$ GeV and $m(\tilde{\chi}_1^0) = 20 - 160$ GeV in steps of 20 GeV. However, to assure a large enough mass-gap between the slepton and $\tilde{\chi}_1^0$ (which directly affects the acceptance), only grid points with $m(\tilde{\ell})$ satisfying $m(\tilde{\ell}) - m(\tilde{\chi}_1^0) > 30$ GeV are used. Since the direct slepton production has a very small cross section (smallest of the SUSY sparticles), the grids concentrate on low slepton masses.

Both left and right-handed sleptons and sneutrinos, and all allowed combinations of these are included. Right- and left-handed sleptons have identical mass in this grid, and although this is not necessarily true in a realistic model, limits can still be set separately for right and left-handed sleptons by using MC truth information to pick out one or the other type.

With the above model choices, the only possible decay chain of the directly produced sleptons are through lepton+neutralino as Figure 4.9 shows.

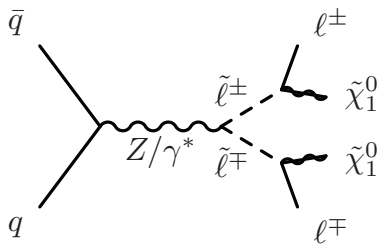

Figure 4.9: Direct slepton production and decay as considered in the pMSSM direct slepton grid.

This concludes the presentation of the signal grids. The next sub-sections present the actual production channels resulting in di-lepton final states, and their characterization.

4.2.5 Di-leptonic final states in direct gaugino and slepton production

The following sections go through the dominant contributions to final-states with two leptons in this direct gaugino and slepton search.

Di-leptonic final states from $\tilde{\chi}_1^{\pm}\tilde{\chi}_2^0$ production

The main production channel for direct $\tilde{\chi}_1^{\pm}\tilde{\chi}_2^0$ was presented in Figure 4.4, which was the s-channel (b) where a virtual W boson acts as the intermediate exchange particle.

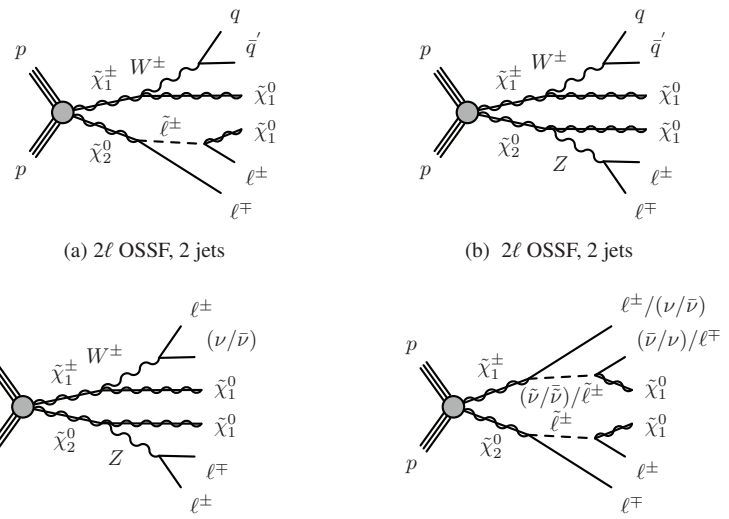

(a) 2ℓ OSSF, 2 jets

(b) 2ℓ OSSF, 2 jets

(c) $2\ell, \ell_{\text{miss}}$ OS, SS, DF, SF

(d) $2\ell, \ell_{\text{miss}}$ OS, SS, DF, SF

Figure 4.10: $\tilde{\chi}_1^{\pm}\tilde{\chi}_2^0$ production leading to two (a and b) or three (c and d) leptons, $E_{\text{T}}^{\text{miss}}$ from the two $\tilde{\chi}_1^0$s and ν's, and in (a) and (b) jets from the quarks. In the three-lepton channels one lepton is assumed mis-reconstructed (l_{miss}). Depending on which lepton fails reconstruction these channels would lead to a combination of OS, SS, DF and SF (opposite sign, same sign, different flavour and same flavour respectively).

According to Table 4.1, a maximum of three leptons can be achieved through the decay alternatives, if both legs decay leptonically. Examples of leading order decay chains are depicted in Figure 4.10. The decay of the $\tilde{\chi}_1^{\pm}$ can proceed through $\tilde{\chi}_1^{\pm} \to W\tilde{\chi}_1^0,\ W \to \ell\nu/q\bar{q}'$ or through $\tilde{\chi}_1^{\pm} \to \ell\tilde{\ell},\ \tilde{\ell} \to \tilde{\chi}_1^0\ell$. Although the branching ratio $\text{Br}(\tilde{\chi}_1^{\pm} \to W\tilde{\chi}_1^0)$ is larger than $\text{Br}(\tilde{\chi}_1^{\pm} \to \nu\tilde{\ell})$, the latter is still the largest contributor to leptons, since the decay rate through W's is reduced by the W leptonic branching fraction ($10.80 \pm 0.09\%$ per lepton [40]).

In the other leg, the $\tilde{\chi}_2^0$ can decay through a slepton via $\ell\tilde{\ell},\ \tilde{\ell} \to \tilde{\chi}_1^0\ell$ or through a Z boson as $\tilde{\chi}_1^0 Z,\ Z \to \ell^{\pm}\ell^{\mp}/q\bar{q}$ if kinematically allowed.

In diagrams 4.10 (a) and (b), exactly two leptons are produced, but in addition (at least[6]) two jets from the hadronically decaying W. These diagrams contribute to the opposite sign same flavour (OSSF) channel. In the case where both the W and the Z decay leptonically, or both legs decay via intermediate sleptons (c and d), a total of three leptons is produced. This final state can still contribute to the di-lepton final state if one of the leptons is not reconstructed due to acceptance or reconstruction inefficiencies. Depending on which of the leptons fail reconstruction these two chains contribute to the same sign (SS) or opposite sign (OS), and to the different (DF) or same flavour (SF) channels. Both channels are jet-free if one disregards initial-state radiation, underlying events, and pile-up.

Di-leptonic final states in direct production of $\tilde{\chi}_1^{\pm}\tilde{\chi}_1^{\mp}$

Direct production of $\tilde{\chi}_1^{\pm}\tilde{\chi}_1^{\mp}$ proceeds through the s-channel in this SUSY scenario (no t-channel), with an intermediate Z or γ^* as already shown in Figure 4.4 (c).

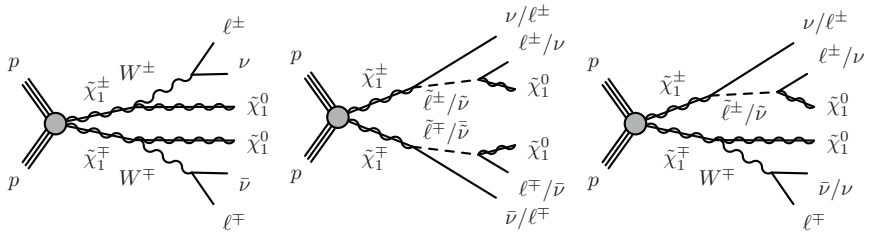

(a) 2ℓ OS, SF, DF (b) 2ℓ OS, SF, DF (c) 2ℓ OS, SF, DF

Figure 4.11: Leptonic decays of $\tilde{\chi}_1^{\pm}\tilde{\chi}_1^{\mp}$ all leading to a 2ℓ OS, SF or DF final state. In all diagrams ν is used to mean both ν and $\bar{\nu}$ to avoid cluttering.

Subsequent decay of the $\tilde{\chi}_1^{\pm}\tilde{\chi}_1^{\mp}$ pair can lead to two uncorrelated leptons in the final states if the decays proceed through leptonically decaying W bosons or through intermediate sleptons, or a combination of both as the diagrams in Figure 4.11 illustrate. These are final states that consist of exactly two leptons and a large fraction of missing energy due to the two $\tilde{\chi}_1^0$ and ν's. The diagrams contribute to the opposite sign (OS) channel, and democratically to same and different lepton flavour (DF, SF), in the following combinations: (OSSF), and (OSDF). No tree-level jets are produced, but hard jets can stem from initial state radiation.

Di leptonic final states in $\tilde{\chi}_2^0\,\tilde{\chi}_2^0$ production

Production of $\tilde{\chi}_2^0\tilde{\chi}_2^0$ leads to two leptons, like in Figure 4.12 where at least one of the Z-bosons in each of the diagrams decays invisibly or hadronically. In this case both diagrams contribute to the OSSF channel, with or without jets, depending on the non-leptonic Z decay, shown here in the top leg of both diagrams. One could also consider the possibility of a di-lepton final state

[6]When quarks are present, gluons can easily be radiated resulting in ≥ 2 jets in this case.

if all Z's in the process decayed leptonically leading to a total of four leptons, but two leptons would be mis-reconstructed. Although this is a very small contribution (initially $\tilde{\chi}_2^0\tilde{\chi}_2^0$ has a small production cross section to start with), it could still add to both the OS and SS channels, either flavour combinations, depending on which leptons were mis-reconstructed. We should also keep in mind that the Z-veto which is required in some of the signal regions reduces the sensitivity to this production channel.

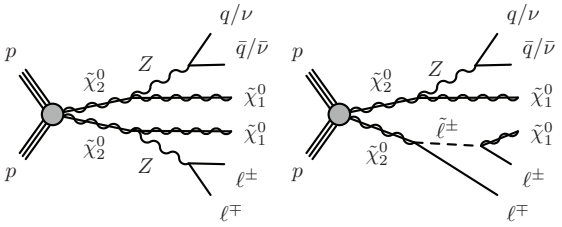

Figure 4.12: Leptonic decays of $\tilde{\chi}_2^0\tilde{\chi}_2^0$, both processes lead to 2ℓ OSSF, and either 2 jets or additional $E_{\mathrm{T}}^{\mathrm{miss,rel}}$ from the two ν's.

Di-leptonic final states in $\tilde{\chi}_1^0\tilde{\chi}_2^0$ production

Figure 4.13 shows two examples of $\tilde{\chi}_1^0\tilde{\chi}_2^0$ production, with decay chains resulting in two final state leptons. The production mechanism leading to this final state were shown in Figure 4.4 (a). Figure 4.13 (a) illustrates $\tilde{\chi}_2^0$ decay via a Z boson, and Figure 4.13 (b) via a slepton. Due to the Z-veto, the first diagram is suppressed, at least when the Z is real. However, both diagrams potentially contribute to the OSSF channel. No hard scattering jets are produced, but as always, initial state radiation jets may be present.

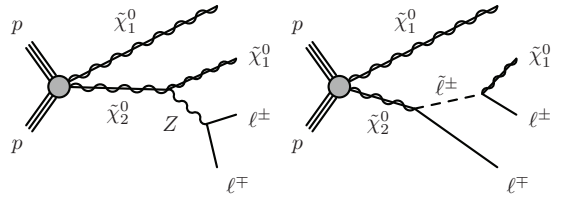

(a) Intermediate Z (b) Intermediate $\tilde{\ell}$

Figure 4.13: Leptonic decays of $\tilde{\chi}_1^0\tilde{\chi}_2^0$, both processes result in an OSSF lepton pair.

Direct $\tilde{\ell}^\pm\tilde{\ell}^\mp$ production

As already discussed, direct slepton production proceeding through Z/γ^* leads to di-leptons, as shown in Figure 4.9.

Since we assume that all gauginos but the LSP are heavier than the sleptons, this is the only possible decay chain. The process features a special signature: Constructing the stransverse

mass m_{T2} (detailed in Chapter 3.4) of the two leptons gives a maximum endpoint which can be shown ([140]) to be expressed as

$$m_{\mathrm{T2}}^{\mathrm{max}}(m_{\chi}) = \frac{m_{\tilde{\ell}}^2 - m_{\tilde{\chi}_1^0}^2}{2m_{\tilde{\ell}}} + \sqrt{\left(\frac{m_{\tilde{\ell}}^2 - m_{\tilde{\chi}_1^0}^2}{2m_{\tilde{\ell}}}\right)^2 + m_{\chi}^2}\,, \tag{4.1}$$

where the mass of the visible decay particle (electron or muon) is neglected. The expression depends on the test-mass m_{χ}. It has been shown (in Ref. [140]) that $m_{\mathrm{T2}}^{\mathrm{max}}$ grows with increasing m_{χ}. Assuming $m_{\mathrm{T2}}(m_{\chi} = 0)$ therefore leads to the conservative prediction

$$m_{\mathrm{T2}}^{\mathrm{max}}(m_{\chi} = 0) = \frac{m_{\tilde{\ell}}^2 - m_{\tilde{\chi}_1^0}^2}{m_{\tilde{\ell}}}\,.$$

Hence m_{T2} gives a prediction about the mass difference between the mother particle $\tilde{\ell}$, and the invisible particle $\tilde{\chi}_1^0$.

The m_{T2} variable is a useful SM discriminator, since the new physics (SUSY) endpoint lies much above the endpoint corresponding to SM topologies. This is discussed further in Section 5.1, where I discuss the signal regions, and after I have presented the relevant SM backgrounds.

With the most important diagrams contributing to two final state leptons presented and discussed, it is now convenient to summarize what the signal footprints are and how the SM processes enter as backgrounds.

4.2.6 Signal footprints

All processes described illustrated in Figures 4.9 to 4.12, were jet-free at lowest order, except the processes in Figure 4.10 (a), and 4.10 (b), where exactly two jets are produced from $\tilde{\chi}_1^{\pm}\tilde{\chi}_2^0 \rightarrow (l^{\pm}l^{\mp}\tilde{\chi}_1^0) + (q\bar{q}'\tilde{\chi}_1^0)$, or from Figure 4.12, where the jets stem from the intermediate Z-boson. All production and decay chains lead to large missing energy, and by definition two reconstructed leptons.

The processes discussed are now grouped together according to their final state signature, and summarized in Table 4.2. Taking the first row as an example, the gaugino pair $\tilde{\chi}_2^0\tilde{\chi}_1^{\pm}$ decay leads to a combination of OS, SS, SF, and DF depending on which lepton is mis-reconstructed. The final lepton configurations could then be OSSF, OSDF, SSSF or SSDF. There are no jets (from LO production and decay), and the process involves the usual $E_{\mathrm{T}}^{\mathrm{miss}}$ from the two lightest neutralinos, and possibly neutrinos.

If we sort the processes above into categories depending on final states we arrive to four main categories as presented in Table 4.3. Each category, or signal region, is given a descriptive name. The SR-OSjveto region contains an opposite sign lepton pair, either SF or DF, and a jet veto. The SR-SSjveto region contains a SS lepton pair of either flavour combination. The SR-2jets region has an OSSF lepton pair and at least two jets, and finally the SR-mT2 region contains an OSSF lepton pair, a jet veto and a requirement on the stransverse mass m_{T2}. All regions contain a certain amount of $E_{\mathrm{T}}^{\mathrm{miss}}$ (to be quantified later) due to the two LSPs, and in some cases neutrinos.

ID	Process	Signature		
		Sign	Flavour	Experimental objects
1	$\tilde{\chi}_2^0\tilde{\chi}_1^\pm \to (\ell^+\ell^-\tilde{\chi}_1^0) + (\ell^\pm\nu\tilde{\chi}_1^0),\ \ell_{miss}$	OS,SS	SF,DF	2ℓ, no jets, $E_{\mathrm{T}}^{\mathrm{miss}}$
2	$\tilde{\chi}_2^0\tilde{\chi}_1^\pm \to (\ell^+\ell^-\tilde{\chi}_1^0) + (\bar{q}q\tilde{\chi}_1^0)$	OS	SF	2ℓ, >= 2jets, $E_{\mathrm{T}}^{\mathrm{miss}}$
3	$\tilde{\chi}_1^\mp\tilde{\chi}_1^\pm \to (\ell^\pm\nu\tilde{\chi}_1^0) + (\ell^\mp\nu\tilde{\chi}_1^0)$	OS	SF,DF	2ℓ, no jets, $E_{\mathrm{T}}^{\mathrm{miss}}$
4	$\tilde{\chi}_2^0\tilde{\chi}_2^0 \to (q\bar{q}/\nu\bar{\nu}\ \tilde{\chi}_1^0) + (\ell^\pm\ell^\mp\tilde{\chi}_1^0)$	OS	SF	2ℓ, ≥ 2 jets, $E_{\mathrm{T}}^{\mathrm{miss}}$
5	$\tilde{\chi}_2^0\tilde{\chi}_2^0 \to (\ell^\pm\ell^\mp\tilde{\chi}_1^0) + (\ell^\pm l^\mp\tilde{\chi}_1^0),\ 2\ell_{miss}$	OS,SS	SF,OF	2ℓ, no jets, $E_{\mathrm{T}}^{\mathrm{miss}}$
6	$\tilde{\chi}_2^0\tilde{\chi}_1^0 \to (\tilde{\chi}_1^0) + (\ell^\pm\ell^\mp\tilde{\chi}_1^0),$	OS	SF	2ℓ, no jets, $E_{\mathrm{T}}^{\mathrm{miss}}$
7	$\tilde{\ell}^\pm\tilde{\ell}\mp \to (\ell\tilde{\chi}_1^0) + (\ell\tilde{\chi}_1^0)$	OS	SF	2ℓ, no jets, $E_{\mathrm{T}}^{\mathrm{miss}}$, m_{T2}

Table 4.2: The signature of each signal production channel and di-lepton final state. Any mis-reconstructed leptons are labelled ℓ_{miss}, and can be ℓ^+ or ℓ^-. A running ID-number from 1-7 is assigned to each process for easy reference later.

Short-name	Requirement
SR-OSjveto	OSSF, OSDF, jet veto, $E_{\mathrm{T}}^{\mathrm{miss}}$
SR-SSjveto	SSSF, SSDF, jet veto, $E_{\mathrm{T}}^{\mathrm{miss}}$
SR-2jets	OSSF, ≥ 2 jets, $E_{\mathrm{T}}^{\mathrm{miss}}$
SR-mT2	OSSF, jet veto, $E_{\mathrm{T}}^{\mathrm{miss}}$, m_{T2}

Table 4.3: Final state requirements divided into signal-regions. These regions are further developed in Section 5.1 in order to optimize the signal to background ratio.

The signal regions defined in Table 4.3 are based solely on the signal processes. Exact cuts and further requirements are determined depending on what SM background processes contribute to each signal region. This is the topic of the next section.

4.3 Standard Model background processes, and the means to suppress them

With two leptons, missing energy, and in some cases jets, there are several SM processes that enter the game. In the following sections I describe each of the contributing SM processes, in what way they could pass the signal selection, and how they can be reduced. I start by the processes which are well described in the SM, namely the electroweak processes leading to exactly two leptons. Then in Section 4.3.4 I turn to the main focus of this thesis, namely processes

involving so-called fake leptons, those which stem either from jets or from conversions.

4.3.1 $t\bar{t} \rightarrow (bl^+\nu) + (\bar{b}l^-\bar{\nu})$

The production of $t\bar{t}$ pairs with both W-bosons decaying leptonically, leading to two opposite (same or different flavour) leptons, is expected to be one of the main background sources in the di-lepton channel of the direct gaugino and slepton searches. The top row of Figure 4.14 shows the leading production mechanisms, while the leptonic decay chain is shown in the bottom row. The background leptons are marked in red. This background features two b-jets, and $E_{\mathrm{T}}^{\mathrm{miss}}$ from

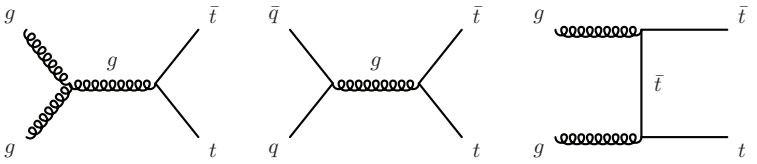

(a) s-chan gluon fusion (b) s-chan quark fusion (c) t-chan quark exchange

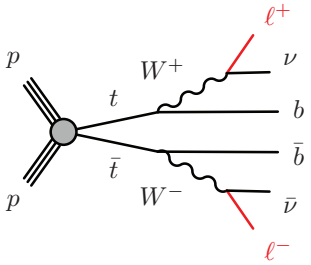

(d) Leptonic decay of $t\bar{t}$

Figure 4.14: Leading order production mechanisms for $t\bar{t}$ in the top row, and production and leptonic decay of $t\bar{t}$, leading to OS SF and DF leptons, in the bottom.

the two ν's. While $E_{\mathrm{T}}^{\mathrm{miss}}$ is part of the SUSY signal footprint, b-jets are not. Therefore a b-jet veto is expected to reduce the $t\bar{t}$ background, without affecting any SUSY signals significantly, as demonstrated by Figure 4.15, which shows the b-jet multiplicity for SM background and a selection of SUSY signal points. The single top (blue), to be introduced later in this section, and $t\bar{t}$ (red) SM distributions clearly contain more b-jets than the SUSY (Simplified Model Mode C) benchmark points overlaid, which peak at zero b-jets. Requiring the event to be free of b-jets removes as much as 82% of the top background in the di-muon channel, and 81% in the di-electron channel. While taking the simplified model mode C point with $\tilde{\chi}_1^{\pm} = 150$ GeV and $\tilde{\chi}_1^0 = 50$ GeV as an example, as much as 98% and 97% of the signal is kept in the di-muon and di-electron channel respectively, thus demonstrating the efficiency of the cut. Another way to suppress the $t\bar{t}$ background is to veto events that satisfy the kinematical signature of $t\bar{t}$ events as given by the top-tagger presented in Section 3.4. For $t\bar{t}$ production with both top quarks decaying through $t \rightarrow Wb$, $W \rightarrow l\nu$, we get one invariant mass $m^{max}(b, l)$, and three m_{CT}'s, with

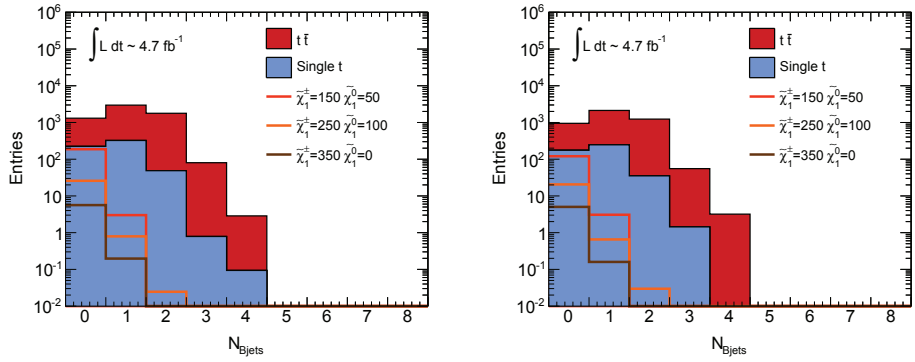

(a) Muons (b) Electrons

Figure 4.15: Number of b-jets in opposite sign di-muon or di-electron events, for three different Simplified Model Mode C signal grid points, and $t\bar{t}$ and single top MC background.

end-point values bounded above [116] by

$$\begin{aligned} m^{max}(b,l) &= 152.6 \text{ GeV} \\ M_{CT}^{max}(b,b') &= 135.0 \text{ GeV} \\ M_{CT}^{max}(l,l') &= 80.4 \text{ GeV} \\ M_{CT}^{max}([bl],[b'l']) &= 307.5 \text{ GeV} . \end{aligned}$$

A top-tag is issued for an event if the actual M_{CT} values calculated for the lepton and jet

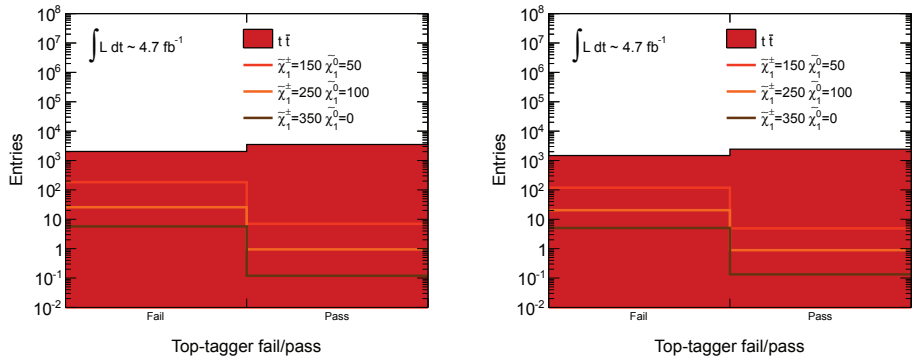

(a) Muons (b) Electrons

Figure 4.16: Number of events that fail (0) or pass (1) the top-tagger for $t\bar{t}$ background and a handful of simplified model signal points.

combinations given above, are less than M_{CT}^{MAX}, and if the invariant mass satisfies $m(b,l) < m^{max}(b,l)$. The combination of these kinematical constraints, together with the b-veto gives a very strong handle on the $t\bar{t}$ background. The pass (1) or fail (0) of the top-tagger is shown in Figure 4.16 for $t\bar{t}$ events and a few signal processes. The signal has a much higher probability to fail the top-tagger (96%) compared to the $t\bar{t}$ events (37%), which together with the b-jet veto help reduce the background, while not harming the signal.

4.3.2 Z/γ^*+jets

The Drell-Yan process $q\bar{q} \rightarrow Z/\gamma^* \rightarrow l^+l^-$ is a natural background in this search, due to the opposite sign (same flavour) final state leptons. It in fact also contributes to the SS di-electron channel due to so-called charge-flips, to be discussed in Section 4.3.4. The leading order hard production mechanisms of Z/γ^* are shown in Figure 4.17. One or more jets can be produced in

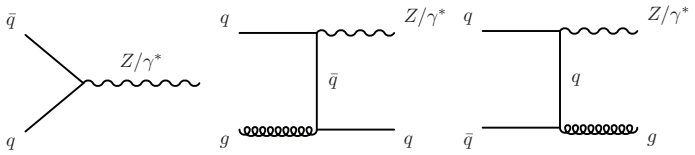

(a) s-chan (b) t-chan (c) t-chan

Figure 4.17: Leading order hard production mechanisms for Z/γ^* + jets.

this process, due to accompanying gluons or quarks. In Figure 4.18 three different di-lepton final states are shown. In (a) the decay involves a di-lepton pair and nothing else: in (b) the process

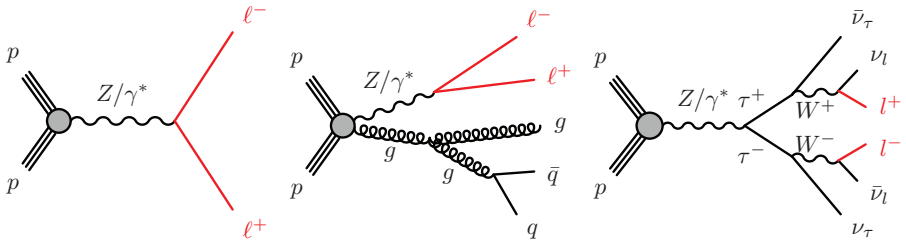

(a) ee or $\mu\mu$ (b) ee or $\mu\mu$ +jets (c) $\tau\tau \rightarrow (\mu\mu/ee/\mu e)$

Figure 4.18: Example of three Z/γ^* processes leading to a pair of charged leptons. Diagram (a) illustrates DY-production with no additional decay-products, in diagram (b) a Z/γ^* is produced with three accompanying jets. Both these diagrams give an OS SF lepton pair. Diagram (c) shows a final state that leads to an OS, SF or DF lepton pair: ee, $\mu\mu$ or $e\mu$ via leptonic τ decay.

in addition includes a gluon (stemming from 4.17(c)), which in this case leads to three jets; finally, in (c) is shown an example of $Z/\gamma^* \rightarrow \tau\tau$, where both τ's decay leptonically. Except for (c) and the resulting ν's, Z/γ^* production (and decay) does not produce $E_{\mathrm{T}}^{\mathrm{miss}}$ directly related to

the hard interaction process. But like for any other process, $E_{\mathrm{T}}^{\mathrm{miss}}$ can still be caused by detector resolution and efficiency. To deal with this background a Z-veto is applied to the opposite sign signal regions. This is a brute-force handling of the Z contribution, and automatically reduces the sensitivity to the SUSY signal processes involving decays through Z's, like in Figure 4.10 (b and c). Therefore more recent analysis ([141]) have developed signal regions which handle the SM Z-background without harming the signal. However, for signal processes with no real Z, the cut is efficient, as illustrated by Figure 4.19 which shows the invariant mass of opposite sign same-flavour lepton pairs. Whereas there is a clear peak from the SM Z and diboson samples (discussed in the following section), there is no such peak for the signal, therefore removing events in the Z-mass window reduces background, with minor effect on the signal.

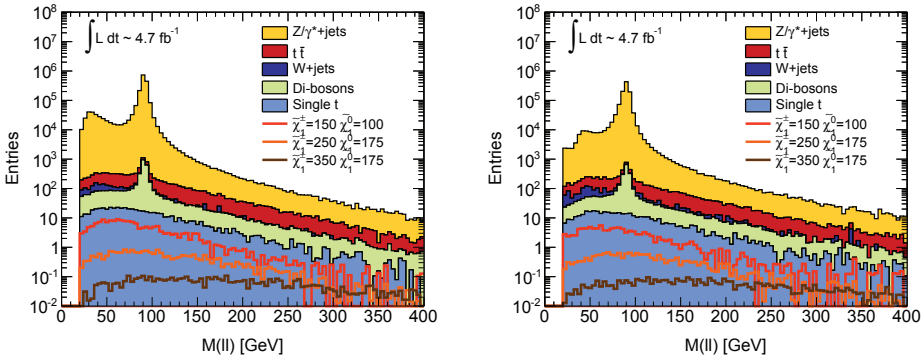

(a) Muons (b) Electrons

Figure 4.19: Invariant mass of opposite-sign same-flavour di-lepton pairs in SM background and in a selection of simplified model signal grid points. Muons to the left, and electrons to the right.

4.3.3 *WZ*, *WW*, *ZZ*

Di-boson production in form of WZ, WW or ZZ (Figure 4.20) leads to two reconstructed leptons in an analogous way to the direct gaugino production processes $\tilde{\chi}_1^{\pm}\tilde{\chi}_2^0$, $\tilde{\chi}_1^{\pm}\tilde{\chi}_1^{\mp}$, and $\tilde{\chi}_2^0\tilde{\chi}_2^0$. In diagrams Figure 4.20 (c) and (d) the sign is omitted on the W-boson since this depends on the charges and flavour of the partons in the hard process. Exactly two leptons can be produced in various ways, of which three examples are given in Figure 4.21. In the case of a third lepton, for instance if the W in Figure 4.21 (b) decays leptonically, the diagram can still contribute to the di-lepton signal selection if one of the leptons is mis-reconstructed, in the same way as discussed for the corresponding signal production. Mis-reconstruction can also cause the $ZZ \rightarrow 4l$ to only produce two reconstructed leptons. However, the probability of two mis-reconstructed leptons can be expressed as $(1 - \varepsilon_l)^2$, were ε_l is the lepton reconstruction efficiency which is close to 1.0. Therefore this contribution is in practice negligible.

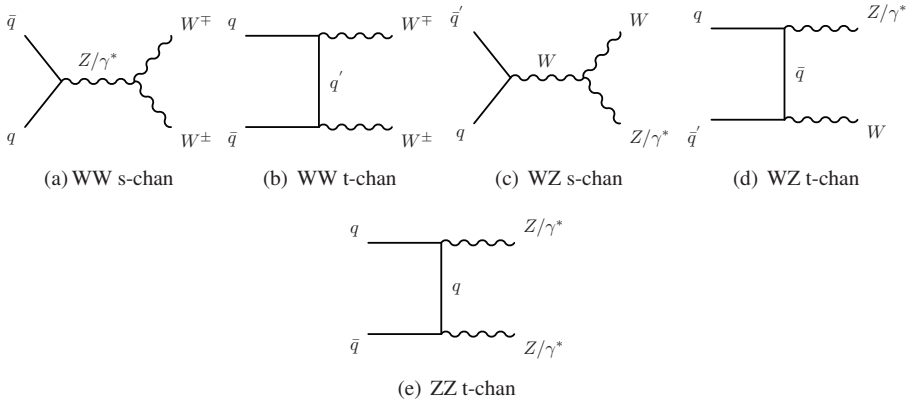

(a) WW s-chan (b) WW t-chan (c) WZ s-chan (d) WZ t-chan

(e) ZZ t-chan

Figure 4.20: Leading order hard di-boson production mechanisms.

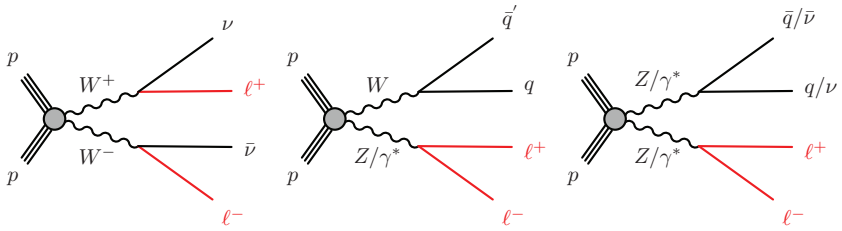

(a) WW (b) WZ (c) ZZ

Figure 4.21: Hard production of WZ, WW, and ZZ which lead to a pair of di-leptons and zero (a) or two jets (b and c). The first diagram results in an OSSF or OSDF lepton pair, while the last two give an OSSF lepton pair.

Since considerable $E_{\mathrm{T}}^{\mathrm{miss}}$ is expected from the WW production, the $E_{\mathrm{T}}^{\mathrm{miss}}$ cut is most effective against the WZ and ZZ production. The latter two processes are further reduced by the Z-veto which is applied in all but the SS-jveto signal regions. So, although WZ and ZZ are efficiently reduced, we do expect some contribution from WW in the signal region.

4.3.4 Background processes involving fake leptons

Up until now I have discussed SM processes where prompt (isolated) real leptons are part of the final state, as decay products of W or Z bosons, t-quarks or τ leptons. There is another category of leptons that contributes to the di-lepton sample, and those are the *fake* leptons. Whereas the SM predictions for the processes contributing to real leptons are well established, the fake lepton contribution is not, and is the main subject of this thesis.

The definition of fake leptons depends on the perspective of the analysis. Here fake leptons are all objects that are reconstructed as leptons, but do not originate from the above mentioned

sources (nor gaugino or slepton decays). They therefore include leptons from weak decays of b (or c)-quarks (or hadrons), and leptons that are created from the hadronic contents of light jets, like for instance from weak decay of $\pi^{\pm}$ or $K^{\pm}$ (which mainly are μ's), but also mis-identified jets and single hadrons like π^0. In the weak decay processes listed here, actual real leptons are created. However they must be seen as a part of a jet, either a light or heavy, and not as isolated leptons. They are part of a jet structure and hence for the purpose of this analysis defined as fake leptons. It must be noted that many of the potential fake leptons are removed by the isolation criteria used for both electrons and muons (see Section 3.5, Figures 3.10 and 3.11 for comparison of isolation for fake and real leptons). However, a fair amount of these fake leptons still pass the isolation requirement, and hence they must be estimated with care, as studied and discussed at length in Chapter 6.

Another source of fake leptons (electrons), is when electromagnetic activity around a jet is falsely misidentified as an electron. This can happen when (stray) deposits in the ECal by chance match a track in the inner detector. Or for instance if $\pi^0 \rightarrow \gamma\gamma$ is reconstructed as a single electron, which can occur when the separation between the two photons is too small for individual reconstruction, and instead seen as one cluster from the detector/software point of view, and this cluster by chance points to a track in the inner detector. These types of electrons could be called *true fake* electrons, as there is no actual electron created, but the signals in the detector just mimic one.

As well as fake leptons from QCD processes described above, we consider another source of fake leptons, namely those stemming from γ conversions. An electron or to a lesser extent muon, can radiate a (real) photon which subsequently pair-produces an e^+e^- pair. Conversion into a $\mu^+\mu^-$ can occur, but the probability for this is suppressed by the inverse square of the muon mass, which means that such conversions are $O(10^{-5})$ less likely conversions into e^+e^-, hence negligible for all practical purposes. If one of these electrons is picked up in an otherwise single prompt lepton process, for instance in production and decay of W+jets, the event, from the analysis point of view, passes as a di-lepton event. Since the photon typically travels a certain distance before it converts, the two electrons do not produce hits in inner-most pixel layer, which is as mentioned in Section 3.5.1 used to reduce this background. However, a certain amount still contributes, and must therefore be considered.

In addition to the conversions described above, which are called *external* and occur due to the photon interaction with the detector material, we also have *internal* conversion, where the γ is virtual. Internal conversions produce $\mu^+\mu^-$ and e^+e^- pairs with the same probability, and are not dependent on the detector material. Only external conversions are simulated in the MC used for this analysis, therefore the focus in the following is on these[7]. It must be noted though, that if the leptons from internal conversions are sufficiently non-isolated, fake lepton estimation through the Matrix Method to be described in Section 6, can in fact successfully estimate also these (even if not optimized for it).

In the following I give an overview of the production processes which contribute to the di-lepton signal region through one or two fake leptons.

[7]However, recent studies focusing on Higgs production [142], suggest that this is in fact not a negligible fake lepton contribution.

W+jets and fake leptons

A W boson with possible associated jets can come from the hard processes of Figure 4.22 (a-b). With subsequent leptonic decay of the W boson as shown in (c), the process can mimic a di-lepton final state if the quark leads to a fake lepton. Furthermore, the $E_{\mathrm{T}}^{\mathrm{miss}}$ from the neutrino ν increases the probability that the event contributes to the SUSY signal region, either with jet veto (if a single jet is faked by a lepton), or jet requirement, depending on the number of accompanying partons.

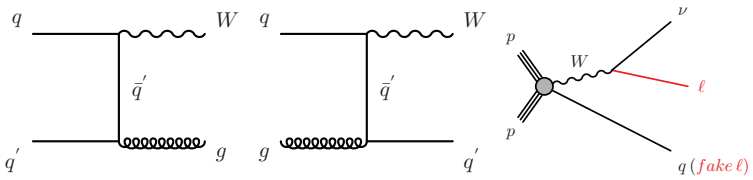

(a) t-chan g (b) t-chan q (c) Leptonic decay

Figure 4.22: Leading order hard production mechanisms for W(+jets), and a decay leading to a fake lepton.

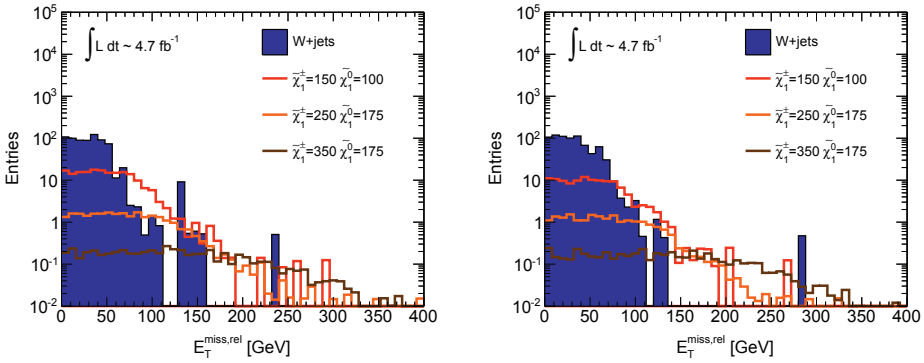

(a) Muons (b) Electrons

Figure 4.23: $E_{\mathrm{T}}^{\mathrm{miss,rel}}$ distribution for the W+jets background and three simplified grid SUSY model (mode C) points. Exactly two opposite-sign same-flavour leptons have been selected.

Even though this process naturally contains $E_{\mathrm{T}}^{\mathrm{miss}}$ from the ν, it is typically less than in a SUSY event. Figure 4.23 compares the $E_{\mathrm{T}}^{\mathrm{miss,rel}}$ distribution for the W+jets background and for a handful of different simplified model grid points, and shows how the SUSY samples have larger tails of high $E_{\mathrm{T}}^{\mathrm{miss,rel}}$.

A cut applied at for instance 100 GeV removes as much as 98% of the muon background and 99% of the electron background from W+jets production.

Single top and fake leptons

Top quarks can be produced not only in pairs, but also singly as shown in Figure 4.24 (a-c). The top is then accompanied with either a b-quark, a lighter down-type quark (down or strange), or a W-boson. If the single top quark decays leptonically, the production channels constitutes

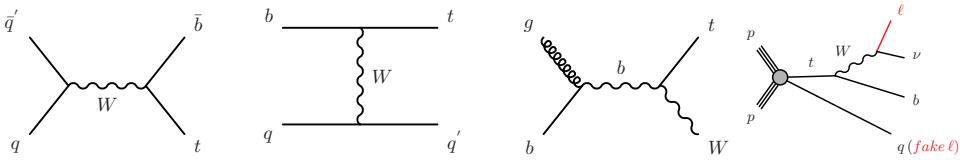

(a) s-channel (b) t-channel (c) Wt-channel (d) Leptonic decay

Figure 4.24: Leading order diagrams for single top production (top), and an example of leptonic decay (bottom).

background for the di-lepton SUSY search for instance if the lepton from the weak decay of the b-quark in Figure 4.24 (a) passes the lepton requirements. This type of lepton is defined as fake in this analysis. In this case the software reconstruction could mistakenly interpret the b-jet as a lepton, and a b-veto which would otherwise help reduce this background, would not be useful. Furthermore, an accompanying quark can result in a fake lepton as subfigure (d) illustrates. And finally, leptonic decay of the W boson in subfigure (c) also results in a di-lepton final state.

Except if the b-jet is mistaken for a lepton as mentioned above, the b-jet veto is useful to suppress this background.

Fake lepton contribution from QCD

Quark or gluon production does not lead to real leptons. However if the quarks decay weakly and semi-leptonically, an actual lepton is produced from the decaying W, however such leptons are in this thesis defined as fake. This is the case in the left diagram in Figure 4.25. However, quark production also leads directly to jets in the case of the lighter quarks, as in the diagram to the right, and can lead to two fake leptons. Both these contributions are considered as double fake lepton final states.

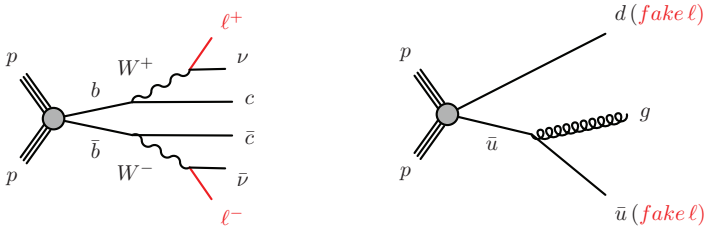

Figure 4.25: Quark/jet production.

The QCD cross section is enormous, many orders of magnitude larger than a typical EW or SUSY cross section (see Figure 4.2 and 4.3 for comparisons). Even if the probability of

a falsely reconstructed di-lepton final state is extremely small, it can still be non-negligible due to the very large initial QCD cross section. Therefore fake leptons from QCD jets could potentially be a harmful background and require careful estimation. Figure 4.26 illustrates this point, showing the $E_{\mathrm{T}}^{\mathrm{miss,rel}}$ distribution of OS di-muon MC and di-electron MC events, where both leptons satisfy the tight lepton requirement. As we see there are plenty of di-lepton events especially populating the low $E_{\mathrm{T}}^{\mathrm{miss,rel}}$ region.

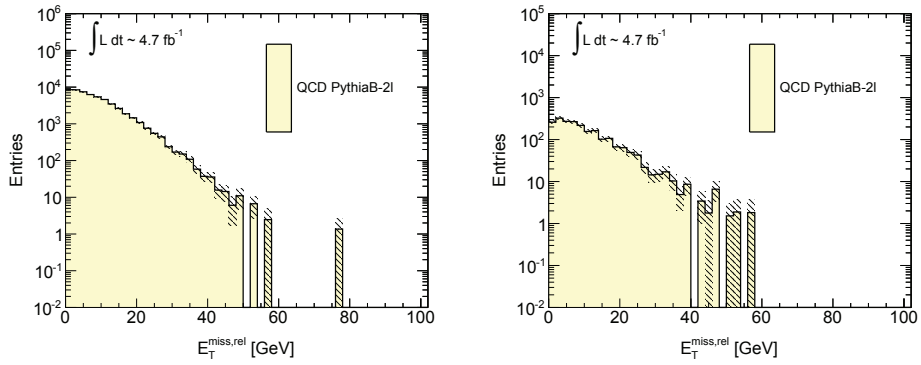

(a) Muons (b) Electrons

Figure 4.26: The $E_{\mathrm{T}}^{\mathrm{miss,rel}}$ distribution for di-muons (left) and di-electrons (right) from the heavy flavour MC QCD sample PythiaB_2L. Both leptons satisfy tight lepton requirements.

External conversions

To illustrate the effect converted photons could have on the number of final state leptons, Figure 4.27 serves as an example. Here two situations are shown, the production and decay of W+jets in (a), and of Z+jets in (b). In both cases one of the leptons radiates a photon. The resulting number of leptons are three in the W process (a) and four in the Z process (b), and therefore these processes should naively not contribute to the di-lepton channel. However, it is not unusual that the radiated γ is *hard*, which leaves the original lepton soft after radiating, and hence could fail the signal lepton requirements. In addition the energy could be distributed unequally between the pair-produced e^+e^- with one soft and one hard electron, and again the soft electron might fail the requirements and be discarded from the analysis.

For the W+jets process one would in either case end up with two hard leptons and not only one as expected from the hard interaction process. Figure 4.28 (a) gives an example of such a case. Here the red circles indicate which lepton passed the signal selection, and the black crosses which lepton failed it. In the Z/γ^*+jets of (b) we see an example of how only two out of the total of four produced leptons survive to the final state. Depending on which leptons fail reconstruction the final state lepton configuration could here be $e\mu$ or ee with any sign combination, as opposed to the usual OSSF pair from a prompt DY process. In the case of a resulting SS ee pair, the configuration is dubbed "charge-flip" events, since it appears as if the original

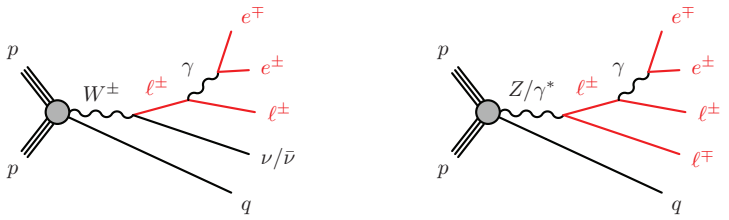

(a) W+jets + $\gamma \to e^+e^-$ (b) Z+jets + $\gamma \to e^+e^-$

Figure 4.27: Example of processes where final state γ radiation results in additional electrons.

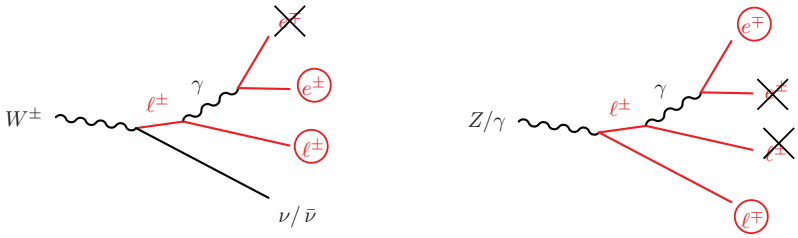

(a) W+jets + $\gamma \to e^+e^-$ (b) Z+jets + $\gamma \to e^+e^-$

Figure 4.28: Example of processes where final state γ radiation results in additional electrons, and where some electrons fail reconstruction resulting in a SS event, so-called charge-flip events.

opposite sign *ee* event had flipped charge to a same-sign *ee* event.

A final note on the fake lepton contribution: In the SS channel, the real lepton SM contributions are negligible. However, any lepton charge combination is equally probable for fake leptons, thus the fake leptons are an important background in the SS channel.

With the signal and background processes defined, the signal regions can be defined and optimized. In this context, I also define the event selection procedure, and the data and MC samples used in this analysis. The next chapter deals with all this.

Chapter 5

Signal regions, the data, and the event selection procedure

This chapter presents the signal regions based on the processes that contribute to the signal and the background, as defined in the previous chapter. It also briefly goes through the optimization strategy employed to arrive to the final signal regions. Finally the event selection procedure adopted in the current direct gaugino and slepton search is defined and discussed, together with a summary of the data sets used.

5.1 Signal regions

For the purpose of this thesis, where the main focus is on the estimation of the fake lepton background contribution to the direct gaugino and slepton searches, signal regions are defined as in [134]. The optimization of the direct gaugino signal regions is performed within the framework of two different SUSY grids, the simplified models (Section 4.2.3) for the jet-veto gaugino regions, and the pMSSM DGemt (Direct Gaugino e=e, m=μ, t=τ, Section 4.2.2) grids for the jet-requirement gaugino region. The currently used simplified model MC samples have five times larger statistics then DGemt, and therefore the preferred model to use for optimizing the direct gaugino limits. In the regions with jets, however, where more complex diagrams are involved, the simplified models are not suited, and therefore the DGemt grids are used instead.

Then for the direct slepton signal regions, we optimize using the direct slepton grid (described in Section 4.2.4).

The optimization parameter used here is the significance Z_n defined as

$$Z_n = \sqrt{2}\,\mathrm{erf}^{-1}(1-2p) \tag{5.1}$$

where p is the so-called p-value to be described below, and erf is the error-function, defined as

$$\mathrm{erf}(\gamma) = \frac{2}{\sqrt{\pi}} \int_0^{\gamma} e^{-x^2} dx \tag{5.2}$$

and is related to the cumulative Gaussian. It gives the probability for a random variable to lie

within a certain standard deviation σ of the Gaussian distribution. So erf(γ=1) corresponds to the variable lying within 1 σ, and so on.

The p-value p is a way to quantify how probable it is to observe the actual number of events q_{obs} or more, if the experiment is repeated many times. This follows from the definition

$$p(n \geq q_{\text{obs}}|b) = \sum_{n=q_{\text{obs}}}^{\infty} \frac{b^n}{n!} e^{-b} \,. \tag{5.3}$$

The expression simply says that the p-value is the integral of the distribution (here Poisson) from the value $q_{obs} \rightarrow \infty$, where $q_{obs} = q_s + b$, i.e. the sum of the signal expectancy and the background. The p-value gives the probability of observing n number of events, where n is equal or larger than the actually observed events q_{obs}, assuming (here) a background (b) only hypothesis. The smaller the p-value, the larger is the deviation of the observed data from the background only hypothesis, and the better we can exclude the hypothesis. If the p-value is large, the data is said to be consistent with the hypothesis.

In order for the SUSY signal regions to have the power to actually discover SUSY, we require a significance Z_n <1.64, which corresponds to a 95% exclusion confidence level (C.L.) of the background. When testing for discovery however, a 5σ level, which corresponds to a probability (p-value) of p=2.87·10^{-7}, is conventionally required.

The optimization procedure is then carried through for each of the signal grid points, by varying a set of cuts, such that the signal to background is optimized. The set of cuts, and cut-values that yield a 95% exclusion level of the background are then selected to define the signal regions.

In the following sections I present each of the signal regions (SR) used in this analysis, and what cuts are used to optimize the region. For all SR optimizations we assume a 10% background uncertainty, which is roughly the order of the background cross section uncertainty. In some cases the optimization is also performed with a 20% uncertainty to check the effect on the signal sensitivity, and is commented on where relevant. I start with the opposite sign jet-veto region SR-OSjveto.

5.1.1 SR-OSjveto

The SUSY direct gaugino processes 1, 3, and 5-7 of Table 4.2 contribute to the OS jet-veto signal region. Figure 5.1 (a) shows the $E_{\text{T}}^{\text{miss,rel}}$ for opposite sign (OS) muon pairs, with dominating processes: Z/γ^*+jets and $t\bar{t}$, followed by W+jets, di-bosons and single top. A Z-veto defined as $|m_{ll} - m_Z| < 10$ GeV removes more than 80% of the Z events and almost 50% of the diboson events, while the signal events are mostly kept, as Figure 5.1 (b) illustrates. The electron distributions are not shown, but electrons behave as muons.

Since the signal events do not contain leading order jets, we in addition apply a jet veto. This is effective for reducing in particular the $t\bar{t}$ background which produces multiple jets. Several jet-definitions are tested. First the p_{T} cut is varied between 20, 30 and 40 GeV. Additional cuts

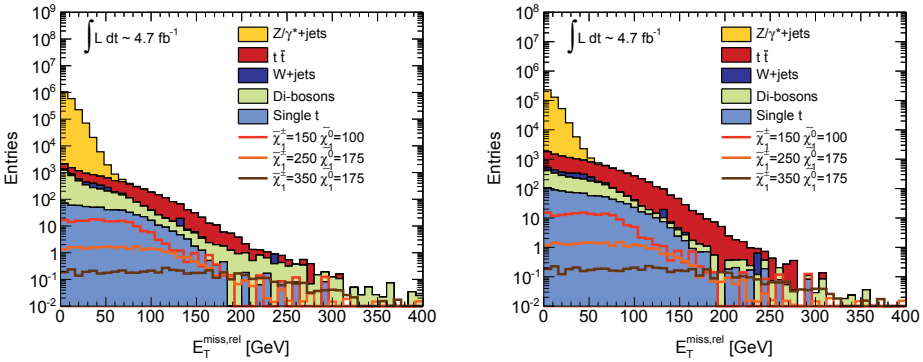

(a) Muons OS (b) Muons OS + Z-veto

Figure 5.1: $E_{\mathrm{T}}^{\mathrm{miss,rel}}$ of opposite sign muons before Z-veto (left) and after (right). Three different simplified model signal region points are used for illustration of a possible signal.

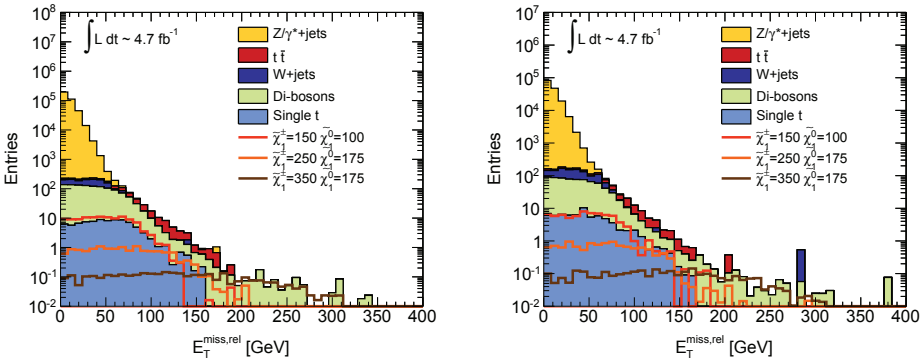

(a) Muons OS + Z-veto + jet-veto (b) Electrons OS + Z-veto + jet-veto

Figure 5.2: $E_{\mathrm{T}}^{\mathrm{miss,rel}}$ of opposite sign muons (left) and electrons (right) after applying both the Z-veto and the jet-veto. Three different Simplified model signal region points are used for illustration of a possible signal.

on $|\eta|$ and the jet vertex fraction (JVF) are then included. The resulting optimal jet definition requires p_{T}>30 GeV, $|\eta| < 2.5$ and JVF> 0.75. Figure 5.2 shows the $E_{\mathrm{T}}^{\mathrm{miss,rel}}$ distribution for OS muons (left) and electrons (right) after requiring both the Z-veto and a jet-veto. We see that the $t\bar{t}$ background now is efficiently reduced. Finally the signal region is optimized with respect to $E_{\mathrm{T}}^{\mathrm{miss,rel}}$. The optimization of the region yielded a cut $E_{\mathrm{T}}^{\mathrm{miss,rel}}$>100 GeV.

Figure 5.3 shows the expected significance versus $m(\tilde{\chi}_1^{\pm})$ and $(m(\tilde{\chi}_1^0))$. The red curve outlines the expected 95% confidence region, which covers a triangular area up until about $m(\tilde{\chi}_1^0) \sim 100$ GeV, $m(\tilde{\chi}_1^{\pm}) \sim 320$ GeV. For this result, no background uncertainty is applied.

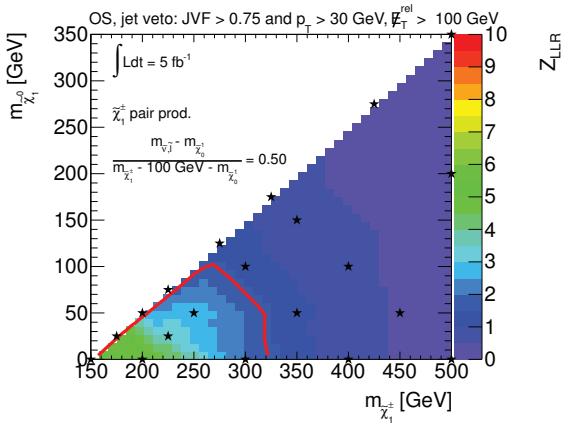

Figure 5.3: The expected significance Z_n for the optimal definition of SR-OSjveto signal region, with an applied cut on $E_{\mathrm{T}}^{\mathrm{miss,rel}}$ of 100 GeV, the Z-veto, and the jet veto requiring p_{T}> 30 GeV, $|\eta|$ <2.50 and JVF>0.75. No background uncertainty is included. The red curve outlines the expected 95% confidence region. Plot extracted from ATLAS Internal note [133], which is the support material of [134].

5.1.2 SR-SSjveto

In the same-sign no-jets signal region, the two production and decay chains are $\tilde{\chi}_2^0\tilde{\chi}_1^\pm \rightarrow (\ell^+\ell^-\tilde{\chi}_1^0)+(l^\pm\nu\tilde{\chi}_1^0)$, $l^\pm_{\mathrm{miss}}$, and $\tilde{\chi}_2^0\tilde{\chi}_2^0 \rightarrow (l^\pm l^\mp\tilde{\chi}_1^0)+(l^\pm l^\mp\tilde{\chi}_1^0)$, $2l^\pm_{\mathrm{miss}}$, (number 1 and 5 in Table 4.2). The first chain must have one lepton mis-reconstructed, and the second two leptons . The signal region is optimized for the first, and more important of these two. Due to the required mis-reconstructed third lepton, the signal region SR-SSjveto functions mainly as complementary to the three-lepton channel. While SS is known to be a very frequently occurring signature in SUSY, this is in fact the case only with strong production. In electroweak production there is no natural diagram which gives a di-lepton SS final state, however a three-lepton final-state can easily occur as we saw in Section 4.2.

To reduce the SM background a cut on $E_{\mathrm{T}}^{\mathrm{miss,rel}}$ is applied, in addition to the same jet-veto as for SR-OSjveto. Figure 5.4 shows the $E_{\mathrm{T}}^{\mathrm{miss,rel}}$ distribution for muon (left) and electrons (right), after applying the jet-veto. We see that in the electron channel there is a large contribution from Z/γ^* which is due to the charge-flip contribution mentioned in Section 4.3.4. With an optimized cut of $E_{\mathrm{T}}^{\mathrm{miss,rel}} > 100$ GeV the significance Z_n in the $m(\tilde{\chi}_1^0)$, $m(\tilde{\chi}_1^\pm)$ plane is shown in Figure 5.5, where the red curve indicates the expected 95% CL boundary.

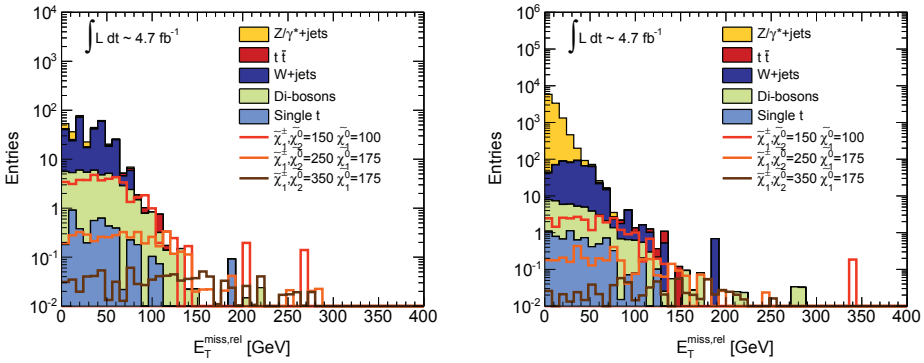

(a) Muons SS + jet-veto

(b) Electrons SS + jet-veto

Figure 5.4: $E_{\mathrm{T}}^{\mathrm{miss,rel}}$ of same-sign muons (left) and electrons (right) after applying the jet-veto. Three different Simplified model signal region points are used for illustration of a possible signal.

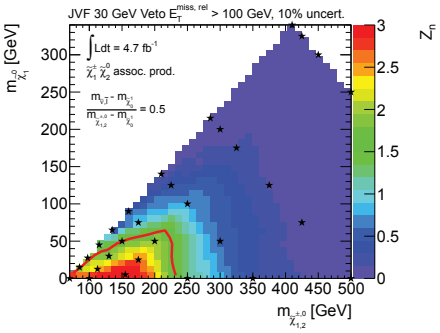

Figure 5.5: The expected significance of same-sign events (SR-SSjveto) after applying a jet-veto and a $E_{\mathrm{T}}^{\mathrm{miss,rel}}$ cut of 100 GeV. A 10% uncertainty on the SM background is used. The red curve outlines the expected 95% confidence region. Plot extracted from ATLAS Internal note [133], which is the support material of [134].

5.1.3 SR-2jets

For optimization of SR-2jets the two diagrams contributing to $\tilde{\chi}_2^0\tilde{\chi}_1^\pm \rightarrow (\ell^+\ell^-\tilde{\chi}_1^0) + (\bar{q}q\tilde{\chi}_1^0)$ either with an intermediate slepton or a Z-boson, were used. This is chain 2 of Table 4.2. Although not optimized for, the region also serves $\tilde{\chi}_2^0\tilde{\chi}_2^0$ production (chain 4 in Table 4.2), where one leg decays hadronically.

As in SR-OSjveto, the important backgrounds are mainly Z/γ^*+jets and $t\bar{t}$. We reduce the latter by exploiting the fact that the $t\bar{t}$ background is accompanied by b-jets. Figure 5.6 shows the $E_{\mathrm{T}}^{\mathrm{miss,rel}}$ distribution for OS di-muon events before (left) and after (right) applying a b-veto and the m_{CT}-veto (which was described in Section 4.3.1). With these cuts, both the Z and the $t\bar{t}$

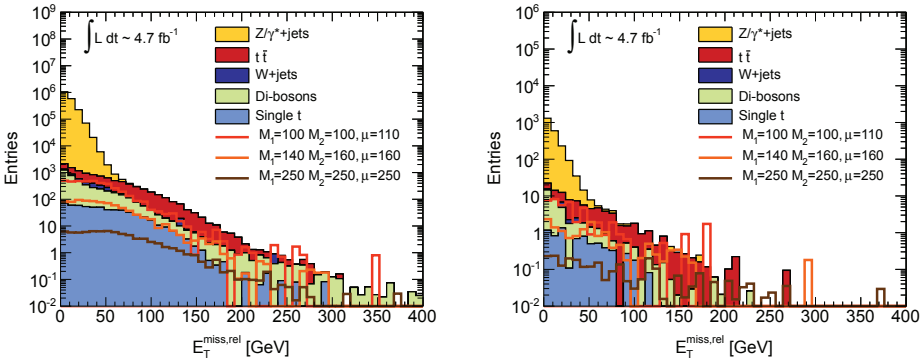

(a) $\mu\mu$, OS (b) $\mu\mu$, OS, b-veto m_{CT}-veto

Figure 5.6: The $E_{\mathrm{T}}^{\mathrm{miss,rel}}$ distribution for opposite sign di-muon events before (left) and after (right) requiring a b-veto and the m_{CT}-veto. Three different pMSSM (Direct Gaugino DG) model signal region points are used for illustration of a possible signal.

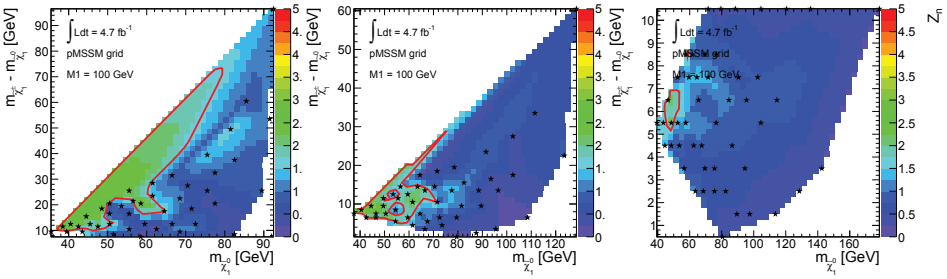

(a) M_1=100 GeV (b) M_1=140 GeV (c) M_1=250 GeV

Figure 5.7: The expected significance in SR-2jets signal region, as a function of $m_{\tilde{\chi}_1^0}$ and $m_{\tilde{\chi}_1^\pm} - m_{\tilde{\chi}_1^0}$, for three benchmark values of M_1 in the DGemt MC grid (denoted M1 in the plots), namely M_1=100 GeV (left), M_1=140 GeV (middle) and M_1=250 GeV (right). The red curve outlines the expected 95% confidence region. A 10% uncertainty on the SM background is applied. Note that there is a typo on the M1 value in the text-box of these figures. The correct values are presented in the caption. Plot extracted from ATLAS Internal note [133], which is the support material of [134].

background (as well as the di-boson background, that also contributes) are reduced by more than 90%. To reduce the the Z-background further, we apply the usual Z-veto $|m_{ll} - m_Z| < 10$ GeV. As the signal contains two tree-level jets, we require at least 2 signal jets.

The optimization of this signal region was done with the DGemt grid, and Figure 5.7 shows the result using the above cuts for the three values of M_1, namely from left to right, M_1 =

100, 140, and 250 GeV. The optimal $E_{\mathrm{T}}^{\mathrm{miss,rel}}$ cut turned out to be at 50 GeV. A 10% uncertainty is used for the SM background.

5.1.4 SR-m_{T2}

Signal region SR-m_{T2} is constructed and optimized for the direct slepton $\tilde{\ell}\tilde{\ell} \to l\tilde{\chi}_1^0, l\tilde{\chi}_1^0$ search, but it is also sensitive to $\tilde{\chi}_1^+\tilde{\chi}_1^- \to W^+\tilde{\chi}_1^0 W-\tilde{\chi}_1^0 \to l^+\nu\tilde{\chi}_1^0, l^-\bar{\nu}\tilde{\chi}_1^0$ production (process 3 in Table 4.2), when the two leptons have the same flavour.

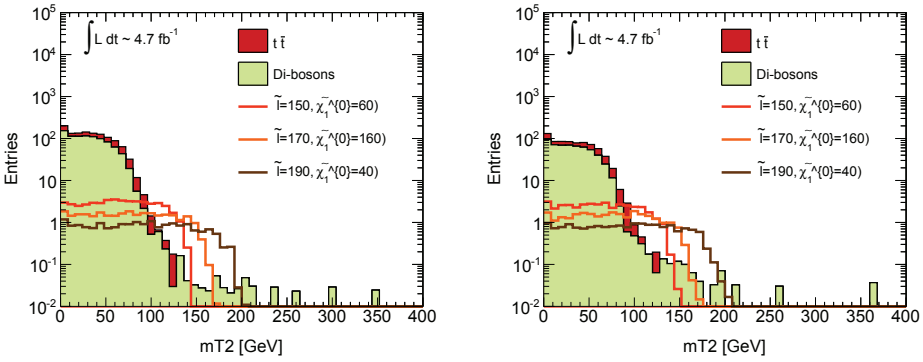

(a) Muons (b) Electrons

Figure 5.8: m_{T2} for two direct slepton SUSY (DS) MC grid points, and WW SM MC sample. A jet-veto is required, in addition to OSSF lepton pairs.

The m_{T2} is a key variable in this region, and is important to reduce SM background, especially $t\bar{t}$ and W^+W^-, as the m_{T2} signal is expected to extend beyond the background. Figure 5.8 shows the m_{T2} distribution for opposite sign di-muon (left) and di-electron (right) pairs, together with a selection of direct slepton grid points. Here the background is reduced by an additional jet-veto requirement. Although the background is much larger than the signal, the difference between the shapes of m_{T2} for background and signal is clearly visible, with the signal featuring a sharp endpoint at higher values than the background. It is clear from this plot that although the signal and background could potentially be separated with m_{T2} it is essential with further background-suppression.

To suppress the Z background we apply the Z-veto $|m_{ll} - m_Z| < 10$, and the jet-veto helps in further reduction of the $t\bar{t}$ background. Finally the signal region is optimized against different combinations of m_{T2} and $E_{\mathrm{T}}^{\mathrm{miss,rel}}$. A low m_{T2} cut gives a good sensitivity to low mass splitting $m(\tilde{\ell}) - m(\tilde{\chi}_1^0)$, a high m_{T2} cut is effective for the region of phase-space with higher mass-splitting. Figure 5.9 (a) shows the m_{T2} distribution endpoint values in the $m_{\tilde{\ell}}$, $m_{\tilde{\chi}_1^0}$ mass plane, ranging from ~50-190. We find the bulk of the points at $m_{\mathrm{T2}} > 80$ GeV. There is however a trade-off between background suppression and signal cross section. At low values of m_{T2} the

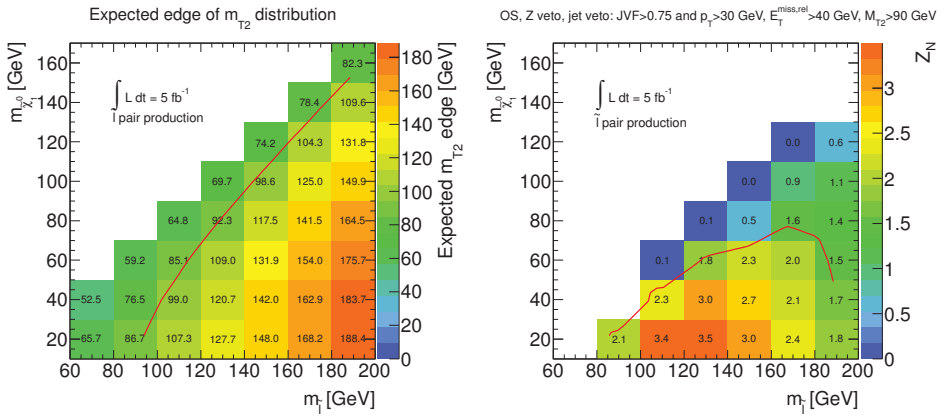

(a) m_{T2} endpoint values

(b) Significance

Figure 5.9: The expected endpoint of the m_{T2} distribution (left) and significance in SR-m_{T2} (right), in the $m_{\tilde{\ell}}$, $m_{\tilde{\chi}_1^0}$ mass plane . The red line in the left figure represents the contour where the m_{T2} endpoint value is exactly 90 GeV. In the significance plot to the right, signal region cuts are applied as indicated in the plots header, and discussed in the text. The expected 95% C.L. contour is outlined in red. Plot extracted from ATLAS Internal note [133], which is the support material of [134]

SM background is still a challenge, but at high m_{T2} the signal cross section is reduced. In this analysis, the point of compromise was found with $E_{\mathrm{T}}^{\mathrm{miss,rel}} > 40$ GeV and $m_{T2} > 90$ GeV. The 90 GeV contour is marked in Figure 5.9 (a) with a red line. In Figure 5.9 the expected 95% C.L. contour when including all cuts, is outlined by a red curve in the plane spanning $m_{\tilde{\ell}}$, $m_{\tilde{\chi}_1^0}$ values.

A final note on the optimization procedure. In all OS regions (SR-OSjveto, SR-2jets, and SR-m_{T2}) the level of uncertainty on the background greatly affects the significance. If instead of applying a 10% uncertainty, we use 20%, the signal region satisfying the expected 95% CL is considerably reduced (which was shown in in the Internal ATLAS note [133]). It is therefore important to keep systematic uncertainties under control. The SS region (SR-SSjveto) is to a lesser extent affected by the background uncertainty, as the SM background is much smaller compared to OS.

For clarity, a summary of the four independent signal regions is presented in Tables 5.1 and 5.2, explicitly stating all cuts.

This finalizes the discussion and definition of the signal regions. In the following section the event selection will be presented, including treatment of overlap between objects (electron, muons and jets), and the trigger strategy. The following section summarizes all the data samples - real and simulation, signal and backgrounds.

Direct gaugino

Shorthand	Description	Cuts
SR-OSjveto	Opposite sign leptons, no jets	jet veto $\|m_Z - m_{ll}\| > 10$GeV $E_{\mathrm{T}}^{\mathrm{miss,rel}} > 100$GeV
SR-SSjveto	Same sign leptons, no jets	jet veto $E_{\mathrm{T}}^{\mathrm{miss,rel}} > 100$GeV
SR-2jets	Opposite sign same flavour leptons, jet requirement	≥2 jets b-jet veto m_{CT} top-tag veto $\|m_Z - m_{ll}\| > 10$GeV $E_{\mathrm{T}}^{\mathrm{miss,rel}} > 50$GeV

Table 5.1: The definition of the three signal regions SR_OSjveto, SR_SSjveto and SR_2jets used in the direct gaugino search

Direct slepton and chargino

Shorthand	Description	Cuts
SR-m_{T2}	Opposite sign same flavour, with m_{T2} cut, no jets	jet veto $\|m_Z - m_{ll}\| > 10$GeV $m_{T2} > 90$GeV $E_{\mathrm{T}}^{\mathrm{miss,rel}} > 40$GeV

Table 5.2: The definition of the signal region used in the direct slepton search, region SR-m_{T2}.

5.2 General event selection

The data I analyzed in the search for direct gauginos and sleptons, were collected by ATLAS during LHC runs in the period from March to October 2011. In this period LHC provided a collision energy of $\sqrt{s}$ =7 TeV, and the total integrated luminosity collected amounted to $\int \mathcal{L}\,dt = 5.0\,\mathrm{fb}^{-1}$. Of this a total of $\int \mathcal{L}\,dt = 4.7\,\mathrm{fb}^{-1}$ met the standard required to perform physics analysis, and is the integrated luminosity this thesis is based upon [1].

An event, or the collection of data from one collision instance, is only accepted for the anal-

[1] In 2012 LHC continued colliding protons, and with a higher collision energy of $\sqrt{8}$ TeV, ATLAS collected a total of 20.3 fb^{-1} integrated luminosity for physics analysis. This thesis is however based on the 2011 data set, although the method developed is used also for the $\sqrt{8}$ TeV analysis [141].

ysis if it passes a set of requirements, mostly related to the ability to identify and measure the remnants from the proton-proton interaction. Roughly speaking, if a sub-detector is in a state that does not allow for a reliable measurement, and software reconstruction cannot recover the performance, the event is rejected. The overall data-quality is based on the collective assessment of all sub-detectors and is done centrally in ATLAS by the Data-Quality group. They provide a so-called "Good run list" (GRL) which all physics analysis groups apply. It is the GRL that is responsible for the necessary reduction of the integrated luminosity from 5.0 to 4.7 fb^{-1}. In addition several analysis-dependent event criteria are enforced. These are discussed briefly in the following.

For the event to likely stem from a head-on parton collision, in ATLAS we require that a primary vertex (the vertex connected to the collection of tracks with the highest sum of p_{T}) with at least 5 tracks must be present. This increases the probability that we suppress out the abundant softer interactions, which are not relevant for high p_{T} physics. The resulting final-states of interest include electrons, muons, jets and $E_{\text{T}}^{\text{miss}}$: all these objects and variables must be reconstructed and determined reliably, as detailed in Section 3.5. Actually, since the analysis depends on $E_{\text{T}}^{\text{miss}}$, this alone requires excellent performance from all sub-detectors. This is because $E_{\text{T}}^{\text{miss}}$ is inferred from the total transverse energy in the event and based on energy conservation from the initial hard interaction process. Without all hard physics objects observed, and properly identified and measured, the $E_{\text{T}}^{\text{miss}}$ cannot be reliably determined.

For the jets, the liquid argon detector has a blind spot after an unrecoverable failure of some components resulting in dead front-end boards (FEB), therefore the events are vetoed that contain jets that point in this direction. In addition events are removed if they contain jets that are likely to stem from detector/hardware effects or cosmic showers. The latter is also relevant for muons, if a cosmic muon is found, the event is rejected. And finally, some muon candidates are of such bad quality that the whole event is considered unreliable, these are muons where the total uncertainty of the charge over momentum (q/p) is larger than 20%.

With the use of electrons, muons and jets, a careful geometrical *overlap removal procedure* must be applied. This is because an object is not necessarily uniquely identified. Electrons can leave energy in the hadronic calorimeter and result in a falsely reconstructed jet. An actual jet can leave traces in the electromagnetic calorimeter through π^0 decays, or even contain leptons through weak decays of hadrons. An electron or (at a less extent) muon can emit bremsstrahlung resulting in the reconstruction of additional electrons when the photon converts. For all these cases a careful and ordered overlap removal procedure has been defined, ordered after the level of trust we have that the object is what it appears to be. This order is listed below, and is performed on objects that have already passed *baseline* object definitions, as presented in Chapter 3.5, Tables 3.1 (electrons), 3.2 (muons) and 3.3 (jets). The ΔR variable is used to measure the geometrical separation between objects, and is defined as $\Delta R = \sqrt{(\Delta\eta)^2 + (\Delta\phi)^2}$.

1. $\Delta R(e_1, e_2) < 0.1$: If two electrons (e_1, e_2) are closer than $\Delta R = 0.1$, it is probable that the softer electron is due to conversion from electron bremsstrahlung, therefore only the most energetic electron is kept.
2. $\Delta R(j, e) < 0.2$: If a jet (j) and an electron (e) which have already passed criterion 1 are within $\Delta R < 0.2$ the jet is most probably mis-reconstructed and is removed.
3. $\Delta R(j, l) < 0.4$: If either a muon or electron (l) and a jet (j), both having passed criteria

1 and 2 are within $\Delta R < 0.4$, the lepton is removed (and the jet kept) as the lepton most probably stems from jet-remnants.

4. $\Delta R(e,\mu) < 0.1$: Finally, if an electron (e) and muon (μ) are within $\Delta R < 0.1$ both leptons are rejected. This is because the muon in this case most probably has emitted a photon which has converted, leaving both the muon and the electron(s) badly reconstructed.

This summarizes the main "event-cleaning" and object overlap removal procedure, but another important ingredient in the data selection is the trigger. This is discussed in the following section.

5.3 Data sets and triggers

The data is divided into "periods" where each period typically corresponds to different LHC run-conditions, as we learn how to improve LHC. For each period the instantaneous luminosity increases, thus triggers are adjusted to complement each period. An overview of the different periods, and the corresponding integrated and instantaneous luminosity is presented in Table 5.3.

Period	Run-range	Luminosity	
		Integrated [pb]	Peak inst. [10^{30}cm^{-1}s^{-1}]
B	178044-178109	11	46
D	179710-180481	162	659
E	180614-180766	48	832
F	182013-182519	128	1100
G	182726-183462	505	1263
H	183544-184169	257	1264
I	185353-186493	334	1887
J	186516-186755	229	1995
K	186873-187815	593	2328
L	188921-190343	1409	3252
M	190503-191933	1040	3848
Tot integrated luminosity 4716 pb			

Table 5.3: Summary of the data taking periods, with run-ranges, and integrated and instantaneous (inst.) luminosity. Periods A and C are omitted as they do not contribute to the 2011 data-set used in this analysis. These were runs with special conditions.

Since this SUSY search is focused on final states with electrons and muons, both the `Muon` and `Egamma` trigger streams[2] were used. The triggers selected for each data taking period were those which were unprescaled[3] with the lowest p_{T} threshold available. They are listed in Tables 5.4-5.6. For all channels (ee, $\mu\mu$ and $e\mu$) both single and di-lepton triggers were used. The trigger p_{T} are online thresholds/cuts. The p_{T} value where the trigger starts to be at its most efficient is quoted as the offline trigger threshold. The p_{T} region below features a so-called turn-on-curve from zero to maximum efficiency, as Figure 5.10 gives an example of.

[2] A stream refers to the routing of collision data into collection of files depending on the physics content.

[3] Prescaling is a method to only select a fraction of events, according to a defined prescale value of a trigger.

Electron Triggers

Period	Single		Double	
	Trigger	Offline p_T Threshold	Trigger	Offline p_T Threshold
A-J	e20_medium	25 GeV	2e12_medium	17 GeV
K	e22_medium	25 GeV	2e12T_medium	17 GeV
L-M	e22vh_medium1	25 GeV	2e12Tvh_medium	17 GeV

Table 5.4: Single (left) and di- (right) electron triggers used for each period of data analyzed.

In the electron trigger strategy, all triggers require `medium` electron identification quality, which corresponds to the baseline electrons (as presented in Section 3.5.1 Table 3.1). The single `medium` electron trigger efficiency is shown as a function of p_T in Figure 5.10 for the three different electron definitions used in this analysis. As the plot shows the efficiency is about 90-95% above the threshold of around 25 GeV.

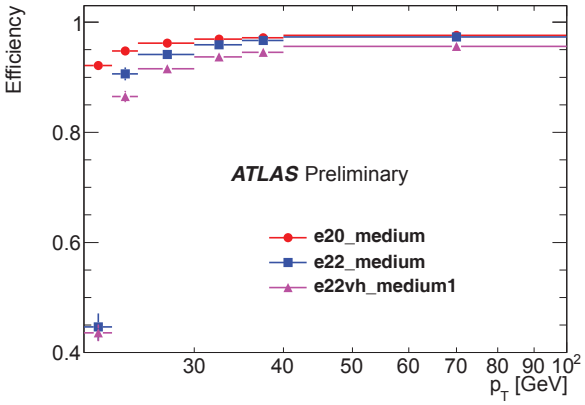

Figure 5.10: Electron trigger efficiencies versus p_T offline, using the tag-and-probe method with Z events. The "vh" refers to an additional hadronic suppression. [143]

For the single triggers, the lowest unprescaled online p_T threshold was increased from 20 to 22 GeV during the data taking period, but with both still corresponding to a 25 GeV offline threshold. For the di-electron triggers a 12 (17) GeV online (offline) threshold was kept throughout. In later data taking periods the hadronic suppression was tightened, referred to with a "vh" added to the trigger name.[4], and a tightening of the p_T threshold of the L1 seeding was introduced, indicated by the "T". In the latest single trigger a "medium1" requirement was constructed to trigger on the `pp` (such as `tightpp`) electron identification objects, which have stricter requirements on shower shapes and additional requirements on tracks. For further technical details on the electron (and photon) triggers see [143].

[4]More specifically "vh" implies that an η dependent threshold was applied, in addition to limiting events with hadronic leakage by requiring the energy in the core of the hadronic calorimeter to be < 1 GeV.

Muon Triggers

Period	Single		Di	
	Trigger	Offline p_T Threshold	Trigger	Offline p_T Threshold
A-I	mu18	20 GeV	2mu10_loose	12 GeV
J-M	mu18_medium	20 GeV	2mu10_loose	12 GeV

Table 5.5: Single- (left) and di-muon (right) triggers used for each period of data analyzed.

The muon triggers also evolved somewhat with the increasing instantaneous luminosity. The early single muon triggers did not apply muon quality cuts, but in the later periods (J-M) a `medium` quality requirement was introduced. Single muon trigger efficiencies above the threshold of 20 GeV are roughly 70% in the barrel and 90% in the end-caps, as Figure 5.11 shows, with the lower efficiency for the barrel (left), and the higher for the end-cap (right).

For the di-muon triggers a `loose` muon quality cut was applied throughout. The p_T cuts were kept at the same level over the course of the whole data taking period: 18 (20) GeV online (offline) for the single muon trigger and 10 (12) GeV online (offline) for the di-muon trigger.

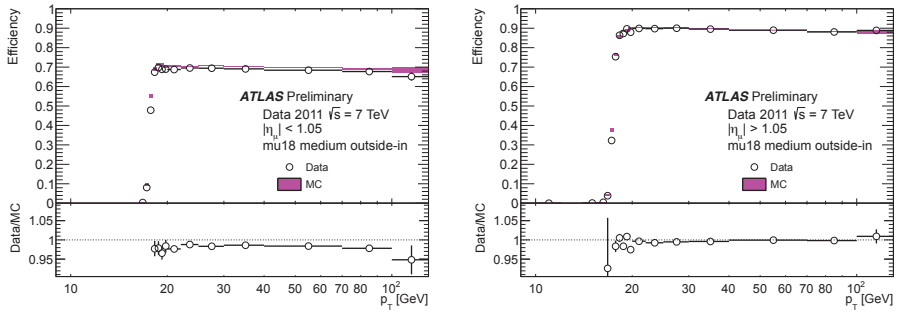

Figure 5.11: Muon trigger efficiencies versus offline p_T measured in Z-events. Left figure shows the efficiency measured in the barrel ($\eta < 1.05$), and the right figure in the end-caps ($\eta > 1.05$). The label "outside-in" refers to the initial triggering which in this case is in the Muon Spectrometer. Corresponding "inside-out" (initialized in Inner Detector) results give similar results. From Ref. [144].

Electron-muon Trigger

Period	Di	
	Trigger	Offline p_T Thresholds
A-M	e10_medium_mu6	$p_T(e) > 15$ GeV, $p_T(\mu) > 8$ GeV

Table 5.6: Di- electron and muon trigger.

Finally the $e\mu$ di-lepton trigger used throughout the whole 7 TeV data period applied a `medium` electron quality requirement (no requirement on the muon quality), and an online p_T

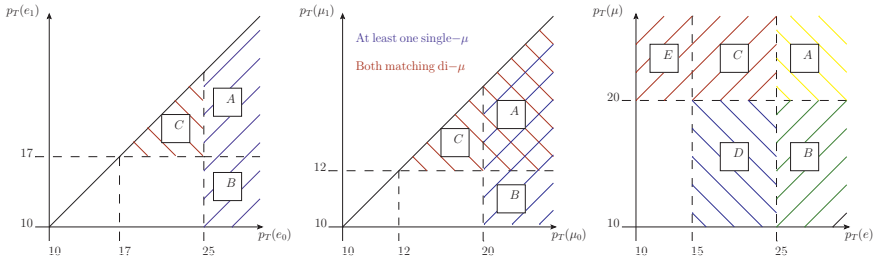

(a) e^+e^- (b) $\mu^+\mu^-$ (c) $e\mu$

Figure 5.12: The coverage of the di-lepton trigger in the 2D transverse momentum parameter space. From left to right e^+e^- (a), $\mu^+\mu^-$ (b) and $e\mu$ (c). Each region is given a label A,B and so on for practical reasons when explaining the trigger strategy in the text. Figure from ATLAS Internal Note [133], supporting material to [134].

threshold of 10 GeV for the electron and 6 GeV for the muon, corresponding to an offline threshold of 15 and 8 GeV respectively.

A careful trigger strategy is implemented in order to cover as much of the p_T phase space as possible, and to obtain a high total trigger efficiency. This is illustrated in Figure 5.12, where the p_T phase-space of the two leptons is divided into regions A-C for ee and $\mu\mu$ or A-E for $e\mu$. The regions within each channel are colour-coded according to which trigger is used. In region A of the $\mu^+\mu^-$ channel in Figure 5.12(b), two triggers contribute.

In this direct gaugino and slepton search, MC trigger simulation is not used, instead the MC event is given a weight according to the measured trigger efficiency in the current p_T and η phase-space. In areas of p_T phase-space where the trigger efficiency is high, typically ≥95%, the single most efficient trigger is used (either single or di-lepton trigger). Only where a significant increase in the trigger efficiency is obtained, an `ORing` of the single and di-lepton triggers is applied. The resulting trigger strategy depicted in Figure 5.12 reflects this. Table 5.7 summarizes the regions and triggers for each channel. Note that MC trigger weights are only computed for leptons above p_T threshold, which is sufficient for the baseline SUSY analysis defined in this thesis. However, it does somewhat effect the fake lepton distributions, which I get back to in Chapters 6 and 7.

For the di-electron channel in Figure 5.12(a), regions A and B are both characterized by the leading electron p_T> 25 GeV and in these regions the single electron trigger is used, as the top row of Table 5.7 shows. This trigger is known to have a 95% trigger efficiency on the trigger-plateau (of 25 GeV), see Section 3.2.6 for more details. In region C with both electron's p_T below 25 GeV the di-electron trigger is used.

In the di-muon channel we apply a combination of the single and di-muon trigger in region A where the leading muon p_T is >20 GeV. This is as mentioned because the single muon trigger only has an 80% overall efficiency on the trigger plateau. That combination is shown by the red and the blue hatching overlapping in this region of Figure 5.12(b). The event is accepted if the single `OR` di-muon trigger is passed. In Region B where the leading (sub-leading) muon p_T is > 20 (< 12) GeV the single muon trigger is used, and in Region C where leading (sub-

	Single		Di		
Chan	e	μ	ee	$\mu\mu$	$e\mu$
ee	A,B		C		
$\mu\mu$		A,B		A,C	
$e\mu$	A,B	A,C,E			D

Table 5.7: The trigger strategy divided into phase-space regions as illustrated in Figure 5.12. For the p_{T} thresholds, see the figure or text.

leading) muon p_{T} is $< 20\,(< 20)$ GeV the di-muon trigger is applied. See also the middle row of Table 5.7.

The electron-muon channel phase-space is divided into 5 regions. The region A with $p_{\mathrm{T}}^{e} > 25, p_{\mathrm{T}}^{\mu} > 20$ is covered either by a single electron or single muon trigger. In Region B where $p_{\mathrm{T}}(e) > 25$, $p_{\mathrm{T}}(\mu) < 20$ the single electron trigger is used. In Regions E and C with $p_{\mathrm{T}}(e) < 25$, $p_{\mathrm{T}}(\mu) > 20$ the single muon trigger is used, and finally in region D with $p_{\mathrm{T}}(e) < 25$, $p_{\mathrm{T}}(\mu) < 20$ the di-lepton $e\mu$ trigger is used. The bottom row of Table 5.7 summarizes the strategy.

5.3.1 Monte Carlo SM background samples

The di-lepton direct gaugino and slepton searches use MC background samples from several MC generators in order to cover the variety of channels considered, and to model higher order corrections as well as possible. Because of limited computer power, only a few crucial processes have been fully simulated to NLO. For the rest, so-called global k-factors are applied to scale the cross section up from LO to NLO, the k-factor being defined as

$$k = \frac{\sigma^{NLO}}{\sigma^{LO}}$$

correction to the LO results. This is the simplest way of taking into account important effects, without reprocessing all fully simulated MC processes again to NLO. The latter is impossible in practice (with today's methods) due to limited resources. All samples used in this analysis are briefly described below. The generators used, the cross sections and k-factors of the MC samples, are all summarized in Table 5.8. In addition slightly more detailed tables which also give the MC sample ID numbers, and cross sections divided into sub-samples, can be found in Appendix B.3.

For both the Z and W boson production we use the Alpgen Jimmy (+Herwig for hadronization) samples, made up of sub-samples according to the number of accompanying partons in the hard scattering event, from 0-5 partons. Only light quarks are directly produced, but gluon-splitting into all flavours adds also heavy flavour quarks to the events. An inclusive Z and W

boson sample is achieved by combining the Z/γ^*/W+jets with the $Z/\gamma^*/W, b\bar{b}$ + jets samples[5].

The Z/γ^*+jets production samples are further divided into two sets according to the invariant mass of the lepton pair. A di-lepton invariant mass filter is used to split the production into a low-mass Drell-Yan sample with $10 < m(ll) < 40$ GeV, and a high mass sample with $40 < m(ll) < 2000$ GeV. This is done due to the usual argument of saving processing time, and producing enough high-mass samples, since each sample then can be given separate luminosity scaling weights. We include both samples to cover the whole invariant mass spectrum.

The $Z/\gamma^* + b\bar{b}$+jets samples are divided into 0-3 additional light partons as in the Z/γ^*+jets-samples. The total cross section for Z/γ^* including the $b\bar{b}$ samples, is $1.50 \cdot 10^4$ pb. This is after including k-factors and leptonic branching ratios. See Table 5.8 for a summary of the key features, and for more details, Appendix Table B.2.

The W+jets samples mainly follow the same scheme as Z/γ^*, where the samples are divided into W+jets with light partons (and gluons with subsequent splitting), and separate $Wb\bar{b}$+jets samples. The total cross section amounts to $3.14 \cdot 10^4$ pb. Table 5.8 summarizes the sample, while details are collected in Appendix Table B.3.

SM MC samples I					
Type	Description	Generator	eff σ [pb]	Unc.	k-factor
γ^*+jets	Zee/$\mu\mu$/$\tau\tau$NpX Mll10to40	ALPG JIM	11900	5%	1.24
$Z\gamma^*$+jets	Zee/$\mu\mu$/$\tau\tau$NpX	ALPG JIM	3210	5%	1.24
$Z\gamma^* bb$+jets	Zee/$\mu\mu$/$\tau\tau$bbNpX	ALPG JIM	38.5		1.24
W+jets	Weν/$\mu\nu$/$\tau\nu$NpX	ALPG JIM	31400	5%	1.20
Wbb+jets	WbbNpX	ALPG JIM	9.65		1.20
$t\bar{t}$	Semi-leptonic T1	PHeg PYT	90.6	+9.9-10.7%	–
$t\bar{t}$	All-hadronic T0	MCNLO JIM	76.2	+9.9-10.7%	–
t-chan	single top	MCNLO JIM	64.57*	+2.63 – 1.74	[145]
s-chan			4.63*	+0.20 -0.18	[146]
Wt-chan			15.74	+1.17 -1.21	[147]
Di-boson	WW, WZ, ZZ (single-lep req.)	Herwig	24.2	5%(7% WZ)	1.48, 1.70, 1.35
Di-boson	WW, WZ, ZZ(4l), ZZ(ll$\nu\nu$) (di-lep req.)	Sherpa	16.4	5%(7% WZ)	1.09, 1.08, 1.14, 1.17

Table 5.8: Summary of the contributing SM backgrounds (not including di- or multijet processes, for these see Table 5.9), their generator, the effective cross section, uncertainty on cross section, and k-factor. Abbreviations: ALPG= Alpgen, JIM=Jimmy, PHeg=PowHeg, MCNLO=MC@NLO, PYT=Pythia. The samples with NpX includes X=0-3 or 5 Number of partons (Np) depending on the sample. For more technical details on the samples, see Appendix B.3. Note that in the single top s- and t-channel, the total cross section is given (*). Each lepton channel contributes with a branching ratio of 10.8%.

[5]For completeness also cc samples should be included, however at the time of performing this analysis, these samples were not available.

Separate samples are available for the di-boson background. Here we use two different sets, namely Herwig and Sherpa. The Sherpa samples are used when the event selection includes jets, since Sherpa features associated tree-level jets contrary to Herwig which only includes jets from the underlying event. In events that have passed the jet-veto, the Herwig sample is sufficient, since the jet contribution in this case is much less important. The total cross sections including branching ratio to leptons and k-factors for the di-boson samples are 24.2 pb for the Herwig sample and 16.4 pb for the Sherpa sample. The cross sections differ since this Herwig sample includes a single lepton requirement, while the Sherpa samples use a di-lepton requirement. Table 5.8 summarizes the features of the two samples, and Appendix Table B.4 gives more details.

The top-background is divided into single top and $t\bar{t}$ production. In the simulation of the single top production, the s, t, and Wt channels (Figure 4.24) are treated separately. Only leptonic decays of the W are considered, and samples are divided by lepton flavour. All samples are generated with MC@NLO interfaced with Jimmy. The details of the cross sections are presented in Table 5.8. The cross sections totals up to 38.1 pb, with uncertainties of the order of 2-7%. No k-factors are used.

The $t\bar{t}$ background is divided into leptonic (T1) and fully hadronic (T0) final states. In this analysis we use the PowHeg Pythia for the leptonic channel, while for the fully hadronic sample, the MC@NLO interfaced with Jimmy is used. Originally MC@NLO was used for both T1 and T0, however, as the W-line shape was found to be better described in PowHeg Pythia, the representation of the more important leptonic channel was finally done with PowHeg Pythia. The total $t\bar{t}$ theoretical cross section is taken as $166.8^{+16.5}_{-17.8}$ pb (corresponding to +9.9-10.7% uncertainty) following the ATLAS Top Working groups recommendations ([148]). Technical details about the sample are collected in Appendix Table B.5, and as usual, Table 5.8 summarizes the key features.

The QCD MC is not used in the final SUSY limit-setting, since it instead relies on the results of the fake lepton estimation to be detailed in Chapter 6. However, in the fake estimation analysis itself, four different Pythia QCD MC are used for validation, and compared to find the best suited for fake lepton representation. These are the general purpose QCD samples J0-5 (dubbed JX) with either an electron or a muon filter, the general purpose jet-filter sample JF17 (a jet above 17 GeV is required at generator level), and two heavy flavour filtered samples; one with a single lepton filter (PythiaB_1L, a single lepton with p_{T} above 15 GeV is required) and the other with a di-lepton filter (PythiaB_2L, two leptons both with p_{T} above 10 GeV required). Since this analysis requires leptons in the final state, it is practical to use samples that require one or more leptons, when these are available.

All samples include the following six sub-processes $q_iq_j \rightarrow q_iq_j$, $q_i\bar{q}_i \rightarrow q_k\bar{q}_k$, $q_i\bar{q}_i \rightarrow gg$, $q_ig \rightarrow q_ig$, $gg \rightarrow q_k\bar{q}_k$, and $gg \rightarrow gg$, where q is a quark of any flavour (both heavy and light, except t), and g is a gluon. Here the sub-scripts i, j denote different incoming partons, and k is used for the outgoing parton if it not the same flavour as the incoming ones. This is Pythia's so-called standard QCD mixture.

The JF17 sample incorporates the standard mixture plus the following sub processes: $q_i\bar{q}_i \rightarrow t\bar{t}$, $gg \rightarrow t\bar{t}$, $q_i\bar{q}_i \rightarrow g\gamma$, $gq_i \rightarrow q_i\gamma$, $q_i\bar{q}_i \rightarrow Z/\gamma^*$, $q_i\bar{q}_j \rightarrow W^{\pm}$. Since this sample requires at least one jet, both the $t\bar{t}$ and the $Z\gamma^*$ and $W^{\pm}$ decay modes are hadronic or in the case of $t\bar{t}$, at the most semi-

SM MC samples II - QCD			
Description	Generator	eff σ [pb]	k-factor
JF17 jet-filter	PYT	9.20 E+07	–
PythiaB 2-lep filter	PYTB	8.04E+03	–
PYthiaB 1-lep filter	PYTB	2.32E+05	–
JX 1-el filter	PYT	2.23 E+06	–
JX 1-mu filter	PYT	3.94 E+06	–

Table 5.9: Summary of the SM QCD samples used for validating the fake lepton estimation to be described in Chapter 6.For more technical details on the samples, see Appendix B.3.

leptonic. The two processes with γ in the final-state are so-called prompt photon production.

Information on the sample and cross sections for these QCD samples used are listed in the Appendix Tables B.6-B.7.

5.3.2 Monte Carlo signal grid files

For consistency I also summarize the SUSY signal grids used in this analysis. For the direct gaugino (chargino and neutralino) search we use the pMSSM DGemt grid, and the simplified model grids. For the direct slepton we use the pMSSM direct slepton grid. The MC ID numbers, and the defining parameters for each grid is listed in Table 5.10. For more details on the SUSY signal grids, see Sections 4.2.2-4.2.4 for the pMSSM DGemt grid, the simplified model grid, and the pMSSM direct slepton grid respectively.

Type	MC ID	Parameters [GeV]	Generator
DGemt	138422-138567	M_1={100,140,250}, $M_2=\mu$=[100-250]	Prospino2.1
DGemt	143782-143943	M_1={100,140,250}, $M_2=\mu$=[100-400]	ISASUSY 7.8
DGemt	163509-163637	M_1={100,140,250}, $M_2=\mu$=[100-500]	Herwig++
SM A no slep	140790-140827	$\tilde{\chi}_1^{\pm} = \tilde{\chi}_2^0$ 70-500 $\tilde{\chi}_1^0$ =0-430	Prospino2.1
SM A slep	144867-144897		Herwig++
SM C no slep	144898-144928		
SM C slep	157784-157805		
DS	142708-142742	$\tilde{\chi}_1^{\pm} = \tilde{\chi}_2^0$ 70-190 , $\tilde{\chi}_1^0$ 20-60	Prospino, ATLFastII, Herwig++

Table 5.10: An overview of the SUSY signal datasets. The pMSSM DGemt grid is fully simulated, while the simplified model (SM) grid and direct slepton (DS) grid use ATLFastII. The simplified model grids are divided into modes A and C, with or without intermediate sleptons (slep). The DGemt uses Prospino2.1 for the cross section calculations, and ISASUSY 7.8 as spectrum generator, the simplified models use SDECAY [149] and SOFTSUSY [150] for decay calculator and spectrum generator respectively.

Chapter 6

Fake lepton background estimation with the Matrix Method

This chapter presents the estimation of background from so-called *fake* leptons, using the Matrix Method (MM) [151]. In the context of this analysis, electrons and muons are fake if they originate from sources other than prompt decay of Z, W bosons, including those stemming from leptonic decay of the W boson in top-quark or τ lepton decays, all of which are already described in Section 4.3.4. Real leptons naturally also come from decay of SUSY particles. The denomination "fake" is used since non-prompt leptons can mimic "real" isolated prompt leptons. As fakes we include leptons from light flavour jets, weak decay of b- or c-hadrons[1], and electrons from converted photons. The light component also includes contribution from $\pi^{\pm}$, $K^{\pm}$ decays, and what can be interpreted as "real fakes" from π^0 overlap.

While fake muons predominately originate from heavy flavour jets, the electron contribution stems from a richer mixture of processes, both where the light jet is misidentified as an electron, for instance from electromagnetic deposits from hadrons in a jet, and from heavy flavour sources as for muons. One important additional source of fake electrons is photon conversions. From the point of view of this analysis, electrons from conversions are divided into two main categories, the charge-flip events, and the rest of the conversion events (internal and external). Only the latter is estimated with the Matrix Method, as the charge flip contribution is estimated with the MC-based Charge-Flip package, which is briefly described in the next section.

The work presented in this and the following two chapters, is a result of the analysis performed in connection to several ATLAS publications, and other related material. In Internal ATLAS supporting notes: [152–154], (35 pb^{-1}, 1 fb^{-1}, and 4.7 fb^{-1} respectively), in ATLAS (internal) Communication notes: [133, 155], and in three publications, Europhysics Journal [156] (35 pb^{-1}) and Physics Letters [134, 157] (1 fb^{-1}, and 4.7 fb^{-1} respectively). The approach developed in this work has also been used (and developed further) in some follow-up work using the full 2012 data statistics, such as the most recent conference note [141], and the related internal note [158]. The method has undergone a series of changes compared to what was done in the first publication, performed on the 2010 data with 35 pb^{-1}. In this thesis the approach follows the work described in [134], and the related internal note [133], which applies the method on the 4.7 fb^{-1} 2011 data. However, details in the analysis, such as choice of control regions and sys-

[1] One may argue that electrons or muons from weak decays of b- and c-quarks are prompt, but in this analysis they are treated as part of the QCD background

tematic uncertainties have been re-evaluated, and the full analysis chain has been gone through in course of writing this thesis. It is important to point out that this does not change the main conclusions in [134], but reconfirms, and slightly improves the results.

The fake estimation in all the above-mentioned publications and notes was developed and carried through in close cooperation with Eirik Gramstad, PhD from the University of Oslo who defended his thesis on September 27, 2013 [159]. As Eirik and myself were the only ones performing the fake estimation for the di-lepton SUSY search analysis, the cooperation has been important both for cross checks on results and for fruitful discussions on the development of the method. In the three rounds of publications, we alternated the responsibilities within the analysis, in particular the more heavy technical aspects of implementing the object definitions and event selections, and producing final analysis files in 100% agreement with the rest of the SUSY di-lepton group (so-called cutflow agreement). This applies also to various sub-analysis and in-depth investigations within the MM.

In the next section, I present the motivations for using the data-driven Matrix Method to estimate the fake lepton background. This is followed by the description of the method itself and the terminology used (Section 6.2). The derivation of fake and real efficiencies is one of the main challenge of the method, and is described from Section 6.3. The implementation of the method, and the final real efficiencies and fake rates used, together with a discussion of their systematic uncertainties are all described in Chapter 7, where also the results are presented.

6.1 Fake leptons in MC, and the need for a data-driven estimation method

MC simulations carefully constructed to reproduce the Standard Model, or any other model of interest, are extremely useful for making predictions for a physics analysis. Data is nature's blueprint, but MC can help us understand the underlying truth. However, the study of hadronic fake leptons is especially challenging with regards to MC. There are limitations connected to simulating events corresponding to the large cross section, which are orders of magnitude larger than the electroweak cross section (see Section 4.1 for details), challenges in modelling the initial and final state radiation, and in taking into account the underlying event and the pile up. All these points result in considerably large uncertainty as to whether QCD fakes are correctly represented or not. Fake electrons from conversions are also estimated by separate methods, and not taken directly from MC. In the 35pb^{-1} analysis [156], the rate of charge-flip events in MC was approximately 20% larger than in data, and therefore a separate method was developed to estimate this contribution as mentioned in the introduction. The discrepancy was presumed to be due to differences in the material budget in the real and simulated detector, and discrepancies in the absolute positioning of the beam-pipe. In this version of the analysis however, with updated MC samples, and more data, the discrepancy is no longer significant (at the 8% level, see Appendix D for details). However, the charge-flip estimation method is still carried out for the final results, as it gives a reliable and precise determination of this important source of same-sign (SS) electron events. For the charge-flip events in this analysis, we therefore use

the Charge-Flip package, which is part of the SUSYTools software package. The method estimates the amount of SS ee or $e\mu$ pairs based on opposite sign (OS) pairs in MC, and provides charge-flip weights as a function of p_{T} and η. The weights are the probability for an electron to have "flipped charge", and summing all weights gives the total number of charge-flipped electrons. The package also provides a correction for the p_{T} and m_{ll} measurement to account for the energy-loss due to the γ radiation. Whenever the electron contribution is estimated with the Charge-Flip method briefly presented above, this is stated specifically.

Before proceeding it is convenient to add a note about the plotting scheme used throughout the whole thesis. In all distributions, such as Figure 6.1 showing the p_{T} of the leading lepton for tight (signal) di-muon events in the SS channel, the default MC selection is the full set of SM MC samples as detailed in Appendix B.3 which include processes described in Section 4.3, unless stated otherwise. These are the W+jets, Z/γ^*+jets, $t\bar{t}$, WW, WZ, ZZ (di-boson), and single top. Which QCD MC sample is used, or whether it is omitted is explicitly stated. For the di-boson background the Herwig sample is the default, and if the Sherpa samples are used instead, because of the somewhat better handling of additional jets, this is specifically indicated. In some cases I refer to MC EW samples. I then mean the full set of SM MC samples mentioned above, but omitting QCD.

All samples are scaled to the correct integrated luminosity (4.7 fb^{-1}, see Appendix B.4 for exact scaling values), and include all trigger, smearing and reconstruction weights, as described in Section 3.5. The errors in all plots with MC include cross section and luminosity uncertain-

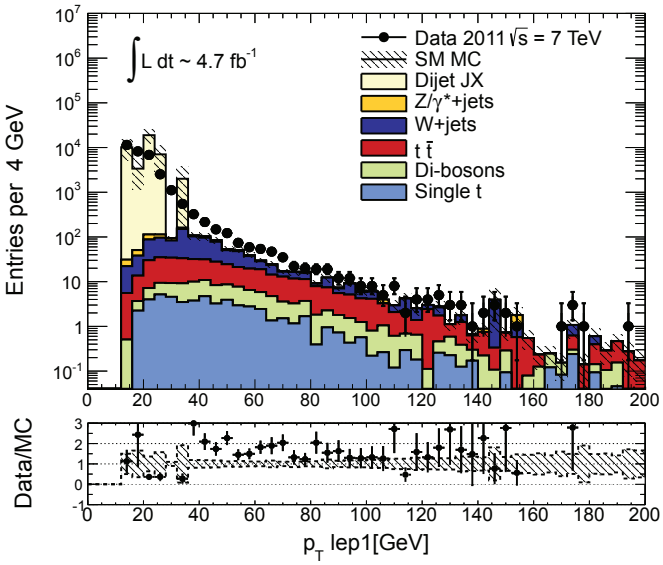

Figure 6.1: The p_{T} of the leading lepton in SS $\mu\mu$ events. The Pythia JX sample is used to model QCD, and all contributing electroweak MC SM samples are included. In the ratio plot some bins apparently do not have any data-points as they are beyond the plotted range [-1,3].

ties, added in quadrature with the statistical uncertainty. The uncertainty on the luminosity is 3.9% [160, 161]. The cross section uncertainties follow the recommendations from the various Standard Model sub-groups and were already summarized in Section 5.3.1, specifically in Table 5.8.

Let us continue with Figure 6.1 to illustrate the challenges with QCD MC. The selected QCD sample is the general purpose Pythia J0-J5 [104], here named JX for short, which has a mixture of light and heavy jets, and is in principle a good sample to study fake leptons from jets. See Table 5.9 and the discussion in Section 5.3.1 that includes a description of the different QCD samples I use in this analysis. We see in Figure 6.1 that the full SM MC does not reproduce data, with a data to MC ratio in the bottom part of the plot which for the most of the p_{T} spectrum is far from 1. It is clearly caused by a QCD MC sample (cream-coloured histograms) that performs very poorly, with large fluctuations in the lower p_{T} bins, and lack of statistics in the higher p_{T} bins, leading to large errors (black hatched area). The root of the problem stems partly from challenges in simulating enough QCD MC. In order to achieve decent QCD statistics with fake leptons corresponding to 4.7 fb^{-1}, one would have to simulate billions of events, which is not practically possible with a limited amount of resources. Instead, smaller samples are used, that have to be scaled up to the correct integrated luminosity. This particular sample is scaled up by several thousands (see Table B.4 in Appendix), even though it in fact has a single lepton requirement which helps in reducing the cross section by a large amount. However, this is evidently not enough, as the large spikes witness.

If we instead use a QCD MC sample which already at generator level requires two leptons, namely the heavy flavour filtered PythiaB_2L (see Table 5.9), we arrive to a distribution as in Figure 6.2 (a). The muon agreement between data and MC is much better here, although not perfect, but there are enough QCD events to avoid spiky bins. The data to MC agreement suggests that most of the muon fakes are caused by heavy flavour decays, owing to the fact that the

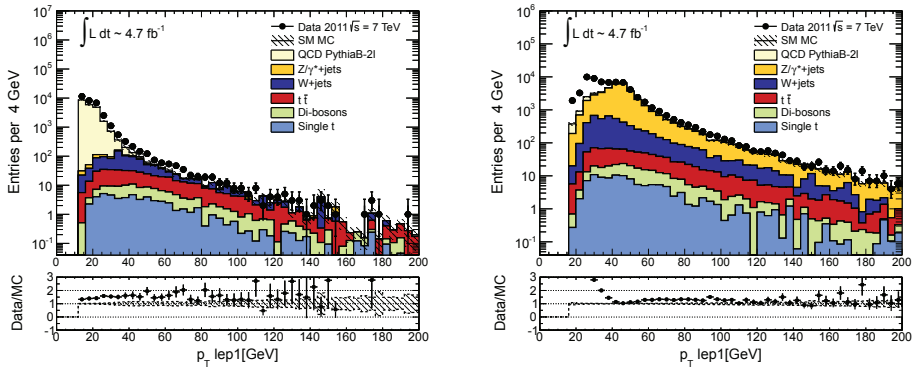

(a) Muons (b) Electrons

Figure 6.2: The p_{T} of the leading lepton in SS $\mu\mu$ (left) and ee (right), with the full SM MC, and PythiaB_2L used to represent QCD. Again some data-points are missing in the ratio-plot for the same reason as discussed in Figure 6.1.

heavy flavour QCD more or less reproduces data. The remaining discrepancies could either be explained by missing fake components, like for instance from light flavour jets (pion and kaon decays), or by an uncertainty on the QCD cross section, or a combination of both. However, we expect the latter to be the main reason, as the light flavour component is not expected to be large for muons. In the muon channel conversions are not a concern, as discussion in Section 4.3.4.

The situation is different for electrons, since we do in fact expect a significant contribution from light flavour, as well as from conversions. Figure 6.2 (b) shows how the full SM MC including the PythiaB_2L QCD sample clearly does not reproduce data. However, in lack of a good light flavour QCD sample (JX does an equally poor job for electrons as for muons), we also in this channel use the heavy flavour filtered sample, and assume that it at least models the heavy flavour contribution satisfactorily. Any under-representation of light jets is accounted for by adding systematic uncertainties (presented in Section 7.1.2.3). The conversion component is estimated separately, and is detailed in Section 6.4.2.

In order to largely surpass the challenges discussed above, data control regions are constructed, in order not to rely only on MC. The procedure to do so, and the definition of the control regions are discussed in several sections to follow. But first, I start by introducing the Matrix Method, which aims at estimating the fake lepton background in a more or less data-driven approach.

6.2 The Matrix Method (MM)

Two different lepton selection criteria, which are named *tight* and *loose*, are needed in the MM. The tight selection is the default signal lepton selection, while the loose corresponds to the baseline selection, both already presented with some detail in Section 3.5. According to Table 3.2, the baseline (loose) muon has the same definition as a signal (tight) muon, except from the isolation requirement [2] which is omitted. The baseline (loose) electron has the same definition as the signal (tight) electron (Table. 3.1), except that the `mediumPP` criterion is used instead of `tightPP` . While `tightPP` includes cuts on number of TRT-hits and on the E/p ratio, the `mediumPP` does not. These cuts are particularly used to filter against fake and conversion electrons. In addition the isolation requirement[3] is omitted also for loose electrons.

To derive the equations used in the MM, one must first define the fake rate f and real efficiency r

$$r = \frac{N_T^R}{N_L^R}, \qquad f = \frac{N_T^F}{N_L^F} \tag{6.1}$$

i.e. the probability that a real (^{R}) or fake (^{F}) inclusive loose lepton ($_L$) also passes the tight lepton ($_T$) criteria, where "inclusive loose" refers to a lepton which has passed the baseline lepton

[2] An isolated muon is defined as not being surrounded by tracks with more than $\sum p_{\mathrm{T}} > 1.8$ GeV within a cone of $\Delta R < 0.2$, see Section 3.5.2 for details.

[3] An isolated electron is defined as not being surrounded by tracks with more than $\sum p_{\mathrm{T}}/p_{\mathrm{T}} > 0.1$ within a cone of $\Delta R < 0.2$, see Section 3.5.1 for details.

$$\begin{bmatrix} N_{TT} \\ N_{Tl} \\ N_{lT} \\ N_{ll} \end{bmatrix} = \begin{bmatrix} r_1 r_2 & r_1 f_2 & f_1 r_2 & f_1 f_2 \\ r_1(1-r_2) & r_1(1-f_2) & f_1(1-r_2) & f_1(1-f_2) \\ (1-r_1)r_2 & (1-r_1)f_2 & (1-f_1)r_2 & (1-f_1)f_2 \\ (1-r_1)(1-r_2) & (1-r_1)(1-f_2) & (1-f_1)(1-r_2) & (1-f_1)(1-f_2) \end{bmatrix} \begin{bmatrix} N_{LL}^{RR} \\ N_{LL}^{RF} \\ N_{LL}^{FR} \\ N_{LL}^{FF} \end{bmatrix}$$

Table 6.1: The matrix expressing the various two-lepton tight or loose combinations as functions of real efficiencies and fake rates, and the numbers of real or fake leptons. Subscripts T, L and l mean tight, inclusive loose and exclusive loose (non-right) respectively, r and f are the real efficiencies and fake rates, and finally superscripts R and F denote real or fake leptons. The labelling (1,2) of the real and fake rates refer to the p_{T} ordering of the leptons, and their individual real efficiency and fake rate.

requirements as defined in Sections 3.5.1 and 3.5.2 for electrons and muons respectively. Here N^R and N^F are by definition real or fake respectively. In the actual data-driven determination of these efficiencies, we make use of samples with as high purity as possible, to ensuring that the data-sample contains mostly real leptons in the real control region, and fake leptons in the fake control region.

The number of inclusive loose leptons N_L is the sum of the tight N_T and exclusive loose (or equivalently non-tight) N_l leptons.

$$N_L = N_l + N_T \tag{6.2}$$

From (6.1) follows that when a sample consists of both real and fake leptons, then

$$N_T = N_T^R + N_T^F = r \cdot N_L^R + f \cdot N_L^F \,, \tag{6.3}$$

and in a similar fashion and using (6.2) we find

$$N_l = N_L - N_T = N_L^R + N_L^F - (N_T^R + N_T^F) = N_L^R \cdot (1-r) + N_L^F \cdot (1-f). \tag{6.4}$$

In the presence of two leptons equations (6.3) and (6.4) expand to a 4×4 matrix as shown in Table 6.1. The left hand terms are the observed number of loose and tight combinations of di-lepton events in a particular signal region. Here N_{TT} is the number of events with two tight leptons, N_{ll} is the number of events with two loose leptons that both fail the tight criteria (non-tight), and N_{lT} and N_{Tl} are the number of events with exactly one tight and one non-tight lepton. The subscripts "1" and "2" indicate that the leptons are p_{T} ordered such that the fake rate and real efficiency accompanies each lepton independently. The right-most column represents the number of estimated *inclusive loose* real-real pairs N_{LL}^{RR}, real-fake pairs N_{LL}^{RF}, fake-real pairs N_{LL}^{FR} and fake-fake pairs N_{LL}^{FF}.

Once the fake and real efficiencies are measured, which is shown in this chapter, and the number of observed loose or tight di-lepton events are determined, the matrix in Table 6.1 is inverted, yielding the estimated number of real and fake lepton pairs, $N_{LL}^{RR}, N_{LL}^{RF}, N_{LL}^{FR}$ and N_{LL}^{FF}. However, this gives us an estimate of the number of *inclusive* loose real and fake di-leptons. To find the composition in a *tight* sample corresponding to the signal selection, one must multiply

by the respective real efficiencies and fake rates

$$\begin{aligned} N_{TT}^{RR} &= r_1 r_2 \cdot N_{LL}^{RR} \\ N_{TT}^{RF} &= r_1 f_2 \cdot N_{LL}^{RF} \\ N_{TT}^{FR} &= f_1 r_2 \cdot N_{LL}^{FR} \\ N_{TT}^{FF} &= f_1 f_2 \cdot N_{LL}^{FF} \end{aligned} \quad . \tag{6.5}$$

In this implementation of MM we are interested in events with either one or two fake leptons, and such event types are both defined as fake events. Thus the total amount of fake events in a particular signal region is defined as

$$N_{\text{fake}}^{\text{tot}} = N_{TT}^{RF} + N_{TT}^{FR} + N_{TT}^{FF} \, . \tag{6.6}$$

Purity in control regions, truth subtraction, and truth classification

In the MM, data-driven control regions can be used to extract real efficiencies and fake rates. A useful quantity which characterizes the control regions is their level of *purity*. This is defined as the relative amount of fake (real) leptons in a fake (real) control region. As purity is mainly a concern in the fake control regions (and not real), the following discussion defines purity as how small the "contamination" of real leptons is, in a fake control region. The goal is to achieve a control region that measures a *true* fake rate. Real leptons naturally have a larger $N_L \rightarrow N_T$ probability which falsely increases the fake rate. This is why all control regions undergo real-lepton subtraction. As there is no way of determining the actual true amount of fake and real leptons in data, MC is used to subtract the real contamination stemming from the well known and controlled SM processes (not including QCD):

$$\text{purity}_{fake} = \frac{N_{\text{data}}^{\text{leptons}} - N_{\text{MC real}}^{\text{leptons}}}{N_{\text{data}}^{\text{leptons}}} \quad = \quad \frac{N_{\text{fake}}^{\text{leptons}}}{N_{\text{data}}^{\text{leptons}}} \, . \tag{6.7}$$

Purity therefore depends on the expected number of real leptons from Monte Carlo $N_{\text{MC real}}^{\text{leptons}}$, normalized to the same luminosity as data $N_{\text{data}}^{\text{leptons}}$. Naturally both numbers $N_{\text{data}}^{\text{leptons}}$ and $N_{\text{MC real}}^{\text{leptons}}$ are extracted from the same control region. All important processes contributing to the real di-lepton baseline selection are considered (Z, W, t, and τ).

An example of the effect of the real lepton subtraction is shown in Figure 6.3 for muons in SS events. The p_{T} distribution is shown for data and MC including PythiaB_2L MC representing QCD. As we see the real lepton subtraction seems to be more or less successful, as the QCD MC now dominates explaining data rather well (except in the higher p_{T} bins, which is discussed later). Note that the other MC processes left over ($t\bar{t}$, W+jets, single top, Z+jets) contribute since in these events at least one lepton turns out to be fake. For more distributions including corresponding plots for electrons, see Appendix C.2.

MC truth is needed both for identifying real leptons for control-region subtraction, but also

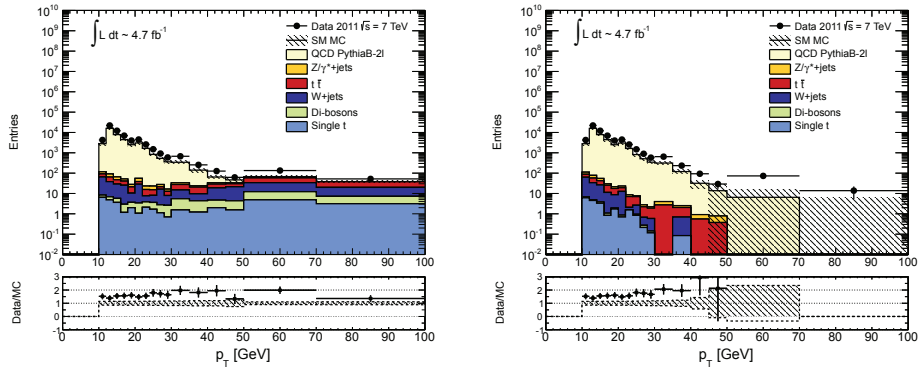

(a) No subtraction

(b) With subtraction

Figure 6.3: p_{T} of muon in SS events before (left) and after (right) statistical subtraction of real muons.

in general to validate the Matrix Method. The truth-information is supplied by the Athena-based `MCTruthClassifier` tool. In this tool, the truth-matching is performed by geometrically correlating reconstructed objects (after passing through the detector simulation) to generator level truth objects. A reconstructed object is said to match if it is closer than 0.1 in the η, ϕ distance ΔR. In the MC samples used in this analysis, the truth-matching is already in place, via the `MCTruthClassifier` tool. In addition to matching reconstructed particle to truth particle, `MCTruthClassifier` can climb up the decay chain to find the origin of each particle. This is possible, since each vertex has a so-called "bar-code" which uniquely identifies it. Using a reconstructed electron as an example, if the `MCTruthClassifier` finds a match to a generator level electron, it travels up each vertex of that generated electron until it finds its origin, its "mother". This could for instance be a Z or W boson, or maybe a γ. Since the electron might radiate without changing its identity, the tool continues until it finds the first vertex for this particle. In this way, for each matched object one could potentially[4] have stored the whole history of its journey from primary generated particle to the final particle as seen by the detector.

In some cases when the particle structures are very complicated, for instance in jets, the reconstructed lepton can fail the matching procedure and be categorized as "not-matched". In Table 6.2 I list the `MCTruthClassifier` ids corresponding to each lepton origin. In the context of the fake estimation leptons are divided into origin-categories "Heavy", "Light", and "Conversion", where "heavy" and "light" refer to the mother jet flavour in QCD events. As the table shows, the "not-matched" electron (el) events are included in the light category, while for muons they are not.

A dedicated study was performed on electrons by Eirik Gramstad and documented in his PhD thesis [159]. He showed that most of the electrons which fell into the "not-matched" category, in fact originated from light flavoured quarks. Therefore I treat the "not-matched" electrons as electrons from light jets in the context of this fake estimation analysis. This category

[4] In practice, sample size restricts the information kept, and in for instance jet events, not all particles have physical mothers due to methods in simulation.

id	origin	category
5	conversions	**Conversions**
25	c-meson	**Heavy**
26	b-meson	
27	$c\bar{c}$-meson	
28	J/ψ	
29	$b\bar{b}$-meson	
32	c-baryon	
33	b-baryon	
0	not-matched (el)	**Light**
23	light-meson	
24	s-meson	
30	light-baryon	
31	s-baryon	
34	π	
35	K	

id	origin	category
9	τ	**Real**
10	top	
12	W boson	
13	Z boson	

Table 6.2: The origin of the leptons as classified in the `MCTruthClassifier` tool of the four categories “Real”, “Heavy”, “Light” and “Conversions” used in this analysis.

makes up about 7% of all SS fake baseline electrons, see Figure 6.4 (a) for the proportion of each category of fakes.

The contribution is smaller for muons, as the dominant production of fake muons is from heavy flavour. In Figure 6.4 (b) I show that less than 1% of all fake muons are “not-matched”.

This finalizes the theoretical introduction to the Matrix Method and related definitions. In the next sections the experimental procedure is described. I first determine the real efficiency r

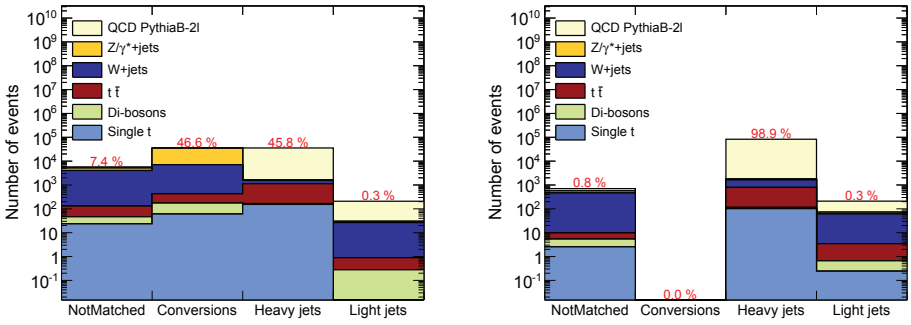

(a) Electrons (b) Muons

Figure 6.4: Composition of fake leptons in SS events, using the default MC sample with PythiaB_2L for the QCD component.

and fake rate f, two necessary ingredients before implementing the MM, with the final goal to estimate the fake lepton background in possible di-lepton SUSY signals.

6.3 Real efficiency

Real efficiencies are measured in data from a control region dominated by (real) leptons from Z bosons. The region is defined by events with opposite sign same-flavour (OSSF) di-leptons which have an invariant mass in the Z-mass peak range $\in (86, 96)$ GeV. A total of ~1.4 million di-muon and ~1.0 million di-electron data events are used to determine the real efficiency

$$r = \frac{N_T^R}{N_L^R}$$

where N_T is the number of tight leptons and N_L is the number of inclusive loose leptons. The superscript (^{R}), where R stands for Real, indicates that the region predominantly consists of real leptons, and hence the ratio yields the real efficiency r.

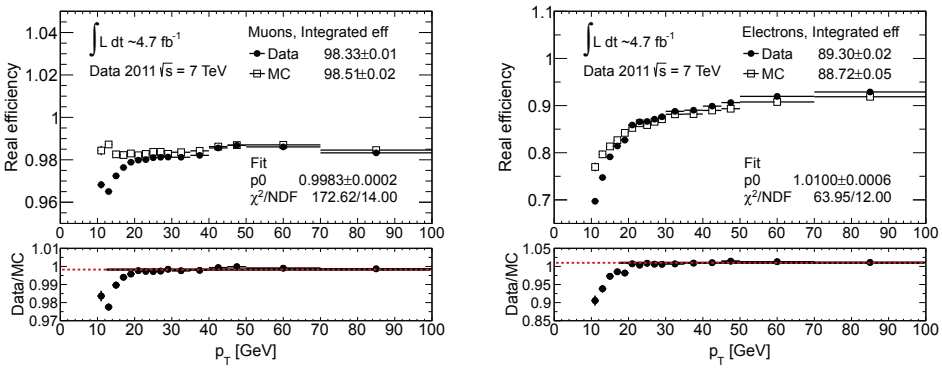

(a) Muon real efficiency versus p_{T}

(b) Electron real efficiency versus p_{T}

Figure 6.5: The real efficiency for muons (left) and electrons (right) as function of p_{T}. Errors are purely statistical. Data is plotted with closed squares and MC is overlaid with open squares.

Figures 6.5 and 6.6 show the real efficiency as a function of p_{T} and η respectively for muons (left) and electrons (right). The data measurement is shown in closed markers, and for comparison the $Z \to \ell^+\ell^-$ MC efficiency is plotted with open marker. Only MC Z/γ^*+jets samples are used. The data/MC ratio is fitted with a straight line from the trigger threshold of 12 GeV in the muon, and 17 GeV in the electron channel. In both channels the agreement is excellent, with a

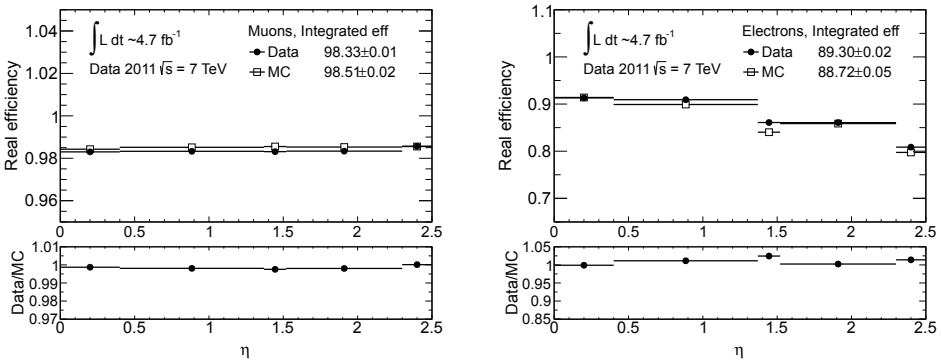

(a) Muon real efficiency versus $|\eta|$

(b) Electron real efficiency versus $|\eta|$

Figure 6.6: The real efficiency for muons (left) and electrons (right) as function of $|\eta|$. Errors are purely statistical. Data is plotted with closed squares and MC is overlaid with open squares.

ratio ~ 1.0. The small discrepancy in the low p_{T} region for both lepton flavours can be due to sensitivity to the trigger thresholds. First of all, MC weights are as we remember (Section 5.3) only calculated for leptons above the threshold, secondly the weights themselves might not be perfectly adjusted in this sensitive region. The effect is very small, though, with a maximum deviation of 3% between data and MC. When it comes to the electron η distribution in Figure 6.6, muons show no dependency, while in the electron channel the geometrical features are reflected. This is as expected for electron efficiencies, and reproduces the trend ATLAS sees for electron reconstruction efficiencies (see Section B.2). We also see that MC slightly mis-models the electron behaviour in the transition region between the barrel and endcap at around η =1.4, and close to the end of the acceptance region at η =2.47. Overall though, the agreement between data and MC in both channels can also here be said to be very good.

The p_{T} dependence is used directly in the final computation of the fake lepton background, while the η dependency in fact turns out to be insignificant with respect to the final fake lepton estimation, which is shown in Section 7.1.5.

Instead of simply counting the total amount of loose and tight leptons, and defining the real efficiency as the ratio of these numbers, one could have used a tag and probe method, since one in Z-events expects two correlated leptons. The tag would then be a tight lepton, and the probe the other lepton, which is loose or tight. Only events with at least one tight lepton would then be considered. However, using inclusive samples, give similar results as tag and probe, while allowing an even larger data sample, and is therefore the preferred method in this analysis.

6.4 Fake rates

As mentioned in the introduction of this chapter, fake leptons are not a uniform group of objects, but stem from a variety of sources. The fake rate, which together with the real efficiency is of

major importance to the Matrix Method, might be different for each individual source. In this implementation of the MM, we separate QCD fakes from conversions, and in addition account for differences between heavy and light flavour QCD fakes.

The fake rate from hadronic sources has deserved special attention in this thesis, since this is the contribution which is hardest to determine reliably. A number of QCD data control regions are therefore constructed in order to perform cross checks between regions, and to limit bias to the region definitions. Two main types of QCD control regions are studied, general mixture regions targeting both light and heavy flavour jets, and a special heavy flavour control region, all described in Section 6.4.1.

A separate data control region is constructed in order to measure the conversion fake rate for electrons. Section 6.4.2 describes the procedure used, as well as its validation with MC.

A final fake rate is then computed using MC-based weights to represent the relative amount of each component, including the various systematic uncertainties, including those related to the absolute size of the light and the heavy jet fake contributions. This is all described in Section 7.1.

This implementation of the MM [134] relies on MC fake rates for the hadronic component. In Chapter 7.2 I perform the fake estimates with fake rates and real efficiencies all from data, i.e. a fully data-driven estimation. First though, let us determine the separate fake rates, starting by the hadronic component.

6.4.1 Fake leptons from hadrons

Hadronic fakes refer to all (fake) leptons that stem from QCD processes. Data control regions are used as a basis for measuring the hadronic fake rate. To achieve a fake dominated region, cuts are required on variables that separate events with real and fake leptons such as missing (relative) transverse energy $E_{\mathrm{T}}^{\mathrm{miss,rel}}$, transverse mass m_{T}, and the azimuthal angle between the directions of a lepton and missing energy $E_{\mathrm{T}}^{\mathrm{miss}}$: $\Delta\phi(lep, E_{\mathrm{T}}^{\mathrm{miss}})$. Any remaining real leptons are statistically subtracted with the help of MC, as described in Section 6.2. In fact MC is also used to remove conversion electrons from the QCD control regions, as the conversion fake rate is measured in a dedicated conversion control region which is described in Section 6.4.2. The MC removal of conversions include the charge-flip electrons. In the following "MC lepton subtraction" refers to removal of both real leptons and conversion electrons, unless otherwise stated.

Three main types of QCD data control regions labelled as A, B, and C, and variations within these have been examined. These are single-lepton control regions (CR-A), di-lepton same-sign same-flavour (SSSF) control regions (CR-B) and a single lepton b-tagged control region (CR-C). Control-regions A and B are constructed to pick up a mixture of QCD-leptons (heavy and light), while CR-C targets heavy-flavour fakes. The cuts used to select the three control region types are listed in Table 6.3 and are on $E_{\mathrm{T}}^{\mathrm{miss,rel}}$ or m_{T} ($E_{\mathrm{T}}^{\mathrm{miss,rel}}$ < [20,30,60] GeV, m_{T} < [40,60] GeV). Naturally one specific region only uses a single m_{T} and/or $E_{\mathrm{T}}^{\mathrm{miss,rel}}$ cut. Each enumerated item defines one class of control regions, with a certain collection of cuts. For CR-C the bullet list presents the requirements used for defining the tag-and-probe regions, which includes a b-jet requirement, a so-called "far-jet" requirement, and a muon tagged inside the b-jet (mutag). The enumerated list classifies the various combinations tested, including additional

CR-A	- single lepton, mixed QCD
	I. $m_{\mathrm{T}} < (40, 60)$ GeV
	II. $m_{\mathrm{T}} < (40, 60)$ GeV, $\Delta\phi(l, E_{\mathrm{T}}^{\mathrm{miss,rel}}) < 1.0$
	III. $E_{\mathrm{T}}^{\mathrm{miss,rel}} < (20, 30)$ GeV, $\Delta\phi(l, E_{\mathrm{T}}^{\mathrm{miss,rel}}) < 1.0$
CR-B	- SS di-lepton, mixed QCD
	I. $E_{\mathrm{T}}^{\mathrm{miss,rel}} < (20, 30, 60)$ GeV (Z-veto for electrons)
CR-C	- single lepton, heavy flavour QCD
	• Exactly one b-jet (btag)
	• Lepton's distance from any jet is $\Delta R > 1.0$ (far jet)
	• Additional muon within $\Delta R < 0.4$ of a b-jet (mutag)
	I. Btag, $m_{\mathrm{T}} < (40, 50)$ GeV, w muontag, w/wo far jet
	II. Btag, $E_{\mathrm{T}}^{\mathrm{miss,rel}} < (10, 20, 30, 40)$ GeV, $m_{\mathrm{T}} < (40, 50)$ GeV, w/wo far jet

Table 6.3: Definition of main control regions CR-A, CR-B and CR-C.

cuts on m_{T} or $E_{\mathrm{T}}^{\mathrm{miss,rel}}$.

From the multitude of control regions, one region from each main region CR-A, CR-B, and CR-C is selected to act as a representative for this region. Finally a single region for each lepton flavour is chosen to represent the hadronic fake, and is used to perform comparisons with MC. The variations seen in the fake rate across regions are used to estimate the systematic uncertainties, and are discussed further in Section 7.1. The variations within regions are, as shown later, taken into account by an uncertainty on the $E_{\mathrm{T}}^{\mathrm{miss,rel}}$ dependency.

6.4.1.1 Single lepton CR-A

Figure 6.7 displays the variables used in the single lepton CR-A, namely $E_{\mathrm{T}}^{\mathrm{miss,rel}}$ (top left), m_{T} (top right), and $\Delta\phi(l, E_{\mathrm{T}}^{\mathrm{miss,rel}})$ (bottom), for baseline (inclusive loose) single muon events. The MC includes all contributing SM processes except QCD. Any missing components, visible by a gap in the distributions between the SM MC and data, is interpreted as fake leptons, predominately from QCD. MC QCD is not used, since as explained in the introduction, the available samples do not (always) reproduce the expected contribution. As expected for a single lepton control region, the W+jets background is the largest and displays clear features which differ from the other SM backgrounds, with $E_{\mathrm{T}}^{\mathrm{miss,rel}}$ clearly peaking at around 50 GeV, m_{T} peaking between 50-80 GeV then falling abruptly, and $\Delta\phi(lep, E_{\mathrm{T}}^{\mathrm{miss}})$ tending towards π, i.e. with the muon and the $E_{\mathrm{T}}^{\mathrm{miss}}$ back to back. All three variables can be used to remove the bulk of W+jet events where the single lepton is expected to be real. Of these three variables, m_{T} is the best discriminator since the separation between QCD and electroweak SM works better than $E_{\mathrm{T}}^{\mathrm{miss,rel}}$, while not significantly affecting the QCD events (assumed to be represented by white space between data and SM MC). Applying a strict cut on $\Delta\phi(lep, E_{\mathrm{T}}^{\mathrm{miss}})$ on the other hand, removes a fair amount of QCD as well, since the QCD distribution is rather flat.

A closer look reveals that an m_{T} cut of 40 GeV removes about 95% of the W events, and preserves more than 85% of the QCD events, while a cut on $\Delta\phi(lep, E_{\mathrm{T}}^{\mathrm{miss}}) < 1.0$ removes about 50% W and keeps 70% QCD events.

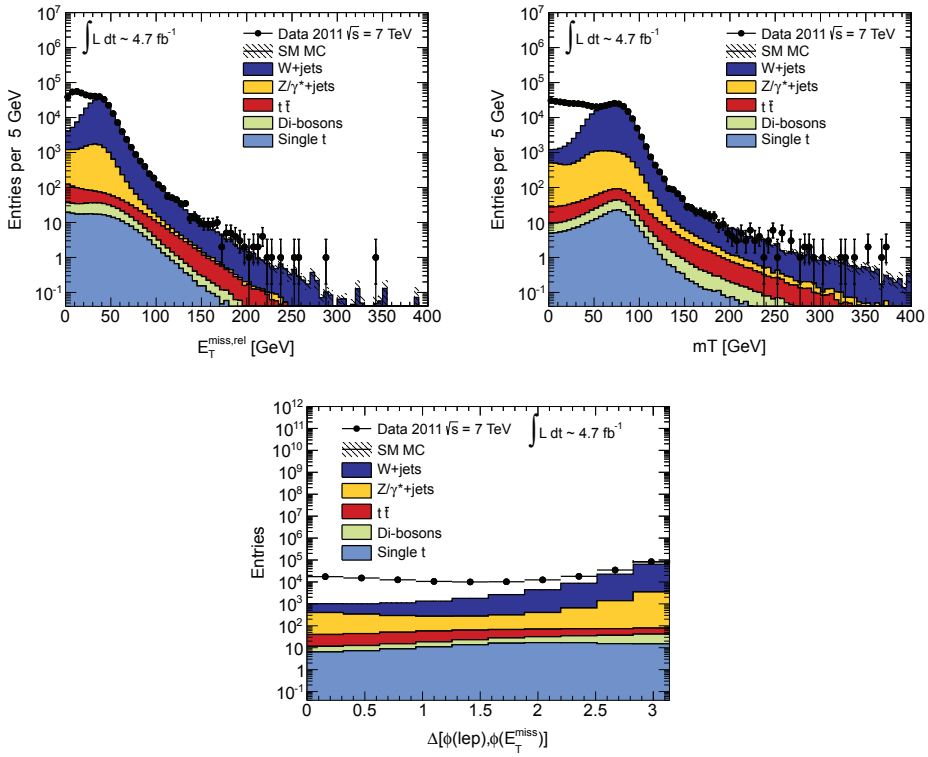

Figure 6.7: Kinematic distributions for single muon events. $E_{\mathrm{T}}^{\mathrm{miss,rel}}$ top left, m_{T} top right, and $\Delta\phi(lep, E_{\mathrm{T}}^{\mathrm{miss}})$ bottom.The muon have passed the baseline selection (inclusive loose). SM MC is represented by coloured histograms, and data with black dots. QCD MC is not included.

Table 6.4 summarizes the statistics and purity for the inclusive loose muons (and electrons) in the regions considered. This is a representative subset of a larger set of control regions listed in Appendix C.1. Muon fake purities range from 73% to 91%. The region with lowest purity (73.8%) corresponds to $E_{\mathrm{T}}^{\mathrm{miss,rel}} < 30$ GeV. We also observe that when increasing the cut on $E_{\mathrm{T}}^{\mathrm{miss,rel}}$, the purity decreases, which is explained by the fact that more real leptons contribute, predominantly from W decays (compare R01 and R07 or R05 and R11). The highest purity is obtained for $m_{\mathrm{T}} < 40$ GeV, see regions R13 and R17. There is only a slight improvement to the muon purity in R13 when including a $\Delta\phi$ cut (R17), which is likely to be explained by the m_{T} cut which already very efficiently handles the W-background.

The corresponding kinematic distributions for events with single electrons are shown in Figure 6.8. The trends are very similar to the muon distributions, but for electrons the Z events are shifted towards lower values of $E_{\mathrm{T}}^{\mathrm{miss,rel}}$, m_{T}, and $\Delta\phi$ compared to muon events. The relative amount of the two is on the other hand the same, around 8%. Ideally one would not expect Z events with a single real lepton. However, the reconstruction efficiency is not 100% (see Appendix B.2), which means that one of the leptons from the Z decay can fail reconstruction,

	Muons		Electrons		
Reg	N_L	purity [%]	N_L	purity [%]	Description
R01	198705	85.1	327689	91.0	$E_{\mathrm{T}}^{\mathrm{miss,rel}} < 20$
R05	134652	87.1	221865	91.3	$E_{\mathrm{T}}^{\mathrm{miss,rel}} < 20, \Delta\phi_{E_{\mathrm{T}}^{\mathrm{miss}},l} < 1.0$
R07	284056	73.8	444755	85.7	$E_{\mathrm{T}}^{\mathrm{miss,rel}} < 30$
R11	185150	78.3	296339	87.5	$E_{\mathrm{T}}^{\mathrm{miss,rel}} < 30, \Delta\phi_{E_{\mathrm{T}}^{\mathrm{miss}},l} < 1.0$
R13	214125	90.6	327769	93.7	$M_T < 40$
R17	153963	91.3	248474	93.6	$M_T < 40, \Delta\phi_{E_{\mathrm{T}}^{\mathrm{miss}},l} < 1.0$
R19	298381	74.5	451228	87.5	$M_T < 60$
R23	196625	78.8	310513	89.0	$M_T < 60, \Delta\phi_{E_{\mathrm{T}}^{\mathrm{miss}},l} < 1.0$

Table 6.4: The muon (left) and electron (right) statistics and QCD purity in single lepton control regions (CR-A). In the muon channel two candidate optimal regions are highlighted in grey (R13 and R17), while in the electron channel only R13 is highlighted.

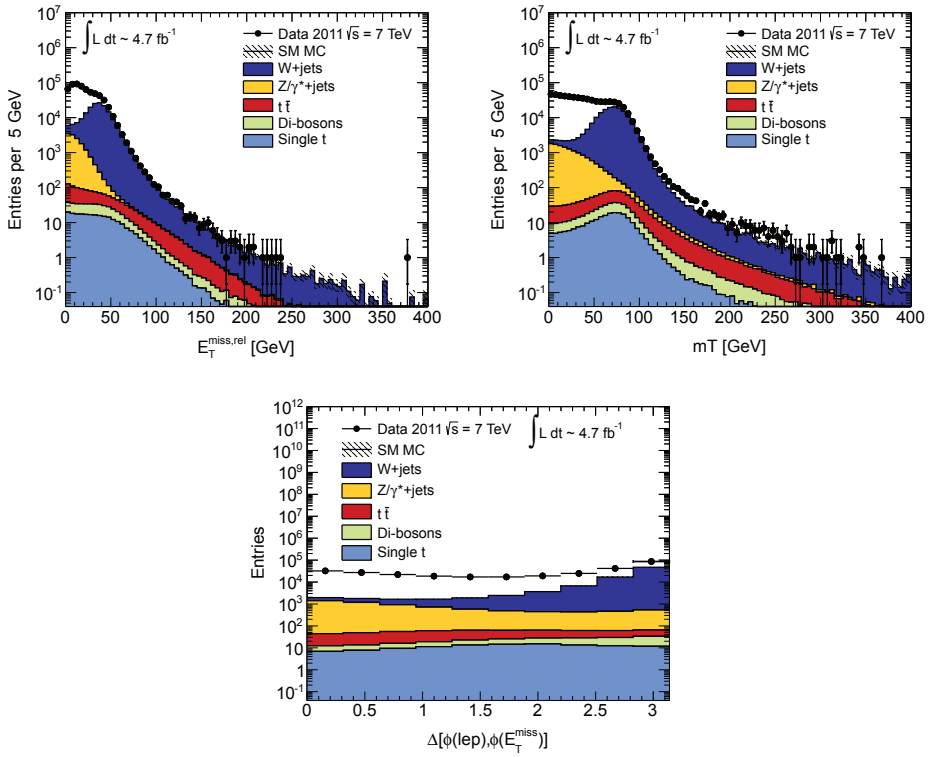

Figure 6.8: Kinematic distributions for single electron events. $E_{\mathrm{T}}^{\mathrm{miss,rel}}$ top left, m_{T} top right, and $\Delta\phi(lep, E_{\mathrm{T}}^{\mathrm{miss}})$ bottom. The electrons have passed the baseline selection (inclusive loose).

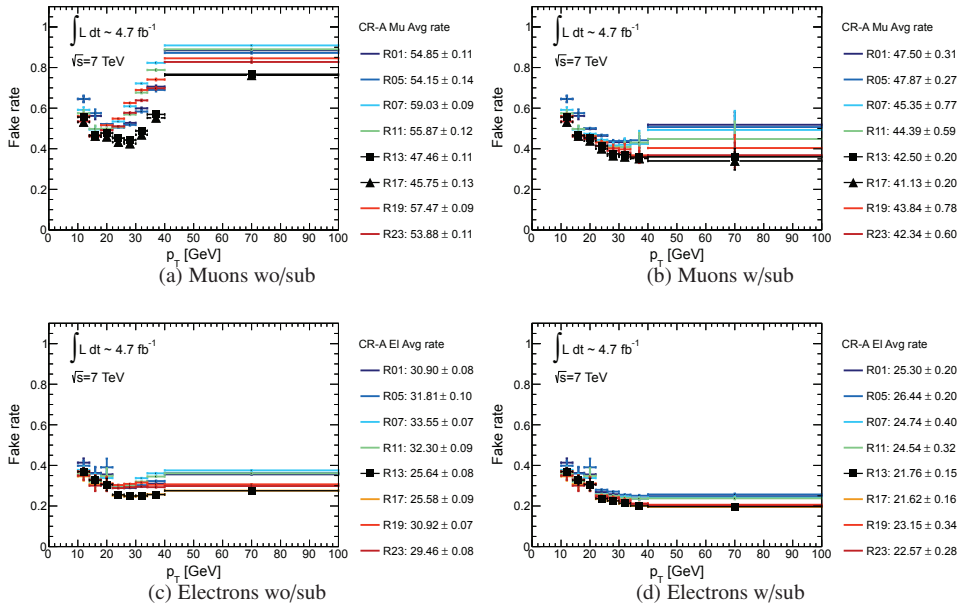

(a) Muons wo/sub (b) Muons w/sub

(c) Electrons wo/sub (d) Electrons w/sub

Figure 6.9: Fake rates versus p_{T} and their integrated rates (avg) for single lepton data control regions CR-A, before (left) and after (right) MC lepton subtraction. Muons in the top row and electrons in the bottom row.

thus end up as single-lepton in the point of view of the analysis.

Comparing statistics and purity for muons (two left columns) and electrons (the next two columns) in Table 6.4 we see that the electron purity is a bit higher for each control region, with values in the range 85% to 93% (compared to 73-91% for muons). This means that the relative amount of fake leptons is somewhat larger for electrons.

Also for electrons, the m_{T}< 40 regions score highest on purity, and as for muons the $\Delta\phi$ cut does not make a large impact.

According to purity alone the ultimate region is for muons R17 ($m_{\mathrm{T}} < 40$ GeV, $\Delta\phi < 1.0$), with a purity of 91.3%, and for electrons R13 ($m_{\mathrm{T}} < 40$ GeV), with a purity of 93.7% (highlighted with grey in Table 6.4). However, it is interesting to see how the fake rates behave for the different control regions, before choosing a baseline region, especially considering the small impact on the purity when adding the $\Delta\phi < 1.0$ cut. Figure 6.9 shows the fake rate before (left) and after (right) MC real lepton and electron conversion subtraction for muons (top) and electrons (bottom) as function of p_{T}. First of all it is reassuring to see that the fake rates are reduced after subtraction of real (and conversion) leptons. This is consistent with the expected behaviour of the real leptons, of driving the fake rate up. That the reduction is largest in the tail of the distribution coincides with larger relative amount of real leptons in the tail (see study in Appendix C.4 for further details).

The favoured control regions R17 for muons and R13 for electrons are marked with black squares in the figures legend. For muons control region R13 ($m_{\mathrm{T}} < 40$) is also highlighted,

marked with black triangles. It is evident from Figure 6.9 (b) that although the purity was slightly better for R17, the two regions are practically identical after MC subtraction. As there is no noticeable difference between R17 and R13, the latter, which only includes an m_{T} cut, is chosen as a baseline region for both muons and electrons.

6.4.1.2 Di-lepton same-sign CR-B

The di-lepton SS regions (CR-B) have, unlike the single lepton control regions, no electroweak SM contribution at all (at truth-level). They contain fake leptons from OS events with charge mis-reconstruction, from di- and multi-jet events, or from OS di-lepton events where one real lepton is not reconstructed, but instead a fake lepton from the jet is. Since EW SM suppression is less important the only cut studied is $E_{\mathrm{T}}^{\mathrm{miss,rel}}$.

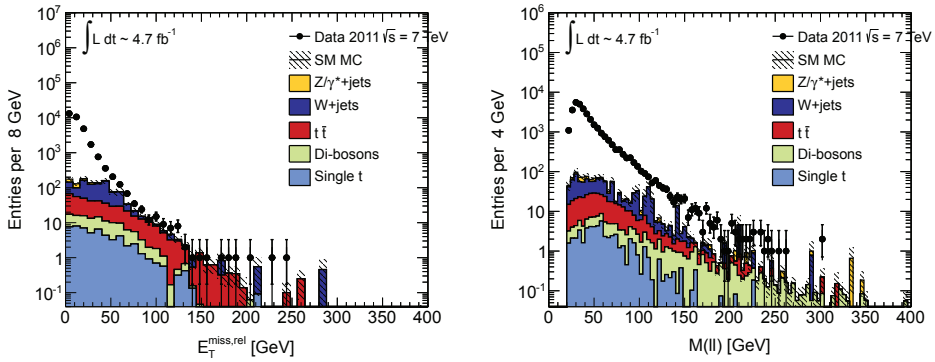

Figure 6.10: $E_{\mathrm{T}}^{\mathrm{miss,rel}}$ (left) and invariant mass (right),in SS same-flavour di-muon events. Both leptons have passed the baseline selection (inclusive loose). No QCD MC is included.

Figure 6.10 displays the $E_{\mathrm{T}}^{\mathrm{miss,rel}}$ (left) and invariant mass distribution (right) for di-muon SS events. As for the single lepton events, fake leptons (gap between SM MC and data) dominate at low $E_{\mathrm{T}}^{\mathrm{miss,rel}}$, and over a large range of m_{ll}.

The equivalent SS di-electron distributions in Figure 6.11 feature two distinct differences compared to the muons. The first is the expected contribution from charge-flip Z/γ^* events described in Section 4.3.4, and appearing as a Z-peak. The second is the larger contribution from W+jets, where one real lepton from the W is accompanied by a fake lepton of same charge. In the electron case the larger contribution of W's is due to a significant amount of conversion electrons (about 40% of all leptons in the W-sample).

To reduce the charge-flip background in the electron channel, (where the largest contribution is from Z), we apply a Z-veto. As this cut is not 100% efficient we remove the remaining conversion electrons statistically with the help of MC. Most electrons that have flipped charge in fact behave much like real electrons, and are often identified as such by `MCTruthClassifier`. See Figure 6.12 which shows the origin reported by `MCTruthClassifier` in SS events, with

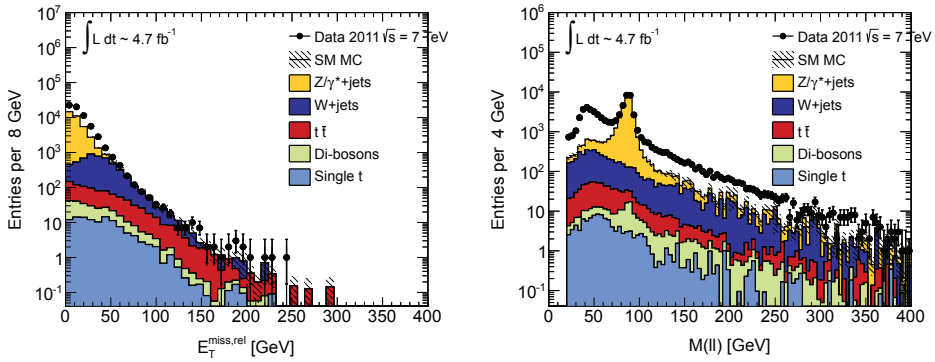

Figure 6.11: $E_{\mathrm{T}}^{\mathrm{miss,rel}}$ (left), and invariant mass (right) in SS same-flavour di-electron events. Both leptons have passed the baseline selection (inclusive loose). No QCD MC is included.

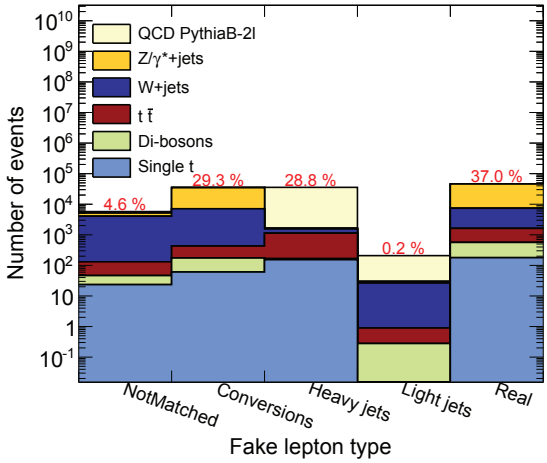

(a) Electrons SS

Figure 6.12: The composition of SS electrons from the full SM MC, with PythiaB_2L representing QCD.

a large amount of real electrons from the Z sample. We do naturally expect at least one real electron, and hence it is no surprise that the Z contributes. However, the proportion of real-real electron SS pairs (which ideally should be non-existent) is found to be roughly 20%. Real lepton subtraction is therefore particularly important in these control regions. This is as usual also applied to the muon channel, where the main purpose is to remove any real leptons from Z+jets, W+jets, top or diboson production (although this background is small as discussed earlier).

From Table 6.5, which presents the statistics and purity for the pre-selected SS di-lepton control regions, we see that the purities are overall very high for muons (>98%), and about

75% for electrons. The Z-veto applied only for the electron channel is denoted in the table by ($\not{Z}$). Control region R02 yields the highest purity for muons (99.3%), and R07 for electrons (76.7%). Both regions are highlighted in grey. The CR-B fake rates as a function of p_{T} shown

	Muons		Electrons		
Reg	N_L	purity [%]	N_L	purity [%]	Description
R02	60980	99.3	-	-	$E_{\mathrm{T}}^{\mathrm{miss,rel}} < 20$
R03	69194	99.0	-	-	$E_{\mathrm{T}}^{\mathrm{miss,rel}} < 30$
R04	73462	98.4	-	-	$E_{\mathrm{T}}^{\mathrm{miss,rel}} < 60$
R06	-	-	62360	76.2	$E_{\mathrm{T}}^{\mathrm{miss,rel}} < 20, \not{Z}$
R07	-	-	77404	76.7	$E_{\mathrm{T}}^{\mathrm{miss,rel}} < 30, \not{Z}$
R08	-	-	89558	74.7	$E_{\mathrm{T}}^{\mathrm{miss,rel}} < 60, \not{Z}$

Table 6.5: The muon (left) and electron (right) statistics and purity in SS di-lepton control regions (CR-B). The regions with highest purity are highlighted in grey, which is R02 for muons and R07 for electrons. Only the electron regions include a Z-veto ($\not{Z}$).

in Figure 6.13, follow the same plotting scheme as the corresponding Figure 6.9 for CR-A. In both the electron and muon channels, the three selected fake rates are similar. The reduction of the fake rate after the MC real (and conversion) subtraction is clearly more prominent for electrons than muons, when comparing left and right plots (before and after subtraction). This is as expected, as the purity is already very high in the muon channel. It is only the high p_{T} tail of the muon fake rate which is affected by the real lepton removal. Control regions R02 for muons and R07 for electrons, which are the regions with the highest purity, are marked with black squares. In the muon channel, control region R02 which requires $E_{\mathrm{T}}^{\mathrm{miss,rel}} < 20$ GeV, has a slightly higher fake rate at low p_{T}, but is the lowest at high p_{T}. For the electrons the selected region R07 is centred between the two other distributions. However, as already stated, all rates are very close for all regions shown.

6.4.1.3 Heavy flavour CR-C

In control region C (CR-C), the goal is to measure the fake rate of leptons from heavy flavour jets in $b\bar{b}$ events. Events with exactly one b-tagged jet identified are selected (first bullet point of the CR-C list in Table 6.3). At truth-level one expects two b-jets, but for this control region, the second b-jet is assumed misidentified either as a regular jet and/or as a lepton. To further improve the b-tag one requires that a muon is found in the centre of the b-tagged jet ($\Delta R(jet, \mu) < 0.4$), which means that we only use events where the tagged b-quark decays semi-leptonically. In CR-C we can also enhance the overlap-removal requirement, using $\Delta R > 1.0$ between the probed lepton and any jet, compared to the usual 0.4. This is to increase the probability that the probe lepton stems from the other b-jet, and hence is more back-to-back (than 0.4) to the other b-jet.

As already explained, real leptons from W-boson production (and to a less extent from single top and $t\bar{t}$ production) are a potential contamination in single lepton control regions, and hence

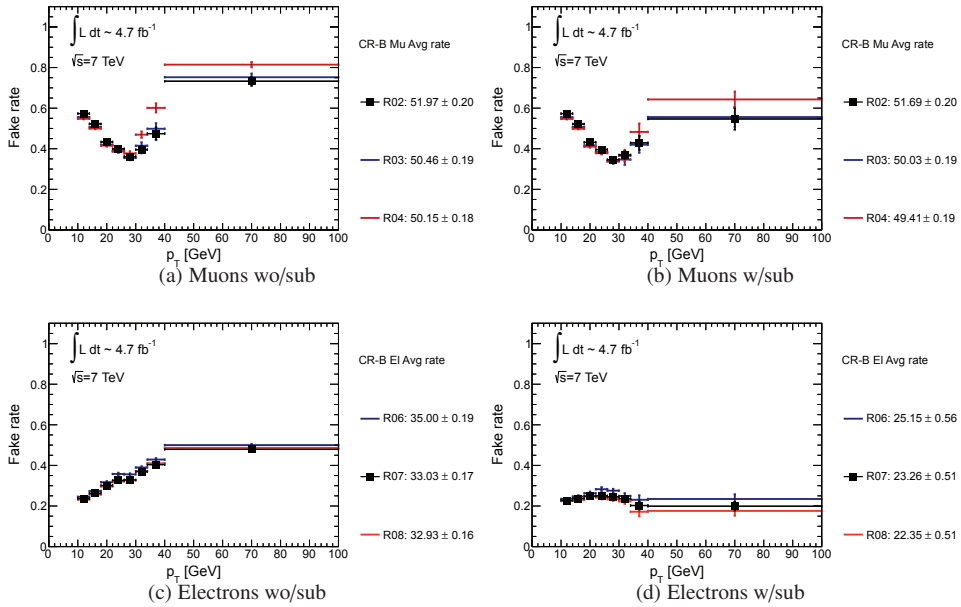

Figure 6.13: Fake rates for SS di-lepton control regions CR-B, before (left) and after (right) MC real lepton and conversion electron subtraction. Muons in the top row and electrons in the bottom row.

this CR-C region[5]. The cuts on $E_{\mathrm{T}}^{\mathrm{miss,rel}}$ and/or m_{T} are used to strongly reduce this background.

Figure 6.14 shows the $E_{\mathrm{T}}^{\mathrm{miss,rel}}$ (left) and m_{T} (right) distribution for muons (top) and electrons (bottom) in events satisfying CR-C above. Again we see that hadron fakes populate mainly the low $E_{\mathrm{T}}^{\mathrm{miss,rel}}$ and m_{T} regions, evident from the gap between data and the SM MC. It is interesting to note that the W+jets background (dark blue) has a much flatter trend at low $E_{\mathrm{T}}^{\mathrm{miss,rel}}$ than in CR-A, which implies that the region is not as sensitive to this cut, as is CR-A in Figures 6.8 and 6.7. The m_{T} distribution however (right plot of Figure 6.14) displays the usual Jacobian peak, and a cut $m_{\mathrm{T}} < 40$ GeV would therefore be fairly effective in order to remove events with (potential) real leptons from the large W+jets background. In the muon channel there is a certain contribution from Z events. The real lepton MC subtraction takes care of this, as well as the other SM processes contributing with real leptons (in both channels).

Studying the statistics and purity of variations on CR-C in Table 6.6, we see that all tested combinations give a high purity (>90%), and that muon purities are slightly lower than electron purities. The first 14 regions are omitted, which are the regions that require a jet separation of $\Delta R > 1.0$. It was found that this cut in fact does not have a large impact, neither on purity, nor on the fake rate. They are however documented in Appendix C.1.

As statistics is reduced when cuts are added and tightened, whilst the purity does not in-

[5]It is defined as a single lepton region, even though we operate with two leptons, one tag muon and one probe lepton (electron or muon). This is because the tag lepton (which is part of the b-jet), fails the standard overlap-removal with the jet, and therefore is categorized as a single lepton region.

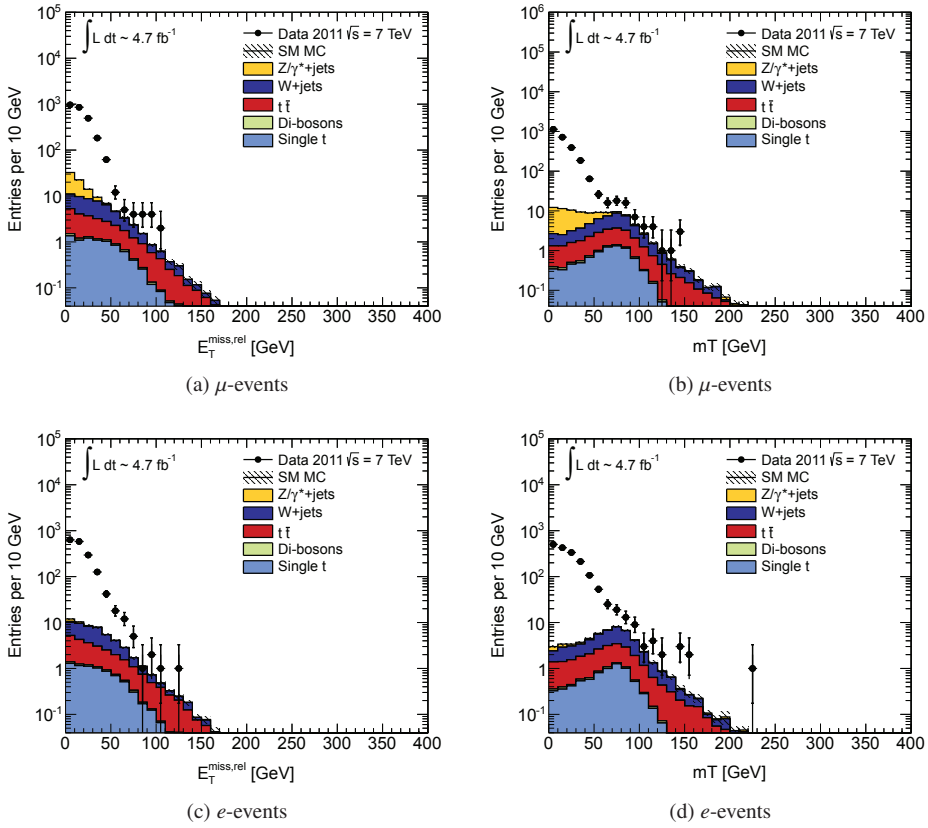

(a) μ-events (b) μ-events

(c) e-events (d) e-events

Figure 6.14: The $E_{\mathrm{T}}^{\mathrm{miss,rel}}$ (left) and m_{T} after $E_{\mathrm{T}}^{\mathrm{miss,rel}}<$ 40 cut (right) for baseline single muon (top) and electron (bottom) events, where a single mu-tagged b-jet is identified (CR-C).

crease, the optimal region in CR-C is R19, where only a cut on $m_{\mathrm{T}}<$ 40 GeV is used, in addition to the muon-tag. This region is highlighted in grey in Table 6.6.

Since CR-C uses a b-tagger to define its region, and since the b-tagger has a very low probability to mistake light jets for b-jets (order of 1%-2% [162]), we expect a very pure heavy flavour control region. However, there is a possible remaining source of *real* leptons from $t\bar{t}$ or single top events, with leptonically decaying W bosons, even after the m_{T} cut. This contribution is removed with MC subtraction, as well as any conversion electrons, as in CR-A and CR-B.

Figure 6.15 displays the fake rates versus p_{T} for regions R15-R24, listed in Table 6.6. Again distributions before subtraction are to the left, and after to the right, with muons in the top row, and electrons in the bottom. The favoured control region R19 is plotted with black squares. The subtraction of real leptons (and for electrons, conversions) has little overall effect, as expected since the regions are already very pure. In both electron and muon channels a separation between groups of control regions is seen, with a couple of regions (dark blue R15 and yellow

R20) with fake rates above the rest. Both these are regions that apply a tight $E_{\mathrm{T}}^{\mathrm{miss,rel}}$ cut of 10 GeV. Regions with a looser $E_{\mathrm{T}}^{\mathrm{miss,rel}}$ cut give as the figure shows lower fake rates. This suggests a dependence on $E_{\mathrm{T}}^{\mathrm{miss,rel}}$.

	Muons		Electrons		
Reg	N_L	purity [%]	N_L	purity [%]	Description
R15	273	91.1	225	97.4	$E_{\mathrm{T}}^{\mathrm{miss,rel}}$<10, m_{T}<40
R16	515	92.9	428	97.8	$E_{\mathrm{T}}^{\mathrm{miss,rel}}$<20, m_{T}<40
R17	627	93.5	530	97.9	$E_{\mathrm{T}}^{\mathrm{miss,rel}}$<30, m_{T}<40
R18	661	93.6	576	97.9	$E_{\mathrm{T}}^{\mathrm{miss,rel}}$<40, m_{T}<40
R19	684	93.7	605	97.86	m_{T}<40
R20	280	90.7	241	97.2	$E_{\mathrm{T}}^{\mathrm{miss,rel}}$<10, m_{T}<50
R21	540	92.4	473	97.6	$E_{\mathrm{T}}^{\mathrm{miss,rel}}$<20, m_{T}<50
R22	661	92.8	591	97.6	$E_{\mathrm{T}}^{\mathrm{miss,rel}}$<30, m_{T}<50
R23	697	92.8	641	97.6	$E_{\mathrm{T}}^{\mathrm{miss,rel}}$<40, m_{T}<50
R24	723	92.8	673	97.4	m_{T}<50

Table 6.6: The muon (left) and electron (right) statistics and purity in tag-and-probe CR-C.

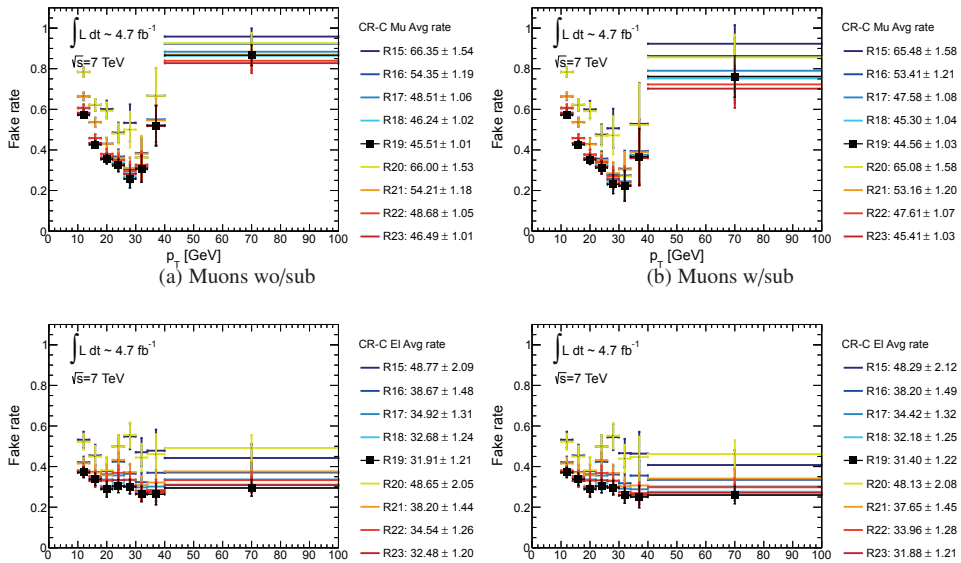

(a) Muons wo/sub (b) Muons w/sub

(c) Electrons wo/sub (d) Electrons w/sub

Figure 6.15: Fake rates for heavy flavour tag and probe control regions CR-C, before (left) and after (right) MC lepton subtraction. Muons in the top row and electrons in the bottom row.

6.4.1.4 Comparison of QCD control regions

In the previous section three optimal baseline regions were selected from a larger pool of sub-regions. In this section I take a closer look at the three control regions, investigating the fake rates as a function of p_{T}, η and $E_{\mathrm{T}}^{\mathrm{miss,rel}}$. I also compare the control regions in order to extract a systematic uncertainty from the differences seen between them. I from here on refer to the three regions just as CR-A, CR-B and CR-C, which is meant to mean CR-A R13, CR-B R02, and CR-C R19 for muons, and CR-A R13, CR-B R07, and CR-C R19 for electrons. These are summarized in Table 6.7, together with the integrated fake rate, total amount of inclusive loose leptons in the region, and the description of the cuts used.

		Data		
	Region	f [%]	N_L	Description
Muons	CR-A R13	42.38 ± 0.15	191664	$M_T < 40$
	CR-B R02	51.67 ± 0.20	60583	$E_{\mathrm{T}}^{\mathrm{miss}} < 20$
	CR-C R19	33.25 ± 1.73	822	m_{T}<40, mutag
Electrons	CR-A R13	21.70 ± 0.10	305984	$M_T < 40$
	CR-B R07	23.26 ± 0.32	59349	$E_{\mathrm{T}}^{\mathrm{miss}} < 30, \not{Z}$
	CR-C R19	28.04 ± 1.72	711	m_{T}<40, mutag

Table 6.7: The optimal control regions in the three main control regions CR-A (single lepton), CR-B (di-lepton SS), and CR-C (single lepton b-tagged). Both lepton flavours use the same optimal regions, except for CR-B where the electron channel includes the Z-veto.

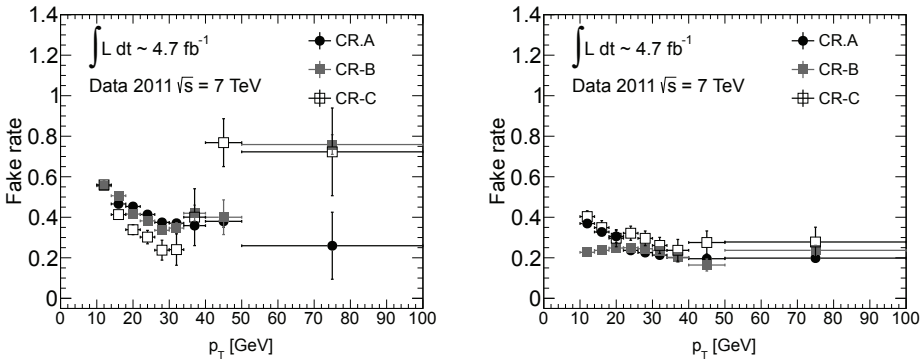

Figure 6.16: Comparison of the data fake rates versus p_{T} from the selected control regions from CR-A, B and C for muons (left) and electrons (right).

Figure 6.16 shows each of the fake rates versus p_{T} for muons (left) and electrons (right). In the muon channel CR-A and CR-B seem to agree well, while CR-C systematically lies below these except for the very first bin. Above 40 GeV we start running out of statistics, especially

for CR-C, leading to fluctuations. In CR-B and CR-C we again see the increase at high p_{T}, which as discussed earlier is a region sensitive to the real lepton subtraction.

For the electron channel a disagreement between the di-lepton CR-B, and the two single-lepton regions CR-A or CR-C is seen at low p_{T}. This is clearly trigger-related, as we remember from Section 5.3 that MC trigger weights are only supplied for leptons above the trigger threshold. Therefore the real and conversion MC lepton subtraction has no effect in the sub-threshold p_{T} range, hence resulting in the higher rates for CR-A since the real lepton contamination drives the rate up. At higher values of p_{T} (above the trigger plateau) all rates agree well.

To compare fake rates versus η or $E_{\mathrm{T}}^{\mathrm{miss,rel}}$ (integrated over p_{T}) I must first take into account the trigger thresholds. Otherwise the comparison would not be fair, as there are very few single muons(electrons) below 20(25) GeV, and the p_{T} dependency would thus result in a skewed fake rate distribution when plotted against η or $E_{\mathrm{T}}^{\mathrm{miss,rel}}$. Therefore the single lepton in CR-A and CR-C, and the hardest muon(electron) in CR-B, must satisfy $p_{\mathrm{T}} > 20(25)$ GeV.

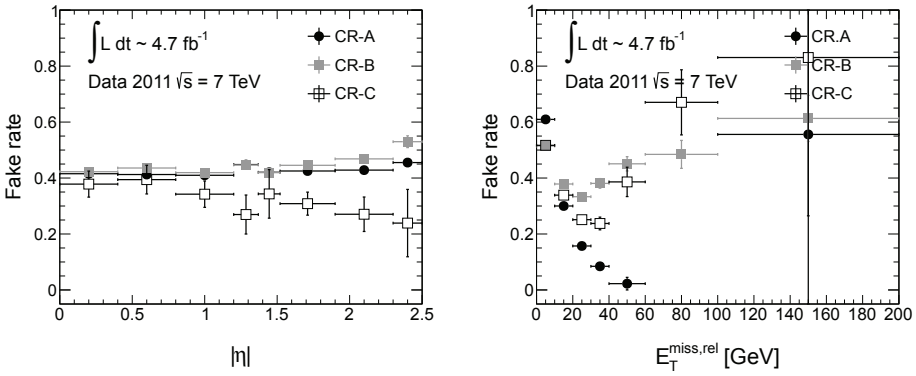

Figure 6.17: Muon fake rates in data versus $|\eta|$ (left) and $E_{\mathrm{T}}^{\mathrm{miss,rel}}$ (right). The optimal control regions listed in Table 6.7 are used, except for obtaining the $E_{\mathrm{T}}^{\mathrm{miss,rel}}$ distribution where the $E_{\mathrm{T}}^{\mathrm{miss,rel}}$ cut naturally is omitted.

The muon fake rates for the three control regions are plotted as a function of $|\eta|$ and $E_{\mathrm{T}}^{\mathrm{miss,rel}}$ in Figure 6.17. We see that there is no significant η dependency for CR-A and CR-B. There seems to be a slightly more pronounced dependency in CR-C. There is however an $E_{\mathrm{T}}^{\mathrm{miss,rel}}$ dependency worth noting since $E_{\mathrm{T}}^{\mathrm{miss,rel}}$ is an important SUSY variable. Each control region exhibits a rather different trend; whilst CR-A drops monotonously (except for the upward fluctuation in the last bin), CR-B and CR-C drop until around 30 GeV, but then rise again. It is reasonable to assume that part of the explanation of the rise at high $E_{\mathrm{T}}^{\mathrm{miss,rel}}$ is caused by the fact that the real lepton subtraction is not 100% efficient. Figure 6.18 (left) shows how the muon fake rate versus $E_{\mathrm{T}}^{\mathrm{miss,rel}}$ after real lepton subtraction (and conversions) behaves in CR-B type regions (SS di-lepton, but omitting the $E_{\mathrm{T}}^{\mathrm{miss,rel}}$ cut), as the cross section on the electroweak background is scaled up and down. We see that the high $E_{\mathrm{T}}^{\mathrm{miss,rel}}$ tail (starting at around 40 GeV) is in fact affected by the scaling, with the rate increasing when MC is down-scaled, and decreasing when

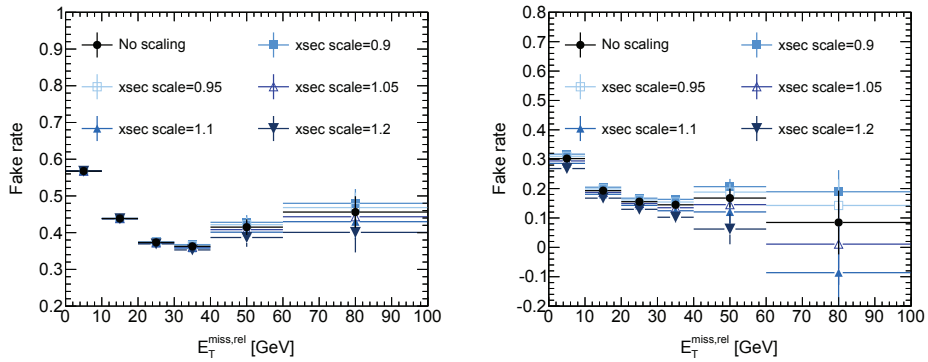

(a) Muons CR-B

(b) Electrons CR-B

Figure 6.18: Fake rate versus $E_{\mathrm{T}}^{\mathrm{miss,rel}}$ in SS di-lepton events (CR-B), in data after statistical subtraction of real leptons. In the electron channel conversion electrons are also removed. The fake rates are shown after scaling the MC electroweak cross section up or down according to the legend. "No scaling" denotes nominal MC cross sections. The rates are extracted in "control regions" where the quotes indicate that no $E_{\mathrm{T}}^{\mathrm{miss,rel}}$ cuts are applied.

up-scaled, supporting the statement above about the sensitivity to real lepton subtraction at high $E_{\mathrm{T}}^{\mathrm{miss,rel}}$ (although errors are large). For distributions in CR-A and CR-C, see Figure C.8 in Appendix C.7.

For electrons (Figure 6.19), the dependency on η is more prominent than for muons, decreasing with increasing η, and with a clear dip at the crack region around $\eta = 1.37 - 1.52$. However, as already mentioned the η dependency is not important for the final fake estimation, this will be shown in Section 7.1.5. When it comes to the $E_{\mathrm{T}}^{\mathrm{miss,rel}}$ dependency it is again CR-A which drops quickest, but all regions mainly follow the same trend, with a dependency that drops rather fast until around 40 GeV, and after this either flattens (CR-A, CR-B) or rises somewhat (CR-C). Figure 6.18 (right) shows how the $E_{\mathrm{T}}^{\mathrm{miss,rel}}$ dependency in CR-B is affected by the real lepton subtraction, when the SM MC (non-QCD) is scaled up or down. The conclusion is much like in the muon channel, when more real leptons are subtracted the rate flattens at high $E_{\mathrm{T}}^{\mathrm{miss,rel}}$.

Of the dependencies observed, the $E_{\mathrm{T}}^{\mathrm{miss,rel}}$ is potentially the most important, as it is directly related to the signal region cuts, and hence to the signal kinematics. I therefore look closer at this dependency using MC in Section 6.4.1.5 below, where the final control regions above are compared to MC.

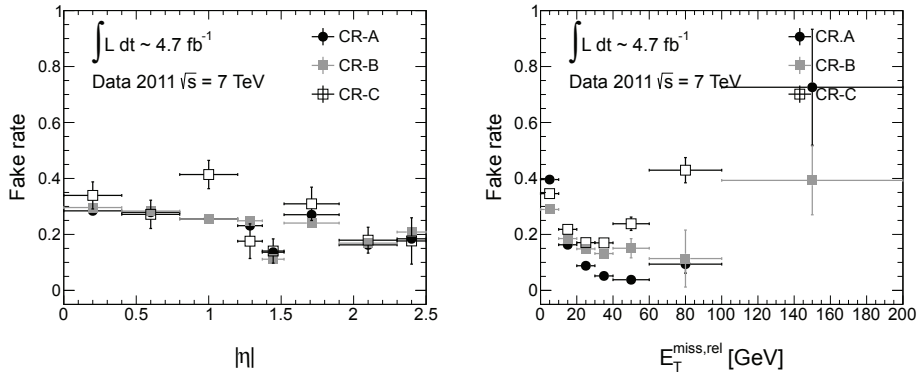

Figure 6.19: Electron fake rates in data versus $|\eta|$ (left) and $E_{\mathrm{T}}^{\mathrm{miss,rel}}$ (right). The optimal control regions listed in Table 6.7 are used, except for obtaining the $E_{\mathrm{T}}^{\mathrm{miss,rel}}$ distribution where the $E_{\mathrm{T}}^{\mathrm{miss,rel}}$ cut naturally is omitted.

6.4.1.5 Data and MC comparison for QCD fakes

Up until now we have only considered the control regions with respect to data (apart from statistical subtraction of real and conversion leptons using MC). We can apply the same cuts in MC, and compare the two. The full SM MC is used, and for QCD either PythiaB_1L or PythiaB_2L, depending on the control region. Also for MC real MC leptons identified through the `MCTruthClassifierTool` are statistically subtracted. In the electron channel, conversion electrons are also removed. As the general effect of the MC subtraction is already discussed above, here I mainly concentrate on the comparison between data and MC.

		Data		MC		
	Region	f [%]	N_L	f [%]	N_L	Description
Muons	CR-A R13	42.38 ± 0.15	191664	33.67 ± 1.82	266113	$M_T < 40$
	CR-B R02	51.67 ± 0.20	60583	48.61 ± 2.21	40236	$E_{\mathrm{T}}^{\mathrm{miss}} < 20$
	CR-C R19	33.25 ± 1.73	822	31.97 ± 2.16	980	m_{T}<40, mutag
Electrons	CR-A R13	21.70 ± 0.10	305984	34.01 ± 1.69	89969	$M_T < 40$
	CR-B R07	23.26 ± 0.32	59349	28.89 ± 4.15	4776	$E_{\mathrm{T}}^{\mathrm{miss}} < 30, \not{Z}$
	CR-C R19	28.04 ± 1.72	711	27.91 ± 1.67	948	m_{T}<40, mutag

Table 6.8: Fake rate f and statistics N_L for data and MC in the selected control regions, after statistical subtraction of real and conversion MC leptons. Muons in the top and electrons in the bottom. Note that in the single lepton control regions (CR-A, CR-C), the fake rates are integrated from the trigger threshold and beyond, specifically not including the sub-threshold points (where there is no MC due to trigger), in order to give a fair comparison between data and MC.

Table 6.8 displays the integrated statistics N_L and fake rate f after MC subtraction for both

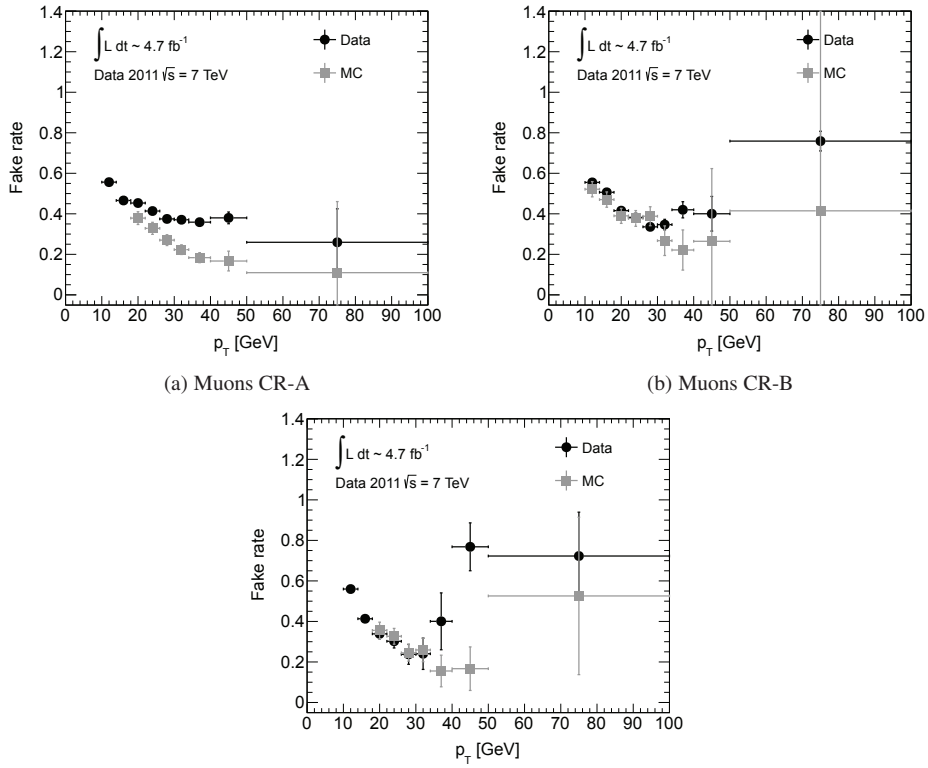

(a) Muons CR-A

(b) Muons CR-B

(c) Muons CR-C

Figure 6.20: The muon fake rates in CR-A (left top), CR-B (right top) and CR-C (bottom) after statistical removal of real MC leptons. Data is plotted in black circles, and MC in grey squares, as the legend indicates. For definition of the control regions, see Table 6.3. Only statistical uncertainty, and systematic uncertainty on the cross section and luminosity are included in the errors. Note that for single muon control regions (CR-A and CR-C) the MC fake rate is not plotted below 20 GeV due to missing trigger weights.

muons (top) and electrons (bottom) for the selected regions (from Table 6.7).

For muons (top row) we see a good agreement between fake rates in data and MC for CR-B and CR-C. In CR-A however, we observe a discrepancy, with (integrated) fake rates of 42.38±0.15 in data versus 33.67±1.82 in MC. Both the overall agreement in CR-B and C, and the discrepancy in CR-A can be recognized in the p_{T} dependent fake rates in data and MC in Figure 6.20. The disagreement between data and MC in CR-A is seen to increase with p_{T}. The effect seen in CR-A can be due to several reasons. (i) The actual MC modelling of the fake composition and its kinematical behaviour just might not reproduce fakes in data. (ii) We could have forgotten some processes contributing with real lepton, thus removing too few, and hence not properly dealing with the high p_{T} tail. It is worth noting though that for muons, the MC overestimates the event yield, (see Table 6.8 top row). This might suggest that there are no important missing real SM components. (iii) All processes are indeed included, but the

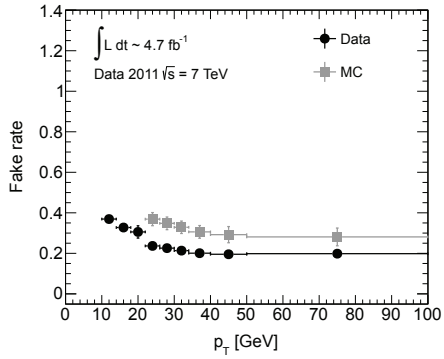

(a) Electrons CR-A

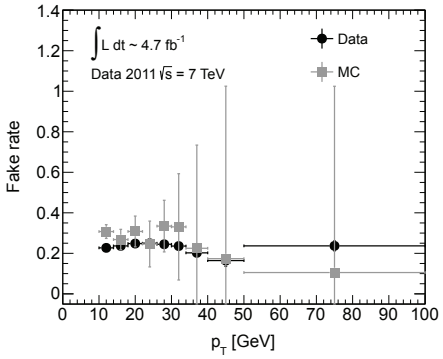

(b) Electrons CR-B

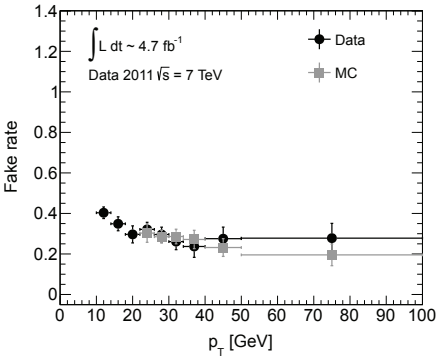

(c) Electrons CR-C

Figure 6.21: The electron fake rates in CR-A (left top), CR-B (right top) and CR-C (bottom) after statistical removal of real and conversion MC leptons. Data is plotted in black circles, and MC in grey squares, as the legend indicates. For definition of the control regions, see Table 6.3. Only statistical uncertainty, and systematic uncertainty on the cross section and luminosity are included in the errors. Note that for single lepton control regions (CR-A and CR-C) no MC points are available below 25 GeV for electrons (there are no trigger weights below this value).

data distribution is sensitive to the statistical MC lepton subtraction. I already showed that the subtraction procedure could be part of the explanation for the apparent $E_{\mathrm{T}}^{\mathrm{miss,rel}}$ dependence. Similar studies were also performed for p_{T}, and although the effect is less prominent, we see an effect in the high p_{T} (low $E_{\mathrm{T}}^{\mathrm{miss,rel}}$ control region) tail (Appendix C.5 Figure C.6). Also, the tails are sensitive just due to the fact that we are subtracting close to all leptons, as the tail is highly dominated by real leptons. Note that the points given above are relevant for all control regions where we see data and MC disagreement, and not only in CR-A, naturally. In particular these points relate to the $E_{\mathrm{T}}^{\mathrm{miss,rel}}$ dependency in all control regions, and differences we will see in data and MC, which is discussed further in Section 6.4.1.5.

Thus at least part, but probably not all of the behaviour can be explained by a slightly inefficient real lepton subtraction. Note that the uncertainty on the truth identification itself is

negligible for real leptons, and does therefore not contribute to this possible inefficiency.

For the electrons we see from Table 6.8 (bottom part) as for muons, a good agreement in CR-B, and CR-C between data and MC, while CR-A differs. The picture is however reversed, with MC yielding the highest (integrated) fake rate of 34.01±1.69 compared to 21.70±0.10 in data for CR-A. Figure 6.21 reveals that the difference is constant in p_{T}. In CR-B and CR-C the good agreement is confirmed over the whole p_{T} range, although errors on MC are large, especially in CR-B due to the statistical subtraction of real and conversion electrons. The same possible explanation for the differences between data and MC in CR-A, given in the muon discussion above, could also apply for electrons. However, for electrons we do expect a fair additional contribution of conversions and of light fakes, and the latter is underrepresented in the selected QCD PythiaB_1L sample, therefore can certainly affect the data to MC agreement. The variation with cross section (scaling of MC) however, hardly affects the data to MC agreement, as studies in Appendix C.5 Figure C.6 shows. This means that the most probable explanation is that the MC QCD is simply not appropriately reproducing the fakes as seen in data.

While CR-B is a di-lepton control region, and thus is similar to the di-lepton final-state we wish to estimate, and CR-C is a heavy flavour dominated region well suited to learn about the heavy flavour fake rate, the single lepton CR-A seems neither to give a good data and MC agreement, nor does it reflect our final-state. We therefore in the following, mainly use CR-B and CR-C for further studies.

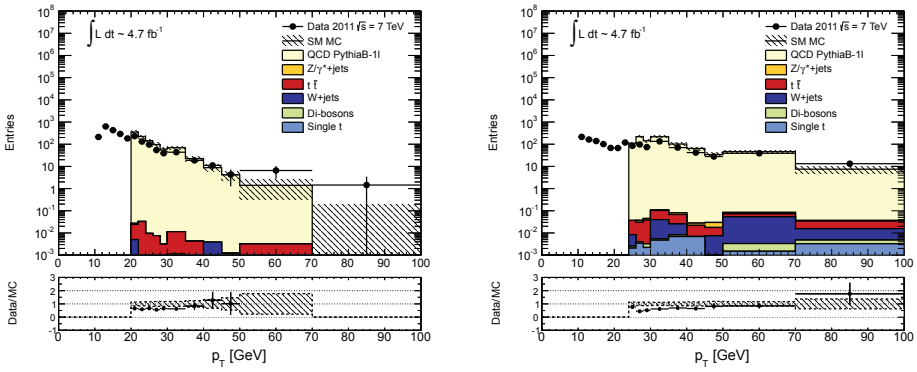

(a) Muons CR-C

(b) Electrons CR-C

Figure 6.22: Transverse momentum of muons (left) and electrons (right) in CR-C for data and MC after statistical subtraction of real and conversion electrons. There is no MC below the trigger threshold at 20 and 25 GeV for muons and electrons respectively.

To compare data and MC quantitatively, we must have in mind the under-representation of the light component in the QCD samples available to us. Therefore, a fair comparison can only be achieved for the heavy flavour component. Figure 6.22 shows the data and MC comparison of the number of inclusive loose events versus p_{T} for the muon and electron channel respectively in the heavy flavour control region CR-C. Real (and conversion) leptons have been statistically removed. As we see, MC explains data fairly well, and there does not seem to be any missing QCD component. In fact, MC overestimates data somewhat in both channels (except in the high

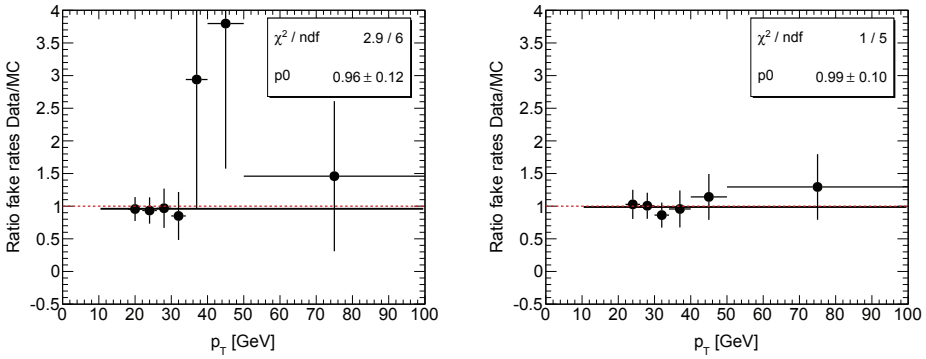

(a) Muons (b) Electrons

Figure 6.23: The ratio of fake rates obtained in data and MC, fitted with horizontal lines for both the muon channel (left), and the electron channel (right). CR-C is used. The 1:1 agreement is indicated with a dashed red line.

Scale factor Data/MC	
Muons	Electrons
0.96±0.12	0.99± 0.10

Table 6.9: The scale factor between data and MC, as extracted in CR-C for muons and electrons.

p_T bins), but this is expected to be due an overall scale uncertainty. We therefore go ahead and compare the data and MC fake rates in Figure 6.23, which gives the ratio between the data and MC fake rates in the mentioned control region. In both channels data and MC agree very well within errors, as it must be noted that statistics is very low beyond ~35 GeV for muons. The straight line fit gives a ratio of 0.96±0.12 for muons and 0.99±0.10 for electrons, summarized in Table 6.9.

Fake rate dependency on $E_T^{miss,rel}$ in MC

In order to study the fake rate's $E_T^{miss,rel}$ dependency, di-lepton SS events are used, which is a CR-B type. However, no cuts on the $E_T^{miss,rel}$ are included, which means that the region is inclusive, and not a control region in the strict sense. For electrons though, a Z-veto has as usual been added to suppress the large contribution of real (and conversion) electrons from (charge-flipped) Z decays. The goal of this study is two-fold: First to demonstrate how the dependencies behave for different processes ($t\bar{t}$, $b\bar{b}$ and so on), and for heavy versus light flavour fakes; Second to compare data and MC in order to determine to what extent we can trust MC. For the latter it is favourable to use a control region that is expected to include both heavy and light flavour fakes, which is why CR-B is chosen, and not CR-C which by construction is heavy flavour dominated. This is mostly important in the electron channel, naturally, where a substantial light component is expected.

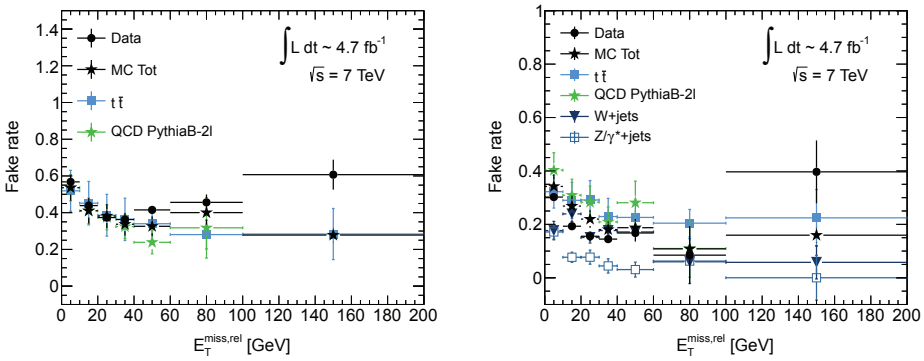

(a) Muons CR-B

(b) Electrons CR-B

Figure 6.24: Fake rate versus $E_{\mathrm{T}}^{\mathrm{miss,rel}}$ in MC for muons (left) and electrons (right) selecting only leptons from QCD. The rates are extracted in a CR-B type region, which means use of events with SS same-flavour di-leptons, but otherwise using no cuts.

Figure 6.24 shows the muon (left) and electron (right) fake rate versus $E_{\mathrm{T}}^{\mathrm{miss,rel}}$ for data and all MC, and separately for the most important processes. These are for muons the $t\bar{t}$ and PythiaB_2L QCD (which is dominated by $b\bar{b}$ events, with $< 0.1\%$ light flavour jets). The rest of the processes (single top, W+jets Z/γ^*+jets and the di-boson background) each contribute less than 1%. They are not plotted separately, but are still included in the total MC distribution. However, in the electron channel the W+jets and Z/γ^*+jets samples are plotted in addition, as they contribute with about 30% and 7% respectively. Real (and conversion) leptons have as usual been subtracted.

In the muon channel $t\bar{t}$ and QCD show similar behaviour, with fake rates that agree well over the whole $E_{\mathrm{T}}^{\mathrm{miss,rel}}$ scale. The distributions fall off with increasing $E_{\mathrm{T}}^{\mathrm{miss,rel}}$, but flattens off from about 40 GeV. Data and MC agree quite well at the low $E_{\mathrm{T}}^{\mathrm{miss,rel}}$, however from around $E_{\mathrm{T}}^{\mathrm{miss,rel}} \geq 40$ GeV we, as already discussed (Figure 6.18), see the characteristic increase in the muon data fake rate. This is as explained most probably due to some remaining real leptons driving the data rate up, and other possible effects listed earlier in this section.

The electron channel is shown in the right plot of Figure 6.24. Again we see that fake rates from $t\bar{t}$ and QCD (mainly $b\bar{b}$, $< 0.1\%$ light flavour jets) events agree. The W+jets and Z/γ^*+jets events yield lower fake rates (especially in the Z/γ^*-sample). These samples are simulated with light flavour quark jets (however, gluon jets are allowed to split into all flavours), and thus indicate that we should expect a lower fake rate for the light flavour fake contribution.

In Figure 6.25 the MC fake rates are broken down into heavy or light flavour fakes. Overlaid is also data after subtraction of real leptons (and for electrons, conversions in addition). In the muon channel (left) the data is seen to follow the heavy flavour fakes. The light flavour fake rate is lower than for heavy flavour, but fluctuates considerably due to the small event count. In the electron channel (right) data instead follows the light flavour distribution, except for the

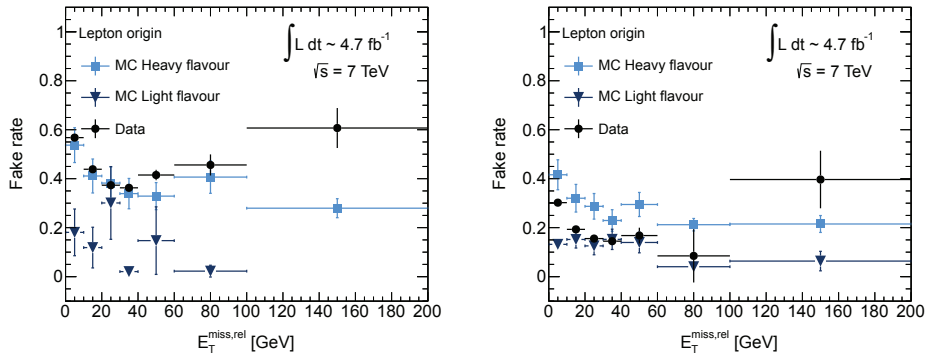

(a) Muons CR-B

(b) Electrons CR-B

Figure 6.25: Fake rate versus $E_{\mathrm{T}}^{\mathrm{miss,rel}}$ for truth-selected heavy and light flavour MC fake leptons, and for data. The rates are extracted in a CR-B type region, which means use of events with SS same-flavour di-leptons, but otherwise using no cuts. For the data distribution MC lepton subtraction has been performed, and in the electron channel a Z-veto is also applied.

very first bin where data is found somewhere between the heavy and light flavour rates. Again the light flavour rate is lower than the heavy flavour rate.

Both Figures 6.24 and 6.25 confirm that a $E_{\mathrm{T}}^{\mathrm{miss,rel}}$ dependency is seen in data as well as in MC. It also confirms that it is not (only) due to different processes contributing at high $E_{\mathrm{T}}^{\mathrm{miss,rel}}$ each with their own behaviour and importance (for instance $t\bar{t}$, $b\bar{b}$ or W+jets), since in fact each process itself exhibits a dependency. We also see that both the heavy and light jet fake rates depend on $E_{\mathrm{T}}^{\mathrm{miss,rel}}$, although the rates themselves differ. Finally, it is reassuring that both data and MC show the same behaviour.

To take into account the $E_{\mathrm{T}}^{\mathrm{miss,rel}}$ dependency one could think of at least two main approaches. One is to actually incorporate the dependency and make fake rates both p_{T} and $E_{\mathrm{T}}^{\mathrm{miss,rel}}$ dependent. Due to lack of time this was not attempted for the published work [134]. In Chapter 7.2 I follow this fully data-driven approach.

The approach that is carried through in [134] and which I present in Section 7.1, however relies on the agreement between data and MC described above, and avoids the most prominent dependency at low $E_{\mathrm{T}}^{\mathrm{miss,rel}}$, by extracting the QCD fake rate from MC at intermediate $E_{\mathrm{T}}^{\mathrm{miss,rel}}$.

First though, I introduce the fake rate for the conversion electrons, as this must be in place in order to construct the final combined fake rate used in the electron channel.

6.4.2 Fake rate from conversion electrons

For electron final-states, the contribution from the conversions described in Chapter 4.3.4 must be considered. In previous sections the conversion component was subtracted from the hadron

data control regions simply by using MC. However, to actually determine the conversion fake rate, a separate control region is used. This region is constructed in order to be dominated by $Z \rightarrow \mu^+\mu^- + \gamma$. There are two main reasons for that. The first is in order not to overlap with the "charge-flip"contribution. This background is estimated separately by another independent method, and we therefore do not include it in the Matrix Method. Requiring $Z \rightarrow \mu^+\mu^- + \gamma$ ensures a charge-flip free region, since charge-flip of muons results either in a SS $\mu^+\mu^-$ pair, or a μe pair, if one of the muons is not reconstructed. The most important motivation for the $Z \rightarrow \mu^+\mu^- + \gamma$ control region is, however, to unambiguously identify the conversion electron from the γ, assuming that one electron is mis-reconstructed.

The cuts described in Table 6.10 define the region, where the three first requirements guarantee the dominance of muonic decay of Z bosons, such that the only electron in the event is most likely to stem from a γ. These include the requirement that the invariant mass of the $\mu\mu e$ are within the Z-mass peak (80-100 GeV), that the di-muon pair fulfils the baseline lepton selection cuts, has opposite charge, and that at least one of the muons is above the online trigger threshold of 18 GeV, and finally that there is exactly one baseline electron present. The trigger threshold requirement is only put on one lepton, as the second lepton might have lost energy due to the bremsstrahlung process. The next cuts limit the contamination of other processes, Drell-Yan (4.), $t\bar{t}$ (5.), and single t or W production (6. and 7.).

1. Exactly two baseline muons with opposite sign. At least one muon with p_{T}>18 GeV
2. Exactly one loose electron
3. $M_{\mu\mu e} \in (80, 100)$ GeV
4. $M_{\mu\mu} > 20$ GeV
5. B-jet veto
6. $E_{\mathrm{T}}^{\mathrm{miss,rel}} < 50$ GeV
7. $M_T(e, E_{\mathrm{T}}^{\mathrm{miss}}) < 40$ GeV

Table 6.10: Cuts for the conversion control region.

The region is validated with truth information from MC. All the baseline MC samples presented in Chapter 5.3.1 are included, with the Sherpa samples chosen to represent the di-boson contribution. For the QCD component the PythiaB di-lepton filter sample (PythiaB_2L) is used. Figure 6.26 shows the expected composition of electrons with a dominance of conversion electrons. Almost 78% of all fake electrons belong to this category. There is in fact also a contribution from heavy and light flavour jet electron fakes (in total 21%), but the proportion of real leptons is very small (1.1%).

Even though the real component is small in this control region, we statistically subtract it from data (and from MC), as we did in the QCD control regions described earlier. The fake rates after subtraction are shown in Figure 6.27. MC from the same control region is also plotted for comparison, both an inclusive sample (MC incl), and the truth-determined conversion leptons only (MC conv). The comparison between the MC inclusive and the MC conversion rates is to check whether the contamination of QCD fakes affects the conversion fake rate. As we see in

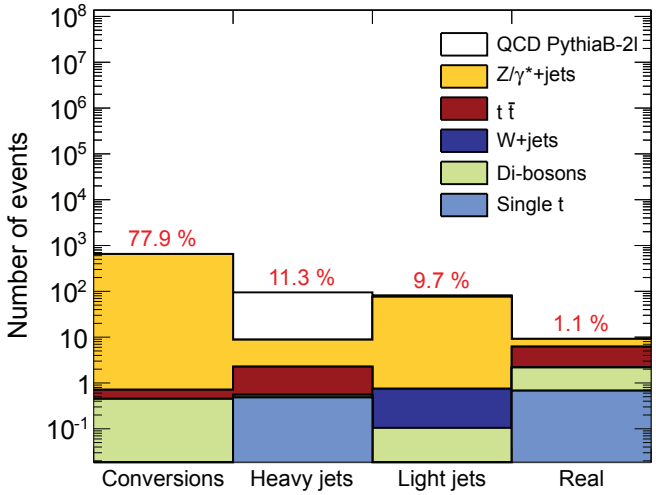

Figure 6.26: The MC origin of the baseline (inclusive loose) electron in the conversion control region. The percentage above the bins shows the relative amount of each component.

the figure both the MC distributions agree within errors. The MC inclusive integrated fake rate is 21.23±2.67% and the MC conversion fake rate of 21.28±1.74%. Note that the inclusive rate has larger errors due to the subtraction of the real leptons. We conclude with this that the contamination of non-conversion leptons (mostly QCD) can be ignored. In the bottom part of the plot, the ratio between data and the MC conversion rate is shown. A fit is performed assuming a straight line, and as the fit-result of 1.01±0.08 shows, the data agrees with MC within errors.

The same fake rates are plotted versus η and and $E_{\mathrm{T}}^{\mathrm{miss,rel}}$ in Figure 6.28, left and right respectively. In the $E_{\mathrm{T}}^{\mathrm{miss,rel}}$ plot, the control region is adapted omitting the $E_{\mathrm{T}}^{\mathrm{miss,rel}}$ and m_{T} cut (cuts 6 and 7 in Table 6.10), to not bias the $E_{\mathrm{T}}^{\mathrm{miss,rel}}$ distribution (remembering that m_{T} and $E_{\mathrm{T}}^{\mathrm{miss,rel}}$ are correlated). Again we see good agreement between data and MC. The η dependency (left) is as expected for electrons, reflecting the detector geometry, as commented in Section 6.3.

Neither data nor MC show any dependency on $E_{\mathrm{T}}^{\mathrm{miss,rel}}$ beyond the second bin, even if statistics is sparse at higher $E_{\mathrm{T}}^{\mathrm{miss,rel}}$ since this is a control region dominated by Z decays. This is in contrast to the QCD rates where a more important dependency is found, as discussed in the previous section.

Now that we have measured the real efficiencies, the QCD fake rates and the conversion fake rate, both in data and in MC, and investigated the most important dependencies, we can proceed with putting all the pieces together in order to achieve a set of final rates with dependencies and systematic uncertainties accounted for. In the following chapter I present the procedure to do

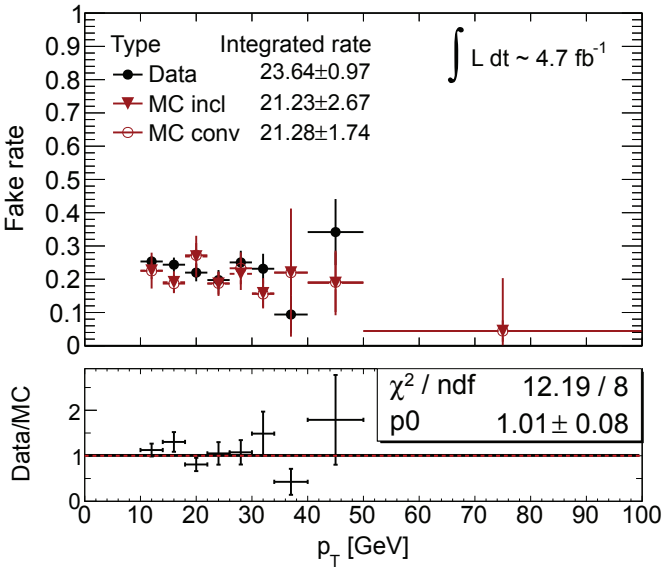

Figure 6.27: The conversion region electron fake rate versus p_{T}. Black dots represent data. Two distributions are shown for MC. In red closed triangles the MC inclusive - where inclusive means that all electrons in the control region, except real electrons are included. In red open circles, only the MC conversion electrons are used. The integrated rates quoted in the legend are in percent.

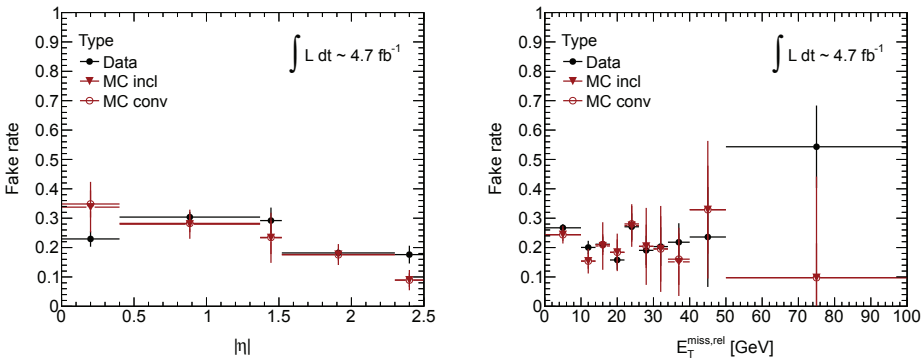

Figure 6.28: The conversion region electron fake rate versus η (left) and $E_{\mathrm{T}}^{\mathrm{miss,rel}}$ (right). Black dots represent data. Two distributions are shown for MC. In red closed triangles the MC inclusive - where inclusive means that all electrons in the control region are included, with no truth-filtering. In red open circles, the MC conversion electrons only, were used. In the $E_{\mathrm{T}}^{\mathrm{miss,rel}}$ plot, both the $E_{\mathrm{T}}^{\mathrm{miss,rel}}$ cut and the m_{T} cuts are omitted.

so, first as carried through in [134], then in a fully data-driven way in Section 7.2.

Chapter 7

Implementation of the fake lepton estimation with the Matrix Method

In the previous chapter the foundation for extracting fake rates and real efficiencies was prepared, with extensive use of control regions and comparison between them. In this chapter I follow two main approaches. One is to describe the procedure resulting in the publication [134], where we take the real efficiency and conversion fake rate from data control regions, but the QCD fake rate from MC, after validation using data. The other is a fully data-driven procedure where also the QCD fake rate is extracted from data control regions.

I start by describing the procedure followed in [134], and in the course of that, discuss the relevant systematic uncertainties related to the method.

7.1 Semi-data driven procedure

This section describes the procedure as followed in [134], but with the systematic uncertainties to some degree re-evaluated for practical reasons[1]. Based on the good agreements achieved between MC and data in the previous chapter, the $E_{\mathrm{T}}^{\mathrm{miss,rel}}$ dependency is taken into account by extracting the QCD fake rate from MC in an "intermediate" $E_{\mathrm{T}}^{\mathrm{miss,rel}}$ region chosen between 40-100 GeV. This choice is based on the observation in Figure 6.24 that the dependency flattens with increasing $E_{\mathrm{T}}^{\mathrm{miss,rel}}$ and, more importantly, both data and MC show the same trend for both muons and electrons. By avoiding the lowest $E_{\mathrm{T}}^{\mathrm{miss,rel}}$ bins, we can operate with a fake rate with less pronounced dependency, and still get a precise estimate of the fake lepton contribution at high $E_{\mathrm{T}}^{\mathrm{miss,rel}}$, which is the region of most interest for the SUSY searches we perform. The data control regions discussed at length in the previous chapter are used to derive systematic uncertainties, and for further consistency checks, as addressed later on.

Figure 7.1 shows the MC QCD intermediate $E_{\mathrm{T}}^{\mathrm{miss,rel}}$ fake rates for muons and electrons as function of p_{T}. The full SM MC is included, and PythiaB_2L is used to represent QCD. As we are operating with MC, we directly select leptons that stem from hadrons (QCD processes). As expected, due to the nature of the $E_{\mathrm{T}}^{\mathrm{miss,rel}}$ dependency, the fake rates are noticeably lower than

[1]The analysis was performed in spring of 2012 and in most cases it was practical to redo the analysis with slight changes, both due to new insights into the approaches used, and due to rewriting of analysis scripts. Any important change is commented.

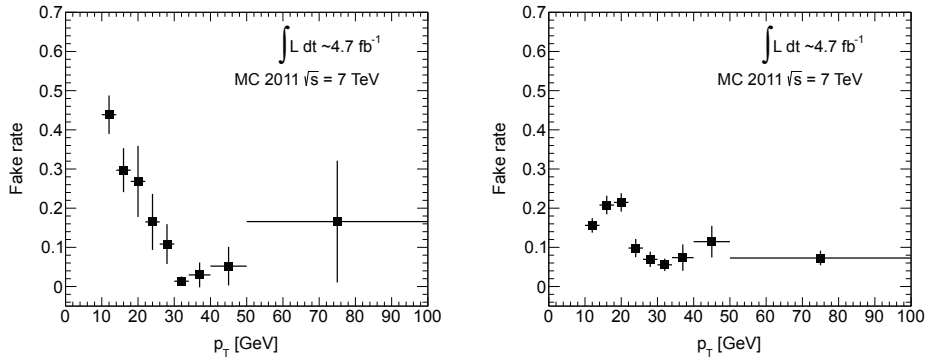

(a) Muons (b) Electrons

Figure 7.1: The QCD fake rates from the MC intermediate $E_{\mathrm{T}}^{\mathrm{miss,rel}}$ region 40-100 GeV using only fake leptons. The full SM MC is included, with PythiaB_2L to represent QCD.

those obtained in the low $E_{\mathrm{T}}^{\mathrm{miss,rel}}$ control regions in the previous chapter.

In the electron channel, we must in addition to the QCD fake rate, take into account the conversions, and we therefore construct a combined weighted fake rate of the QCD and conversion components. In principle we could have attempted to extract separate rates and weights for light and heavy flavour fakes. However, we know that PythiaB_2L, which although was the best we could do, does not reproduce the light component, as clearly demonstrated by Figure 6.2 (b) (in Section 6.1), and therefore such a procedure would be driven by large uncertainties. We therefore treat QCD as a whole. The final fake rate is expressed by

$$\mathrm{f}_{\mathrm{e}}^{\mathrm{FIN}}(p_{\mathrm{T}}) = \sum_{i=\mathrm{QCD,conv}} \mathrm{f_i}(p_{\mathrm{T}}) \cdot \mathrm{w_i}(p_{\mathrm{T}}) \cdot \mathrm{s_i}\,. \tag{7.1}$$

Here the subscript i denotes the types of fakes relevant for electrons, which are QCD and conversions, $\mathrm{w_i}$ the relative amount of each fake-type (the weight), $\mathrm{s_i}$ the scale-factor measured between fake rates in data and MC, and $\mathrm{f_i}$ are the MC QCD fake rates shown in Figure 7.1, and the data-driven conversion fake rate for electrons previously shown in Figure 6.27. All rates are p_{T} dependent, and likewise the weights.

Before going into details on the systematic uncertainties, and the resulting final fake rates, I below explain the calculation of the weights.

7.1.1 Calculating fake rate weights

To obtain a more or less realistic relation between conversions and QCD fakes, knowing we can not rely on QCD MC to correctly reproduce the expected component for electrons (Figure 7.2), we use data as the overall scale of events (N_{data}), and MC truth to get the amount of real leptons that contribute (N_{real}^{MC}). In this way we obtain the total expected number of fake leptons N_{fake} without relying on the QCD MC sample itself as follows $N_{fake} = N_{data} - N_{MC}^{real}$.

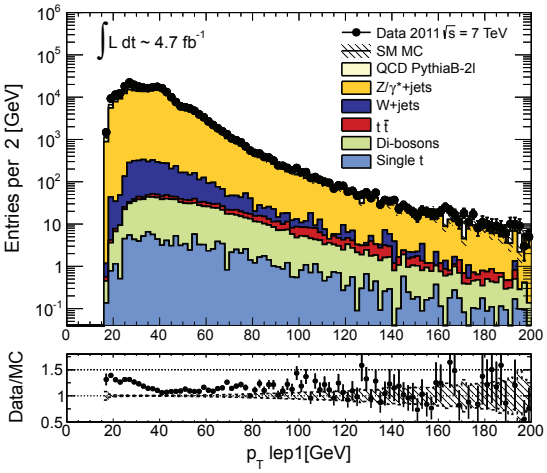

Figure 7.2: Electron inclusive loose distribution in SR-OSjveto (excluding $E_{\mathrm{T}}^{\mathrm{miss,rel}}$ cut) showing the discrepancy between data and MC at low p_{T} due to the insufficiency of the QCD PythiaB_2L MC sample.

The conversion component estimated by the Matrix Method is, as we remember, only the non-charge-flip (as charge-flip is estimated by a separate method). We extract the total amount of these conversions directly from MC (N_{conv}^{MC}). We can do so by using OS events, as the non-charge flip conversion contribution is expected to be equally large in SS and OS events (all electrons and muons have the same probability to radiate photons, independent of whether the event is OS or SS). The QCD component is then defined as $N_{fake} - N_{conv}^{MC}$. The weights are then simply

$$\begin{aligned} w_{conv} &= \frac{N_{conv}^{MC}}{N_{fake}}, \\ w_{QCD} &= \frac{N_{fake} - N_{conv}^{MC}}{N_{fake}}, \end{aligned}$$

where $w_{conv} + w_{QCD} \equiv 1$.

To predict the weights as close as possible to what is expected in the actual signal regions, we perform the calculation with events that satisfy the SR-OSjveto region, however omitting the $E_{\mathrm{T}}^{\mathrm{miss,rel}}$ requirement to gain statistics. Figure 7.3 presents the resulting SR-OSjveto weights as a function of p_{T}. The conversion component is in fact rather small, especially at low p_{T}, but increases somewhat with increasing p_{T} until about 45 GeV, then decreases and flattens again. These p_{T} dependent weights are then applied to the separate QCD and conversion fake rates as formulated in Equation 7.1.

The resulting fake rate for the electron channel, after combining the conversion and QCD fake rates with the appropriate weights, is shown in Figure 7.4. The muon fake rate in Figure 7.1

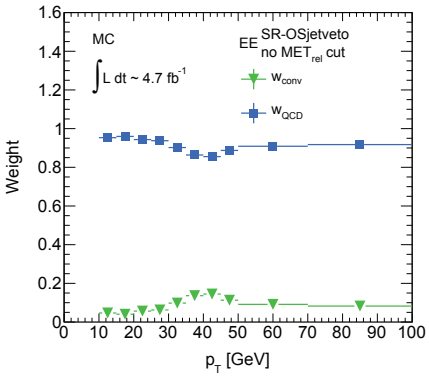

Figure 7.3: The conversion and QCD weights in opposite sign events (SR-OSjveto) using the full $E_{\mathrm{T}}^{\mathrm{miss,rel}}$ range. The weights are obtained by gauging the total amount of fake leptons with data, as described in the text.

(a) is used unchanged because of the negligible conversion contribution.

In principle, each signal region could use different weights, and hence a different final fake rate. Fake estimation in the SR-2jets region would thus be performed using weights extracted from a SR-2jets-like region, and so on. Table 7.1 shows how using separate weights from SR-OSjveto, SR-SSjveto, and SR-2jets (SR-m_{T2} has too little statistics) affect the integrated fake rate with respect to the baseline, which uses weights from the SR-OSjveto region as outlined above. We see that although the conversion weight increases from 6.8% to as much as 12.9% (corresponding to a relative increase of 89.8%) in SR-2jets, this only affects the resulting combined fake rate by 3.5%.

We see therefore that the effect on the final fake rate is small, even when regarding the

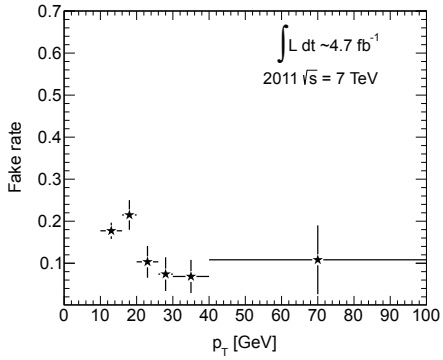

Figure 7.4: The combined weighted fake rate for electrons, constructed from the data-driven conversion fake rate, and the MC-driven QCD fake rate. The errors are purely statistical.

SR-SSjveto region, where we naively would expect a much larger overall contribution of conversions. However, as charge-flips makes up most of this, and they are removed as they are not estimated by the MM but by the separate Charge-Flip method, the conversions left over are approximately of the same order as in OS regions, and only give a 1% effect on the combined fake rate. Hence the weights extracted from the OS-jveto region do well also here. In fact, it is from SR-2jets that the weights differ most from the weights extracted from SR-OSjveto, as pointed out above. We therefore assign a conservative 4% systematic on the combined weighted fake rate to account for any bias we introduce by using SR-OSjveto weights for all signal regions. For more details on how the weights are calculated, and the actual weight distribution as a function of p_{T} from each signal region, see Appendix C.10.

	Conversions		QCD		Conversions+QCD	
	wgt [%]	diff [%]	wgt [%]	diff [%]	f^{COMB} [%]	$\sigma(f^{\mathrm{COMB}})$[%]
SR-OSjveto	6.8 ± 0.1	–	93.2 ± 0.1	–	15.7	–
SR-SSjveto	8.5 ± 0.2	+26.0	91.5 ± 0.2	-1.9	15.8	+1.0
SR-2jets	12.9 ± 1.3	+89.8	87.1 ± 1.0	-6.5	16.2	+3.5

Table 7.1: The calculated relative amount (weight) of conversions and QCD in three different signal-regions (before $E_{\mathrm{T}}^{\mathrm{miss,rel}}$ cut), and the relative difference of the weights (diff) for SR-SSjveto and SS-2jets relative to SR-OSjveto. In addition is shown the resulting combined fake rate f^{COMB}, and the corresponding relative uncertainty with respect to the baseline using SR-OSjveto weights. All numbers are in percent.

Now that we have established the combined fake rate, it is time to have a closer look at the systematic uncertainties connected with the Matrix Method fake lepton estimation. In the next sections I present what I consider the most important systematic uncertainties, and attempt to motivate why and how they are implemented.

7.1.2 Systematic uncertainty on the QCD MC fake rate

I start with the uncertainties related to the QCD MC fake rate, which is the component that has the largest uncertainty. The methods used are as carried through in [134], with slight improvements where stated. The evaluated effects are (presented in their order of importance): the uncertainty related to the $E_{\mathrm{T}}^{\mathrm{miss,rel}}$ dependency; the effect varying the relative contribution of the heavy flavour fakes from $t\bar{t}$ and $b\bar{b}$; the effect on the fake rate when varying the relative amount of light and heavy fakes; differences between fake rates in OS and SS events; and finally differences between the data-control regions, which serve as a basis for validating the MC based fake rate. All uncertainties are in the end summarized in Table 7.5, Section 7.1.2.6.

7.1.2.1 $E_{\mathrm{T}}^{\mathrm{miss,rel}}$ MC QCD fake rate dependency

An important source of systematic uncertainty is related to the $E_{\mathrm{T}}^{\mathrm{miss,rel}}$ dependency, especially since we rely on MC predictions at high $E_{\mathrm{T}}^{\mathrm{miss,rel}}$, whereas validation is performed through data control regions at low $E_{\mathrm{T}}^{\mathrm{miss,rel}}$. To evaluate this component, we normalize the fake rates versus $E_{\mathrm{T}}^{\mathrm{miss,rel}}$ shown in Figure 6.24 to the integrated fake rate in the $E_{\mathrm{T}}^{\mathrm{miss,rel}}$ 40-100 GeV region (the

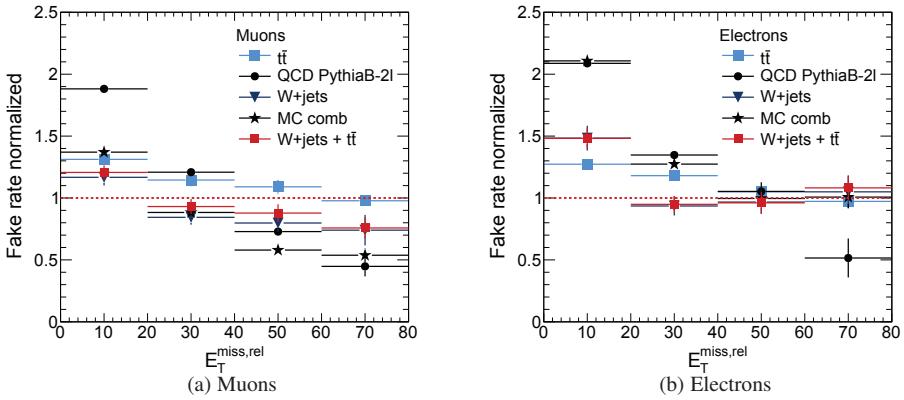

(a) Muons (b) Electrons

Figure 7.5: The normalized MC fake rate versus $E_{\mathrm{T}}^{\mathrm{miss,rel}}$ for muons (left) and electrons (right) for QCD leptons only. The normalization applied is the integrated fake rate measured in the intermediate $E_{\mathrm{T}}^{\mathrm{miss,rel}}$ region 40-100 GeV process by process. A dashed red line indicates the 1:1 agreement between the integrated fake rate in the intermediate region and the fake rate over the whole $E_{\mathrm{T}}^{\mathrm{miss,rel}}$ spectrum.

baseline MC QCD rate) corresponding to each process. The deviation from 1 is used as an estimate of the uncertainty. Since it is $t\bar{t}$ and W+jets that dominate at high $E_{\mathrm{T}}^{\mathrm{miss,rel}}$, the combined fake rate of these samples will be used to extract the uncertainty. The relative rates for $t\bar{t}$ and W+jets events are shown in Figure 7.5, and the red markers represent their combined rate. The QCD fake rate extracted from the PythiaB_2L sample (black circles) shows a stronger dependency, the total MC (MC comb) is dominated by this component at low $E_{\mathrm{T}}^{\mathrm{miss,rel}}$, but less so at higher $E_{\mathrm{T}}^{\mathrm{miss,rel}}$, where $t\bar{t}$ and W+jets become more important.

From the figure we see that the maximum deviations from 1.0 for the combined W+jets plus $t\bar{t}$ rate are roughly ±20% for muons and +50-0% for electrons[2]. In the publication [134], we opted for a conservative approach and used this directly as the systematic uncertainty due to the $E_{\mathrm{T}}^{\mathrm{miss,rel}}$ dependency. Here however, I wish to instead use the weighed average uncertainty across bins, to achieve a more realistic systematic uncertainty. With approximate statistics for the combined W+jets and $t\bar{t}$ events, distributed as 26(24), 38(37), 26(27), 10(12) % in each $E_{\mathrm{T}}^{\mathrm{miss,rel}}$ bin of the muon (electron) channel respectively, I arrive to a systematic uncertainty of +20-12% in the muon channel, and +35-5%in the electron channel. This is summarized in Table 7.5.

7.1.2.2 Heavy flavour QCD MC ($b\bar{b}$) versus $t\bar{t}$ MC fake rates

It is known that the QCD-production cross section has a large theoretical uncertainty. In this analysis we use the heavy-flavour dominated PythiaB_2L, which mostly contains $b\bar{b}$, to repre-

[2]Note that although from Figure 7.5 it seems that the muon fake rate continues to fall, it in fact flattens, which can be inferred from Figure 6.24.

sent QCD . However, the heavy flavour component also includes fakes from $t\bar{t}$, and the relative amount of $b\bar{b}$ and $t\bar{t}$ will affect the total heavy flavour fake rate if the individual fake rates differ. We combine the $t\bar{t}$ rate with the heavy flavour QCD rate (from now on called $b\bar{b}$) according to their relative importance to give a combined weighted heavy flavour fake rate. This can be expressed as

$$\begin{aligned} f^{\text{heavy}} &= f_{\text{bb}} \cdot w_{\text{bb}} + f_{\text{tt}} \cdot (w_{\text{tt}}) \\ &= f_{\text{bb}} \cdot w_{\text{bb}} + f_{\text{tt}} \cdot (1 - w_{\text{bb}}) , \end{aligned} \tag{7.2}$$

where f_{bb} and f_{tt} are the integrated fake rates of the $b\bar{b}$ and $t\bar{t}$ components respectively, and w_{bb} and w_{tt} are the weights, or relative contribution of $b\bar{b}$ and $t\bar{t}$.

From this formula we can investigate how f^{heavy} changes if the $b\bar{b}$ contribution (w_{bb}) is increased or reduced, as a consequence of the $b\bar{b}$ cross section uncertainty. This is however only relevant if the two fake rates differ. Figure 7.6 presents the MC fake rates as a function of p_{T}, separately for $t\bar{t}$ and $b\bar{b}$ (QCD heavy flavour PythiaB_2L), for muons to the left, and electrons to the right. In the muon distribution, I use SS events, as this is what is used for the final fake rate, while the electrons use SS+OS, to be discussed in Section 7.1.2.4. We select directly heavy flavour truth leptons, and the full $E_{\text{T}}^{\text{miss,rel}}$ range is included to give a clear comparison between rates, instead of using just the intermediate $E_{\text{T}}^{\text{miss,rel}}$ region which has limited statistics. We see that the overall fake rate is slightly lower for $t\bar{t}$ events, both for muons and electrons. The legends give the integrated fake rates of 46.57±7.15% for muon $b\bar{b}$ events, and 38.62±2.83% for muon $t\bar{t}$ events, and 31.35±6.13% and 28.46±2.33% for electron $b\bar{b}$ and $t\bar{t}$ events respectively. In Figure 7.6 the fakes from the $b\bar{b}$ (PythiaB_2L) are much more abundant than from the $t\bar{t}$ sample, making up as much as 99.3% in the muon channel, and 97.9% in the electron channel. A combined $t\bar{t}$, $b\bar{b}$ fake rate would thus be completely dominated by the latter.

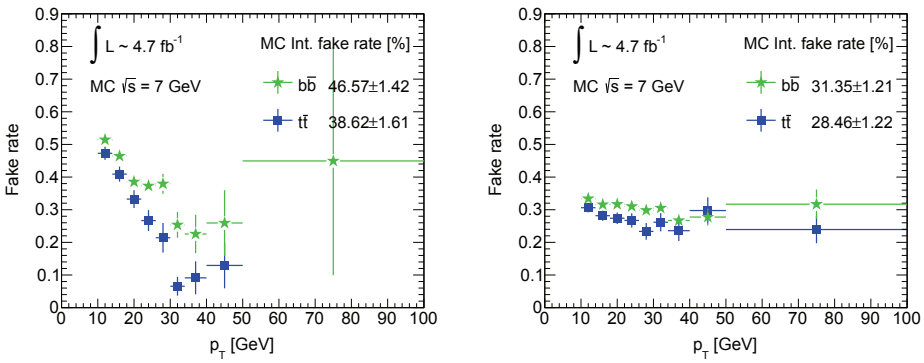

(a) Muons (b) Electrons

Figure 7.6: The MC fake rates for heavy flavour fakes for $t\bar{t}$ and $b\bar{b}$ (the latter in form of the PythiaB QCD sample). The full $E_{\text{T}}^{\text{miss,rel}}$ range is used. The errors include the statistical error, and the systematic uncertainty on cross section and luminosity.

With the integrated fake rates as given in the legend, we can now evaluate what effect more, or less $b\bar{b}$ events have on the total heavy flavour fake rate, using Equation 7.2. We chose to vary the $b\bar{b}$ contribution up to 100% $b\bar{b}$ and down by a factor of two, with respect to the nominal (99.3% for muon and 97.9% for electrons), given the large cross section uncertainty on QCD.

The resulting combined fake rates are presented in the top part of Table 7.2. The combined fake rate with the maximum (f^{bb-max}) or minimum (f^{bb-min}) amount of $b\bar{b}$ are shown in the two next to last columns. The deviation from the nominal values (f^{nom}) are then taken as the systematic uncertainty, and is explicitly shown in the last column, with $+0.1 - 8.5\%$ for muons and $+0.2 - 4.5\%$ for electrons.

As the final QCD fake rate is in fact calculated in the intermediate $E_{\mathrm{T}}^{\mathrm{miss,rel}}$ region, we do the same exercise for events satisfying the $E_{\mathrm{T}}^{\mathrm{miss,rel}}$ cut. At higher $E_{\mathrm{T}}^{\mathrm{miss,rel}}$ values, $t\bar{t}$ starts to be more important. In this region the contribution of $b\bar{b}$ is 78.8% of the total for muons, and 84.3% for electrons, so slightly lower than integrating over the full $E_{\mathrm{T}}^{\mathrm{miss,rel}}$. The rates are also different, as expected due to the $E_{\mathrm{T}}^{\mathrm{miss,rel}}$ dependency, see the bottom part of Table 7.2, two first columns. Now the $b\bar{b}$ rates are in fact lower than the $t\bar{t}$, in contrast to the upper table. This is explained by the different $E_{\mathrm{T}}^{\mathrm{miss,rel}}$ dependencies of the two processes. The $b\bar{b}$ fake rate falls much more steeply with $E_{\mathrm{T}}^{\mathrm{miss,rel}}$ compared to $t\bar{t}$, see again Figure 7.5. The final relative uncertainties on the fake rates used are therefore $+10.0 - 5.4\%$ for muons and $+17.2 - 6.4\%$ for electrons, as given in the last column of the bottom row of Table 7.2 (see also the summary in Table 7.5).

	$t\bar{t}$		$b\bar{b}$		$t\bar{t}$+$b\bar{b}$			
	f_{tt}	w_{tt}	f_{bb}	w_{bb}	$f_{\mathrm{tt+bb}}^{\mathrm{nom}}$	$f_{\mathrm{tt+bb}}^{\mathrm{bb-max}}$	$f_{\mathrm{tt+bb}}^{\mathrm{bb-min}}$	σ
Integrated over $E_{\mathrm{T}}^{\mathrm{miss,rel}}$								
Mu	38.6±1.6	0.7	46.6±1.4	99.3	46.5±1.4	46.6±1.1	42.6±1.4	+0.1-8.5
El	28.5± 1.2	2.1	31.3± 1.2	97.9	31.3±1.2	31.3±0.9	29.9±1.2	+0.2-4.5
$E_{\mathrm{T}}^{\mathrm{miss,rel}}$ 40-100 GeV								
Mu	31.1±1.9	21.1	24.6±3.6	78.9	25.9±2.9	24.6±1.8	28.5±3.6	+10.0-5.4
El	24.7± 1.3	15.7	17.2± 1.4	84.3	18.4±1.2	17.2±1.0	21.5±1.4	+17.2-6.4

Table 7.2: The integrated fake-efficiencies and weights of the heavy-flavour components $t\bar{t}$ and $b\bar{b}$ in the first two main columns. The third column shows the weighted average of the two components, while the next to last and last column show the combined fake-efficiency when varying the weight of the $b\bar{b}$ component up or down. All numbers are in percent.

7.1.2.3 Light versus heavy flavour fakes in the MC QCD fake rate

For electrons we know the light component is important, however there is no reliable MC, nor dedicated data control regions for this contribution. We therefore instead consider the light component as a source of systematic uncertainty. Again the heavy flavour sample PythiaB_2L

is used for QCD, hence the light flavour component is necessarily underestimated.

We evaluate the uncertainty by varying the light flavour component up and down in the same manner as explained in Section 7.1.2.2, but instead of $b\bar{b}$ and $t\bar{t}$, we now consider heavy flavour versus light flavour QCD fakes from PythiaB_2L MC. Both weights (w) and fake rates (f) are extracted from MC truth, in the intermediate $E_{\mathrm{T}}^{\mathrm{miss,rel}}$ range, and are quoted in Table 7.3. The exercise is carried out for muons as well as electrons, but the effect in the muon channel is negligible (below 1%), and is therefore not considered here.

Heavy		Light		Combined
f [%]	w [%]	f [%]	w [%]	f [%]
19.3±3.2	55.7	10.6±1.7	44.3	15.5±1.9

Table 7.3: The electron QCD PythiaB_2L MC integrated (average) fake-efficiencies of the heavy and light flavour fake components, as given by truth, and the corresponding relative weights. The last column quotes the weighted average of the two components. All numbers are in percent.

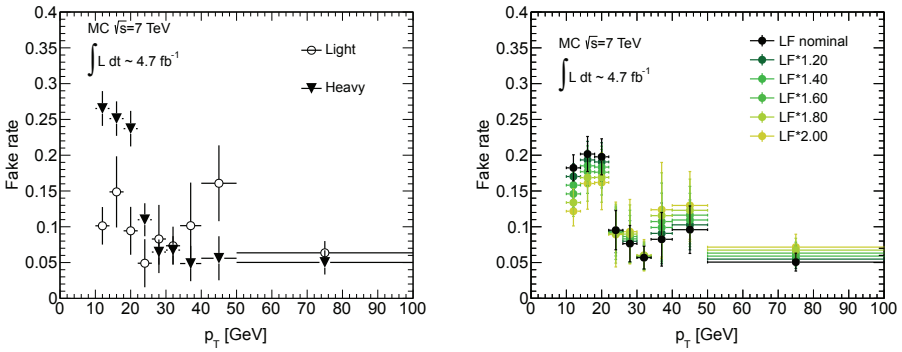

Figure 7.7: The MC PythiaB_2L QCD fake rate for events with $E_{\mathrm{T}}^{\mathrm{miss,rel}}$ 40-100 GeV. To the left is shown the heavy and light components separately. To the right, the integrated rate (heavy and lighted combined) is shown in black with nominal weights, while the coloured markers represent the resulting rates when varying the light flavour (LF) component up by 20-100%. The errors on the light and heavy flavour fake rates are purely statistical. In particular, no error is added due to cross section uncertainty.

Figure 7.7 shows the light and heavy flavour MC fake rates separately (left), and how they combine to an integrated fake rate (right, black markers). The coloured markers in the right plot show how the integrated fake rate varies as the light flavour component is increased up to twice its original contribution, in steps of 0.2 (and the heavy flavour component is scaled down correspondingly so that the total weight is one). The relative contribution of the light component and the combined fake rate is given in Table 7.4, for the nominal value extracted directly from

MC using PythiaB_2L as the QCD sample, and for the maximum twice increase. Since the fake rate changes linearly with the variation of the weights, I only quote the two values (0.44 and 0.89) corresponding to doubling the scale from 1 to 2, and not the ones in between, which can be inferred from Figure 7.7.

Scale	w [%]	f [%]	σ^{MAX} [%]	σ^{avg} [%]
1.0	44.3	15.5	–	–
2.0	88.6	11.6	+45.3-36.4	+0-24.8

Table 7.4: The weight of light flavour fakes in MC (w), the combined light+heavy flavour fake rates (f) and the maximum deviation in any bin from the nominal fake rate (σ^{MAX}) corresponding to Figure 7.7. σ^{avg} is the difference between the nominal integrated fake rate (15.5) and the scaled integrated fake rate (11.6). All numbers (except scale) are in percent.

In [134] we chose to take the systematic uncertainty on the light flavour normalization as the maximum reduction from the nominal fake rate, similar to what Figure 7.7 shows. This corresponded to an uncertainty of -40% compared to the nominal rate. The re-calculated values in Table 7.4, based on Figure 7.7 quotes 36.4% as the minimal bin-wise fake rate. When it comes to variation upwards seen in the bins above 20 GeV (corresponding to the 45.3% in Table 7.4) we regard these as due to the statistical fluctuations on the light component, based on the left plot in Figure 7.7, and are thus ignored.

If I instead calculate the integrated effect on the fake rate, the maximum systematic uncertainty arrives to -24.8% as shown in the last column of Table 7.4 (when assuming double as much light flavour jets, as in the nominal MC QCD sample, and again ignoring the upward fluctuations on the light flavour component). This is explained by the fact that the second bin contributes most, and in this bin the deviation is only roughly 22% from the nominal value (well below the 36.39% which corresponds to the maximum bin-wise deviation). In this re-evaluation of the systematic uncertainty, I wish to be less conservative than we were in [134]. I therefore instead of +0-36.4% (which corresponded to the re-calculated uncertainties), assign +0-24.8% to the uncertainty on the light component. This is summarized in Table 7.5.

7.1.2.4 SS and OS MC QCD fake rate comparison

With MC representing the QCD fake rate, and with the possibility to use truth information, we can now in addition to the SS information used in the previous chapter and shown to give very good agreement between data and MC, also use OS events to extract the fake rates (as we with truth can avoid the large contamination of real leptons). We do not use single lepton events however, as we saw that data and MC do not agree as well as the di-leptons do (Figures 6.20 and 6.21).

How the SS, OS and inclusive (SS+OS) MC QCD fake rates compare, is shown in Figure 7.8 for muons and electrons. The full MC is used, and PythiaB_2L represents QCD. To model the fake rate from jets, we directly select leptons that originate from heavy or light flavour hadron events with $E_{\mathrm{T}}^{\mathrm{miss,rel}}$ in the intermediate region 40-100 GeV. This corresponds to the region used

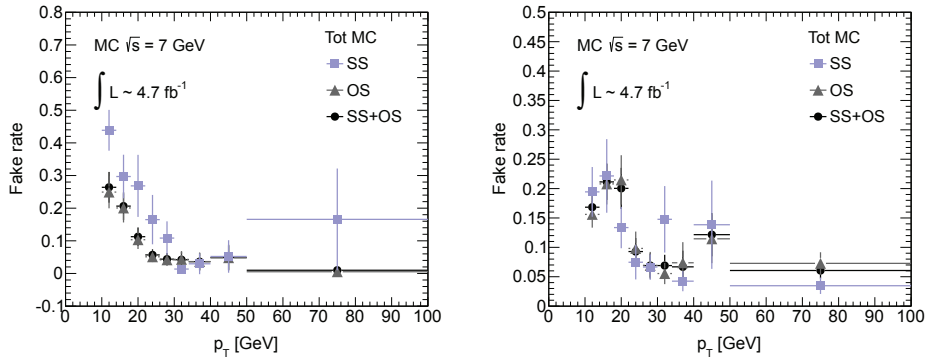

(a) Muons Full MC

(b) Electrons Full MC

Figure 7.8: The MC fake rate for muons (left) and electrons (right) in the intermediate $E_{\mathrm{T}}^{\mathrm{miss,rel}}$ region 40-100 GeV. Only leptons that originate from heavy or light flavour QCD are selected with the help of truth information. The same-sign (SS), the opposite-sign (OS) and the inclusive distribution (SS+OS) are compared.

for the final fake rates. As the OS+SS combined fake rate in effect is the weighted average fake rate of the separate OS and SS fake rates, we can compare the combined fake rate to the separate fake rates, and with this tell how much each of them contributes. We see that for muons the OS dominates, since the SS+OS rate closely follows the OS distribution. We also see that there is a significant difference between the OS and SS fake rates (and thus OS+SS and SS fake rates, as the SS contributes minorly to the combined rate), with OS yielding an overall lower fake rate. For electrons there is a more democratic contribution from both di-lepton channels, and the two separates fake rates agree better, within statistics. Due to the differences between OS and SS fake rates in the muon channel especially, we select the SS fake rate as baseline for muons. This is based on the studies done in (the same-sign) CR-B control region, where data and MC were found to agree well, see Figure 6.20 (b) Section 6.4.1.5. For the electron channel however, where the differences between OS and SS are not significant, we combine the two to gain statistics. A systematic uncertainty is extracted to account for any possible bias we introduce when choosing either SS (muons) or SS+OS (electrons) to represent the MC QCD fake rate. We take this from the most important background processes at high $E_{\mathrm{T}}^{\mathrm{miss,rel}}$, namely $t\bar{t}$, as demonstrated in Appendix C.3. The ratio of the SS to OS fake rate for $t\bar{t}$ events only, is presented in Figure 7.9 for muons to the left, and electrons to the right. The systematic uncertainty on MC QCD fake rate due to the difference between SS and OS fake rates, is taken as the weighted average of the SS to OS ratio, which is found by a straight line fit, yielding 0.84±0.07 for muons and 0.85±0.08 for electrons. Since we select the SS rate in the muon channel, the uncertainty is applied downward only (since the ratio is SS over OS). In the electron channel we use the combined SS+OS events, but since the error is calculated from $t\bar{t}$ events where OS dominates, the error is applied upward. This translates to a asymmetric uncertainty of +0-16% in the muon channel, and +15-0% in the electron channel.

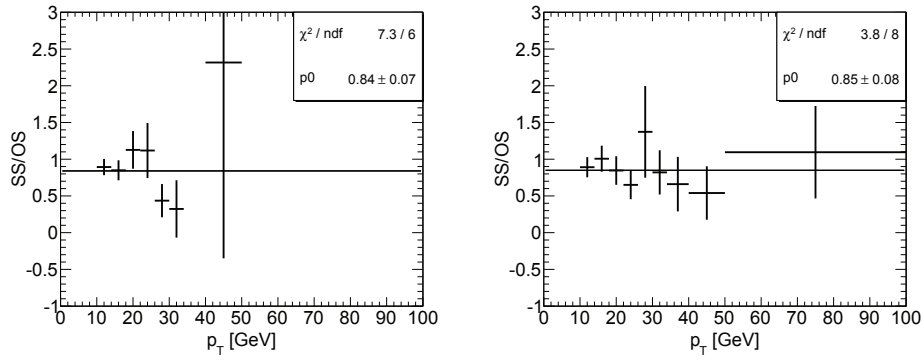

(a) Muons $t\bar{t}$ (b) Electrons $t\bar{t}$

Figure 7.9: The ratio of SS to OS fake rate in $t\bar{t}$ MC, including only heavy and light flavour origin leptons. The ratio is fitted assuming a constant ratio, and is shown as a black line.

7.1.2.5 QCD control region systematics

Since fake control regions CR-A and CR-B both target a mixed QCD fake sample, in contrast to CR-C which deals with heavy flavour fakes, we can compare them against each other in order to extract a systematic uncertainty related to possible variations between data control regions. The ratio of the baseline rates from CR-A and CR-B is shown in Figure 7.10, together

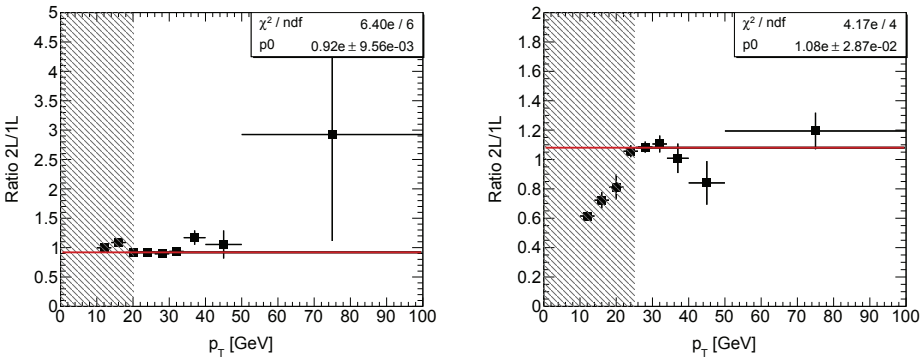

(a) Muons (b) Electrons

Figure 7.10: The ratio of the di-lepton same sign control region (CR-B) and the single lepton control region (CR-A) in data. Muons to the left and electrons to the right. A fit is performed from 20 GeV for muons and 25 GeV for electrons to avoid the single lepton trigger turn-on curve below these values (indicated by the hatched area).

with a fit assuming a constant ratio, performed from 20 GeV for the muons and 25 GeV for the electrons to avoid the turn-on trigger regions for the single lepton triggers, which would otherwise give an unfair comparison. In the muon channel the fit yields a ratio of 0.920±0.009,

and 1.080±0.029 in the electron channel. I therefore assign a ±8% uncertainty on the fake rate due to the difference between CR-A and CR-B, in both the muon and electron channel.

These errors are slightly different compared to Ref. [134], where a total systematic uncertainty of ±12% was found for the muon channel and ±4% for the electron channel. The differences are due to the use of other baseline regions for the single lepton fake rates (CR-A R07 in Ref. [134] using a $E_{\mathrm{T}}^{\mathrm{miss,rel}}$ cut, compared to CR-A R13 here using a m_{T} cut instead). The fact that CR-A is used, leads to a conservative limit, given that this region was disqualified for further use, partly due to its disagreement between data and MC (Section 6.4.1.5). However there is no other choice of control region to be compared to CR-B which is both sensitive to heavy and light flavours.

7.1.2.6 Summary of the MC QCD fake rate uncertainty

Table 7.5 summarizes the systematic uncertainties related to the MC QCD fake rate discussed in the previous sections. In addition to the uncertainties summarized in Table 7.5, comes the uncertainty on the combined final electron QCD and conversion fake rate, due to the uncertainty on the QCD (and conversion) weight, as discussed in Section 7.1.1. This uncertainty was found to be 4%, and is applied to the final fake rate presented in Section 7.1.6.

Uncertainty on the MC-based hadronic fake rate					
	Muons		Electrons		
Description	Up [%]	Down [%]	Up[%]	Down [%]	Reference
Heavy flavour norm.	10.0	5.4	17.2	6.4	Sec. 7.1.2.2
Light flavour norm.	–	–	0.0	24.8	Sec. 7.1.2.3
$E_{\mathrm{T}}^{\mathrm{miss,rel}}$ dependency	20.0	12.0	35.0	5.0	Sec. 7.1.2.1
SS/OS	0.0	16.0	15.0	0.0	Sec. 7.1.2.4
1L/2L	8.0	8.0	8.0	8.0	Sec. 7.1.2.5
Data/MC (sf)	4.0	4.0	1.0	1.0	Sec. 6.4.1.5 (Fig 6.23)
Total σ	24.1	22.6	42.6	27.3	

Table 7.5: A summary of the relative systematic uncertainties related to the QCD fake rate. Numbers are in percent. The last column states the section of figure where the study is presented.

Due to the very good agreement between data and MC found when comparing fake rates in the heavy flavour control region CR-C, where MC is expected to describe data well, we do not directly use a scale-factor on the final fake-rate, but instead assign a systematic uncertainty to it. Section 6.4.1.5, Figure 6.23 lead to a 4% deviation between data and MC in the muon channel, and 1% in the electron channel. These are included in the summary Table 7.5.

As mentioned, these systematic uncertainties are re-evaluated and improved, compared to the results we published in [134]. The largest improvements are in the electron channel, where I now quote +43%-27% compared to +59%-56%. In the muon channel the uncertainties are more or less the same with +24%-23% compared to +25%-26% in the publication. It is the

reduction of the light flavour, and $E_{\mathrm{T}}^{\mathrm{miss,rel}}$ dependency systematic uncertainties, that accounts for the largest reductions. Although the fake contribution is small compared to the total amount of background events, we know that it is important to keep the systematic uncertainty under control, in order to be sensitive in the signal regions. Therefore the improved systematic uncertainties contribute to slightly improve the results.

7.1.3 Conversion systematics

The systematic uncertainty on the data-driven conversion fake rate is taken as the difference between data and MC, illustrated by the ratio plot, and the legend in Figure 6.27, Section 6.4.2. While data gives a fake rate of 23.64±0.97%, the MC conversion fake rate is 21.28±1.74%.

The integrated difference between the two is of the order of 10%, and is here taken as a systematic uncertainty on the conversion fake rate. In the publication we chose to ignore the bin to bin fluctuations and instead use the integrated value, which results in an uncertainty of the order of 1% only (fit-value $1.01 \pm 7.75 \cdot 10^{-2}$). However, in this re-evaluation I instead apply the 10.0% uncertainty, which is more realistic, and in fact in agreement with the fit in Figure 6.27, when considering the $\sim 8\%$ uncertainty on the fit quoted. The uncertainty related to the conversion weight (relative amount of conversions to QCD), is taken into account on the final combined fake rate, and not separately on the conversion fake rate, and is included in the final systematics on the fake rate as described in Section 7.1.6.

Uncertainty on the electron conversion fake rate		
Description	Up[%]	Down [%]
σ(Data/MC)	10.0	10.0

Table 7.6: The relative systematic uncertainty related to the conversion fake rate. Numbers are in percent.

7.1.4 Real efficiency systematics

Finally, the systematic uncertainty on the data-driven real rate is studied. The integrated real efficiencies of 98.33±0.01% and 89.30±0.02%, are measured in the Z-region for electrons and muons respectively, as described in Section 6.3. It is the kinematic properties of leptons from the Z decay that strongly influence these efficiencies. With MC the real lepton efficiency is also estimated from other processes, which is then used to determine to what extent the Z-region biases the real efficiency.

Figure 7.11 compares the real efficiency for truth-filtered real MC leptons from different production processes for muons (left) and electrons (right). The rates are extracted from di-lepton events, and therefore the W+jets and single top processes are omitted. The processes included, display very similar real efficiencies over the whole p_{T} spectrum for both lepton flavours, with

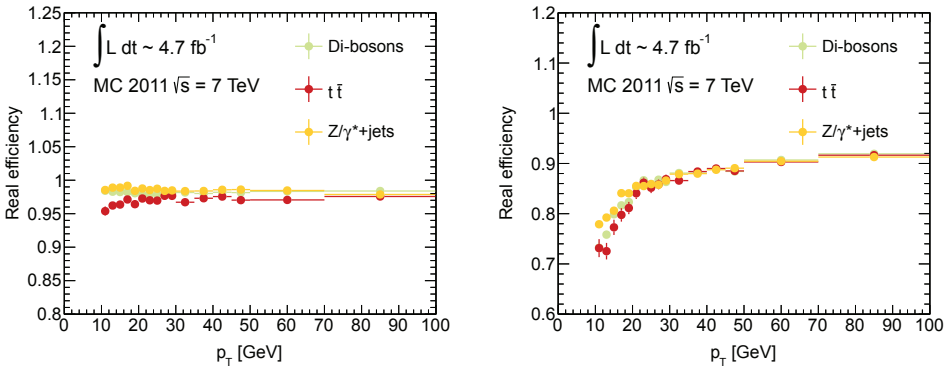

(a) Muons (b) Electrons

Figure 7.11: The real efficiency for electrons (left) and muons (right) as function of p_{T}(left). Each marker represents a different process. Errors are purely statistical.

a maximum deviation from the average rate of 3% in the low p_{T} bins. In the higher p_{T} bins, more relevant to the SUSY search, the uncertainty reduces to $< 1\%$. We therefore assign a 1.5% uncertainty due to the differences in the real efficiency between Z/γ^* and other important di-lepton processes.

Another source of systematic uncertainty is any disagreement between data and MC. The data to MC efficiency ratio in Section 6.3 Figure 6.5 reflects excellent agreement, with a average ratio of 0.9983±0.0002 in the muon channel, and 1.0100±0.0006 for electrons. We therefore only assign a 1% systematic uncertainty due to differences between data and MC, to both channels.

Table 7.7 summarizes the systematic uncertainties assigned to the real lepton efficiencies.

Uncertainty on the real efficiency				
	Muons		Electrons	
Description	Up [%]	Down [%]	Up [%]	Down [%]
Variation from processes	1.5	1.5	1.5	1.5
Data/MC agreement	1.0	1.0	1.0	1.0
Total σ	1.8	1.8	1.8	1.8

Table 7.7: Systematic uncertainty on the real efficiency. Numbers are in percent.

7.1.5 Uncertainty due to η dependency

Finally, the η dependency on the electron fake rate and real efficiency is evaluated. To do this we must jump to conclusions, and have a look at the lepton estimation given by the Matrix Method, since the dependency is seen for both the fake rate and the real efficiency. I give details about how estimates are obtained in the next section, here I just simply refer to the final estimates,

without further explanation.

To determine whether the η dependency seen in the electron fake rate and real efficiency significantly affect the fake lepton estimation, a 2D $p_{\mathrm{T}} - \eta$ real efficiency and fake rate is made. These are plugged into the Matrix Method, and the final estimates when using only the (usual) 1D p_{T} dependent fake rate and real efficiency are compared to the estimates when using the 2D ones.

Table 7.8 shows the result for both the SS and the OS channel after a $E_{\mathrm{T}}^{\mathrm{miss,rel}}$>100 GeV cut is made (signal-like region). As the table shows the effect on the final fake lepton estimation is negligible (< 1%), and much smaller than the statistical error. Therefore we neglect the η dependency altogether.

	SS + $E_{\mathrm{T}}^{\mathrm{miss,rel}} > 100$ GeV	OS + $E_{\mathrm{T}}^{\mathrm{miss,rel}} > 100$ GeV
	ee	*ee*
p_{T} dep.	34.2 ± 9.0	62.3 ± 18.1
p_{T}+η dep.	34.1 ± 10.0	62.2 ± 24.1
max diff. (%)	0.077 (0.22%)	0.121 (0.19%)

Table 7.8: The fake lepton estimation performed using only p_{T} dependent fake rates and real efficiency, and the estimation using a 2D p_{T} and η dependent fake rate and real efficiency. SS and OS channel di-electron channel only, after applying a $E_{\mathrm{T}}^{\mathrm{miss,rel}}$> 100 GeV cut. Extracted from Ref. [159]

7.1.6 Final fake rates and real efficiencies, including systematic uncertainties

The final fake rates for electrons and muons are shown in Figure 7.12. The combined electron fake rate is constructed with the weights calculated in Section 7.1.1, and here the individual fake rates for QCD (blue) and conversions (green) are also shown. The uncertainty on the MC cross section and luminosity is included in the individual fake rates, added in quadrature with the statistical uncertainty.

The hatched area indicates the total error including the statistical and systematic errors, which were summarized in Tables 7.5 and 7.6. In addition is added a 4% uncertainty on the combined electron fake rate, as discussed in Section 7.1.1. In the electron channel it is clear that the conversion fake rate has very little influence on the combined rate, which is as expected given the small conversion contribution shown in Figure 7.3.

The final real efficiency including the statistical and systematic errors added in quadrature is shown in Figure 7.13.

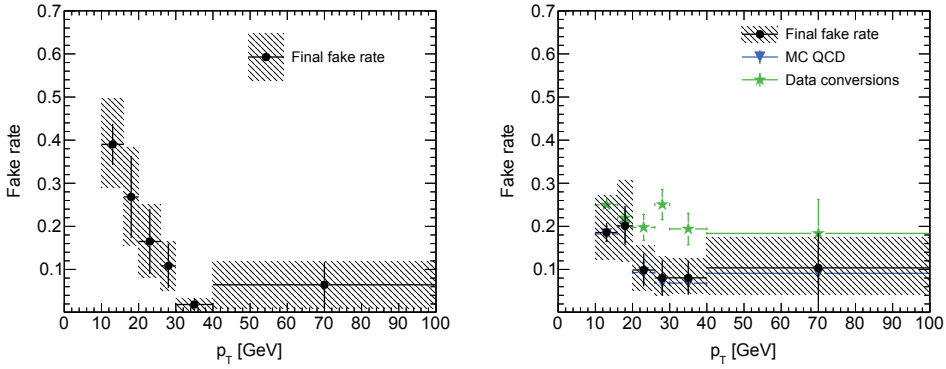

(a) Muons (b) Electrons

Figure 7.12: The final fake rate used for muons (left) and electrons (right). For electrons the fake rate is a weighted average of the bin-wise data-driven conversion fake rate (green) and the MC-based QCD fake rate (blue). The error bars on the final fake rate is the statistical error (which includes the cross section and luminosity uncertainty on MC), and the hashed area shows the total systematic and statistical uncertainties added in quadrature, where the systematic part is as summarized in Table 7.5 (Section 7.1.2.6) for the QCD component, Table 7.6 (Section 7.1.3) for the conversion component, plus for electrons a 4% systematic uncertainty on the fake rate weights detailed in Table 7.1 of Section 7.1.1.

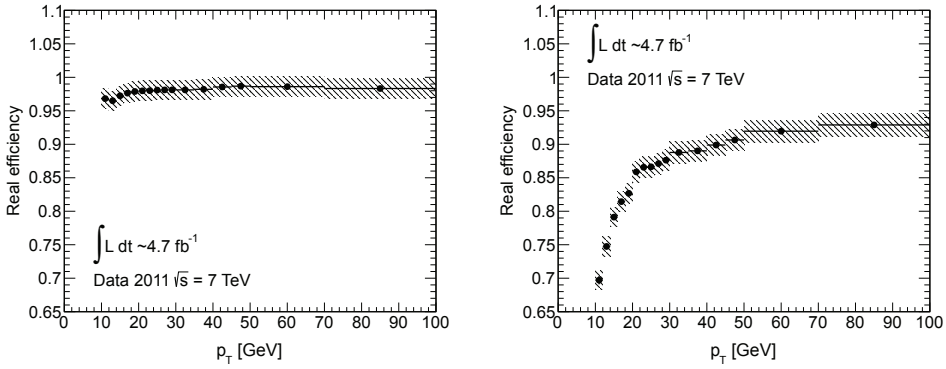

(a) Muon real efficiency versus p_T (b) Electron real efficiency versus p_T

Figure 7.13: The final real efficiency for muons (left) and electrons (right) as function of p_T. The errors bars are the statistical error only, while the hashed area represents the statistical and systematic uncertainties added in quadrature. The systematic uncertainties are detailed in Table 7.7 of Section 7.1.4.

7.1.7 Obtaining the fake lepton estimates with the Matrix Method

We have now established the real efficiencies, and the final fake rates: a combined weighted fake rate consisting of a conversion and QCD component for electrons, and only a QCD component for muons. We have also determined the most important systematic uncertainties, and

are ready to apply them to the Matrix Method.

The fake rates and efficiencies are constructed as a function of p_{T}. This means that when applying them to the Matrix Method, we determine each lepton's fake rate and efficiency according to its p_{T}. In the following I outline the procedure by using a di-muon event as an example, where both muons are exclusive loose (i.e. each muon only satisfies the baseline, and not the signal requirements), which means that in this event we measure $N_{ll} = 1$. Therefore the rather complicated expression we get after inverting the matrix 6.1 to go from the measured quantities $r,\ f, N_{ll}, N_{lT}, N_{Tl}$, and N_{TT} simplifies to only include the N_{ll} term, as all the others N-terms are 0 for this particular event. For instance for N_{LL}^{FF} we would after inverting the matrix, get

$$N_{LL}^{FF} = \frac{(1-r_1)(1-r_2)N_{TT} + r_2(r_1-1)N_{Tl} + r_1(r_2-1)N_{lT} + r_1 r_2 N_{ll}}{(r_1-f_1)(r_2-f_2)}$$

which for this exact event with two exclusive loose muons reduces to

$$N_{LL}^{FF} = \frac{(r_1 r_2)N_{ll}}{(r_1-f_1)(r_2-f_2)} = \frac{r_1 r_2}{(r_1-f_1)(r_2-f_2)}$$

where r_1, r_2, f_1 and f_2 are the real efficiencies and fake rates for the leading and sub-leading muon respectively. The other estimates N_{LL}^{FR}, N_{LL}^{RF} and N_{LL}^{RR} in this example event follow suit, and become

$$N_{LL}^{RF} = \frac{f_1 r_2}{(r_1-f_1)(r_2-f_2)}$$
$$N_{LL}^{FR} = \frac{f_2 r_1}{(r_1-f_1)(r_2-f_2)}$$
$$N_{LL}^{RR} = \frac{f_1 f_2}{(r_1-f_1)(r_2-f_2)}$$

All the terms sum up to 1 by construction: $N_{LL}^{FF} + N_{LL}^{RF} + N_{LL}^{FR} + N_{LL}^{RR} = 1$. The interpretation of the terms is that they each represent the probability of the di-lepton event to be truly fake-fake, real-fake, fake-real, or real-real respectively. The total di-lepton fake probability is the sum of the three first, i.e $N_{LL}^{fake} = N_{LL}^{RF} + N_{LL}^{FR} + N_{LL}^{FF}$. As explained in the presentation of the Matrix Method in Section 6.2, this number is given in the inclusive loose base ($_{LL}$) and must be translated into the tight-tight base ($_{TT}$) in order to give a prediction on the amount of fake signal leptons. The total fake-weight from this doubly inclusive-loose example-event is therefore

$$N_{TT}^{fake} = r_1 f_2 N_{LL}^{RF} + f_1 r_2 N_{LL}^{FR} + f_1 f_2 N_{LL}^{FF}$$

Similar expressions are then obtained for each event according to their lepton combination (N_{Tl}, N_{lT} and N_{TT}, by exchanging the relevant terms according to the matrix in Table 6.1. Summing up all events in a signal region, following the procedure outlined above, finally yields the total number of fake leptons per region.

When it comes to the statistical and systematic uncertainties, they are propagated through the matrix from the measured to the estimated quantities, and result in final statistical and systematic uncertainties on the fake lepton estimation itself.

Let us now finally turn to the validation results of the fake lepton estimation, using the semi-data driven fake rates.

7.1.8 Validation of semi data-driven fake lepton estimation

The validation is performed from all-inclusive opposite sign (OS) and same-sign (SS) events, which are control-region like at low $E_{\mathrm{T}}^{\mathrm{miss,rel}}$ and signal-region like at high $E_{\mathrm{T}}^{\mathrm{miss,rel}}$. The final signal regions in Chapter 8 in addition use several cuts to suppress background and enhance signal. These are omitted in the OS and SS regions used here.

The final fake lepton estimation ("Fake est") is shown in Figure 7.14 for the SS and in Figure 7.15 for the OS samples. The data are confronted with the total prediction which includes the SM MC (electroweak and $t\bar{t}$ in coloured histograms) and the fake estimate. For each SM MC sample, only real-real events are used, since the rest (real-fake, fake-real and fake-fake) is estimated by the MM, and are thus part of the fake estimate. The SS channel is special, as we use the Charge-Flip package to estimate the ee and $e\mu$ contribution from Z/γ^*, $t\bar{t}$, and $W^{\pm}W^{\mp}$, and not the usual SM MC. The error on the total prediction includes the statistical error and systematic error on cross section and luminosity for MC, and the total statistical and systematic uncertainty from the fake lepton estimation, added in quadrature.

The p_{T} distribution of the leading lepton, and the $E_{\mathrm{T}}^{\mathrm{miss,rel}}$ distribution are plotted separately for each lepton flavour combination $\mu\mu$, ee, and $e\mu$. Note that the p_{T} distributions are shown for events with $E_{\mathrm{T}}^{\mathrm{miss,rel}} > 40$ GeV only. This is in order to give a fair validation of results, given that the fake rates are extracted from the intermediate $E_{\mathrm{T}}^{\mathrm{miss,rel}}$ region 40-100 GeV, and not expected to completely accommodate values below this.

Figures 7.14 and 7.15 demonstrate that the fake lepton estimation gives excellent agreement between data and the total prediction in all channels, over all p_{T}, and all but the very first bins of $E_{\mathrm{T}}^{\mathrm{miss,rel}}$. By comparing the two sets of plots, the fake lepton estimation is significantly more important in the SS region compared to the OS, also the OS $e\mu$ channel contains a fair amount of fake leptons. In OSSF channels the contribution is more or less negligible, due to the very large contribution of real opposite sign leptons from Z/γ^* and $t\bar{t}$.

The fake estimation described so far in this chapter, and as published in [134] does as demonstrated, a very good job in describing the fake lepton contribution. However, a wish to be completely data-driven has resulted in the next section, which redoes the estimation using many of the elements already described, but in particular extracts also the QCD fake rate from data. All MC studies performed up to now are mainly used to validate the fully data-driven method, and help extract some of the systematic uncertainties.

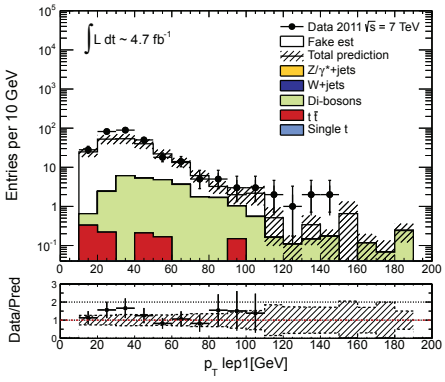

(a) $\mu\mu$ SS $E_{\mathrm{T}}^{\mathrm{miss,rel}} > 40$ GeV

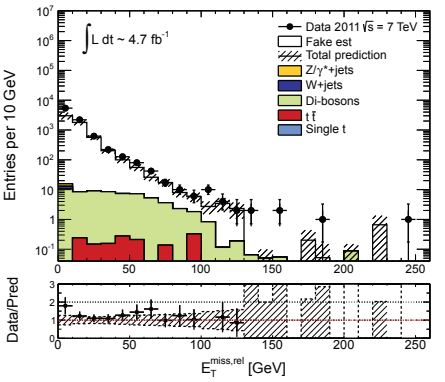

(b) $\mu\mu$ SS

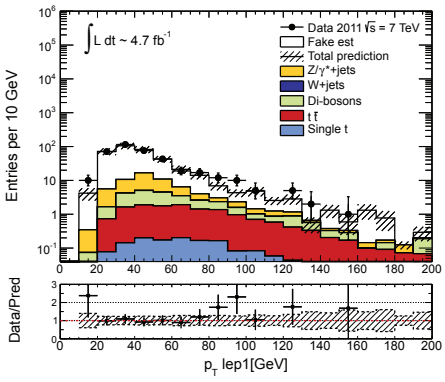

(c) ee SS $E_{\mathrm{T}}^{\mathrm{miss,rel}} > 40$ GeV

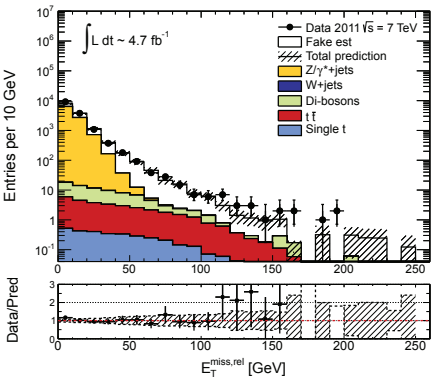

(d) ee SS

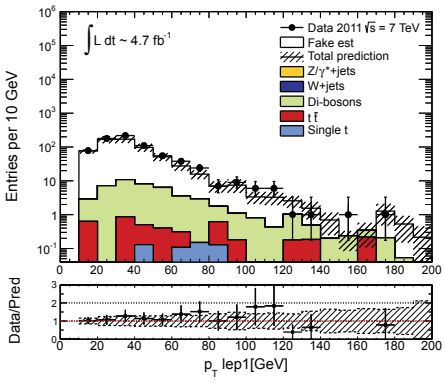

(e) $e\mu$ SS $E_{\mathrm{T}}^{\mathrm{miss,rel}} > 40$ GeV

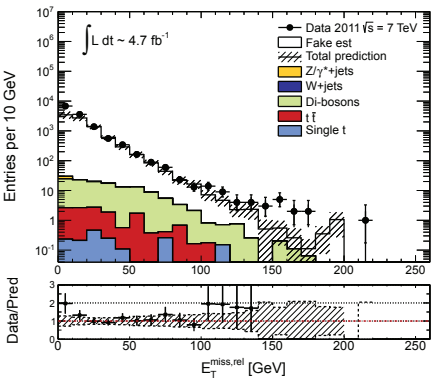

(f) $e\mu$ SS

Figure 7.14: The p_{T} of the leading lepton (left) and $E_{\mathrm{T}}^{\mathrm{miss,rel}}$ (right) in SS events, for $\mu\mu$ (top), ee (middle) and $e\mu$ (bottom). In the emu channel the leading lepton can be either the electron or the muon. A $E_{\mathrm{T}}^{\mathrm{miss,rel}} > 40$ GeV cut is applied to the p_{T} distribution.

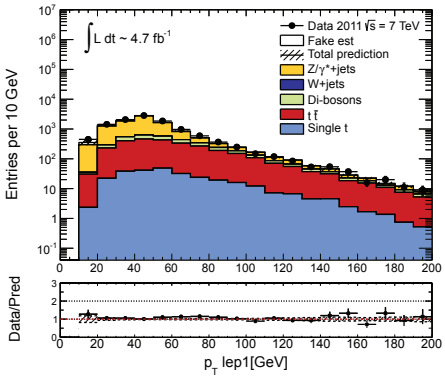

(a) $\mu\mu$ OS $E_{\mathrm{T}}^{\mathrm{miss,rel}} > 40$ GeV

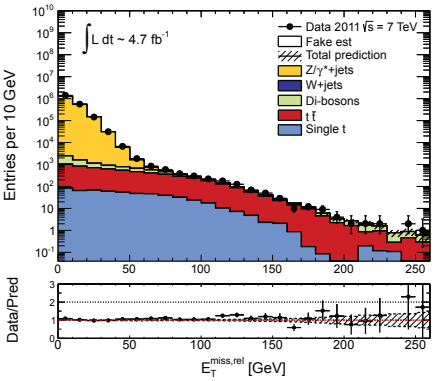

(b) $\mu\mu$ OS

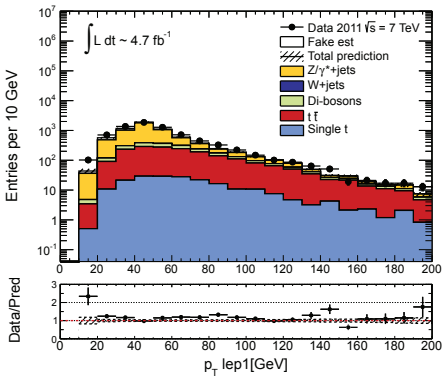

(c) ee OS $E_{\mathrm{T}}^{\mathrm{miss,rel}} > 40$ GeV

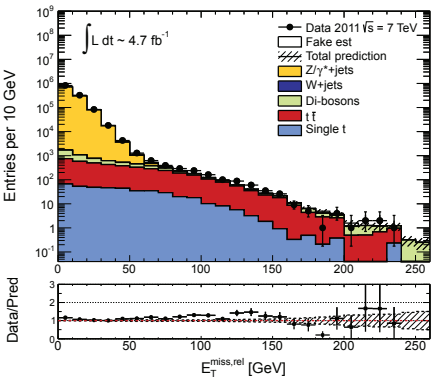

(d) ee OS

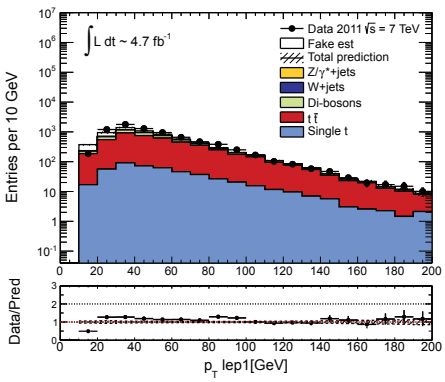

(e) $e\mu$ OS $E_{\mathrm{T}}^{\mathrm{miss,rel}} > 40$ GeV

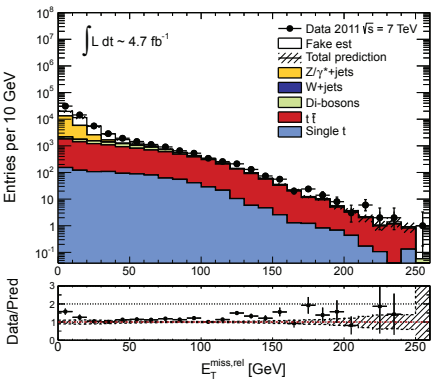

(f) $e\mu$ OS

Figure 7.15: The p_{T} of the leading lepton (left) and $E_{\mathrm{T}}^{\mathrm{miss,rel}}$ (right) in OS events, for $\mu\mu$ (top), ee (middle) and $e\mu$ (bottom). In the emu channel the leading lepton can be either the electron or the muon. A $E_{\mathrm{T}}^{\mathrm{miss,rel}} > 40$ GeV cut is applied to the p_{T} distribution.

7.2 Fully data-driven fake lepton background estimation

In this section I perform the fake lepton estimation using the Matrix Method as in the previous chapter, but instead of using the intermediate $E_{\mathrm{T}}^{\mathrm{miss,rel}}$ MC-based QCD fake rates, I use the fake rates from the data QCD control regions. The motivation for previously using the MC based fake was to be less sensitive to the strong $E_{\mathrm{T}}^{\mathrm{miss,rel}}$ dependency found particularly at low $E_{\mathrm{T}}^{\mathrm{miss,rel}}$. Here I instead incorporate the $E_{\mathrm{T}}^{\mathrm{miss,rel}}$ dependency into the data fake-rate by constructing a p_{T} and $E_{\mathrm{T}}^{\mathrm{miss,rel}}$ dependent rate. The procedure to do so is explained in the following.

7.2.1 Data-driven fake rates and real efficiencies

I take advantage of the studies in the previous chapter, and use the data-driven real p_{T} dependent efficiencies and conversion fake rate determined and validated there, including the systematic uncertainties derived. These were presented in Figure 6.5 (real efficiency) and Figure 6.27 (conversion fake rate).

For the QCD fake rate I use the p_{T} dependent fake rates from CR-B, validated in the previous chapter. These muon and electron fake rate distributions are repeated in Figure 7.16 for clarity. Here only statistical errors are included, as the systematic errors are discussed later in this section. An important aspect with CR-B is that it targets both heavy and light flavour lepton fakes, as opposed to CR-C which targets the heavy flavour component only. The di-lepton control region CR-B is favoured over the single lepton CR-A, since we in the previous chapter saw a better agreement between data and MC for CR-B.

The electron fake rate is as before constructed from the combined weighted conversion and QCD fake rates (Figures 6.27 and 7.16 (b) respectively) (except omitting the data/MC scale

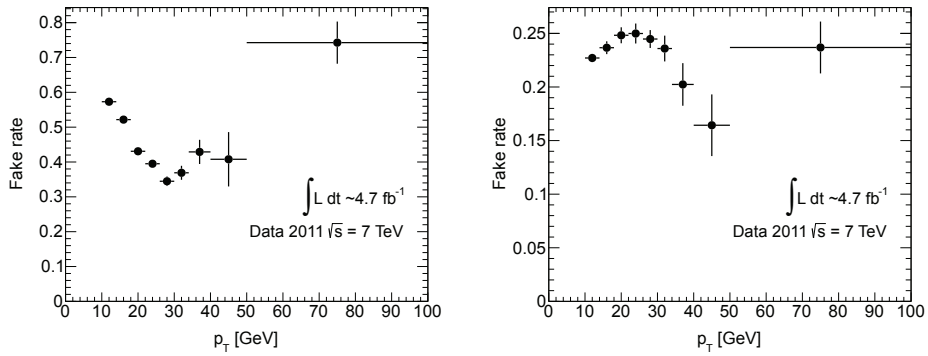

(a) Muons (b) Electrons

Figure 7.16: Data-driven QCD fake rate for muons (left) and electrons (right). CR-B R02 and R07 is used for the muon and electron channel respectively, which were found to be the optimal control regions within CR-B, see Section 6.4.1 for details, and Table 6.3 which presented the control region cuts. Errors are purely statistical.

factor) by

$$\mathrm{f}_{\mathrm{e}}^{\mathrm{FIN}}(p_{\mathrm{T}}) = \sum_{i=\mathrm{QCD,conv}} \mathrm{f_i}(p_{\mathrm{T}}) \cdot \mathrm{w_i}(p_{\mathrm{T}}) \tag{7.3}$$

where we again sum over fake-types i, here QCD and conversions, w_i is the relative amount of fakes of type i (the weights) as a function of p_{T}, and f_i the fake rate for fakes of type i, also a function of p_{T}. We apply the exact same (MC-based) weights as described in the semi data-driven method, and which were presented in Figure 7.3 in Section 7.1.1. The weights must also for this fully data-driven approach, be extracted from MC, as we need access to the overall normalization of QCD and conversion electrons respectively. This can not be obtained straight from data, since we would have to use separate control regions to effectively select QCD or conversion electrons respectively, which in no way can give information about the relative contribution of the two. However, as explained in Section 7.1.1, the overall normalization is taken from data. Again we assume the same weights for all signal regions, and hence the same f^{FIN} for all signal regions. Note that as opposed to the corresponding weighted fake rate in the semi data-driven approach Equation (7.1), we here do not operate with any scale factor s_i, as all fake rates are taken from data.

The final electron and muon fake rate including systematic and statistical errors follow at the end of Section 7.2.3, after the systematic uncertainties have been addressed. In the following section I describe the most important part of this data-driven approach, namely how to take into account the $E_{\mathrm{T}}^{\mathrm{miss,rel}}$ dependency.

7.2.2 Data-driven $E_{\mathrm{T}}^{\mathrm{miss,rel}}$ dependency

Figure 7.17 shows the fake rate versus $E_{\mathrm{T}}^{\mathrm{miss,rel}}$ for SS muons and electrons, after statistical subtraction of real (and conversion) leptons. In the electron channel the Z-veto ($|m_{ll}-m_Z| < 10$ GeV) removes the bulk of the charge-flip events. Otherwise no other cuts are applied[3]. Since the high $E_{\mathrm{T}}^{\mathrm{miss,rel}}$ region coincides with the SUSY signal regions, and in principle could contain signal leptons, we do not use these data points when extrapolating from low to high $E_{\mathrm{T}}^{\mathrm{miss,rel}}$ values. This is illustrated with the hatched area from 40 GeV and up. However, by fitting the bins below 40 GeV only, and using the resulting fit function to extrapolate to higher $E_{\mathrm{T}}^{\mathrm{miss,rel}}$ values, we achieve a fake rate versus $E_{\mathrm{T}}^{\mathrm{miss,rel}}$ for the whole energy range, without the fit being biased by the signal region. The fit is performed using a sum of an exponential and a constant, to account for the exponential fall at low $E_{\mathrm{T}}^{\mathrm{miss,rel}}$, but still allow for a flattening at higher $E_{\mathrm{T}}^{\mathrm{miss,rel}}$. The chosen fit-function is motivated by the corresponding fake rates in MC in Figure 7.18 where the target QCD leptons are selected by the help of truth. Here we see a clear flattening at high $E_{\mathrm{T}}^{\mathrm{miss,rel}}$. As thoroughly explained and studied in connection with Figure 6.18 (Section 6.4.1.4), the increase in data at high $E_{\mathrm{T}}^{\mathrm{miss,rel}}$ is probably due to inefficiencies in the real lepton statistical subtraction, and not an actual behaviour of the fake leptons themselves. Both in the muon and electron channel the fit follows the bins below 40 GeV satisfactorily.

[3] Or said in another way, these are CR-B R02 and R07 control regions for muons and electrons respectively, but omitting the $E_{\mathrm{T}}^{\mathrm{miss,rel}}$ cut.

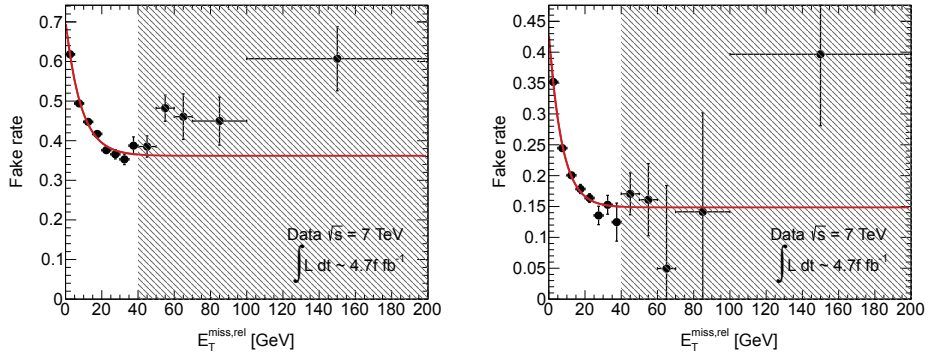

(a) Muons (b) Electrons

Figure 7.17: The muon (left) and electron (right) data QCD fake rate versus $E_{\mathrm{T}}^{\mathrm{miss,rel}}$, and a fit (red) exploiting only the data points up until 40 GeV. A combined exponential and constant fit-function is used for both lepton flavours.

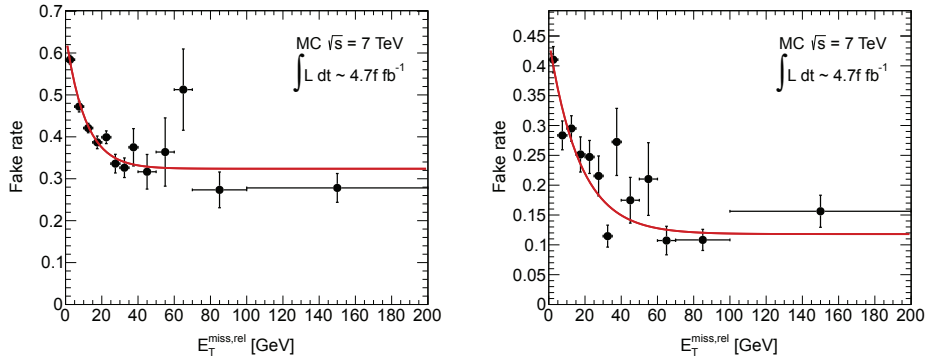

(a) Muons (b) Electrons

Figure 7.18: The MC muon (left) and electron (right) fake rate versus $E_{\mathrm{T}}^{\mathrm{miss,rel}}$, using the same fit-function (red) as the data. All data points are included in the fit in case of QCD MC.

To actually account for the $E_{\mathrm{T}}^{\mathrm{miss,rel}}$ as well as the p_{T} dependency, we construct a "quasi" 2D p_{T}, $E_{\mathrm{T}}^{\mathrm{miss,rel}}$ dependent fake rate, by scaling $f(p_{\mathrm{T}})$ by a factor given by the $f(E_{\mathrm{T}}^{\mathrm{miss,rel}})$. This assumes that the shape of $f(p_{\mathrm{T}})$ is independent of $E_{\mathrm{T}}^{\mathrm{miss,rel}}$, since the scaling procedure just shifts the whole p_{T} dependent fake rate up or down as Figure 7.19 shows. Appendix C.9 shows that this is a reasonable assumption, and that we can assign a 10% systematic uncertainty on the scaling procedure, which is summarized in Table 7.9 as "$E_{\mathrm{T}}^{\mathrm{miss,rel}}$ scaling".

The actual procedure is as follows: For each event a scale factor (sf_{MET}) is first calculated

based on the $E_{\mathrm{T}}^{\mathrm{miss,rel}}$ dependent fake rate, here denoted $f(E_{\mathrm{T}}^{\mathrm{miss,rel}})$:

$$sf_{MET} \quad = \quad f^{\text{QCD-CR}}\left(E_{\mathrm{T}}^{\mathrm{miss,rel}}\right) / f^{\text{QCD-CR}}\left(\text{avg}\right) \,,$$

which says that the scale factor sf_{MET} is the ratio of the fake rate in the current $E_{\mathrm{T}}^{\mathrm{miss,rel}}$ bin $f\left(E_{\mathrm{T}}^{\mathrm{miss,rel}}\right)$ divided by the integrated (average) fake rate from the data control regions $f^{\text{QCD-CR}}\left(\text{avg}\right)$ (which are CR-B R02 for muons and R07 for electrons) (the average fake rate is simply the total N_T/N_L ratio.). The fake rate $f\left(E_{\mathrm{T}}^{\mathrm{miss,rel}}\right)$ are taken from the fits of Figure 7.17.

The resulting factor is then applied to the fake rate corresponding to each lepton p_{T}, $f(p_{\mathrm{T}})$, also from the QCD control regions, in the following way

$$f^{\text{QCD-CR}}\left(p_{\mathrm{T}}, E_{\mathrm{T}}^{\mathrm{miss,rel}}\right) \quad = \quad f\left(p_{\mathrm{T}}\right) \cdot sf_{MET} \tag{7.4}$$

where $f^{\text{QCD-CR}}\left(p_{\mathrm{T}}, E_{\mathrm{T}}^{\mathrm{miss,rel}}\right)$ now is the p_{T} dependent fake rate from the data control region, but normalized according to the scale factor calculated above.

This effectively is a "quasi-2D" fake rate which takes into account both the p_{T} dependency and the $E_{\mathrm{T}}^{\mathrm{miss,rel}}$ dependency, denoted $f^{\text{QCD-CR}}\left(p_{\mathrm{T}}, E_{\mathrm{T}}^{\mathrm{miss,rel}}\right)$ here.

In Figure 7.19 the scaling procedure is illustrated. Here the default p_{T} based fake rate (black dots) is scaled up or down according to $E_{\mathrm{T}}^{\mathrm{miss,rel}}$, following the procedure outlined above. The different colours represent a different bin in the $E_{\mathrm{T}}^{\mathrm{miss,rel}}$ fit. This is shown in the legend together with the resulting scale factor. As the figure (and legend) shows it is only the lowest $E_{\mathrm{T}}^{\mathrm{miss,rel}}$ bins that result in a scale factor above 1, therefore most of the scaled p_{T} dependent fake rate is scaled down. This agrees well with what we have seen in the previous chapter. The intermediate $E_{\mathrm{T}}^{\mathrm{miss,rel}}$ fake rate is generally lower than the fake rates from the low $E_{\mathrm{T}}^{\mathrm{miss,rel}}$ control regions. The strength of this method is however, that the low $E_{\mathrm{T}}^{\mathrm{miss,rel}}$ regions are now also accounted for, and we thus expect a good fake lepton estimation over the whole $E_{\mathrm{T}}^{\mathrm{miss,rel}}$ range.

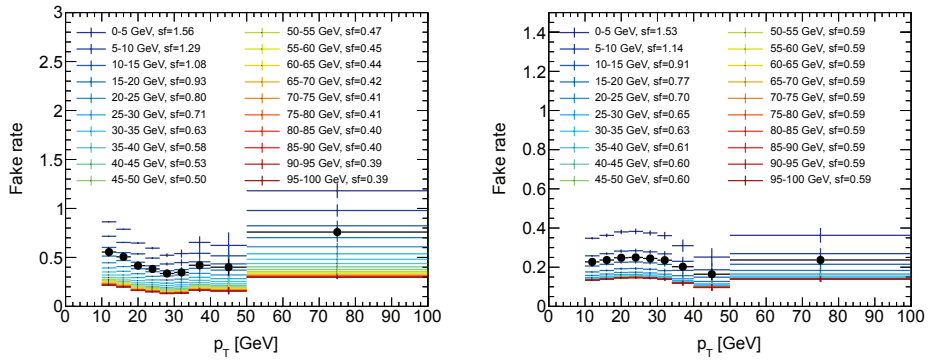

(a) Muons (b) Electrons

Figure 7.19: The muon (left) and electron (right) fake rate versus p_{T}, normalized according to various values of $E_{\mathrm{T}}^{\mathrm{miss,rel}}$, given as bin-wise scale-factors shown in the legend.

7.2.3 Systematic uncertainties and final fake rates

The main systematic uncertainties which are relevant for this approach are the difference between control regions, and uncertainties due to real lepton subtraction from MC, and other unknown effects discussed in Section 6.4.1.5 possibly explaining the raise of the muon fake rate distribution at high p_{T} and $E_{\mathrm{T}}^{\mathrm{miss,rel}}$. Since the $E_{\mathrm{T}}^{\mathrm{miss,rel}}$ dependency is taken into account this automatically accounts for (at least part of) the difference in composition between the control region (low $E_{\mathrm{T}}^{\mathrm{miss,rel}}$) and the signal region (high $E_{\mathrm{T}}^{\mathrm{miss,rel}}$). However, the uncertainty on the $E_{\mathrm{T}}^{\mathrm{miss,rel}}$ dependency itself is taken into account, and is described in the following.

As mentioned there can be several reasons why in particular the muon data fake rate increases with $E_{\mathrm{T}}^{\mathrm{miss,rel}}$ (see discussion Section 6.4.1.5). We do as discussed expect a behaviour more like in MC where the rate flattens after about 40 GeV. The fit in Figure 7.17 reflects this expectation. However, we take into account the difference seen in data and the fit distribution at high $E_{\mathrm{T}}^{\mathrm{miss,rel}}$, by assigning it as a systematic uncertainty. A possible explanation is that the rise stems (partly) from the statistical real lepton removal which is not 100% efficient. The uncertainty is evaluated by taking the absolute difference between the nominal fake rate value and the fit value, bin by bin, but taking into account the statistical error, to not double-count. When ignoring outliers, we arrive to a total systematic uncertainty of 7% in the muon channel, and 0% in the electron channel, as the deviations in the latter are within statistical uncertainties. These are listed in Table 7.9 under "statistical subtr". The procedure is detailed in Appendix C.8.

Furthermore, to account for uncertainties on the $E_{\mathrm{T}}^{\mathrm{miss,rel}}$ scaling procedure itself, the fake rate versus p_{T} is evaluated in bins of $E_{\mathrm{T}}^{\mathrm{miss,rel}}$, and compared. The assumption is that the shape

Uncertainty on the data-driven hadronic fake rate					
	Muons		Electrons		
Description	Up [%]	Down [%]	Up [%]	Down [%]	Reference
1L vs SS	< 1	8.0	8.0	< 1	Sec. 7.1.2.5
statistical subtr.	7.0	7.0	< 1	< 1	App. C.8
$E_{\mathrm{T}}^{\mathrm{miss,rel}}$ scaling	10.0	10.0	10.0	10.0	App. C.9
Total σ	12.2	14.6	12.8	10.0	
Uncertainty on the data-driven conversion fake rate					
	Muons		Electrons		
Description	Up [%]	Down [%]	Up [%]	Down [%]	Reference
Total σ	< 1	< 1	10.0	10.0	Sec. 7.1.3
Uncertainty on the data-driven real efficiency					
	Muons		Electrons		
Description	Up [%]	Down [%]	Up [%]	Down [%]	Reference
Total σ	1.5	1.5	1.5	1.5	Sec. 7.1.4, Fig. 7.11

Table 7.9: The systematic uncertainties assigned to the data-driven p_{T},$E_{\mathrm{T}}^{\mathrm{miss,rel}}$ dependent fake rate. The values are in percent.

of the fake rate versus p_T does not change significantly. I find a 10% effect, which is taken as the systematic uncertainty for the scaling approach, see the "$E_T^{miss,rel}$ scaling" item in Table 7.9, and Appendix C.9 for details.

The difference between the single lepton control region CR-A, and the same-sign control region CR-B was evaluated in the previous chapter and found to be 8% in both channels. This was shown in Figure 7.10 in Section 7.1.2.5, with average ratios CR-B/CR-A of 0.92 in the muon channel and 1.08 in the electron channel. Therefore the uncertainty is here applied downward for muons and upwards for electrons.

The final systematic uncertainties are summarized in Table 7.9, where I also repeat the systematic uncertainty for the real efficiency already discussed in Section 7.1.4 (excluding the data/MC agreement uncertainty), and the conversion fake rate systematics discussed in Section 7.1.3. Note that no explicit uncertainty on the MC cross section and luminosity is included in the table, since this is already accounted for in the real (and conversion) lepton statistical subtraction of the data fake rate.

In addition to the summarized uncertainties, comes the uncertainty on the QCD and conversion weights in the electron channel (4% as described in Section 7.1.1). This uncertainty is included in the final fake rate by propagating it through Equation (7.3).

The resulting fake rates including statistical and systematic errors are plotted in Figure 7.20 as a function of p_T, for muons and electrons respectively. As explained in Section 7.2.2, for each event $f(p_T)$ is scaled according to the $E_T^{miss,rel}$, which is not shown explicitly here, but it was however shown in Figure 7.19 (without final uncertainties). Together with the real efficiencies of Figure 7.13, we now have what we need to calculate the fake estimates in a fully data-driven

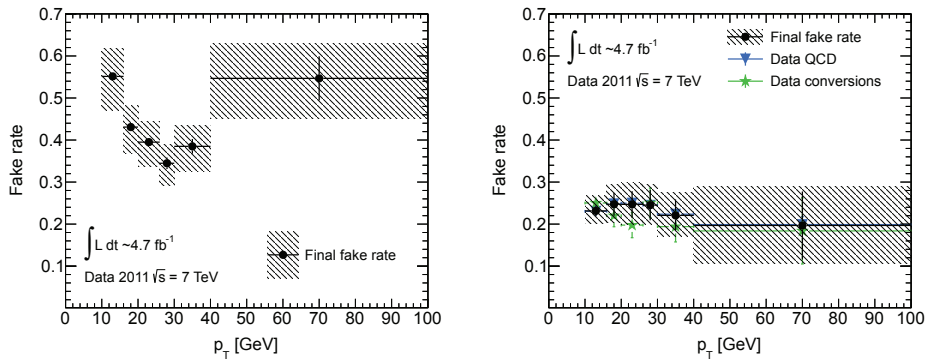

(a) Muons (b) Electrons

Figure 7.20: The p_T dependent fake rate used for muons (left) and electrons (right). For electrons the fake rate is a weighted average of the bin-wise conversion fake rate (green) and the QCD fake rate (blue). The error bars on the final fake rate are the statistical error, plus the propagated error on MC cross section and luminosity from the statistical subtraction of the real (and conversion) leptons. The hashed area shows the total systematic and statistical uncertainties added in quadrature, where the systematic part is as detailed in Table 7.9

way, which the next section presents.

7.2.4 Validation of the fully data-driven fake lepton estimation

The fake lepton contribution in OS and SS events are calculated as usual, inverting the matrix in Table 6.1 event-by-event, using the real efficiencies (Figure 7.13) and fake rates (Figure 7.20) for each of the leptons, to obtain the fake lepton estimate for that event. For details on the event-by-event estimation and inversion of the matrix, see Section 7.1.7. We use p_{T} dependent fake rates, which are scaled event-by-event according to the $E_{\mathrm{T}}^{\mathrm{miss,rel}}$ dependency, as explained in Section 7.2.2.

Figures 7.21 and 7.22 show the fake lepton estimation together with the SM MC prediction and data for SS and OS events respectively. These are the same SS and OS events used for the semi data-driven approach, inclusive in $E_{\mathrm{T}}^{\mathrm{miss,rel}}$, thus are control-region like at low $E_{\mathrm{T}}^{\mathrm{miss,rel}}$ and signal-region like at high $E_{\mathrm{T}}^{\mathrm{miss,rel}}$. The uncertainty on the total prediction includes statistical uncertainty on the MC, and the uncertainty due to luminosity and cross section, in addition to the statistical and full systematic uncertainty on the fake lepton estimation. Errors are added in quadrature. The p_{T} distribution for the hardest lepton, and the $E_{\mathrm{T}}^{\mathrm{miss,rel}}$ are plotted, for each of the channels separately ($\mu\mu$, ee, and $e\mu$). We see an excellent agreement for both OS and SS events, and in all channels, over the whole p_{T} and $E_{\mathrm{T}}^{\mathrm{miss,rel}}$ range.

Now that the good performance of the data-driven estimates has been demonstrated, let us compare with the semi data-driven results in Section 7.1.8.

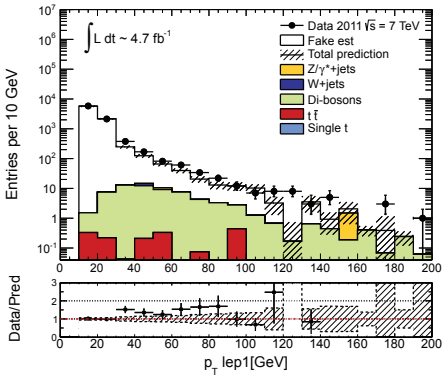

(a) $\mu\mu$ SS

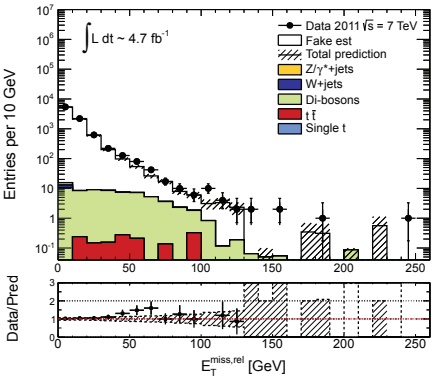

(b) $\mu\mu$ SS

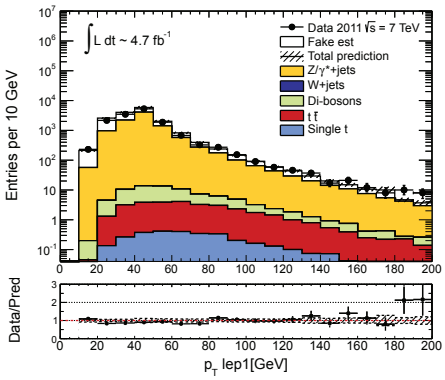

(c) ee SS

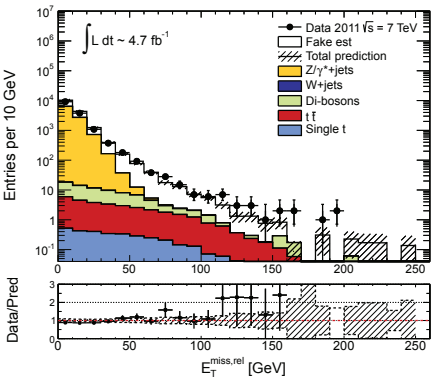

(d) ee SS

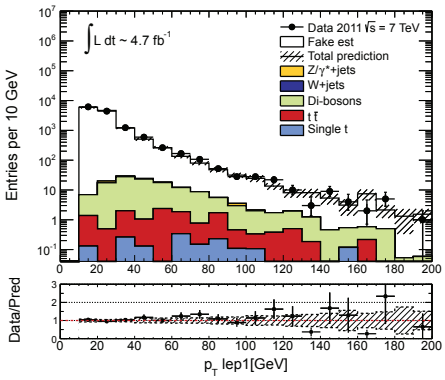

(e) e μ SS

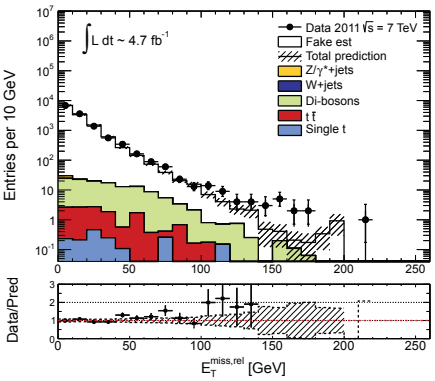

(f) e μ SS

Figure 7.21: The p_{T} of the leading lepton (left) and $E_{\mathrm{T}}^{\mathrm{miss,rel}}$ (right) in SS events, for $\mu\mu$ (top), *ee* (middle) and $e\mu$ (bottom) with full SM MC, and using the fully data-driven method to estimate the fakes. The electron charge-flip component in SS events is estimated using the Charge-flip package. In the $e\mu$ channel the leading lepton can be either the electron or the muon.

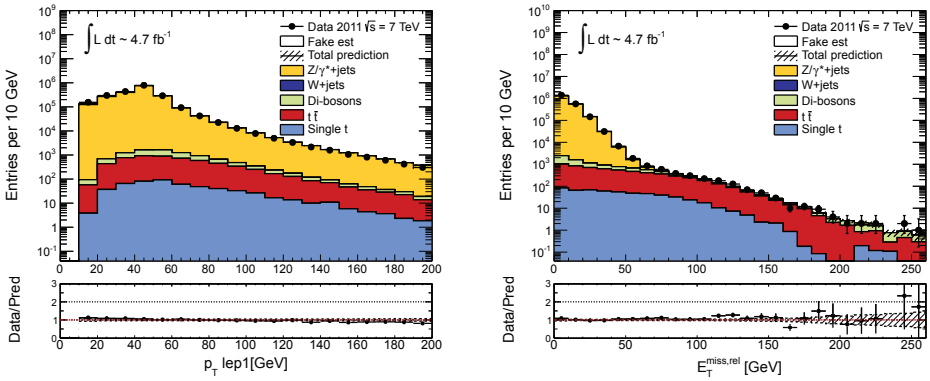

(a) $\mu\mu$ OS (b) $\mu\mu$ OS

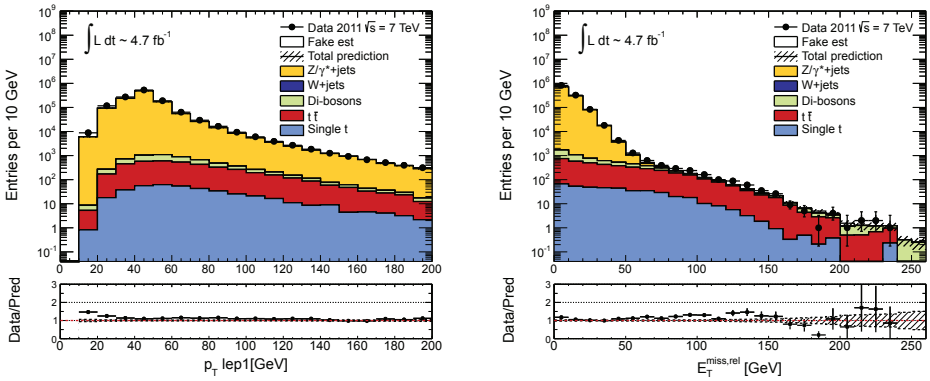

(c) ee OS (d) ee OS

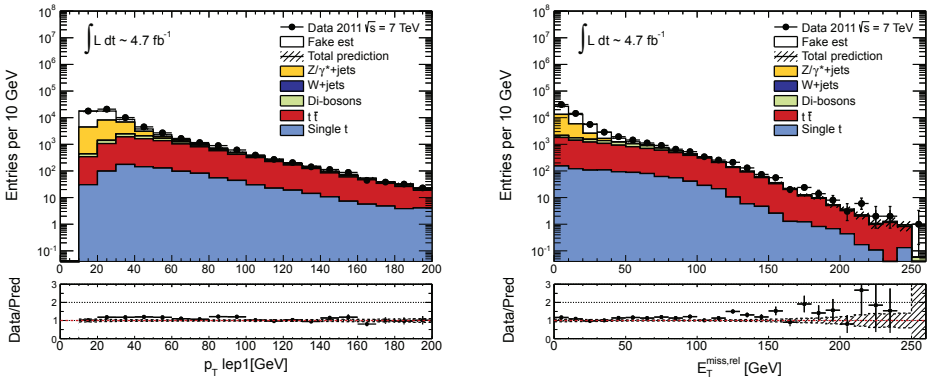

(e) e μ OS (f) e μ OS

Figure 7.22: The p_{T} of the leading lepton (left) and $E_{\mathrm{T}}^{\mathrm{miss,rel}}$ (right) in OS events, for $\mu\mu$ (top), ee (middle) and $e\mu$ (bottom) with full SM MC, and using the fully data-driven method to estimate the fakes. The electron charge-flip component in OS events is estimated using the Charge-flip package. In the $e\mu$ channel the leading lepton can be either the electron or the muon.

7.3 Comparison of data and MC agreement using the two fake lepton estimation methods

In Figures 7.23 and 7.24, the semi data-driven and fully data-driven fake lepton estimations are compared side-by-side, again using inclusive $E_{\mathrm{T}}^{\mathrm{miss,rel}}$ OS and SS events. As before the total prediction is plotted and compared to data, with the same treatment of statistical and systematic uncertainties as already discussed in Sections 7.1.8 and 7.2.4. I only show SS distributions since for the sake of comparison they are more illuminating than OS, where the fake leptons contribute to a much smaller degree.

In general we see that the fully data-driven estimation yields a smaller total uncertainty. This is obvious when comparing the systematic tables of the two approaches Tables 7.5 and 7.9. In the semi data-driven approach the largest error is on the $E_{\mathrm{T}}^{\mathrm{miss,rel}}$ dependency, and this error is greatly reduced in the fully data-driven approach, since the dependency is taken into account by constructing the joint p_{T} and $E_{\mathrm{T}}^{\mathrm{miss,rel}}$ dependent fake rate as discussed. We in particular see that the fully data-driven approach more successfully reproduces data at low p_{T} and $E_{\mathrm{T}}^{\mathrm{miss,rel}}$ compared to the semi data-driven approach. However, both approaches do equally well at high $E_{\mathrm{T}}^{\mathrm{miss,rel}}$, which is the most important for the SUSY searches.

With both procedures well validated, let us turn to the application of the fake lepton estimation in the signal regions. The next chapter presents the full Standard Model prediction in the final signal regions, and interprets the results in the simplified and DGemt SUSY models.

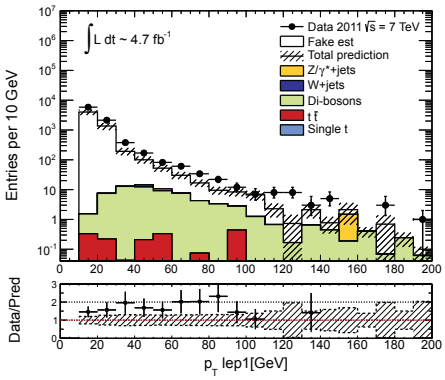

(a) $\mu\mu$ SS semi data-driven

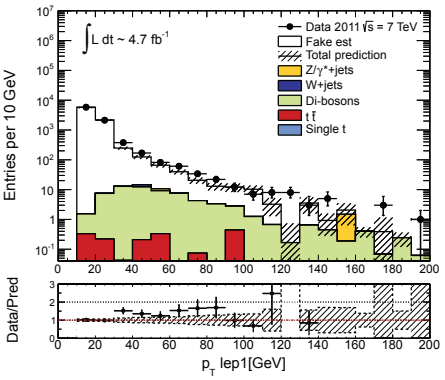

(b) $\mu\mu$ SS fully data-driven

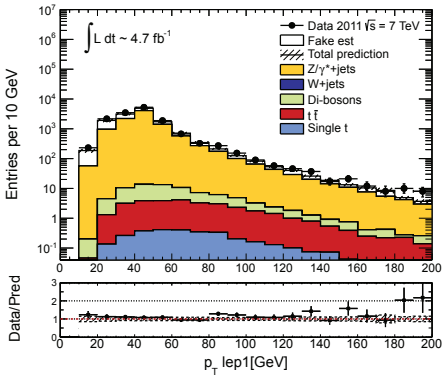

(c) Semi data-driven ee SS

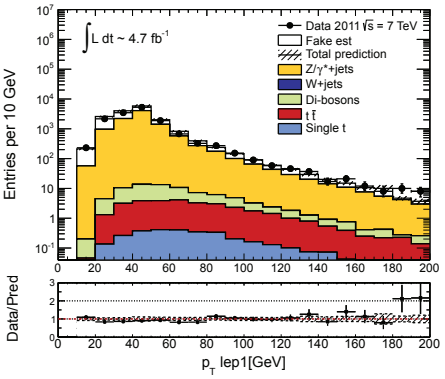

(d) Fully data-driven ee SS

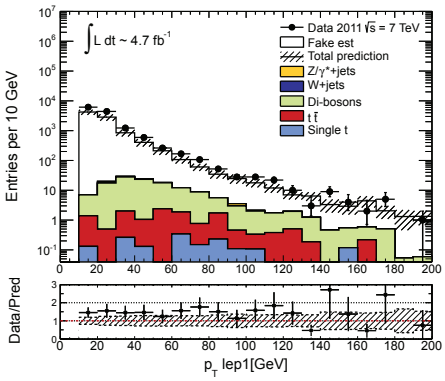

(e) Semi data-driven $e\mu$ SS

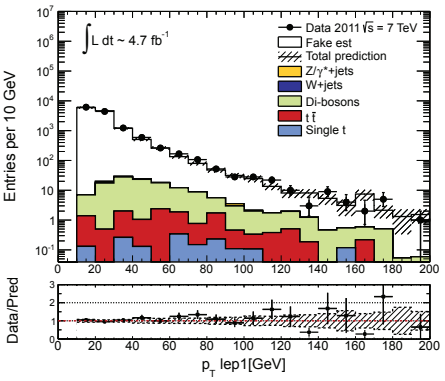

(f) Fully data-driven $e\mu$ SS

Figure 7.23: The p_{T} of the leading lepton in SS $\mu\mu$ (top), ee (middle), and $e\mu$ (bottom) events for data and MC plus the fake lepton estimation, using the semi data-driven procedure (left) and the fully data-driven procedure (right).

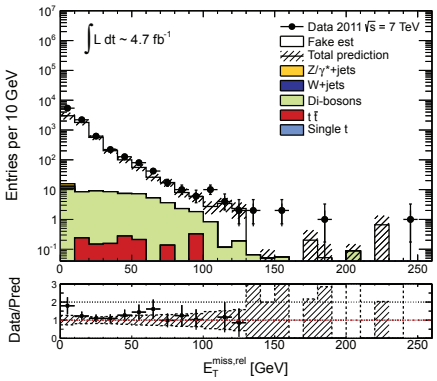

(a) $\mu\mu$ SS semi data-driven

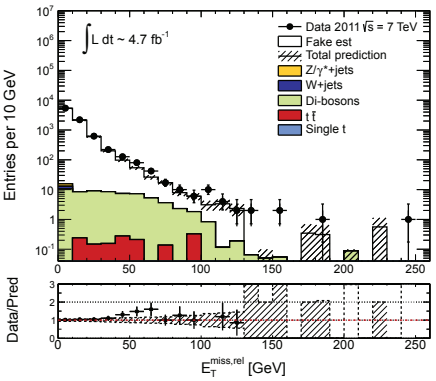

(b) $\mu\mu$ SS fully data-driven

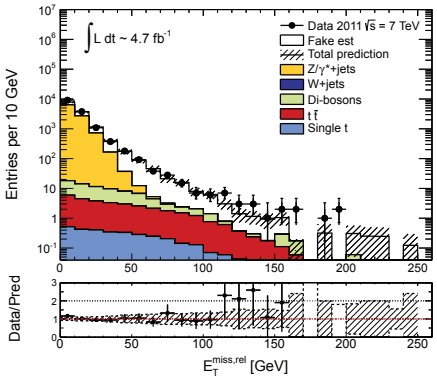

(c) Semi data-driven ee SS

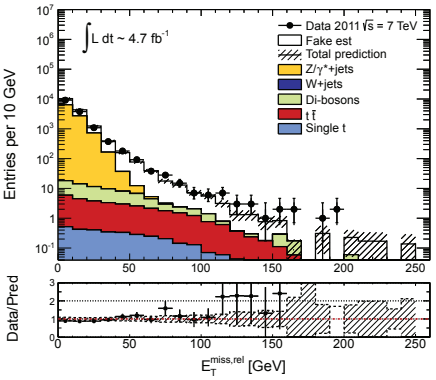

(d) Fully data-driven ee SS

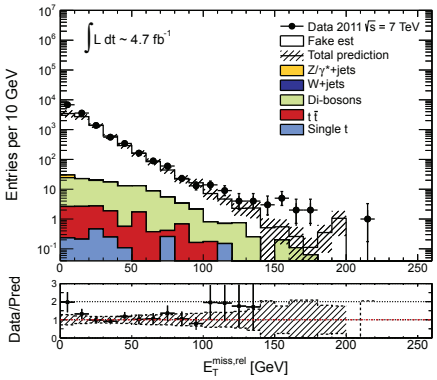

(e) Semi data-driven $e\mu$ SS

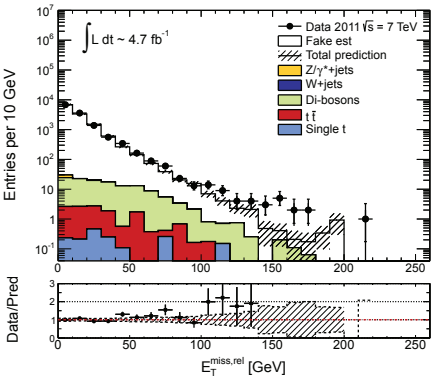

(f) Fully data-driven $e\mu$ SS

Figure 7.24: The $E_{\mathrm{T}}^{\mathrm{miss,rel}}$ in data and MC plus fake lepton estimation using the semi data-driven procedure (left) and the fully data-driven procedure (right) in SS $\mu\mu$ (top), ee (middle), and $e\mu$ events.

Chapter 8

Search for direct gauginos and sleptons in di-lepton final states

In this chapter the final signal region cuts are applied on data to search for hints of a SUSY signal. The results from the Matrix Method fake estimation performed in previous chapters, are combined with the MC predictions of the electroweak background, and the charge-flip contribution from the ChargeFlip package, to yield the total (SM) background prediction.

I first use the semi data-driven estimate of the fake lepton background (detailed in Section 7.1) to compare data and the SM background prediction, and perform the statistical analysis. Then in Section 8.2 as input to the SM background, the fake lepton estimation gained using the fully data-driven fake lepton is used (detailed in Section 7.2).

All fake leptons are estimated with the Matrix Method, and mainly involve W, single top (except the Wt channel), and jet processes, in addition to electron conversions in all processes. Backgrounds that yield exactly two (truth) real leptons are extracted directly from MC and include the di-boson (WW, WZ, ZZ), $t\bar{t}$, part of the single top (Wt), and Z/γ^* backgrounds. Truth-information is used to avoid overlap between the fake lepton estimation and the MC backgrounds. In signal region SR-SSjveto ee and $e\mu$ channels, the SM backgrounds are evaluated using the charge-flip estimation, except ZZ and WZ contributions which are taken directly from MC (as these processes do not contain Charge-Flip), and as usual the fake leptons are estimated through the MM.

I first present the final signal region distributions, where the SUSY signal we seek is expected to show up, if it exists. This is followed by the final event yields, before giving a description of the statistical procedure used when interpreting the results in the pMSSM and simplified models. Finally I compare results using the two fake estimation methods.

8.1 SUSY search based on the semi data-driven fake lepton estimation

Figures 8.1 and 8.2 show how data and the full SM prediction compare as a function of $E_{\mathrm{T}}^{\mathrm{miss,rel}}$ for all four signal regions: SR-OSjveto, SR-SSjveto, SR-2jets and SR-m_{T2} are shown. Each channel is shown separately in the following order: $\mu\mu$, ee, $e\mu$, except for SR-2jets as this signal region only includes same-flavour. For an overview of the exact definition of all signal regions,

I refer to Tables 5.1 and 5.2 of Section 5.1. The statistical error on the observed number of events is the statistical Poisson limit at the 68% confidence level (CL). The total prediction includes the SM MC (which includes the charge flip contribution for SR-SSjveto) and the fake estimation. The former includes statistical errors, and systematic errors on luminosity and cross section, while the latter includes both statistical and systematic uncertainties. The dashed line defines the $E_{\mathrm{T}}^{\mathrm{miss,rel}}$ above which we search for SUSY.

We see that data agrees with the total prediction for all channels and signal regions, unfortunately as no SUSY signal is observed. As seen before, it is mainly in SS region, namely the SR-SSjveto signal region, and in all regions of the $e\mu$ channel, that the fake leptons contribute noticeably. The fake estimation does very well over most of the $E_{\mathrm{T}}^{\mathrm{miss,rel}}$ range, except for a slight underestimation in the very low $E_{\mathrm{T}}^{\mathrm{miss,rel}}$, which is as expected, as the fake rate is tailored for $E_{\mathrm{T}}^{\mathrm{miss,rel}} > 40$.

The observed number of data events in each signal region and channel are compared to the expected SM background in Table 8.1. In addition is shown the upper limit on the observed and expected SUSY cross section in both cases ($\sigma^{obs(exp)}$), which is explained in Section 8.3. The MC includes the full set of systematic uncertainties which are further discussed in Section 8.4. In SR-m_{T2} the same-flavour channels are shown separately, as different flavour combinations are not used in the direct slepton search. However, in the direct gaugino search they are, and therefore the inclusive combination (all) is also shown (as it is for the other signal regions). The total statistical and systematic errors are shown separately. We see that the number of observed data events in all channels and each signal region agrees within errors with the total prediction, and we must therefore unfortunately state that no SUSY signal is observed. We therefore set limits on the signal, but before that I present the results using the fully data-driven fake estimation, and compare the two.

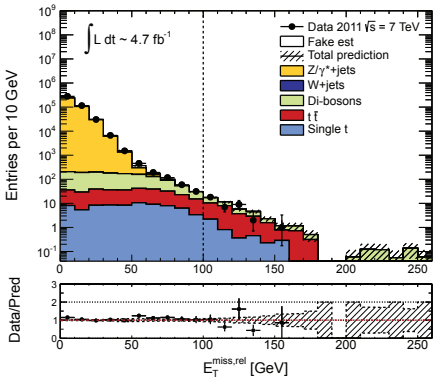

(a) $\mu\mu$ SR-OSjveto

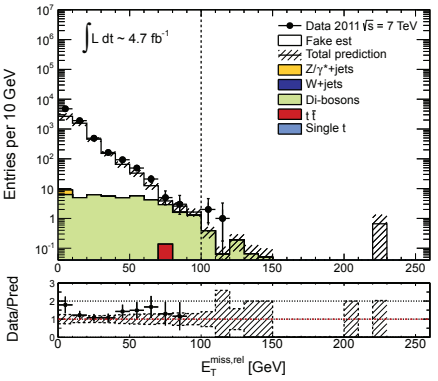

(b) $\mu\mu$ SR-SSjveto

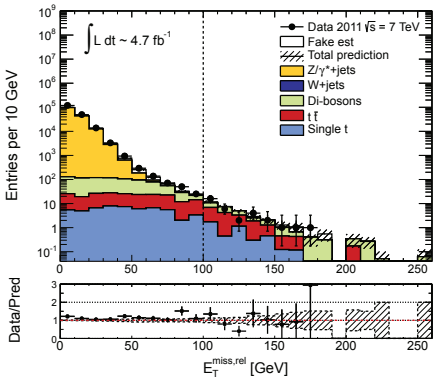

(c) ee SR-OSjveto

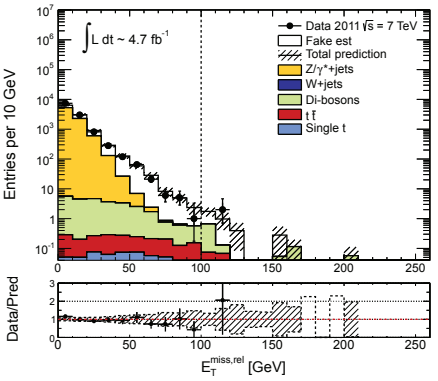

(d) ee SR-SSjveto

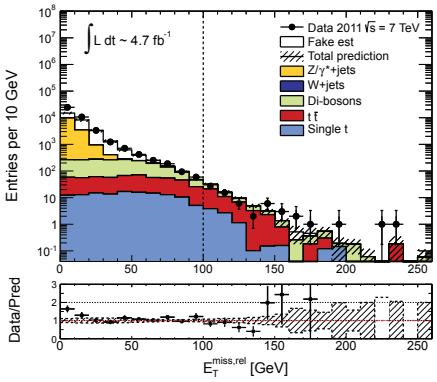

(e) $e\mu$ SR-OSjveto

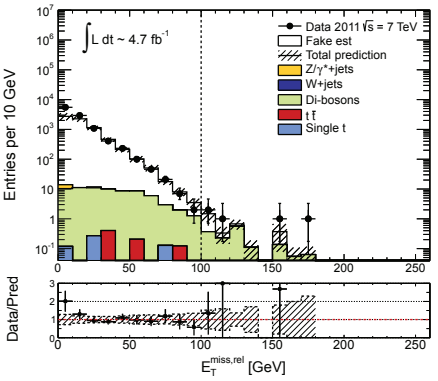

(f) $e\mu$ SR-SSjveto

Figure 8.1: Final $E_{\mathrm{T}}^{\mathrm{miss,rel}}$ distribution for the SR-OSjveto (left) and SR-SSjveto (right) signal regions: data vs total prediction made of SM MC and semi data-driven fake estimation. In SR-SSjveto, the $t\bar{t}$, single top (Wt-channel), Z/γ^*, and WW backgrounds in the ee and $e\mu$ channels are estimated using the Charge-Flip package. The dashed vertical line marks the beginning of the final signal search region.

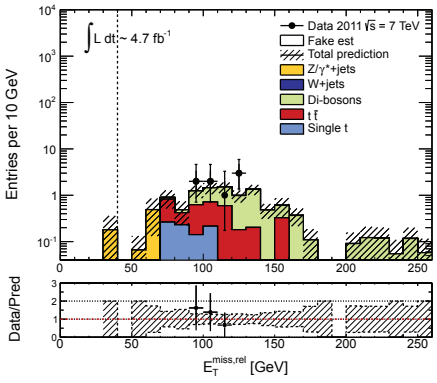

(a) $\mu\mu$ SR-m_{T2}

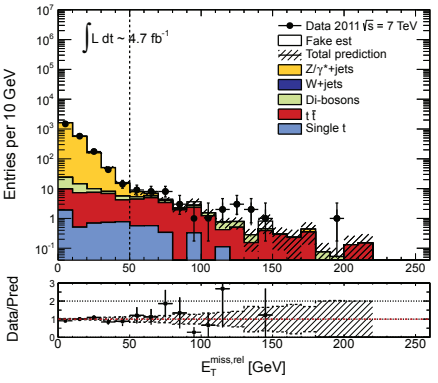

(b) $\mu\mu$ SR-2jets

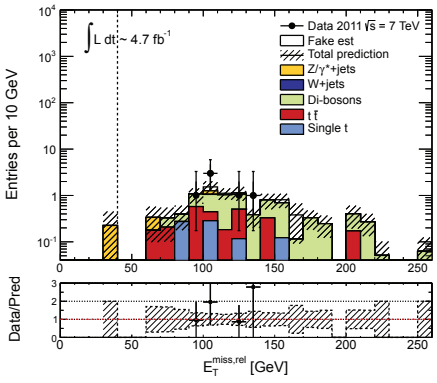

(c) ee SR-m_{T2}

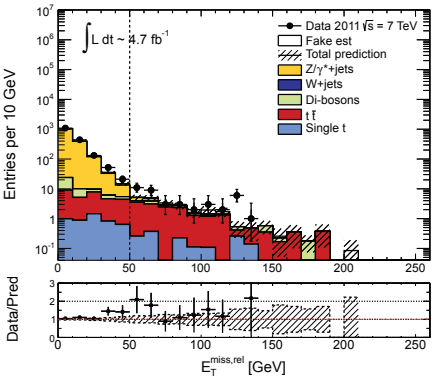

(d) ee SR-2jets

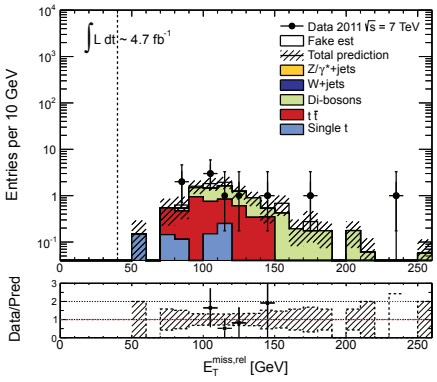

(e) $e\mu$ SR-m_{T2}

Figure 8.2: Final $E_{\mathrm{T}}^{\mathrm{miss,rel}}$ distribution for the SR-m_{T2} (left) and SR-2jets (right) signal regions for the $\mu\mu$, ee, and $e\mu$ channels from top to bottom respectively (except for SR-2jets which is not defined for the $e\mu$ channel). Data vs total prediction made of SM MC and semi data-driven fake estimation. The dashed vertical line marks the beginning of the final signal search region.

SROSjveto

	$e^{\pm}e^{\mp}$	$e^{\pm}\mu^{\mp}$	$\mu^{\pm}\mu^{\mp}$	all
diboson	12.3 ± 0.9 ± 2.1	19.8 ± 1.1 ± 12.0	16.2 ± 1.0 ± 4.8	48.3 ± 1.7 ± 7.6
$t\bar{t}$	14.5 ± 1.6 ± 6.7	37.8 ± 2.6 ± 17.1	23.9 ± 2.0 ± 11.1	76.2 ± 3.6 ± 36.3
single top	4.3 ± 0.8 ± 3.4	8.3 ± 1.1 ± 6.6	4.3 ± 0.8 ± 3.3	16.9 ± 1.5 ± 13.3
fake leptons	2.5 ± 1.6 ± 0.9	5.1 ± 2.3 ± 1.4	0.0 ± 0.3 ± 0.2	7.6 ± 2.9 ± 1.8
Z/γ^*+jets	0.2 ± 0.2 ± 0.1	0.0 ± 0.0 ± 0.0	0.2 ± 0.2 ± 0.1	0.4 ± 0.3 ± 0.3
Total	33.8 ± 2.6 ± 7.9	71.0 ± 3.8 ± 21.9	44.7 ± 2.4 ± 12.5	149.5 ± 5.2 ± 41.7
Data	33	65	37	135
$\sigma^{obs(exp)}$[fb]	4.12 ($4.19^{+1.5}_{-1.0}$)	7.99 ($8.50^{+2.5}_{-2.0}$)	4.41 ($5.07^{+1.7}_{-1.3}$)	13.86 ($14.88^{+4.3}_{-3.4}$)

SRSSjveto

	$e^{\pm}e^{\pm}$	$e^{\pm}\mu^{\pm}$	$\mu^{\pm}\mu^{\pm}$	all
diboson	0.7 ± 0.2 ± 0.1	1.5 ± 0.3 ± 0.9	0.8 ± 0.2 ± 0.2	3.0 ± 0.4 ± 0.5
charge flip	0.3 ± 0.0 ± 0.0	0.1 ± 0.0 ± 0.0	0.0 ± 0.0 ± 0.0	0.4 ± 0.0 ± 0.0
fake leptons	2.4 ± 1.6 ± 0.8	1.6 ± 1.3 ± 0.6	0.6 ± 0.8 ± 0.6	4.6 ± 2.2 ± 1.2
Total	3.5 ± 1.6 ± 0.8	3.2 ± 1.3 ± 1.1	1.4 ± 0.8 ± 0.7	8.1 ± 2.2 ± 1.3
Data	2	5	3	10
$\sigma^{obs(exp)}$[fb]	0.83 ($1.09^{+0.6}_{-0.4}$)	1.54 ($1.16^{+0.6}_{-0.4}$)	1.26 ($0.87^{+0.5}_{-0.3}$)	1.94 ($1.58^{+0.8}_{-0.5}$)

SR2jets

	$e^{\pm}e^{\mp}$	$e^{\pm}\mu^{\mp}$	$\mu^{\pm}\mu^{\mp}$	all
diboson	7.8 ± 0.4 ± 4.5	-	9.6 ± 0.5 ± 6.3	17.4 ± 0.6 ± 9.9
$t\bar{t}$	15.7 ± 1.7 ± 6.9	-	18.5 ± 1.8 ± 8.3	34.3 ± 2.5 ± 14.9
DrellYan	0.2 ± 0.2 ± 0.0	-	0.3 ± 0.3 ± 1.1	0.5 ± 0.4 ± 1.1
single top	1.4 ± 0.5 ± 1.1	-	1.4 ± 0.5 ± 1.1	2.9 ± 0.7 ± 2.2
fake leptons	2.1 ± 1.5 ± 0.9	-	1.0 ± 1.1 ± 1.0	3.1 ± 1.8 ± 1.4
Z/γ^*+jets	2.1 ± 0.7 ± 1.0	-	4.1 ± 1.0 ± 1.9	6.2 ± 1.2 ± 2.7
Total	29.4 ± 2.4 ± 8.4	-	34.9 ± 2.4 ± 10.7	64.3 ± 3.4 ± 19.0
Data	40	-	39	79
$\sigma^{obs(exp)}$[fb]	6.15 ($4.50^{+1.7}_{-1.3}$)	-	5.70 ($5.16^{+1.8}_{-1.3}$)	10.65 ($8.73^{+2.8}_{-2.3}$)

SRmT2

	$e^{\pm}e^{\mp}$	$e^{\pm}\mu^{\mp}$	$\mu^{\pm}\mu^{\mp}$	SF	all
diboson	5.7 ± 0.6 ± 0.5	4.7 ± 0.5 ± 0.5	6.5 ± 0.6 ± 0.4	12.1 ± 0.9 ± 0.8	16.9 ± 1.0 ± 1.2
$t\bar{t}$	2.2 ± 0.6 ± 1.1	4.7 ± 0.9 ± 2.0	3.0 ± 0.7 ± 1.3	5.2 ± 1.0 ± 2.4	9.9 ± 1.4 ± 4.3
single top	0.8 ± 0.3 ± 0.9	0.7 ± 0.3 ± 0.6	0.8 ± 0.3 ± 0.7	1.6 ± 0.5 ± 1.4	2.3 ± 0.6 ± 1.8
fake leptons	0.8 ± 0.9 ± 0.4	0.5 ± 0.7 ± 0.3	0.0 ± 0.1 ± 0.0	0.8 ± 0.9 ± 0.4	1.3 ± 1.2 ± 0.5
Z/γ^*+jets	0.4 ± 0.3 ± 0.1	0.0 ± 0.0 ± 0.0	0.6 ± 0.4 ± 0.4	0.9 ± 0.5 ± 0.5	0.9 ± 0.5 ± 0.5
Total	9.8 ± 1.3 ± 1.5	10.6 ± 1.4 ± 2.2	10.9 ± 1.1 ± 1.6	20.7 ± 1.7 ± 2.9	31.3 ± 2.2 ± 4.9
Data	6	9	8	14	23
$\sigma^{obs(exp)}$[fb]	1.15 ($1.65^{+0.8}_{-0.5}$)	1.61 ($1.83^{+0.8}_{-0.5}$)	1.33 ($1.74^{+0.8}_{-0.5}$)	1.59 ($2.37^{+1.0}_{-0.7}$)	2.22 ($3.10^{+1.3}_{-0.9}$)

Table 8.1: The total number of events observed, and the total SM prediction for all four signal regions (SR-OSjveto, SR-SSjveto, SR-2jets, and SR-m_{T2}), and three channels (ee, $e\mu$ and $\mu\mu$).

8.2 SUSY search based on the fully data-driven fake lepton estimation

In a similar way to the final distributions presented in the previous Section 8.1 for the semi data-driven fake estimation, Figures 8.3 and 8.4 show the final data and total SM prediction when estimating the fake lepton background using the fully data-driven approach. We already saw in Section 7.2.4 when validating the fully data-driven approach that the fake lepton estimation does very well, and in particular also at low $E_{\mathrm{T}}^{\mathrm{miss,rel}}$, the plots here shown for all signal regions confirms this.

Table 8.2 compares the total prediction of the two methods, again we also see the upper limit on the observed and expected SUSY cross section in both cases ($\sigma^{obs(exp)}$), which will be explained in Section 8.3.

Overall we see that the results are compatible in the two methods, across all regions and channels. The table clearly states that the data-driven method performs satisfactory and even reduces the systematical errors somewhat on the fake estimates, although for the fake estimates, the statistical errors drive the total uncertainty.

We have thus shown that both approaches do very well in estimating the fake lepton contribution. Unfortunately though, as already stated, there seems to be no sign of a SUSY signal. The next section presents the statistical interpretation of these results.

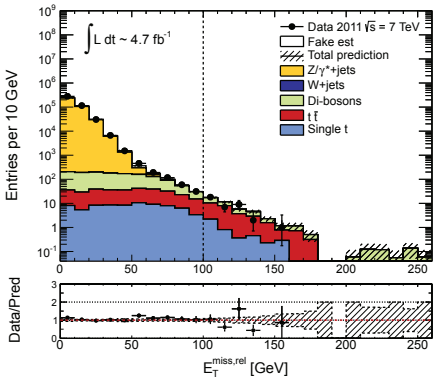

(a) $\mu\mu$ SR-OSjveto

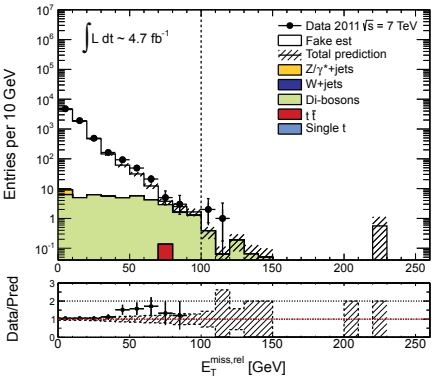

(b) $\mu\mu$ SR-SSjveto

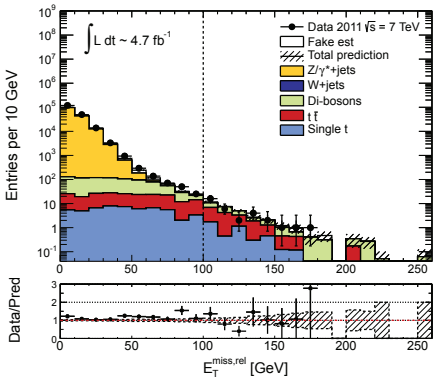

(c) ee SR-OSjveto

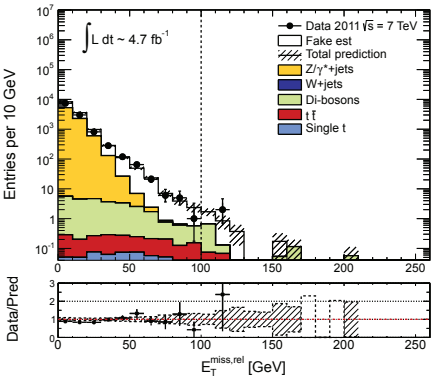

(d) ee SR-SSjveto

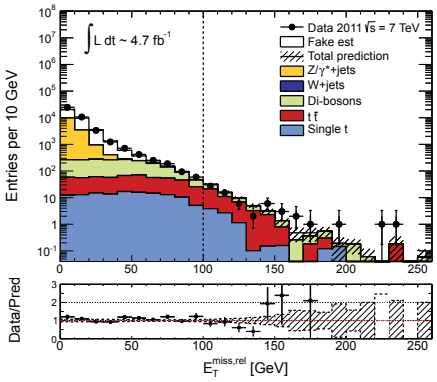

(e) $e\mu$ SR-OSjveto

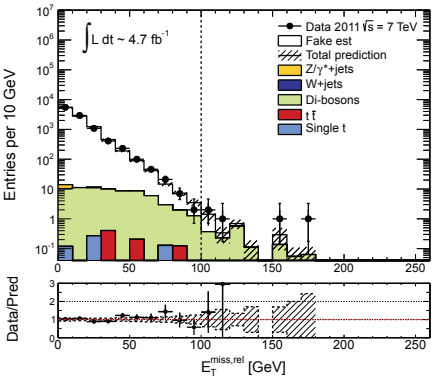

(f) $e\mu$ SR-SSjveto

Figure 8.3: Final $E_{\mathrm{T}}^{\mathrm{miss,rel}}$ distribution for the SR-OSjveto (left) SR-SSjveto (right) signal regions, with $\mu\mu$ in the top, ee in the middle, and $e\mu$ in the bottom row, showing data vs total prediction made of SM MC and fully data-driven fake estimation. In SR-SSjveto, the $t\bar{t}$, single top (Wt-channel), Z/γ^*, and WW backgrounds in the ee channel are estimated using the Charge-Flip package.

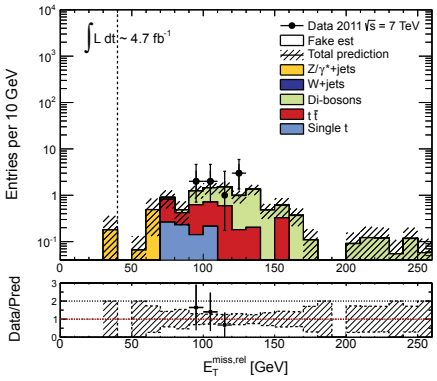

(a) $\mu\mu$ SR-m_{T2}

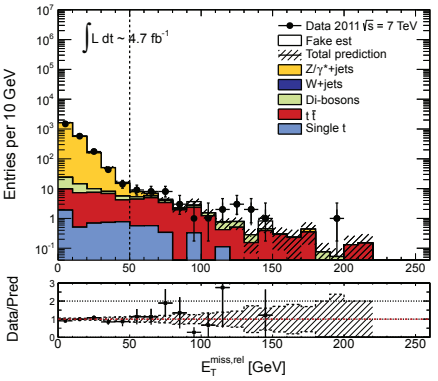

(b) $\mu\mu$ SR-2jets

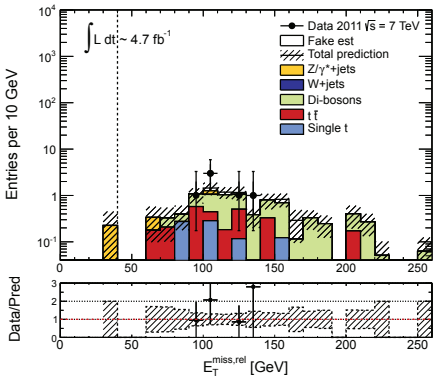

(c) ee SR-m_{T2}

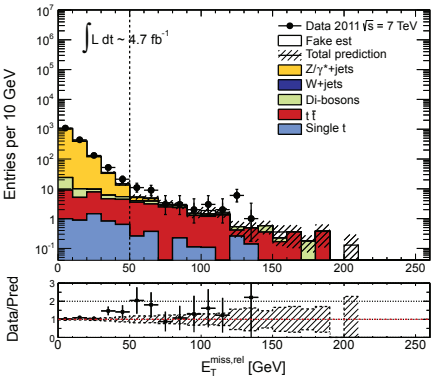

(d) ee SR-2jets

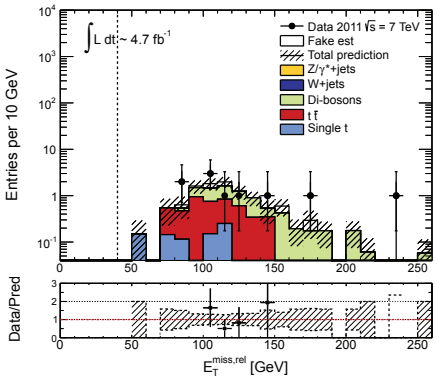

(e) $e\mu$ SR-m_{T2}

Figure 8.4: Final $E_{\mathrm{T}}^{\mathrm{miss,rel}}$ distribution for the SR-m_{T2} (left) and SR-2jets (right) and signal regions, for $\mu\mu$ (top), ee (middle), and $e\mu$ (bottom) (except for SR-2jets which is not defined for $e\mu$). The data vs total prediction made of SM MC and fully data-driven fake estimation.

Results using the semi data-driven fake estimation

	$e^{\pm}e^{\mp}$	$e^{\pm}\mu^{\mp}$	$\mu^{\pm}\mu^{\mp}$	all	
SROSjveto					
fake leptons	2.5 ± 1.6 ± 0.9	5.1 ± 2.3 ± 1.4	0.0 ± 0.3 ± 0.2	7.6 ± 2.9 ± 1.8	
Total	33.8 ± 2.6 ± 7.9	71.0 ± 3.8 ± 21.9	44.7 ± 2.4 ± 12.5	149.5 ± 5.2 ± 41.7	
Data	33	65	37	135	
$\sigma^{obs(exp)}$[fb]	4.12 ($4.19^{+1.5}_{-1.0}$)	7.99 ($8.50^{+2.5}_{-2.0}$)	4.41 ($5.07^{+1.7}_{-1.3}$)	13.86 ($14.88^{+4.3}_{-3.4}$)	
SRSSjveto					
fake leptons	2.4 ± 1.6 ± 0.8	1.6 ± 1.3 ± 0.6	0.6 ± 0.8 ± 0.6	4.6 ± 2.2 ± 1.2	
Total	3.5 ± 1.6 ± 0.8	3.2 ± 1.3 ± 1.1	1.4 ± 0.8 ± 0.7	8.1 ± 2.2 ± 1.3	
Data	2	5	3	10	
$\sigma^{obs(exp)}$[fb]	0.83 ($1.09^{+0.6}_{-0.4}$)	1.54 ($1.16^{+0.6}_{-0.4}$)	1.26 ($0.87^{+0.5}_{-0.3}$)	1.94 ($1.58^{+0.8}_{-0.5}$)	
SR2jets					
fake leptons	2.1 ± 1.5 ± 0.9	-	1.0 ± 1.1 ± 1.0	3.1 ± 1.8 ± 1.4	
Total	29.4 ± 2.4 ± 8.4	-	34.9 ± 2.4 ± 10.7	64.3 ± 3.4 ± 19.0	
Data	40	-	39	79	
$\sigma^{obs(exp)}$[fb]	6.15 ($4.50^{+1.7}_{-1.3}$)	-	5.70 ($5.16^{+1.8}_{-1.3}$)	10.65 ($8.73^{+2.8}_{-2.3}$)	
SRmT2					
fake leptons	0.8 ± 0.9 ± 0.4	0.5 ± 0.7 ± 0.3	0.0 ± 0.1 ± 0.0	0.8 ± 0.9 ± 0.4	1.3 ± 1.2 ± 0.5
Total	9.8 ± 1.3 ± 1.5	10.6 ± 1.4 ± 2.2	10.9 ± 1.1 ± 1.6	20.7 ± 1.7 ± 2.9	31.3 ± 2.2 ± 4.9
Data	6	9	8	14	23
$\sigma^{obs(exp)}$[fb]	1.15 ($1.65^{+0.8}_{-0.5}$)	1.61 ($1.83^{+0.8}_{-0.5}$)	1.33 ($1.74^{+0.8}_{-0.5}$)	1.59 ($2.37^{+1.0}_{-0.7}$)	2.22 ($3.10^{+1.3}_{-0.9}$)

Results using the fully data-driven fake estimation

	$e^{\pm}e^{\mp}$	$e^{\pm}\mu^{\mp}$	$\mu^{\pm}\mu^{\mp}$	all	
SROSjveto					
fake leptons	2.0 ± 1.4 ± 0.7	4.8 ± 2.2 ± 1.3	0.1 ± 0.2 ± 0.3	6.9 ± 2.6 ± 1.6	
Total	33.3 ± 2.5 ± 7.8	70.7 ± 3.7 ± 21.9	44.8 ± 2.4 ± 12.5	148.8 ± 5.1 ± 41.7	
Data	33	65	37	135	
$\sigma^{obs(exp)}$[fb]	4.11 ($4.16^{+1.6}_{-1.1}$)	8.04 ($8.49^{+2.4}_{-2.0}$)	4.41 ($5.07^{+1.7}_{-1.3}$)	13.90 ($14.90^{+4.2}_{-3.5}$)	
SRSSjveto					
fake leptons	2.2 ± 1.5 ± 0.6	1.4 ± 1.2 ± 0.5	0.5 ± 0.7 ± 0.5	4.1 ± 2.0 ± 1.0	
Total	3.2 ± 1.5 ± 0.6	3.1 ± 1.2 ± 1.0	1.3 ± 0.8 ± 0.6	7.6 ± 2.1 ± 1.1	
Data	2	5	3	10	
$\sigma^{obs(exp)}$[fb]	0.84 ($1.06^{+0.6}_{-0.4}$)	1.56 ($1.14^{+0.6}_{-0.4}$)	1.27 ($0.84^{+0.5}_{-0.3}$)	2.00 ($1.53^{+0.7}_{-0.5}$)	
SR2jets					
fake leptons	2.2 ± 1.5 ± 0.8	-	1.3 ± 1.2 ± 1.1	3.5 ± 1.9 ± 1.3	
Total	29.5 ± 2.4 ± 8.4	-	35.3 ± 2.5 ± 10.7	64.7 ± 3.5 ± 19.0	
Data	40	-	39	79	
$\sigma^{obs(exp)}$[fb]	6.14 ($4.51^{+1.7}_{-1.3}$)	-	5.59 ($5.08^{+1.8}_{-1.3}$)	10.44 ($8.56^{+2.8}_{-2.3}$)	
SRmT2					
fake leptons	0.7 ± 0.9 ± 0.4	0.5 ± 0.7 ± 0.3	0.0 ± 0.3 ± 0.0	0.6 ± 0.8 ± 0.4	1.2 ± 1.1 ± 0.5
Total	9.7 ± 1.3 ± 1.5	10.6 ± 1.4 ± 2.2	10.9 ± 1.1 ± 1.6	20.6 ± 1.7 ± 2.9	31.2 ± 2.1 ± 4.9
Data	6	9	8	14	23
$\sigma^{obs(exp)}$[fb]	1.15 ($1.64^{+0.8}_{-0.5}$)	1.59 ($1.82^{+0.8}_{-0.5}$)	1.33 ($1.74^{+0.8}_{-0.5}$)	1.60 ($2.37^{+1.0}_{-0.7}$)	2.22 ($3.10^{+1.3}_{-0.9}$)

Table 8.2: Final event yields produced using the semi data-driven procedure (top) and the fully data-driven procedure (bottom).

8.3 Statistical method for interpretation of results

I here introduce the statistical tools used to compare the observed data with the expectations predicted by the SM, where the latter is extracted from MC and from the fake lepton estimation.

We base the significance test on the profile likelihood ratio λ, which is

$$\lambda(\mu) = \frac{L(\mu, \hat{\hat{\boldsymbol{\theta}}}_\mu)}{L(\hat{\mu}, \hat{\boldsymbol{\theta}})},$$

where μ is the signal strength, and $\boldsymbol{\theta}$ so-called nuisance parameters that parametrize the uncertainties. $\lambda(\mu)$ is a test statistic, i.e. the value that is used for testing hypothesis μ. For a counting experiment the likelihood L itself is just a Poisson distribution, and simply gives the probability of a certain outcome, given a set of parameters θ, μ. When L is maximised (resulting in a minimized λ), this corresponds to the likelihood function which best reproduces one of the hypotheses (signal and background, or just background). This is what the hats ($\hat{}$) represent. The likelihood in the numerator is maximised with respect to the nuisance parameters $\boldsymbol{\theta}$ which give the largest L, assuming some μ ($\mu = 1$, if we are testing signal+background, or $\mu = 0$ if testing the background only hypothesis), and the denominator is constructed from the values of μ and $\boldsymbol{\theta}$ that give the global maximum L. The likelihood is defined as

$$L(\mu, \boldsymbol{\theta}) = \frac{\left[\mu s(\boldsymbol{\theta}_s) + b(\boldsymbol{\theta}_b)\right]^n}{n!} e^{-(\mu s(\boldsymbol{\theta}_s) + b(\boldsymbol{\theta}_b))} \prod_{i=1}^{n_{\text{nuis}}} \boldsymbol{\theta}_{is} \prod_{i=1}^{n_{\text{nuis}}} \boldsymbol{\theta}_{ib}, \tag{8.1}$$

where the first term is the usual Poisson distribution with the signal s and background b hypotheses, which are functions of some uncertainty $\boldsymbol{\theta}_s$ and $\boldsymbol{\theta}_b$ respectively, and the two products over the number of nuisance parameters n_{nuis}, are the signal and background uncertainty terms.

The test statistic $\lambda(\mu)$ is then constructed for $\mu = 1$, and for $\mu = 0$. In fact, what we use for test statistic is not $\lambda(\mu)$, but $q_\mu = -2 \ln \lambda(\mu)$, which is much more practical when dealing with products of nuisance parameters, as we can then instead sum them. To test the hypothesis we use CL_s [163] defined as

$$CL_s = \frac{p_{s+b}}{p_b} \tag{8.2}$$

where the p-values are calculated from the hypothesis distribution, based on the test statistic of the likelihood function. Intuitively using just p_{s+b} would do, however CL_s protects against excluding a model for which we have no sensitivity, i.e. when $b \gg s$, by "moderating" CL_{s+b} by p_b, and is therefore preferred. The hypothesis distribution can be obtained by Monte Carlo experiments where a random dataset is generated from pseudo-experiments, and is what was done for the publication [134]. However, this requires a large number of pseudo-experiments, and is very time-consuming (due to the minimization procedure on every pseudo-experiment). In a large sample limit however, the likelihood approaches a Gaussian, and q_μ follows a χ^2 distribution (Wilks' theorem [164]) for a true hypothesis μ. The p-values can therefore be calculated from the χ^2 distribution instead, which is what is done in the current analysis.

One then obtains an upper limit on the visible cross section $\sigma \times \epsilon \times A$, where ϵ is the efficiency, and A the acceptance, and all signal grid points which yield a value of q_μ above the

defined value of the 95% confidence limit, are excluded.

The statistical analysis is done in HistFitter, an interface to the ROOT-based HistFactory software package [165]. HistFitter is developed by the ATLAS SUSY Working group with the purpose to accommodate statistical analysis in a 2-dimensional parameter plane, which is how Supersymmetry searches are performed in ATLAS. Event yields, and statistical and systematic errors, which are presented below, are fed into HistFitter, which then performs the statistical analysis. Correlation between errors are taken into account by the configuration of nuisance parameters and their impact on the expected number of events.

8.4 Systematic uncertainties

Here I summarize the systematic uncertainties taken into account, and briefly comment on how they are obtained, typically quoting the ROOT packages and tool used, which are all part of the SUSYTools package. In all cases the uncertainty is extracted by comparing estimates (predictions) using nominal values with the estimates obtained after having varied the parameter of interest. The resulting systematic errors from the terms described below, are summarized in Table 8.3. Note that these systematic uncertainties are only applied to the final search analysis, and not on the kinematic distributions shown throughout. An exception is the uncertainty on luminosity and cross section which are included in all plots, unless stated otherwise.

The most important systematic uncertainties on the SM MC (marked in grey for each region in Table 8.3) are the $t\bar{t}$ initial state and final state (strong) radiation, contributing with roughly 20% in the SR-OSjveto and SR-2jets signal regions. The jet energy resolution and jet-energy scale are also relatively important with about 3-10% in the OS signal regions (and negligible with errors $< 1\%$ in the SS). In SR-SSjveto it is in fact the systematic error on the fake lepton estimation of about 10% that dominates. In the OS signal regions however, the error on the fake estimation is relatively small, of the order of 1-2%. The statistical and systematic uncertainties amount to 8.6%(stat.) and 30.8%(syst.) in SR-OSjveto, 11.2%(stat.) and 24.0%(syst.) in SR-2jets, 31.6%(stat.) and 11.3%(syst.) in SR-SSjveto, and 20.8%(stat.) and 23.8%(syst.) in SR-m_{T2}, respectively. In the following I list each of the separate systematic errors together with the combined errors which entered the result Tables 8.1 and 8.2.

The uncertainty on the luminosity (Lumi) is 3.9% and affects scaling to luminosity in the same way for all MC types [160, 161].

The cross section uncertainties (xsec) have already been summarized in Section 5.3.1 Table 5.8. For each uncertainty described below an abbreviation is defined and given in parenthesis, corresponding to the abbreviations used in Table 8.3.

The jet energy scale uncertainties (JES) are evaluated using the MultijetJESUncertaintyProvider, which gives uncertainties on the jet energy scale as a function of jet p_{T} and η. It is implemented using the JetUncertainties-00-03-05 package, and includes uncertainties due to pile-up

and nearby jets.

The jet energy resolution (JER) uncertainty is evaluated by smearing each jet according to a Gaussian distribution, with unity mean and a width given by a p_{T} dependent resolution function. This is implemented using the package JetResolution-01-00-00.

The b-tagging uncertainties (bweight) are the recommended uncertainties for the 80% working point of the JetFitterCombNN algorithm, as provided by the BTagCalibrations (ROOT) file which is part of the SUSYTools-00-00-67 package.

The electron and muon efficiency uncertainties are calculated with the egammaAnalysisUtils-00-02-76 software package. Each MC electron is given a multiplicative event weight to account for differences in efficiency between data and MC, incorporating corrections in identification efficiency for the `tightPP` lepton definition (see Section 3.5 for the definition), for reconstruction and for track quality efficiency. For muons the MuonEfficiencyCorrections-01-00-10 software package is used, and the procedure is the same as for electrons.

Electron resolution and scale uncertainties (ELR,ELSF) are both evaluated using the egammaSFclass in the egammaAnalysisUtils-00-02-76 package.

The uncertainties in muon MS and ID momentum components (MUID,MUMS) are propagated by smearing each of the separate p_{T} ID and MS components, and compare to the nominal smearing on the combined MS and ID track.

The uncertainties in the trigger re-weights (TRG) are extracted using a $\pm 1.5\%$ uncertainty on the trigger weights (studied in the support-material of Ref. [134]), and calculating the resulting MC prediction with the scaled values. This is conservative for most p_{T} and η combinations.

The uncertainties on $E_{\mathrm{T}}^{\mathrm{miss}}$ are obtained by propagating the relevant uncertainties mentioned above to the $E_{\mathrm{T}}^{\mathrm{miss}}$ (and hence $E_{\mathrm{T}}^{\mathrm{miss,rel}}$) using the METUtility tool. This means that the scaled objects (be they electrons, muons or jets) are vectorially removed from the $E_{\mathrm{T}}^{\mathrm{miss}}$ and re-added using the scaled momentum components. The scalar sum of the transverse energy is corrected in an analogous fashion. In addition comes a 5% uncertainty on the magnitude of the soft terms (soft jets and Cell-Out, see Section 3.5.4 for a definition of the latter).

The effect on the factorization and renormalization scales on Z/γ^* production are evaluated for the Alpgen Z/γ^*+jets cross sections, by varying the factorisation and renormalization scales, the so-called 'ktfac" and "qfac" terms, up and down separately, using the ScaleVariationReweighter class in SUSYTools.

The parton shower uncertainty in $t\bar{t}$ production (ifsr_Top,ifsr_ST)) is evaluated using samples generated by the Acer event-generator, yet another generator on the market, using "more" or "less" parton showering . The relative variation upward is taken as (PSmore-AcerMC)/AcerMC and the relative downward variation is taken as (PSless-AcerMC)/AcerMC. This relative uncer-

tainty is then applied to the default Monte Carlo sample, namely PowHeg+Pythia.

The generator uncertainties on $t\bar{t}$ production (gen_Top, gen_ST) are obtained by comparing the nominal estimates (PowHeg+Pythia) with those given by PowHeg+Jimmy and MC@NLO samples. The larger of the two is taken as the final systematic uncertainty.

The di-boson generator uncertainties (gen_Diboson) are considered by comparing Alpgen and Sherpa.

The errors due to the fake lepton estimation (QCD-MM) are as the other uncertainties found by comparing the nominal prediction with those obtained using the upper and lower fake lepton estimates. They are in turn obtained by varying the fake rate and real efficiency as determined in Section 7.1.2.6.

Signal channel	SROSjveto	SR2jets	SRSSjveto	SRmT2
Total statistical ($\sqrt{N_{\text{obs}}}$)	±11.62	±8.89	±3.16	±4.80
Total background systematic	±41.69	±18.99	±1.13	±5.49
Lumi	±0.00	±0.00	±0.00	±0.00
CLUS	±1.31	±0.11	±0.06	±0.11
ELR	±0.18	±0.22	±0.00	±0.11
ELSC	±0.06	±0.21	±0.00	±0.92
ELSF	±2.57	±0.93	±0.05	±0.38
JER	±10.88	±3.60	±0.03	±1.51
JES	±13.21	±2.19	±0.03	±1.46
MUID	±0.05	±0.06	±0.00	±0.03
MUMS	±0.24	±0.51	±0.06	±0.25
MUSC	±0.01	±0.16	±0.00	±0.86
MUSF	±0.42	±0.20	±0.01	±0.09
QCD-MM	±1.58	±1.32	±1.00	±0.47
PILEUP	±1.05	±0.27	±0.08	±0.31
TRG	±2.88	±1.20	±0.06	±0.55
bweight	±0.00	±0.00	±0.00	±0.00
gen_ST	±13.00	±2.22	±0.00	±1.72
gen_Top	±3.05	±0.69	±0.00	±0.20
gen_Diboson	±6.77	±9.73	±0.46	±0.00
ifsr_ST	±0.51	±0.09	±0.00	±0.09
ifsr_Top	±32.77	±14.39	±0.00	±0.00
ktfac	±0.10	±2.25	±0.00	±0.30
lumi	±0.15	±0.09	±0.00	±0.03
qfac	±0.05	±0.91	±0.00	±0.13
xsec	±11.22	±5.04	±0.21	±2.08

Table 8.3: Breakdown of the dominant systematic uncertainties on number of background event estimates in the various signal regions. Note that the individual uncertainties can be correlated, and do not necessarily add up quadratically to the total background uncertainty.

8.5 Interpretation of SUSY search results

As the fully data-driven fake lepton estimation yielded slightly better results, I proceed with these. They are as given in the bottom Table 8.2. The results are interpreted in the framework of three different SUSY grids described in Sections 4.2.2-4.2.4, the direct gaugino pMSSM grid, the direct gaugino simplified model grid, and the direct slepton grid. In the direct gaugino channel, all signal regions and all channels are considered, and the signal region resulting in the best sensitivity is used to set the limits. In the direct slepton search, only same-flavour channels of the SR-m_{T2} are used in the search, as the SUSY signal only yields opposite sign same flavour. In all exclusion plots, the hashed area indicates the excluded region.

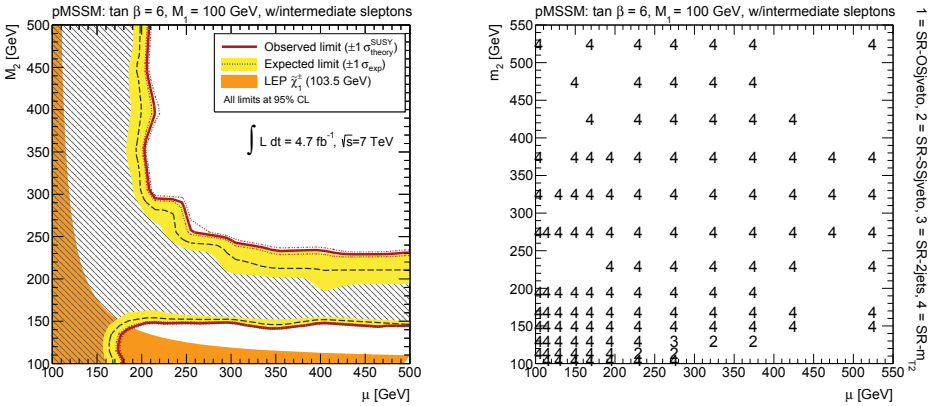

(a) 95% exclusion (b) Most sensitive signal regions

Figure 8.5: The 95% exclusion limits (left) in the M_2, μ plane of the direct gaugino pMSSM grid DGemt, for $M_1 = 100$ GeV. To the right, the signal regions with best sensitivity used for setting the limit, which in this case is mostly region 4, SR-m_{T2} (see side of plot for region description).

In Figures 8.5-8.7 the expected 95% exclusion limits are presented for the direct gaugino pMSSM grid, in the $\mu - M_2$ plane, for three values of M_1: 100, 140, and 250 GeV respectively. The expected limits including the experimental uncertainties are drawn as black dashed lines, with the yellow band representing the $\pm 1\sigma$ expectation, when including the full systematic (and statistical) uncertainty, except the uncertainty on cross section, which instead is evaluated on the observed limit. Also plotted is the observed limit in red, and the effect of $\pm 1\sigma$ uncertainty on the theory cross section. The excluded area is marked by the hashed area. The LEP limits [166] exclude the orange area. In addition is shown the signal regions used to set the limits, which are the ones out of the four regions (defined at right-hand side of plot) which gives the best sensitivity in each grid-point. For all three pMSSM direct gaugino models, it is mostly SR-m_{T2} which yields the best exclusion power, over most of the μ-M_1 plane, as the right plots of Figures 8.5-8.7 demonstrate. At intermediate Higgs mass parameter μ, low gaugino mass parameter M_2 values, the SR-SSjveto contributes slightly for $M_1 = 100$ and $M_1 = 140$ GeV.

Figure 8.5 presents the exclusion limits for $M_1 = 100$ GeV. All values of M_2 are excluded

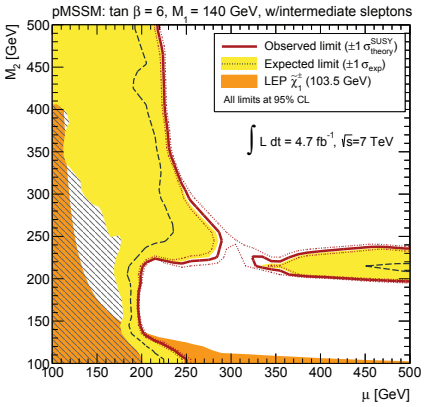

(a) 95% exclusion

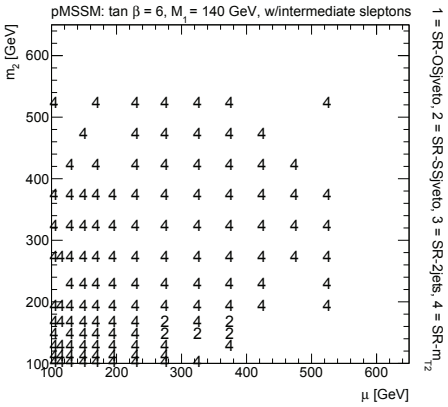

(b) Most sensitive signal regions

Figure 8.6: The 95% exclusion limits (left) in the M_2, μ plane of the direct gaugino pMSSM grid DGemt, for $M_1 = 100$ GeV. To the right, the signal regions with best sensitivity used for setting the limit, and the signal region definitions are shown on the right-hand side of the plot.

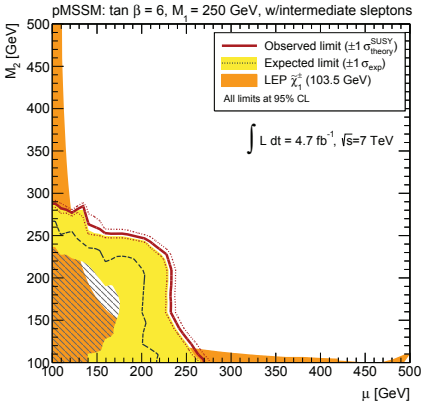

(a) 95% exclusion

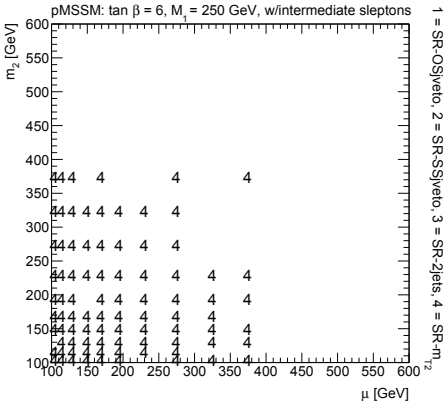

(b) Most sensitive signal regions

Figure 8.7: The 95% exclusion limits (left) in the M_2, μ plane of the direct gaugino pMSSM grid DGemt, for $M_1 = 100$ GeV. To the right, the signal regions with best sensitivity used for setting the limit, and the signal region definitions are shown on the right-hand side of the plot.

for μ up to $\sim$ 180 GeV. All values of μ are excluded for roughly $M_2 \in (150, 230)$ GeV. At M_2 above around 300 GeV a broader area is excluded with μ reaching up until around 200 GeV.

For $M_1 = 140$ GeV in Figure 8.6, the μ region excluded for all M_2 values is slightly wider, reaching to about 225 GeV, however the uncertainty is substantially bigger. Generally the exclusion area looks much like for $M_1 = 100$ GeV, however especially the band reaching from $M_2 \sim$ 200-250 which excluded all values of μ is in this scenario much smaller, with a gap around 300-325 GeV.

Finally, with $M_1 = 250$ GeV in Figure 8.7 we only exclude μ values up until around 225 GeV for M_2 between 0-250 GeV, with slightly better limits at low μ, and low M_2.

When interpreting the data within the simplified models, shown in Figures 8.8-8.9 for mode A and mode C respectively, the limits are set directly in the $m_{\tilde{\chi}_1^\pm}, m_{\tilde{\chi}_1^0}$ plane. In this model there are no LEP limits with compatible assumptions, and they are therefore not shown. In each case the signal regions yielding the best sensitivity are selected for setting limits, and are shown in the right plots for each respective mode. In Mode A ($\tilde{\chi}_1^\pm\tilde{\chi}_2^0 \to \tilde{\ell}\nu(\tilde{\nu}l) + \tilde{\ell}\ell \to l\nu\tilde{\chi}_1^0 + \ell\ell\tilde{\chi}_1^0$) it is only SR-$m_{T2}$ that contributes. In Mode C ($\tilde{\chi}_1^\pm\tilde{\chi}_1^\mp \to 2\times\tilde{\ell}\nu(\tilde{\nu}\ell) \to 2\times\ell\nu\tilde{\chi}_1^0$) SR-$m_{T2}$ is important as in mode A, however, SR-OSjveto and SR-2jets also contribute, the former at low $m_{\tilde{\chi}_1^\pm}, m_{\tilde{\chi}_1^0}$, and the latter in a region following the diagonal in $m_{\tilde{\chi}_1^\pm}, m_{\tilde{\chi}_1^0}$, and with SR-$m_{T2}$ otherwise.

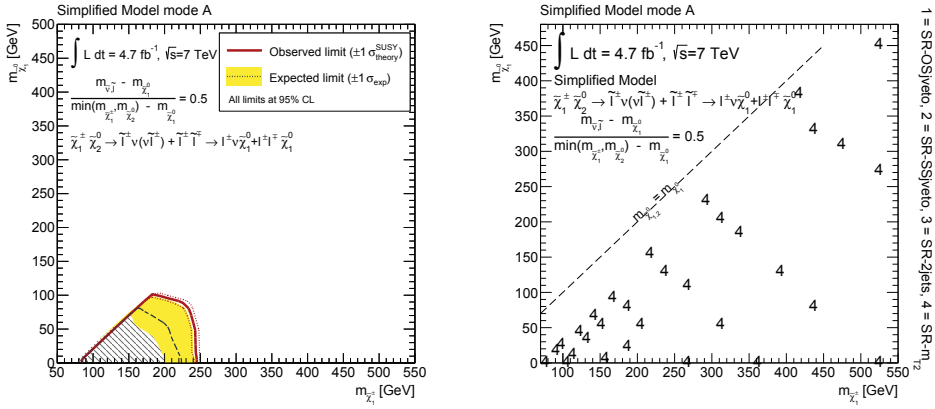

Figure 8.8: The 95% exclusion limits in the $\tilde{\chi}_1^\pm$, $\tilde{\chi}_1^0$ plane of the simplified model grid mode A. The signal regions which yield the best sensitivity are presented in the right plot.

In Mode A (Figure 8.8) $\tilde{\chi}_1^\pm$ masses from around 80-250 GeV are excluded at low $m_{\tilde{\chi}_1^0}$, with a reduced exclusion for higher values of $m_{\tilde{\chi}_1^0}$. In Mode C (Figure 8.9) the exclusion area is broader, from around 120-360 GeV at low $m_{\tilde{\chi}_1^0}$, and follows the same trend at higher $m_{\tilde{\chi}_1^0}$ as in Mode A.

Finally the limits set on the direct slepton model shown in Figure 8.10. The region spanning $\sim m_{\tilde{\ell}} \in (95, 200)$ GeV is excluded for low $m_{\tilde{\chi}_1^0}$, with weaker exclusion at higher $m_{\tilde{\chi}_1^0}$, however, the uncertainty is very large in this model.

While this direct gaugino and slepton SUSY search unfortunately did not result in a claim of discovery, the limits presented improves earlier ATLAS SUSY dilepton searches. More importantly, this is the first analysis addressing direct slepton production. As this process has very low production cross section, the search was finally made possible by the accumulated integrated luminosity of 4.7 fb^{-1} available for this analysis. It is also the first analysis performed within the di-lepton SUSY group explicitly targetting direct gaugino production (and hence low jet activity), as earlier analysis ([156, 157, 167]) focused on strong production, where jet activity is important. It was in fact features in the analysis of [157] that lead to this turn of focus from

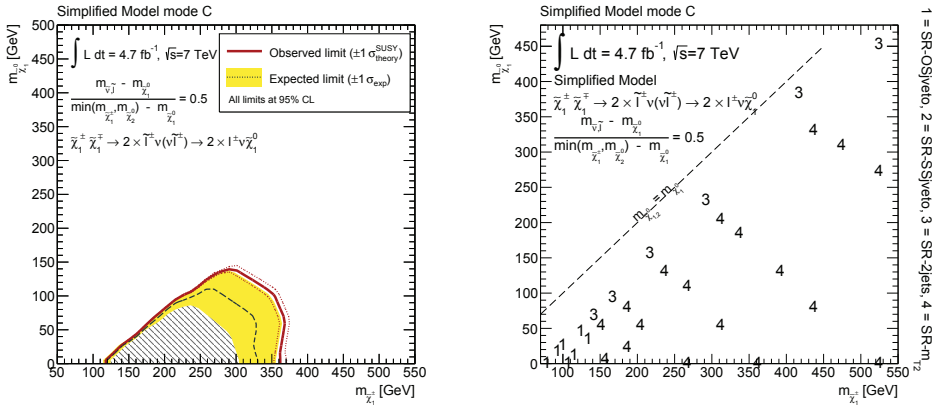

Figure 8.9: The 95% exclusion limits in the $\tilde{\chi}_1^{\pm}$, $\tilde{\chi}_1^0$ plane of the simplified model grids, mode C. The signal regions which yield the best sensitivity are presented in the right plot.

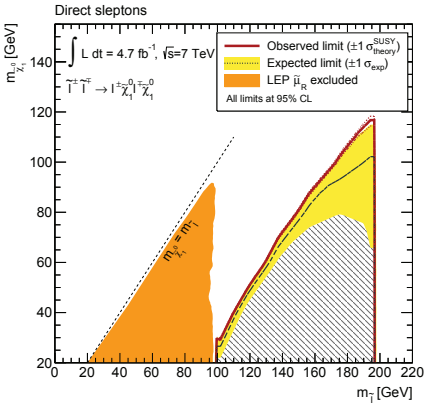

Figure 8.10: The 95% exclusion limits in the $m_{\tilde{\chi}_1^0}$, $m_{\tilde{l}}$ plane of the direct slepton pMSSM grid.

strong to weak SUSY production. One found that a signal region which did not require jets turned out to be sensitive to direct gaugino production, even with cuts not optimized for such a signal. Thus new signal regions were defined and optimized for direct gaugino production, as presented in this thesis.

What if a disccovery was made? This would be exciting indeed. And a taste of it was experienced with the Higgs discovery in 2012. One of the immediate aspects of a discovery is the interest from the public. The Higgs discovery resulted in a huge rush of popular scientific articles, interviews and other media performances. Of course, this is largely due to the increasing attention from scientists and funding agencies on the importance of transmitting, educating and informing the public about research developement. But how could a SUSY discovery be used for public education? Well, the next chapter suggests one possible way.

Chapter 9

Communicating the excitement of discovery

Particle physics is indeed an exciting and fascinating field of research, and one of the most rewarding aspects of being part of this adventure, is to get the opportunity to convey this to others. Especially to young students that are curious to find out more about physics and in particular particle physics. In the course of my Master and PhD studies I have been involved with outreach, mostly within the context of the International Particle Physics Outreach Group (IPPOG [168])[1], but also with popular scientific talks given to both students and teachers on various occasions. I talk about the former here.

So, as this thesis starts with my wonder of the subatomic world, it ends with the transmission of this wonder to young students, through an educational tool I developed. In the following sections I present the "Z-path" [169], an outreach program for LHC collision data from the ATLAS detector. The work has earlier been documented in [170] and [171], and an abstract is in progress of being submitted for ICHEP 2014 on behalf of ATLAS and IPPOG.

The Z-path is incorporated into the IPPOG International Masterclasses [172]. It was first run in 2012, using completely fresh ATLAS data, collected just months earlier. The main goal of the Masterclasses is to motivate and educate high-school students in the exiting field of particle physics, by allowing them to visit research institutes and universities, and work hands-on with real collision data. Through the course of the day, the students learn about the fundamentals of particle physics from expert scientists in the field, and through data analysis get to work as close as possible to the scientific reality. As part of the International program, students hook up with CERN and other Masterclass institutes around the world, for a video-session, to really get the feel of the international collaboration that CERN is.

9.1 The LHC Z-Path emerges

The work with the Z-path started in 2011 as the LHC data was coming in for full, and a subset was released[2] for educational purposes. With LHC data in hand, it was time at last to update the

[1] Earlier EPPOG, the *E*uropean Particle Physics Outreach Group

[2] After request from the IPPOG Masterclass teams

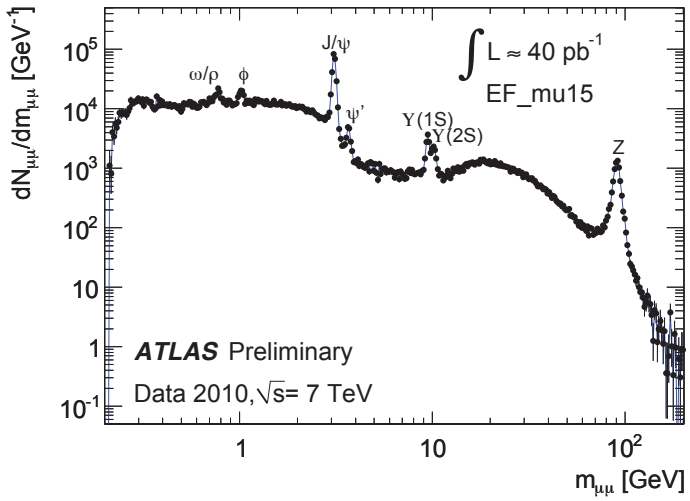

Figure 9.1: ATLAS di-muon opposite sign invariant mass spectra.

old LEP Hands-On-CERN Z-exercise, used since 2005. The goal of the Z-path was, through the invariant mass technique, to make an educational tool that was versatile enough to closely follow the discoveries as they unravelled at the LHC. The Z-path is a discovery path, like the LHC is a discovery machine.

The foundation of the Z-path is naturally the Z-boson. With the invariant mass technique students get to reconstruct the Z-boson mass, from real Z-candidate events, concentrating on the relatively easy decay channels $Z \to e^+e^-/\mu^+\mu^-$. However, to illustrate the point that with the invariant mass technique, all kind of particles with the same decay pattern can be (re)discovered, the path also deals with low mass hadron resonances $J/\psi \to e^+e^-/\mu^+\mu^-$ and $\Upsilon \to e^+e^-/\mu^+\mu^-$, in order to reproduce a similar mass spectrum as shown in the di-muon mass spectrum of Figure 9.1.

The overall goal of the Z-path is to rely on the invariant mass technique to measure properties of know particles and discover new ones, for example new neutral gauge bosons, Z', predicted by various theories extending the SM with new weak interactions. Therefore there is a surprise hiding in the data provided to the students: We planted simulated events with a Z' of mass 1 TeV as the new particle to be "discovered". This lets the students test their ability to trust the analysis even if the results are surprising. Like it would be if a new massive boson would appear at the LHC.

With the 2012 discovery of the Higgs boson, we were able, with the Z-path in place, to promptly apply the invariant mass technique and let the students themselves make the discovery. The 2013 international Masterclasses featured the use of 1fb^{-1} of 7 TeV Higgs $H \to \gamma\gamma$ and $H \to Z^*Z \to 4\ell$ data. This is 10% of the data sample interpreted by the ATLAS physicist for the Higgs discovery. In the 2014 version of the Masterclasses the ATLAS management approved the use of 2fb^{-1} of 8 TeV data, and are eager to accomodate Masterclasses also in the future, by increasing the allowed data sample even more.

What about Supersymmetry or other exotic objects such as gravitons? Well, when observed, the high school students will be able play with them a few months later. Let's get back to the Z-path itself, starting by describing its tools.

9.2 Tools used in the Z-path

To accommodate the Z-path, we developed OPloT [173], a php-based web plotting tool for submission, combination, and discussion of results. In earlier Masterclasses this was typically done by hand using spread-sheets, and was time-consuming. With OPloT, this is all handled automatically. Students upload their own results, and histograms are automatically combined by institute, and also by day, since up to five institutes join an International Masterclass day. This allows for prompt access of results for discussion. OPloT has 5 main views, the Student view, Tutor view, Moderator view and Administrator view. The student view allows for upload and inspection of own results. The Tutor view allows for inspection of the combined results for own institute. The Moderator view accomodates the moderators of the video conference and in addition to each institues results, displays the combined results for that day, plus includes some material (slides) to be used at the video conference to help discuss the results. Finally the Administrator view is made for tutors to administrate the uploaded results, or for allowing (anyone with the password) to create new Masterclass event, typically for stand-alone master-classes. I come back to OPloT later, showing screen shots of the student histograms from a typical Masterclass day.

Another important tool in the Z-Path is the HYPATIA [174] (java-based) event display. HYPATIA builds on the official ATLAS event display ATLANTIS [175], but is tailored for educational purposes. The important feature of HYPATIA is that it includes an "Invariant Mass Table", which allows to select pairs of particles which are subsequently entered to construct an invariant mass. A special release is made to accommodate the Z-path Masterclass, among other things allowing exportation of the results for web-upload, but also incorporating special features to analyse the $H \to \gamma\gamma$ and $H \to 4\ell$ events. Thanks to a pleasant and fruitful collaboration with the HYPATIA team, in particular Christine Kourkoumelis and Stelios Vourakis, our ideas were, and still are, quickly implemented.

Finally, the data events themselves are selected by following ATLAS recommended physics objects cuts, such as those presented in Section 3.5. We run over the ESD files using Athena and the grid (see Section 3.3), in order to generate event-display xml files used by HYPATIA. Using ESD files enables us to produce event-display files with all relevant information such as hits and tracks, needed to realistically depict the event.

The event-mixtured used is as follows: 5% of each low mass resonance, and the simulated Z' events, 50% Z-bosons, 30% $H \to \gamma\gamma$ and 5% $H \to 4\ell$. When it comes to the $H \to 4\ell$, we in fact duplicate those, in order for all students to encounter them, as we only have 40 events available in total. However, OPloT ultimately removes duplication, so that the combined results are correct. The total data-sample amounts to 37.000 (password protected) events, split into data-sets of 50 events each, which is the amount each pair of students analyses[3].

[3] And we have 1000 of these events openly available for anyone to use.

9.3 The Z-path web-material

To prepare the young students for analysing LHC data, they learn about the fundamentals of particle physics, and how to identify particles in the ATLAS detector. A typical Masterclass day would include several in-depth lectures on these subjects. Here, however, I present the educational program as it is implemented through the online Z-path web-material [169], which covers the essential subjects mentioned above. The Oslo group is responsible for the idea, the material and the implementation of the Z-path.

The web-material is implemented as part of the ATLAS Masterclass platform developed for IPPOG by the central administration in Dresden. The Z-path and W-path, which are the two existing ATLAS masterclass packages, share the same framework and some material. This is in particular the sections about particle and event-identification in ATLAS, and related exercises and tools. For the latter, the content is made especially for the Z-path, however for a streamlined web-experience, the layout is the same as used in the W-path.

The path itself is organized in two sections in the following manner

- Z-Path
  - Introducing the Z-boson
  - Introducing the Higgs boson
  - Identifying Events
  - Search and Discover with Mass
  - Get to Work!
- Knowledge Center
  - The Standard Model
  - Research at the LHC
  - More About the Z-boson
  - Energy Units
  - Momentum
  - Vector
  - Histogram
  - Radioactivity
  - Feynman Diagrams

The main part is contained in the "Z-Path" menu, with all the basics needed to perform the analysis, after an introduction to the subjects as LHC collisions, production and decay of short lived particles such as the Z and Higgs bosons, and their role. In the "Knowledge Center" menu, additional information is available in order for the whole Z-path to be more or less self-contained, aimed for teachers that would like to use the Z-path stand-alone, or for students that would like some more details. Here one can briefly learn about the Standard Model, and more about the Z-boson. It also explains the mathematical tools we encounter, such as momentum, vectors, and histograms, in addition to some general information about research at LHC, Feynman diagrams, and some information about radioactivity which relates to the weak force, which the Z-boson is part of.

After having introduced the Z-boson and Higgs boson, which are the first two items of the Z-path menu, explaining their role in Nature, and how they can be detected, the hands-on part begins. This starts with learning how ATLAS performs particle identification, and is accessed

through the "Identifying particles" menu item. By text and multi-media material, the students are guided through how the ATLAS detector is built and functions. Figure 9.2 shows a screenshot of one of the tools used: a slice of ATLAS, visualizing how the different particles interact with the detector material. The students learn about elementary particles such as the electron, muon, photon, and neutrinos, and composite particles such as protons and neutrons, in addition to jets of hadrons.

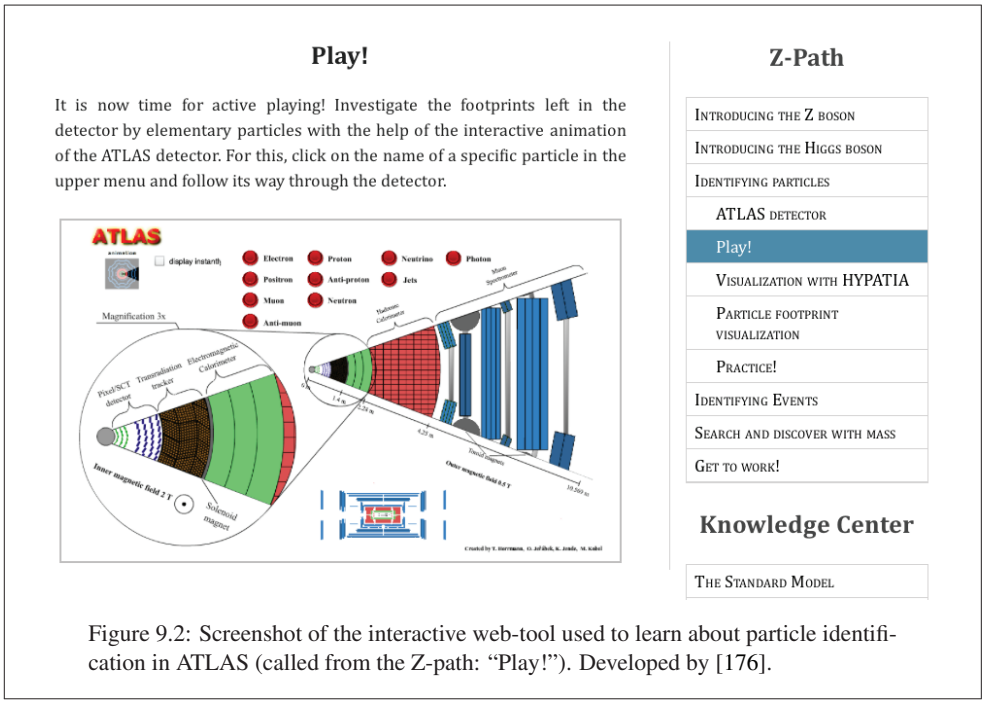

Figure 9.2: Screenshot of the interactive web-tool used to learn about particle identification in ATLAS (called from the Z-path: "Play!"). Developed by [176].

An important aspect is to learn how charged particles leave tracks in the inner detector, and how the different detector technologies are used to identify particles. Electromagnetic particles such as the electron and photon are totally absorbed in the electromagnetic calorimeters, and their energy is measured there. They must also learn that photons are neutral, and although they behave like the electron in the Electromagnetic calorimeter, they are invisible to the inner detector. Protons, neutrons and in general jets of hadrons are stopped in the hadronic calorimeter, where their energy is measured. And like the photon, neutrons are neutral, and thus do not leave tracks in the inner detector, while the positively charged protons do. Muons are special as they traverse the whole detector, and thus leave clear traces in both inner detector and the muon spectrometer (and some minimum signal in the calorimeters), and are therefore the easiest to identify. Neutrinos shoot through the detector without leaving a trace, and result in missing transverse energy. All these features can be tested in the web-application of Figure 9.2.

The HYPATIA event display's particle identification scheme is one of the main skills to learn. Together with the web-material, using screenshots and descriptive text, students work with their own version of HYPATIA, getting to know its features, and the way particles are

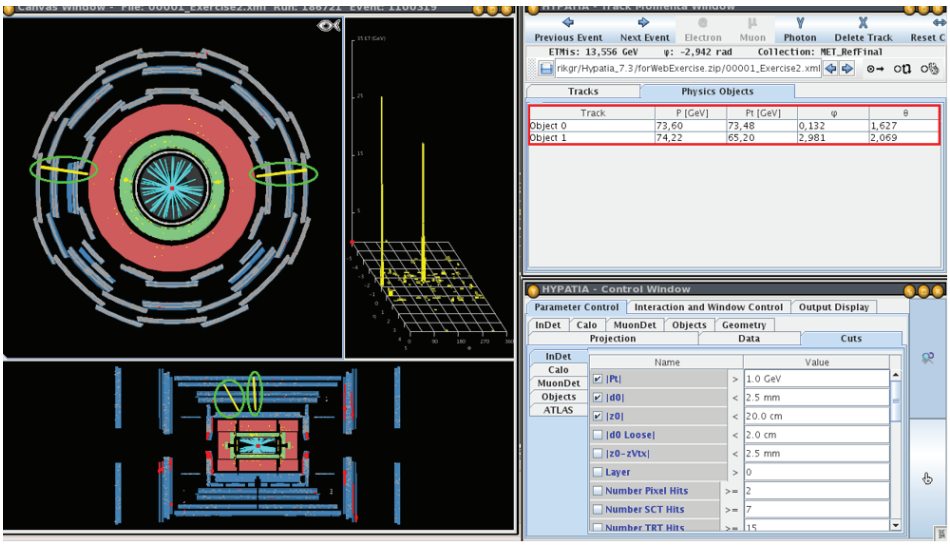

Figure 9.3: Screenshot of text and image explaining how to use HYPATIA. In this case how to use the "Physics Objects" tab to identify photons.

visualized. Figure 9.3 shows how to identify photons. It explains how photons (and electrons) are defined as "Physics Objects" and show up as yellow markers (circled in green) both in the transverse and longitudinal plane. To further decide whether the objects are photons or electrons, the student will use the "Cuts" tab in the bottom "Control Window" and put a minimum p_{T} threshold in order to remove low p_{T} tracks. This way it is easier to decide whether the calorimeter towers (yellow deposits in the (green) Electromagnetic calorimeter), corresponding to the physics object markers, are associated to tracks or not. If not, the objects are most probably photons.

A set of such images and text-boxes guides the students through the basics of particle identification, handling muons, electrons and photons, in addition to neutrinos and jets, and explaining the difference between particles and antiparticles. Finally, to end the session a test allows to check the newly aquired knowledge: The task is to identify different particles as an electron, positron, muon, anti-muon, photon, neutrino(antineutrino) or jet. The test is online, and allows to "check" your answer, and to see the correct answer.

Of all the mentioned particles, the students work mainly with electrons, muons, and photons in the analysis itself. So once they crack the particle identification code it is time to learn how to identify and distinguish the collision events, via the "Identifying Events" menu item. Like in the previous section, students practice with the help of screen shots and text, and learn about the signatures of the di-muon and di-electron resonances (J/ψ, Υ, Z, $Z^{'}$), and the Higgs resonance decaying into di-photons or four leptons. The web-pages also introduce background information to understand the complicated collision environment in ATLAS, and why we must

search for the decay products, and not directly the heavy particles, which we know decay instantly. Thus the students are effectively "event-detectives" and "bump-hunters", searching for the underlying happening, using only traces of the actual event.

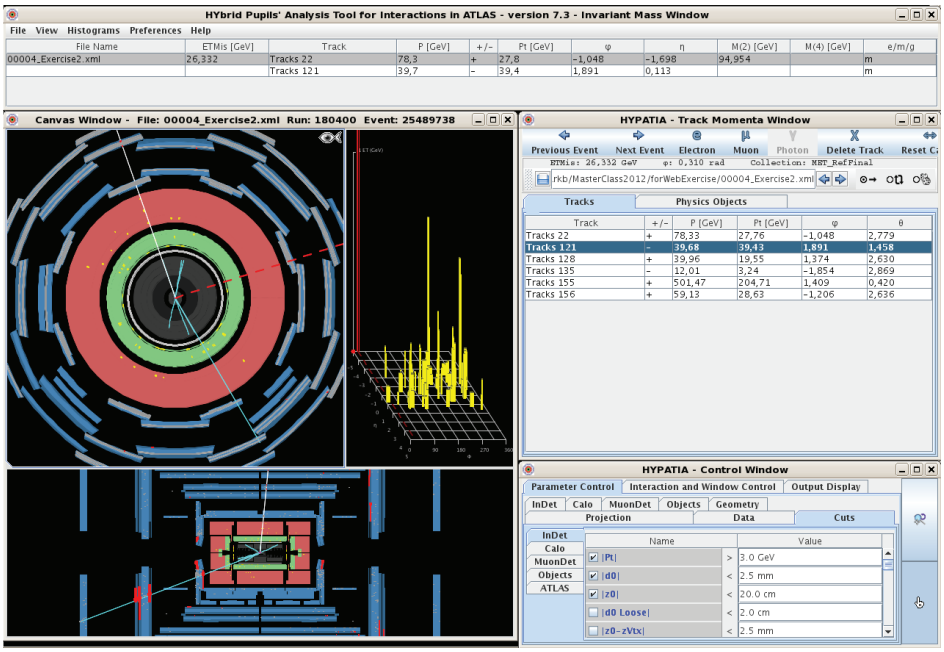

Figure 9.4: Screenshot of a $\mu^+\mu^-$ HYPATIA event display.

Figure 9.4 gives an example of how a di-muon event looks in HYPATIA. In this screenshot we see all the available windows. On the top we find the "Invariant mass Window", under it, the two event-views: transverse and longitudinal (in addition to the η, ϕ electromagnetic calorimeter energy deposit mapping), and to the right the "Track Momenta Window", and the "Control Window". Students click on the tracks, directly, or on on the tracks in the Track Momenta Window, to get information on charge, direction, and momentum of the selected track. In the main analysis, if the track is believed to be a candidate muon from a heavy particle decay, it is inserted into the Invariant Mass table by buttons at the top of the Track Momenta Window. When two particles (or four) are entered in one event, the Invariant Mass Window calculates the invariant mass and displays it in the table.

Finishing off the practise with identifying events, is another web-form test containing 10 e^+e^-, $\mu^+\mu^-$, $\gamma\gamma$, 4ℓ events, in addition to some possible background events.The students submit their answer to the web-form, and can check to see how many correct answers they got, and can then check the "correct answer" by clicking the button.

To understand the connection between the decay products and the original particle, we go more in detail about the concept of invariant mass, and how it is used to uniquely identify

particles. This is introduced in the "Search and discover with mass" menu item. Here they are introduced to Einsteins famous formula

$$E = \sqrt{(\vec{p} \cdot c)^2 + (m_0 \cdot c^2)^2} \tag{9.1}$$

leading to the invariant mass

$$m_0 = \sqrt{\left(\frac{E}{c^2}\right)^2 - \left(\frac{\vec{p}}{c}\right)^2} \tag{9.2}$$

Then, since momentum and energy is conserved in Nature, this implies that also the *invariant mass* m_0 is conserved. Therefore in a given process, like the production and decay of the Z-boson, m_0 before and after decay should be the same. This allows the reconstruction of the Z-mass through the energy and momenta of its decay products

$$m_0^{(Z)} = \sqrt{\left(\frac{E_{\ell^+} + E_{\ell^-}}{c^2}\right) - \left(\frac{\vec{p_{\ell^+}} + \vec{p_{\ell^-}}}{c}\right)^2} \tag{9.3}$$

So the students learn that through the very basic concept of conservation of energy and momenta, and through Einsteins energy-momentum relation, they have all the tools at hand for reconstructing masses of heavy, short-lived particles created in the proton-proton collisions at LHC. And with the mass being an inherit feature of elementary particles, the masses can be used as a mean to identify them, and in particular to reveal new, yet undiscovered particles.

Finally, with all the theory and practise under the skin, students (typically in groups of two) are ready to analyse their own unique data-set containing 50 collision events.

To help students identify the events, they are given a set of identification criteria to be guided by. For the di-lepton events they are asked to look for opposite sign lepton pairs. They must use the track information to identify the charges, as the leptons are so energetic that the charged lepton's trajectory is more or less straight, and not curved much by the magnetic field. Therefore it is usually not possibly to determine the charge by eye, by evaluating the direction of the curve. They furthermore use the cuts available through the Track Momentum Window to only allow tracks with a certain amount of momentum, and thus remove a large portion of background tracks. Depending on whether the resonance is a heavy particle like the Z, or $Z^{'}$, the leptons will be more or less back to back in the transverse plane as Figures 9.5 and 9.4 give examples of, for electrons an muons respectively, or boosted in one direction, which would typically be the case in J/ψ due to the low mass of the resonance.

The $H \rightarrow \gamma\gamma$ offers extra challenges, as we also include events with one or two converted photons. An example of a such an event is depicted in Figure 9.6. In order to distinguish whether the event contains an e^+e^- or photon pair, students are asked to check the invariant mass of the e^+e^- pair, in order to test the photon mass hypothesis. Thus, if the resulting invariant mass is close to 0, the electron-positron pair stems from a converted photon. In the example in Figure 9.6 this is indeed the case, as the invariant mass is found at 0.311 GeV. In addition they can experiment with requiring a certain amount of Inner Detector hits, since photons that convert will typically not leave tracks in the inner most detector layers. This is possible by

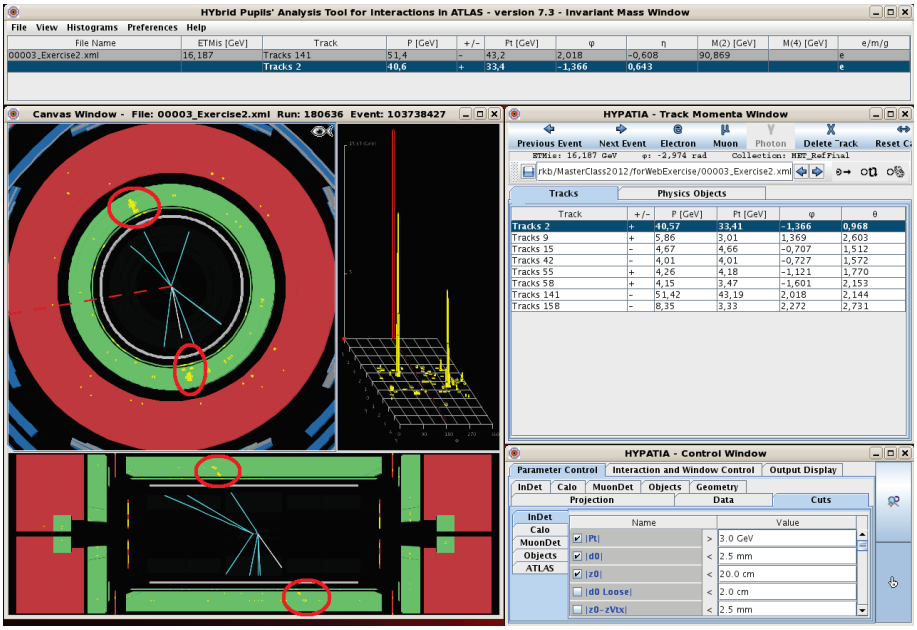

Figure 9.5: Screenshot of an event with a Z decaying to e^+e^-, as displayed in HYPATIA.

toggling the "Cuts" tab of the "Control Window", and for instance requiring at least 2 pixel hits. In the example, both tracks disappear with this requirement.

Another important point when dealing with di-photon events, where one photon has converted, is to help the students understand that we are looking for di-lepton, four-lepton or di-photon events only. If we find a single photon together with either a single or two electrons, it does not fit our event criteria, so more analysis is needed to determine the event-type. In the case of a converted photon and only a single electron track, we can be facing failure in software reconstruction, or very close together electron-positron pairs which are difficult (or impossible) to distinguish. A nice challenge for students, and a great possibility to go more in depth in particle identification and the physics behind it all.

So, the $H \to \gamma\gamma$ really puts the students on the spot, and presents the exact same challenges we as scientists face when analysing events. The only difference being that we do not do it visually event-by-event, but rather write computer programs to perform the selection for us.

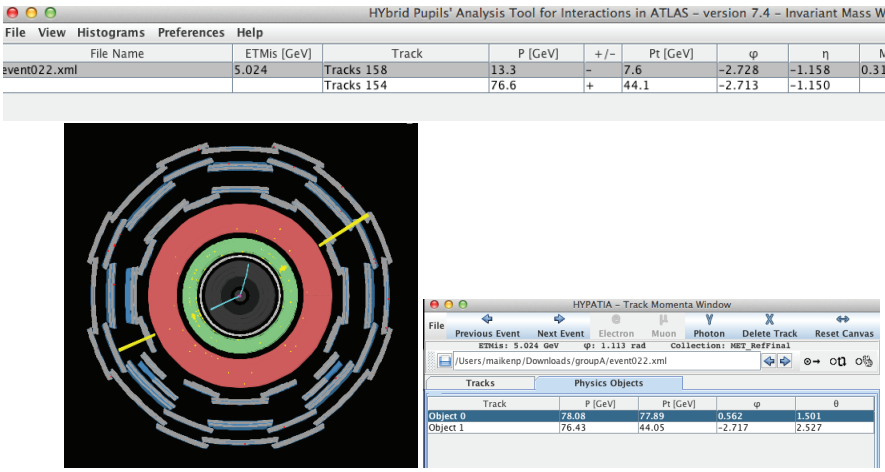

Figure 9.6: Screenshot of an $H \to \gamma\gamma$ event as displayed in HYPATIA. One γ converted (the bottom one), and the invariant mass of the electron-positron pair is found to be close to 0, namely 0.33 GeV as the invariant mass table shows.

9.4 Analysis results in OPloT

After all 50 events are analysed, the students export their Invariant Mass table, and upload it to OPloT. Figure 9.7 shows a screenshot of the student submission page, with drop-down menus to select correct upload folder. After submission, the results in form of histograms, are automatically combined behind the scene.

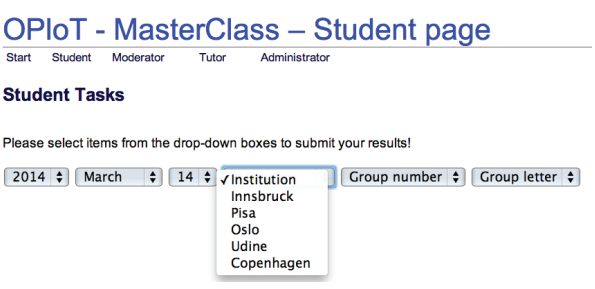

Figure 9.7: Screenshot of the OPloT student submission page.

Figure 9.8 gives an example of the resulting histograms available in OPloT. The top plot displays the di-lepton results, the middle the four lepton result, and the bottom plot the di-photon results. The di-lepton statistics on the right-hand side can be used to discuss the various particle masses and widths, showing the separate information for electrons and muons, and grouped into reasonable mass-ranges. These can however be adjusted by the entry-boxes below the histogram (not shown here), if desired. Finally, there is a table of statistics showing how many events of

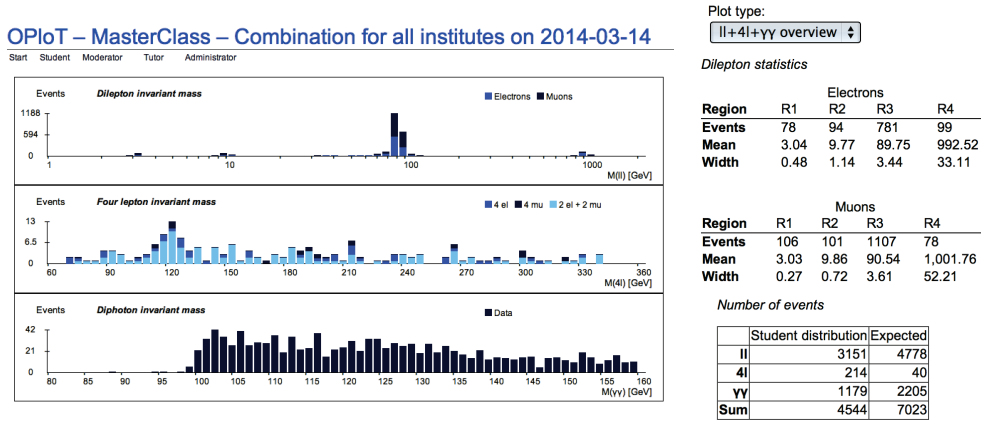

Figure 9.8: An overview of all combined histograms in OPloT.

each type were analysed by the students ("Student distribution") , and how many were available in the samples used that day ("Expected"). The expected number assumes that all events distributed that day were analysed, which is usually not the case, but it gives a nice overview of the expected perfect analysis. In particular we see that the students found more than 5 times the expected 4ℓ events!! A good chance to discuss bias, and mistakes performed in the analysis, which is taken up in the next section. By using the drop-down menu "Plot type" to the right one can select each of these histograms for closer inspection, for instance the di-lepton result, as shown in the example of Figure 9.9. We can clearly recognize the invariant mass peaks of the $J\psi$ at $\sim$ 3 GeV, the Υ at $\sim$ 10 GeV, and the Z boson at $\sim$ 91 GeV. In addition the simulated $Z^{'}$ shows up at $\sim$ 1 TeV. A very nice result indeed!

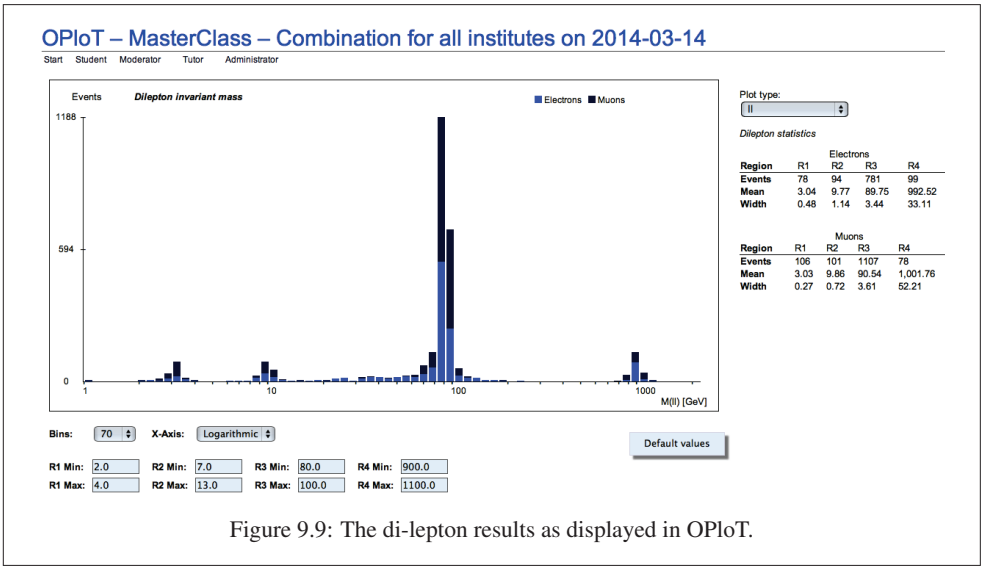

Figure 9.9: The di-lepton results as displayed in OPloT.

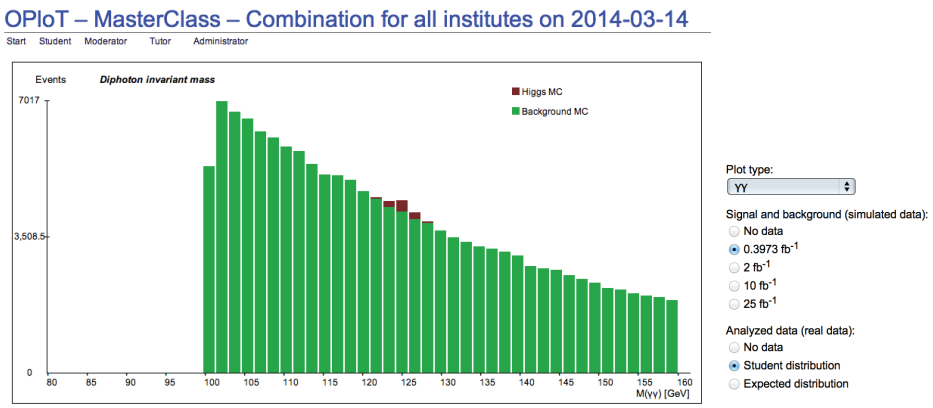

Figure 9.10: The 25fb^{-1} $H \rightarrow \gamma\gamma$ expected results as displayed in OPloT, with the signal results overlaid. The events are simulated.

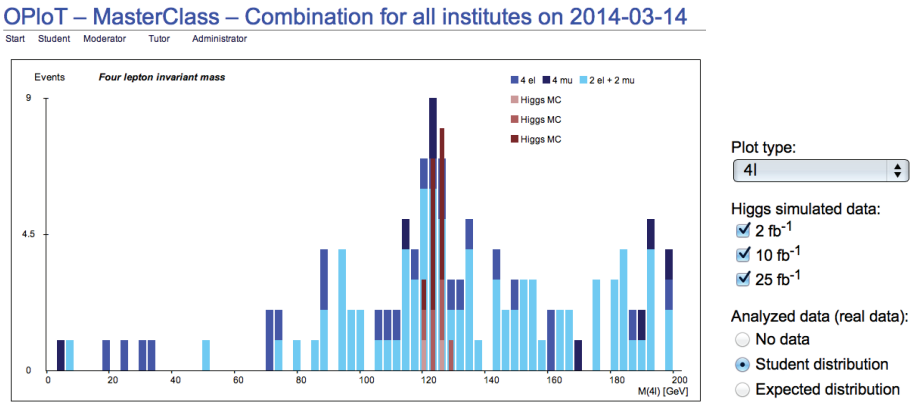

Figure 9.11: The $H \rightarrow 4\ell$ results as displayed in OPloT, with the expected results overlaid.

9.5 Discussion of results

In the discussion of the results, themes like identifying particles by their mass (which particles do you see?), differences between electrons and muons (more muons than electrons?), and wide distribution (why not single mass-values?) are addressed. Widths of particles are discussed in terms of detector resolutions and natural particle widths related to lifetimes. Very often there are more muon events than electron events. This is because muons are easier to identify, and students more often do mistakes with electrons. This is pointed out, as an important result, that we do mistakes, however, when combining the results, the mistakes are not so significant, and we still get a very nice mass peak, thus proving the importance of analysing many events.

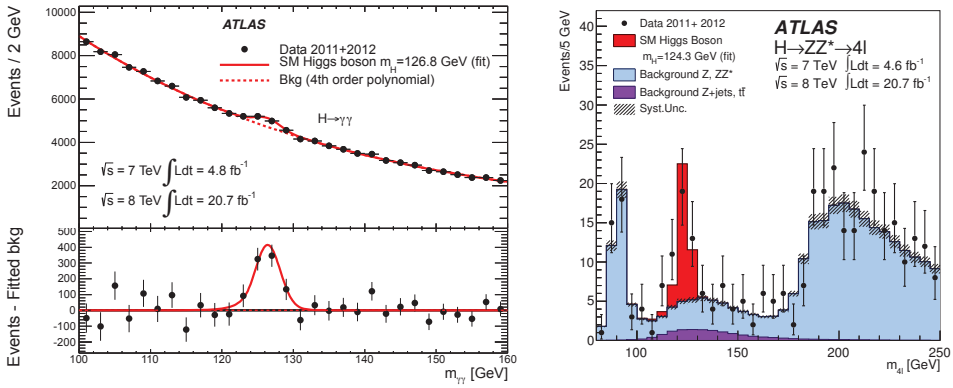

Figure 9.12: ATLAS official $H \to \gamma\gamma$ and $H \to 4\ell$ results.

For the di-photon distribution, an extra challenge is to distinguish between electrons and photons. In the first Masterclass using Higgs events in 2013, we encountered a Z-mass peak in the di-photon channel (!). This was clearly due to mistakenly identifying di-electron events as di-photon events. However, such mistakes are in fact very useful for discussion of results, as it allows to point out the similarities between photons and electrons, and also to explain that in fact this decay channel is forbidden (at tree level) in Nature. The $H \to \gamma\gamma$ also offers an excellent opportunity to discuss the fact that no signal is actually visible in the student results. Although many students interpret the result as a discovery, we can discuss the meaning of a significant result, versus a result where the background completely swamps the signal. This concerns also for the $H \to 4\ell$, although here the background is much smaller, and we can even with very few events claim discovery. Much more important - students learn about how probable it is that a 125 GeV Higgs candidate is in fact a Higgs: as high as 50% for $H \to 4\ell$ and much less for $H \to \gamma\gamma$. To help the discussion of the Higgs results OPloT enables use of expected simulated signal distributions corresponding to 2, 10, and 25 fb^{-1}, which can be overlaid the student distribution. Figures 9.10 and 9.11 demonstrates this feature for $H \to \gamma\gamma$ and $H \to 4\ell$ respectively. The student distribution is shown in blue, and the MC signal in red-tones. In the $H \to \gamma\gamma$ is shown the expected background distribution in green, clearly demonstrating the difficult bump-hunting in the $\gamma\gamma$ channel, as the signal is nothing more than a statistical fluctuation with this amount of data.

However, the student distributions are overall very good, and the final message is therefore that if they had had the full $H \to \gamma\gamma$ and $H \to 4\ell$ statistics used by ATLAS, and shown in Figure 9.12, they would have made the discovery themselves!

9.6 Experiences and improvements, and outlook

Overall, the Z-path is a great success. It is the most popular Masterclass (out of the CMS, ATLAS W, ATLAS Z, ALICE, and LHCb masterclasses arranged by IPPOG), as the concept of invariant mass is very well suited for educational purposes, with its clear interpretation of identifying particles, and clear mass-peak results. The Z-path continues to develop and improve.

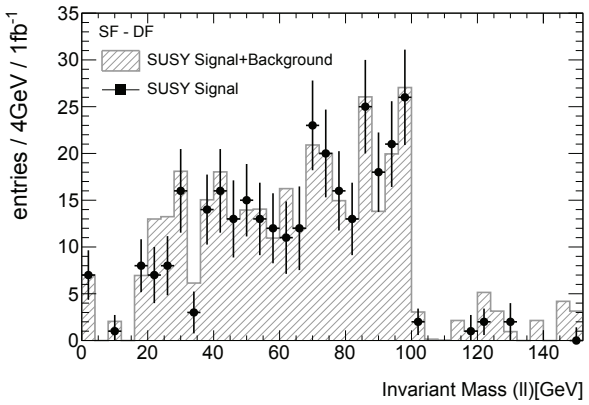

Figure 9.13: SUSY Signal invariant mass endpoint illustration. The black markers are SUSY signal (mSUGRA), and the histogram is the combined signal and background.

The first version only including di-lepton resonances was found on the easy side by many students. With Higgs entering the game we accomodated such students by the extra challenge of identifying photons, and having to deal with $H \to \gamma\gamma$ with one or two converted photons. To not make the task too overwhelming, we this year increased the ratio of non- and singly-converted photons in the bulk of the data-samples, while some additional samples, only used when requested, have a larger fraction of doubly-converted photon events. This has made the overall event-mixture suitably challenging for most students.

In the developement area, we have more recently presented a script (written by Magnar Bugge) to loop through all (xml) events, thus giving possibilities to extend the Z-path tool to more advanced university students. We are working on projects where students first tune their "cuts" using event displays, followed by an automatic analysis with cuts on various variables and possibilities to plot all kinds of relevant quantities. OPloT can easily be extended to include other types of distributions, like $E_{\mathrm{T}}^{\mathrm{miss}}$, or p_{T} for instance, which allows an advanced physics analysis to be accessible for non-expert (higher education) students.

The mission is to bring to young students any discovery made by LHC experiments, and we have already succeeded with the Higgs boson. We are ready to implement some hypothetical graviton resonances to pop-up in dileptons, di-photons and even di-Z bosons. However, my hope is of course that supersymmetric particles are discovered. The Z-path is perfectly suited for invariant mass *endpoint* analysis [177] of supersymmetric particles. SUSY production often leads to decay chains where we have intermediate SUSY particles such as in $\tilde{q} \to q\tilde{\chi}_2^0 \to q\ell^{\pm}\tilde{\ell}^{\mp} \to q\ell^{\pm}\ell^{\mp}\tilde{\chi}_1^0$, i.e. resulting in a final state with an OSSF lepton pair. Constructing the invariant mass of the lepton pairs results in an endpoint which reflects the mass difference between the SUSY particles involved in the chain. Figure 9.13 shows the invariant mass distribution for SUSY di-lepton signal (in mSUGRA) and the total background. It is clear that the SUSY signal features a sharp cut-off at around 100 GeV. Feasability studies to make a suitable analysis for students, are on-going. This would naturally be the great continuation of the Z-path and my analysis with Supersymmetry, as I started off with end-point analysis in relation to my Master degree [178]. Let's hope a discovery is made! The Z-path is ready for a do-it-yourself measurement!

Conclusions and outlook

The timing for my quest into particle physics could not have been better. I begun my PhD programme as the LHC started up, and could analyze the first ATLAS data as it came in. Having to wait one year I got the chance to study cosmic muons in ATLAS, which was very interesting, and a great preparation for collision data.

This thesis describes in detail the work performed on the fake lepton estimation method using the Matrix Method. The fake analysis was first performed in the ATLAS SUSY di-lepton working group, when the focus was still on strong SUSY production, with cascade decays of the squarks and gluinos, and resulting jets in the final-state. First the method was included as a complimentary result on the 35 pb^{-1} data documented in the ATLAS internal (restricted) note: [152], which was the basis for the paper *"Search for supersymmetric particles in events with lepton pairs and large missing transverse momentum in* $\sqrt{s}$ *= 7 TeV proton-proton collisions with the ATLAS experiment"* in Eur.Phys.J.: [156]. For the 1 fb^{-1} data, the fake lepton estimation was the primary method for estimating fakes. This is documented in the ATLAS Internal note [153], which is the support material for the publication in Phys.Lett. B, *"Searches for supersymmetry with the ATLAS detector using final states with two leptons and missing transverse momentum in* $\sqrt{s}$ *= 7 TeV proton-proton collisions"*: [157]. Finally, the work on the fake lepton estimation continued in the di-lepton group, but now with focus on production of direct charginos, neutralinos, and sleptons, using the full 7 TeV dataset collected in 2011. The results in this thesis reflect the approach for the 2011 round of analysis, documented in the Internal ATLAS note [133], which is the support material for the publication in Phys.Lett. B *"Search for direct slepton and gaugino production in final states with two leptons and missing transverse momentum with the ATLAS detector in pp collisions at* $\sqrt{s}$ *= 7 TeV "* [134].

During the course of writing up the thesis, I reworked the semi data-driven fake lepton estimation we published in [134], and re-evaluated some of the systematic uncertainties. The results are compatible with the published ones, with slight improvements, as the systematic uncertainties on the fake lepton estimation are reduced. The results on the limits in the direct slepton search is furthermore improved compared to the publication, as a conservative approach was taken there, and an improved approach was found by E. Gramstad in [159], and has been adapted here.

I further developed a fully data-driven fake lepton estimation, yielding compatible results to the semi data-driven in the high $E_{\text{T}}^{\text{miss,rel}}$ signal regions, and improving the results at low $E_{\text{T}}^{\text{miss,rel}}$. Instead of using MC for the high $E_{\text{T}}^{\text{miss,rel}}$ range, the experimental $E_{\text{T}}^{\text{miss,rel}}$ dependency is taken into account directly together with the p_{T} dependency. The systematic uncertainties were also reduced compared to the semi data-driven results.

Using MC for the real lepton SM background, and the Matrix Method fake lepton estimation, a SUSY search is performed in four dedicated signal regions, defined in order to cover as much of the SUSY direct chargino, neutralino, and slepton final-state topology as possible. The SR-OSjveto, is an opposite-sign (OS), same flavour or different flavour (SF, DF) signal region, with a jet-veto, and a Z-veto. The SR-SSjveto encompasses same-sign (SS) di-lepton events of any flavour combination, and also applies a jet veto. The SR-2jets is for final states with jets, and OS SF di-leptons. Finally, SR-m_{T2} is an OS region, with an m_{T2} cut especially tailored for direct sleptons, in which case only SF leptons are selected. It is also included in the direct chargino and neutralino search, where both DF and SF lepton pairs are used.

No excess of data is found compared to the full SM prediction, in any of the signal regions. Therefore, the results are used to set limits on SUSY masses and cross sections, to narrow down the vast SUSY phase-space still open for discovery. Three different SUSY models are used for the limit-setting, namely the Direct Gaugino pMSSM model, the simplified models, and the direct slepton models. In this summary I only quote the results from the two latter. The best limits are obtained on $\tilde{\chi}_1^{\pm}$ mass limit of 120-360 GeV for $\tilde{\chi}_1^0$ mass of 10 GeV from the direct gaugino production channel, and $\tilde{\chi}_1^{\pm}$ mass limit of 80-250 GeV for $\tilde{\chi}_1^0$ mass of 10 GeV from the direct gaugino, neutralino production channel. In the direct slepton search the limit quotes 95-200 GeV on the mass of the $\tilde{\ell}$ for a $\tilde{\chi}_1^0$ mass of 20 GeV. In all three models the $\tilde{\chi}_1^{\pm}$ the excluded range decreases for increasing $\tilde{\chi}_1^0$. The gaugino results are similar as what we published in [134], and we improved the results on the direct slepton search.

When LHC starts up again in 2015, after almost two years of detector, computing and software upgrading to cope with higher luminosities, the center of mass energy will be increased from the 8 TeV it ran with before shut-down, to 13 TeV. Data-driven methods are always important when new energy-scales are reached, as MC must be tuned to describe the new energy regime. The fully data-driven fake lepton estimation could be an important ingredient at this stage.

The latest ATLAS summary plot on the electroweak gaugino search, based on the full 8 TeV data set, is shown in Figure 9.14. As we can see, the 2l limits shown in the dark blue line have improved significantly compared to the 7 TeV 4.7 fb^{-1} results which spanned the region 120-330 GeV. The new limit is 130-460 GeV, and the Matrix Method was used and developed further, to estimate the fake lepton backgrounds also here.

One might wonder why it is such an accomplishment to keep excluding larger and larger portions of SUSY phase-space. The answer is that if SUSY exists, it exists only at one specific place, and reducing the possibilities helps us focus the search on those areas. There is still hope. LHC has yet only delivered 2% of the scheduled data, and is expected to run until 2035. There are therefore still plenty of opportunities to discover SUSY.

When discovered, the educational material we developed is ready to accommodate a motivating measurement for high-school students to repeat the work performed by physicists. Students who took part in the International Masterclasses have mastered the invariant mass technique to identify and measure properties of known particles, such as Z; they could use the tool to find a hidden hypothetical new particle, Z′; they went on to search for the Higgs boson and

found it!

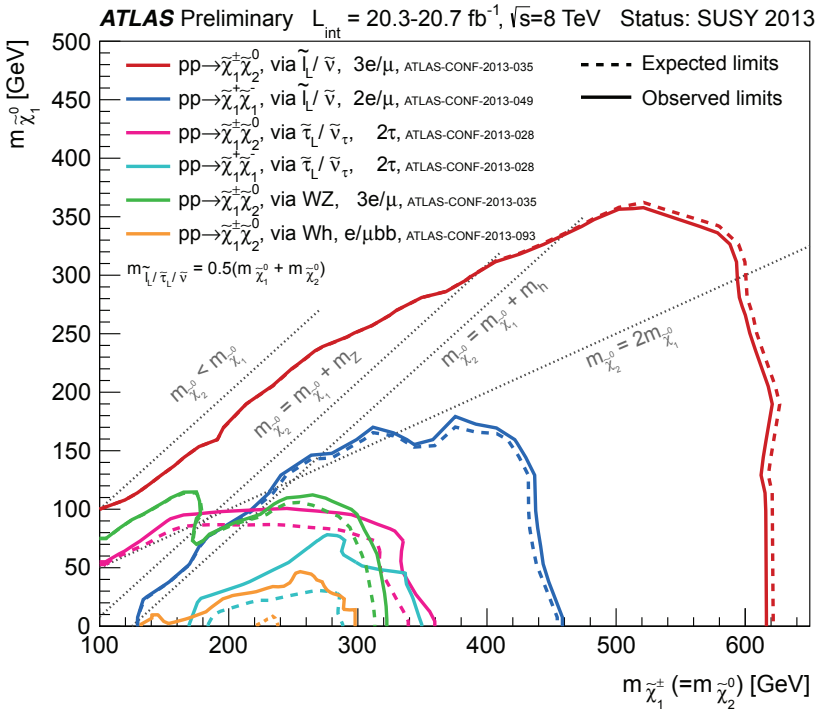

Figure 9.14: Summary of ATLAS searches for electroweak production of charginos $\tilde{\chi}_1^{\pm}$ and neutralinos $\tilde{\chi}_2^0\tilde{\chi}_1^0$ on 20 fb^{-1} of pp collision data at $\sqrt{s} = 8TeV$. Exclusion limits at 95% confidence level are shown in the $m_{\tilde{\chi}_1^{\pm}}$, $m_{\tilde{\chi}_1^0}$ plane. The dashed and solid lines show the expected and observed limits, respectively, including all uncertainties except the theoretical signal cross section uncertainties. This analysis contributes to the $2e\mu$ result shown in dark blue. As this plot is the most recent using 8 TeV data the limits are significantly improved compared to the limits obtained using 7 TeV data shown in this analysis [179].

Appendices

Appendix A

Semi Conducter Tracker noise-occupancy monitoring

As part of the monitoring of the Semi Conducter Tracker (SCT), the noise-occupancy is measured by the "ratio-noise" algorithm [180]. This algorithm replaced the space-point subtraction method in April 2012.

This section describes the algorithm and results obtained using different implementations of the ratio-noise algorithm. The investigation and comparisons of the results encompassed my "ATLAS Qualification work", the service work required for all ATLAS members to qualify as an ATLAS author. First, an overview is given of the online monitoring-system of which the noise monitoring is part of.

A.1 ATLAS DAQ Monitoring

A crucial part of data taking is the online and offline monitoring of the detector and data quality. Here, the main focus is on the online framework in particular. Although the monitoring framework of the online and offline implementation differ, the basic monitoring application is used by both. The difference between them is mainly due to interfaces to transient or persistent storage systems, and is not discussed further here.

The monitoring of both detector hardware and data produced by the detector is managed by four main components. These are the Event Monitoring Service (EM), Error Service (ES), Information Serivce (IS), and Online Histogramming Service (OHS). The services are responsible for collecting and distributing operational data for monitoring purposes, and handle data types from simple counters, to histograms and up to whole events.

Figure A.1 gives a rough schematic overview of the information flow from various stages of the detector's read-out-systems and event processing to the resulting display of monitoring information. All services can receive data at different points of the data processing chain, from the Read Out Driver (ROD), the Read Out Systems (ROS), or from the fully constructed events in the event builder (EB), also known as Sub Farm Input (SFI). The Information, Online Histogram and Error services can also receive events that have passed through the Event

Monitoring Service (EMS), which provides a framework for sampling and distributing events or event fragments.

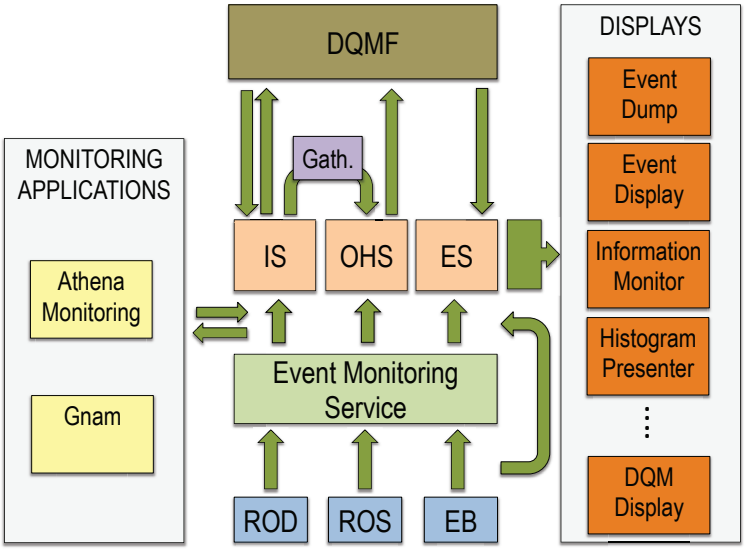

Figure A.1: Framework of online monitoring. Abbreviations are listed here: ROD: Read Out Driver, ROS: Read Out Systems, EB: Event Builder, IS: Information Service, OHS: Online Histogram Service, ES: Error Service, DQMF: Data Quality Framework, Gath: Gatherer, and GNAM: (Gnam is Not AtlMon).

The Error Service (or Message Reporting Service) is in charge of collecting and reporting errors related to the DAQ. Consumers, for instance a display, must subscribe to the service, and the errors are then presented in separate error monitoring displays.

The Information Service (IS) collects and distributes simple information objects suchs as numbers or more complicated objects like histograms. Information collected by the IS, is commonly distributed over several nodes, therefore a Gatherer [181] (marked with "Gath." in Figure A.1) is needed for combination. An example is when several processing tasks (PTs) produce the same histograms for a subset of events, and one needs to merge histograms for the final result. The Gatherer therefore communicates with the IS and the OHS to gather and publish the combined result back into the OHS.

A consumer (for instance a display) subscribes to notifications when changes occur to specified information items. A consumer can also send requests to the information providers, via the service system. Using the IS as an example, an application which has subscribed to a certain type of information, can request a change in the information distribution frequency via the IS.

The actual results (counters, values, histograms and so on), are produced by two main applications, namely GNAM [182] and Athena [183] Monitoring. GNAM is mostly used for monitoring the ATLAS hardware detector status, while the Athena Monitoring is used for the data-quality assessment. GNAM is not discussed further here. The Athena-based monitoring

algorithms use fully assembled events and produce objects like counter, vectors, histograms as well as more complicated data structures. Using histograms as an example, the naming convention follows a UNIX folder structure, and OHS creates folders on the fly as the histograms are published. However in OHS, histograms are in principle published without "knowing" of other histograms belonging to the same run. The Monitoring Data Archiving [184] (MDA) takes care of "connecting" histograms to runs, as it packs histograms from OHS into a single root file, one per run. It inherits the folder-structure following the histogram naming convention. A separate service, the Collection and Cache service [184] (CoCa) bundles up several files from MDA into large archives, and is responsible for storing the files on tape. In addition CoCa caches the most recent runs for easy access. CoCa can also distribute the files to the grid for world-wide access[1].

A separate framework built for the intelligent assessment of results, is the Data Quality Monitoring Framework (DQMF) [185]. It has its own display, namely the Data Quality Monitoring Display (DQMD). The purpose of DQMF is to run algorithms and examine information items from the various Online Services. It can produce alarms in the case that values are outside of predefined limits, and/or display colour-coding green, orange, red for intuitive quality assessment of the information items (such as histograms, or simple values).

The ratio-noise algorithm is implemented as part of the Athena SCT Monitoring package as a separate tool. The tool runs both online and offline. Online histograms produced by the tool, are published through the OHS via IS and the Gatherer, and are also used by the DQMF for checks on important parameters such as module-errors, hit occupancy or noise, to mention just a few.

A.2 The ratio-noise method

"Noise" can be defined as a spontaneous fluctuation of current or voltage, and refers to unwanted electric activity in electronics. It is a collective effect of several phenomena, such a *thermal* noise, fluctuations in number of charges leading to *shot* noise, one has *burst*, and *avalanche* noise, and so on. As noise is unavoidable, it is important to know its magntidue in order to set the appropriate signal to noise threshold. For SCT modules the noise-requirement is $< 5 \cdot 10^{-4}$ per strip. The method to measure noise can be rather complicated. The ratio noise algorithm was proposed as a simple and effective way of measuring noise.

Noise is (most commonly) measured in so-called "empty" events, where empty refers to the absence of collision between 2 beam particles. Empty events are triggered by for instance "L1 RDO Empty" or "L0 RDO Empty". Any hits, or fired strips are interpreted as noise in such an event. The probability that a strip fires is therefore taken as a measure of the noise, and is denoted by p_f.

The name "ratio-noise" refers to the definition of the noise as proportional to the ratio of fired strips (or hits) on a single side of a module to the number of strips with no hits on either side of a module. This is a very simple way to measure the noise and only requires counting hits on each module. In the derivation below we assume that the number of strips with hits on

[1]The two services were separated, as the features of CoCa were useful not only for the monitoring community.

Short-hand	Expressions	Prob	Explanation
p_f	P(s1) or P(s2)	p_f	Prob of a strip to fire
p_f^{not}	P(!s1) or P(!s2)	$(1-p_f)$	Prob of a strip to not fire
$p_f p_f^{\text{not}}$	P(s1 | !s2) or P(s2 | ! s1)	$p_f(1-p_f)$	Prob of a single strip to fire
$p_f p_f$	P(s1 and s2)	p_f^2	Prob of both strips to fire
$p_f^{\text{not}} p_f^{\text{not}}$	P(!s1 and !s2)	$(1-p_f)^2$	Prob of no strips firing

Table A.1: Table of probabilities for combinations of strips to fire or not.

both sides is negligible, which is a reasonable assumption in "empty"/non-physics events.

In order to find an expression for p_f, we must first establish expressions for the various possibilities for strips to fire or not. An SCT-module is built up of 12x128=768 strips, and each module consists of two sides. The probability for a single strip to fire or not depends on the joint hit-probability of all strips on a module. However, we start by considering a toy-module of only one side and two strips, and later generalize to a module of two sides and 768 strips.

The toy-module strips 1 and 2 are denoted as s1 and s2 respectively. For this two-strip single-sided module, the different possibilities can be expressed as in Table A.1.

Furthermore, we need an expression for the probability for at least one strip to fire ($p_f^{\geq=1}$). To find this, we exploit the fact that the sum of all probabilities is 1

$$1 = 2p_f p_f^{\text{not}} + p_f p_f + p_f^{\text{not}} p_f^{\text{not}} \qquad \text{or} \qquad 1 = 2p_f(1-p_f) + p_f^2 + (1-p_f)^2\,, \tag{A.1}$$

where the 2 in front of the first term is due to $p_f p_f^{\text{not}}$ entering once for each of the two strips considered. We use the above Equation (A.1) to express $p_f^{\geq=1} = 2p_f p_f^{\text{not}} + p_f p_f$ in terms of the probability that no strips fires, in the following manner:

$$p_f^{\geq=1} = 1 - p_f^{\text{not}} p_f^{\text{not}} = 1 - (1-p_f)^2 \tag{A.2}$$

We can simplify the probability in Equation (A.2) with a Taylor series expansion. Generalizing now from 2 to N_s, so that $(1-p_f)^2$ becomes $(1-p_f)^{N_s}$ and can be expressed as

$$\begin{aligned}(1-p_f)^{N_s} &= 1 + N_s(-p_f) + \frac{N_s(N_s-1)(-p_f)^2}{2!} + ... \\ &\simeq 1 + N_s(-p_f)\end{aligned} \tag{A.3}$$

This again means that the probability for at least one strip to fire $p_f^{\geq=1} = 1-(1-p_f)^{N_s}$ is to first order (assuming $p_f << 1$)

$$p_f^{\geq=1} \simeq N_s \cdot p_f\,, \tag{A.4}$$

where the Taylor Series expansion from Equation (A.3) has been used to replace $(1-p_f)^{N_s}$.

Moving now to an actual SCT module with 768 strips (on each side), the general probabilities can be expressed in the same way as Table A.1, but instead of two single strips, the

Short-hand	Expressions	Prob	Explanation
p_m	P(m1) or P(m2)	p_m	Prob of hits on a module-side
p_m^{not}	P(!m1) or P(!m2)	$(1-p_m)$	Prob of no hits on a module-side
$p_m p_m^{\text{not}}$	P(m1 | !m2) or P(m2 | ! m1)	$p_m(1-p_m)$	Prob of hits on a single module-side
$p_m^{\text{not}} p_m^{\text{not}}$	P(!m1 and !m2)	$(1-p_m)^2$	Prob of no hits on either module-sides

Table A.2: Table of probabilities for combinations of a module-side to encounter hits or not.

probabilities for hits of either sides of a module are considered. The expressions are equivalent, if one just replaces the word "strip" with "module-side", and p_f (probability of a strip firing) with p_m (probability of hits on one side of the module). This gives us Table A.2 (only showing the relevant probabilities).

We now appreciate that p_m (probability of hits on one module-side) is in fact the same as the probability that one or more strips fire, so p_m is

$$p_m = p_f^{>=1} \simeq N_s \cdot p_f \,.$$

Solving for the noise p_f we find that $p_f \sim p_m/N_s$. Now the challenge is to find an expression for p_m. This can be acquired by a simple ratio. We define the ratio R as the probability of the module to encounter one or more hits on a single side divided by the probability that the module encounters no hits on either side

$$\begin{aligned} R &\sim \frac{2 p_m p_m^{\text{not}}}{p_m^{\text{not}} p_m^{\text{not}}} \\ &= \frac{2 p_m (1-p_m)}{(1-p_m)^2} \,, \end{aligned} \tag{A.5}$$

where the 2 enters since we are considering both sides of the module. The numerator of R is then simply the number of single strips that fire on a module's one side only, while the denominator is the number of strip-pairs that do not fire on any side of a module. We then assume that a single strip only fires once per event. Solving for p_m gives

$$p_m \sim \frac{R}{2+R} \,.$$

We finally have all components needed to find the noise (NO), expressed through p_f:

$$\text{NO} = p_f \sim \frac{p_m}{N_s} = \frac{R}{(2+R)} \frac{1}{N_s} = \frac{R}{(2+R)} \frac{1}{768} \,. \tag{A.6}$$

A.3 Study of the ratio-noise results

The ratio-noise is calculated by the Athena-based tool SCTRatioNoiseMonTool. In the text to follow I refer to "offline" and "online" measurements of the ratio-noise. Both implementations

use the SCTRatioNoiseMonTool. An example of a noise measurement performed on modules in Barrel layer 0 over a certain period of time, can be seen in Figure A.2.

Online and offline differences in the ratio-noise measurements were one of the main incentives for putting the method under scrutiny. One must, however, be aware that it does not necessarily make sense to directly compare the two. This is due to several reasons, which are discussed in the following.

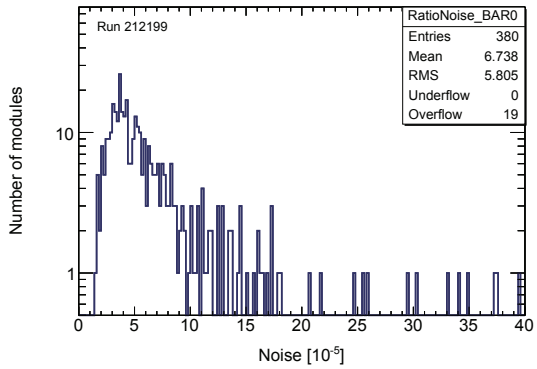

Figure A.2: Ratio-noise distribution for Barrel layer 0, run 212199 module-by-module, produced by SCTRatioMonTool both for online and offline.

The default online results integrate the ratio-noise over the entire run, including periods before stable beam. This complicates the interpretation of the results, since the modules during standby are in a low voltage configuration (typically around 50V) implying a higher noise-level. The offline results however, only use events from luminosity blocks with stable beams, when the SCT modules run with the nominal 150V. Therefore, the online results which include the low voltage period, will alone cause discrepancies when comparing to the offline.

As described in Section A.1 the DQMF receives input (numbers, histograms, events), and performs predefined tests on them. The results are displayed as a function of time. One of the histograms DQMF produces, is the mean ratio-noise per SCT disk or layer versus time. The mean here, refers to the histogram-mean of the ratio-noise for modules in that particular disk or layer, similar to the distribution Figure A.2, produced online in real-time. These athena-online input-histograms are refreshed every 1000 events, and thus give a snapshot of the ratio-noise level at a particular moment. Since DQMF extracts the mean of the athena-online ratio-noise measurement at predefined time-intervals, and stores them as function of time, it serves as a history of the online ratio-noise measurements. Figure A.3 shows an example of how this information can be extracted to produce a history of the ratio-noise. It is worth noting the single measurement performed before stable beams (blue hatched area) which lies considerably above the measurements perfomed with stable beam (hatched green). This is, as explained above, due to the low voltage state of the modules, which gives a higher noise-level.

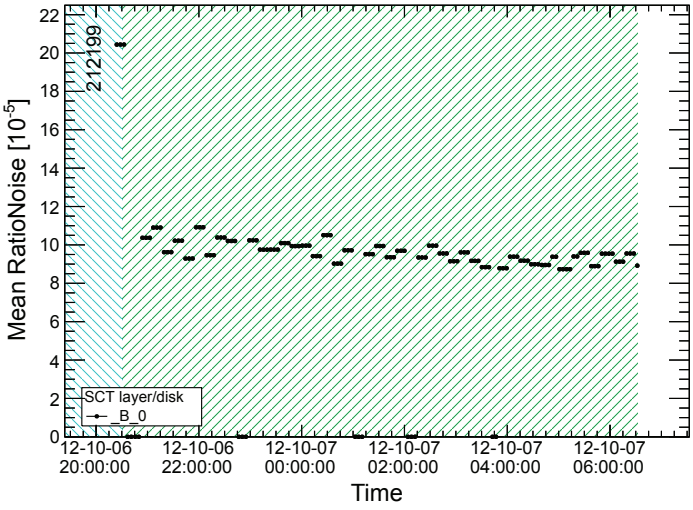

Figure A.3: Mean ratio-noise versus time from DQMF for run 212199. The blue area indicates the period of the run before stable beam, and the green area the period with stable beam. The measurement ends when the run stops (white area).

To be able to easily factor out the luminosity blocks before stable beam, such that an online and offline system comparison can be performed on a more equal footing, I added an online histogram which gives the ratio-noise per luminosity block for ensembles of modules (disks/layers, barrel/endcap and so on). Each measurement is performed by accumulating hits in one luminosity-block, producing the ratio-noise on the accumulated hits. An example of the result is shown in Figure A.4, using the same run as in Figure A.3. Comparing the two we see that they are comparable.

While the online implementation produces (among other things) ratio-noise measurements at designated intervals during the whole run, the offline performs a single measurement per module after accumulating hit information during the entire run, which results in a distribution similar to Figure A.2. A 1:1 comparison of the online and offline results can therefore not be made. However, a reasonable way to compare them is first to calculate the mean ratio-noise run-by-run for a particular layer or disk. For the offline histograms, this is simply the mean of the distributions shown in Figure A.2. For DQMF the mean must be calculated by averaging the measurements performed during stable beam, which corresponds to measurements in the green area in Figure A.3. The ratio between these offline and online (DQMF) results, are finally computed for each layer or disk, and displayed as a function of run number. An example of this ratio performed on runs 208126-210308, is shown in Figure A.5.

A red line is drawn to mark the 1:1 correspondence. We are interested in the general trend of the measurement, and do not pay attention to fluctuations around the main trend, as the comparison is particularly sensitive to the length of run. We see that for this particular layer of the SCT, the typical ratio between the offline and online results is around 0.3, with fluctuations by run varying from 0.2 to 0.4, which is rather far from 1.0. In this comparison only the measure-

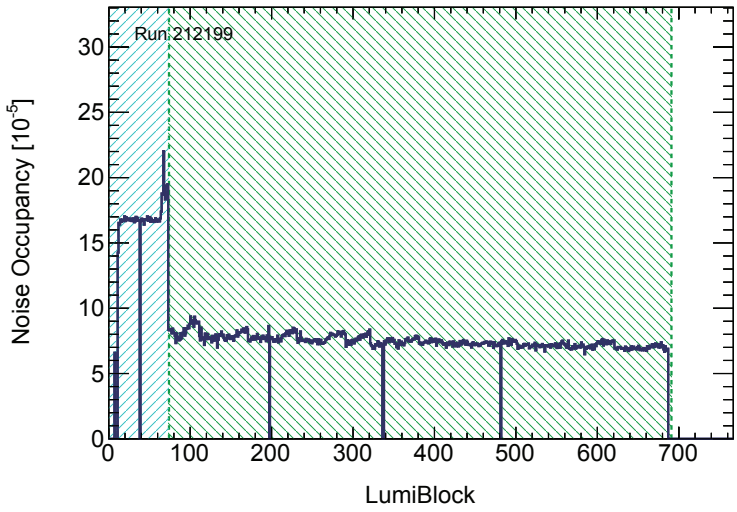

Figure A.4: The ratio-noise integrated over all modules in layer 0 of the barrel, as a function of luminosity block. The green area indicates the stable beam period.

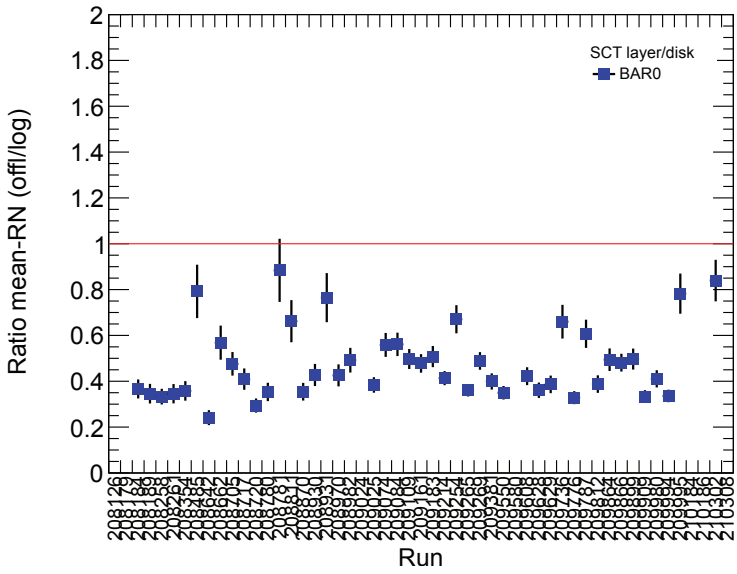

Figure A.5: Ratio between the ratio-noise extracted from offline and DQMF, for Barrel layer 0 as a function of run number

ments during stable-beams were used from the DQMF results, to give a fair comparison with the offline. One did not expect the differences to be so large.

A.3.1 Explanation of online and offline discrepancy

A closer look at the DQMF results revealed puzzling trends. Figure A.6 shows the mean ratio-noise displayed by the DQMF versus time. For both plots the STANDBY period with SCT modules in low voltage is in blue, and the ON period (stable beam), with SCT modules in high-voltage, is in green. The left plot of Figure A.6(a), shows the results for a single example run, run 209980. As expected the noise rather high at the beginning of the run, when SCT is in STANDBY (blue area). The surprising feature however, is that the noise features such a slow and smooth fall-off from STANDBY (blue) to ON (green). One should expect an immediate drop at the low to high voltage transition (as shown in fact already in Figure A.3 taken from a later run when the problem was solved). Figure A.6(b) shows a different run, and features a trend closer to what is expected. In this stable beam period (in green) a special situation occurred, namely that the run stopped and a new run started, causing all software algorithms to be re-started. This is a clear indication that the slow fall-off is a software-effect (a bug), implying that some counters or histograms used by the DQMF were not reset as they should. Effectively, this would mean that the high values measured in the STANDBY period are integrated with the lower values in the ON period, artificially producing a slow fall-off curve.

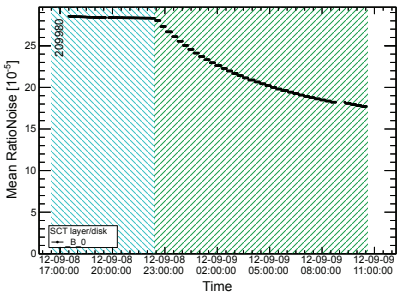

(a) Run 209980

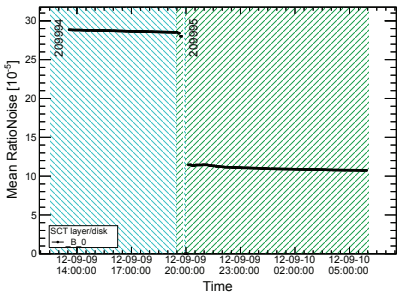

(b) Run 209994 and 209995

Figure A.6: Mean ratio-noise measured by DQMF versus time. The blue area marks the STANDBY-period, the green when SCT in ON. Left plot run 209980, right plot two consecutive runs 20994 and 20995.

This was indeed the case. It turns out that the vectors used to store the number of zero or one-side hits per module, were accumulating over the whole run, including the STANDBY period, and not re-initialized every 1000 events, as they should have been.

The figure we encountered earlier, Figure A.3 already has the bug-fix implemented, and as we see, the fall-off from low to high voltage module state is immediate. Compared to the distributions in Figure A.6 the measurements now fluctuate more, but this is expected, since there is no integration with previous measurements anymore.

A.3.2 Improvement of online and offline results

Figure A.7 shows a clear improvement of the ratio of offline to DQMF results compared to the one shown earlier in Figure A.5. There is still not a 1:1 agreement, but as explained, we do not expect this, as the methods differ.

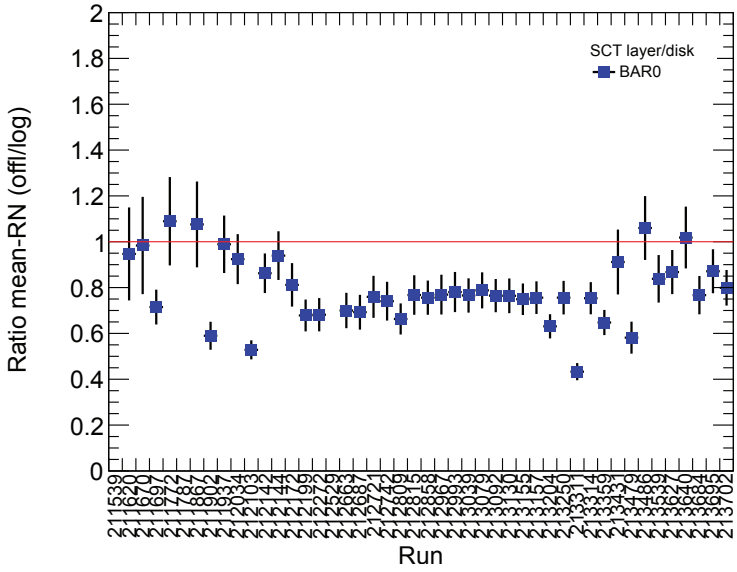

Figure A.7: Ratio between ratio-noise results extracted from offline and DQMF for Barrel layer 0 as a function of run number for runs after the bug-fix.

A more complete picture of the improvements can be found in Figure A.8. For each run and each detector layer and disk, the difference between the ratio noise measurements from two methods, a and b, has been calculated. The difference is defined as

$$\text{diff} = \frac{<\text{RN}^a> - <\text{RN}^b>}{<\text{RN}^a>}$$

where < RN > is the mean ratio-noise calculated as explained in the beginning of this section, depending on what type of method is used (online, offline, DQMF), and the superscript denotes the method.

The left column of Figure A.8 shows the comparison between online and DQMF ratio-noise measurements, and the right column between the offline and DQMF measurements. and the last column between the online and offline measurements. The top row shows the distributions before the correction ("Pre fix"), and the bottom after ("Post fix"). In the bottom-right plot it is in fact the online luminosity block histogram that are used and not the default online ones, since the luminosity-block histogram as explained can exclude measurements outside the stable-beam period. As the histogram was implemented at a later point, they are not used in the earlier runs shown in the top row.

Improvements between all methods can be seen by comparing top and bottom rows. All methods here refer to default online results, the online results using lumi-block info, the DQMF

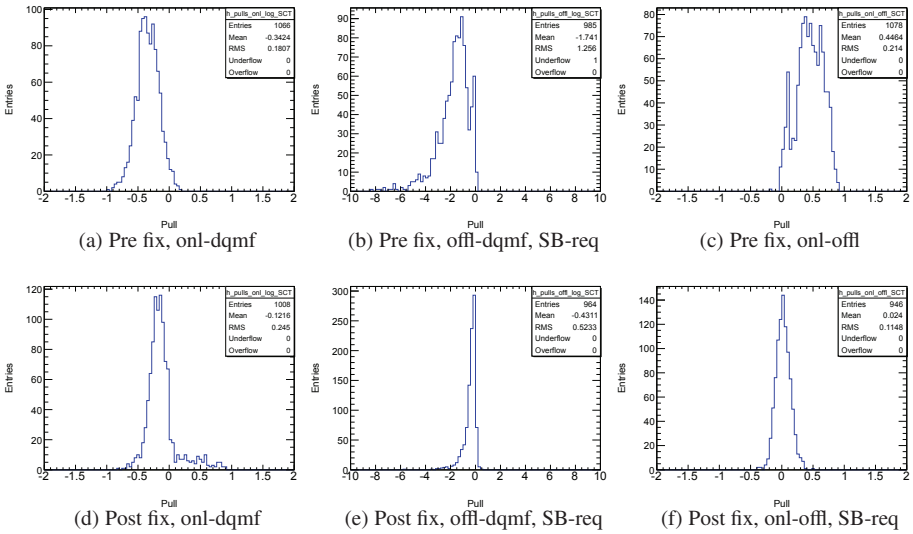

(a) Pre fix, onl-dqmf (b) Pre fix, offl-dqmf, SB-req (c) Pre fix, onl-offl

(d) Post fix, onl-dqmf (e) Post fix, offl-dqmf, SB-req (f) Post fix, onl-offl, SB-req

Figure A.8: Difference between ratio-noise results of the online and DQMF (left), between offline and DQMF (middle), and between online and offline (right). The bottom-right plot uses the luminosity-block online histograms instead of the default online. The rows show the results before (top) or after (bottom) the bug-fix.

and finally the offline results. Especially the online versus offline (bottom-right plot) shows a very good agreement after the code-corrections.

A.4 Conclusion

During the course of fall 2012 I performed my qualification work to become an official ATLAS author. The task was to understand the ratio-noise measurements, and in particular the online and offline discrepancies seen. During the course of this study a bug was found in the software, explaining the discrepancies.

Appendix B

Details on object definitions, event selection and data and MC samples

B.1 Electron object definitions

Type	Description	Name
Loose electron and photon cuts		
Acceptance of the detector	$\|\eta\| < 2.47$ for electrons, $\|\eta\| < 2.37$ for photons ($1.37 < \|\eta\| < 1.52$ excluded)	-
Hadronic leakage	Ratio of E_T in the 1st sampling of the hadronic calorimeter to E_T of the EM cluster (used over the range $\|\eta\| < 0.8$ and $\|\eta\| > 1.37$)	R_{had1}
	Ratio of E_T in the hadronic calorimeter to E_T of the EM cluster (used over the range $\|\eta\| > 0.8$ and $\|\eta\| < 1.37$)	R_{had}
Middle layer of the ECal	Ratio in η of cell energies in 3×7 versus 7×7cells	R_η
	Lateral width of the shower	w_2
Medium electron cuts (in addition to the loose cuts)		
Strip layer of the ECal	Total lateral shower width (20 strips)	w_{stot}
	Ratio of the energy difference between the largest and second largest energy deposits over the sum of these energies	E_{ratio}
Track quality	Number of hits in the pixel detector (≥ 1)	-
	Number of hits in the pixels and SCT (≥ 7)	-
	Transverse impact parameter (<5 mm)	d_0
Track matching	$\Delta\eta$ between the cluster and the track in the strip layer of the ECal	$\Delta\eta 1$
Tight electron cuts (in addition to the medium electron cuts)		
B-layer	Number of hits in the B-layer (at least one)	
Track matching	$\Delta\phi$ between the cluster and the track in the middle layer of the ECal	$\Delta\phi 2$
	Ratio of the cluster energy to the track momentum	E/p
TRT	Total number of hits in the TRT (used over the acceptance of the TRT, $\|\eta\| < 2.0$)	-
	Ratio of the number of high-threshold hits to the total number of TRT hits (used over the acceptance of the TRT, $\|\eta\| < 2.0$)	-

Table B.1: Description of the electron (and photon) identification scheme. [186]

B.2 Muon and electron reconstruction efficiency

The muon ([187]) and electron ([188]) reconstruction efficiencies are presented in Figure B.1. Both efficiencies use tag-and-probe $Z \to \ell^+\ell^-$. Tag and probe refers to the procedure to identify one lepton that has passed the reconstruction requiremenst (tag), and investigate whether the expected second lepton (probe) also does. The relative amount of times the probe passes the reconstruction is then defined as the reconstruction efficiency. We see that in general muons have a higher reconstruction efficiency, compared to electrons. The electrons are much more affected by the detector material due to bremsstrahlung effects, as demonstrated by the dependency on the η geometry.

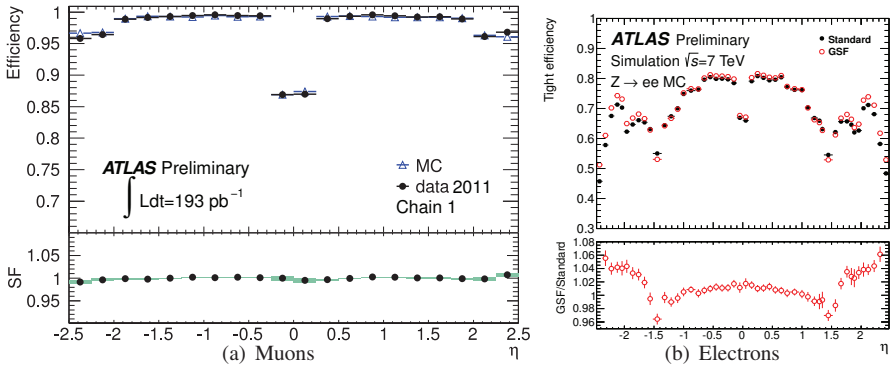

Figure B.1: Muon STACO (Chain 1) combined reconstruction efficiency (left) and electron tight++ reconstruction efficiency (right). The muon results compare data and MC, while the electron results are MC. The electron results are extracted from a study comparing two different track refitting algorithms (Gaussian sum-filter and standard Kalman filter).

B.3 Monte Carlo background samples

The SM MC samples used in this analysis are listed in Tables B.2-B.9. The entries marked in grey are samples used only for specific studies, while the rest make up the default full SM MC samples used throughout the thesis.

Sample ID	Short name	Generator	σxBR [pb]	kfac
116250/116260/116270	Zee/$\mu\mu$/$\tau\tau$Np0_Mll10to40	ALPG JIM	3.05 E+03	1.24
116251/116261/116271	Zee/$\mu\mu$/$\tau\tau$Np1_Mll10to40	ALPG JIM	8.49/8.48/8.49 E+01	1.24
116252/116262/116272	Zee/$\mu\mu$/$\tau\tau$Np2_Mll10to40	ALPG JIM	4.12/4.11/4.13 E+01	1.24
116253/116263/116273	Zee/$\mu\mu$/$\tau\tau$Np3_Mll10to40	ALPG JIM	8.35/8.34/8.35	1.24
116254/116264/116274	Zee/$\mu\mu$/$\tau\tau$Np4_Mll10to40	ALPG JIM	1.85/1.87/1.83	1.24
116255/116265/116275	Zee/$\mu\mu$/$\tau\tau$Np5_Mll10to40	ALPG JIM	4.60 E-01	1.24
		Total σ×BR×k-factor	1.19 E+04	
107650/107660/107670	Zee/$\mu\mu$/$\tau\tau$Np0	ALPG JIM	6.70 E+02	1.24
107651/107661/107671	Zee/$\mu\mu$/$\tau\tau$Np1	ALPG JIM	1.35 E+02	1.24
107652/107662/107672	Zee/$\mu\mu$/$\tau\tau$Np2	ALPG JIM	4.06 E+01	1.24
107653/107663/107673	Zee/$\mu\mu$/$\tau\tau$Np3	ALPG JIM	1.13 E+01	1.24
107654/107664/107674	Zee/$\mu\mu$/$\tau\tau$Np4	ALPG JIM	2.84	1.24
107655/107665/107675	Zee/$\mu\mu$/$\tau\tau$Np5	ALPG JIM	7.60 E-01	1.24
		Total σ×BR×k-factor	3.21 E+03	
109300/109305/109310	Zee/mumu/tautaubbNp0	ALPG JIM	6.57/6.56/6.57	1.24
109301/109306/109311	Zee/mumu/tautaubbNp1	ALPG JIM	2.48/2.47/2.49	1.24
109302/109307/109312	Zee/mumu/tautaubbNp2	ALPG JIM	8.90 E-01	1.24
109303/109308/109313	Zee/mumu/tautaubbNp3	ALPG JIM	3.90 E-01	1.24
		Total σ×BR×k-factor	3.85 E+01	
		Grand Total σ×BR×k-factor	1.51 E+04	

Table B.2: The Z/γ^* MC samples, divided into invariant mass ranges 10-40 (top-table), >40 (middle table), and separate samples with heavy flavour associated parton production (bottom table). The samples in the two top tables only have light associated partons generated. All samples are simulated with Alpgen interfaced with Jimmy (ALPG JIM). Jimmy uses Herwig for parton showering. An inclusive sample is achieved by combining all samples listed in the table.

Sample ID	Short name	Generator	σxBR [pb]	kfac
107680/107690/107700	Weν/$\mu\nu$/$\tau\nu$Np0	ALPG JIM	6.93 E+03	1.20
107681/107691/107701	Weν/$\mu\nu$/$\tau\nu$Np1	ALPG JIM	1.30 E+03	1.20
107682/107692/107702	Weν/$\mu\nu$/$\tau\nu$Np2	ALPG JIM	3.78 E+02	1.20
107683/107693/107703	Weν/$\mu\nu$/$\tau\nu$Np3	ALPG JIM	1.02 E+02	1.20
107684/107694/107704	Weν/$\mu\nu$/$\tau\nu$Np4	ALPG JIM	2.57 E+01	1.20
107685/107695/107705	Weν/$\mu\nu$/$\tau\nu$Np5	ALPG JIM	7.00	1.20
		Total σ×BR×k-factor	3.14 E+04	
106280	WbbNp0	ALPG JIM	3.34	1.20
106281	WbbNp1	ALPG JIM	2.68	1.20
106282	WbbNp2	ALPG JIM	1.39	1.20
106283	WbbNp3	ALPG JIM	6.60 E-01	1.20
		Total σ×BR×k-factor	9.65	
		Grand Total σ×BR×k-factor	3.14E+04	

Table B.3: The W boson production MC samples. As with the Z/γ^* these are also divided according to light and heavy flavour accompanying partons (top and bottom tables respectively).In the heavy flavour samples, all lepton flavours are included in one sub-sample.

Sample ID	Short name	Generator	σxBR [pb]	kfac
105985	WW	Herwig	1.15E+01	1.48
105986	ZZ	Herwig	9.75E-01	1.35
105987	WZ	Herwig	3.48E+00	1.70
		Total σ×BR×k-factor	2.42E+01	
126892	CT10_llnunu_WW	Sherpa	3.67E+00	1.09
126893	CT10_lllnu_WZ	Sherpa	6.26E+00	1.08
126894	CT10_llll_ZZ	Sherpa	4.62E+00	1.14
126895	CT10_llnunu_ZZ	Sherpa	3.38E-01	1.17
		Total σ×BR×k-factor	1.64E+01	

Table B.4: The di-boson production MC samples. Two different samples are shown, the Herwig samples (top), and the Sherpa samples (bottom). The former is used in jet-veto events, while the latter is for events with jets.

Sample ID	Short name	Generator	σxBR [pb]	kfac
105861	T1	PHeg PYT	9.06 E+01	1.00
105204	T0	MCNLO JIM	7.62 E+01	1.00
		Total σ×BR×k-factor	1.67 E+02	
108340/108341/108432	st_tc_$e\nu/\mu\nu/\tau\nu$	MCNLO JIM	6.97	1.00
108343/108344/108345	st_sc_$e\nu/\mu\nu/\tau\nu$	MCNLO JIM	5.00E-01	1.00
108346	st_Wt	MCNLO JIM	1.57E+01	1.00
		Total σ×BR×k-factor	3.81E+01	

Table B.5: The top quark MC samples. The top table shows the $t\bar{t}$ samples. T1 is the leptonic, while T0 is the fully hadronic sample. For the leptonic sample PowHeg Pythia (PHeg PYT) is used, while the fully hadronic sample used MC@NLO with Jimmy (MCNLO JIM). An inclusive sample is achieved by combining both. The single top production is shown in the bottom table, and is divided into sub-samples according to channel (s, t, Wt), and according to lepton flavour final state. All single top samples are simulated with MC@NLO Jimmy (MCNLO JIM). An inclusive single top sample is achieved by combining all three channels and flavours.

Sample ID	Short name	Generator	σxBR [pb]	kfac
109270	J0_jetjet_1elec	PYT	8.90 E+05	1.00
109271	J1_jetjet_1elec	PYT	9.94 E+05	1.00
109272	J2_jetjet_1elec	PYT	2.97 E+05	1.00
109273	J3_jetjet_1elec	PYT	4.30 E+04	1.00
109274	J4_jetjet_1elec	PYT	3.46 E+03	1.00
		Total σ×BR×k-factor	2.23 E+06	
109276	J0_jetjet_1muon	PYT	6.80 E+05	1.00
109277	J1_jetjet_1muon	PYT	7.78 E+05	1.00
109278	J2_jetjet_1muon	PYT	2.19 E+05	1.00
109279	J3_jetjet_1muon	PYT	2.84 E+04	1.00
109280	J4_jetjet_1muon	PYT	1.94 E+03	1.00
109281	J5_jetjet_1muon	PYT	7.07 E+01	1.00
		Total σ×BR×k-factor	1.71 E+06	
		Grand Total σ×BR×k-factor	3.94 E+06	

Table B.6: Pythia (PYT) inclusive di-jet MC samples, with an electron (1elec) or muon (1 muon) filter. The samples are divided into p_{T} ranges, where the number 0-5 indicates the range from low to high. Included are the tree-level $2\rightarrow 2$ processes: $q_iq_j \rightarrow q_iq_j$, $q_i\bar{q}_i \rightarrow q_k\bar{q}_k$, $q_i\bar{q}_i \rightarrow gg$, $q_ig \rightarrow q_ig$, $gg \rightarrow q_k\bar{q}_k$, and $gg \rightarrow gg$. Note: one would naturally expect J5 sample also for the electron-filter set, however, no SUSY_NTUP was available. This has minimal importance since the p_{T} cut is very high from 280-560 GeV, and a vanishing number of events is expected in this range, particularly when requiring two leptons.

Sample ID	Short name	Generator	σxBR [pb]	kfac
105802	JF17_pythia_jet_filter	PYT	9.20 E+07	1.00
		Total σ×BR×k-factor	9.20 E+07	

Table B.7: The so-called jet-filter 17 Pythia MC sample. Sub-processes include those listed in caption of Table B.6, but include in addition $q_i\bar{q}_i \rightarrow Q_k\bar{Q}_k$, $gg \rightarrow Q_k\bar{Q}_k$, $q_i\bar{q}_i \rightarrow q_i\gamma$, $q_i\bar{q}_i \rightarrow Z/\gamma^*$, $q_i\bar{q}_j \rightarrow W^{\pm}$. The two last processes could seem to supply leptonic states, but they are in fact filtered out by the generator jet-filter. Lower-case q implies all quark flavours, while upper-case Q implies heavy flavour only.

Sample ID	Short name	Generator	σxBR [pb]	kfac
105757	PythiaB_mu10mu10X	PYTB	2.44 E+03	1.00
105758	PythiaB_mu10e10X	PYTB	4.38 E+03	1.00
105759	PythiaB_e10e10X	PYTB	1.23 E+03	1.00
		Total σ×BR×k-factor	8.04 E+03	

Table B.8: Heavy flavour filtered Pythia di-jet samples, where a $b\bar{b}$ or $c\bar{c}$ quark pair is required at generator level. Processes included are the same as in Table B.6, but with the additional heavy flavour filter. These samples in addition apply a di-lepton generator level filter, either di-muon, di-electron or muon-electron pair, all with minimum p_{T} of 10 GeV.

Sample ID	Short name	Generator	σxBR [pb]	kfac
108326	PYTB_bbe15X	PYT	8.47E+04	1.00
108327	PYTB_cce15X	PYT	3.09E+04	1.00
108405	PYTB_bbmu15X	PYT	8.47E+04	1.00
106059	PYTB_ccmu15X	PYT	3.16E+04	1.00
		Total σ×BR×k-factor	2.32E+05	

Table B.9: Heavy flavour filtered Pythia di-jet samples, where a $b\bar{b}$ or $c\bar{c}$ quark pair is required at generator level, in addition to the processes listed in the caption of Table B.6. These samples in addition apply a single-lepton generator level filter, (electron or muon), both with minimum p_{T} of 15 GeV.

B.4 Simulated luminosity and luminosity scale factors

The samples presented in the previous section each have a different number of events simulated, which corresponds to a certain integrated luminosity. The samples, their total cross-section (including branching ratios, efficiencies and k-factors), the sample's integrated luminosity, and the luminosity scale factor needed to scale up to $4.71 fb^{-1}$ is presented in the tables to follow.

Sample ID	σ [pb]	lumi-sim [fb^{-1}]	lumi-sf
107650	8.33e+02	7.94e+00	0.59
107651	1.67e+02	7.98e+00	0.59
107652	5.05e+01	3.97e+01	0.12
107653	1.40e+01	3.93e+01	0.12
107654	3.53e+00	4.25e+01	0.11
107655	9.45e-01	5.29e+01	0.09
107660	8.33e+02	7.95e+00	0.59
107661	1.67e+02	7.98e+00	0.59
107662	5.05e+01	3.96e+01	0.12
107663	1.40e+01	3.78e+01	0.12
107664	3.53e+00	4.25e+01	0.11
107665	9.45e-01	5.29e+01	0.09
107670	8.33e+02	1.27e+01	0.37
107671	1.67e+02	1.99e+01	0.24
107672	5.05e+01	1.99e+01	0.24
107673	1.40e+01	3.64e+01	0.13
107674	3.53e+00	4.11e+01	0.11
107675	9.45e-01	4.76e+01	0.10

Table B.10: Z/γ^*+jets samples.

Sample ID	σ [pb]	lumi-sim [fb^{-1}]	lumi-sf
116250	3.80e+03	2.62e-01	17.99
116251	1.06e+02	2.84e+00	1.66
116252	5.12e+01	1.95e+01	0.24
116253	1.04e+01	1.44e+01	0.33
116254	2.30e+00	1.74e+01	0.27
116255	5.72e-01	1.75e+01	0.27
116260	3.80e+03	2.63e-01	17.91
116261	1.05e+02	2.85e+00	1.66
116262	5.11e+01	1.96e+01	0.24
116263	1.04e+01	1.45e+01	0.33
116264	2.33e+00	1.72e+01	0.27
116265	5.72e-01	1.75e+01	0.27
116270	3.80e+03	2.63e-01	17.91
116271	1.06e+02	2.84e+00	1.66
116272	5.13e+01	9.72e+00	0.48
116273	1.04e+01	1.44e+01	0.33
116274	2.28e+00	1.76e+01	0.27
116275	5.72e-01	1.75e+01	0.27

Table B.11: γ^*+jets samples.

Sample ID	σ [pb]	lumi-sim [fb^{-1}]	lumi-sf
105757	2.44e+03	1.22e+00	3.86
105758	4.38e+03	6.81e-01	6.93
105759	1.23e+03	2.38e+00	1.98

Table B.12: PythiaB heavy flavour QCD sample with di-lepton filter.

Sample ID	σ [pb]	lumi-sim [fb^{-1}]	lumi-sf
108326	8.47e+04	5.31e-02	88.81
108327	3.09e+04	4.85e-02	97.19
108405	8.47e+04	5.29e-02	89.03
106059	3.16e+04	4.74e-02	99.40

Table B.13: Pythia heavy flavour QCD sample with lepton filter.

Sample ID	σ [pb]	lumi-sim [fb^{-1}]	lumi-sf
107680	8.29e+03	4.17e-01	11.29
107681	1.56e+03	1.60e+00	2.94
107682	4.52e+02	8.32e+00	0.57
107683	1.22e+02	5.57e+00	0.85
107684	3.07e+01	8.14e+00	0.58
107685	8.37e+00	8.36e+00	0.56
107690	8.29e+03	4.18e-01	11.28
107691	1.56e+03	1.60e+00	2.94
107692	4.52e+02	8.34e+00	0.57
107693	1.22e+02	8.28e+00	0.57
107694	3.07e+01	8.30e+00	0.57
107695	8.37e+00	8.36e+00	0.56
107700	8.29e+03	4.12e-01	11.43
107701	1.56e+03	1.60e+00	2.94
107702	4.52e+02	7.48e+00	0.63
107703	1.22e+02	8.29e+00	0.57
107704	3.07e+01	8.14e+00	0.58
107705	8.37e+00	7.77e+00	0.61

Table B.14: W+jets samples.

Sample ID	σ [pb]	lumi-sim [fb^{-1}]	lumi-sf
105985	1.70e+01	1.46e+02	0.032
105986	1.32e+00	1.90e+02	0.025
105987	5.92e+00	1.69e+02	0.028

Table B.15: Di-boson samples.

Sample ID	σ [pb]	lumi-sim [fb^{-1}]	lumi-sf
105861	9.06e+01	3.31e+01	0.14

Table B.16: $t\bar{t}$ samples.

Sample ID	σ [pb]	lumi-sim [fb^{-1}]	lumi-sf
108340	6.97e+00	2.54e+01	0.19
108341	6.97e+00	2.54e+01	0.19
108342	6.97e+00	2.53e+01	0.19
108343	5.00e-01	5.07e+02	0.009
108344	5.00e-01	5.07e+02	0.009
108345	5.00e-01	5.07e+02	0.009
108346	1.57e+01	5.06e+01	0.09

Table B.17: Single top samples.

Sample ID	σ [pb]	lumi-sim [fb^{-1}]	lumi-sf
109276	6.80e+05	1.18e-03	4008.8
109277	7.78e+05	1.29e-03	3665.6
109278	2.19e+05	2.28e-03	2066.3
109279	2.84e+04	1.76e-02	268.0
109280	1.94e+03	1.29e-01	36.53

Table B.18: Pythia J0-4 QCD samples with muon filter.

Sample ID	σ [pb]	lumi-sim [fb^{-1}]	lumi-sf
109270	8.90e+05	8.97e-04	5251.4
109271	9.94e+05	1.01e-03	4686.2
109272	2.97e+05	1.68e-03	2805.2
109273	4.30e+04	1.16e-02	405.9
109274	3.46e+03	7.22e-02	65.26

Table B.19: Luminosity scaling for Pythia J0-4 QCD samples with electron filter.

Sample ID	σ [pb]	lumi-sim [fb^{-1}]	lumi-sf
105802	9.20e+07	1.09e-05	433757.1

Table B.20: Pythia JF17 QCD sample with jet filter.

Appendix C

Supporting material for the Matrix Method fake estimation

C.1 Purity, statistics and fake rates in all control regions

The following tables give an overview over all the control regions tested for both muons and electrons, with event counts, fake rates and purity, in addition to the exact definition of the regions. They are the full set of QCD control regions studied related to Section 6.4.1.

Muon single lepton QCD control regions (CR-A)

	Before subtraction			After subtraction		
Region	f_{data} [%]	N_L	purity [%]	$f_{data}^{MC\,sub}$ [%]	N_L	Selection
R00	71.30 ± 0.07	447659	51.00	45.33 ± 0.97	228323	
R01	54.81 ± 0.11	196634	85.11	47.36 ± 0.17	167362	$E_{\mathrm{T}}^{\mathrm{miss,rel}} < 20$
R02	51.94 ± 0.19	71954	85.17	44.10 ± 0.25	61282	$E_{\mathrm{T}}^{\mathrm{miss,rel}} < 20, N_j \geq 1$
R05	54.07 ± 0.14	133012	87.11	47.70 ± 0.18	115860	$E_{\mathrm{T}}^{\mathrm{miss,rel}} < 20, \Delta\phi_{E_{\mathrm{T}}^{\mathrm{miss}},l} < 1.0$
R06	51.61 ± 0.21	54857	87.29	45.05 ± 0.26	47886	$E_{\mathrm{T}}^{\mathrm{miss,rel}} < 20, \Delta\phi_{E_{\mathrm{T}}^{\mathrm{miss}},l} < 1.0, N_j \geq 1$
R07	59.08 ± 0.09	281420	73.79	45.25 ± 0.31	207648	$E_{\mathrm{T}}^{\mathrm{miss,rel}} < 30$
R08	48.95 ± 0.17	90829	83.32	39.34 ± 0.25	75680	$E_{\mathrm{T}}^{\mathrm{miss,rel}} < 30, N_j \geq 1$
R11	55.91 ± 0.12	183064	78.25	44.27 ± 0.26	143240	$E_{\mathrm{T}}^{\mathrm{miss,rel}} < 30, \Delta\phi_{E_{\mathrm{T}}^{\mathrm{miss}},l} < 1.0$
R12	46.85 ± 0.19	69354	86.24	38.93 ± 0.25	59809	$E_{\mathrm{T}}^{\mathrm{miss,rel}} < 30, \Delta\phi_{E_{\mathrm{T}}^{\mathrm{miss}},l} < 1.0, N_j \geq 1$
R13	47.42 ± 0.11	211276	90.58	42.38 ± 0.14	191374	$m_{\mathrm{T}} < 40$
R14	41.03 ± 0.17	84927	91.72	36.21 ± 0.19	77897	$m_{\mathrm{T}} < 40, N_j \geq 1$
R17	45.71 ± 0.13	151673	91.33	41.00 ± 0.15	138528	$m_{\mathrm{T}} < 40, \Delta\phi_{E_{\mathrm{T}}^{\mathrm{miss}},l} < 1.0$
R18	40.27 ± 0.19	69341	91.76	35.45 ± 0.21	63629	$m_{\mathrm{T}} < 40, \Delta\phi_{E_{\mathrm{T}}^{\mathrm{miss}},l} < 1.0, N_j \geq 1$
R19	57.54 ± 0.09	295460	74.50	43.75 ± 0.33	220103	$m_{\mathrm{T}} < 60$
R20	44.80 ± 0.16	95194	86.33	36.67 ± 0.21	82178	$m_{\mathrm{T}} < 60, N_j \geq 1$
R23	53.94 ± 0.11	194299	78.82	42.24 ± 0.27	153148	$m_{\mathrm{T}} < 60, \Delta\phi_{E_{\mathrm{T}}^{\mathrm{miss}},l} < 1.0$
R24	42.90 ± 0.18	74699	88.02	35.75 ± 0.22	65753	$m_{\mathrm{T}} < 60, \Delta\phi_{E_{\mathrm{T}}^{\mathrm{miss}},l} < 1.0, N_j \geq 1$
R29	56.06 ± 0.45	12085	66.22	35.06 ± 0.81	8002	$N_j \geq 2, \Delta\phi_{E_{\mathrm{T}}^{\mathrm{miss}},l} < 1.0$
R30	53.44 ± 0.51	9588	74.51	38.36 ± 0.74	7144	$N_j \geq 2, \Delta\phi_{E_{\mathrm{T}}^{\mathrm{miss}},l} < 1.0, E_{\mathrm{T}}^{\mathrm{miss,rel}} < 30$
R31	43.41 ± 0.53	8776	84.57	33.88 ± 0.64	7422	$N_j \geq 2, \Delta\phi_{E_{\mathrm{T}}^{\mathrm{miss}},l} < 1.0, m_{\mathrm{T}} < 40$
R32	47.41 ± 0.50	9965	78.73	34.17 ± 0.67	7845	$N_j \geq 2, \Delta\phi_{E_{\mathrm{T}}^{\mathrm{miss}},l} < 1.0, m_{\mathrm{T}} < 60$

Table C.1: The muon fake rates, purities and event count before and after subtraction of real muons in single muon control regions. In the tables N_j means number of signal jets. m_{T}, $E_{\mathrm{T}}^{\mathrm{miss}}$, and $E_{\mathrm{T}}^{\mathrm{miss,rel}}$ are in GeV.

Muon same-sign QCD control regions (CR-B)

	Before subtraction			After subtraction		
Region	f_{data} [%]	N_L	purity [%]	$f_{data}^{MC\,sub}$ [%]	N_L	Selection
R00	50.25 ± 0.18	74022	98.23	49.40 ± 0.19	72708	
R02	51.97 ± 0.20	60980	99.38	51.69 ± 0.20	60604	$E_{\mathrm{T}}^{\mathrm{miss}} < 20$
R03	50.46 ± 0.19	69194	99.09	50.03 ± 0.19	68562	$E_{\mathrm{T}}^{\mathrm{miss}} < 30$
R04	50.15 ± 0.18	73462	98.47	49.41 ± 0.19	72334	$E_{\mathrm{T}}^{\mathrm{miss}} < 60$
R06	52.01 ± 0.20	59448	99.42	51.75 ± 0.21	59103	$E_{\mathrm{T}}^{\mathrm{miss}} < 20, \not{Z}$
R07	50.48 ± 0.19	67370	99.15	50.08 ± 0.20	66796	$E_{\mathrm{T}}^{\mathrm{miss}} < 30, \not{Z}$
R08	50.15 ± 0.19	71460	98.58	49.46 ± 0.19	70441	$E_{\mathrm{T}}^{\mathrm{miss}} < 60, \not{Z}$
R10	50.92 ± 0.48	10780	97.80	49.90 ± 0.49	10543	$N_j \geq 1, E_{\mathrm{T}}^{\mathrm{miss}} < 20$
R11	47.69 ± 0.43	13258	97.39	46.39 ± 0.45	12911	$N_j \geq 1, E_{\mathrm{T}}^{\mathrm{miss}} < 30$
R12	46.41 ± 0.41	14982	96.45	44.57 ± 0.43	14450	$N_j \geq 1, E_{\mathrm{T}}^{\mathrm{miss}} < 60$
R14	50.84 ± 0.49	10504	97.97	49.91 ± 0.50	10290	$N_j \geq 1, \not{Z}, E_{\mathrm{T}}^{\mathrm{miss}} < 20$
R15	47.54 ± 0.44	12892	97.58	46.33 ± 0.46	12579	$N_j \geq 1, \not{Z}, E_{\mathrm{T}}^{\mathrm{miss}} < 30$
R16	46.22 ± 0.41	14546	96.69	44.51 ± 0.43	14064	$N_j \geq 1, \not{Z}, E_{\mathrm{T}}^{\mathrm{miss}} < 60$
R17	50.38 ± 0.90	3120	88.45	44.39 ± 1.04	2759	$N_j \geq 2$
R19	50.53 ± 1.01	2434	92.12	46.59 ± 1.12	2242	$N_j \geq 2, E_{\mathrm{T}}^{\mathrm{miss}} < 30$
R20	49.38 ± 0.93	2904	90.10	44.19 ± 1.05	2616	$N_j \geq 2, E_{\mathrm{T}}^{\mathrm{miss}} < 60$
R22	51.98 ± 1.14	1922	93.26	48.76 ± 1.24	1792	$N_j \geq 2, \not{Z}, E_{\mathrm{T}}^{\mathrm{miss}} < 20$
R23	50.13 ± 1.04	2324	92.57	46.40 ± 1.14	2151	$N_j \geq 2, \not{Z}, E_{\mathrm{T}}^{\mathrm{miss}} < 30$
R24	48.95 ± 0.95	2766	90.59	44.02 ± 1.07	2505	$N_j \geq 2, \not{Z}, E_{\mathrm{T}}^{\mathrm{miss}} < 60$

Table C.2: The muon fake rates, purities and event counts before and after subtraction of real muons in same-sign di-lepton muon control regions. N_j means number of signal jets, and $\not{Z}$ denotes a z-veto (mainly relevant for electrons). $E_{\mathrm{T}}^{\mathrm{miss,rel}}$ is in GeV.

Muon single-lepton heavy flavour QCD control regions (CR-C)

	Before subtraction			After subtraction		
Region	f_{data} [%]	N_L	purity [%]	f_{data}^{MCsub} [%]	N_L	Selection
R01	59.00 ± 3.18	239	90.71	54.91 ± 3.52	216	$E_{\mathrm{T}}^{\mathrm{miss,rel}}$<10, m_{T}<40,mutag, $\Delta R(l, j) > 1.0$
R02	44.57 ± 2.34	451	92.63	40.26 ± 2.54	417	$E_{\mathrm{T}}^{\mathrm{miss,rel}}$<20, m_{T}<40,mutag, $\Delta R(l, j) > 1.0$
R03	40.69 ± 2.09	553	93.27	36.53 ± 2.25	515	$E_{\mathrm{T}}^{\mathrm{miss,rel}}$<30, m_{T}<40,mutag, $\Delta R(l, j) > 1.0$
R04	38.53 ± 2.01	584	93.42	34.33 ± 2.17	545	$E_{\mathrm{T}}^{\mathrm{miss,rel}}$<40, m_{T}<40,mutag, $\Delta R(l, j) > 1.0$
R05	37.46 ± 1.97	606	93.51	33.26 ± 2.11	566	m_{T}<40,mutag, $\Delta R(l, j) > 1.0$
R06	58.85 ± 3.16	243	90.30	54.54 ± 3.51	219	$E_{\mathrm{T}}^{\mathrm{miss,rel}}$<10, m_{T}<50,mutag, $\Delta R(l, j) > 1.0$
R07	44.80 ± 2.29	471	92.09	40.17 ± 2.50	433	$E_{\mathrm{T}}^{\mathrm{miss,rel}}$<20, m_{T}<50,mutag, $\Delta R(l, j) > 1.0$
R08	41.58 ± 2.04	582	92.61	37.04 ± 2.22	538	$E_{\mathrm{T}}^{\mathrm{miss,rel}}$<30, m_{T}<50,mutag, $\Delta R(l, j) > 1.0$
R09	39.51 ± 1.97	615	92.68	34.88 ± 2.14	570	$E_{\mathrm{T}}^{\mathrm{miss,rel}}$<40, m_{T}<50,mutag, $\Delta R(l, j) > 1.0$
R10	38.65 ± 1.93	639	92.65	33.94 ± 2.09	592	m_{T}<50,mutag, $\Delta R(l, j) > 1.0$
R11	42.03 ± 0.29	29549	95.85	39.58 ± 0.30	28323	$E_{\mathrm{T}}^{\mathrm{miss,rel}}$<30, m_{T}<40, $\Delta R(l, j) > 1.0$
R12	40.66 ± 0.28	30977	95.84	38.15 ± 0.29	29688	$E_{\mathrm{T}}^{\mathrm{miss,rel}}$<40, m_{T}<40, $\Delta R(l, j) > 1.0$
R13	43.04 ± 0.28	31475	94.54	39.85 ± 0.30	29757	$E_{\mathrm{T}}^{\mathrm{miss,rel}}$<30, m_{T}<50, $\Delta R(l, j) > 1.0$
R14	41.90 ± 0.27	33190	94.39	38.54 ± 0.29	31327	$E_{\mathrm{T}}^{\mathrm{miss,rel}}$<40, m_{T}<50, $\Delta R(l, j) > 1.0$
R15	57.88 ± 2.99	273	91.08	53.86 ± 3.29	248	$E_{\mathrm{T}}^{\mathrm{miss,rel}}$<10, m_{T}<40, mutag,
R16	44.27 ± 2.19	515	92.90	40.12 ± 2.37	478	$E_{\mathrm{T}}^{\mathrm{miss,rel}}$<20, m_{T}<40, mutag
R17	40.67 ± 1.96	627	93.46	36.64 ± 2.11	586	$E_{\mathrm{T}}^{\mathrm{miss,rel}}$<30, m_{T}<40, mutag
R18	38.58 ± 1.89	661	93.60	34.51 ± 2.03	618	$E_{\mathrm{T}}^{\mathrm{miss,rel}}$<40, m_{T}<40, mutag
R19	37.57 ± 1.85	684	93.66	33.49 ± 1.99	640	m_{T}<40, mutag
R20	57.14 ± 2.96	280	90.70	52.87 ± 3.27	253	$E_{\mathrm{T}}^{\mathrm{miss,rel}}$<10, m_{T}<50, mutag
R21	44.07 ± 2.14	540	92.36	39.56 ± 2.32	498	$E_{\mathrm{T}}^{\mathrm{miss,rel}}$<20, m_{T}<50, mutag
R22	41.15 ± 1.91	661	92.78	36.70 ± 2.07	613	$E_{\mathrm{T}}^{\mathrm{miss,rel}}$<30, m_{T}<50, mutag
R23	39.17 ± 1.85	697	92.84	34.62 ± 2.00	647	$E_{\mathrm{T}}^{\mathrm{miss,rel}}$<40, m_{T}<50, mutag
R24	38.31 ± 1.81	723	92.78	33.67 ± 1.96	670	m_{T}<50, mutag
R25	41.97 ± 0.27	32504	95.91	39.55 ± 0.29	31173	$E_{\mathrm{T}}^{\mathrm{miss,rel}}$<30, m_{T}<40
R26	40.63 ± 0.27	34050	95.89	38.15 ± 0.28	32650	$E_{\mathrm{T}}^{\mathrm{miss,rel}}$<40, m_{T}<40
R27	42.99 ± 0.27	34820	94.63	39.85 ± 0.28	32949	$E_{\mathrm{T}}^{\mathrm{miss,rel}}$<30, m_{T}<50
R28	41.88 ± 0.26	36697	94.47	38.58 ± 0.27	34667	$E_{\mathrm{T}}^{\mathrm{miss,rel}}$<40, m_{T}<50
R29	40.12 ± 0.26	34671	95.83	37.59 ± 0.28	33224	m_{T}<40

Table C.3: The muon fake rates, purities and event counts before and after subtraction of real muons in tag and probe heavy flavour control regions. $\Delta R(l, j)$ is the geometrical distance between the probe lepton and the jet, "mutag" refers to the requirement of a muon inside the b-jet. m_{T}, and $E_{\mathrm{T}}^{\mathrm{miss,rel}}$ are in GeV.

Electron single-lepton QCD control regions (CR-A)

	Before subtraction			After subtraction		
Region	f_{data} [%]	N_L	purity [%]	$f_{data}^{MC\,sub}$ [%]	N_L	Region
R00	44.07 ± 0.06	610907	71.68	27.19 ± 0.53	437910	
R01	30.87 ± 0.08	326542	90.96	25.23 ± 0.12	297025	$E_{\mathrm{T}}^{\mathrm{miss,rel}} < 20$
R02	30.36 ± 0.11	166892	92.09	25.38 ± 0.14	153685	$E_{\mathrm{T}}^{\mathrm{miss,rel}} < 20, N_j \geq 1$
R05	31.78 ± 0.10	221057	91.27	26.38 ± 0.13	201769	$E_{\mathrm{T}}^{\mathrm{miss,rel}} < 20, \Delta\phi_{E_{\mathrm{T}}^{\mathrm{miss}},l} < 1.0$
R06	31.35 ± 0.13	120970	92.53	26.70 ± 0.16	111929	$E_{\mathrm{T}}^{\mathrm{miss,rel}} < 20, \Delta\phi_{E_{\mathrm{T}}^{\mathrm{miss}},l} < 1.0, N_j \geq 1$
R07	33.54 ± 0.07	443328	85.74	24.68 ± 0.19	380094	$E_{\mathrm{T}}^{\mathrm{miss,rel}} < 30$
R08	28.39 ± 0.10	207297	91.43	22.87 ± 0.13	189525	$E_{\mathrm{T}}^{\mathrm{miss,rel}} < 30, N_j \geq 1$
R11	32.29 ± 0.09	295344	87.48	24.49 ± 0.17	258360	$E_{\mathrm{T}}^{\mathrm{miss,rel}} < 30, \Delta\phi_{E_{\mathrm{T}}^{\mathrm{miss}},l} < 1.0$
R12	28.04 ± 0.11	152908	92.30	23.10 ± 0.14	141127	$E_{\mathrm{T}}^{\mathrm{miss,rel}} < 30, \Delta\phi_{E_{\mathrm{T}}^{\mathrm{miss}},l} < 1.0, N_j \geq 1$
R13	25.61 ± 0.08	326284	93.72	21.69 ± 0.10	305791	$m_{\mathrm{T}} < 40$
R14	23.85 ± 0.10	182373	94.80	20.59 ± 0.11	172894	$m_{\mathrm{T}} < 40, N_j \geq 1$
R17	25.55 ± 0.09	247407	93.60	21.57 ± 0.11	231583	$m_{\mathrm{T}} < 40, \Delta\phi_{E_{\mathrm{T}}^{\mathrm{miss}},l} < 1.0$
R18	23.90 ± 0.11	148866	94.69	20.56 ± 0.12	140954	$m_{\mathrm{T}} < 40, \Delta\phi_{E_{\mathrm{T}}^{\mathrm{miss}},l} < 1.0, N_j \geq 1$
R19	30.91 ± 0.07	449650	87.49	23.10 ± 0.17	393403	$m_{\mathrm{T}} < 60$
R20	25.37 ± 0.09	215283	92.89	20.81 ± 0.11	199969	$m_{\mathrm{T}} < 60, N_j \geq 1$
R23	29.45 ± 0.08	309400	88.97	22.52 ± 0.15	275259	$m_{\mathrm{T}} < 60, \Delta\phi_{E_{\mathrm{T}}^{\mathrm{miss}},l} < 1.0$
R24	24.94 ± 0.11	165576	93.30	20.66 ± 0.12	154475	$m_{\mathrm{T}} < 60, \Delta\phi_{E_{\mathrm{T}}^{\mathrm{miss}},l} < 1.0, N_j \geq 1$
R29	30.48 ± 0.27	28786	85.56	21.14 ± 0.34	24629	$N_j \geq 2, \Delta\phi_{E_{\mathrm{T}}^{\mathrm{miss}},l} < 1.0$
R30	31.18 ± 0.30	23458	88.43	23.81 ± 0.36	20743	$N_j \geq 2, \Delta\phi_{E_{\mathrm{T}}^{\mathrm{miss}},l} < 1.0, E_{\mathrm{T}}^{\mathrm{miss,rel}} < 30$
R31	24.60 ± 0.29	22114	92.59	19.96 ± 0.32	20474	$N_j \geq 2, \Delta\phi_{E_{\mathrm{T}}^{\mathrm{miss}},l} < 1.0, m_{\mathrm{T}} < 40$
R32	26.32 ± 0.28	25522	90.55	20.27 ± 0.31	23108	$N_j \geq 2, \Delta\phi_{E_{\mathrm{T}}^{\mathrm{miss}},l} < 1.0, m_{\mathrm{T}} < 60$

Table C.4: The fake rates, purities and event counts, before and after subtraction of real electrons for the electrons in single electron control regions

Electron same-sign QCD control regions (CR-B)

	Before subtraction			After subtraction		
Region	f_{data} [%]	N_L	purity [%]	$f_{data}^{MC\,sub}$ [%]	N_L	Selection
R00	43.93 ± 0.13	141086	47.68	18.86 ± 0.89	67264	
R02	47.53 ± 0.15	104906	44.89	21.73 ± 1.07	47092	$E_{\mathrm{T}}^{\mathrm{miss}} < 20$
R03	44.98 ± 0.14	124972	47.09	19.69 ± 0.96	58850	$E_{\mathrm{T}}^{\mathrm{miss}} < 30$
R04	43.89 ± 0.13	139288	47.91	18.91 ± 0.89	66736	$E_{\mathrm{T}}^{\mathrm{miss}} < 60$
R06	35.00 ± 0.19	62360	76.19	25.15 ± 0.34	47512	$E_{\mathrm{T}}^{\mathrm{miss}} < 20, \not{Z}$
R07	33.03 ± 0.17	77404	76.67	23.26 ± 0.31	59349	$E_{\mathrm{T}}^{\mathrm{miss}} < 30, \not{Z}$
R08	32.93 ± 0.16	89558	74.73	22.35 ± 0.32	66924	$E_{\mathrm{T}}^{\mathrm{miss}} < 60, \not{Z}$
R10	42.49 ± 0.31	25866	59.66	24.09 ± 0.70	15431	$N_j \geq 1, E_{\mathrm{T}}^{\mathrm{miss}} < 20$
R11	39.95 ± 0.27	31966	62.18	22.49 ± 0.60	19877	$N_j \geq 1, E_{\mathrm{T}}^{\mathrm{miss}} < 30$
R12	38.37 ± 0.25	37086	63.15	21.07 ± 0.55	23418	$N_j \geq 1, E_{\mathrm{T}}^{\mathrm{miss}} < 60$
R14	34.13 ± 0.34	18920	80.28	25.86 ± 0.49	15188	$N_j \geq 1, \not{Z}, E_{\mathrm{T}}^{\mathrm{miss}} < 20$
R15	32.14 ± 0.30	23934	81.04	24.03 ± 0.42	19397	$N_j \geq 1, \not{Z}, E_{\mathrm{T}}^{\mathrm{miss}} < 30$
R16	31.30 ± 0.28	28350	79.94	22.59 ± 0.40	22662	$N_j \geq 1, \not{Z}, E_{\mathrm{T}}^{\mathrm{miss}} < 60$
R17	41.03 ± 0.51	9476	61.62	23.21 ± 0.97	5839	$N_j \geq 2$
R19	41.95 ± 0.56	7674	61.25	24.14 ± 1.08	4700	$N_j \geq 2, E_{\mathrm{T}}^{\mathrm{miss}} < 30$
R20	40.59 ± 0.52	9022	62.23	22.88 ± 0.98	5614	$N_j \geq 2, E_{\mathrm{T}}^{\mathrm{miss}} < 60$
R22	36.58 ± 0.69	4836	77.59	27.21 ± 0.97	3752	$N_j \geq 2, \not{Z}, E_{\mathrm{T}}^{\mathrm{miss}} < 20$
R23	35.48 ± 0.62	5924	77.56	25.91 ± 0.87	4594	$N_j \geq 2, \not{Z}, E_{\mathrm{T}}^{\mathrm{miss}} < 30$
R24	34.81 ± 0.57	7092	76.55	24.53 ± 0.82	5428	$N_j \geq 2, \not{Z}, E_{\mathrm{T}}^{\mathrm{miss}} < 60$

Table C.5: The electron fake rates, purities and event counts before and after subtraction of real electrons in same-sign di-lepton electron control regions. N_j means number of signal jets, and $\not{Z}$ denotes a z-veto. $E_{\mathrm{T}}^{\mathrm{miss,rel}}$ is in GeV.

Electron single lepton heavy flavour QCD control regions (CR-C)

	Before subtraction			After subtraction		
Region	f_{data} [%]	N_L	purity [%]	f_{data}^{MCsub}[%]	N_L	Selection
R01	51.79 ± 3.58	195	97.45	50.69 ± 3.67	190	$E_{\mathrm{T}}^{\mathrm{miss,rel}}$<10, m_{T}<40,mutag, $\Delta R(l, j) > 1.0$
R02	37.87 ± 2.50	375	97.92	36.66 ± 2.56	367	$E_{\mathrm{T}}^{\mathrm{miss,rel}}$<20, m_{T}<40,mutag, $\Delta R(l, j) > 1.0$
R03	33.55 ± 2.18	471	98.01	32.33 ± 2.22	461	$E_{\mathrm{T}}^{\mathrm{miss,rel}}$<30, m_{T}<40,mutag, $\Delta R(l, j) > 1.0$
R04	30.92 ± 2.04	511	98.03	29.68 ± 2.09	500	$E_{\mathrm{T}}^{\mathrm{miss,rel}}$<40, m_{T}<40,mutag, $\Delta R(l, j) > 1.0$
R05	29.50 ± 1.96	539	97.98	28.25 ± 2.01	528	m_{T}<40,mutag, $\Delta R(l, j) > 1.0$
R06	52.15 ± 3.46	209	97.32	51.01 ± 3.55	203	$E_{\mathrm{T}}^{\mathrm{miss,rel}}$<10, m_{T}<50,mutag, $\Delta R(l, j) > 1.0$
R07	37.02 ± 2.37	416	97.75	35.72 ± 2.42	406	$E_{\mathrm{T}}^{\mathrm{miss,rel}}$<20, m_{T}<50,mutag, $\Delta R(l, j) > 1.0$
R08	32.70 ± 2.05	526	97.79	31.34 ± 2.09	514	$E_{\mathrm{T}}^{\mathrm{miss,rel}}$<30, m_{T}<50,mutag, $\Delta R(l, j) > 1.0$
R09	30.35 ± 1.93	570	97.74	28.93 ± 1.97	557	$E_{\mathrm{T}}^{\mathrm{miss,rel}}$<40, m_{T}<50,mutag, $\Delta R(l, j) > 1.0$
R10	29.45 ± 1.86	601	97.58	27.97 ± 1.91	586	m_{T}<50,mutag, $\Delta R(l, j) > 1.0$
R11	28.33 ± 0.24	34227	96.35	25.97 ± 0.25	32978	$E_{\mathrm{T}}^{\mathrm{miss,rel}}$<30, m_{T}<40, $\Delta R(l, j) > 1.0$
R12	26.93 ± 0.23	36444	96.42	24.60 ± 0.24	35138	$E_{\mathrm{T}}^{\mathrm{miss,rel}}$<40, m_{T}<40, $\Delta R(l, j) > 1.0$
R13	28.57 ± 0.23	38756	95.61	25.76 ± 0.24	37056	$E_{\mathrm{T}}^{\mathrm{miss,rel}}$<30, m_{T}<50, $\Delta R(l, j) > 1.0$
R14	27.43 ± 0.22	41338	95.62	24.58 ± 0.23	39526	$E_{\mathrm{T}}^{\mathrm{miss,rel}}$<40, m_{T}<50, $\Delta R(l, j) > 1.0$
R15	49.33 ± 3.33	225	97.36	48.12 ± 3.42	219	$E_{\mathrm{T}}^{\mathrm{miss,rel}}$<10, m_{T}<40, mutag,
R16	36.45 ± 2.33	428	97.84	35.17 ± 2.38	418	$E_{\mathrm{T}}^{\mathrm{miss,rel}}$<20, m_{T}<40, mutag
R17	32.64 ± 2.04	530	97.91	31.34 ± 2.08	518	$E_{\mathrm{T}}^{\mathrm{miss,rel}}$<30, m_{T}<40, mutag
R18	30.03 ± 1.91	576	97.92	28.71 ± 1.95	564	$E_{\mathrm{T}}^{\mathrm{miss,rel}}$<40, m_{T}<40, mutag
R19	28.76 ± 1.84	605	97.86	27.43 ± 1.88	592	m_{T}<40, mutag
R20	49.79 ± 3.22	241	97.20	48.53 ± 3.31	234	$E_{\mathrm{T}}^{\mathrm{miss,rel}}$<10, m_{T}<50, mutag
R21	35.94 ± 2.21	473	97.64	34.55 ± 2.26	461	$E_{\mathrm{T}}^{\mathrm{miss,rel}}$<20, m_{T}<50, mutag
R22	32.15 ± 1.92	591	97.65	30.70 ± 1.97	577	$E_{\mathrm{T}}^{\mathrm{miss,rel}}$<30, m_{T}<50, mutag
R23	29.80 ± 1.81	641	97.60	28.27 ± 1.85	625	$E_{\mathrm{T}}^{\mathrm{miss,rel}}$<40, m_{T}<50, mutag
R24	28.97 ± 1.75	673	97.42	27.38 ± 1.80	655	m_{T}<50, mutag
R25	28.43 ± 0.23	37282	96.36	26.08 ± 0.24	35924	$E_{\mathrm{T}}^{\mathrm{miss,rel}}$<30, m_{T}<40
R26	27.04 ± 0.22	39690	96.42	24.71 ± 0.23	38268	$E_{\mathrm{T}}^{\mathrm{miss,rel}}$<40, m_{T}<40
R27	28.64 ± 0.22	42397	95.64	25.85 ± 0.23	40548	$E_{\mathrm{T}}^{\mathrm{miss,rel}}$<30, m_{T}<50
R28	27.49 ± 0.21	45212	95.64	24.67 ± 0.22	43239	$E_{\mathrm{T}}^{\mathrm{miss,rel}}$<40, m_{T}<50
R29	26.16 ± 0.22	41188	96.43	23.85 ± 0.23	39719	m_{T}<40

Table C.6: The electron fake rates, purities and event counts before and after subtraction of real electron in tag and probe heavy flavour control regions. $\Delta R(l, j)$ is the geometrical distance between the probe lepton and the jet, "mutag" refers to the requirement of a muon inside the b-jet. m_{T}, and $E_{\mathrm{T}}^{\mathrm{miss,rel}}$ are in GeV.

C.2 Data and MC comparison before and after statistical subtraction of MC leptons

The effect of the subtraction of real and conversion leptons on the p_{T} distribution of the selected control regions CR-A R13, CR-B R02 (mu) / R07 (el), and CR-C R19, is presented in Figures C.1 and C.2 for muons and electrons respectively. In the di-lepton same-sign region CR-B both leptons are used. The distributions are relevant in connection to Section 6.4.1, in particular the comparison of data and MC fake rates, Figures 6.20 and 6.21. QCD is modelled by the heavy flavour filtered PythiaB samples, and as usual the full MC SM background is included. Here a 30% uncertainty is used for the QCD sample cross section.

In the muon channel (Figure C.1) the data and MC agreement is quite good in all control regions. Looking more in detail, the QCD seems to be overestimated in CR-A and CR-C, and somewhat underestimated in CR-B. With all control regions, MC underestimates the data in the last high p_{T} bins, however we in fact run out of statistics here.

The electron distributions in Figure C.2 give a somewhat different picture. Especially in CR-B (but also in CR-A) QCD is underestimated, which as discussed in Chapter 6 is expected to be due to light flavour fakes which are not well represented in the PythiaB samples. CR-C however shows a good agreement in the low p_{T} bins (however, with a slight overstimation as in the muon channel), and as for muons, we see a slight underestimation in the last high p_{T} bin, but here the statistical error is large.

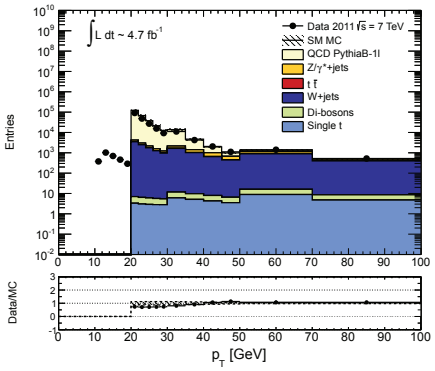

(a) Muons CR-A R13 Wo/Subtr

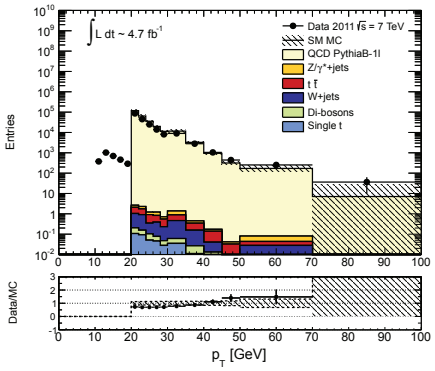

(b) Muons CR-A R13 W/Subtr

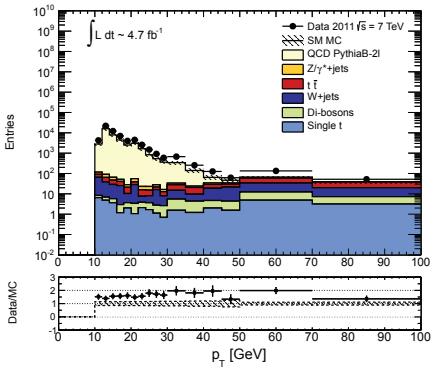

(c) Muons CR-B R02 Wo/Subtr

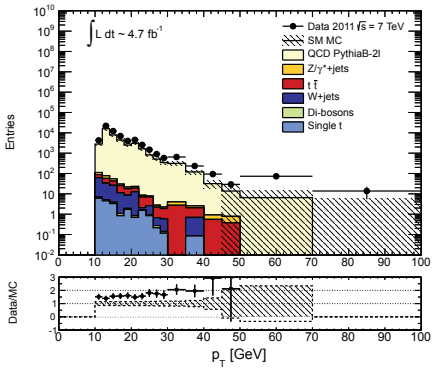

(d) Muons CR-B R02 W/Subtr

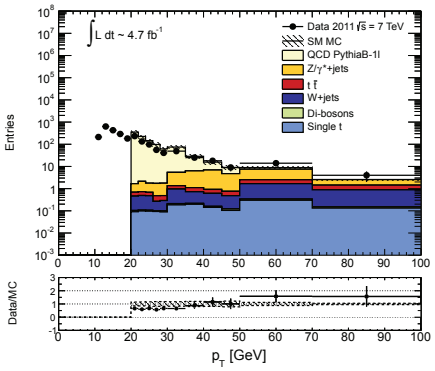

(e) Muons CR-C R19 Wo/Subtr

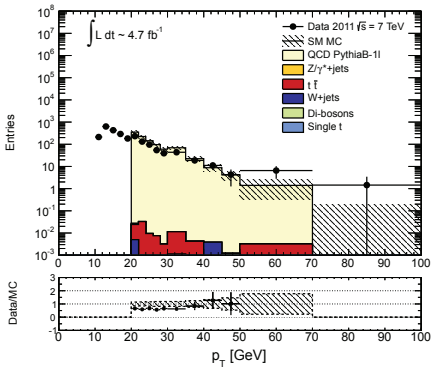

(f) Muons CR-C R19 W/Subtr

Figure C.1: Muon p_{T} in CR-A (top) CR-B (middle) and CR-C (bottom) before (left) and after (right) subtraction of real muons. Subtraction is done statistically in data. In the ratio plots some data points are apparently missing, as they are beyond the ratio-plot scale. The MC error band includes statistical uncertainty, and systematic uncertainty on luminosity and cross section.

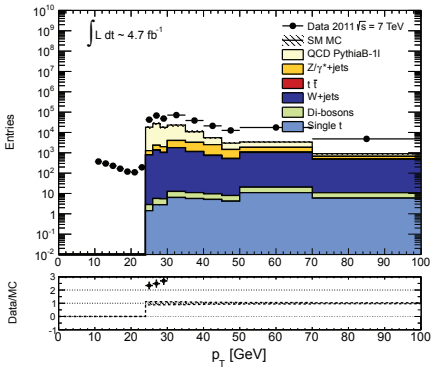

(a) Electrons CR-A R13 Wo/Subtr

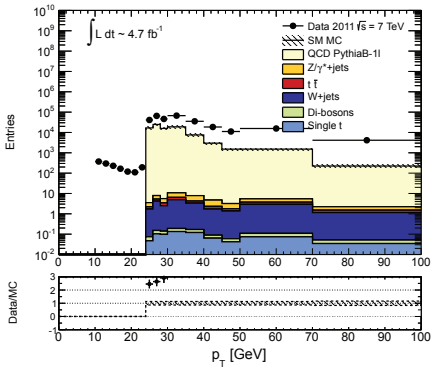

(b) Electrons CR-A R13 W/Subtr

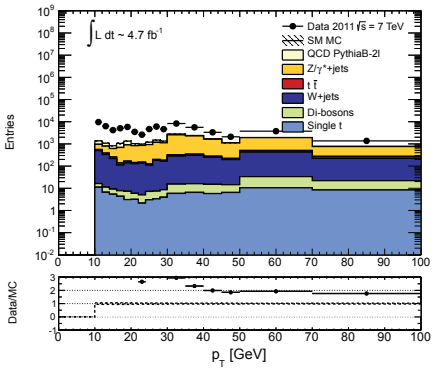

(c) Electrons CR-B R07 Wo/Subtr

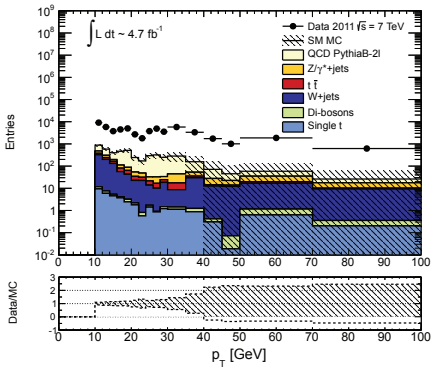

(d) Electrons CR-B R07 W/Subtr

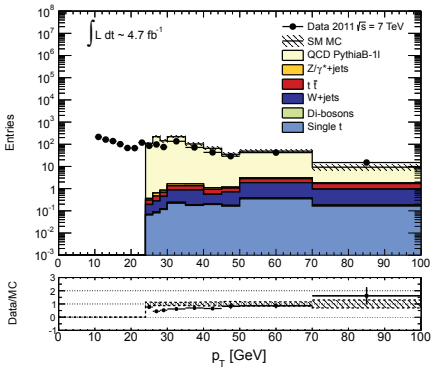

(e) Electrons CR-C R19 Wo/Subtr

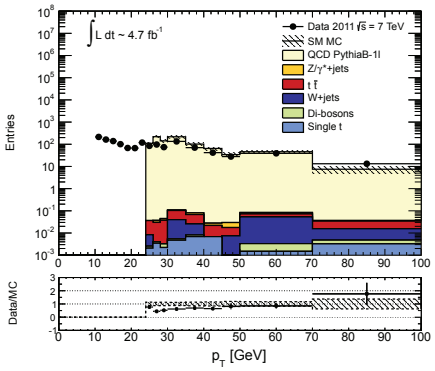

(f) Electrons CR-C R19 W/Subtr

Figure C.2: Electon p_{T} in CR-A (top) CR-B (middle) and CR-C (bottom) before (left) and after (right) subtraction of real and conversion electrons. Subtraction is done statistically in data.In the ratio plots some data points are apparently missing, as they are beyond the ratio-plot scale. The MC error band includes statistical uncertainty, and systematic uncertainty on luminosity and cross section.

C.3 Relative importance of processes versus $E_{\mathrm{T}}^{\mathrm{miss,rel}}$ in MC

Figure C.3 shows the relative amount of inclusive loose leptons versus $E_{\mathrm{T}}^{\mathrm{miss,rel}}$. All contributing MC samples are included, and each sample is relative to the total MC sample. Note however, that the heavy flavour sample PythiaB_2L is used for both channels, which means that the light flavour component, and hence the total QCD component is underestimated for electrons. At low $E_{\mathrm{T}}^{\mathrm{miss,rel}}$ we see that for both muons (left) and electrons (right) in the OS channel (top) that Z/γ^* dominates as expected, while at high $E_{\mathrm{T}}^{\mathrm{miss,rel}}$ $t\bar{t}$ takes over. In the SS channel (bottom) the QCD MC sample is most important at low $E_{\mathrm{T}}^{\mathrm{miss,rel}}$ for muons, while in the electron channel Z/γ^* dominates due to the charge-flip contribution. At high $E_{\mathrm{T}}^{\mathrm{miss,rel}}$ $t\bar{t}$ again dominates, together with some contribution also from W+jets in the electron channel.

Figure C.4 shows the same distribution, but now only using leptons from QCD processes (within all MC samples). At high $E_{\mathrm{T}}^{\mathrm{miss,rel}}$ $t\bar{t}$ and W+jets are important also here, but at low $E_{\mathrm{T}}^{\mathrm{miss,rel}}$ the QCD sample dominates as expected.

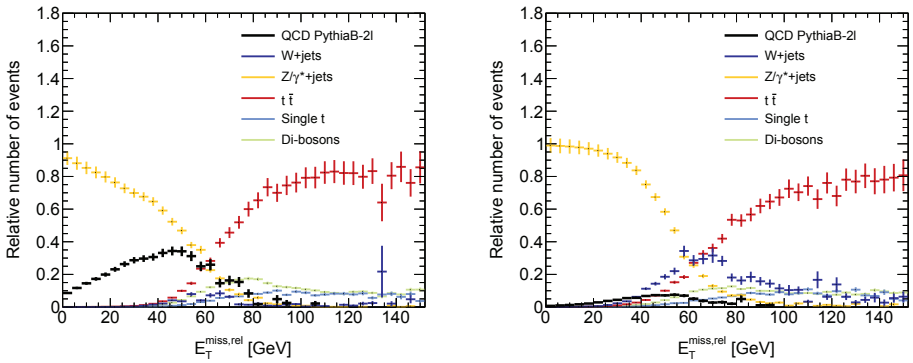

(a) Muons OS

(b) Electrons OS

(c) Muons SS

(d) Electrons SS

Figure C.3: Relative amount of inclusive loose muons (left) and electrons (right) in the OS channel (top) and SS channel (bottom) versus $E_{\mathrm{T}}^{\mathrm{miss,rel}}$. An all-inclusive sample is used, specifically meaning that all types of leptons, both real and fake are included.

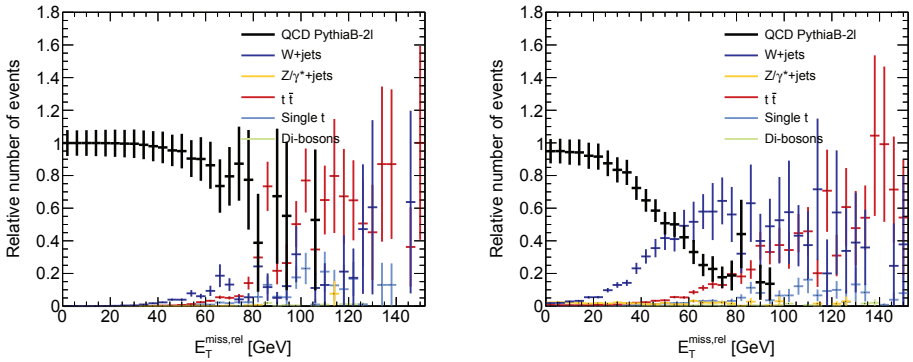

(a) Muons OS

(b) Electrons OS

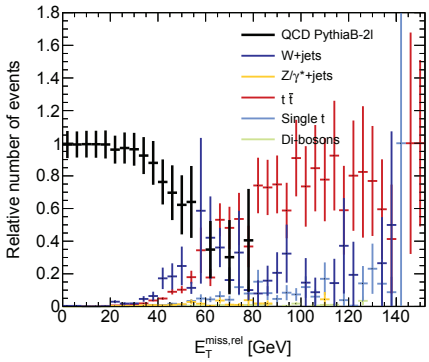

(c) Muons SS

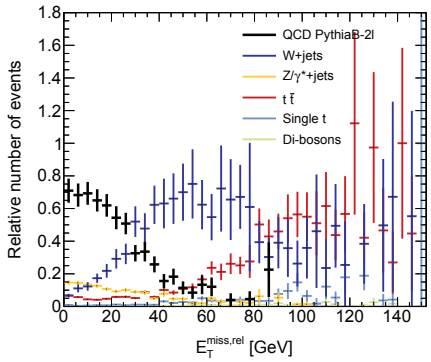

(d) Electrons SS

Figure C.4: Relative amount of inclusive loose muons (left) and electrons (right) in the OS channel (top) and SS channel (bottom) versus $E_{\mathrm{T}}^{\mathrm{miss,rel}}$. Only leptons from QCD processes are selected.

C.4 Relative amount of real MC leptons to total data leptons

As the fake rate depends on p_{T} it is interesting to see how important the real leptons are as a function of this variable. Figure C.5 shows the ratio of MC real muons (electrons), to the total number of muons (electrons) in data for a selection of control regions, for all inclusive loose leptons NL or tight leptons NT. The figures demonstrate that the real leptons' importance grows strongly with p_{T}, or said in other words: there are relatively more real leptons at high p_{T}. We see that especially for the muons the relative amount of real leptons is large in the last bins. Table C.7 shows the absolute number of events in the very last bin of the distributions in Figure C.5. In the muon channel the remaining leptons after subtraction is very low, 36 events remain in CR-A, 14 in CR-B, and only 1.5 in CR-C. In CR-A we are in fact extremely sensitive to the cross section uncertainty. With around 7% more real leptons, we remove all data. In CR-B and CR-C we are less sensitive to the cross section, however, there are very few events left, and therefore a large uncertainty on the number itself.

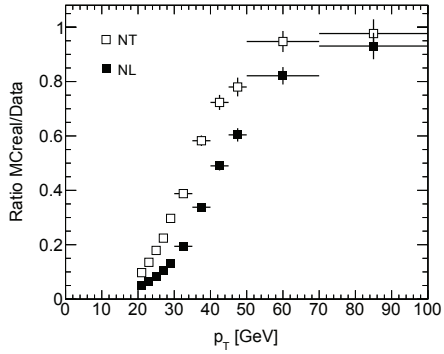

(a) Muons CR-A R13

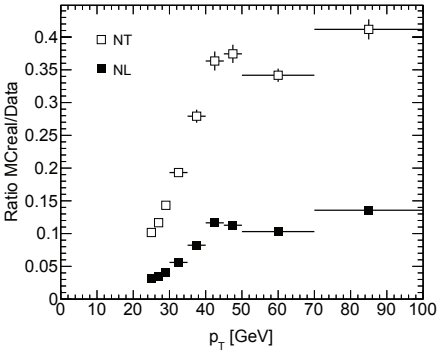

(b) Electrons CR-A R13

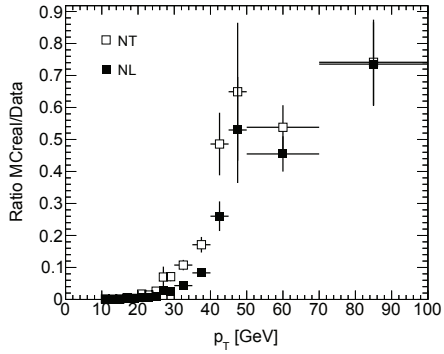

(c) Muons CR-B R02

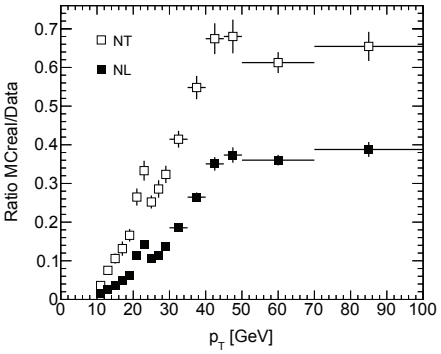

(d) Electrons CR-B R07

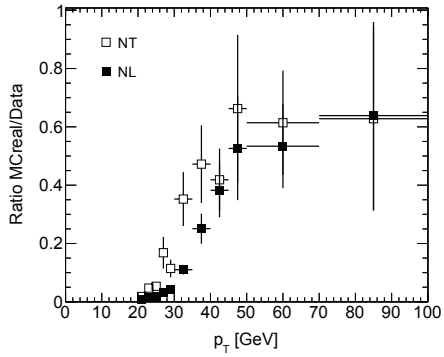

(e) Muons CR-C R19

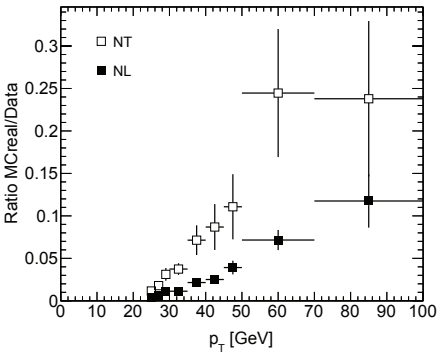

(f) Electrons CR-C R19

Figure C.5: The relative amount of real MC muons to the total data count in the muon channel (left) and electron channel (rigth), for each main type of control region CR-A, -B, and -C. Both the number of tight (NT) and inclusive loose (NL) leptons are shown.

	Reg	N_{Data}	N_{MC}^{real}	Diff
Mus	CR-A	524	487.65	36.35
	CR-B	52	38.25	13.8
	CR-C	4	2.55	1.46
Els	CR-A	826	654.74	4171.26
	CR-B	1369	530.98	838.02
	CR-C	15	1.76	13.24

Table C.7: Number of inclusive loose leptons in data, real leptons in MC, and the difference after real lepton subtraction, in the last bin of the p_{T} distribution in Figure C.5.

C.5 Effect on fake rate versus p_{T} when varying MC cross section

In Section 6.4.1.4 we saw that the high $E_{\mathrm{T}}^{\mathrm{miss,rel}}$ tail of the muon fake rate is reduced when scaling up the MC cross section, since more real leptons are then removed in the statistical removal procedure. The effect of the same scaling for muons versus p_{T} in the data control regions (low $E_{\mathrm{T}}^{\mathrm{miss,rel}}$) is shown in Figure C.6. The effect is most noticeable in CR-A for muons, and CR-B for electrons, while the other control regions are not much affected. The dramatic effect in CR-A is as expected as we already saw in Appendix C.4 that very few muons are left after the statistical subtraction, and that a small cross section variation removes all (and more) of the data.

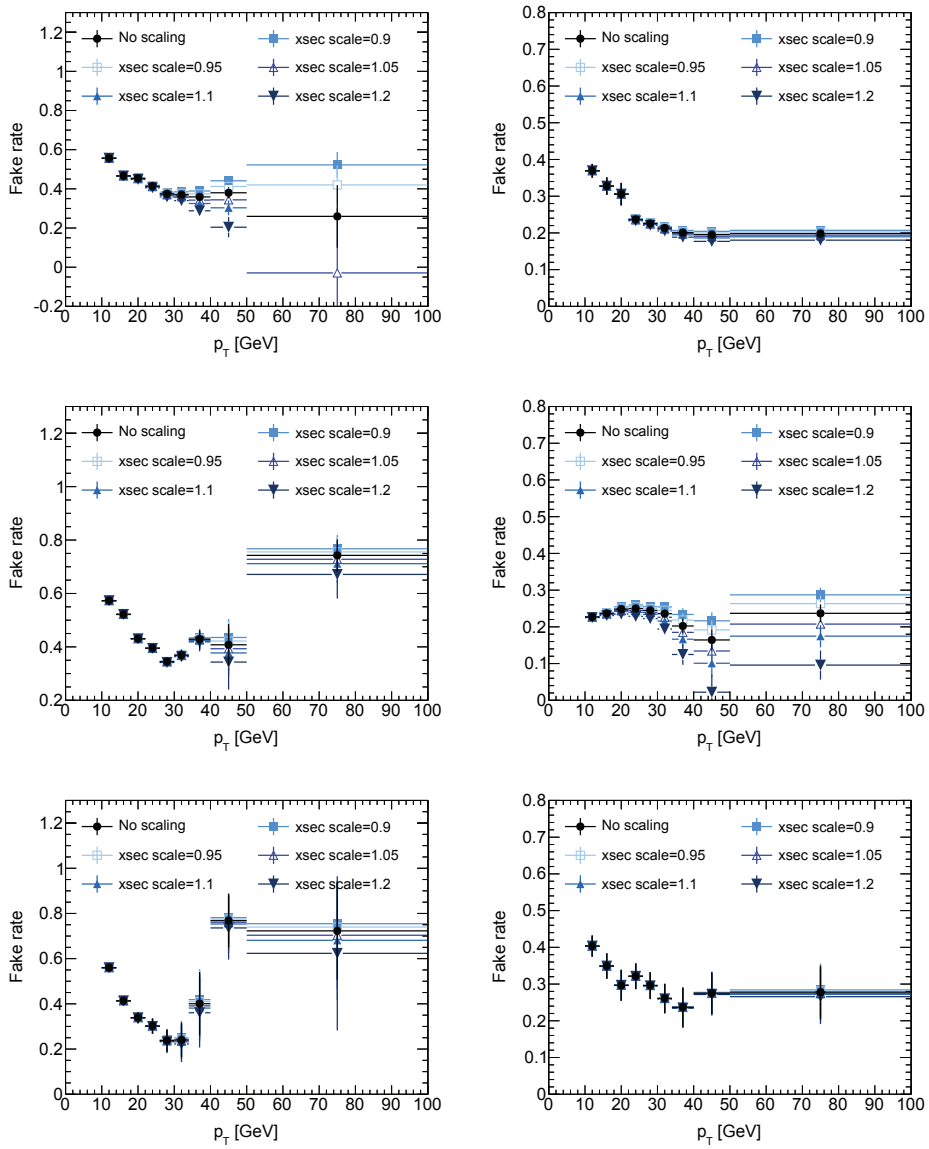

Figure C.6: The data fake rate versus p_T in CR-A (top), -B (middle), and -C (bottom) for muons (left) and electrons (right). The black markers shows the fake rate distribution after statistical removal of MC real (and conversion) leptons using nominal cross section ("No scaling") on MC. The blue markers show the resulting fake rate when scaling the MC cross section up or down by a constant factor compared to the nominal cross section.

C.6 Subtracting conversion electrons in QCD control regions

The impact on the fake rate when removing conversion electrons in addition to real electrons is shown in Tables C.8 and C.9 for di-lepton same-sign, and single electron control regions respectively. In the tables $f^{w/sub}$ and $f^{wo/sub}$ refer to the fake rate including ("w/sub") or excluding ("wo/sub") subtraction of conversion electrons. The column "Ratio" shows the ratio of the two fake rates, which reflects the impact of the conversion removal. Both data and MC are presented.

As the tables show, only di-lepton same-sign control regions (CR-B) in Table C.8 are affected when also subtracting conversions. In CR-A in Table C.9 all ratios are compatible with 1.0. This is expected, since the largest contribution of conversion electrons stem from the charge flip electrons from Z di-lepton events. We also see that the effect seems to be larger in the MC samples than in data. This can be explained by the fact that we do not have the required amount of QCD fake leptons included, as the QCD samples are known to underestimate the contribution for electrons, see e.g. discussion in Section 6.1.

	Data				MC		
Region	$f^{\text{w/sub}}$ [%]	$f^{\text{wo/sub}}$ [%]	Ratio	Region	$f^{\text{w/sub}}$ [%]	$f^{\text{wo/sub}}$ [%]	Ratio
R02	21.7±2.5	30.7±1.4	0.71±0.09	R02	30.0±44.7	45.9±5.9	0.65±0.98
R03	19.7±2.3	28.2±1.3	0.70±0.09	R03	27.9±37.7	43.6±5.7	0.64±0.87
R04	18.9±2.1	26.7±1.2	0.71±0.08	R04	25.4±29.1	40.8±5.2	0.62±0.72
R05	30.5±0.7	32.8±0.6	0.93±0.03	R05	34.8±14.0	44.2±4.2	0.79±0.33
R06	25.2±0.6	27.2±0.5	0.92±0.03	R06	30.8±11.0	38.7±3.8	0.80±0.30
R07	23.3±0.5	25.1±0.4	0.93±0.03	R07	28.9±9.6	35.8±3.5	0.81±0.28
R08	22.4±0.5	24.0±0.4	0.93±0.03	R08	26.0±7.9	31.8±3.1	0.82±0.26

Table C.8: Fake rate after subtracting both conversion and real leptons, $f^{\text{w/sub}}$, after subtracting only real leptons $f^{\text{wo/sub}}$, and the ratio between the two, for same-sign di-lepton control regions CR-B.

	Data				MC		
Region	$f^{\text{w/sub}}$ [%]	$f^{\text{wo/sub}}$ [%]	Ratio	Region	$f^{\text{w/sub}}$ [%]	$f^{\text{wo/sub}}$ [%]	Ratio
R01	25.3±0.2	25.3±0.2	1.00±0.01	R01	42.7±3.4	42.7±3.4	1.00±0.11
R05	26.4±0.2	26.5±0.2	1.00±0.01	R05	44.3±3.5	44.3±3.4	1.00±0.11
R07	24.7±0.4	24.8±0.4	1.00±0.02	R07	38.2±3.7	38.3±3.6	1.00±0.13
R11	24.5±0.3	24.6±0.3	1.00±0.02	R11	38.2±3.4	38.3±3.4	1.00±0.12
R13	21.8±0.2	21.8±0.2	1.00±0.01	R13	34.0±2.9	34.0±2.9	1.00±0.12
R17	21.6±0.2	21.6±0.2	1.00±0.01	R17	33.2±2.8	33.1±2.8	1.00±0.12
R19	23.1±0.3	23.2±0.3	1.00±0.02	R19	34.7±3.3	34.8±3.2	1.00±0.13
R23	22.6±0.3	22.6±0.3	1.00±0.02	R23	33.7±3.1	33.7±3.0	1.00±0.13

Table C.9: Fake rate after subtracting both conversion and real leptons, $f^{\text{w/sub}}$, after subtracting only real leptons $f^{\text{wo/sub}}$, and the ratio between the two, for single electron control regions CR-A

C.7 $E_{\mathrm{T}}^{\mathrm{miss,rel}}$ dependency QCD control regions

The fake rate versus $E_{\mathrm{T}}^{\mathrm{miss,rel}}$ is studied in data and MC.

Figure C.7 shows the MC fake rate versus $E_{\mathrm{T}}^{\mathrm{miss,rel}}$ broken down into heavy and light flavour QCD leptons using truth information in MC, and compared to data. Only processes contributing significantly are included, in order not to clutter the plots with large error bars. In the muon channel, data closely follows the heavy flavour MC curve in all control regions, except for the high $E_{\mathrm{T}}^{\mathrm{miss,rel}}$ bins for CR-C, where data rises but MC keeps falling. The rise in data (also seen in CR-B) is probably due to sensitivity on the subtraction of real leptons, where the MC cross section plays an important role. Indeed, this is confirmed by Figure C.8 which shows the data fake for muons and electrons in the different control regions CR-A, CR-B, and CR-C, when having scaled the MC sample by factors ranging from 0.9-1.2. In these figures, the control region cuts used follow the control region definitions, but the m_{T} and $E_{\mathrm{T}}^{\mathrm{miss,rel}}$ cuts are omitted in order to produce the fake rate versus $E_{\mathrm{T}}^{\mathrm{miss,rel}}$. We see a clear effect in both lepton channels and all control regions as the MC cross section is varied, when MC is down-scaled the fake rate increases, and when it is upscaled the fake rate decreases. This is because we remove more real leptons in the latter case, and real leptons could be causing the increase at high $E_{\mathrm{T}}^{\mathrm{miss,rel}}$. In the two last bins the fake rate is negative in some cases (e.g. CR-A muons), which means that the scaling resulted in subtracting more events than given in the data. The goal of this exercise is however just to show that the high $E_{\mathrm{T}}^{\mathrm{miss,rel}}$ bins are sensitive to the cross section uncertainty, which affect the data fake rate through the statistical lepton subtraction, and that the fake rate is reduced when the cross section is increased. There can be other reasons for the muon fake rate increasing with $E_{\mathrm{T}}^{\mathrm{miss,rel}}$, these are discussed in Section 6.4.1.5.

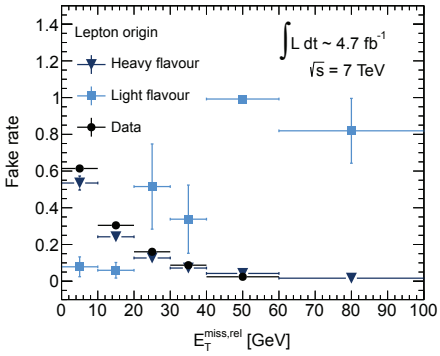

(a) Muons CR-A

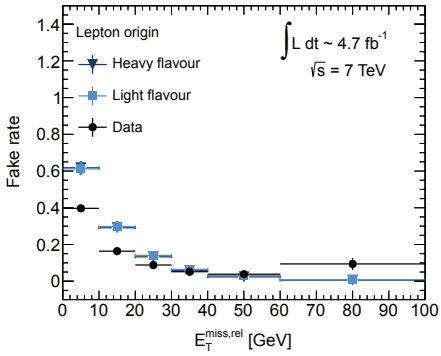

(b) Electrons CR-A

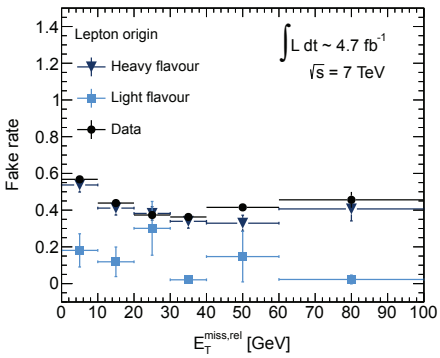

(c) Muons CR-B

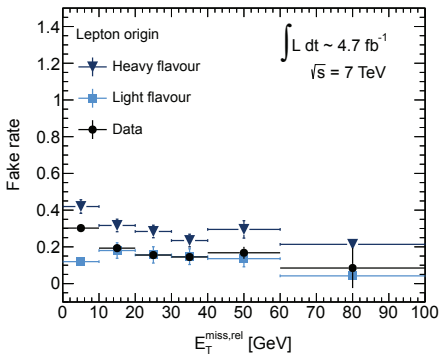

(d) Electrons CR-B

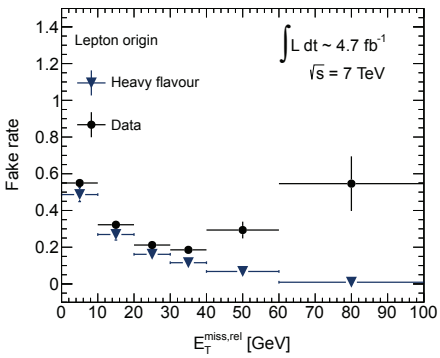

(e) Muons CR-C

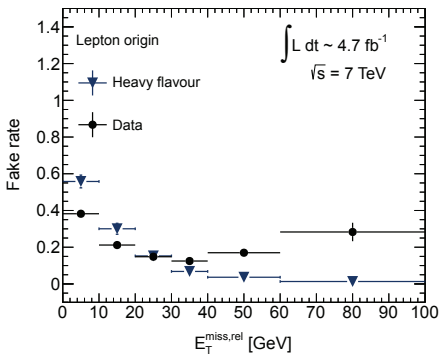

(f) Electrons CR-C

Figure C.7: Fake rate versus $E_{\mathrm{T}}^{\mathrm{miss,rel}}$ for truth selected MC leptons, and for data. The rates are extracted in "control regions" where the quotes indicate that no $E_{\mathrm{T}}^{\mathrm{miss,rel}}$ cut which defines the control regions, are applied. The only requirements are: in CR-A a single lepton requirement, CR-B a di-lepton same-sign requirement, and CR-C a single b-tagged jet, and a single lepton requirement. To suppress real leptons from W decays, a cut on $\Delta\phi < 1.5$ between the lepton and $E_{\mathrm{T}}^{\mathrm{miss}}$ is required in CR-A and CR-C.

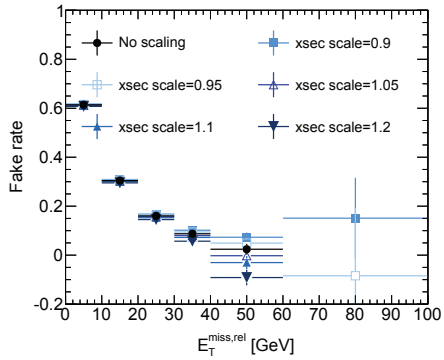

(a) Muons CR-A

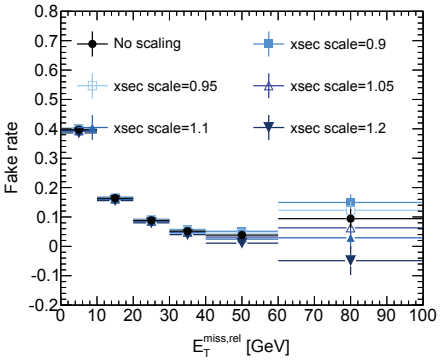

(b) Electrons CR-A

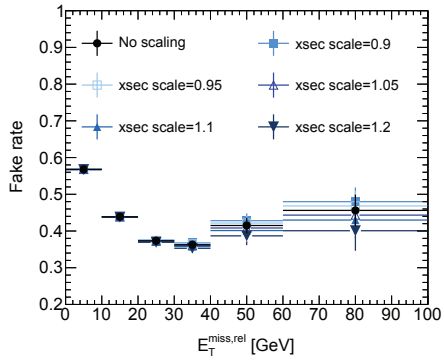

(c) Muons CR-B

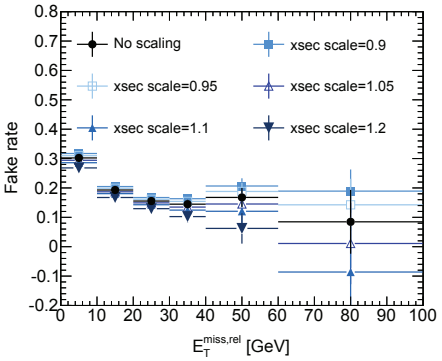

(d) Electrons CR-B

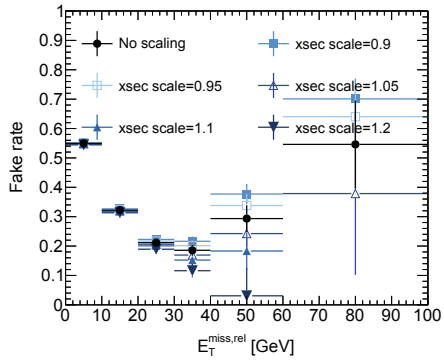

(e) Muons CR-C

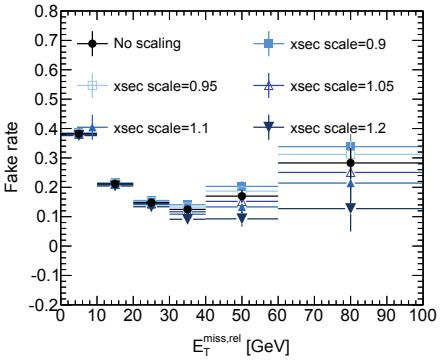

(f) Electrons CR-C

Figure C.8: Fake rate versus $E_{\mathrm{T}}^{\mathrm{miss,rel}}$ in data after statistical subtraction of real leptons. In the electron channel conversion electrons are also removed. The fake rates are shown after scaling the MC electroweak cross section up or down according to the legend. "Default" is when MC is used with the nominal cross section. The rates are extracted in "control regions" where the quotes indicate that no $E_{\mathrm{T}}^{\mathrm{miss,rel}}$ cut which defines the control regions, are applied. The only requirements are: in CR-A a single lepton requirement, CR-B a di-lepton same-sign requirement, and CR-C a single b-tagged jet, and a single lepton requirement. To suppress real leptons from W decays, a cut on $\Delta\phi < 1.5$ between the lepton and $E_{\mathrm{T}}^{\mathrm{miss}}$ is required in CR-A and CR-C.

C.8 MC subtraction uncertainty on data fake rate versus $E_{\mathrm{T}}^{\mathrm{miss,rel}}$

To extract the $E_{\mathrm{T}}^{\mathrm{miss,rel}}$ dependency for the fully data-driven fake lepton estimation, the fake rate versus $E_{\mathrm{T}}^{\mathrm{miss,rel}}$ in CR-B (omitting the $E_{\mathrm{T}}^{\mathrm{miss,rel}}$ cut) is fitted using bins below 40 GeV only, as explained in Section 7.2.2. The data fake rate has then already undergone the statistical subtraction of real MC leptons. We saw there (and reproduced in Figure C.9, to be commented below), that the fitted function for both channels nicely follows the data points below 40 GeV, but especially for muons continues below the data points. The increasing data fake rate as we move towards higher $E_{\mathrm{T}}^{\mathrm{miss,rel}}$ can be related to several aspects, as discussed at various places throughout the analysis chapters 6, 6.4.1.5, and 7, and in Appendices related to these: C.5 and C.7. One of the possibilities is that the real lepton subtraction procedure does not suceed in removing all real leptons, thus pushes the fake rate up at high $E_{\mathrm{T}}^{\mathrm{miss,rel}}$ where we expect a relatively more real leptons than fake leptons.

Figure C.9 shows the fake rate versus $E_{\mathrm{T}}^{\mathrm{miss,rel}}$ including fits (black curve) (a) for muons and (a) for electrons. The black points correspond to the fake rate when subtracting real MC leptons using the nominal cross section (SF=1.0). The coloured distributions show how the fake rate changes when scaling the real MC component by values 0.9,1.1,1.2, and 1.4. The rest of the plots correspond to the inclusive loose lepton events for the full data before applying any subtraction and the full MC, where MC is scaled by the mentioned factors, using the same colour-coding as in the fake rate distribution. The total MC are the coloured histograms, and data are the hashed histograms. As we expect the high $E_{\mathrm{T}}^{\mathrm{miss,rel}}$ tail to be dominated by real leptons (and the low to be dominated by fake leptons), the agreement in the tail tells us how well the real MC data is modelled.

The distributions show that faulty real lepton subtraction could be one of the explanations why we see a rising muon fake rate as $E_{\mathrm{T}}^{\mathrm{miss,rel}}$ increases. We see that the fake rate at high $E_{\mathrm{T}}^{\mathrm{miss,rel}}$ is reduced when scaling up the real MC lepton component. We also see that for muons the correct scale factor seems to be roughly 1.4, judging the inclusive (no real lepton subtraction) data and MC agreement in Figure C.9 (f). Looking at (a) this corresponds to the data points that lie somewhat below the fit-function, but agrees within errors, and is already covered by the cross section uncertainty. We evaluate the systematic uncertainty due to the subtraction procedure in the following way: From Figure C.9 (a) we take the absolute error as the difference between the nominal value and the fit value, bin by bin, but subtract the statistical error on the nominal fake rate from this difference. We then obtain the additional uncertainty from the subtraction procedure only. To get the relative uncertainty we normalize to the nominal fake rate in that bin. Ignoring the outliers of the third and last bin, we find systematic bin-wise errors of the order of 7%.

In the electron channel, we see that already at a scaling of 1.1 (which corresponds to the cross section uncertainties) MC starts to overshoot data above 80 GeV (Figure C.9(j)). However, for the electrons, the fit in fact follows the data points very well over the full $E_{\mathrm{T}}^{\mathrm{miss,rel}}$ range (except the very last bin), and therefore we do not expect a need for a cross section adjustement here. Particularly because this difference is already covered by the uncertainty on the MC cross section. Note that the discrepancy in the data and MC comparison at low $E_{\mathrm{T}}^{\mathrm{miss,rel}}$ particularly seen in the electron channel is due to the use of the non-optimal MC heavy flavour dominated PythiaB_2L QCD sample, as discussed at length in the main part of the thesis.

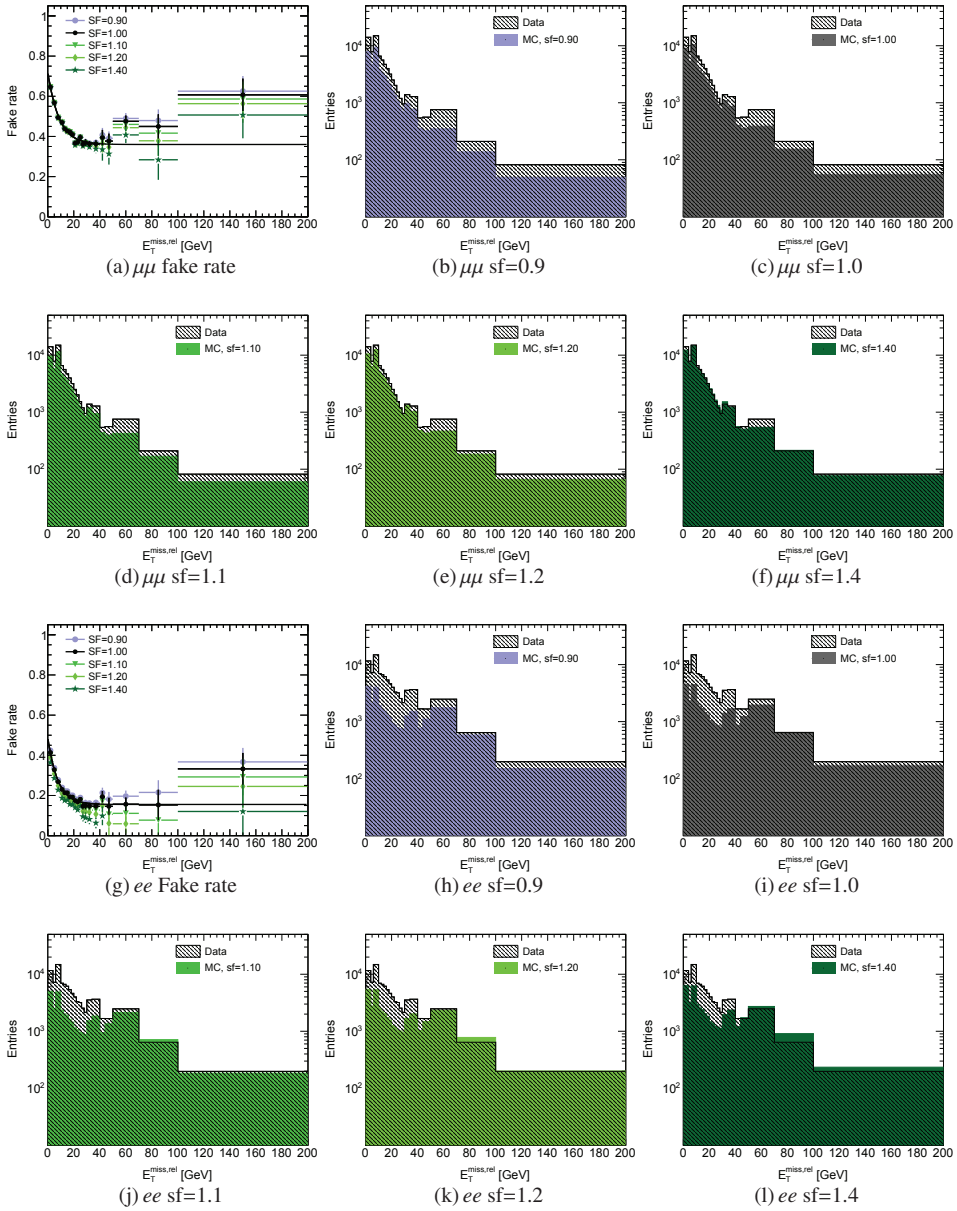

(a) $\mu\mu$ fake rate (b) $\mu\mu$ sf=0.9 (c) $\mu\mu$ sf=1.0

(d) $\mu\mu$ sf=1.1 (e) $\mu\mu$ sf=1.2 (f) $\mu\mu$ sf=1.4

(g) *ee* Fake rate (h) *ee* sf=0.9 (i) *ee* sf=1.0

(j) *ee* sf=1.1 (k) *ee* sf=1.2 (l) *ee* sf=1.4

Figure C.9: The data fake rate versus $E_{\mathrm{T}}^{\mathrm{miss,rel}}$ for same-sign di-muons (a) and di-electrons (g) when scaling the nominal MC by five different scale factors (SF=0.9,1.0,1.1,1.2,1.4), which affects the data fake rate when statistically subtracting real leptons. Figures (h)-(l) shows how the corresponding inclusive loose events in data and full MC including PythiaB_2L QCD MC compares, using the scaling and colour-coding as indicated in the fake rate plots. Included in the fake rate plot is the fit of the unscaled data-points using a exponential+constant fit, and only taking into account bins < 40 GeV. The error on the data fake rate is purely statistical.

C.9 Data based QCD fake rate versus p_T for different $E_T^{miss,rel}$ ranges

In Section 7.2 I claim that the shape of the fake rate distribution versus p_T is (practically) independent on $E_T^{miss,rel}$. Therefore it is justified to scale the p_T dependent fake rate in order to take into account $E_T^{miss,rel}$, instead of applying a real 2D p_T-$E_T^{miss,rel}$ fake rate. The latter would suffer from low statistics at high $E_T^{miss,rel}$ and high p_T. Figure C.10 shows the fake rate versus p_T for muons and electrons in different intervalls of $E_T^{miss,rel}$. The shape of the distributions (within channel) are similar, when ignoring the high p_T bins with low statistics. From the differences between the distributions (in the low p_T region), we find on average a 10% effect in both muon and electron channel, which we assign as a systematic uncertainty.

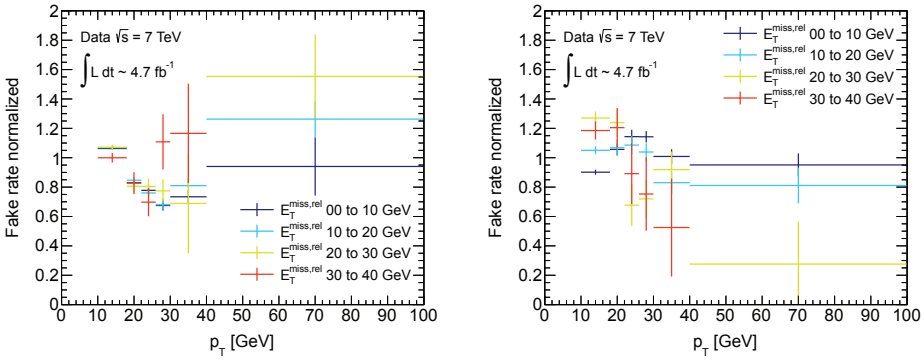

(a) Muons (b) Electrons

Figure C.10: The muon (left) and electron (right) fake rate versus p_T for different values of $E_T^{miss,rel}$ as indicated in the legend.

C.10 QCD and conversion weights in signal regions

The relative amount of conversion and QCD electrons is likely to vary between the different signal regions. Therefore they are evaluated in the three regions SR-OSjveto, SR-SSjveto and SR-2jets before the $E_T^{miss,rel}$ cut. The SR-m_T2 region is left out, as the statistics is too low.

The relative amount of conversion and QCD electrons (or weights for short) have been calculated as follows: First the expected amount of fake electrons has been calculated from data, by using the total number of data electrons and subtracting the expected number of real electrons as given in MC. The amount of conversions is calculated in different ways according to whether the signal region is OS or SS. In the OS regions the conversions are simply extracted from MC truth information. However, in SS events the conversion electrons include electrons in events with two real electrons, and any event with conversion electrons. The reason for also including the "real-real" events, is the contribution from the charge-flips which most often are

identified as real electrons in the SS channel. To extract the actual non-charge flip contribution (which is what we are interested in here) the calculated number of charge-flip electrons, using the Charge flip package is removed from the total amount of conversion electrons as extracted above from MC. The QCD component is finally defined as the total expected fake electrons minus the conversion contribution.

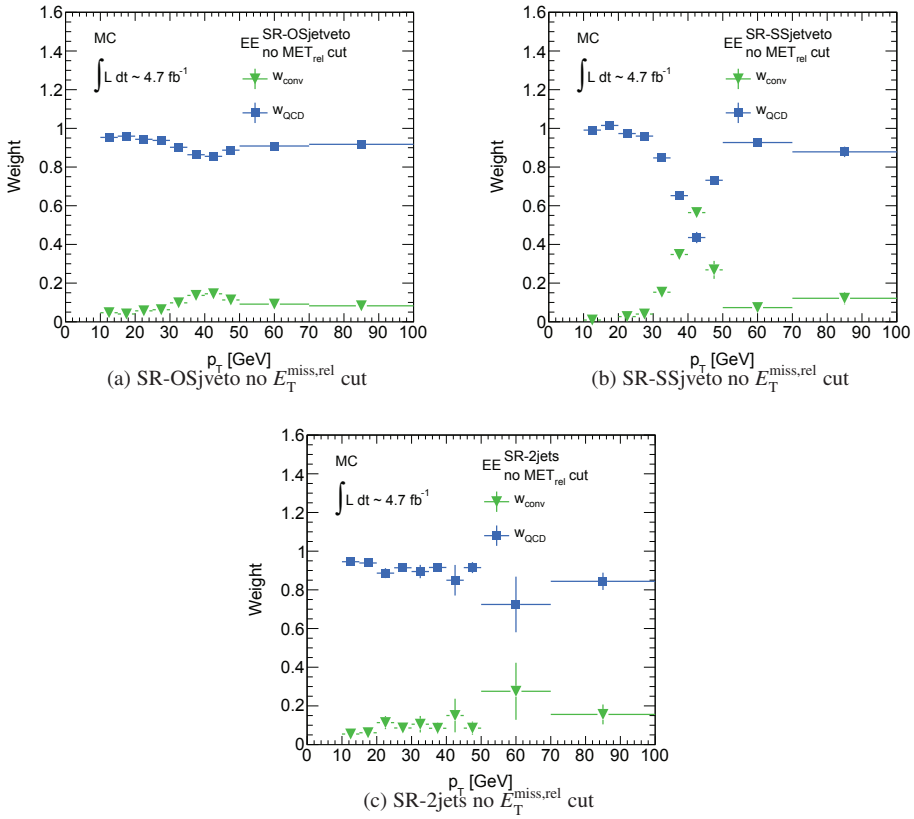

(a) SR-OSjveto no $E_{\mathrm{T}}^{\mathrm{miss,rel}}$ cut

(b) SR-SSjveto no $E_{\mathrm{T}}^{\mathrm{miss,rel}}$ cut

(c) SR-2jets no $E_{\mathrm{T}}^{\mathrm{miss,rel}}$ cut

Figure C.11: Relative amount of conversion and QCD electrons in regions with cuts as SR-OSjveto (top left) SR-SSjveto (top right), and SR-2jets (bottom). No $E_{\mathrm{T}}^{\mathrm{miss,rel}}$ cut has been applied in any of the regions to ensure sufficient statistics.

Figure C.11 shows the result in SR-OSjveto (top left), SR-SS-jveto (top right) and SR-2jets (bottom). The plots display some differences between the weights in the different regions, most noticeably around 40 GeV area, where in the SS-jveto region the conversion weight increases more than in the OS events. However, given the complexity in the steps to obtain the SS weights, it is reasonable to assign at least part of the 40 GeV increase to systematic uncertainty. However, the total effect on the fake estimates, when applying the different weights is small, as Table C.10 shows. All numbers are presented in percent. Here the weights (integrated) are calculated separately for the three signal regions, and the relative difference (diff) compared to the selected baseline weight, namely SR-OSjveto, is shown. Also shown is the effect the

different weights have on the combined fake rate (f^{COMB}), which is calculated following the standard formula explained in Equation (7.1) of Section 7.1, but repeated here for clarity (and using "COMB" rather than "FIN" as the latter is reserved for the final fake rate used in the fake lepton estimation)

$$\mathrm{f}^{\mathrm{COMB}}(p_{\mathrm{T}}) = \sum_{i=\mathrm{QCD,conv}} \mathrm{f_i}(p_{\mathrm{T}}) \cdot \mathrm{w_i}(p_{\mathrm{T}}) \cdot \mathrm{s_i}$$

The combined fake rates are calculated using the MC based QCD fake rate from the semi data-driven approach (see details in Section 7.1) or the QCD CR-B fake rate from the fully data-driven approach (see details in Section 7.2). We see that the maximum relative effect on the SR-OSjveto combined fake rate is 3.5% on the semi data-driven combined fakerate, and <1% when applying the fully data-driven fake rates. The latter small effect is due to the conversion and QCD fake rates being of very similar size. For simplicity the OS-jveto weights were therefore applied in all signal regions, and a systematic uncertainty is applied to account for the differences seen.

	Conv		QCD		Semi data-driven Conv+QCD		Fully data-driven Conv+QCD	
	wgt	diff	wgt	diff	f^{COMB}	$\sigma(f^{\mathrm{COMB}})$	f^{COMB}	$\sigma(f^{\mathrm{COMB}})$
SR-OSjveto	6.8 ± 0.1	–	93.2 ± 0.1	–	15.7	–	23.31	-
SR-SSjveto	8.5 ± 0.2	26.0	91.5 ± 0.2	-1.9	15.8	1.0	23.23	0.05
SR-2jets	12.9 ± 1.3	89.8	87.1 ± 1.0	-6.5	16.2	3.5	23.35	0.18

Table C.10: The calculated relative amount (weight) of conversions and QCD in three different signal-regions (before $E_{\mathrm{T}}^{\mathrm{miss,rel}}$ cut), and the relative difference of the weights (diff) for SR-SSjveto and SS-2jets relative to SR-OSjveto. In addition is shown the resulting combined fake rate f^{COMB}, and the corresponding relative uncertainty with respect to the baseline using SR-OSjveto weights. All numbers are in percent.

Appendix D

Charge flip, data and MC

Updates in the MC simulation have reduced the discrepancy between data and MC in charge-flip events, see Figure D.1.

Where we in earlier analyses in 2010, saw a 20% overshoot in MC, MC now underestimates data somewhat, see ratio plot with black markers, which shows data divided by the MC prediction. The red markers in the same ratio plot shows how the charge-flip estimate compares to MC. Note that the $|\eta|$ plots includes the whole m_{ll} range, and while only selected MC backgrounds are included, the data is all-inclusive. This might therefore explain some of the data-overshoot in the $|\eta|$ plots, as for instance fake leptons are not represented. However, in the m_{ll} Z-mass window plot, any such effect should be negligible. Comparing the data/MC ratios the agreement is also better for the latter, supporting this explanation.

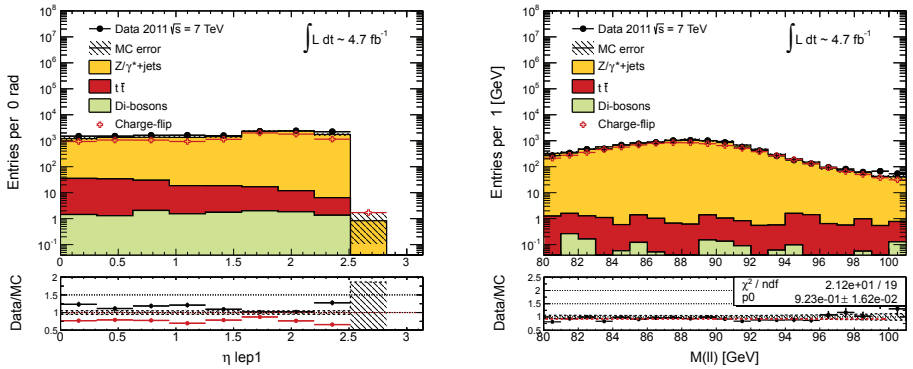

(a) $|\eta|$ lep1 (b) Mll

Figure D.1: Comparison of data, MC and charge-flip estimate for η of the leading electron (left), and for the Z-mass window 80-100 GeV (right).

List of Figures

1.1 The connections between the various formulations of quantum physics. 5
1.2 The SM particle content. 6
1.3 Parabolic and mexican hat scalar potential. 18
1.4 The η,ξ plane of the Higgs potential. 19
1.5 The evolution of the electromagnetic, weak and strong coupling constants as a function of the energy scale. 22
1.6 Coulomb self-energy and electron positron annihilation diagrams. 28
1.7 One-loop quantum corrections to scalar field mass terms. 30
1.8 Example of proton decay through a squark. 35
1.9 Examples of two mass spectres obtained assuming two different SUSY models. 38
1.10 The running of the mSUGRA mass parameters. 40
1.11 Example of messenger fields connecting to sparticles by loops. 41
1.12 An example of a suitable diagram to be interpreted in a Simplified Model. . . . 41

2.1 Illustration of a pp collision. 44
2.2 A Feynman diagram of a fermion-fermion annihilation process. 46
2.3 Three diagrams illustrating the Mandelstam variables. 47
2.4 Feynman diagrams illustrating LO and NLO. 48
2.5 Proton parton distribution function as measured at HERA, versus Bjørken x. . . 50
2.6 The Q^2, x reach of LHC, HERA and fixed target experiments 51
2.7 An illustration of gluon showering from two quarks, giving rise to parton jets. . 52
2.8 Schematic presentation of the string (left) and cluster (right) QCD models. . . . 53

3.1 The LHC accelerator complex. 57
3.2 Schematic overview of the ATLAS detector. 58
3.3 ATLAS magnet system 60
3.4 Overview of the ATLAS inner detector. 61
3.5 Layout of the ATLAS inner detector. 62
3.6 The ATLAS electromagnetic and hadronic calorimeters. 63
3.7 Overview of the ATLAS Muon system. 64
3.8 Schematic overview of the ATLAS Trigger system. 66
3.9 Schematic overview of the ATLAS data chain. 67
3.10 Isolation variable `pTcone20`/p_{T} for real and fake electrons in MC. 73
3.11 Isolation variable `pTcone20` for real and fake muons in MC. 76
3.12 Illustration of the stages forming a QCD jet. 78

3.13 Cartoon showing the definition of the transverse impact parameter d_0. 80
3.14 Ratio of ratio-noise measured offline versus online versus run-number. 83
3.15 Mean ratio-noise in run 209980 measured by DQMF versus time. 84
3.16 Mean ratio-noise for consecutive runs 20994 and 20995. 84
3.17 Mean ratio-noise versus time from DQMF for run 212199. 85
3.18 Difference between ratio-noise online and offline results. 86
3.19 The Δz_0 and Δd_0 difference between the MS and the ID. 87
3.20 The correlation between ϕ and θ in the bottom MS and ID detectors. 87
3.21 The relative p_{T} resolution as a function of p_{T} for ID, MS, and CB tracks. 88
3.22 The frequency in which charges in the ID and MS disagree (OS). 89
3.23 Illustration of cosmic ray showers. 90
3.24 Cosmic muon charge ratio measured in ATLAS and at BESS. 90
3.25 The invariant mass spectrum of opposite sign di-muons in early data. 91

4.1 Illustration of diffractive events. 93
4.2 Predicted SM cross sections as a function of energy. 94
4.3 Expected cross sections for mSUGRA gaugino production at $\sqrt{s} = 2$ or 14 GeV. 95
4.4 The dominant di-lepton gaugino and slepton production channels. 96
4.5 The total di-lepton gaugino pMSSM cross-section, and breakdown into sub-processes. 99
4.6 pMSSM Direct neutralino-chargino signal grid branching ratios. 100
4.7 Feynman diagrams for simplified model decay modes A, B, C, and D. 101
4.8 Cross sections for simplified models mode A, C and D versus the mass of $\tilde{\chi}_1^{\pm}/\tilde{\chi}_2^0$. 101
4.9 Production and decay of $\tilde{\ell}\tilde{\ell}$. 102
4.10 Leptonic decays of $\tilde{\chi}_1^{\pm}\tilde{\chi}_2^0$. 103
4.11 Leptonic decays of $\tilde{\chi}_1^{\pm}\tilde{\chi}_1^{\mp}$. 104
4.12 Leptonic decays of $\tilde{\chi}_2^0\tilde{\chi}_2^0$. 105
4.13 Leptonic decays of $\tilde{\chi}_1^0\tilde{\chi}_2^0$. 105
4.14 Leading order production mechanisms for $t\bar{t}$, and leptonic decays. 108
4.15 Number of b-jets in OS events for SUSY signal and $t\bar{t}$ and single t MC background. 109
4.16 Number of top-tagged SUSY signal events and MC $t\bar{t}$ background events. . . . 109
4.17 Leading order hard production mechanisms for Z/γ^* + jets. 110
4.18 Example of three Z/γ^* processes leading to a pair of charged leptons. 110
4.19 Invariant mass of OS SF leptons in SM MC, and SUSY signal. 111
4.20 Leading order hard di-boson production mechanisms. 112
4.21 Di-leptons from hard production of WZ, WW, and ZZ. 112
4.22 Leading order hard production mechanisms for W(+jets) 114
4.23 $E_{\mathrm{T}}^{\mathrm{miss,rel}}$ distribution for the SM W+jets background and SUSY signal. 114
4.24 Leading order diagrams for single top production, and leptonic decay. 115
4.25 Quark/jet production. 115
4.26 The $E_{\mathrm{T}}^{\mathrm{miss,rel}}$ distribution for di-muons and di-electrons QCD PythiaB_2L MC. . 116
4.27 γ radiation resulting in additional electrons in a W+jets process. 117
4.28 γ radiation resulting in SS event - charge-flip. 117

5.1 $E_{\mathrm{T}}^{\mathrm{miss,rel}}$ of opposite sign muons before Z-veto and after. 120

5.2 $E_{\mathrm{T}}^{\mathrm{miss,rel}}$ of opposite sign muons and electrons after applying the Z- and jet-veto. 120
5.3 The expected significance in SR-OSjveto signal region, using simplified model. 121
5.4 $E_{\mathrm{T}}^{\mathrm{miss,rel}}$ of same-sign muons and electrons after the jet-veto. 122
5.5 The expected significance in SR-SSjveto signal region, using simplified model. 122
5.6 The $E_{\mathrm{T}}^{\mathrm{miss,rel}}$ distribution for OS di-muon events w, w/o a b-veto and m_{CT}-veto. . 123
5.7 The expected significance in SR-2jets signal region, using pMSSM. 123
5.8 m_{T2} for two direct slepton SUSY MC samples, and WW SM MC sample. . . . 124
5.9 Expected m_{T2} end-point value and significance in SR-m_{T2} in the $m_{\tilde{\ell}}$, $m_{\tilde{\chi}_1^0}$ mass plane. 125
5.10 Electron trigger efficiencies versus p_{T}. 129
5.11 Muon trigger efficiencies versus offline p_{T}. 130
5.12 The coverage of the di-lepton trigger in the 2D p_{T} parameter space. 131

6.1 p_{T} of the leading lepton in SS $\mu\mu$ events using Pythia JX QCD MC. 138
6.2 p_{T} of the leading lepton in SS $\mu\mu$ and ee events using PythiaB_2L QCD MC. . 139
6.3 Muon p_{T} in SS events before and after statistical removal of real leptons. 143
6.4 Truth composition of fake leptons in SS events with PythiaB_2L QCD MC. . . 144
6.5 The real efficiency for muons and electrons as function of p_{T}. 145
6.6 The real efficiency for muons and electrons as function of $|\eta|$. 146
6.7 $E_{\mathrm{T}}^{\mathrm{miss,rel}}$, m_{T}, and $\Delta\phi(lep, E_{\mathrm{T}}^{\mathrm{miss}})$ distributions for single muon events. 149
6.8 $E_{\mathrm{T}}^{\mathrm{miss,rel}}$, m_{T}, and $\Delta\phi(lep, E_{\mathrm{T}}^{\mathrm{miss}})$ for single electron events. 150
6.9 Data fake rates in CR-A for single muon and electrons events. 151
6.10 $E_{\mathrm{T}}^{\mathrm{miss,rel}}$ and m_{ll} for SS same-flavour di-muon events. 152
6.11 $E_{\mathrm{T}}^{\mathrm{miss,rel}}$ and m_{ll} for SS same-flavour di-electron events. 153
6.12 Truth composition of SS electron MC with PythiaB_2L QCD. 153
6.13 Fake rates for SS di-lepton control regions CR-B, before and after MC real lepton and conversion electron subtraction. 155
6.14 The $E_{\mathrm{T}}^{\mathrm{miss,rel}}$ (left) and m_{T} after $E_{\mathrm{T}}^{\mathrm{miss,rel}} < 40$ cut in CR-C. 156
6.15 Fake rates for CR-C, before and after MC lepton subtraction. 157
6.16 Comparison of CR-A, -B, and -C data muon and electron fake rates versus p_{T}. . 158
6.17 Muon fake rates in data versus $|\eta|$ and $E_{\mathrm{T}}^{\mathrm{miss,rel}}$ for CR-A, -B, and -C. 159
6.18 Fake rate versus $E_{\mathrm{T}}^{\mathrm{miss,rel}}$ in SS di-lepton events (CR-B) after scaling MC cross sections. 160
6.19 Electron fake rates in data versus $|\eta|$ and $E_{\mathrm{T}}^{\mathrm{miss,rel}}$ in CR-A, -B, and -C. 161
6.20 Comparison of data and MC muon fake rates in CR-A, -B, and C. 162
6.21 Comparison of data and MC electron fake rates in CR-A, -B, and C. 163
6.22 m_{T} distribution of muons and electrons in data and MC in CR-C, after real lepton subtraction. 164
6.23 Ratio of data and MC fake rates in CR-C for muons and electrons. 165
6.24 MC QCD fake rates versus $E_{\mathrm{T}}^{\mathrm{miss,rel}}$ for muons and electrons in CR-B. 166
6.25 MC fake rate versus $E_{\mathrm{T}}^{\mathrm{miss,rel}}$ for heavy and light flavour QCD muon and electron fakes in CR-B. 167
6.26 MC electron origin in the conversion control region. 169
6.27 Conversion region fake rate versus p_{T} in data and MC. 170

6.28 The conversion region fake rate versus η in data and MC. 170

7.1 The QCD fake rates from MC, $E_{\mathrm{T}}^{\mathrm{miss,rel}}$ 40-100 GeV using only fake leptons. . . 172
7.2 Electron inclusive loose distribution in SR-OSjveto. 173
7.3 The conversion and QCD weights in SR-OSjveto. 174
7.4 The combined weighted fake rate for electrons. 174
7.5 The normalized MC fake rate versus $E_{\mathrm{T}}^{\mathrm{miss,rel}}$ for muons and electrons for QCD leptons only. 176
7.6 The MC fake rates for heavy flavour fakes for $t\bar{t}$ and $b\bar{b}$. 177
7.7 Systematic study of MC QCD fake rate $E_{\mathrm{T}}^{\mathrm{miss,rel}}$ 40-100 GeV with varying light flavour component. 179
7.8 The OS, SS, and OS+SS MC fake rate for muons and electrons in the intermediate $E_{\mathrm{T}}^{\mathrm{miss,rel}}$ region 40-100 GeV. 181
7.9 Ratio of SS to OS QCD fake rates in $t\bar{t}$ MC. 182
7.10 The ratio of CR-B and CR-A data fake rates. 182
7.11 The real MC efficiency for electrons and muons as function of p_{T}. 185
7.12 The final fake rate used for muons and electrons. 187
7.13 The final real efficiency for muons and electrons as function of p_{T}. 187
7.14 Results of the semi data-driven fake lepton estimation in SS events. 190
7.15 Results of the semi data-driven fake lepton estimation in OS events. 191
7.16 The QCD fake rates used for the fully data-driven fake lepton estimation. . . . 192
7.17 The muon and electron data QCD fake rate and fit versus $E_{\mathrm{T}}^{\mathrm{miss,rel}}$. 194
7.18 The muon and electron MC QCD fake rate and fit versus $E_{\mathrm{T}}^{\mathrm{miss,rel}}$. 194
7.19 The muon and electron fake rate versus p_{T}, normalized according to $E_{\mathrm{T}}^{\mathrm{miss,rel}}$. . . 195
7.20 The fp_{T} dependent fully data-driven muon and electron fake rates. 197
7.21 Results of the fully data-driven fake lepton estimation in SS events. 200
7.22 Results of the fully data-driven fake lepton estimation in OS events. 201
7.23 The p_{T} distribution of the semi- and fully data-driven fake lepton estimation in SS events. 203
7.24 The $E_{\mathrm{T}}^{\mathrm{miss,rel}}$ distribution of the semi- and fully data-driven fake lepton estimation in SS events. 204

8.1 Final $E_{\mathrm{T}}^{\mathrm{miss,rel}}$ distribution for the SR-OSjveto and SR-SSjveto signal regions with semi data-driven fake lepton estimation. 207
8.2 Final $E_{\mathrm{T}}^{\mathrm{miss,rel}}$ distribution for the SR-2jets and SR-m_{T2} signal regions with semi data-driven fake lepton estimation. 208
8.3 Final $E_{\mathrm{T}}^{\mathrm{miss,rel}}$ distribution for the SR-OSjveto and SR-SSjveto signal regions with fully data-driven fake lepton estimation. 211
8.4 Final $E_{\mathrm{T}}^{\mathrm{miss,rel}}$ distribution for the SR-2jets and SR-m_{T2} signal regions with fully data-driven fake lepton estimation. 212
8.5 pMSSM M_1 = 100 95% exclusion limit. 219
8.6 pMSSM M_1 = 140 95% exclusion limit. 220
8.7 pMSSM M_1 = 250 95% exclusion limit. 220
8.8 The 95% exclusion limits in simplified model, mode A. 221
8.9 The 95% exclusion limits in simplified model mode C. 222

8.10 The 95% exclusion limits for the direct slepton pMSSM model. 222

9.1 ATLAS di-muon opposite sign invariant mass spectra. 224
9.2 "Play!" with ATLAS, web-tool. 227
9.3 Screenshot of text and image explaining how to use HYPATIA. 228
9.4 Screenshot of a $\mu^+\mu^-$ HYPATIA event display. 229
9.5 Screenshot of an event with a Z decaying to e^+e^-, as displayed in HYPATIA. . 231
9.6 Screenshot of $H \to \gamma\gamma$ event. 232
9.7 Screenshot of the OPloT student submission page. 232
9.8 An overview of all combined histograms in OPloT. 233
9.9 The di-lepton results as displayed in OPloT. 233
9.10 The 25fb^{-1} $H \to \gamma\gamma$ expected results as displayed in OPloT, with the signal results overlaid. The events are simulated. 234
9.11 The $H \to 4\ell$ results as displayed in OPloT, with the expected results overlaid. . 234
9.12 ATLAS official $H \to \gamma\gamma$ and $H \to 4\ell$ results. 235
9.13 SUSY Signal invariant mass endpoint illustration. 236
9.14 Summary of ATLAS searches for electroweak production of charginos and neutralinos. 239

A.1 Framework of online ATLAS monitoring. 242
A.2 Ratio-noise distribution module-by-module, run 212199. 246
A.3 Mean ratio-noise versus time from DQMF, run 212199. 247
A.4 The ratio-noise integrated over all modules. 248
A.5 Ratio between the ratio-noise extracted from offline and DQMF. 248
A.6 Mean ratio-noise measured by DQMF versus time, runs 209980 and 209994-209995. 249
A.7 Ratio between ratio-noise results extracted from offline and DQMF for Barrel layer after fix. 250
A.8 Comparison of offline and online ratio-noise measurement results. 251

B.1 Muon STACO (Chain 1) combined reconstruction efficiency and electron tight++ reconstruction efficiency. 253

C.1 Muon p_{T} in CR-A, -B, and -C, before and after MC lepton subtraction. 267
C.2 Electron p_{T} in CR-A, -B, and -C, before and after MC lepton subtraction. . . . 268
C.3 Relative amount of inclusive loose all-inclusive muons and electrons the OS, and SS events versus $E_{\mathrm{T}}^{\mathrm{miss,rel}}$. 269
C.4 Relative amount of inclusive loose QCD muons and electrons the OS, and SS events versus $E_{\mathrm{T}}^{\mathrm{miss,rel}}$. 270
C.5 The relative amount of real MC to total data in the muon and electron channel respectively. 271
C.6 The data fake rate after MC real lepton subtraction, and after scaling cross section. 273
C.7 Fake rate versus $E_{\mathrm{T}}^{\mathrm{miss,rel}}$ for truth selected MC leptons, and for data. 276
C.8 The data and MC fake rates versus $E_{\mathrm{T}}^{\mathrm{miss,rel}}$ after statistical subtraction of real leptons, and the effect of MC scaling. 277

C.9 The data fake rate versus $E_{\mathrm{T}}^{\mathrm{miss,rel}}$ for SS di-muons and di-electrons and the effect of scaling MC. 279
C.10 The muon and electron fake rate versus p_{T} for different intervals of $E_{\mathrm{T}}^{\mathrm{miss,rel}}$. . . . 280
C.11 Conversion and QCD weights from MC in SR-OSjveto, SR-SSjveto, and SR-2jets. 281

D.1 Comparison of data, MC and the charge-flip estimate. 283

List of Tables

1.1 The full MSSM particle content. . . . 31
1.2 Chiral supermultiplet fields in the MSSM. The right-handed terms are written in two ways, either in terms of the left-handed fields, or as charge-conjugates of the right-handed fields. Extracted from Ref. [37] . . . 33
1.3 Gauge supermultiplet fields in the MSSM. Extracted from Ref. [37] . . . 33

3.1 The baseline and signal electron. . . . 74
3.2 The baseline and signal muon selection criteria. . . . 76
3.3 The baseline and signal jet definitions. . . . 79
3.4 ID and MS alignement with cosmic muons. . . . 88

4.1 Possible leptonic decays of $\tilde{\chi}_1^{\pm}$, $\tilde{\chi}_2^0$, and $\tilde{\ell}$. . . . 98
4.2 Signatures of the signal di-lepton final states. . . . 107
4.3 Final state requirements divided into signal-regions. . . . 107

5.1 The definition the direct gaugino signal regions. . . . 126
5.2 The definition of the direct slepton signal region. . . . 126
5.3 Summary of the data taking periods, run-ranges and integrated luminosity. . . . 128
5.4 Single and di-electron triggers. . . . 129
5.5 Single- and di-muon triggers. . . . 130
5.6 Di- electron and muon trigger. . . . 130
5.7 The trigger strategy divided into phase-space regions. . . . 132
5.8 Summary of the contributing SM EW and $t\bar{t}$ backgrounds. . . . 133
5.9 Summary of the SM MC QCD samples. . . . 135
5.10 SUSY Signal datasets . . . 135

6.1 The 4×4 matrix of the Matrix Method. . . . 141
6.2 Overview of MC truth origin categories. . . . 144
6.3 Definition of main control regions CR-A, CR-B and CR-C. . . . 148
6.4 Muon and electron statistics and purity in CR-A. . . . 150
6.5 Muon and electron statistics and purity in CR-B. . . . 154
6.6 The muon and electron statistics and purity in CR-C. . . . 157
6.7 The optimal control regions in control regions CR-A , CR-B, and CR-C. . . . 158
6.8 Fake rate and statistics for data and MC in the selected control regions for muons and electrons respectively. . . . 161
6.9 Data and MC scale factor CR-C. . . . 165

6.10 Cuts for the conversion control region. . . . 168

7.1 The conversions and QCD weights in three different signal-regions. . . . 175
7.2 Systematics due to the relative $b\bar{b}$ and $t\bar{t}$ contribution. . . . 178
7.3 Electron truth heavy and light flavour fake rates. . . . 179
7.4 MC light flavour weight systematic study. . . . 180
7.5 A summary of the relative systematic uncertainties related to the QCD fake rate. 183
7.6 The relative systematic uncertainty related to the conversion fake rate. . . . 184
7.7 Systematic uncertainty on the real efficiency. . . . 185
7.8 Comparison of fake lepton estimation with p_{T} dependent fake rates and efficiencies, and with joint p_{T} and η dependent ones. . . . 186
7.9 The relative systematic uncertainties on the data-driven fake rate. . . . 196

8.1 Final event yield using semi data-driven fake lepton estimation. . . . 209
8.2 Comparison of final event yield using semi or fully data-driven fake lepton estimation. . . . 213
8.3 Breakdown of uncertainty on background estimates 218

A.1 Table of probabilities for combinations of SCT strips to fire or not. . . . 244
A.2 Table of probabilities for combinations of a SCT module-side to encounter hits or not. . . . 245

B.1 Description of the electron (and photon) identification scheme. . . . 252
B.2 The Z/γ^* MC samples. . . . 254
B.3 The W boson production MC samples. . . . 255
B.4 The di-boson production MC samples. . . . 255
B.5 The top quark MC samples. . . . 256
B.6 The Pythia QCD di-jet MC samples. . . . 256
B.7 The Pythia JF17 MC sample. . . . 257
B.8 The PythiaB di-lepton filter MC sample. . . . 257
B.9 The PythiaB single lepton MC samples. . . . 257
B.10 Luminosity scaling for Z/γ^*+jets MC samples. . . . 258
B.11 Luminosity scaling for γ^*+jets MC samples. . . . 258
B.12 Luminosity scaling for PythiaB QCD MC sample with di-lepton filter. . . . 258
B.13 Luminosity scaling for PythiaB single-lepton QCD MC sample. . . . 258
B.14 Luminosity scaling for W+jets MC samples. . . . 259
B.15 Luminosity scaling for di-boson MC samples. . . . 259
B.16 Luminosity scaling for the top MC sample. . . . 259
B.17 Luminosity scaling for single top MC samples. . . . 259
B.18 Luminosity scaling for muon-filtered di-jet Pythia MC QCD samples. . . . 259
B.19 Luminosity scaling for electron-filtered di-jet Pythia MC samples. . . . 259
B.20 Luminosity scaling for Pythia JF17 QCD MC sample. . . . 259

C.1 Muon fake rates and purities in CR-A. . . . 260
C.2 Muon fake rates and purities in CR-B. . . . 261
C.3 Muon fake rates and purities in CR-C. . . . 262

C.4 Electron fake rates and purities in CR-A. 263
C.5 Electron fake rates and purities in CR-B. 264
C.6 Electron fake rates and purities in CR-C. 265
C.7 Number of inclusive loose leptons in data, real leptons in MC, and the difference after real lepton subtraction. 272
C.8 Effect of subtracting conversion electrons in di-lepton control regions. 274
C.9 Effect of subtracting conversion electrons in single lepton control regions. . . . 274
C.10 Conversion and QCD weights from MC in SR-OSjveto, SR-SSjveto, and SR-2jets. 282

Bibliography

[1] *The Large Hadron Collider*, http://home.web.cern.ch/topics/large-hadron-collider.

[2] ATLAS Collaboration. http://atlas.ch.

[3] ALICE Collaboration, *A Large Ion Collider Experiment*, http://aliceinfo.cern.ch.

[4] ISOLDE Collaboration, *The ISOLDE Radioactive Ion Beam facility*, http://isolde.web.cern.ch.

[5] The LHCb Collaboration. http://lhcb-public.web.cern.ch/lhcb-public/.

[6] *AD, The Antiproton Decelerator*, http://home.web.cern.ch/about/accelerators/antiproton-decelerator.

[7] *CERN neutrinos to Gran Sasso*, http://home.web.cern.ch/about/accelerators/cern-neutrinos-gran-sasso.

[8] http://home.web.cern.ch/about/experiments/cloud.

[9] D. H. Lawrence, *Pansies: Poems*. Martin Secker, 1929. http://rpo.library.utoronto.ca/poems/relativity-0.

[10] M. Kuhlmann, *Stanford Encyclopedia*, 2012. http://plato.stanford.edu/entries/quantum-field-theory.

[11] G. F. Guidice, *A Zeptospace Oddysey*. Oxford University Press, USA, 2010.

[12] S.-I. Tomonaga, J. Schwinger, and R. P. Feynman, *The Nobel Prize in Physics 1965*, Web. 28 mar 2014. http://www.nobelprize.org/nobel_prizes/physics/laureates/1965/. Nobelprize.org. Nobel Media AB 2013.

[13] S. L. Glashow, A. Salam, and S. Weinberg, *The Nobel Prize in Physics 1979*, Web. 28 mar 2014. http://www.nobelprize.org/nobel_prizes/physics/laureates/1979/. Nobelprize.org. Nobel Media AB 2013.

[14] CDF Collaboration, F. Abe et al., *Observation of Top Quark Production in pp Collisions with the Collider Detector at Fermilab*, Phys. Rev. Lett. **74** (1995) 2626–2631.

[15] D0 Collaboration, S. Abachi et al., *Search for High Mass Top Quark Production in pp Collisions at sqrts = 1.8 TeV*, Phys. Rev. Lett. **74** (1995) 2422–2426.

[16] S. W. Herb et al., *Observation of a Dimuon Resonance at 9.5 GeV in 400-GeV Proton-Nucleus Collisions*, Phys. Rev. Lett. **39** (1977) 252–255.

[17] DONUT Collaboration, K. Kodama et al., *Observation of tau neutrino interactions*, Phys.Lett. **B504** (2001) 218–224, arXiv:hep-ex/0012035 [hep-ex].

[18] CMS Collaboration. http://cms.web.cern.ch/content/cms-collaboration.

[19] CMS Collaboration, S. Chatrchyan et al., *Observation of a new boson at a mass of 125 GeV with the CMS experiment at the LHC*, Phys.Lett. **B716** (2012) 30–61, arXiv:1207.7235 [hep-ex].

[20] ATLAS Collaboration, G. Aad et al., *Observation of a new particle in the search for the Standard Model Higgs boson with the ATLAS detector at the LHC*, Phys.Lett. **B716** (2012) 1–29, arXiv:1207.7214 [hep-ex].

[21] E. Wigner, *The Collected Works of Eugene Paul Wigner*, vol. VI. Springer-Verlag, Berlin, 1995.

[22] M. Thomson, *Modern Particle Physics*. Cambridge University Press, 2013. http:www.cambridge.org/MPP.

[23] S. L. Glashow, *Partial Symmetries of Weak Interactions*, Nucl. Phys. **22** (1961) 579–588.

[24] A. Salam, *in Elementary Particle Theory*, 1968. Proc. 8th Nobel Symp.

[25] S. Weinberg, *A Model of Leptons*, Phys. Rev. Lett. **19** (1967) 1264–1266.

[26] T. W. B. Kibble, *Symmetry Breaking in Non-Abelian Gauge Theories*, Phys. Rev. **155** (1967) 1554–1561.

[27] P. W. Higgs, *Spontaneous Symmetry Breakdown without Massless Bosons*, Phys. Rev. **145** (1966) 1156–1163.

[28] G. S. Guralnik, C. R. Hagen, and T. W. B. Kibble, *Global Conservation Laws and Massless Particles*, Phys. Rev. Lett. **13** (1964) 585–587.

[29] P. W. Higgs, *Broken Symmetries and the Masses of Gauge Bosons*, Phys. Rev. Lett. **13** (1964) 508–509.

[30] P. Higgs, *Broken symmetries, massless particles and gauge fields*, Physics Letters **12** (1964) no. 2, 132–133.

[31] F. Englert and R. Brout, *Broken Symmetry and the Mass of Gauge Vector Mesons*, Phys. Rev. Lett. **13** (1964) 321–323.

[32] J. Goldstone, *Field theories with "Superconductor" solutions*, Il Nuovo Cimento **19** (1961) no. 1, 154–164.

[33] *The Nobel Prize Institute home-pages*, http://www.nobelprize.org/nobel_prizes/physics/laureates/2004/popular.html.

[34] D. Green, *High P_T Physics at Hadron Colliders*. Cambridge University Press, 2005. Press Syndicate of the University of Cambridge.

[35] H. D. Politzer, *Reliable Perturbative Results for Strong Interactions?*, Phys. Rev. Lett. **30** (1973) 1346–1349.

[36] D. J. Gross and F. Wilczek, *Ultraviolet Behavior of Non-Abelian Gauge Theories*, Phys. Rev. Lett. **30** (1973) 1343–1346.

[37] S. P. Martin, *A Supersymmetry primer*, arXiv:hep-ph/9709356 [hep-ph].

[38] Q. R. Ahmad et al., *Direct Evidence for Neutrino Flavor Transformation from Neutral-Current Interactions in the Sudbury Neutrino Observatory*, Phys. Rev. Lett. **89** (2002) 011301.

[39] (Super-Kamiokande) Collaboration, Y. Fukuda et al., *Evidence for Oscillation of Atmospheric Neutrinos*, Phys. Rev. Lett. **81** (1998) 1562–1567.

[40] Particle Data Group Collaboration, J. Beringer et al., *Review of Particle Physics*, Phys. Rev. D **86** (2012) 010001.

[41] F. Zwicky, *On the redshift of spectral lines through interstellar space*, Proceedings of the National Academy of Sciences **15** (1929) no. 10, 773–779, http://www.pnas.org/content/15/10/773.

[42] Planck Collaboration, P. Ade et al., *Planck 2013 results. XVI. Cosmological parameters*, arXiv:1303.5076 [astro-ph.CO].

[43] R. Barbieri and G. Giudice, *Upper Bounds on Supersymmetric Particle Masses*, Nucl.Phys. **B306** (1988) 63.

[44] B. de Carlos and J. Casas, *One loop analysis of the electroweak breaking in supersymmetric models and the fine tuning problem*, Phys.Lett. **B309** (1993) 320–328, arXiv:hep-ph/9303291 [hep-ph].

[45] ATLAS Collaboration, CDF Collaboration, CMS Collaboration, D0 Collaboration Collaboration, *First combination of Tevatron and LHC measurements of the top-quark mass*, arXiv:1403.4427 [hep-ex].

[46] H. Murayama, *Supersymmetry phenomenology*, arXiv:hep-ph/0002232 [hep-ph].

[47] P. A. M. Dirac, *The Quantum Theory of the Electron*, Proceedings of The Royal Society **117** (1928) no. 10, 610–624.

[48] S. Dimopoulos and H. Georgi, *Softly Broken Supersymmetry and SU(5)*, Nucl. Phys. **B193** (1981) 150.

[49] E. Witten, *Dynamical Breaking of Supersymmetry*, Nucl. Phys. **B188** (1981) 513.

[50] M. Dine, W. Fischler, and M. Srednicki, *Supersymmetric Technicolor*, Nucl. Phys. **B189** (1981) 575–593.

[51] S. Dimopoulos and S. Raby, *Supercolor*, Nucl. Phys. **B192** (1981) 353.

[52] N. Sakai, *Naturalness in Supersymmetric Guts*, Zeit. Phys. **C11** (1981) 153.

[53] R. Kaul and P. Majumdar, *Cancellation of quadratically divergent mass corrections in globally supersymmetric spontaneously broken gauge theories*, Nucl. Phys. **B199** (1982) 36.

[54] P. Fayet, *Supersymmetry and Weak, Electromagnetic and Strong Interactions*, Phys. Lett. **B64** (1976) 159.

[55] P. Fayet, *Spontaneously Broken Supersymmetric Theories of Weak, Electromagnetic and Strong Interactions*, Phys. Lett. **B69** (1977) 489.

[56] G. R. Farrar and P. Fayet, *Phenomenology of the Production, Decay, and Detection of New Hadronic States Associated with Supersymmetry*, Phys. Lett. **B76** (1978) 575–579.

[57] P. Fayet, *Relations Between the Masses of the Superpartners of Leptons and Quarks, the Goldstino Couplings and the Neutral Currents*, Phys. Lett. **B84** (1979) 416.

[58] A. Djouadi, *The anatomy of electroweak symmetry breaking Tome II: The Higgs bosons in the Minimal Supersymmetric Model*, Physics Reports **459** (2008) no. 1-6, 1 – 241.

[59] H. Baer and X. Tata, *Weak Scale Supersymmetry, From Superfields to Scatttering Events*. Cambridge University Press, 2006.

[60] A. H. Chamseddine, R. Arnowitt, and P. Nath, *Locally Supersymmetric Grand Unification*, Phys. Rev. Lett. **49** (1982) 970–974.

[61] R. Barbieri, S. Ferrara, and C. A. Savoy, *Gauge Models with Spontaneously Broken Local Supersymmetry*, Phys. Lett. **B119** (1982) 343.

[62] L. E. Ibanez, *Locally Supersymmetric SU(5) Grand Unification*, Phys. Lett. **B118** (1982) 73.

[63] L. J. Hall, J. D. Lykken, and S. Weinberg, *Supergravity as the Messenger of Supersymmetry Breaking*, Phys. Rev. **D27** (1983) 2359–2378.

[64] N. Ohta, *Grand Unified Theories Based on Local Supersymmetry*, Prog. Theor. Phys. **70** (1983) 542.

[65] G. L. Kane, C. F. Kolda, L. Roszkowski, and J. D. Wells, *Study of constrained minimal supersymmetry*, Phys. Rev. **D49** (1994) 6173–6210.

[66] S. Dimopoulos and D. W. Sutter, *The Supersymmetric flavor problem*, Nucl.Phys. **B452** (1995) 496–512, `arXiv:hep-ph/9504415 [hep-ph]`.

[67] MEGA Collaboration Collaboration, M. Brooks et al., *New limit for the family number nonconserving decay $\mu^+ \to e^+\gamma$*, Phys.Rev.Lett. **83** (1999) 1521–1524, arXiv:hep-ex/9905013 [hep-ex].

[68] N. Cabibbo, *Unitary Symmetry and Leptonic Decays*, Phys. Rev. Lett. **10** (1963) 531–533.

[69] M. Kobayashi and T. Maskawa, *CP-Violation in the Renormalizable Theory of Weak Interaction*, Progress of Theoretical Physics **49** (1973) no. 2, 652–657. http://ptp.oxfordjournals.org/content/49/2/652.

[70] M. Dine and W. Fischler, *A Phenomenological Model of Particle Physics Based on Supersymmetry*, Phys. Lett. **B110** (1982) 227.

[71] L. Alvarez-Gaume, M. Claudson, and M. B. Wise, *Low-Energy Supersymmetry*, Nucl. Phys. **B207** (1982) 96.

[72] C. R. Nappi and B. A. Ovrut, *Supersymmetric Extension of the SU(3) x SU(2) x U(1) Model*, Phys. Lett. **B113** (1982) 175.

[73] M. Dine and A. E. Nelson, *Dynamical supersymmetry breaking at low-energies*, Phys. Rev. **D48** (1993) 1277–1287, arXiv:hep-ph/9303230.

[74] M. Dine, A. E. Nelson, and Y. Shirman, *Low-energy dynamical supersymmetry breaking simplified*, Phys. Rev. **D51** (1995) 1362–1370, arXiv:hep-ph/9408384.

[75] M. Dine, A. E. Nelson, Y. Nir, and Y. Shirman, *New tools for low-energy dynamical supersymmetry breaking*, Phys.Rev. **D53** (1996) 2658–2669, arXiv:hep-ph/9507378 [hep-ph].

[76] N. Arkani-Hamed, P. Schuster, N. Toro, J. Thaler, L.-T. Wang, et al., *MARMOSET: The Path from LHC Data to the New Standard Model via On-Shell Effective Theories*, arXiv:hep-ph/0703088 [HEP-PH].

[77] J. Alwall, P. C. Schuster, and N. Toro, *Simplified models for a first characterization of new physics at the LHC*, Phys. Rev. D **79** (2009) 075020. http://link.aps.org/doi/10.1103/PhysRevD.79.075020.

[78] J. Alwall, M.-P. Le, M. Lisanti, and J. G. Wacker, *Model-independent jets plus missing energy searches*, Phys. Rev. D **79** (2009) 015005.

[79] D. Alves, E. Izaguirre, and J. Wacker, *Where the sidewalk ends: jets and missing energy search strategies for the 7 TeV LHC*, Journal of High Energy Physics **2011** (2011) no. 10, 1–36.

[80] LHC New Physics Working Group Collaboration, D. Alves et al., *Simplified models for LHC new physics searches*, Journal of Physics G: Nuclear and Particle Physics **39** (2012) no. 10, 105005. http://stacks.iop.org/0954-3899/39/i=10/a=105005.

[81] C. F. Berger, J. S. Gainer, J. L. Hewett, and T. G. Rizzo, *Supersymmetry Without Prejudice*, JHEP **0902** (2009) 023, arXiv:0812.0980 [hep-ph].

[82] A. Djouadi, J.-L. Kneur, and G. Moultaka, *SuSpect: A Fortran code for the supersymmetric and Higgs particle spectrum in the MSSM*, Comput.Phys.Commun. **176** (2007) 426–455, arXiv:hep-ph/0211331 [hep-ph].

[83] S. S. AbdusSalam et al., *Fitting the phenomenological MSSM*, Phys. Rev. D **81** (2010) 095012.

[84] R. P. Feynman, *Very high-energy collisions of hadrons*, Phys.Rev.Lett. **23** (1969) 1415–1417.

[85] C. G. Tully, *Elementary Particle Physics in a Nutshell*. Princeton University Press, 2011.

[86] R. P. Feynman, *Space-Time Approach to Quantum Electrodynamics*, Phys. Rev. **76** (1949) 769–789.

[87] J. D. Bjorken, *Asymptotic Sum Rules at Infinite Momentum*, Phys. Rev. **179** (1969) 1547–1553. http://link.aps.org/doi/10.1103/PhysRev.179.1547.

[88] *Hadron Electron Ring Accelerator at DESY, Hamburg Germany*, Home-page. http://www.desy.de/research/facilities__projects/hera/index_eng.html.

[89] V. N. Gribov and L. N. Lipatov Soviet Journal of Nuclear Physics **15** (1972) 438.

[90] V. N. Gribov and L. N. Lipatov Soviet Journal of Nuclear Physics **15** (1972) 675.

[91] G. Altarelli and G. Parisi, *Asymptotic freedom in parton language*, Nuclear Physics B **126** (1977) no. 2, 298 – 318.

[92] Y. L. Dokshitzer Sov. Phys. JETP **46** (1977) 641.

[93] R. Placakyte, *Parton Distribution Functions*, arXiv:1111.5452 [hep-ph].

[94] A. Martin, W. Stirling, R. Thorne, and G. Watt, *Parton distributions for the LHC*, Eur.Phys.J. **C63** (2009) 189–285, arXiv:0901.0002 [hep-ph]. Plots available at http://mstwpdf.hepforge.org/plots/plots.html.

[95] B. Andersson, G. Gustafson, G. Ingelman, and T. Sjöstrand, *Parton fragmentation and string dynamics*, Physics Reports **97** (1983) no. 2-3, 31 – 145.

[96] B. Webber, *A QCD model for jet fragmentation including soft gluon interference*, Nuclear Physics B **238** (1984) no. 3, 492 – 528.

[97] D. Amati and G. Veneziano, *Preconfinement as a property of perturbative QCD*, Physics Letters B **83** (1979) no. 1, 87 – 92.

[98] N. Metropolis and S. Ulam, *The Monte Carlo Method*, Journal of the American Statistical Association **44** (1949) no. 247, pp. 335–341. http://www.jstor.org/stable/2280232.

[99] *Proton Synchrotron Division*, http://ps-div.web.cern.ch/ps-div/LHC-PS/LHC-PS.html.

[100] ATLAS Collaboration, G. Aad et al., *The ATLAS Experiment at the CERN Large Hadron Collider*, Journal of Instrumentation **3** (2008) no. 08, S08003. http://stacks.iop.org/1748-0221/3/i=08/a=S08003.

[101] M. Capeans, O. Rohne, et al., *ATLAS Insertable B-Layer Technical Design Report*, Tech. Rep. CERN-LHCC-2010-013. ATLAS-TDR-19, CERN, Geneva, Sep, 2010. http://cds.cern.ch/record/1291633/files/ATLAS-TDR-019.pdf.

[102] ATLAS Collaboration, G. Aad et al., *Performance of the ATLAS Trigger System in 2010*, Eur.Phys.J. **C72** (2012) 1849, arXiv:1110.1530 [hep-ex].

[103] P. Calafiura et al., *The athena control framework in production, new developments and lessons learned*, . http://cds.cern.ch/record/865624/files/p456.pdf.

[104] T. Sjostrand, S. Mrenna, and P. Z. Skands, *PYTHIA 6.4 Physics and Manual*, JHEP **0605** (2006) 026, arXiv:hep-ph/0603175 [hep-ph].

[105] G. Corcella et al., *HERWIG 6: An Event generator for hadron emission reactions with interfering gluons (including supersymmetric processes)*, JHEP **0101** (2001) 010, arXiv:hep-ph/0011363 [hep-ph].

[106] T. Gleisberg et al., *Event generation with SHERPA 1.1*, JHEP **0902** (2009) 007, arXiv:0811.4622 [hep-ph].

[107] S. Frixione and B. R. Webber, *Matching NLO QCD computations and parton shower simulations*, JHEP **0206** (2002) 029, arXiv:hep-ph/0204244 [hep-ph].

[108] M. L. Mangano et al., *ALPGEN, a generator for hard multiparton processes in hadronic collisions*, Journal of High Energy Physics **2003** (2003) no. 07, 001. http://stacks.iop.org/1126-6708/2003/i=07/a=001.

[109] P. Nason, *A New method for combining NLO QCD with shower Monte Carlo algorithms*, JHEP **0411** (2004) 040, arXiv:hep-ph/0409146 [hep-ph].

[110] J. Butterworth, J. R. Forshaw, and M. Seymour, *Multiparton interactions in photoproduction at HERA*, Z.Phys. **C72** (1996) 637–646, arXiv:hep-ph/9601371 [hep-ph].

[111] GEANT4 Collaboration, S. Agostinelli et al., *GEANT4: A Simulation toolkit*, Nucl.Instrum.Meth. **A506** (2003) 250–303.

[112] J. Allison et al., *Geant4 developments and applications*, Nuclear Science, IEEE Transactions on **53** (2006) no. 1, 270–278.

[113] I. Ueda, *ATLAS Distributed Computing Operations in the first Two Years of Data Taking*, University of Tokyo. 2012. http://pos.sissa.it/archive/conferences/153/013/ISGC%202012_013.pdf.

[114] I. Antcheva et al., *ROOT – A C++ framework for petabyte data storage, statistical analysis and visualization*, Computer Physics Communications **180** (2009) no. 12, 2499 – 2512.

[115] C. Lester and D. Summers, *Measuring masses of semi-invisibly decaying particles pair produced at hadron colliders*, Phys.Lett. **B463** (1999) 99–103, arXiv:hep-ph/9906349 [hep-ph].

[116] G. Polesello and D. R. Tovey, *Supersymmetric particle mass measurement with the boost-corrected contransverse mass*, JHEP **1003** (2010) 030, arXiv:0910.0174 [hep-ph].

[117] D. R. Tovey, *On measuring the masses of pair-produced semi-invisibly decaying particles at hadron colliders*, JHEP **0804** (2008) 034, arXiv:0802.2879 [hep-ph].

[118] B. Gripaios, *Transverse observables and mass determination at hadron colliders*, JHEP **0802** (2008) 053, arXiv:0709.2740 [hep-ph].

[119] S. Hassani et al., *A muon identification and combined reconstruction procedure for the ATLAS detector at the LHC using the (MUONBOY, STACO, MuTag) reconstruction packages*, Nuclear Instruments and Methods in Physics Research Section A: Accelerators, Spectrometers, Detectors and Associated Equipment **572** (2007) no. 1, 77 – 79. Frontier Detectors for Frontier Physics, Proceedings of the 10th Pisa Meeting on Advanced Detectors.

[120] B. Resende, *Muon identification algorithms in ATLAS*, Tech. Rep. ATL-PHYS-PROC-2009-113, CERN, Geneva, Sep, 2009. https://cds.cern.ch/record/1209632/files/EPS-HEP%202009_431.pdf.

[121] M. Cacciari, G. P. Salam, and G. Soyez, *The Anti-k(t) jet clustering algorithm*, JHEP **0804** (2008) 063, arXiv:0802.1189 [hep-ph].

[122] S. D. Ellis and D. E. Soper, *Successive combination jet algorithm for hadron collisions*, Phys. Rev. D **48** (1993) 3160–3166. http://link.aps.org/doi/10.1103/PhysRevD.48.3160.

[123] Y. L. Dokshitzer, G. Leder, S. Moretti, and B. Webber, *Better jet clustering algorithms*, JHEP **9708** (1997) 001, arXiv:hep-ph/9707323 [hep-ph].

[124] A. B. Galtieri, F. Margaroli, and I. Volobouev, *Precision measurements of the top quark mass from the Tevatron in the pre-LHC era*, Reports on Progress in Physics **75** (2012) no. 5, 056201. http://stacks.iop.org/0034-4885/75/i=5/a=056201.

[125] The ATLAS Collaboration, *Studies of the performance of the ATLAS detector using cosmic-ray muons*, The European Physical Journal C **71** (2011) no. 3, 1–36.

[126] *The Expected Performance of the ATLAS Inner Detector*, Tech. Rep. ATL-PHYS-PUB-2009-002. ATL-COM-PHYS-2008-105, CERN, Geneva, Aug, 2008. https://cds.cern.ch/record/1118445?ln=no.

[127] Hyperphysics. http://hyperphysics.phy-astr.gsu.edu/hbase/astro/cosmic.html.

[128] S. Haino et al., *Measurements of primary and atmospheric cosmic - ray spectra with the BESS-TeV spectrometer*, Phys.Lett. **B594** (2004) 35–46, arXiv:astro-ph/0403704 [astro-ph].

[129] ATLAS Collaboration, G. Aad et al., *Rapidity gap cross sections measured with the ATLAS detector in pp collisions at* $\sqrt{s} = 7$ *TeV*, Eur.Phys.J. **C72** (2012) 1926, arXiv:1201.2808 [hep-ex].

[130] ATLAS Collaboration, G. Aad et al., *Measurement of the Inelastic Proton-Proton Cross-Section at* $\sqrt{s} = 7$ *TeV with the ATLAS Detector*, Nature Commun. **2** (2011) 463, arXiv:1104.0326 [hep-ex].

[131] E. G. R. W. Pages, *Predicted SM cross section as function of energy*, http://www.hep.ph.ic.ac.uk.

[132] W. Beenakker et al., *The Production of charginos / neutralinos and sleptons at hadron colliders*, Phys.Rev.Lett. **83** (1999) 3780–3783, arXiv:hep-ph/9906298 [hep-ph].

[133] I. Santoyo Castillo, B. Gjelsten, E. Gramstad, F. Ould-Saada, M. Pedersen, et al., *Searching for direct gaugino production and direct slepton production with two leptons and missing transverse momentum at* $\sqrt{s} = 7TeV$ *(supporting INT note)*, Tech. Rep. ATL-COM-PHYS-2011-1721, CERN, Geneva, Dec, 2011. https://cds.cern.ch/record/1408807?ln=no.

[134] The ATLAS Collaboration, G. Aad et al., *Search for direct slepton and gaugino production in final states with two leptons and missing transverse momentum with the ATLAS detector in pp collisions at* $\sqrt{s} = 7$ *TeV*, Phys.Lett. **B718** (2013) 879–901, arXiv:1208.2884 [hep-ex].

[135] *Search for squarks and gluinos with the ATLAS detector in final states with jets and missing transverse momentum and 20.3* fb^{-1} *of* $\sqrt{s} = 8$ *TeV proton-proton collision data*, Tech. Rep. ATLAS-CONF-2013-047, CERN, Geneva, May, 2013. https://cds.cern.ch/record/1547563?ln=no.

[136] T. A. Collaboration, *Search for direct production of charginos and neutralinos in events with three leptons and missing transverse momentum in pp collisions with the {ATLAS} detector*, Physics Letters B **718** (2013) no. 3, 841 – 859.

[137] F. E. Paige, S. D. Protopopescu, H. Baer, and X. Tata, *ISAJET 7.69: A Monte Carlo event generator for pp, anti-p p, and e+e- reactions*, arXiv:hep-ph/0312045 [hep-ph].

[138] W. Beenakker et al., *Production of Charginos, Neutralinos, and Sleptons at Hadron Colliders*, Phys. Rev. Lett. **83** (1999) 3780–3783.

[139] W. Beenakker et al., *Erratum: Production of Charginos, Neutralinos, and Sleptons at Hadron Colliders [Phys. Rev. Lett. 83, 3780 (1999)]*, Phys. Rev. Lett. **100** (2008) 029901.

[140] W. S. Cho, K. Choi, Y. G. Kim, and C. B. Park, *Measuring superparticle masses at hadron collider using the transverse mass kink*, JHEP **0802** (2008) 035, arXiv:0711.4526 [hep-ph].

[141] *Search for direct-slepton and direct-chargino production in final states with two opposite-sign leptons, missing transverse momentum and no jets in 20/fb of pp collisions at sqrt(s) = 8 TeV with the ATLAS detector*, Tech. Rep. ATLAS-CONF-2013-049, CERN, Geneva, May, 2013. https://cds.cern.ch/record/1547565?ln=en.

[142] R. C. Gray, C. Kilic, M. Park, S. Somalwar, and S. Thomas, *Backgrounds To Higgs Boson Searches from Asymmetric Internal Conversion*, arXiv:1110.1368 [hep-ph].

[143] ATLAS Collaboration, *Performance of the ATLAS Electron and Photon Trigger in p-p Collisions at sqrts = 7 TeV in 2011*, . http://inspirehep.net/record/1204270/files/ATLAS-CONF-2012-048.pdf.

[144] ATLAS Collaboration, *Performance of the ATLAS muon trigger in 2011*, . http://inspirehep.net/record/1204318/files/ATLAS-CONF-2012-099.pdf.

[145] N. Kidonakis, *Next-to-next-to-leading-order collinear and soft gluon corrections for t-channel single top quark production*, Phys. Rev. D **83** (2011) 091503.

[146] N. Kidonakis, *Next-to-next-to-leading logarithm resummation for s-channel single top quark production*, Phys. Rev. D **81** (2010) 054028.

[147] N. Kidonakis, *Two-loop soft anomalous dimensions for single top quark associated production with a WH*, Phys. Rev. D **82** (2010) 054018.

[148] https://twiki.cern.ch/twiki/bin/viewauth/AtlasProtected/TopMC11#MC11CommonConventions. Internal ATLAS recommendation.

[149] M. Muhlleitner, A. Djouadi, and Y. Mambrini, *SDECAY: A Fortran code for the decays of the supersymmetric particles in the MSSM*, Comput.Phys.Commun. **168** (2005) 46–70, arXiv:hep-ph/0311167 [hep-ph].

[150] B. Allanach, *SOFTSUSY: a program for calculating supersymmetric spectra*, Comput.Phys.Commun. **143** (2002) 305–331, arXiv:hep-ph/0104145 [hep-ph].

[151] ATLAS Collaboration, G. Aad et al., *Measurement of the top quark-pair production cross section with ATLAS in pp collisions at* $\sqrt{s} = 7$ *TeV*, Eur.Phys.J. **C71** (2011) 1577, arXiv:1012.1792 [hep-ex].

[152] P. Bechtle, B. K. Gjelsten, E. Gramstad, F. Ould-Saada, M. Pedersen, et al., *SUSY searches with dileptons and high missing transverse momentum*, Tech. Rep. ATL-PHYS-INT-2011-030, CERN, Geneva, Apr, 2011. https://cds.cern.ch/record/1341811. Restricted ATLAS material.

[153] A. Alonso, B. Kile Gjelsten, E. Gramstad, Ould-Saada, M. Pedersen, et al., *Searching for Supersymmetry with two leptons and missing transverse momentum at* $\sqrt{s} = 7TeV$, Tech. Rep. ATL-PHYS-INT-2011-091, CERN, Geneva, Nov, 2011. https://cds.cern.ch/record/1398592/. Restricted ATLAS material.

[154] A. Alonso, B. Gjelsten, E. Gramstad, F. Ould-Saada, M. Pedersen, et al., *Constraining the gauge-mediated Supersymmetry breaking model in final states with two leptons, jets and missing transverse momentum with the ATLAS experiment at* $\sqrt{s} = 7TeV$, Tech. Rep. ATL-PHYS-INT-2011-096, CERN, Geneva, Nov, 2011. https://cds.cern.ch/record/1402507. Restricted ATLAS material.

[155] A. Alonso, , B. Kile Gjelsten, E. Gramstad, F. Ould-Saada, M. Pedersen, et al., *Searching for Supersymmetry with two leptons and missing transverse momentum at sqrt(s)=7 TeV*, Tech. Rep. ATL-COM-PHYS-2011-649, CERN, Geneva, Jun, 2011. https://cds.cern.ch/record/1355699. Restricted ATLAS material.

[156] ATLAS Collaboration, G. Aad et al., *Search for supersymmetric particles in events with lepton pairs and large missing transverse momentum in* $\sqrt{s} = 7$ *TeV proton-proton collisions with the ATLAS experiment*, Eur.Phys.J. **C71** (2011) 1682, arXiv:1103.6214 [hep-ex].

[157] The ATLAS Collaboration, G. Aad et al., *Searches for supersymmetry with the ATLAS detector using final states with two leptons and missing transverse momentum in* $\sqrt{s} = 7$ *TeV proton-proton collisions*, Phys.Lett. **B709** (2012) 137–157, arXiv:1110.6189 [hep-ex].

[158] C. Clement, B. Gjelsten, E. Gramstad, F. Ould-Saada, M. Pedersen, et al., *Searching for direct gaugino production and direct slepton production with two leptons and missing transverse momentum at* $\sqrt{s} = 8TeV$., Tech. Rep. ATL-PHYS-INT-2013-002, CERN, Geneva, Jan, 2013. https://cds.cern.ch/record/1503511. Restricted ATLAS material.

[159] E. Gramstad, F. Ould-Saada, and A. L. Read, *Searches for Supersymmetry in Di-Lepton Final States with the ATLAS Detector at* $\sqrt{s} = 7$ *TeV*. PhD thesis, Oslo U., Jun, 2013. https://cds.cern.ch/record/1631043?ln=no. Presented 27 Sep 2013.

[160] ATLAS Collaboration, G. Aad et al., *Luminosity Determination in pp Collisions at* $\sqrt{s} = 7$ *TeV Using the ATLAS Detector at the LHC*, Eur.Phys.J. **C71** (2011) 1630, arXiv:1101.2185 [hep-ex].

[161] ATLAS Collaboration, *Luminosity Determination in pp Collisions at sqrt(s) = 7 TeV using the ATLAS Detector in 2011*, ATLAS-CONF-2011-116. http://cdsweb.cern.ch/record/1376384.

[162] The ATLAS Collaboration, *Commissioning of the ATLAS high-performance b-tagging algorithms in the 7 TeV collision data*, Tech. Rep. ATLAS-CONF-2011-102, CERN, Geneva, Jul, 2011. http://cds.cern.ch/record/1369219?ln=en.

[163] A. L. Read, *Modified frequentist analysis of search results (the CL_s method)*, . https://cds.cern.ch/record/451614/files/open-2000-205.pdf.

[164] S. S. Wilks, *The Large-Sample Distribution of the Likelihood Ratio for Testing Composite Hypotheses*, The Annals of Mathematical Statistics **9** (1938) no. 1, 60–62.

[165] ROOT Collaboration, K. Cranmer et al., *HistFactory: A tool for creating statistical models for use with RooFit and RooStats*, Tech. Rep. CERN-OPEN-2012-016, New York U., New York, Jan, 2012. https://cds.cern.ch/record/1456844.

[166] *Lep susy working group*, On web. http://lepsusy.web.cern.ch/lepsusy/.

[167] ATLAS Collaboration Collaboration, G. Aad et al., *Search for an excess of events with an identical flavour lepton pair and significant missing transverse momentum in $\sqrt{s} = 7$ TeV proton-proton collisions with the ATLAS detector*, Eur.Phys.J. **C71** (2011) 1647, arXiv:1103.6208 [hep-ex].

[168] *International Particle Physics Outreach Group*, http://ippog.web.cern.ch.

[169] M. Pedersen and F. Ould-Saada, *Z-Path*, http://atlas.physicsmasterclasses.org/en/zpath.htm.

[170] F. Ould-Saada, M. Pedersen, et al., *International Particle Physics Masterclasses - Bringing LHC data into the Classroom*, 36th International Conference on High Energy Physics. 2012. http://pos.sissa.it/archive/conferences/174/559/ICHEP2012_559.pdf. To appear in http://www.epj-conferences.org.

[171] M. Bugge, E. Gramstad, V. Morisbak, F. Ould-Saada, and M. Pedersen, *ATLAS Masterclasses, W and Z path physics and presentation of the Z path measurement*, International Conference on New Frontiers of Physics. European Physical Journal Web of Conferences, 2013. http://indico.cern.ch/event/198153/overview.

[172] *IPPOG Masterclasses*, http://physicsmasterclasses.org.

[173] V. Morisbak, M. Pedersen, and F. Ould-Saada, *Oslo PLotting Tool, a web-based plotting tool for Z-path Masterclasses*, http://cernmasterclass.uio.no. University of Oslo.

[174] C. Kourkoumelis, C. Fassouliotis, S. Vourakis, and D. Vudragovic, *HYPATIA, Hybrid Pupil's Analysis Tool for Interactions in ATLAS*, http://hypatia.phys.uoa.gr. University of Athens and Institute of Physics Belgrade.

[175] *ATLAS Atlantis event-display*, http://www.hep.ucl.ac.uk/atlas/atlantis/.

[176] T. Herman, O. Jerabek, K. Jende, and M. Kobel, *Interactive ATLAS wedge*, http://atlas.physicsmasterclasses.org/en/wpath_teilchenid1.htm. Technical University Dresden.

[177] B. Gjelsten, D. Miller, and P. Osland, *Determining masses of supersymmetric particles*, arXiv:hep-ph/0511008 [hep-ph]. http://arxiv.org/abs/hep-ph/0511008v1.

[178] M. Pedersen and F. Ould-Saada, *Supersymmetry : A study of the supersymmetric opposite sign di-lepton channel*, Master's thesis, University of Oslo, 2008. http://urn.nb.no/URN:NBN:no-20534.

[179] *Summary of ATLAS searches for electroweak production of charginos and neutralinos*, Public online plots. https://atlas.web.cern.ch/Atlas/GROUPS/PHYSICS/CombinedSummaryPlots/SUSY/ATLAS_SUSY_EWSummary/history.html.

[180] S. McMahon, *Ratio Noise algorithm*, Mar, 2011. http://indico.cern.ch/event/74480/contribution/5/material/slides/1.pdf. SCT Monitoring Meeting, Restricted ATLAS Indico page.

[181] P. Conde-Muíño et al., *Portable Gathering System for Monitoring and Online Calibration at ATLAS*, tech. rep., CERN, Geneva, 2004. http://inspirehep.net/record/1197233.

[182] A. Dotti et al. IEEE Trans.Nucl.Sci. **53** (2006) .

[183] *Atlas Computing: technical design report*. CERN, Geneva, 2005. http://cds.cern.ch/record/837738?ln=en. See also: http://atlas-computing.web.cern.ch/atlas-computing/packages/athenaCore/athenaCore.php.

[184] P. Zema, *The Monitoring Data Archiving Service for ATLAS*, in *Nuclear Science Symposium Conference Record, 2006. IEEE*, vol. 1, pp. 12 –19. 29 2006-nov. 1, 2006.

[185] M. Hauschild et al., *Data Quality Monitoring Framework for the ATLAS experiment at LHC*, IEEE Trans.Nucl.Sci. **55** (2008) 417–420.

[186] *Electron and photon reconstruction and identification in ATLAS: expected performance at high energy and results at 900 GeV*, Tech. Rep. ATLAS-CONF-2010-005, CERN, Geneva, Jun, 2010. http://cds.cern.ch/record/1273197.

[187] ATLAS. Public results. https://twiki.cern.ch/twiki/bin/view/AtlasPublic/MuonPerformancePublicPlots#AnchorPlots2011.

[188] ATLAS Collaboration, *Improved electron reconstruction in ATLAS using the Gaussian Sum Filter-based model for bremsstrahlung*, Tech. Rep. ATLAS-CONF-2012-047, CERN, Geneva, May, 2012. https://cds.cern.ch/record/1449796.